

Organic Room-Temperature Phosphorescent and Thermally Activated Delayed Fluorescent Small Molecules: Efficiency Vs Processability for Lighting Application

by

Nidhankar Aakash Deepakrao
10CC17J26016

A thesis submitted to the
Academy of Scientific & Innovative Research
for the award of the degree of
DOCTOR OF PHILOSOPHY
in SCIENCE

Under the supervision of

Dr. Santhosh Babu Sukumaran



CSIR-National Chemical Laboratory, Pune

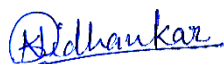


Academy of Scientific and Innovative Research
AcSIR Headquarters, CSIR-HRDC campus
Sector 19, Kamla Nehru Nagar,
Ghaziabad, U.P. – 201 002, India

September-2022

Certificate

This is to certify that the work incorporated in this Ph.D. thesis entitled, “Organic Room-Temperature Phosphorescent and Thermally Activated Delayed Fluorescent Small Molecules: Efficiency Vs Processability for Lighting Application”, submitted by Nidhankar Aakash Deepakrao to the Academy of Scientific and Innovative Research (AcSIR), in partial fulfilment of the requirements for the award of the Degree of Doctor of Philosophy in Science, embodies original research work carried-out by the student under my/our supervision/guidance. I/We, further certify that this work has not been submitted to any other University or Institution in part or full for the award of any degree or diploma. Research material(s) obtained from other source(s) and used in this research work has/have been duly acknowledged in the thesis. Image(s), illustration(s), figure(s), table(s) *etc.*, used in the thesis from other source(s), have also been duly cited and acknowledged.



Research Student

Mr. Nidhankar Aakash Deepakrao

Date: 08/09/2022



Research Supervisor

Dr. Santhosh Babu Sukumaran

Date: 08/09/2022

STATEMENTS OF ACADEMIC INTEGRITY

I, Nidhankar Aakash Deepakrao a Ph.D. student of the Academy of Scientific and Innovative Research (AcSIR) with Registration No. 10CC17J26016 hereby undertake that, the thesis entitled “Organic Room-Temperature Phosphorescent and Thermally Activated Delayed Fluorescent Small Molecules: Efficiency Vs Processability for Lighting Application” has been prepared by me and that the document reports original work carried out by me and is free of any plagiarism in compliance with the UGC Regulations on “Promotion of Academic Integrity and Prevention of Plagiarism in Higher Educational Institutions (2018)” and the CSIR Guidelines for “Ethics in Research and in Governance (2020)”.



Signature of the Student

Date: 08/09/2022

Place: CSIR-NCL, Pune

It is hereby certified that the work done by the student, under my supervision, is plagiarism-free in accordance with the UGC Regulations on “Promotion of Academic Integrity and Prevention of Plagiarism in Higher Educational Institutions (2018)” and the CSIR Guidelines for “Ethics in Research and in Governance (2020)”.

NA

Signature of the Co-Supervisor (If any)

Dr.

Date:

Place:



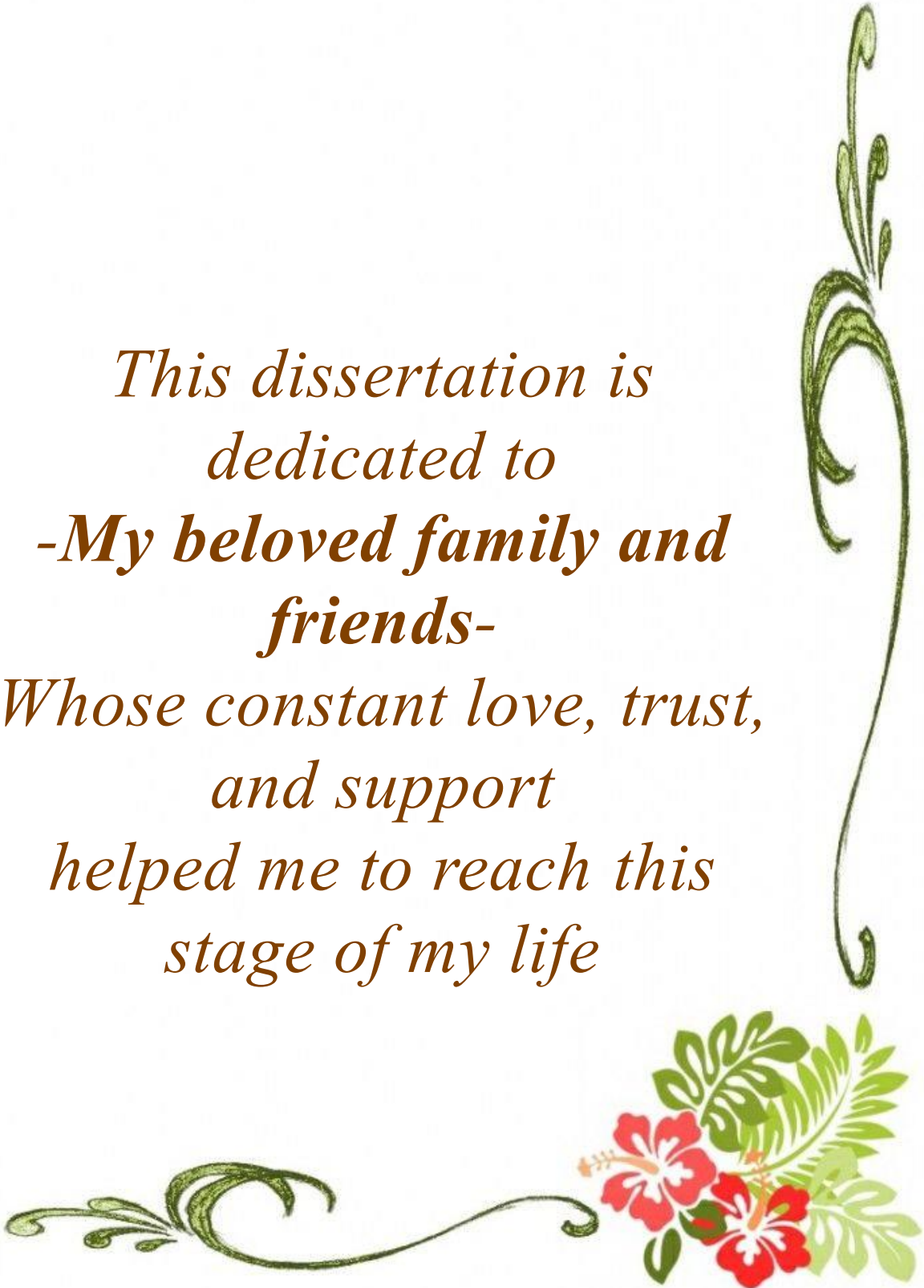
Signature of the Supervisor

Dr. Santhosh Babu Sukumaran

Date: 08/09/2022

Place: CSIR-NCL, Pune.

*This dissertation is
dedicated to
-My beloved family and
friends-
Whose constant love, trust,
and support
helped me to reach this
stage of my life*



ACKNOWLEDGMENT

Ph.D. is like a long journey; an experience that takes you through the untraversed path, the green lush meadows, and the island of Cyclopes to conquer the final goal fixed in mind. Once you achieve the target and turn back, you realize that all your efforts and the pain were worth going through. The small successes & the serendipitous discoveries, the frustrating failures & unexpected crystallizations, the imparted chemical wisdom & the laboratory camaraderie; they are all important parts of this beautiful voyage. But one can't succeed in this journey without the guidance and support of the research supervisor, labmates, friends, and well-wishers. I am taking this opportunity to express my deepest gratitude to everyone who has helped and supported me throughout my research journey.

*First and foremost, I would like to express my deep gratitude to my research supervisor, **Dr. Santhosh Babu Sukumaran**, Principal Scientist for allowing me to carry out this research work, whose expertise, understanding and patience added considerably to my doctoral degree experience. His sincerity and hard work have deeply inspired me. I greatly appreciate the freedom he gave me to find my path and the support he offered whenever I needed the most. I much appreciate the confidence he had in me, enabling me to grow as an independent researcher. With profound gratitude, I acknowledge:” Thank you, Sir.”*

*I wish to express my sincere thanks to the Doctoral Advisory Committee members, **Dr. K. Selvaraj**, **Dr. J. Nithyanandhan** and **Dr. K. Shanmuganadhan** for thesis contribution in stimulating suggestions and encouragement to co-ordinate my work.*

*I am grateful to **Prof. A. K. Nangia**, **Dr. Ashish Lele**, Director CSIR-NCL, **Dr. N. P. Argade** (Head, Organic Chemistry Division), **Dr. S. P. Chavan** (Former Head, Organic Chemistry Division), for giving me this opportunity and providing all necessary infrastructure and facilities to carry out my research work.*

I especially thank my seniors **Dr. Goudappagouda**, **Dr. Vivek Wakchaure** and **Dr. Ranjeesh K. C.**, for the continuous valuable suggestions, guidance for manuscript writing and support they offered whenever I needed the most.

Special thanks to my labmates who have helped me on various occasions, for providing a friendly, cooperative, lively working environment, helping nature and a kind attitude to share knowledge: **Sangram Dongre**, **Sairam Veer**, **Kiran Asokan**, **Viksit Kumar**, **Aswini Narayanan**, **Thanasekar C.**, **Geethu Venugopal**, **Bhagyasree**, **Abdulla** and **Dr. Rashmi Nayak** and many others who have worked alongside me.

I am extending my thanks to the master's student **Ms. Arya** whom I co-mentored for her master's project. Also, I thank the master's students **Asiya**, **Syno**, **Lekshmi**, **Amal T. Babu**, **Tajmon Tony**, **Nasif** and **Akhil** whom I helped with their master's projects.

My sincere thanks to my collaborators for their support and contributions, **Mr. S. K. Chaubey** and **Dr. Pavan Kumar** (IISER, Pune-Maharashtra) for their optical waveguide measurements, **Ms. Divya S. Mohana Kumari** and **Dr. K. Rethesh** (Gov. college for women, Thiruvananthapuram-Kerala) for their phosphorescence measurements, **Ms. Kavya Rajeev** and **Dr. K. N. Narayanan Unni** (NIIST Thiruvananthapuram-Kerala), **Mr. Premkumar Kothavade** and **Dr. K. Shanmuganathan** for their 3D printing applications, **Mr. Soumya Ranjan Dash** and **Dr. Rashmi Nayak** for their TD-DFT calculations and **Dr. Rajesh Gonnade** for solving the single-crystal structure.

I would like to thank **Dr. Ravindar Kontham** for giving me an opportunity to work in his group and for initial support in my research. Also, Sincere thanks to **Dr. Pramod Pillai** (IISER, Pune) for providing frequent access to the phosphorescence emission spectra measurements facility.

*I wish to convey my thanks to AcSIR coordinators **Dr. B. L. V. Prasad, Dr. Mahesh Kulkarni, Dr. M. Sasidhar, Dr. Santosh Mhaske** and student academic office staff, **P. K. Purushothaman, Poornima Kohle, Vaishali, Komal, Vijaya** and **Purnima** for their help and cooperation. I also thank **Mrs. Catherine** and the technical team of the Organic Chemistry Division, Glass Blowing department, and DIRC, for their continuous help and support.*

*I would like to extend my sincere thanks to **Dr. P. R. Rajamohanan, Dr. T. G. Ajithkumar** and **Dr. U. K. Marelli** for their timely help in NMR analysis, **Dr. Santhakumari** for the HRMS facility, **Mrs. Sanas** for HPLC facility, **Mrs. Damase** for IR facility, and **Mr. Sadafule** for LC-MS.*

*I would also like to acknowledge **Dr. Sunita Barve, Mr. Gati Krushna Nayak** and other staff members of the library for all kinds of support and for giving access to the library.*

*My sincere thanks to **Marathi@NCL** group for their support and to make my journey joyful and a memorable one.*

*Special thanks must go to my colleagues from NCL **Dr. Madhukar Said, Dr. Sagar Thorat, Dr. Rohini, Ashok, Balasaheb, Ashwini, Priyanka, Madhukar, Dr. Mahesh Shinde, Dr. Mahesh Pisal, Dr. Venkannababu Mullapudi, Dr. Ravindar Phatake, Dr. Rahul Jagtap, Mahendra Wagh, Dr. Poonam, Pramod, Shubhangi, Hemant, Dr. Digambar, Mahendra, Dr. Popat, Satish, Kishor, Sathish, Dinesh, Abha, Ashwini, Dr. Anupam Tripathi, Jagjivan, Sazia, Swapnil, Kailash, Dr. Abdul, Nirshad, Lakshmi, Himanshu, Kranti, Pooja, Lavanya, Someshwar, Manish, Pavan, Archana, Dharmendra, Rashid, Nilu, Priyanka, Sameer, Sachin, Dr. Amol, Kavita, Anurag, Priyanka, Pavan, Bhupendra, Christy, Ambarish, Bharat, Prashant, Rohit, Sachin, Yogesh, Prachi, A. K. Wale, Shrikant, Navnath, Pooja, Rakesh, Vinay, Ashish, and Dipesh.** I would also like to thank my friends, **Chidi, Manmath, Amol, Sangram, Aishwarya, Jagdish, Chandan, Sagar, Ashwini, Nitin, Vasudev, Ravi, and Swapnil.***

*My family is always a source of inspiration and great moral support for me in pursuing my education. I owe a lot to my beloved parents who encouraged and helped me at every stage of my personal and academic life and longed to see this achievement come true. At this moment, I invariably feel short of words to express my sincere thanks to my father **Mr. Deepak R. Nidhankar** and my beloved mother **Mrs. Meera D. Nidhankar** for their relentless hard work and sacrifice in bringing me up besides providing constant moral support and encouragement can hardly be acknowledged in few words. I express my deep and paramount gratitude to my brother **Mr. Dinesh** and **Mr. Sagar** for their support in critical situations and who stood behind me throughout my Ph.D. career and became my strong moral support. Also, I would like to thank **Vibha**, for her support and constant encouragement. I cherish you forever and thank you for being real. Thanks for being there for me today.*

In conclusion, this research would not have been possible without the financial support of the University Grants Commission (CSIR-UGC), New Delhi and the Academy of Scientific and Innovative Research (AcSIR).

I wish to thank the great scientific community whose achievements are a constant source of inspiration for me. Above all, I extend my gratitude to the Almighty God for giving me the wisdom, health, and strength to undertake this research work and enabling me to its completion.

Thank you all...!!!

Yours Sincerely

Aakash D. Nidhankar

Contents:

Abbreviations	15-17
Synopsis report	18-28

Chapter-1, Section 1 29-82

Introduction to Phosphorescence and Efficient Metal-free Organic Room Temperature Phosphors

1.1.1 Introduction	30
1.1.2 Jablonski Diagram	31-33
1.1.3 Ways to Improve the RTP Lifetime and Efficiency	34-38
1.1.3a Rate of Intersystem Crossing (k_{isc})	36
1.1.3b Energy Gap (ΔE_{ST})	36
1.1.3c Rate of Non-radiative Decay (k_{nr})	37
1.1.3d Rate of Radiative Decay (k_p)	37
1.1.3e Rate of Quenching (k_q)	38
1.1.3f Triplet Exciton Diffusion	38
1.1.4 Efficient Organic Phosphors	39-68
1.1.4.1 Single and Two Component Organic Phosphors	39
1.1.4.2 Host-Guest Based Organic Phosphors	53
1.1.4.3 Polymer-Based Organic Phosphors	60
1.1.4.4 Polymer Supported Organic Phosphors	65
1.1.5 Applications	69-73
1.1.6 Future Perspectives	74-75
1.1.7 Conclusions	76
1.1.8 References	76-82

Chapter-1, Section 2 83-121

Introduction to Thermally Activated Delayed Fluorescence Emitters for Lighting Applications

1.2.1 Introduction	84-86
1.2.2 Fundamental Principles for the Designing of TADF Emitters	87-88

1.2.2.1 Evidence for the Existence of Charge Transfer States	89
1.2.2.2 Molecular Design	90-91
1.2.3 Mechanism and Basic Understanding	92-98
1.2.3.1 Prompt Fluorescence Yield (Φ_{PF}) and Lifetime (τ_{PF})	94
1.2.3.2 Delayed-to-Prompt Fluorescence ratio, (Φ_{DF}/Φ_{PF})	94
1.2.3.3 Reverse Intersystem Crossing Rate Constant (k_{RISC})	95
1.2.3.4 Temperature Dependence of TADF	96
1.2.3.5 Dependence of TADF with Excitation Dose	97
1.2.4 Organic TADF emitters and their applications	99-113
1.2.4.1 Diphenyl sulfone Based TADF Emitters	99
1.2.4.2 Triazine-Based TADF Materials	103
1.2.4.3 Phosphine Oxide Derivatives for TADF materials	105
1.2.4.4 Cyano and Benzonitrile substituted TADF Emitters	106
1.2.4.5 Triarylborane based TADF Emitters	109
1.2.4.6 Benzoylpyridine and Di(pyridinyl)methanone-Carbazole Derivatives	110
1.2.4.7 Triazole derivatives	112
1.2.4.8 Triphenylamine derivatives based TADF materials	113
1.2.5 Future Perspective	116
1.2.6 Conclusion	117
1.2.7 References	118-121

Chapter-1, Section 3**122-133****Introduction to Room-Temperature Solvent-free Luminescent Organic Liquids (SLOLs)**

1.3.1 Introduction	123
1.3.2 Features of SLOL	123-131
1.3.3 Conclusion	132
1.3.4 References	132-133

Chapter-2**134-170****Self-assembled Helical Arrays for Stabilizing the Triplet State**

2.1 Introduction	135
------------------	-----

2.2 Experimental section	136-138
2.2.1 Details of DFT Calculations	136
2.2.2 Crystallization	137
2.2.3 Phosphorescence waveguiding	137
2.2.4 X-ray intensity data measurements	137
2.2.5 Phosphorescence experiments	138
2.3 Synthesis	139-144
2.3.1 Procedure for synthesis of 9H-carbazole	139
2.3.2 Procedure for synthesis of 9-hexyl-9H-carbazole	141
2.3.3 Procedure for synthesis of (9-Hexyl-9H-carbazol-3-yl)(phenyl)methanone	142
2.3.4 Synthesis of (9-hexyl-9H-carbazole-3,6-diyl)bis(phenylmethanone)	143
2.3.5 Synthesis of (9-hexyl-9H-carbazole-3,6-diyl)bis((4-bromophenyl)methanone)	144
2.4 Result and discussions	145-164
2.5 Conclusion	165
2.6 References	165-170

Chapter-3**171-210****Room-Temperature Phosphorescence from Metal-Free Organic Phosphors**

3.1 Introduction	173
3.2 Experimental section	174-175
3.2.1 Crystallization	174
3.2.2 X-ray intensity data measurements	175
3.2.3 Phosphorescence experiments	175
3.3 Synthesis	176-187
3.3.1 Procedure for synthesis of 9-propyl-9H-carbazole	176
3.3.2 Procedure for synthesis of 9-butyl-9H-carbazole	178
3.3.3 Procedure for synthesis of 9-pentyl-9H-carbazole	178
3.3.4 Procedure for synthesis of 9-heptyl-9H-carbazole	179
3.3.5 Procedure for synthesis of 9-octyl-9H-carbazole	179
3.3.6 Synthesis of (9-propyl-9H-carbazole-3,6-diyl)bis(phenylmethanone)	180
3.3.7 Synthesis of (9-butyl-9H-carbazole-3,6-diyl)bis	

(phenylmethanone)	181
3.3.8 Synthesis of (9-pentyl-9H-carbazole-3,6-diyl)bis (phenylmethanone)	181
3.3.9 Synthesis of (9-heptyl-9H-carbazole-3,6-diyl)bis (phenylmethanone)	182
3.3.10 Synthesis of (9-octyl-9H-carbazole-3,6-diyl)bis (phenylmethanone)	183
3.3.11 Synthesis of (9-hexyl-9H-carbazole-3,6-diyl)bis (p-tolylmethanone)	184
3.3.12 Synthesis of (9-hexyl-9H-carbazole-3,6-diyl) bis((4-chlorophenyl)methanone)	184
3.3.13 Procedure for Synthesis of 4,4'-(9-hexyl- 9H-carbazole-3,6-dicarbonyl)dibenzonitrile	185
3.3.14 Procedure for Synthesis of (S)-2-methylbutyl methanesulfonate	186
3.3.15 Procedure for Synthesis of (S)-9-(2-methylbutyl) -9H-carbazole	187
3.3.16 Procedure for Synthesis of (S)-(9-(2-methylbutyl) -9H-carbazole-3,6-diyl)bis(phenylmethanone)	187
3.4 Result and discussions	188-205
3.5 Conclusion	206
3.6 References	207-210

Chapter-4**211-266****Thermally Activated Delayed Fluorescent Solvent-free Organic Liquid
Hybrids for Tunable Emission Applications**

4.1 Introduction	212
4.2 Experimental section	213-217
4.2.1 RTP and TADF Experiments	213
4.2.2 Temperature-Dependent Emission and Lifetime Decay Measurements	214
4.2.3 Preparation of TADF Hybrids for Energy Transfer	214
4.2.4 Preparation of PLA/ SOL Filaments	214
4.2.5 Computational Methods	215
4.2.6 Fused Filament Fabrication (FFF) 3D Printing	

of PLA/SOL Filaments	216
4.2.7 Experimental Details of OLED device	217
4.3 Synthesis	218-227
4.3.1 Synthesis of 6-(4,4,5,5-tetramethyl-1,3,2-dioxaborolan-2-yl)-2-(tricosan-12-yl)-1H-benzo[de]isoquinoline-1,3(2H)-dione	220
4.3.2 Synthesis of 2-butyl-6-(4,4,5,5-tetramethyl-1,3,2-dioxaborolan-2-yl)-1H-benzo[de]isoquinoline-1,3(2H)-dione	221
4.3.3 Synthesis of 6-methoxy-2-(tricosan-12-yl)-1H-benzo[de]isoquinoline-1,3(2H)-dione	222
4.3.4 Synthesis of 6-(diethylamino)-2-(tricosan-12-yl)-1H-benzo[de]isoquinoline-1,3(2H)-dione	222
4.3.5 Synthesis of 6-(4-(dimethylamino)phenyl)-2-(tricosan-12-yl)-1H-benzo[de]isoquinoline-1,3(2H)-dione	223
4.3.6 Synthesis of (E)-6-(4-(bis(2-ethylhexyl)amino)styryl)-2-(tricosan-12-yl)-1H-benzo[de]isoquinoline-1,3(2H)-dione	224-226
4.3.7 Synthesis of 2,9-di(tricosan-12-yl)anthra[2,1,9-def:6,5,10-d'e'f']diisoquinoline-1,3,8,10(2H,9H)-tetraone	227
4.4 Results and Discussion	228-259
4.5 Conclusion	260
4.6 References	260-266

Chapter-5**267-300****Luminescent Solvent-free Organic Liquid Naphthalimides for lighting applications**

5.1 Introduction	268
5.2 Experimental section	269
5.2.1 RTP and TADF Experiments	269
5.2.2 Emission and Lifetime Decay at 77 K and 298 K Temperature Measurements	269
5.2.3 Preparation of Polymerizable Hybrid Liquids	269
5.2.4 Preparation and Purification of Polymer Films	273
5.3 Synthesis	270-274
5.3.1 Synthesis of 6-(10,11-dihydro-5H-dibenzo[b,f]azepin-5-yl)-2-(tricosan-12-yl)-1H-benzo[de]isoquinoline-1,3(2H)-dione (Az-NMI)	270

5.3.2 6-(3-chloro-10,11-dihydro-5H-dibenzo[b,f]azepin-5-yl)-2-(tricosan-12-yl)-1H-benzo[de]isoquinoline-1,3(2H)-dione	271
5.3.3 Synthesis of 6-((1H-benzo[d][1,2,3]triazol-1-yl)oxy)-2-(tricosan-12-yl)-1H-benzo[de]isoquinoline-1,3(2H)-dione	272
5.3.4 Synthesis of 6-(4-(dimethylamino)phenyl)-2-(tricosan-12-yl)-1H-benzo[de]isoquinoline-1,3(2H)-dione	273
5.3.5 Synthesis of 6-(diallylamino)-2-(tricosan-12-yl)-1H-benzo[de]isoquinoline-1,3(2H)-dione	274
5.4 Result and discussions	275-292
5.5 Conclusion	293
5.6 References	293-296
Characterization details of the synthesized compounds	297-358
Abstract	359
List of Publications and Patents	360
List of National / International Conferences	361
List of Oral and Poster Presentations	362
Awards & honours	362
Publications	363

Abbreviations

A		DMSO- <i>d</i> ₆	Deuterated dimethyl sulfoxide
<i>α</i>	Alpha	DFT	Density functional theory
Å	Angström	D	Donor (charge)
a.u.	arbitrary unit	DMF	Dimethylformamide
A	Acceptor (charge)	<i>θ</i>	Dihedral angle
ACN	Acetonitrile	DF	Delayed fluorescence
AIE	Aggregation induced emission	E	
ACQ	Aggregation-caused quenching	ESI	Electron spray ionization
B		eV	electron-volt
<i>β</i>	Beta	EQE	External quantum efficiency
C		ET	Energy Transfer
CIE	International Commission on Illumination	DMSO- <i>d</i> ₆	Deuterated dimethyl sulfoxide
calcd	Calculated	F	
CDCl ₃	chloroform-d	FTIR	Fourier transform infrared
°C	degree Celcius	FRET	Förster resonance energy transfer
CT	Charge transfer	FWHM	Full-width half maximum
CCDC	Cambridge crystallographic data center	G	
CL	Cross-linker	<i>T_g</i>	Glass transition temperature
CD	Circular dichroism	<i>γ</i>	Gamma
CPL	Circularly polarised luminescence	G	Gauss
CH ₂ Cl ₂	Dichloromethane (DCM)	gm	Gram
D		<i>g_{lum}</i>	Dissymmetry factor
<i>d</i>	doublet (NMR)	H	
DMSO	Dimethyl sulfoxide	h	Hour
DSC	Differential scanning calorimetry	Hz	Hertz
<i>δ</i>	Delta chemical shift (NMR)	HFC	Hyperfine-coupling

HPLC	High-performance liquid chromatography	OLED	Organic light-emitting diode
I		OM	Optical Microscope
		OPVs	Oligo(p-phenylvinylene)s
ISC	Intersystem crossing	P	
IC	Internal conversion	ppm	Parts per million
IPA	Isophthalic acid	PMMA	Poly(methyl methacrylate)
ICT	Intermolecular charge transfer	PVA	Polyvinyl alcohol
IQE	Internal quantum efficiency	PLA	Poly(Lactic acid)
K		PL	Photoluminescence
K	Kelvin	PF	Prompt fluorescence
L		POCl ₃	Phosphorous oxytrichloride
LUMO	Lowest unoccupied molecular orbital	Q	
λ	Lambda Wavelength	QY	Quantum yield
M		R	
mp	Melting point	RT	Room temperature
MS	Mass spectrometry	RB	Round bottom (flask)
T_m	Melting temperature	RTP	Room temperature phosphorescence
MALDI	Matrix-assisted laser	rISC	Reverse intersystem crossing
-TOF	desorption ionization-time of flight mass spectrometry	Ref.	Reference
MA	Melamine		
MTHF	2-methyl tetrahydrofuran	S	
N		s	singlet (NMR)
NIR	Near-Infrared	SC	Single crystal
n-BuLi	n-butyl lithium	SEM	Scanning electron microscopy
NMI	Napthalenemonoimide	SOC	Spin-orbit coupling
nm	Nanometer	SOL	Solvent-free organic liquids
NMR	Nuclear magnetic resonance	SLOL	Solvent-free luminous organic liquids
O			

T

t	triplet (NMR)
TEM	Transmission electron microscopy
THF	Tetrahydrofuran
TCSPC	Time correlated single photon counting
TADF	Thermally activated delayed fluorescence
TGA	Thermogravimetric analysis
TTA	Triplet-triplet annihilation
TBAB	Tetrabutylammonium bromide

U

UV-Vis	Ultraviolet-visible spectroscopy
UOP	Ultralong organic phosphorescence

V


V	Volt
Vis	Visible

W

W	Watt
w%	Weight percentage
WG	Waveguiding

X

XRD	X-ray diffraction
-----	-------------------

	Synopsis of the thesis to be submitted to the Academy of Scientific and Innovative Research for the award of the degree of Doctor of Philosophy in Sciences/ Engineering
Name of the Candidate	Mr. Nidhankar Aakash Deepakrao
Enrollment No. and Date	Ph. D. in Chemical Sciences (10CC17J26016); January 2017
Title of the Thesis	“Organic Room-Temperature Phosphorescent and Thermally Activated Delayed Fluorescent Small Molecules: Efficiency Vs Processability for Lighting Application”
Research Supervisor	Dr. Santhosh Babu Sukumaran (CSIR-NCL, Pune)

1. **Introduction**: The current thesis describes Organic Room-Temperature Phosphorescent and Thermally Activated Delayed Fluorescent Small Molecules and their efficiency, processability for lighting applications. This entitled thesis is categorized into four working chapters. Initially we describes the general introduction about Room Temperature Phosphorescence (RTP) and Thermally Activated Delayed Fluorescence (TADF). Organic molecules exhibiting Room Temperature Phosphorescence (RTP) and Thermally Activated Delayed Fluorescence (TADF) that efficiently harvest triplet excitons and convert to light have emerged as promising light-emitting materials. The advantages of both intersystem crossing (ISC) in RTP and reverse intersystem crossing (rISC) in TADF materials heavily supported achieving an internal quantum efficiency of 100%. RTP and TADF organic molecules have attracted scientific interest due to their wide applications in bio-imaging, organic optoelectronics, anti-counterfeiting, sensing, flexible display and lighting devices etc. The second chapter deals with Self-assembled Helical Arrays for Stabilizing the Triplet State, the third chapter deals with Room-Temperature Phosphorescence from Metal-Free Organic Phosphors, the fourth chapter deals with Thermally Activated

Delayed Fluorescent Solvent-free Organic Liquid Hybrids for Tunable Emission Applications, and the fifth chapter deals with the Processable Luminescent Solvent-free Organic Liquid Naphthalimides for Lighting Applications.

2. Statement of a problem: For the past many decades, heavy metal complexes were explored as phosphors because of the presence of ligand-metal and metal-ligand charge transfer (CT) and strong spin-orbit coupling, which improves the intersystem crossing (ISC) and controls the triplet decay rate. Despite many advantages, organometallic complexes have the drawbacks of high toxicity, limited resources, and high cost. Hence this situation promoted the search for metal-free organic molecules as alternative phosphors. However, for organic materials, the non-radiative (k_{nr}) and quenching (k_q) rates of the triplet states are much larger than the radiative decay rate (k_p) under ambient conditions. Moreover, the triplet states are vulnerable to quenching by molecular oxygen, and hence RTP and TADF from metal-free organic molecules under ambient conditions continue to be challenging. In this context, set our approach to develop concisely, practically and synthetically benign organic molecules which are technologically advanced for lighting and display applications with improved processability and luminescence features.

3. Objectives:

Inspired by interesting applications of organic molecules containing RTP and TADF properties, we aimed to develop concise, practically and synthetically benign organic molecules which are technologically advanced for lighting and display applications with improved processability and luminescence features. We explore the variation of alkyl chain and chirality induced room temperature phosphorescence from phenylmethanone unit containing carbazole-based organic phosphors and its photophysical studies assisted by alkyl chain and molecular packing in the crystal-state and we came up with a new strategy of helical array

to support long-lived phosphorescence under ambient conditions. Further, we have explored thermally activated delayed fluorescent solvent-free organic liquid naphthalimides and analysed the TADF emission with various dopants to demonstrate the tunable emission and show a practical demonstration of 3D printing applications and polymerized luminescent thin films for lighting applications.

4. Methodology and results:

Chapter 2: Self-assembled Helical Arrays for Stabilizing the Triplet State

Room-temperature phosphorescence of metal and heavy atom-free organic molecules has emerged as an area of great potential in recent years. A rational design played a critical role in controlling the molecular ordering to impart efficient intersystem crossing and stabilize the triplet state to achieve room-temperature ultralong phosphorescence. However, in most cases, the strategies to strengthen phosphorescence efficiency have resulted in a reduced lifetime, and the available nearly degenerate singlet-triplet energy levels impart a natural competition between delayed fluorescence and phosphorescence, with the former one having the advantage. Herein, an organic helical assembly supports the exhibition of an ultralong phosphorescence lifetime. In contrary to other molecules, 3,6-phenylmethanone functionalized 9-hexylcarbazole exhibits a remarkable improvement in phosphorescence lifetime (> 4.1 s) and quantum yield (11%) owing to an efficient molecular packing in the crystal state. A right-handed helical molecular array act as a trap and exhibits triplet exciton migration to support the exceptionally longer phosphorescence lifetime.

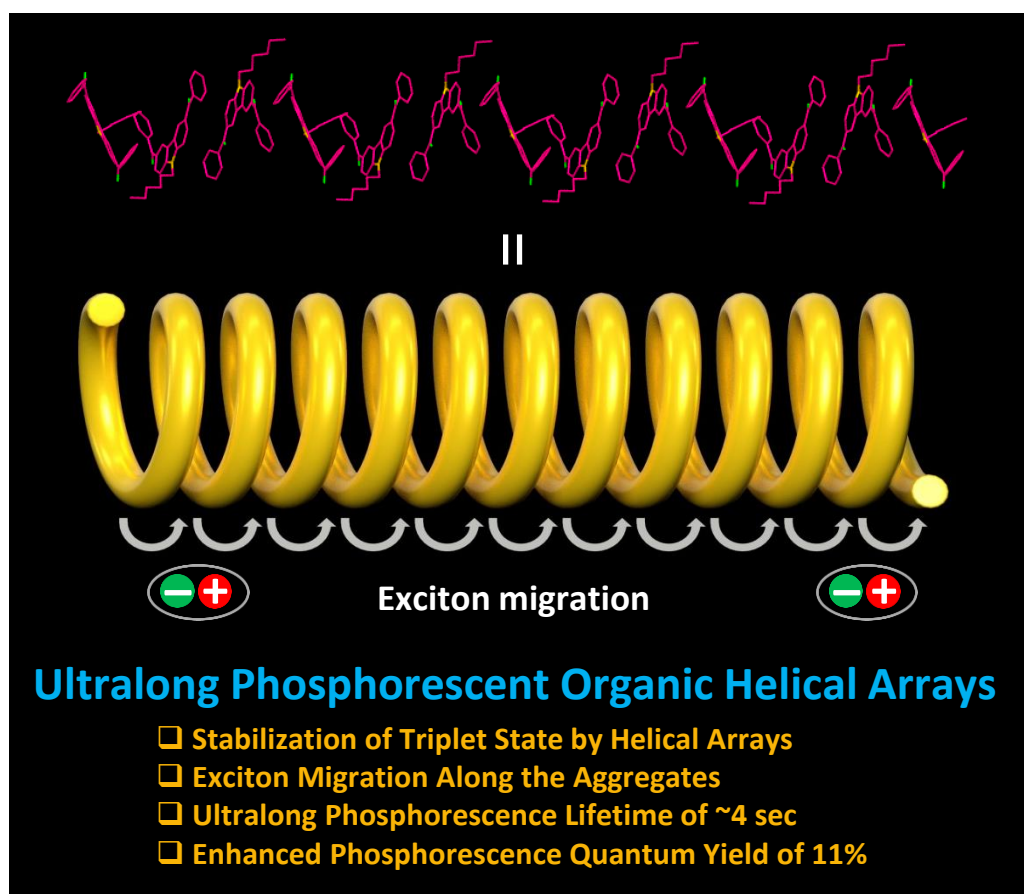


Figure 1. 3,6-bis(phenylmethanone) substituted 9-hexylcarbazole-based self-assembled helical arrays for the stabilization of the triplet state.

Chapter 3: Room-Temperature Phosphorescence from Metal-Free Organic Phosphors

In continuation with chapter 2, in this chapter we have describes the variation of alkyl chain and chirality induced room temperature phosphorescence from phenylmethanone unit containing carbazole-based organic phosphors and its photophysical studies assisted by alkyl chain and its molecular packing in the crystal-state. We planned to study not only the effect of aliphatic alkyl chain as well as keeping the chiral alkyl chain onto 3,6-bis(phenylmethanone) substituted carbazole molecules but also by changing the substitution on phenylmethanone unit functionalization, which exhibits RTP property with good lifetime. No such

Helical molecular packing was observed in other substituted carbazole molecules and from a single crystal study, we concluded that Only the C-6 alkyl chain played a crucial role for Helical packing of 3,6-bis(phenylmethanone) substituted 9-hexylcarbazole in the crystal lattice.

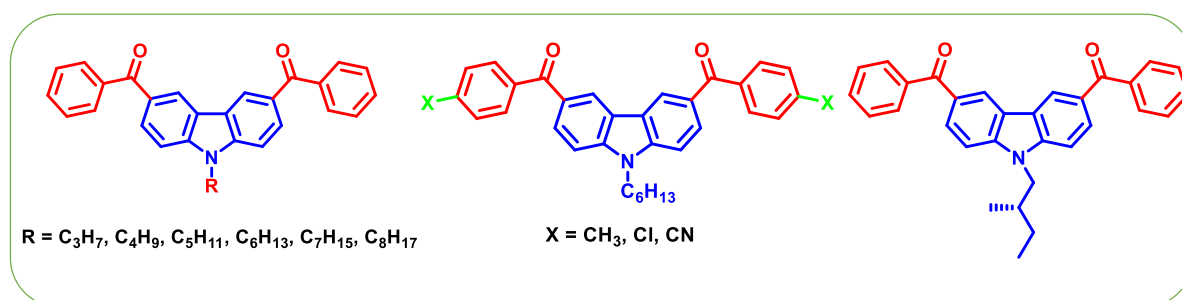


Figure 6. Chemical structures of metal-free organic phosphors 3,6-bis(phenylmethanone) substituted carbazole molecules.

Chapter 4: Thermally Activated Delayed Fluorescent Solvent-free Organic Liquid Hybrids for Tunable Emission Applications

The synthetic feasibility and excellent luminescence features of organic molecules attracted much attention and were eventually found useful in lighting applications. In this context, a solvent-free organic liquid having attractive thermally activated delayed fluorescence features in bulk along with high processability has prime importance. Herein, we report a series of naphthalene monoimide-based solvent-free organic liquids exhibiting blue to red thermally activated delayed fluorescence with luminescence quantum yields up to 80% and lifetimes between 8 to 45 μ s. An effective approach explored energy transfer between liquid donors with various emitters exhibiting tunable emission colours, including white. The high processability of liquid emitters improved the compatibility with polylactic acid and was used for developing multicolour emissive objects using 3D printing. Besides, the first example of a thermally

activated delayed fluorescent liquid as an emitter in OLED with moderate performance is promising. Our demonstration will be much appreciated as a processable alternate emissive material suitable for large-area lighting, display, and related applications.

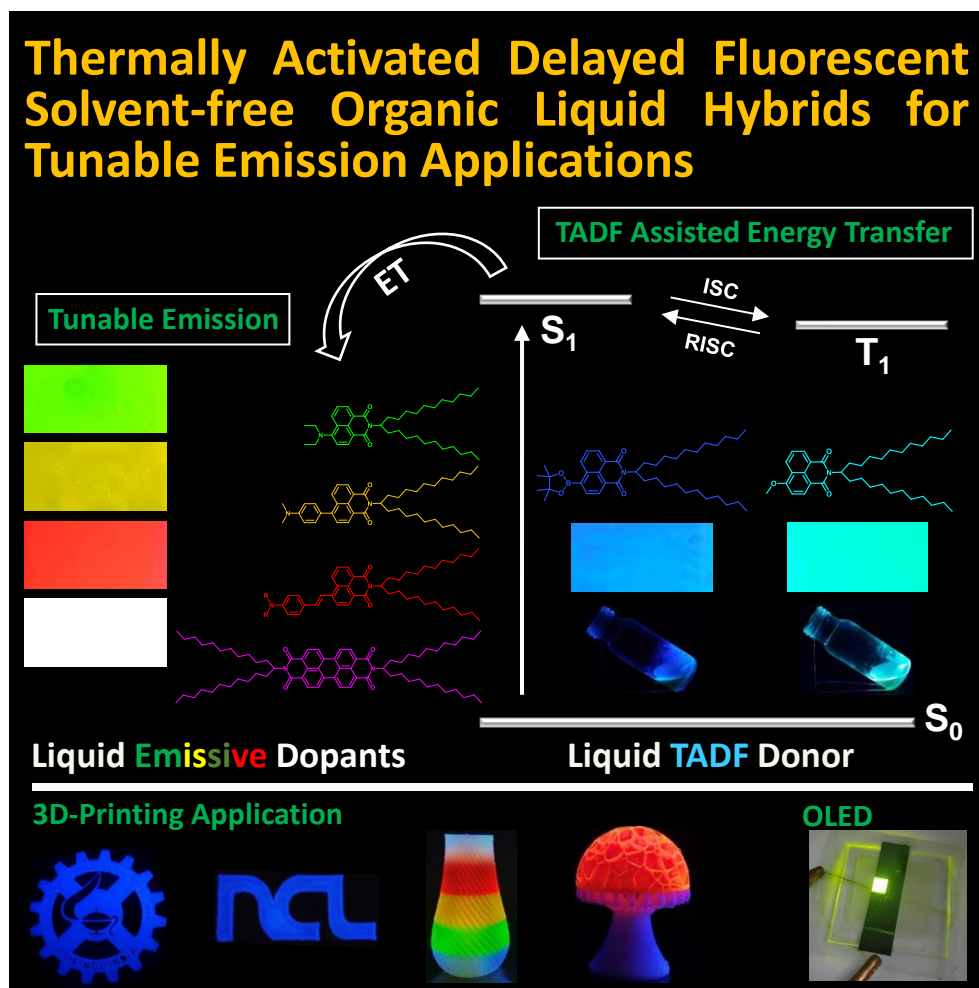


Figure. Schematic of the TADF-assisted energy transfer for tunable emission and 3D printing applications.

Chapter 5: Processable Luminescent Solvent-free Organic Liquid Naphthalimides for Lighting Applications

The synthetic feasibility and excellent luminescence features of organic molecules attracted much attention and were eventually found useful in lighting

applications. In this context, a solvent-free organic liquid having attractive thermally activated delayed fluorescence features in bulk along with high processability has prime importance. similar to the previous chapter, herein, we report a series of naphthalene monoimide-based solvent-free organic liquids exhibiting thermally activated delayed fluorescence with high luminescence quantum yields and lifetimes between 11.5 to 78.6 μ s. In the previous chapter, we describe the advantages of solvent-free organic liquids and their processability with applications. Solvent-free liquids have more advantages over solvated systems. They are good in Tunable optoelectronic properties, Non-volatility and Usable in bulk, Processability and easily printable or paintable. Still, they are having some disadvantages like Stickiness of the layer surface while using and having least curability of the final films. So new approach that can overcome all these issues is highly desirable. A non-volatile, low-viscosity and highly emissive room-temperature liquid photopolymerizable luminescent organic liquid material is a promising candidate for lighting applications. In this context, we planned to synthesize the solvent-free organic liquid Naphthalimides for TADF property and photopolymerizable luminescent organic liquid to show practical demonstration of polymerized luminescent thin films for lighting applications.

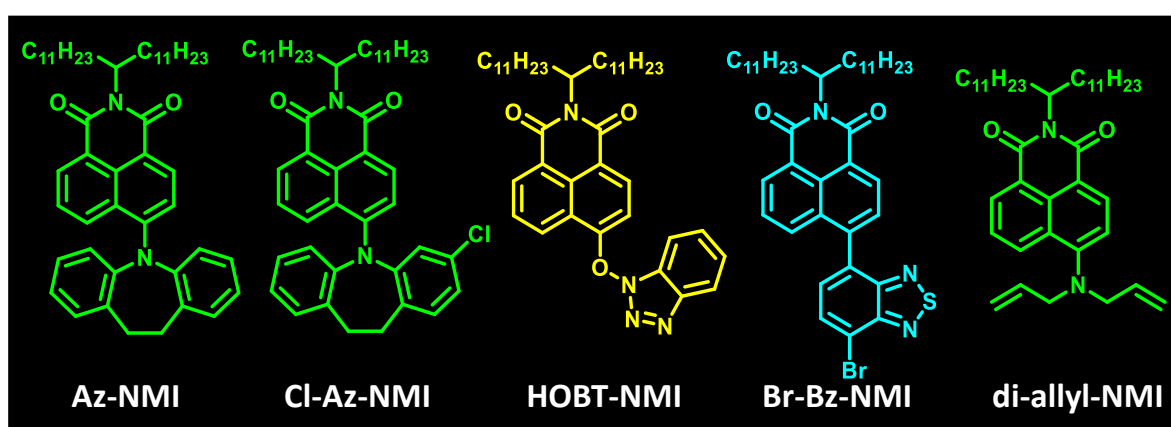


Figure. Chemical structures of processable luminescent solvent-free organic liquid naphthalimides for lighting applications.

5. Conclusion:

The thesis comprises new synthetic methodologies for metal-free organic room temperature phosphorescent, thermally activated delayed fluorescent and solvent-free organic liquids molecules for lighting applications. In chapter 2, we have reported a new series of phenylmethanone functionalized N-alkylated carbazoles exhibiting UOP. A helical array by the peculiar molecular packing of 3,6- bis(phenylmethanone) substituted 9-hexylcarbazole in the crystal state enabled to mix up the singlet-triplet states to create hybrid triplets to enhance the intersystem crossings. By optimizing the molecular structure and a strained crystal packing, a metal- and heavy atom-free carbazole derivative resulted in a significant improvement of phosphorescence lifetime and quantum yield. A combined experimental and theoretical study sheds light on the stabilization of the triplet state by the helical arrays and the presence of triplet exciton migration results in the longer phosphorescence lifetime, so far reported for a single molecule crystal. The findings put forth a new strategy of helical arrays to support long-lived phosphorescence under ambient conditions and will invoke the development of new organic phosphors.

Chapter 3, demonstrates the series of phenylmethanone compounds by attaching different alkyl chains. After carefully understanding the photophysical studies, we come to conclude that all are exhibiting RTP properties. Single-Crystal structures help to find the molecular packing involved in the molecules. Only the C-6 alkyl chain playing a crucial role for helical packing of 3,6-bis(phenylmethanone) substituted 9-hexylcarbazole in the crystal lattice. No such helical molecular packing was observed in other substituted carbazole molecules.

In chapter 4, the successful demonstration of the TADF liquid accomplished a series of molecules having varying TADF emission colors through structural modification. The host-guest combination of TADF liquid emitters exhibited ET-assisted tunable emission. A cascade ET between the TADF liquids demonstrated

white light-emitting hybrid liquids. The attractive features such as the capability to form a large-area thin luminescent film and tunable emission by doping enable TADF liquids to be a potential candidate in lighting and display applications. Interestingly, the high QY and uniform dispersibility of SOLs supported the very low loading of the emitters (1wt%) to deliver 3D printed objects with multicolor light emission. The detailed photophysical studies indicate that neither the same SOLs in solution nor the crystalline structural analogs exhibit TADF, and it points to the importance of molecular design in developing the hitherto unknown TADF liquids. The high processability of TADF liquids to form large-area thin films without compromising the emission features offer a bright future for TADF SOLs.

In chapter 5, the successful demonstration of the TADF liquid accomplished a series of molecules having TADF through structural modification. The solvent-free TADF liquid exhibit cyan to yellow colour emission with a delayed lifetime of up to **79** μs . Furthermore, a polymerizable group on one of the solvent-free TADF liquid utilize for thermal and photo-polymerization. **Di-allyl-NMI** liquid provides a low viscous fluid matrix for cross-linker (**CL**) by simple physical mixing to develop polymerizable blends. The hybrid liquid films enabled to development of stable polymer films on the surface by photo as well as thermal polymerization. Even though we are able to prepare polymer film, our efforts will be continued to make free-standing stable polymer film. The high processability of TADF liquids to form large-area thin films without compromising the emission features offer a bright future for TADF SOLs and is a potential candidate in lighting and display applications.

6. Future directions:

In chapter 2, we show that 3,6-phenylmethanone functionalized 9-hexylcarbazole exhibits a remarkable improvement in phosphorescence lifetime (> 4.1 s) and quantum yield (11%) owing to an efficient molecular packing in the

crystal state. We came up with a new mechanism strategy for the stabilization of triplet excitons. Helical arrays of organic small molecules and polymers exhibit exciting optoelectronic properties by controlling the spatial organization of the structural units. Hence, the design of a helical assembly to modulate the triplet state to achieve a longer phosphorescence lifetime will be highly appreciated. The findings put forth a new strategy of helical arrays to support long-lived phosphorescence under ambient conditions and will invoke the development of new organic phosphors. It can be achieved only through unexplored molecular designs and with the rigorous assistance of molecular packing.

We believe that our solvent-free organic liquid strategies (Chapter-4) and the developed enhanced luminescent materials (Chapter-5) would find an enormously wide range of applications in fluorescent sensors, bioimaging, optoelectronics large-scale flat panel displays, and soft optical device applications. The high processability of solvent-free organic liquids TADF emitters improved the compatibility with polylactic acid and was used for developing multicolour emissive objects using 3D printing. Our demonstration of the thermally activated delayed fluorescence liquid will be much appreciated as a processable alternate emissive material suitable for large area lighting, display, and related applications. The study related to the direct application in various fields of these luminescent materials would be undertaken further in our laboratory. In the future, we plan to utilize our solvent-free organic liquid strategy to prepare large-scale and highly emissive room-temperature photopolymerizable luminescent organic liquid materials.

References:

1. **A. D. Nidhankar**, Goudappagouda, V. C. Wakchaure and S. S. Babu, Efficient Metal-free Organic Room Temperature Phosphors, *Chem. Sci.* **2021**, *12*, 4216-4236.

2. **A. D. Nidhankar**, Goudappagouda, D. S. M. Kumari, S. K. Chaubey, R. Nayak, R. G. Gonnade, G. V. P. Kumar, R. Krishnan and S. S. Babu, Self-assembled Helical Arrays for Stabilizing the Triplet State, *Angew. Chem. Int. Ed.* **2020**, *59*, 13079-13085. **Hot Paper**
3. **A. D. Nidhankar**, and S. S. Babu, Room-Temperature Phosphorescence from Metal-Free Organic Phosphors, *Manuscript under preparation*.
4. **A. D. Nidhankar**, Goudappagouda, P. Yadav, S. D. Dongre, S. D. Veer, S. R. Dash, K. Rajeev, K. N. N. Unni, K. Shanmuganathan and S. S. Babu, Thermally Activated Delayed Fluorescent Solvent-free Organic Liquid Hybrids for Tunable Emission Applications, *Manuscript communicated (under revision)*.
5. **A. D. Nidhankar**, and S. S. Babu, Processable Luminescent Solvent-free Organic Liquid Naphthalimides for Lighting Applications, *Manuscript under preparation*.



Signature of the Supervisor



Signature of the Candidate

Chapter 1: Section 1

Introduction to Phosphorescence and Efficient Metal-free Organic Room Temperature Phosphors

1.1.1 Introduction

The term “Luminescence” was introduced by Eilhardt Wiedemann in 1888 as the Emission of light by a substance. It occurs when an electron returns from an excited to ground level, leaving the energy as a phonon. Luminescence is classified mainly into three types- 1) fluorescence, 2) phosphorescence, and 3) thermally activated delayed fluorescence (TADF) which depends on the type of the excited state. The first class of luminescence is fluorescence, in which deexcitation is from singlet excited states to singlet ground states. In this process, there is no change in spin orientation, and hence fluorescence is spin allowed process. Conventionally, rates of fluorescence emission are 10^8 s^{-1} , so the average lifetime range of fluorescence is 10^{-9} to 10^{-6} sec. Phosphorescence is the process of emitting light from triplet excited states to the ground state. In this process, change in the spin occurs from the triplet state to the ground state, which is a forbidden transition, and hence the emission rate is slow in the range of 10^{-3} to 10 sec. Therefore phosphorescence lifetimes of organic molecules range from milliseconds to seconds. The third type of luminescence is TADF, which is light emission from singlet excited states through reverse intersystem crossing (RISC) from the triplet excited state. During the TADF process, the triplet state of the molecules undergoes thermally activated RISC and is further de-excited to the ground state.

The application of fluorescence, phosphorescence, and TADF materials in organic optoelectronics and biological sciences has increased dramatically during the last two decades. Our daily life encircles around the constant use of electronic devices such as computers, laptops, television, mobile phones, and many more devices. Mostly these devices are built on inorganic semiconductors. Still, due to the technological difficulties concerned with silicon, a significant amount of effort has been invested in developing organic electronics.¹ Recently, organic electronics have emerged as an active field of research promising efficient large-area lighting emitting material and light-harvesting devices.

1.1.1. Jablonski Diagram

The Jablonski diagram is often used to depict the processes between light absorption and emission. For explaining absorption and emission, Jablonski diagrams are used as a starting point. Jablonski diagram displays the variety of molecular processes which occurs in excited states. Professor Alexander Jablonski is known as the "Father of Fluorescence Spectroscopy" for his numerous achievements, including descriptions of concentration depolarization and the definition of the terminology "anisotropy" to describe the polarised emission from solutions. The Jablonski diagram depicts a molecule's electronic states and transitions between them. The states are arranged horizontally by spin multiplicity and vertically by energy. Transitions between radiation and non-radiation are denoted by straight arrows. Each electronic state's higher vibrational levels and vibrational ground states are denoted by thick lines.²

Figure 1.1.1 depicts a typical Jablonski diagram, S_0 represents the singlet ground state, and S_1 - S_3 represents the first and higher electronic states, respectively. To demonstrate the instantaneous nature of light absorption, transitions between states are depicted as vertical lines. Following are the processes that occur during light absorption. When the fluorophore is excited to a higher vibrational level, such as S_2 or S_3 , molecules quickly relax to S_1 , the lowest vibrational level. This process is known as internal conversion and usually takes 10^{-11} seconds or less. When the S_1 states of molecules can undergo spin inversion to the first triplet state, T_1 , this process is known as intersystem crossing. Phosphorescence is the emission of light from the T_1 state to the singlet (S_0) ground state, and it is usually at longer wavelengths (lower energy) than fluorescence. Since the transitions from T_1 to S_0 state are prohibited, the rate constants for triplet emission are lower than fluorescence. The incorporation of heavy atoms, i.e., bromine and iodine, and heteroatoms such as O, N, S, and Te, mainly enables to display phosphorescence. The heavy atoms promote the rate of

intersystem crossing through spin-orbit coupling, thereby increasing phosphorescence lifetime and quantum yields.²

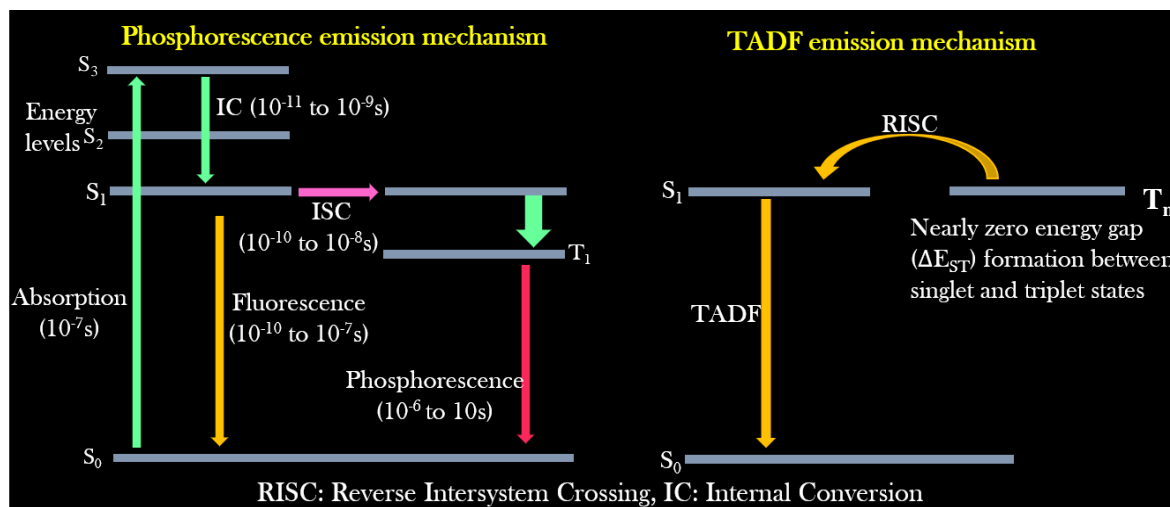


Figure 1.1.1. Schematic energy level diagram (Jablonski diagram) of three types of luminescent organic molecules.

Organic room temperature phosphorescence (ORTP) has attracted scientific interest because of the large Stokes shift, long lifetime, and strong afterglow that enable applications in bio-imaging, organic optoelectronics, anti-counterfeiting, sensing, etc.^{24,25,33,34} For the past many decades, heavy metal complexes have been explored as phosphors because of the presence of ligand-metal and metal-ligand charge transfer (CT) and intense spin-orbit coupling (SOC), which increases the rate of intersystem crossing (ISC) and controls the triplet decay rate.²⁷ Despite many advantages, organometallic complexes have the disadvantages like high toxicity, limited resources, and high cost. Hence this situation promoted the search for metal-free organic molecules as alternative phosphors. However, for organic materials, the non-radiative (k_{nr}) and quenching (k_q) rates of the triplet states are much larger than the radiative decay rate (k_p) under ambient conditions. Moreover, the triplet states are vulnerable to quenching by molecular oxygen, and hence RTP from metal-free organic molecules under ambient conditions continues to be challenging.¹ Nonetheless, the recent past has witnessed a massive jump in the exploration of metal-free organic phosphors

through innovative molecular designs and control over the radiative and nonradiative decay processes associated with triplet excitons. The critical parameters that are being considered while designing organic RTP (ORTP) molecules include (1) populating the triplet state by efficient singlet-to-triplet ISC, (2) minimizing the nonradiative relaxation pathways, and (3) delaying the radiative decay. In accordance with that, heteroatoms such as N, O, S, Te, and halogens are incorporated as an integral part of the molecular design of organic phosphors.^{4–27}

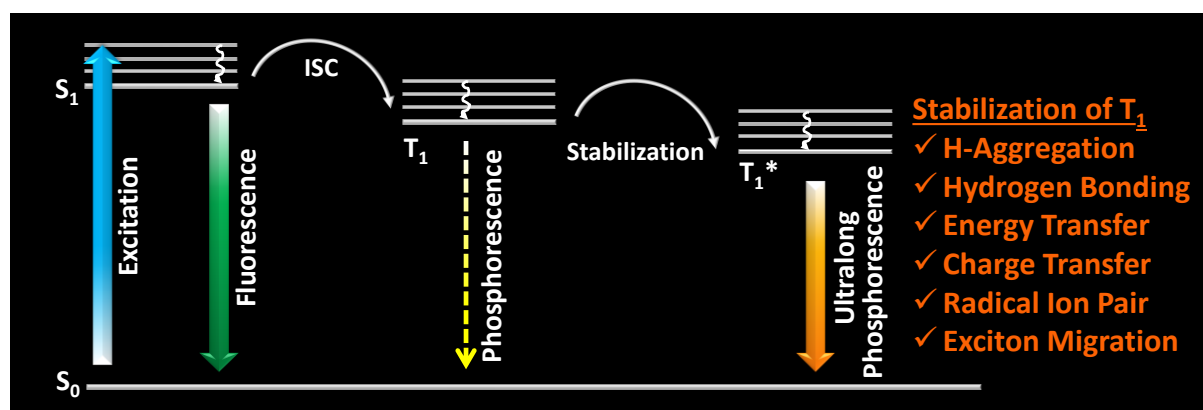


Figure 1.1.2. Schematic of stabilization of the triplet state, leading to ultralong phosphorescence in organic molecules.

Besides, nonradiative relaxation pathways are controlled by molecular packing in the crystalline state and with the help of supportive media such as polymers and cavitands. The compact molecular packing with the assistance of various intermolecular interactions, provided extra stabilization of the triplet excitons to extend the lifetimes beyond seconds. In this way, a synergistic effect of all the supportive features resulted in enhanced RTP of metal-free organic phosphors.^{5–9} Besides, stabilization of the triplet excitons is found to be a conceptually new and exciting strategy to achieve newer heights for RTPs (Figure. 1.1.2).²⁰ Many new concepts such as suppression of the nonradiative deactivation pathways of the triplet state through hydrogen bonding, H-aggregation, helical arrays, and excited-state manipulations such as charge transfer (CT), energy transfer (ET), radical ion pair formation, energy migration,

etc. have been introduced to stabilize the triplet state.^{20,21} Until now, many attempts to understand the relationship between ultralong RTP (URTP) and molecular packing have been reported.⁸⁻¹⁰ Those studies uncovered the vital role of ordered molecular arrays in tailoring lifetime,¹⁴⁻¹⁶ emission efficiency,¹⁸ luminescent colour,¹⁹ and even realizing the unique dynamic URTP features. Even though the structure-property correlation of organic phosphors has been achieved to a certain extent, the involvement of complex factors limits a complete understanding of the underlying mechanism of URTP. Hence a deeper understanding of the supportive role of adequate molecular packing, rigidification by polymers and hosts, and related controlling factors is of great significance. Even though URTP is a fascinating concept, a slow radiative decay leading to a long-lived lifetime is not supportive for any device applications, especially in light-emitting diodes (LEDs).^{31,32} However, compared to short-lived fluorescent materials, the advantages of an ultralong lifetime and large Stokes shifts make URTP materials promising candidates for applications such as bio-imaging, information storage, data encryption, anti-counterfeiting, sensing, and photodynamic therapy.^{24,25,33,34} Besides, the most critical aspect of URTP is that the triplet state excitons are susceptible to deactivation by molecular motions, oxygen, and humidity.^{1,3,35} Hence, it has been highly challenging to prolong the phosphorescent emission of organic materials at room temperature by overcoming all these hurdles. In this context, URTP of small molecule-based metal-free ORTPs has prime importance as a fundamental challenge. Numerous design strategies and self-assembly methods have been found successful in achieving an ultralong lifetime.

1.1.3 Ways to Improve the RTP Lifetime and Efficiency

The main challenges in metal-free organic room temperature phosphors (ORTPs) include weak spin-orbit coupling (SOC) ($< 0.1 \text{ cm}^{-1}$), resulting in inefficient ISC, enhanced k_{nr} due to many deactivation pathways, the

susceptibility of T₁ state to oxygen and temperature.^{3,30} Hence to design efficient ORTPs and estimate the performance, the following discussion can be helpful. The important parameters such as quantum efficiency of ISC (ϕ_{isc}) (from S₁ to T₁), quantum yield (ϕ_p), lifetime (τ_p) and radiative decay (k_p) of phosphorescence can be defines as

$$\begin{aligned}\phi_{isc} &= k_{isc}/(k_f + k_{ic} + k_{isc}) && \dots\dots 1 \\ \phi_p &= \phi_{isc}k_p\tau_p && \dots\dots 2 \\ \tau_p &= 1 / k_p + k_{nr} && \dots\dots 3 \\ k_p &= (64\pi^4/3h^4c^2)\Delta E^3_{T1\rightarrow S0} |\mu_{T1\rightarrow S0}|^2 && \dots\dots 4\end{aligned}$$

Where k denotes the rates of singlet emission processes such as k_f , k_{ic} and k_{isc} related to the fluorescence (from S₁ to S₀) and internal conversion (IC) (from S_n to S₁) and ISC (from S₁ to T₁), respectively. At the same time, the rates related to the triplet state are denoted as k_p and k_{nr} for radiative and non-radiative decays (from T₁ to S₀), respectively. It has to be noted that all these rate parameters related to singlet and triplet transitions completely control the characteristic phosphorescence features of pure ORTPs. A more in-depth analysis of equations 1-3 reveals that an enhanced k_{isc} , a reduced k_{nr} , and a slow k_p are highly essential for improved RTP lifetime. Another critical parameter not discussed much is the triplet quenching rate k_q and which can be minimized by rigidification of the phosphor using a host or polymer support.^{20,28,29} Besides, equations 1-3 indicate that conditions such as enhanced ϕ_{isc} and $k_p > k_{nr}$ is required to improve ϕ_p . However, to achieve a long τ_p a reduction of both k_p and k_{nr} is needed. Hence the impact of k_p is ultimate in deciding high ϕ_p and long τ_p . Equation 4 shows that an increment in the singlet-triplet energy gap $\Delta E_{T1\rightarrow S0}$ will accelerate the k_p and eventually reduce the k_{nr} . The above two conditions related to k_p are contradictory when looking for a long lifetime and a high efficiency. Hence, the simultaneous enhancement of both ϕ_p and τ_p is challenging. The below sessions describe the various parameters controlling the RTP features.

1.1.3a. Rate of Intersystem Crossing (k_{isc})

There have been several attempts to obtain an enhanced k_{isc} necessary for efficient RTP, such as effective SOC and small singlet-triplet energy gap (ΔE_{ST}).³¹⁻³³ In this direction, the major directive for a high k_{isc} through effective SOC has come from the El-Sayed's rule, which expresses that effective orbital overlapping is possible in a singlet to triplet transition with different molecular-orbital configurations.¹ In other words, compared to the transition from $^1(n,\pi^*)$ to $^3(n,\pi^*)$ or from $^1(\pi,\pi^*)$ to $^3(\pi,\pi^*)$, effective ISC can be observed in transitions from $^1(n,\pi^*)$ to $^3(\pi,\pi^*)$ or from $^1(\pi,\pi^*)$ to $^3(n,\pi^*)$ states. Many recent successful designs showed that the presence of n orbitals perpendicular to π orbitals is favourable to help a strong SOC and thereby encourage the ISC from singlet to triplet excited states.^{12,14} Hence the presence of hybrid (n,π^*) and (π,π^*) transitions are supportive for URTP. An enhanced k_{isc} through efficient SOC significantly contributed to achieving high ϕ_p ; however, along τ_p heavily depends on the stabilization of triplet excitons through multiple pathways.

1.1.3b. Energy Gap (ΔE_{ST})

One of the reasons for the inefficient RTP in organic molecules is the large singlet-triplet energy gap ΔE_{ST} due to inadequate molecular design. It has been noticed that k_{isc} can be significantly promoted by small ΔE_{ST} , which depends on the spatial overlap of HOMO and LUMO wavefunctions. In this direction, a charge transfer (CT) interaction between the donor and acceptor building units of a phosphor can be influential because the CT interaction can control the spatial overlap. A CT state can be introduced either by bridging donor-acceptor groups or through the assistance of intermolecular interactions between donor, acceptor molecules. Such examples for enhanced RTP through small ΔE_{ST} are driven by CT state³³ and through aggregation-controlled management of ΔE_{ST} ³⁴ are available in the literature. The formation of various aggregates can dictate the ΔE_{ST} value and thereby influence ISC for RTP.

1.1.3c. Rate of Non-radiative Decay (k_{nr})

The current era of organic phosphors and the sudden developments are indebted to crystallization to a greater extent. The crystallization of phosphors using intermolecular interactions such as π - π stacking, van der Waals, halogen and hydrogen bonding suppresses the non-radiative decay pathways to facilitate RTP.³⁵ Besides, host-guest assemblies, immobilization of phosphors in frameworks, and polymers also supported the phosphors from non-radiative decays. In this case, the most celebrated “H-Aggregation” was found effective in stabilizing the triplet excitons to achieve long-lived RTP.³⁶ As per equations 2 and 3, a variation in k_{nr} also significantly alters the values of both ϕ_p and τ_p . Hence the design strategies should consider the incorporation of corresponding functional moieties to impart various noncovalent interactions to regulate k_{nr} . Another vital strategy adopted to reduce k_{nr} through the reduction of the reorganization energy is deuteration, which blocks the molecular vibrations.³⁷ The high $\Delta E_{T1 \rightarrow S0}$ value was also found effective in suppressing the non-radiative decay.¹⁻³

1.1.3d. Rate of Radiative Decay (k_p)

Equation 4 shows that k_p is complicated and mainly determined by many factors involving both the singlet and triplet states, such as SOC between singlet and triplet states, transition dipole moment $\mu_{T1 \rightarrow S0}$, and energy gap $\Delta E_{T1 \rightarrow S0}$. A high $\Delta E_{T1 \rightarrow S0}$ accelerates k_p to facilitate RTP with a reduced lifetime and is the same as the transition dipole moment.¹⁻³ It has been found that in ORTPs showing excellent features, an exceptional stabilization of the triplet excitons through various supports delays the radiative decay. In such systems, k_p is suppressed to achieve a long lifetime over 1 s. A slow k_p , in turn, enhances τ_p to realize URTP, whereas it inversely affects ϕ_p .

1.1.3e. Rate of Quenching (k_q)

Along with other factors controlling the efficiency of RTP, the suppression of k_q is also equally important. Even though recent studies employ crystalline assemblies and the support of polymers, hosts, and porous structures to avoid the effect of moisture and oxygen, the quenching rate of the triplet excitons is also crucial to deliver excellent RTP features under ambient conditions. It has been noticed that k_{nr} will be relatively low in such host supported systems, and hence the deactivation patterns of the triplet excitons require more attention. The current studies on efficient ORTPs lack a deeper understanding of the effect of k_q , assuming that stabilization through self-assembly or other supports will manage k_q .²⁰

1.1.3f. Triplet Exciton Diffusion

Recent studies have shown the importance of triplet exciton diffusion length on persistent RTP.³⁸ It has been suggested that short-range triplet exciton diffusion can suppress k_q by stopping the excitons from reaching the trap sites. The importance of exciton diffusion length is more dominant in the case of crystalline arrays with more traps. However, a very recent demonstration indicated that the efficient triplet exciton diffusion with the assistance of helical arrays of phosphor played an essential role in delaying the triplet radiative decay to extend lifetime beyond 4 s.³⁹ Hence the quality of the generated crystals or thin films and efficient management of triplet excitons can impart excellent RTP features. More studies in this direction are required for detailed understanding and further development. In addition, hyperfine-coupling (HFC) driven intersystem crossing in CT complexes and radical ion pair (RIP),⁴⁰ singlet fission⁴¹ etc. were also found effective in controlling the RTP features.

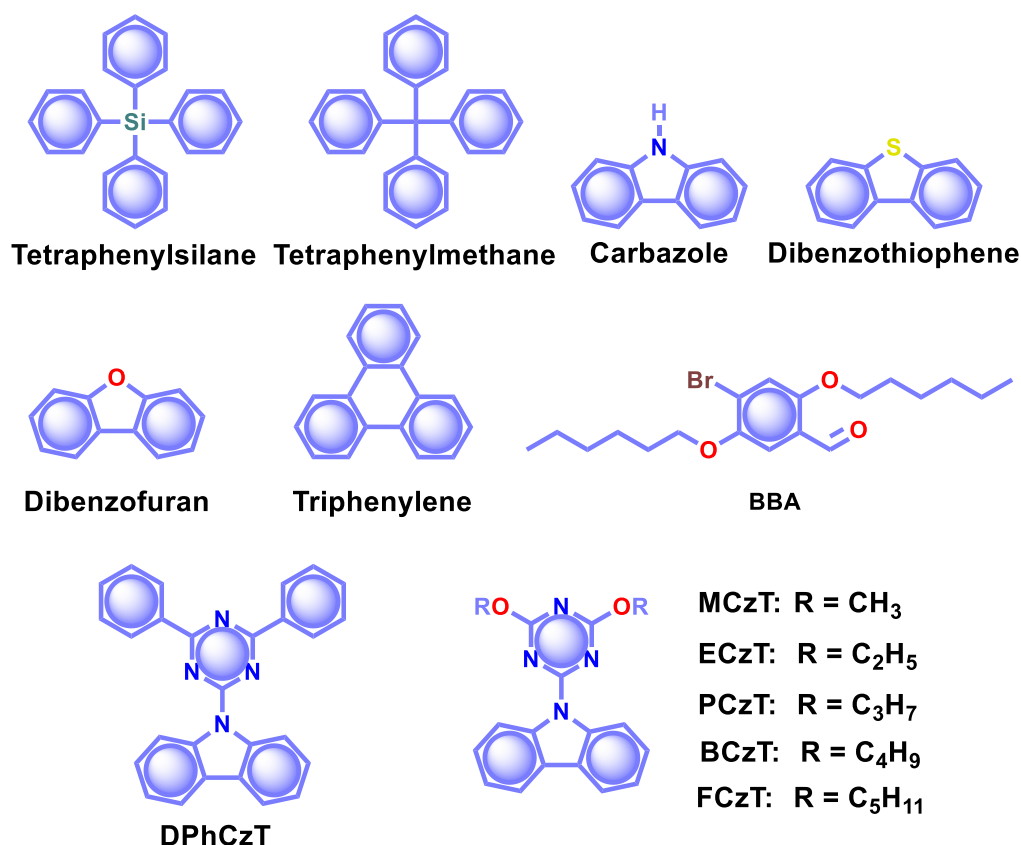
The above sections describe the possible ways to improve the ORTP feature to achieve enhanced RTP features. The implemented molecular design strategies have been found successful to a certain extent and thus delivered some

exceptional RTP candidates exhibiting a lifetime longer than 1 s. In this way, we attempt to reveal the special effects in molecular design and ground state arrangements for metal-free organic phosphors to exhibit prodigious RTP qualities. The recent advancement in lifetime, quantum yield, and afterglow properties of these unusual candidates promoted metal-free ORTPs as a capable material in many functional applications. We would like to mention that the dedicated efforts of various research groups across the globe made significant contributions in this area to gain an admirable position for ORTPs in the current research.¹⁻²⁶

1.1.4. Efficient Organic Phosphors

1.1.4.1. Single and Two Component Organic Phosphors

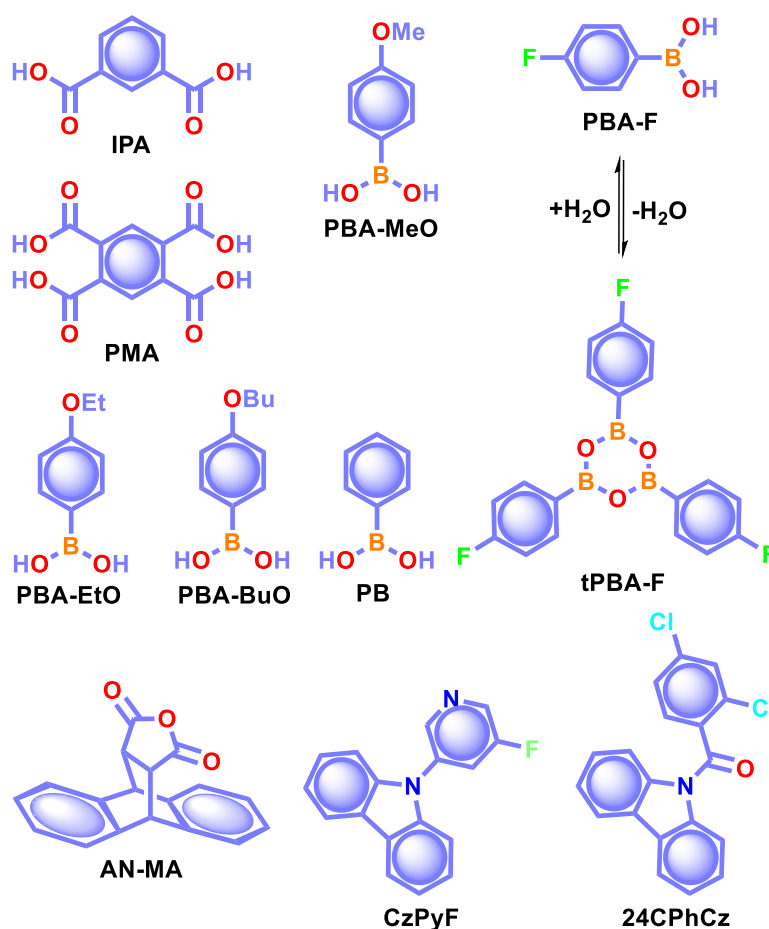
Recently, significant developments have occurred in single-component crystalline assemblies that exhibit a long phosphorescence lifetime with good quantum yields.⁴² In general, RTP of such single-component assemblies is enhanced by crystallization mainly because 1. availability of specific intermolecular interaction in the crystal state to improve ISC through SOC 2. intact molecular packing suppresses the molecular motions and eventually helps to minimize k_{nr} of triplet excitons, 3. crystalline assemblies will protect from triplet quenching by oxygen. The recent exciting development of URTPs is strongly supported by molecular organization in the crystal state, which stabilizes the excited triplet state by trapping triplet excitons and controls both radiative and non-radiative decays.



Scheme 1.1.1. Chemical structure of phosphors **Tetraphenylsilane**, **Tetraphenylmethane**, **Carbazole**, **Dibenzothiophene**, **Dibenzofuran**, **Triphenylene**, **BBA**, **DPhCzT**, **MCzT**, **ECzTPCzT**, **BCzT**, and **FCzT**.

The early report on phosphorescence appeared in 1939 by Clapp and coworkers on **Tetraphenylsilane** and **Tetraphenylmethane** (Scheme 1) crystals with a duration of up to 23 s by bare eyes.⁴³ Later in 1978, Bilen and coworkers studied the afterglow of **Carbazole**, **Dibenzothiophene**, **Dibenzofuran**, **Triphenylene** (Scheme 1.1.1) etc., having a lifetime up to 4.85 s in the crystal state.⁴⁴ Even though many attempts of RTP and afterglow were noticed in the early days, a drastic development happened in the last decade due to the technological advancements in materials chemistry. For example, RTP of 2,5-dihexyloxy-4-bromobenzaldehyde **BBA** (Scheme 1.1.1) was reported by Kim and coworkers in 2011. This molecule shows weak fluorescent emission in solution; however, it exhibits a green phosphorescence emission at 500 nm with

a lifetime of 5.4 ms in the crystal state.⁴⁵ Single-crystal XRD analysis revealed that the phosphorescence property of this small molecule is due to the presence of close contact between the bromine and the carbonyl oxygen of the neighbouring molecule ($C=O \cdots Br-C$, 2.86 Å). RTP retains a lifetime longer than 100 ms, with an afterglow approaching seconds after cessation of excitation. This study was one of the finest reports, which attracted the attention of organic phosphors and hence resulted in a visible change in the area.



Scheme 1.1.2. Chemical structure of benzoic acids **IPA**, **PMA**, boron-containing phosphors **PBA-MeO**, **PBA-EtO**, **PBA-BuO**, **PBA-F**, **tPBA-F**, **PB** and **AN-MA**, **CzPy** and **24CPhCz**.

In 2012, Chen, Liu, Huang, and co-workers synthesized a series of organic molecules of carbazole and triazine having N, O, and P atoms (Scheme 1.1.1).³⁶ Notably, the presence of hetero atoms facilitates the spin-forbidden transition of

singlet-to-triplet excited states through $n-\pi^*$ transitions to populate triplet excitons. In this series, 9-(4,6-diphenyl-1,3,5-triazin-2-yl)-9H-carbazole **DPhCzT** and 9-(4,6-diethoxy-1,3,5-triazin-2-yl)-9H-carbazole **ECzT** (Scheme 1.1.1) exhibited efficient τ_p up to 1.35 s and 1.05 s, respectively. The enhanced ISC in these molecules is because of an increase in the number of energy transitions, which are supported by the H-aggregated dimers formed by **DPhCzT** and **ECzT** in the single crystals. The strong coupling *via* $\pi-\pi^*$ stacking in H-aggregate dimers with wide transition dipole moment provides stabilization and thus protects the triplet excitons. The stabilized triplet excited state (T_1^*) acts as an energy trap at a lower energy level, offering a suppression of radiative and non-radiative deactivation rates in favour of long-lived excited states and UOP.

As a continuation, by varying the alkyl chain length on the triazine unit, the same group achieved photoactivation assisted smart URTP materials.⁴⁶ Among the molecules, the lifetime of **BCzT** (Scheme 1.1.1) drastically increased from 1.8 to 1.33 s upon photoirradiation for 10 min. The prolonged irradiation of molecules with UV light suppresses k_{nr} by controlling the molecular motion to enhance both RTP emission intensity and lifetime. After photo-activation, a significant difference in intermolecular interactions between adjacent molecules was observed. As the alkoxy chain increased, the phosphorescence lifetime of both photoactivation and deactivation for URTP decreased dramatically from **MCzT** to **FCzT**. This study points to the importance of photo-irradiation assisted control of non-radiative transition in ORTPs.

In 2015, Yuasa and his team explained the nuclear spin magnetism-assisted spin-exchange of a radical ion pair (RIP).⁴⁰ In this study, the afterglow property of benzoic acid derivatives such as isophthalic acid **IPA** and pyromellitic acid **PMA** (Scheme 1.1.2) was observed by the naked eye for several seconds. Phosphorescence measurements of **IPA** and **PMA** reveal the presence of emission bands at 532 and 533 nm with 0.970 and 1.1 s lifetime, respectively.

The photoexcitation of these carboxylic acid derivatives leads to the generation of singlet and further triplet RIPs through hyperfine-coupling (HFC) induced spin conversion, mediated through the magnetic field of neighbouring ^1H nuclear spins. Here deuterium labeling of carboxylic acid derivatives suppressed the phosphorescence intensity, confirming the HFC mechanism and a nuclear spin magnetism-assisted spin conversion (^1RIP - ^3RIP) for URTP. In another report, the phosphorescence lifetime of **IPA** in the crystal state is reported as 1.11 s and points to the presence of only one type of hydrogen bonding interaction in **IPA** that stabilizes the carboxylic acid dimers.⁴⁷

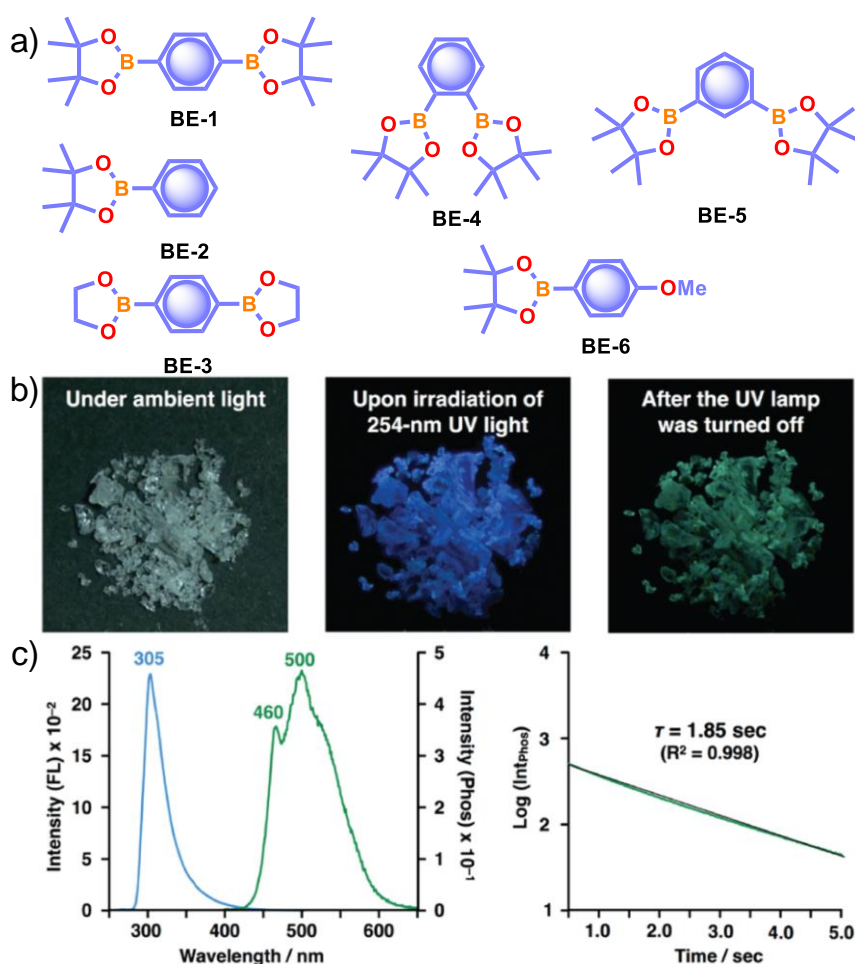


Figure 1.1.3. a) Chemical structure of arylboronic esters **BE-1-5**. b) Photographs of **BE1** under ambient light (left), irradiation with 254 nm UV light in the dark (middle), and after the UV light was turned off in the dark (right). c) Fluorescence and phosphorescence spectra (left) and corresponding phosphorescence decay

profile of **BE-1** (right). *Reproduced with permission from ref. 48. Copyright 2017, American Chemical Society.*

It is well known that the boron-containing compounds are sensitive to its intramolecular motions and collisions with quenching species. Recently, many aryl boronic acids and esters with stable and extended RTP features have been reported. As one of the first reports, Nakai, Fukushima and coworkers reported long-lived RTP of a series of arylboronic esters **BE1-5** (Figure. 1.1.3a).⁴⁸ **BE1** displayed RTP in the solid-state with a green afterglow lasted for several seconds (Figure. 1.1.3b, c). In this series **BE1-5**, the value of τ_p varied as 1.85, 1.79, 1.65, 1.73, 1.57, 1.39 s, respectively (Figure. 1.1.3c). Comparing experimental and theoretical studies revealed that an out-of-plane distortion is introduced on (pinacol) B-C_{ipso} moiety in the T₁* state. This sustained distortion enables the mixing of π and σ orbitals to enhance SOC and thereby lead to RTP with an ultralong lifetime. Later, Li and co-workers studied RTP of many commercially available phenylboronic acids and their thermally prepared triphenylborazine derivatives.³⁵ The phosphorescence spectrum of 4-methoxyphenyl boronic acid (**PBA-MeO**) (Scheme 1.1.2) shows two emission bands at 457 and 488 nm with τ_p of 2.24 and 2.19 s, respectively. The long lifetime is due to rigid conformation and strong hydrogen bonding, which decrease k_{nr} . Even an effective π - π stacking stabilizing the triplet excitons also contributes to achieving bright and prolonged RTP. The importance of π - π stacking interactions was further analyzed by theoretical calculations of dimers and indicated that strong π - π stacking decreases the ΔE_{ST} , thereby favouring ISC. By changing the length of the alkyl chains, authors studied RTP and found that **PBA-EtO** and **PBA-BuO** also showed RTP with τ_p of 1.11 s and 1.28 s, respectively. In this series of boronic acids, the support of hydrogen bonding through C-H...F interactions enabled **PBA-F** and thermally prepared triphenylborazine **tPBA-F** derivative (Scheme 1.1.2) also to show a long lifetime of 1.34 and 1.96 s, respectively.

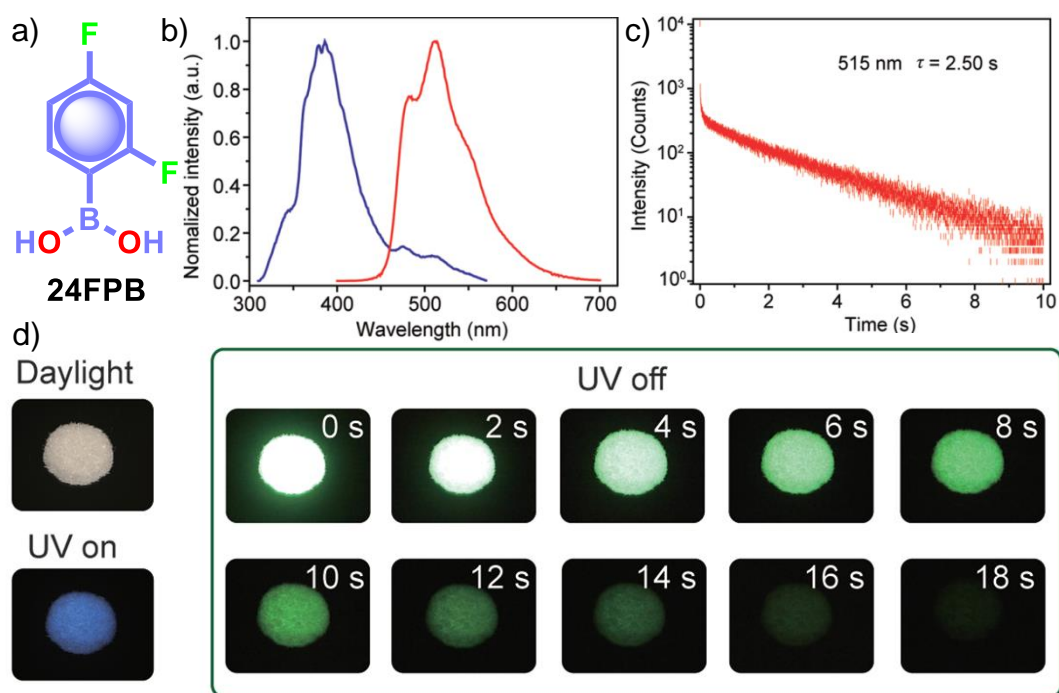


Figure 1.1.4. a) Chemical structure of **24FPB** and b) steady-state photoluminescence (blue line) and phosphorescence (red line) spectra of **24FPB**. c) Phosphorescence decay profile of the emission band at 515 nm. d) Photographs of **24FPB** crystal taken at different time intervals before and after removing the excitation of a 365 nm UV lamp. *Reproduced with permission from ref. 50. Copyright 2019, WILEY-VCH.*

In the same year, HFC driven ISC in CT complexes was reported by Yuasa and coworkers by taking phenylboronic acid derivatives (**PBs**) such as phenylmono-boronic acid **PB** (Scheme 2) and *p*-phenylenediboronic acid ethyleneglycol ester **BE-3** (Figure. 1.1.3a) as examples.⁴⁹ The phosphorescence intensities of **PBs** mainly depend on the magnetic-field and spin-isotope effects, which are controlled by HFC. Interestingly, **PB** showed RT afterglow for several seconds with τ_p of 1.2 s. Further, the authors investigated the effect of steric bulkiness on phosphorescence by taking **BE-3** as an example, which showed a pale blue afterglow property for about 12 s with τ_p of 1.6 s. The luminescence quantum yield of **PB** and **BE-1** was found to be 18 and 77%, respectively. The phosphorescence mechanism was summarized to follow the transitions: $S_0 \rightarrow {}^1CT$

→ $^3\text{CT} \rightarrow \text{T}_1 \rightarrow \text{S}_0$, indicating the direct involvement of both singlet and triplet CT states. Further, studies on the effect of halogen on RTP of **PBs** showed that among the series, only 2-(4-fluorophenyl)-1,3,2-dioxaborolane **PBA-F** exhibited a high τ_p of 1.7 s. In this line, Huang and his group worked on enhancing τ_p by introducing multiple fluorine atoms on the phenylboronic acid **24FPB** (Figure. 1.1.4a,b).⁵⁰ The maximum lifetime of 2.50 s was exhibited by 2,4-difluorophenylboronic acid **24FPB** crystals (Figure. 1.1.4c). The prolonged lifetime is because of the stabilization of the triplet excited state by H-aggregation and intramolecular O-H...F hydrogen bonding (2.22 Å) in the crystal. The hydrogen bonding in crystals fixed the dihedral angle (θ) between the benzene ring and the boronic acid group and thus resulted in rotation confinement leading to a longer lifetime. Interestingly, a persistent green luminescence for **24FPB** was observed for more than 20 s after the UV irradiation was turned off (Figure. 1.1.4d).

Yuan and co-workers reported a long lifetime for the cycloaddition product **AN-MA** of anthracene and maleic anhydride (Scheme 1.1.2).⁵¹ Out of the two polymorphs form A and form B, afterglow emission of form B lasted for several seconds with τ_p of 1.6 s and ϕ_p of 8%, because of its much stronger intramolecular π - π interactions. The presence of carbonyl group and oxygen atoms with lone pairs, together with the effective intra- and intermolecular interactions, help to achieve bright green RTP emission. The relatively low k_{nr} value resulting from the more rigid conformations significantly contributed towards the long lifetime. To understand the effect of a heavy atom to obtain longer RTP, Sasabe, Kido and co-workers studied the RTP features of a series of 3-pyridylcarbazole derivatives with H, F, Cl, Br, and I as substituents on the pyridine ring.⁵² The crystals of the fluorine-substituted derivative **CzPyF** (Scheme 1.1.2) show an ultralong τ_p of 1.1 s and ϕ_p of 1.2%. By comparing theoretical and experimental data shows that the n orbital on the central pyridine ring enhances the intersystem crossing between

$^1\text{CT}^*$ and $^3\text{LE}^*$ states. Single crystal studies indicated that fluorine atoms and pyridine ring contribute to an increase in RTP because of the hydrogen-bonding interactions between $\text{C-H}\cdots\text{N}$ and $\text{H}\cdots\text{F}$. The presence of a halogen atom with larger electronegativity enabled long RTP. Similarly, in 2019, Shi, An, Huang, and co-workers provided a detailed study related to the critical role of molecular stacking in generating efficient triplet excitons by using a series of carbazole derivatives having chlorine substitution at different positions.⁵³ A combined experimental and calculated results revealed that **24CPhCz** (Scheme 1.1.2) with robust intermolecular coupling between carbazoles exhibited long τ_p of 1.06 s and ϕ_p of 2.5%. Studying the crystal structure of **24CPhCz** showed that the existence of intermolecular interactions played the main role in enhancing the lifetime. The molecules were rigidly restricted by abundant interactions, including $\text{CCl}\cdots\pi$, $\text{C=O}\cdots\text{Cl}$, $\text{CCl}\cdots\text{H-C}$, $\text{Cl}\cdots\text{Cl}$, and $\text{C-H}\cdots\pi$. The restricted non-radiative transitions through molecular packing in the crystal state prolong the lifetime. However, a very weak interchromophoric coupling between carbazoles resulted in weak phosphorescence for the other derivatives in the series.

Tunable emission organic phosphors are rare and are difficult to achieve in a single component phosphor. A tunable phosphorescence under different excitation wavelengths was reported by Gu *et al.*, utilizing the available multiple emitting centers in a single-component phosphor (Figure. 1.1.5a).⁵⁴ A triazine derivative, 2-chloro-4,6-dimethoxy-1,3,5-triazine **DMOT** (Figure. 1.1.5a, b), contains various hetero atoms that improve the k_{isc} to boost triplet excitons. The planar structure of the molecule strongly supports H-aggregation through multiple intermolecular interactions such as $\text{N}\cdots\text{C}$, $\text{CH}\cdots\text{C}$, and π - π interactions with the surrounding six molecules (Figure. 1.1.5a). Besides, H-aggregation assisted restricted molecular motion in the crystal ensures excellent phosphorescence features with τ_p of 2.45 s and ϕ_p of 31.2% (Figure. 1.1.5b-d). Interestingly, upon changing the excitation wavelength from 250 to 400 nm, the

emission colour of **DMOT** was tuned from violet to sky blue, arising from single-molecule and H-aggregate phosphorescence, respectively (Figure. 1.1.5c). Such tunable emission smart RTP material will be useful for displays, sensors, and imaging applications.

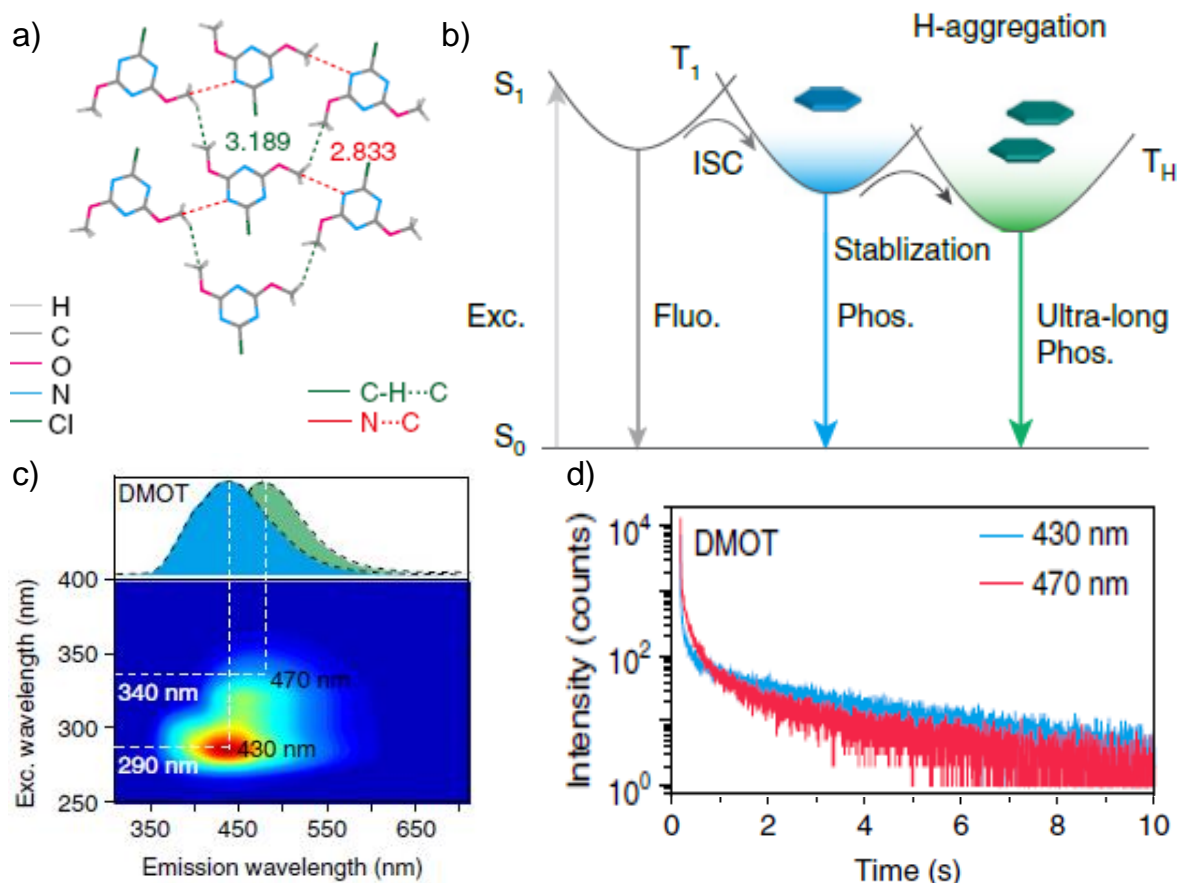


Figure 1.1.5. a) Top-view crystal structure of **DMOT** showing detailed information on the intermolecular interactions. b) Proposed mechanism and molecular design for excitation-dependent colour-tunable URTP. c) Excitation-phosphorescence mapping of **DMOT**. d) Phosphorescence decay profiles of emission bands at 430 and 470 nm for **DMOT**. *Reproduced with permission from ref. 54. Copyright 2019, Springer Nature Limited.*

Similarly, Yuan and co-workers worked on an unexplored pyrimidine molecule hydantoin (**HA**) (Figure. 1.1.6a) with tunable emission colour by changing excitation wavelength.⁵⁵ The available synergistic effect of through-

space conjugation between nitrogen heteroatoms and carbonyls as well as intermolecular interactions through various hydrogen-bonds enabled **HA** as an excellent RTP emitter. Most importantly, **HA** exhibited tunable URTP efficiency with ϕ_p up to 21.8% and τ_p 1.74 s, respectively. Crystals of **HA** displayed sky-blue to yellowish-green afterglows persisting for over 10 s upon exciting with 312 and 365 nm UV irradiation, respectively. A stable self-assembled network with the adjacent molecules using various H-bonds, $O=C\cdots C=O$ π - π , $C=O\cdots H$, and interactions at a relatively shorter distance strengthen the assembly and imply extended through-space delocalization. A dimer of **HA**, 1,1'-methylenedihydantoin **MDHA**, also exhibited tunable URTP with comparatively lower efficiency consisting of τ_p of 1.27 and ϕ_p of 3.6%. The tunable RTP feature is supported by the clustering-triggered emission mechanism, where the presence of different clusters with efficient through-space conjugation and formation of rigidification resulted in tunable RTP. In 2020, Shan and co-workers reported URTP of organic micro rods of **OMR-h**, which is synthesized by heating the mixture of melamine and benzoic acid in an aqueous solution (Figure. 1.1.6a).⁵⁶ In the presence of water, the micro rods form a hydrogen-bonded network and rigidify the molecular motion. A significant enhancement in RTP features with τ_p of 1.64 s and ϕ_p of 11.4% was observed in the wet condition. The observed lifetime of the hydrogen-bonded structure of **OMR-h** is one of the extended lifetimes of ORTP materials in water.

Very recently, Babu and co-workers came up with a new strategy of stabilizing triplet excitons by helical molecular packing (Figure. 1.1.6).³⁹ An N-alkylated carbazole decorated with phenylmethanone units **PCz** (Figure. 1.1.6a) exhibited URTP with high efficiency ($\tau_p > 4.1$ s and ϕ_p of 11%) (Figure. 1.1.6b, c). A helical molecular array of **PCz** in the crystal state enabled to mix up the singlet-triplet states to create hybrid triplets to enhance ISC.

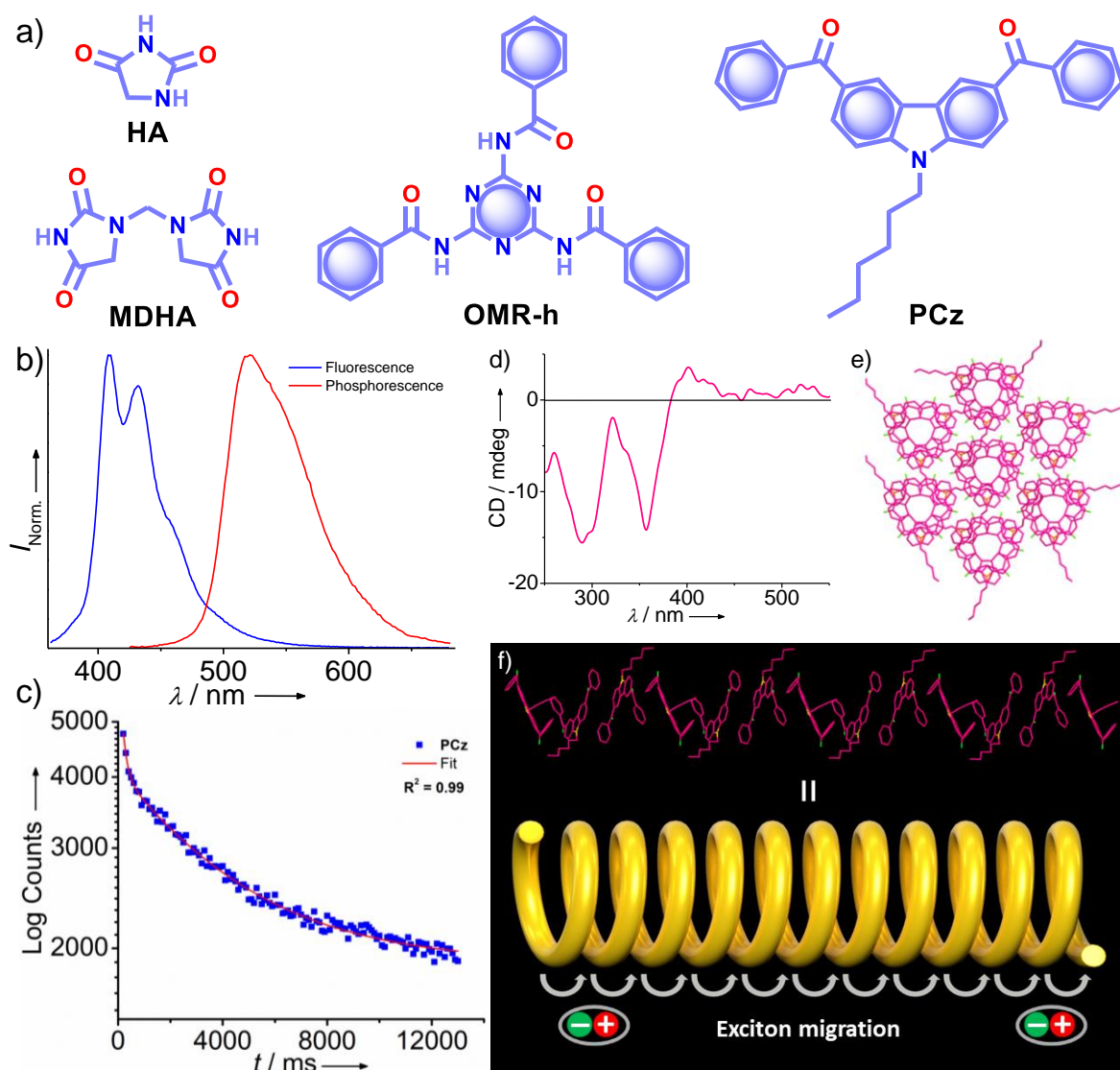


Figure 1.1.6. a) Chemical structure of HA, MDHA, OMR-h, and PCz. b) Steady-state photoluminescence (blue line) in solution and phosphorescence (red line) spectra in crystal state of PCz. c) Phosphorescence decay profile of PCz crystals. d) The solid-state CD spectrum of PCz crystals. e) Six adjacent helical arrays of PCz leading to extended columnar packing in the c-axis. f) Schematic of the helical array of PCz leading to triplet exciton migration. *Reproduced with permission from ref. 39. Copyright 2020, WILEY-VCH.*

A right-handed helical array of PCz acts as a trap and manifests triplet exciton migration to deliver an outstandingly long lifetime (Figure. 1.1.6d, e). An extended molecular array was formed by the arrangement of molecules mainly

through π - π interaction (3.34 Å) between carbazole and phenylmethanone units of adjacent molecules. Thus, the formed 1D-helical array is stabilized by $\text{CH}\cdots\pi$ interaction between the alkyl chain on carbazole and phenylmethanone unit in the adjacent helical columns. The formation of space-filled packing in molecular packing rigidifies and remarkably blocks the non-radiative decay. A combination of experimental and theoretical investigation sheds light on the stabilization of the triplet state by the helical arrays, and the presence of triplet exciton migration results in the efficient RTP (Figure. 1.1.6f).

Similar to single-component RTPs, many attempts have been reported to stabilize the triplet state through multiple interactions between two different structural units with complimentary recognition parts. This section primarily summarizes the developments in the area of efficient two-component RTP systems. An, Huang, and co-workers reported that co-crystals formed by the assembly of melamine **MA** and **IPA** resulted in a stable framework *via* multiple interactions (Figure. 1.1.7).⁵⁷ The two-component assembly **MA-IPA** exhibited URTP with τ_p of 1.91 s and ϕ_p of 24.3% under ambient conditions (Figure. 1.1.7c-d). The rigid framework confined the molecules in a three-dimensional network (Figure. 1.1.7e) and thus helped to limit k_{nr} of the triplet excitons and improved k_{isc} . Similarly, the co-crystals of **MA-TPA** also presented excellent RTP features with τ_p of 1.09 s and ϕ_p of 19.4. The efficient RTP of the co-crystal is confirmed by the faster k_{isc} ($9.3 \times 10^7 \text{ s}^{-1}$) of **MA-IPA** framework than that of the individual components **MA** ($1.7 \times 10^6 \text{ s}^{-1}$) and **IPA** ($8.7 \times 10^6 \text{ s}^{-1}$). It has to be noted that the SOC $\zeta(S_1, T_n)$ of **MA-TPA** and **MA-IPA** increased to 16.1 cm^{-1} and 33.9 cm^{-1} , respectively, compared to the relatively lower values of monomers. It indicates that two-component crystalline assemblies promote the singlet to triplet ISC and enable them to display efficient RTP. However, the co-assembly of **MA-PA** exhibited comparatively less efficient RTP features with τ_p of 0.68 s and ϕ_p of 0.82%. Further, a detailed mechanistic aspect of this significantly high RTP

feature of the co-crystals was explained by Yan and co-workers through TADF-assisted Förster resonance energy transfer from the energy donor **MA** to the phosphor acceptor acids leading to a longer lifetime.⁴⁷ This study also explained the triplet state stabilization by additional charge-mediated hydrogen bonding and π - π stacking. If we compare **MA-IPA** and **MA-TPA**, the k_{nr} and k_p varied as 0.13, 0.18 s⁻¹ and 0.39, 0.74 s⁻¹, respectively. The advantages of two-component phosphor enabled to have simultaneous enhancement of τ_p and ϕ_p .

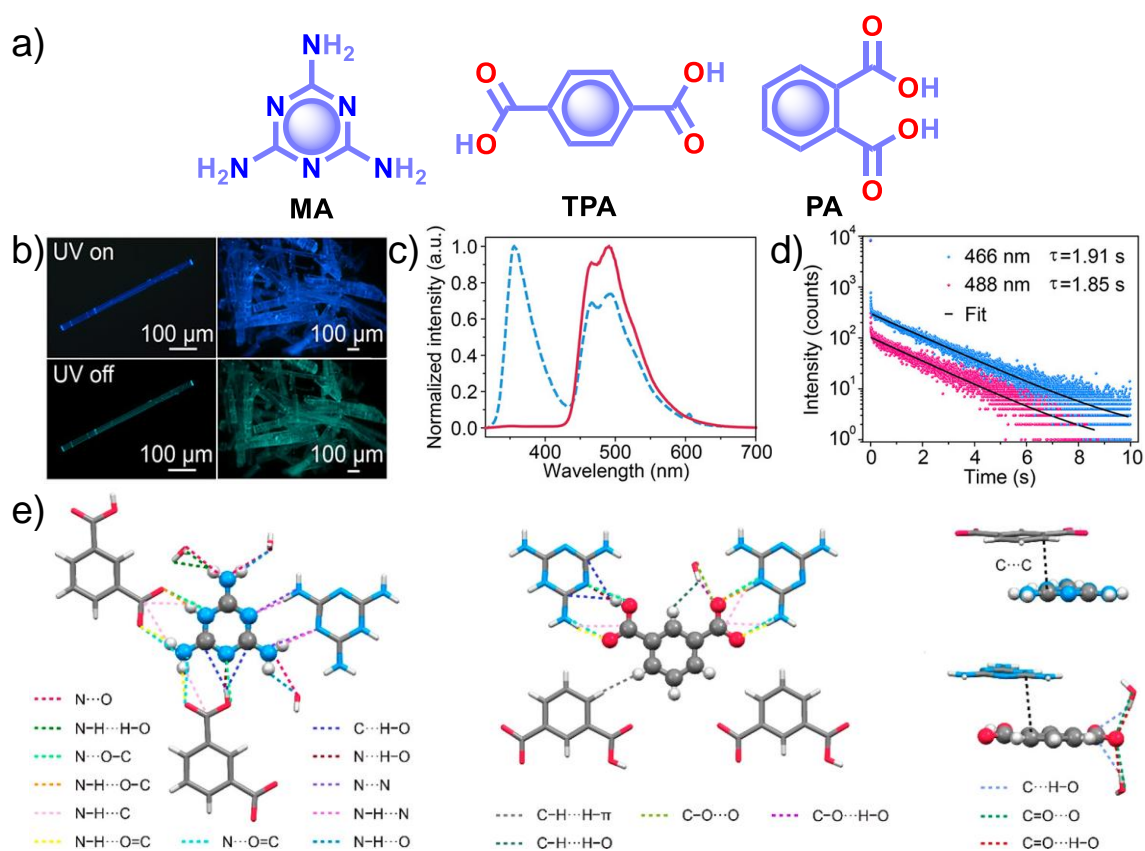


Figure 1.1.7. a) Chemical structure of **MA**, **TPA** and **PA**. b) Photographs of emission (top) and phosphorescence (bottom) of **MA-IPA** co-crystal. c) Steady-state photoluminescence (blue dotted line) and phosphorescence (red line) spectra along with d) phosphorescence decay of the emission bands at 466 and 488 nm, respectively, of **MA-IPA**. *Reproduced with permission from ref. 57. Copyright 2018, American Chemical Society.*

The above section pointed out the recent developments in the area of organic crystalline phosphorescent materials. Many single and multi-component assemblies have been examined to understand the underlying design principles for achieving high quantum yield and extended lifetime up to seconds. However, crystalline RTP materials lack processability and require tedious optimizations for practical applications. This situation demands alternate candidates to troubleshoot the problems in such materials. Hence the organic materials chemists took up this challenge and introduced various new methods to improve RTP features, and the recent developments will be discussed in the following sections.⁵⁸

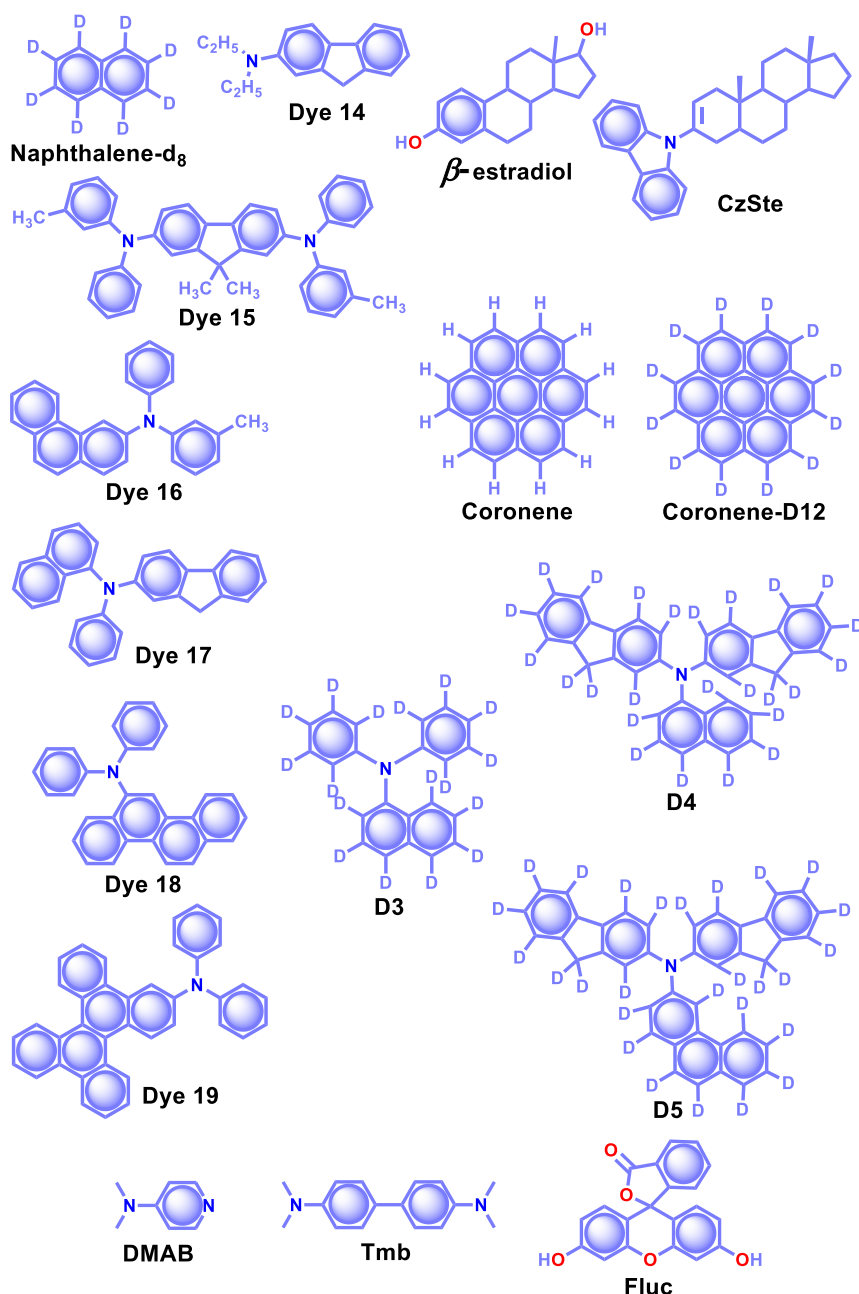
1.1.4.2. Host-Guest Based Organic Phosphors

In the field of supramolecular chemistry, the effective control of the host and guest assemblies to create a wide variety of soft materials gathered attention. Recently, researchers have accomplished RTP of pure organic host-guest systems through controlling various noncovalent interactions.⁵⁹ The host-guest interactions are particularly selective because various factors like shape, size, polarity, charge etc. restrict the host's inclusion behaviour on the guests. Hence, the selection of an appropriate host and guest combination is very critical. In general, the cavity of the host molecule recognized by the guest molecule and gives a rigid environment, and restricts the vibration of the guest molecules. The support is obtained not only from cavitants but other hosts such as small molecules and frameworks that also efficiently support phosphors. Organic host-guest based persistent RTP materials are mainly developed by minimizing k_{nr} of triplet excitons and keeping it smaller than the small k_p .⁵⁹ Since the triplet deactivation pathways heavily depend on non-radiative deactivation of the guest and quenching by the diffusional motion of the host as well as molecular oxygen, the selection of a suitable host-guest combination remains challenging. Herein,

the development of ORTP systems that rely on interactions between hosts and guests is reviewed.

Alfimov and co-workers realized long-lived RTP in the presence of oxygen from arene- β -cyclodextrin (β -CD) cage-hydrocarbon complexes.⁶⁰ Among the different combinations, the complex **Naphthalene-d₈- β -CD** (Scheme 1.1.3) cage with various hydrocarbons showed variable RTP lifetime as 11.9 s for diadamantyl, 9.4 s for diamantine, and 10.3 s for adamantine in the presence of oxygen. However, the RTP lifetime of these complexes further increased in the absence of oxygen. The ternary complexes aggregated in water to form micro-particles, which prevents molecular motions and reduces the quenching effect from oxygen to achieve a large lifetime. In another attempt, the same group demonstrated URTP from the supramolecular complex of **Naphthalene-d₈- β -CD-cyclohexane (I)** with a lifetime of around 16 s while **Naphthalene-d₈- β -CD-cyclohexane-benzophenone (II)** complex showed 14.7 s.⁶¹ More interestingly, the high lifetime of complex (II) is attributed to the triplet-triplet (T-T) energy transfer from benzophenone (donor) to naphthalene-d₈ (acceptor).

Another work in the field of host-guest supramolecular systems was reported by Liu and coworkers using cucurbit[6]uril (**CB[6]**) as host and phenylmethylpyridinium as guest (Figure. 1.1.8a).⁶² The complex **PBC/CB[6]** formed by grinding showed a phosphorescence band at 510 nm having ultralong τ_p of 2.62 s with 9.7% of ϕ_p (Figure. 1.1.8b-d). The encapsulation in **CB[6]** facilitate ISC in phenylmethylpyridinium, which enhances the prevalence of triplet states. Moreover, **CB[6]** provides a rigid matrix for the guest molecule to suppress the molecular motions such as vibrations, rotations, and inter-collisions as well as to prevent the quencher oxygen. Eventually, the successful **PBC/CB[6]** complex prolonged the phosphorescence lifetime. Notably, the unique lifetime and strong phosphorescence features of **PBC/CB[6]** enabled the triple lifetime-encoding for anti-counterfeiting and information encryption applications.



Scheme 1.1.3. Chemical structure of β -estradiol, CzSte and DMAB (host) and Naphthalene- d_8 , Dyes14-19, Coronene, Coronene- d_{12} , D3-5, Tmb (guest) molecules.

The steroidal compound β -estradiol gives rigidity and oxygen blocking properties (Scheme 1.1.3) with high T_1 energy motivated the research group of Adachi to use them used as host material to suppress the triplet quenching.^{63,64} Besides, the use of deuterated aromatic hydrocarbon as the guest minimized non-

radiative deactivation. Red-green-blue persistent emission with RTP $\tau_p > 1$ s and $\phi_p > 10\%$ were observed for dyes **14-19** (Scheme 1.1.3).⁶³ The persistent RTP emission for dyes was noticed for several seconds with single exponential decay. In 2016, the same group reported 3-(N-carbazolyl)-androst-2-ene (CzSte) as a new host molecule (Scheme 1.1.3) to enhance the performance of afterglow light-emitting diodes (LEDs).⁶⁴ To maximize the τ_p of afterglow emission, the authors used **Coronene-d₁₂** as the emitter and found significant improvement in RTP features. **Coronene-d₁₂** planar structure was found ideal for building a rigid host matrix through CH- π intermolecular interactions with steroid moiety of CzSte. The inhibitions of molecular vibration and non-radiative decay of the guest emitter resulted in an extended τ_p of 4.7 s and ϕ_p of 5.3%. Furthermore, the prepared host-guest system was found useful in LEDs exploring higher external quantum efficiency and longer afterglow.

Hirata and co-workers reported a new heavy atom-free organic molecular design consisting of a secondary amine as an RTP antenna substituted with different RTP centers **D3-5** (Scheme 1.1.3) having smaller T_1 energy, exhibiting persistent RTP properties (Scheme 1.1.3).⁶⁵ The notable feature of the molecular design is the steric hindrance introduced between the RTP antenna and the RTP center that decreases k_f and thereby enables efficient ϕ_{isc} . The authors cleverly extended the conjugation of the RTP antenna in anticipation of obtaining $k_p > k_{nr}$. To validate the design strategy, RTP candidates (0.3 wt%) were dispersed in β -estradiol host and observed a persistent emission from 470 to 800 nm. The ϕ_p and τ_p of the host-guest systems varied as 11, 50 and 46%, and 1.60, 1.00, and 1.40 s for **D3**, **D4**, and **D5**, respectively.

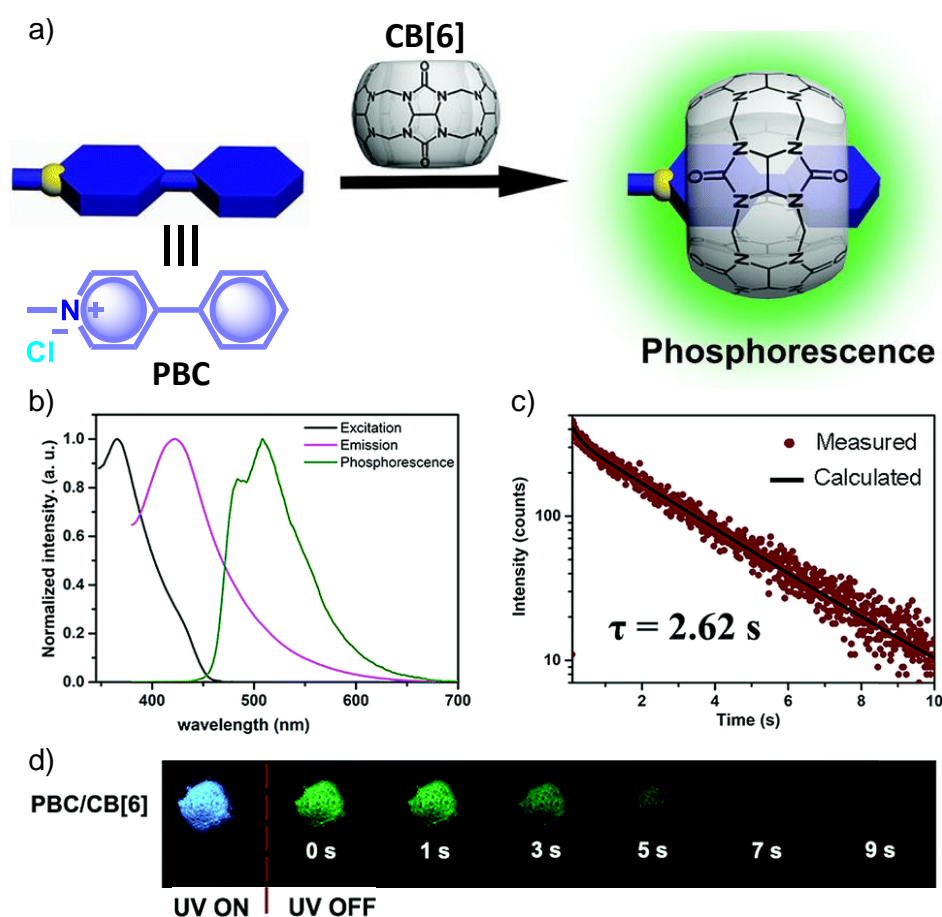


Figure 1.1.8. a) Schematic illustration of the solid-state supramolecular strategy of **PBC** and **CB[6]** for URTP. b) Excitation, emission and phosphorescence spectra of **PBC/CB[6]** in the solid state. c) Phosphorescence decay of **PBC/CB[6]** at 510 nm. d) Photographs of **PBC/CB[6]** powder under 365 nm UV irradiation and at different time intervals after removal of the ultraviolet lamp. *Reproduced with permission from ref. 62. Copyright 2019, Royal Society of Chemistry.*

Recently, an efficient thermoresponsive RTP has been reported by taking advantage of intermolecular charge transfer and energy transfer between *N,N*-dimethylpyridin-4-amine **DMAP** (host) and *N,N,N',N'*-tetramethylbenzidine **Tmb** (guest) (Scheme 1.1.3).⁶⁶ The cocrystals of **DMAP** and **Tmb** displayed efficient blue RTP emission with τ_p 2.08 s and ϕ_p up to 13.4%, respectively. In addition, the authors studied the concentration-dependent emission changes by incorporating an additional energy acceptor fluorescein **Fluc** (Scheme 1.1.3) into

a ternary blend. Upon changing the concentration of **Fluc**, blue to yellow colour-tunable afterglow was noticed. More interestingly, on heating, both **DMAP-Tmb** and **DMAP-Tmb-Fluc** exhibited turn-on RTP with an increasing lifetime from 1.39 s to 1.97 s. Here the enhanced intermolecular interactions in **DMAP-Tmb** and **DMAP-Tmb-Fluc** played a significant role in enhancing phosphorescence lifetime. Further, the thermoresponsive nature of the host-guest RTP materials has been used for multicolour thermal printing.

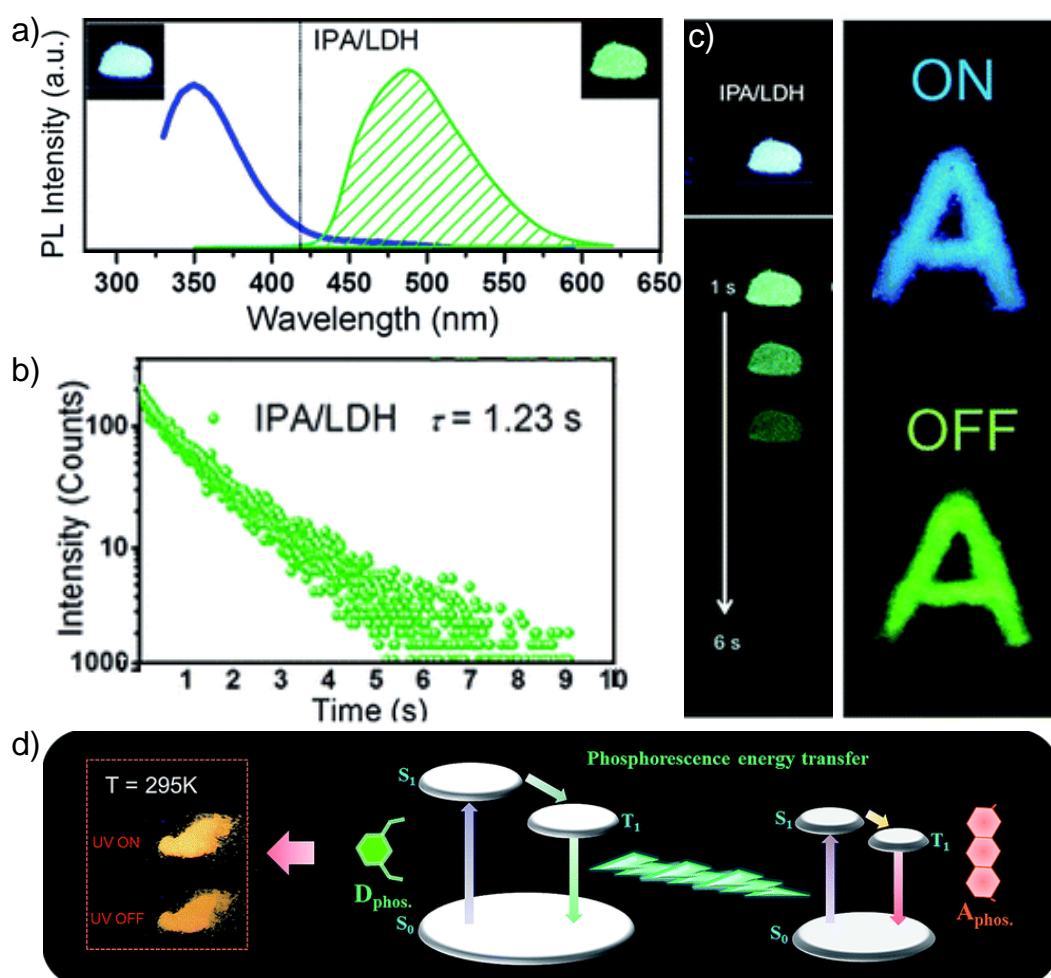


Figure 1.1.9. a) Steady-state emission (left) and phosphorescence (right) spectra of **IPA/LDH** nanohybrids (Insets show the corresponding photographs). b) Phosphorescence decay profile of **IPA/LDH** ($\lambda_{\text{mon}}= 489 \text{ nm}$, $\lambda_{\text{ex}}= 320 \text{ nm}$). c) The letter ‘A’ made with **IPA/LDH** can be unmistakably identified by the naked eye after the excitation is switched off. d) Schematic representation of the proposed

mechanism for PET. *Reproduced with permission from ref. 68. Copyright 2017, Royal Society of Chemistry.*

Metal-organic frameworks (MOFs) are capable of encapsulating guest species in their cavities, and guest confinement can deliver significant improvement in RTP. In this line, Kabe, Adachi, and co-workers describe a long-lived emission by encapsulating **Coronene** in ZIF-8 host.⁶⁷ It is confirmed that the entire **coronene** found in pores of the ZIF-8 MOF suppresses the non-radiative decay and molecular vibration motions, enabling the long-lived RTP. The **Coronene@ZIF-8** exhibited τ_p of 7.4 s, However, under the same experimental conditions, **Coronene-d₁₂@ZIF-8** was able to reach an extended lifetime of 22.4 s. The C-D stretching mode has lower vibrational energy than C-H stretching mode, and hence it assists **Coronene-d₁₂@ZIF-8** to show an enhanced lifetime. Moreover, the suppression of non-radiative deactivation of **Coronene** was confirmed by temperature-dependent lifetime measurement.

In 2017, Yan and co-workers explored a phosphorescence energy transfer (PET) by incorporating donor and acceptor guest molecules in the interlayer nanogallery of layered double hydroxide (LDH) as an inorganic graphene-like host material (Figure. 1.1.9).⁶⁸ The authors used different benzene dicarboxylic acid isomers, namely, **IPA** (Scheme 2), **TPA**, and **PA** (Figure. 1.1.7a), as potential donors assembled *via* co-precipitation method into interlayer of Zn-Al-LDH host. Interestingly, among the nanohybrids, the **IPA/LDH** nanohybrid showed a green phosphorescence emission with the longest τ_p up to 1.23 s and ϕ_p of 3.02% (Figure. 1.1.9b-d). An H-type aggregation between **IPA** dimers and LDH nanosheets stabilized the lowest triplet excited state and minimized the non-radiative decay to prolong the RTP lifetime. Besides, **IPA/LDH** showed thermoresponsive RTP by varying the temperature between 295 to 335 K. Subsequently, co-intercalation of **IPA** as donor and Eosin Y as an acceptor into

the nanogalleries of LDH nanosheets imparted efficient triplet-triplet energy transfer ($E_P = 99.7\%$) (Figure. 1.1.9e).

1.1.4.3. Polymer-Based Organic Phosphors

The crystal-based URTP materials have problems with reproducibility, processability, and flexibility, which significantly impede the development of crystalline URTP materials for practical applications.⁶⁹ Special attention has been made to progress in polymeric organic materials susceptible of URTP in order to overcome these fundamental barriers. Recently, significant improvements have been made in extending the lifetime of organic polymeric materials through homopolymerization, ring-opening polymerization, radical binary copolymerization, and covalent cross-linking reaction, as well as embedding rigid polymer matrix with small molecules.⁶³ Polymer-based RTP materials have been receiving increased attention because of the large molecular weight of the polymer and the availability of functional group chains that can help to rigidify the molecular vibrational and rotational motions of the phosphors. Moreover, it can decrease the effects of oxygen and moisture from the surrounding environment, enabling the triplet excitons to achieve prolonged lifetimes. More importantly, polymer-based RTPs exhibit easy processability, excellent flexibility, and high thermal stability as well.

In 2016, Chen *et al.*, reported the intramolecular charge transfer (ICT) state of polylactic acid-based N-substituted naphthalimide polymers to obtain RTP enhancement.³⁵ It has been noticed that either the ICT state or a heavy atom i.e., Cl, Br promotes efficient ISC and results in strong RTP. In this series, polymer **1,2-OPh-OLA** (Scheme 1.1.4) showed strong ICT and, thereby, a favourable ΔE_{ST} to support RTP. The presence of ICT state served as a link between excited singlet and triplet states and hence increased ISC leading to τ_p of 1.12 s. Additionally, N-substituted naphthalimides conjugated with natural

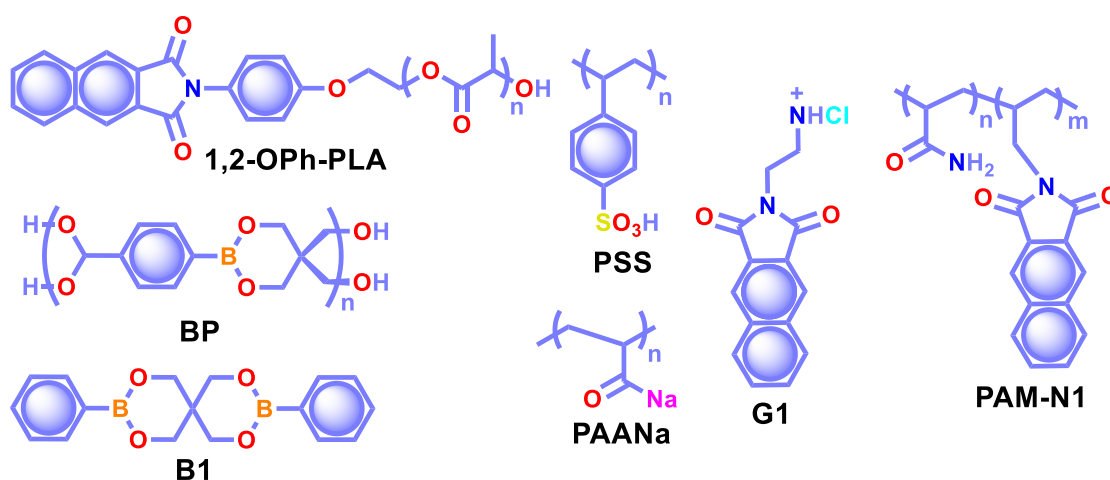
biomacromolecules like i) chitosan and ii) bovine serum albumin also displayed RTP and found useful applications in time-resolved bioimaging.

Ogoshi and coworkers reported URTP with a lifetime of up to 1.22 s from poly(styrene sulfonic acid)-based polymers in the dry solid-state (Scheme 1.1.4).⁷⁰ The measured lifetime is one of the longest RTP lifetimes for non-doped ORTP polymers. The sulfonic acid group in the polymer can form strong inter/intrachain hydrogen bonds in the solid state that reduce the non-radiative decay and eventually lead to ultralong RTP. The RTP lifetime was affected by the introduction of sulfonic acid groups into polymers. The phosphorescence lifetime extended with an increasing ratio due to efficient hydrogen bond formation between sulfonic acid groups. Furthermore, the reversible RTP observed by the uptake and removal of water into the polymer contributed to the encoding application. Detailed studies revealed that the deuteration of SO₃H and exchanging SO₃Na or SO₃K for SO₃H resulted in an increased RTP lifetime. In contrast, a decrease in RTP lifetime was noticed when **PSS** was neutralized by NaOH or KOH.

Cai *et al.*, demonstrated that the ionic cross-linking between chromophores is critically supportive of suppressing non-radiative transitions for URTP, and by extending the concept, a lifetime of 2.1 s for an amorphous polymer is obtained.⁷¹ The replacement of **PSS** with different ions such as Li⁺, K⁺, Rb⁺, NH₄⁺, Mg²⁺, Ca²⁺, Al²⁺, and Gd²⁺ imparted a significant effect on the URTP of polymers. The size of the ionic radius controls RTP features, and as the size increases, the URTP lifetimes gradually decrease. The replacement with Li⁺ and Mg²⁺ resulted in a lifetime of 1.3 and 1.1 s, respectively, and thereafter a gradual decrease in the lifetime is observed. It has been concluded that even though the large ionic radius prevents the prolonged URTP, the high ion charge state is found supportive. Hence a balance between the ionic radius and charge state can significantly alter the lifetime values. Here the k_{nr} is at least one order of magnitude higher than k_p ,

indicating the former played a dominant role in manipulating the URTP of ionic polymer phosphors. The results of ionic cross-linking assisted URTP have even been extended to nonaromatic ionic polymers and found that **PAANa** (Scheme 1.1.4) with blue URTP exhibited a τ_p of 1.4 ms and 2.1 s, respectively, when monitored at 450 nm and 480 nm bands.

Recently, boronic acid/ester-based organic phosphors also excelled as strong RTP candidates. In this line, Kubo and co-workers reported boronate particles **BP** (Scheme 1.1.4) as a self-assembled system showing URTP in both solid and dispersion in water.⁷² Solid **BP** showed phosphorescence peaks located between 450 to 550 nm with a long lifetime of 1.95 s and ϕ_p of 5% under ambient conditions. The RTP properties of **BP** were compared with a model derivative 3,9-dibenzo-2,4,8,10-tetraoxa-3,9-diborospiro [5.5] undecane **B1** (Scheme 1.1.4). Theoretical calculation and crystal structure of **B1** suggest that boron-containing CT interactions and the presence of intermolecular electron coupling facilitate RTP. Notably, When Rhodamine B fluorophores were grafted onto the surface, the ET process from the triplet excited state of **BP** to the singlet state of the fluorophore was made possible, producing an afterglow with dual luminescence at 500 and 600 nm.



Scheme 1.1.4. Chemical structure of polymers **1,2-OPh-PLA**, **BP**, **PSS**, **PAANa**, **G1**, **PAM-N1**, and model derivative **B1**.

In 2020, Ling and co-workers reported the colourful afterglow through regulation of clusterization-triggered RTP of non-conjugated amorphous polyacrylamides (PAMs).⁷³ The emission features of these non-conjugated polymers containing carbonyl and amine groups depend on the aggregation, which can result in electronic interactions by n- π and π - π interactions. Furthermore, the clusterization of amides can form a rigid conformation of polymer chains, which is helpful in inhibiting the non-radiative decay of excitons and stabilizing the excited state through hydrogen bonding. When PAM was blended with naphthalimide **G1** (Scheme 1.1.4), URTP with τ_p up to 1.7 s and ϕ_p of 13.4% was observed in solid powders. Computational studies revealed the possibility of such a clusterization-triggered phosphorescence mechanism. When naphthalimide was covalently linked with the PAMs, **PAM-N1** (Scheme 1.1.4) exhibited an efficient visible-light-excited URTP with τ_p of 1.5 s and ϕ_p of 12%.

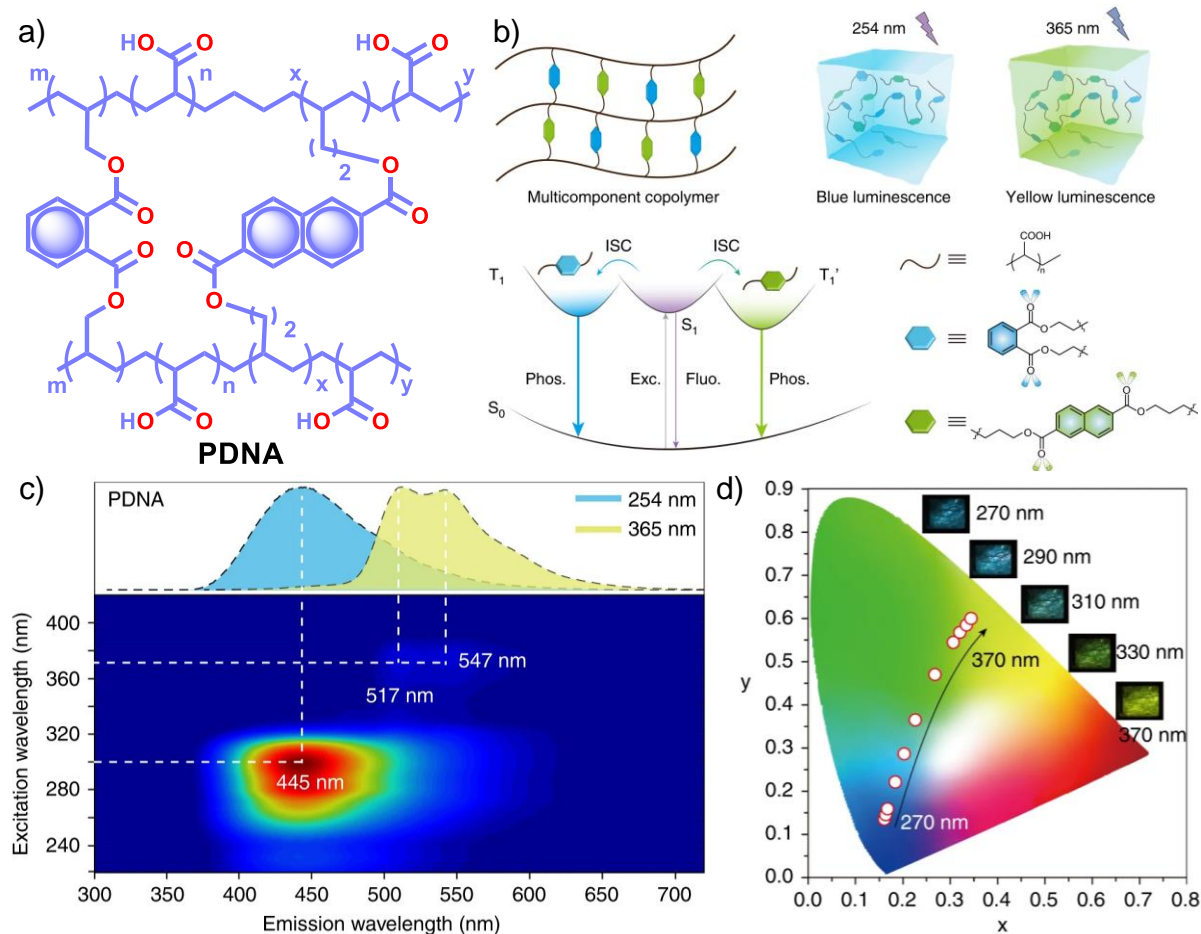


Figure 1.1.10. a) Chemical structure of **PDNA**. b) Schematic illustration of the proposed mechanism of colour-tunable URTP of **PDNA** c) Excitation-phosphorescence mapping of **PDNA** under ambient conditions, inset displays the phosphorescence spectra excited by 254 nm (blue) and 365 nm (yellow). d) CIE chromaticity diagram for **PDNA** with excitation varied from 270 to 370 nm; inset shows the UOP photographs of **PDNA** excited at various wavelengths. *Reproduced with permission from ref. 74. Copyright 2020, Springer Nature Limited.*

In 2020, Gu *et al.*, discovered the colour-tunable URTP in polymers through multi-component cross-linked polymerization by using acrylic acid and multiple luminophores.⁷⁴ A copolymer **PDNA** (Figure. 1.1.10a) prepared using vinyl derivatives of naphthalene (MND), and benzene (MDP), acrylic acid (MND/MDP/AA ratio 1/200/10,000) displayed excitation-dependent multicolour RTP emission spanning from blue to yellow with a long-lived τ_p of 1.1 s and ϕ_p of 23.2% (Figure. 1.1.10b-d). As the ratio of MND/MDP/AA varied, the phosphorescence intensity has gradually decreased. Two other polymers with varying ratios of MND/MDP/AA, namely, **PDNA-5** (1/5/1000) and **PDNA-10** (1/10/1000), also exhibited excellent RTP features with τ_p of 1.22, 1.07 s and ϕ_p of 13, 37.5%, respectively. The excitation spectra of **PDNA** revealed that the origin of blue and yellow emission bands is from two entirely different excited triplet states of benzene and naphthalene components in the polymer and is confirmed by the detailed analysis of the individual polymers. The numerous carbonyl and hydroxyl groups of **PDNA** assist in forming inter or intramolecular hydrogen bonds with polyacrylic acid chains. Thus, eventually, created rigid environment suppressed the non-radiative decay of the excited state and prevented the quenching of triplet excitons. The presence of hydrogen bonding assisted RTP in **PDNA** was revealed by the significant decrease in RTP features in the presence of moisture, which leads to the breakage of the hydrogen bonds

among polymer chains. The overall tunable emission URTP achieved by PDNA is demonstrated in Figure. 1.1.10d.

1.1.4.4. Polymer Supported Organic Phosphors

Apart from incorporating the functional phosphors as a part of the polymer backbones, polymer-supported phosphors also found URTP active. In 2019, Zhao and co-workers achieved URTP from **2-HC** (Figure. 1.1.11a) by co-assembling with polyvinyl alcohol (PVA).⁷⁵ The confinement of **2-HC** in PVA restricts the molecular motions to stabilize the triplet state and thereby generate URTP ($\tau_p = 1.21$ s and $\phi_p = 16\%$) with afterglow lasting for more than four seconds in the dark.

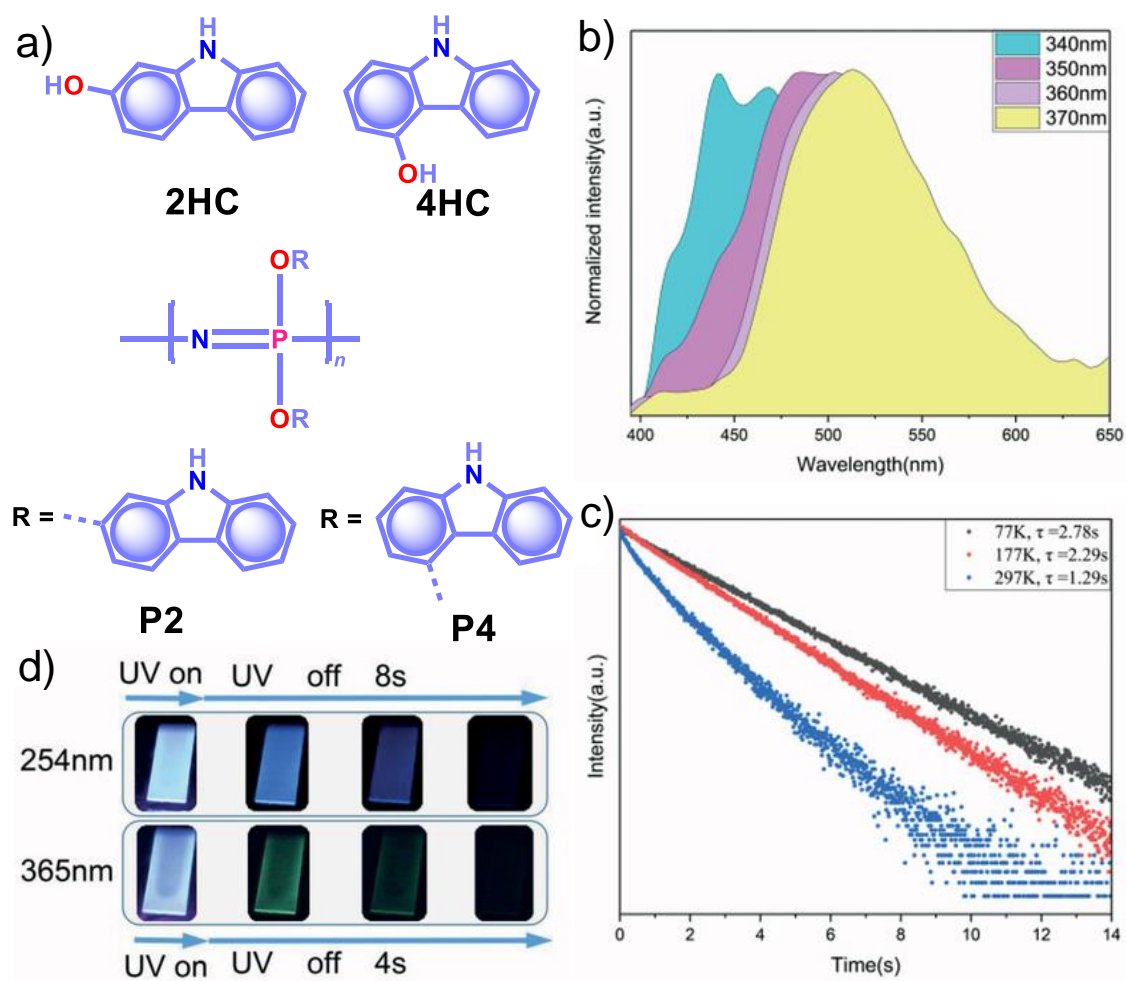


Figure 1.1.11. a) Chemical structure of monomers **2-HC**, **4-HC**, and polymers **P2** and **P4**. b) Excitation wavelength-dependent phosphorescence spectra and c) temperature-dependent phosphorescence decay curves of **PVA-100-P4-1** film. d) Photographs of persistent luminescence of **PVA-100-P4-1** film under ambient conditions. *Reproduced with permission from ref. 70. Copyright 2020, WILEY-VCH.*

The same group demonstrated the excitation-dependent persistent emission by constructing multiple emission centers in polymeric systems with the help of hydrogen bonding.⁷⁶ A polyphosphazene derivative **P4** containing carbazole unit **4-HC** was synthesized and mixed with PVA to develop a composite **PVA-100-P4-1** (Figure. 1.1.11a).

As shown in Figure. 1.1.11b, an excitation wavelength-dependent (340 to 370 nm) redshift of phosphorescence (468 to 522 nm) was observed for **PVA-100-P4-1**. The afterglow of **PVA-100-P4-1** persisted for 12 s, and the corresponding τ_p reached up to 1.29 s with ϕ_p of 1.0% (Figure. 1.1.11c). The presence of strong hydrogen bonding between the polyphosphazene polymer chains and PVA plays a critical role in the afterglow. The k_{nr} for **PVA-100-P4-1** film has significantly come down to 0.77 s^{-1} as compared with that of **PVA-100-4HC-1** precursor film (2.59 s^{-1}). An excitation wavelength-dependent persistent luminescence colour from blue to green obtained indicates the presence of multiple radiation channels in the system (Figure. 1.1.11d). Even though the monomer **2-HC**-PVA composite exhibited a longer lifetime, the corresponding polymer **PVA-100-P2-1** failed to extend the lifetime.

Recently, George and co-workers reported a delayed sensitization assisted triplet to singlet energy transfer in polymer-supported donor-acceptor pairs.⁷⁷ The authors used PVA matrix to host Coronene tetracarboxylate salt **CS** as a triplet energy donor and fluorescent dyes Sulpharhodamine101 **SR101** and

Sulpharhodamine G **SRG** as acceptors to demonstrate PET (Figure. 1.1.12a). Since both the donor and acceptors are water-soluble dyes having polar side-groups, it facilitates co-assembly with PVA *via* ion-dipole and hydrogen bonding interactions. The hybrid of **CS** in PVA matrix showed a phosphorescence band in the range of 500 to 700 nm with an average ultralong τ_p of 2.46 s with ϕ_p 23.4% (Figure. 1.1.12b, c). The emission spectra of **SR101/SRG** doped **CS**-PVA films showed a gradual decrease of **CS** phosphorescence emission with an enhancement of acceptor emission in 550-700 nm regions due to ET from the triplet state of a donor to the singlet state of the acceptors. The hybrid thin films are self-standing and flexible with stable afterglow features (Figure. 1.1.12d). The same group reported deep blue URTP form triazatruxene **TAT** (Figure. 1.1.12a) with an average τ_p of 2.26 s and ϕ_p of 17.5% in PVA matrix.⁷⁸ The deep-blue emission of **TAT**-PVA hybrid films persisted over 10 s points to the efficient RTP from the spatially isolated **TAT** in PVA matrix, supported by strong hydrogen-bonding interaction between **TAT** and PVA. Interestingly, a mixed RTP hybrid of **CS-TAT**-PVA exhibited excitation-dependent multicolour afterglow emission, including ambient white afterglow with the CIE coordinates of (0.29, 0.33).

With the understanding of ORTP of amorphous polymer materials, Reineke and coworkers reported a new family of halogen-free organic luminescent derivatives called aromatic phosphonates (Figure. 1.1.12a).⁷⁹ A series of aromatic phosphonates 4,4'-bis(diethylphosphonomethyl)biphenyl **BDPB** and its derivatives **BDPB-Ac** and **BDPD-PPT** were embedded in polymethyl methacrylate (PMMA) host matrix and covered with Exceval to prepare a hybrid RTP system (Figure. 1.1.12e-g). The presence of PMMA and Exceval ensures hydrogen bonding to rigidify the matrix, acts as an oxygen barrier layer, and efficiently suppresses vibrational dissipation to achieve bright long-lived RTP. In the PMMA matrix, when excited at 300 nm, τ_p varied as

BDPB-Ac = 1.7 s, **BDPB** = 1.8 s, and **BDPD-PPT** = 2.1 s and further varied as 2.0 s, 2.4 s, and 2.6 s, respectively when excited at 275 nm (Figure. 1.1.12f). Furthermore, the RTP of the aromatic phosphonates revealed that the main reason for the long lifetimes is the presence of diethyl-phosphonomethyl units. Interestingly, the lifetime is increased by around 250 ms upon rising from two to three phosphonate groups.

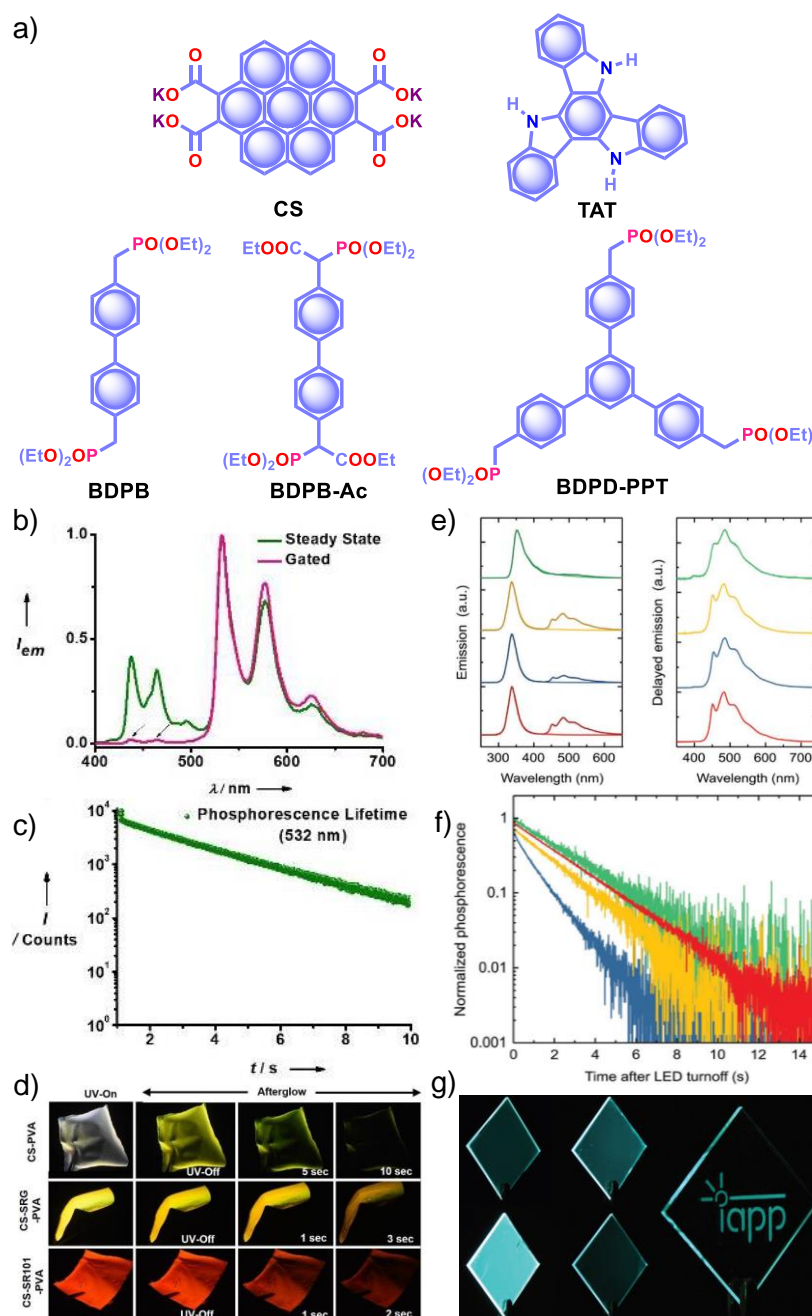


Figure 1.1.12. a) Chemical structure of **CS**, **SRG**, **SR101**, **TAT**, and aromatic phosphonates **BDPB**, **BDPB-Ac**, **BDPD-PPT**. b) Steady-state and gated emission spectra, and c) phosphorescence decay profile of **CS-PVA** film. d) Photographs of **SRG/SR101** doped **CS-PVA** hybrid films showing ambient afterglow properties. e) Emission spectra of aromatic phosphonates under aerated (light colour) and nitrogen atmosphere (dark colour) (left), and delayed spectra showing RTP in Exceval, aerated atmosphere (right) along with corresponding f) phosphorescence decays. g) Photographs of **BDPB-Ac**, **BDPB**, **BDPD-PPT** in Exceval, and delayed phosphorescent image written by masked UV illumination in a **PMMA:BDPB** sample covered with Exceval. *Reproduced with permission from a)-d) ref. 77. Copyright 2020, WILEY-VCH, and e)-g) ref. 79. Copyright 2020, WILEY-VCH.*

1.1.5. Applications

As mentioned in the introduction, the sudden developments of URTPs in recent years have engaged them in various potential applications, including organic electronics, optical recording, anti-counterfeiting, bioimaging, and sensing.⁸⁰⁻⁸⁵ Since many reviews have already summarized the applications of various ORTPs,^{21-25,59,80-85} we discuss only the recent developments of very efficient ORTPs. Li and co-workers utilized the strong interactions of the aryl boronic acids *via* hydrogen bonds to develop an inkjet printing technology suitable for optoelectronic displays.³⁶ The comparable intensities of the RTP crystals and samples from solvent evaporation enabled to use the aryl boronic acid-derived phosphors as a low-cost ink. The fluorescence colour and intensity difference associated with the thermally formed boroxines **tPBA-MeO**, **tPBA-Cl** and **tPBA-Br** (Scheme 1.1.5) from different monomer phosphors **PBA-MeO** (Scheme 1.1.2), **PBA-Cl** and **PBA-Br** (Scheme 5) helped to make distinguishable RTP patterns (Figure. 1.1.16a). As a significant advantage, the brightness of the inkjet-printed designs can be improved by cyclic printing (Figure. 1.1.16b). The

scalable synthesis of phosphors, and stability, accuracy, and reproducibility of the images point to impressive printing technology. Besides, **PBA-MeO** exhibited less toxicity when fed to *Bombyxmori* silkworms and enabled it as a potential candidate for biological applications.

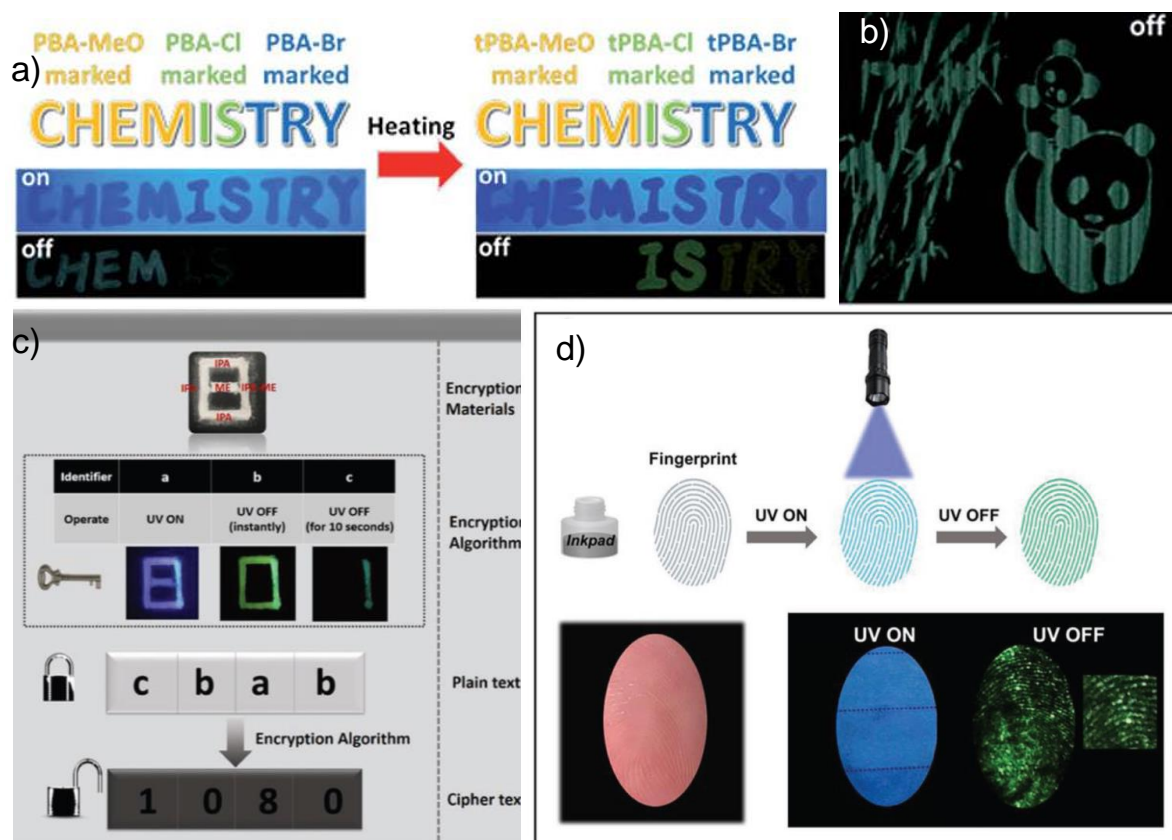


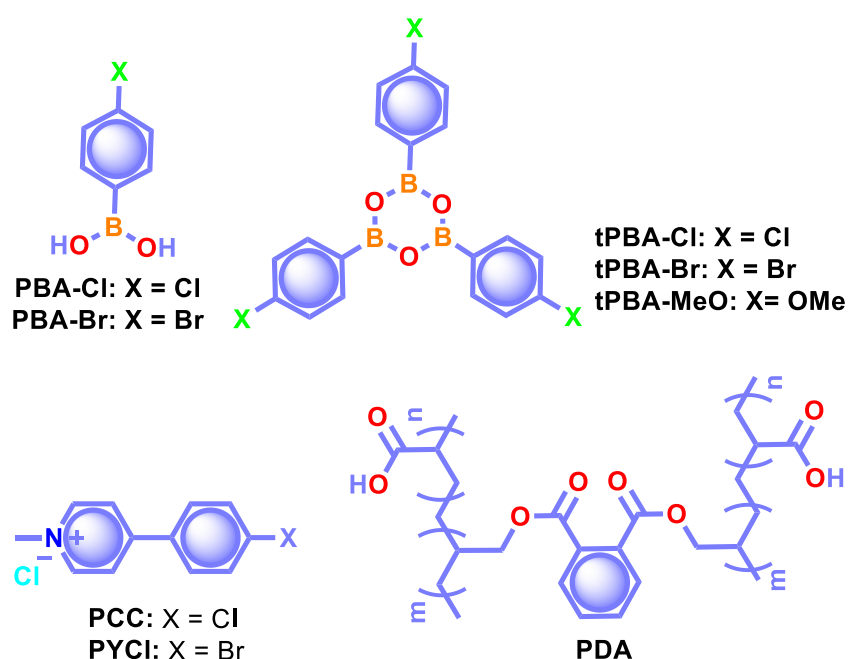
Figure 1.1.16. a) Demonstration of security documents with **tPBA-MeO**, **tPBA-Cl** and **tPBA-Br** before and after heating. b) A pattern of panda printed with **PBA-MeO** for 8 cycles after stopping excitation. The schematic diagram of c) encryption to decryption and d) back-free fingerprint identification and luminescent images of the fingerprint with a special ink pad under UV excitation and after stopping UV excitation using **IPA**, **MA**, and **IPA-MA**. *Reproduced with permission from a), b) ref. 36. Copyright 2017, Royal Society of Chemistry and c), d) ref. 48. Copyright 2019, WILEY-VCH.*

An encryption algorithm having three different modes of operation has been used to develop information safety applications using URTP materials.⁴⁸ As

shown in Figure. 1.1.16c, different modes “a”, “b”, and “c”, were encrypted by using **IPA-ME** and **MA** and **IPA** (Scheme 1.1.2), respectively, and the encryption algorithm enables hiding the real information. Besides, the URTP of **IPA-MA** was effectively used to prove personal identity through fingerprints. An inkpad prepared using **IPA-MA** with polyacrylic acid was used to develop the fingerprint on paper (Figure. 1.1.16d). The supramolecular framework of **MA-IPA** has been used to create a 2-dimensional barcode pattern on filter paper by screen-printing.⁵⁸ The blue-green URTP of **MA-IPA** enabled to identify the information by scanning the barcode in darkness. RTP emission helps in recording the detailed fingerprint characteristics, which can be identified in the darkness. Similarly, the distinctly different lifetime, quantum yield, and robust RTP features of **PBC/CB[6]**, **PCC/CB[6]** (Figure. 1.1.8a), and **PYCI/CB[6]** (Scheme 1.1.5) complexes were used for triple encoding (Figure. 1.1.17a).⁶³ The initial colourless pattern turned to a bright green display after excitation with 365 nm due to the high quantum yield of **PYCI/CB[6]**. The difference in lifetime enabled sequential phosphorescence displays of **PYCI/CB[6]**, **PCC/CB[6]**, and **PBC/CB[6]**.

URTP of amorphous **PSS** (Scheme 1.1.4) and its off/on switching by water vapour has been used for lifetime-encoding application (Figure. 1.1.17b).⁷⁰ The green RTP emission of **PSS** film can be masked by making patterns using water. Since the fluorescence remains intact, no change is observed under UV light, even in the presence of water. However, the pattern “KU” created by the water is no anymore RTP active and can be observed by the naked eye. The reversibility of the water-induced patterns increases the applicability of this method. The excitation-dependent UOP emission property has been used for multilevel information encryption using polymers **PDA** (Scheme 1.1.5) and **PDNA** (Figure. 1.1.10a).⁷⁴ As shown in Figure. 1.1.17c, the patterns NTU and RP in the encrypted information “RNTUP” was fabricated using the polymers **PDNA** and **PDA**,

respectively, as inks. The initial blue emission under 254 nm irradiation was changed to long-lived blue luminescence to show false information upon turning off the excitation source. However, after excitation with 365 nm UV light, the correct information of “NTU” was visualized as long-lived yellow emission. Interestingly, the reversibility of encryption has been achieved by erasure using water and regain by thermal treatment. Similarly, the difference in persistent luminescence intensity of **PVA-100-2HC-1** and **PVA-100-P4-1** (Figure. 1.1.11a) inks has also been used for anti-counterfeiting applications.⁷⁶ In another attempt, the excellent afterglow property of **PAM-N1** (Scheme 4) films was found advantageous for the detection of volatile solvent vapors (Figure. 1.1.17d).⁷³ The strong URTP and green afterglow disappeared in the presence of vapors, and NH₃ imparted drastic quenching. The afterglow restoration achieved by thermal removal of NH₃ ensures an afterglow switch using NH₃ vapour and temperature. Moreover, the security ink developed using **PAM-N1** was found useful for anti-counterfeiting applications.



Scheme 1.1.5. Chemical structure of the supporting phosphors used for various applications.

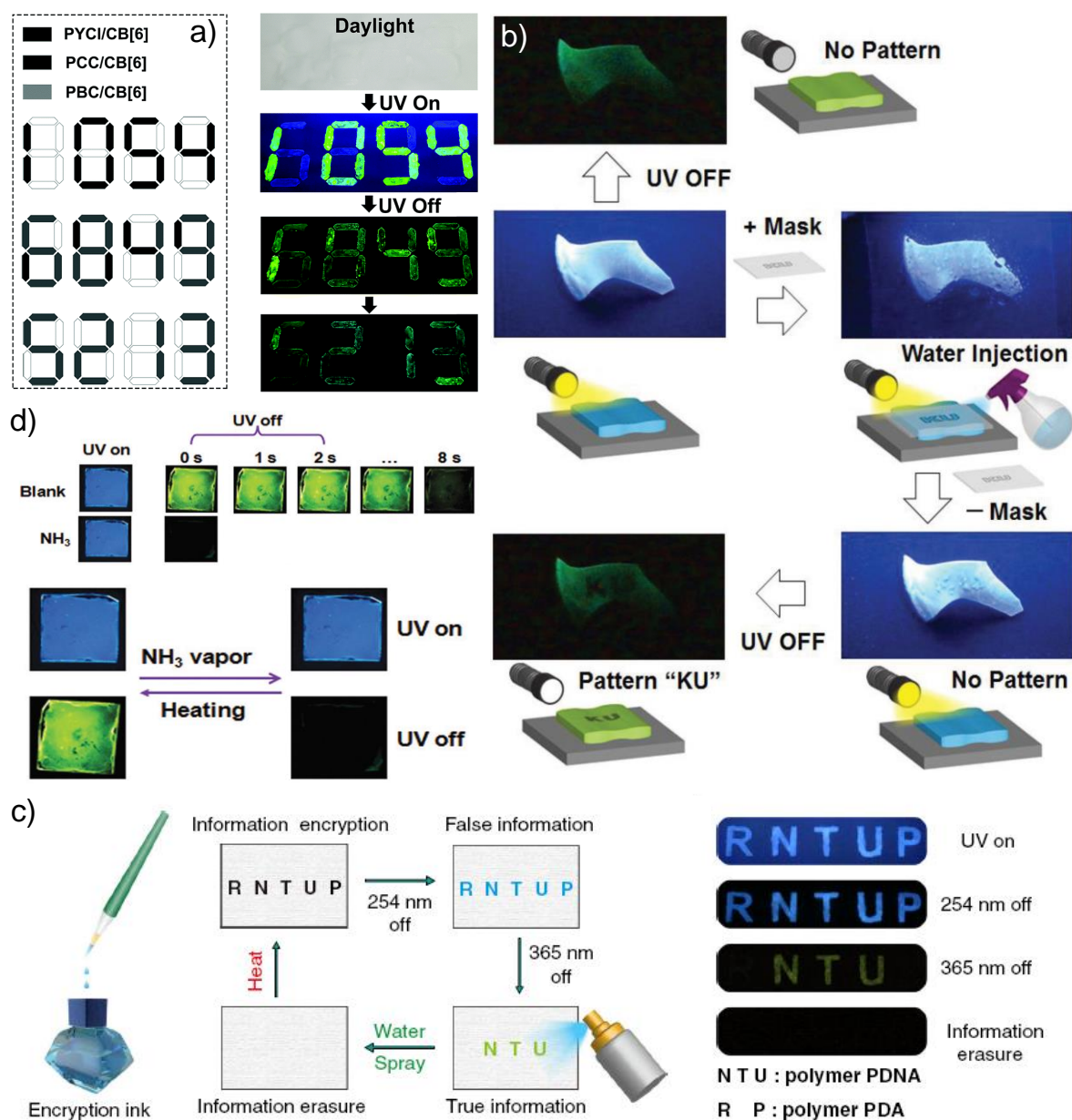


Figure 1.1.17. Lifetime-encoding for security applications using a) **PYCl/CB[6]**, **PCC/CB[6]** and **PBC/CB[6]**, and b) **PSS**. c) Process of information encryption by using the multi-component copolymer **PDNA** (NTU) and **PDA** (RP) as encryption ink and long-lived luminescence photographs of letters (RNTUP and NTU) before and after switching off the UV light of 254 and 365 nm. d)

Photographs of **PAM-N1** films in NH₃ vapors, taken under 365 nm UV light, and after turning off the UV light and afterglow switching based on **PAM-N1** films obtained by stimuli of NH₃ vapour and heating. *Reproduced with permission from a) ref. 53. Copyright 2019, Royal Society of Chemistry and b) ref. 70. Copyright 2018, WILEY-VCH, and c), ref. 74, Springer Nature Limited and d) ref. 73, Copyright 2020, Royal Society of Chemistry.*

1.1.6. Future Perspectives

At the moment, crystallization is a prerequisite for small molecule-based organic phosphors to exhibit RTP with a long lifetime and high quantum yield. One of the limitations associated with crystalline assembly is the processability of such materials in developing optoelectronic devices. There has been a continuous search for noncrystalline RTP materials, and significant progress has been achieved by using amorphous systems such as polymers,⁷⁰⁻⁷⁵ polymers supported phosphors⁷⁶⁻⁷⁹ and organic solvent-free liquids.⁸⁶ However, in most of the systems, the amount of optically inactive molecular components used as a support unit is high, leading to the content of active luminophores being very low. It points to the need for new concepts and designs to develop processable luminogens having excellent RTP efficiency.

ORTPs have exhibited many fascinating features useful for imaging and anti-counterfeiting applications. One of the areas that need to be improved is the stimuli-responsive RTP features, which will enable to develop tunable emission smart RTP materials. More concrete demonstrations in the field of multi-stimuli sensitive RTP materials are highly required to widen the scope.⁸⁷⁻⁸⁹ Another area that can be explored is the nonlinear optical properties of RTP materials, which will bring out newer concepts in a demonstration. Even though a few attempts are there with lasing and waveguiding applications of ORTPs, more detailed studies are envisioned for RTP materials.

ORTPs with emissions spanning from blue to orange colours have been mainly reported, and the red emissive phosphorescence is rare for metal-free systems. The availability of red or NIR emissive RTP systems will be appropriate to explore the applications of organic phosphors in biological applications. However, such a target seems to be the most awaited due to the many hurdles associated with ORTPs. Besides, biological applications demand the biocompatibility of organic phosphors, which is another challenge due to the current scarcity of high-performing RTPs under physiological conditions. It provides an opportunity to explore further the exciting molecular design of ORTPs suitable for biological applications. In the same line, RTP molecules with two-photon and multi-photon induced emissions also will be highly beneficial due to the possible operation of NIR excitation. Recently Liu and co-workers reported the effect of impurity on the afterglow features of carbazole derivatives.⁹⁰ It imposes a serious concern on the efficiency of organic phosphors. An isomer present in the commercially available carbazole imparts a significant effect on RTP. Hence it is advised to check the purity of the samples before analysis thoroughly.

1.1.7. Conclusions

In summary, ORTPs have been widely exploited in the last decade due to the advancement in molecular design, control over intermolecular interactions, and fundamental understanding. In this review, we explained the various successful strategies adopted to improve the efficiency of RTP in metal-free organic systems and attempted to discuss the exceptionally high RTP lifetime above 1 s along with quantum efficiency, and remarkable afterglow properties. The major experiments were centered on important aspects such as the population of the triplet excited state through efficient ISC (ϕ_{isc}), suppression of non-radiative decay (k_{nr}) pathways, and slowing down the decay rate of the triplet excited state (k_p). The successful examples pointed out the incorporation of heavy

atoms, hetero atoms, and carbonyls groups to improve SOC and control the non-radiative decay of the triplet excitons through crystallization, framework formation, host-guest interactions, and polymer support to obtain efficient RTP candidates. The most interesting observation is the use of such efficient RTPs in applications from organic electronics, anti-counterfeiting, and bioimaging to sensing. Even though many improvised ways to elevate the efficiency of organic phosphors are in place, the fundamental understanding of mechanistic aspects is still missing. Hence this area is expected to have serious revelations shortly through combined experimental and theoretical investigations. The recent increase in the quality and quantity of publications indicates that RTPs have a bright future. Similarly, the latest developments in this area also highlight the vital role of organic functional materials in futuristic applications.

1.1.8. References

1. a) V. Coropceanu, J. Cornil, D. A. Da Silva Filho, Y. Olivier, R. Silbey, J.-L. Bre´das, *Chem. Rev.* 2007, **107**, 926. b) M. A. El-Sayed, *Acc. Chem. Res.* 1968, **1**, 8-16.
2. a) J. R. Lakowicz, *Principles of Fluorescence Spectroscopy (Third Edition)*, University of Maryland School of Medicine, Baltimore, Maryland, USA, 2006. b) T. Itoh, *Chem. Rev.* 2012, **112**, 4541-4568.
3. G. Baryshnikov, B. Minaev, H. Ågren, *Chem. Rev.* 2017, **117**, 6537.
4. M. Baroncini, G. Bergamini, P. Ceroni, *Chem. Commun.* 2017, **53**, 2081-2093.
5. A. Forni, E. Lucenti, C. Botta, E. Cariati, *J. Mater. Chem. C* 2018, **6**, 4603-4626.
6. X. Ma, J. Wang, H. Tian, *Acc. Chem. Res.* 2019, **52**, 738-748.
7. L. Xiao, H. Fu, *Chem. Eur. J.* 2018, **25**, 714-723.
8. M. Hayduk, S. Riebe, J. Voskuhl, *Chem. Eur. J.* 2018, **24**, 12221-12230.

9. W. Zhao, Z. He, J. W.Y. Lam, Q. Peng, H. Ma, Z. Shuai, G. Bai, J. Hao, B. Z. Tang, *Chem* 2016, **1**, 592-602.
10. F. B. Dias, K. N. Bourdakos, V. Jankus, K. C. Moss, K. T. Kamtekar, V. Bhalla, J. Santos, M. R. Bryce, A. P. Monkman, *Adv. Mater.* 2013, **25**, 3707-3714.
11. X. Yang, G. Zhou, W-Y. Wong, *Chem. Soc. Rev.* 2015, **44**, 8484-8575.
12. Z. Yang, Z. Mao, X. Zhang, D. Ou, Y. Mu, Y. Zhang, C. Zhao, S. Liu, Z. Chi, J. Xu, Y. C. Wu, P. Y. Lu, A. Lien, M. R. Bryce, *Angew. Chem. Int. Ed.* 2016, **55**, 2181-2185.
13. G. Zhang, G. M. Palmer, M. W. Dewhurst, C. L. Fraser, *Nat. Mater.* 2009, **8**, 747-751.
14. Y. Xie, Y. Ge, Q. Peng, C. Li, Q. Li, Z. Li, *Adv. Mater.* 2017, **29**, 1606829.
15. J. Yang, X. Zhen, B. Wang, X. Gao, Z. Ren, J. Wang, Y. Xie, J. Li, Q. Peng, K. Pu, Z. Li, *Nat. Commun.* 2018, **9**, 840.
16. S. Tian, H. Ma, X. Wang, A. Lv, H. Shi, Y. Geng, J. Li, F. Liang, Z. Su, Z. An, W. Huang, *Angew. Chem. Int. Ed.* 2019, **58**, 6645-6649.
17. J. Yang, Z. Ren, B. Chen, M. Fang, Z. Zhao, B. Z. Tang, Q. Peng, Z. Li, *J. Mater. Chem. C* 2017, **5**, 9242-9246.
18. H. Wu, W. Chi, G. Baryshnikov, B. Wu, Y. Gong, D. Zheng, X. Li, Y. Zhao, X. Liu, H. Ågren, L. Zhu, *Angew. Chem. Int. Ed.* 2019, **58**, 4328-4333.
19. H. Wu, C. Hang, X. Li, L. Yin, M. Zhu, J. Zhang, Y. Zhou, H. Agren, Q. Zhang, L. Zhu, *Chem. Commun.* 2017, **53**, 2661-2664.
20. S. Hirata, *Adv. Optical Mater.* 2017, **5**, 1700116.
21. S. Xu, R. Chen, C. Zheng, W. Huang, *Adv. Mater.* 2016, **28**, 9920-9940.
22. Q. Li, Y. Tang, W. Hu, Z. Li, *Small* 2018, **14**, 1801560.
23. S. Mukherjee, P. Thilagar, *Chem. Commun.* 2015, **51**, 10988-11003.
24. Kenry, C. Chen, B. Liu, *Nat. Commun.* 2019, **10**, 2111.
25. W. Zhao, Z. He, B. Z. Tang, *Nat. Rev. Mater.* 2020, DOI:10.1038/

- s41578-020-0223-z.
26. V. C. Wakchaure, Goudappagouda, K. C. Ranjeesh, T. Das, K. Vanka, R. Gonnade and S. S. Babu, *Chem. Commun.* 2018, **54**, 6028-6031.
 27. Y.-C. Lin, M. Karlsson, M. Bettinelli, 2016, Inorganic Phosphor Materials for Lighting. In N. Armaroli & H. J. Bolink (Eds.), *Photoluminescent Materials and Electroluminescent Devices*, 309-355, Springer, Berlin.
 28. M. -M. Fang, J. Yang, Z. Li, *Chin J Polym Sci.* 2019, **37**, 383-393.
 29. S. Tao, S. Zhu, T. Feng, C. Zheng, B. Yang, *Angew. Chem. Int. Ed.* 2020, **59**, 9826-9840.
 30. H. Ma, Q. Peng, Z. An, W. Huang, Z. Shuai, *J. Am. Chem. Soc.* 2019, **141**, 1010-1015.
 31. M. Baba, *J. Phys. Chem. A* 2011, **115**, 9514-9519.
 32. C. M. Marian, *WIREs ComputMolSci* 2012, **2**, 187-203.
 33. H. Yuasa, S. Kuno, *Bull. Chem. Soc. Jpn.* 2018, **91**, 223-229.
 34. X. Chen, C. Xu, T. Wang, C. Zhou, J. Du, Z. Wang, H. Xu, T. Xie, G. Bi, J. Jiang, X. Zhang, J. N. Demas, C. O. Trindle, Y. Luo, G. Zhang, *Angew. Chem. Int. Ed.* 2016, **55**, 9872-9876.
 35. Z. Chai, C. Wang, J. Wang, F. Liu, Y. Xie, Y.-Z. Zhang, J.-R. Li, Q. Li, Z. Li, *Chem. Sci.* 2017, **8**, 8336-8344.
 36. Z. An, C. Zheng, Y. Tao, R. Chen, H. Shi, T. Chen, Z. Wang, H. Li, R. Deng, X. Liu, W. Huang, *Nat. Mater.* 2015, **14**, 685-690.
 37. S. Hirata, K. Totani, T. Watanabe, H. Kaji, M. Vacha, *Chem. Phys. Lett.* 2014, **591**, 119-125.
 38. K. Narushima, Y. Kiyota, T. Mori, S. Hirata, M. Vacha, *Adv. Mater.* 2019, 1807268.
 39. A. D. Nidhankar, Goudappagouda, D. S. M. Kumari, S. K. Chaubey, R. Nayak, R. G. Gonnade, G. V. P. Kumar, R. Krishnan, S. S. Babu, *Angew. Chem. Int. Ed.* 2020, **59**, 13079-13085.

40. S. Kuno, H. Akeno, H. Ohtani, H. Yuasa, *Phys. Chem. Chem. Phys.* 2015, **17**, 15989-15995.
41. M. Koch, K. Perumal, O. Blacque, J. A. Garg, R. Saiganesh, S. Kabilan, K. K. Balasubramanian, K. Venkatesan, *Angew. Chem. Int. Ed.* 2014, **53**, 6378-6382.
42. W. Jia, Q. Wang, H. Shi, Z. An, W. Huang, *Chem. Eur. J.* 2020, **26**, 4437-4448.
43. D. B. Clapp, *J. Am. Chem. Soc.* 1939, **61**, 523-524.
44. C. S. Bilen, N. Harrison, D. J. Morantz, *Nature* 1978, **271**, 235-237.
45. O. Bolton, K. Lee, H. -J. Kim, K. Y. Lin, J. Kim, *Nat. Chem.* 2011, **3**, 205-210.
46. L. Gu, H. Shi, M. Gu, K. Ling, H. Ma, S. Cai, L. Song, C. Ma, H. Li, G. Xing, X. Hang, J. Li, Y. Gao, W. Yao, Z. Shuai, Z. An, X. Liu, W. Huang, *Angew. Chem. Int. Ed.* 2018, **57**, 8425-8431.
47. B. Zhou, D. Yan, *Adv. Funct. Mater.* 2019, **29**, 1807599.
48. Y. Shoji, Y. Iwabata, Q. Wang, D. Nemoto, A. Sakamoto, N. Tanaka, J. Seino, H. Nakai, T. Fukushima, *J. Am. Chem. Soc.* 2017, **139**, 2728-2733.
49. S. Kuno, T. Kanamori, Z. Yijing, H. Ohtani, H. Yuasa, *Chem. Photo. Chem.* 2017, **1**, 102-106.
50. M. Li, K. Ling, H. Shi, N. Gan, L. Song, S. Cai, Z. Cheng, L. Gu, X. Wang, C. Ma, M. Gu, Q. Wu, L. Bian, M. Liu, Z. An, H. Ma, W. Huang, *Adv. Optical Mater.* 2019, 1800820.
51. T. Zhang, Z. Zhao, H. Ma, Y. Zhang, W. Z. Yuan, *Chem. Asian J.* 2019, **14**, 884-889.
52. H. Sasabe, Y. Kato, Y. Watanabe, T. Ohsawa, N. Aizawa, W. Fujiwara, Y.-J. Pu, H. Katagiri, J. Kido, *Chem. Eur. J.* 2019, **25**, 16294-16300.
53. N. Gan, X. Wang, H. Ma, A. Lv, H. Wang, Q. Wang, M. Gu, S. Cai, Y. Zhang, L. Fu, M. Zhang, C. Dong, W. Yao, Hu. Shi, Z. An, W. Huang, *Angew. Chem. Int. Ed.* 2019, **58**, 14140-14145.

54. L. Gu, H. Shi, L. Bian, M. Gu, K. Ling, X. Wang, H. Ma, S. Cai, W. Ning, L. Fu, H. Wang, S. Wang, Y. Gao, W. Yao, F. Huo, Y. Tao, Z. An, X. Liu and W. Huang, *Nat. Photon.* 2019, **13**, 406-411.
55. Y. Wang, S. Tang, Y. Wen, S. Zheng, B. Yang, W. Z. Yuan, *Mater. Horiz.* 2020, **7**, 2105-2112.
56. Y.-C. Liang, Y. Shang, K.-K. Liu, Z. Liu, W.-J. Wu, Q. Liu, Q. Zhao, X.-Y. Wu, L. Dong, C.-X. Shan, *Nano Res.* 2020, **13**, 875-881.
57. L. Bian, H. Shi, X. Wang, K. Ling, H. Ma, M. Li, Z. Cheng, C. Ma, S. Cai, Q. Wu, N. Gan, X. Xu, Z. An, W. Huang, *J. Am. Chem. Soc.* 2018, **140**, 10734-10739.
58. T. Zhang, X. Ma, H. Wu, L. Zhu, Y. Zhao, H. Tian, *Angew. Chem. Int. Ed.* 2020, **59**, 11206-11216.
59. G. Qu, Y. Zhang, X. Ma, *Chinese Chem. Lett.* 2019, **30**, 1809-1814.
60. V. B. Nazarov, V. G. Avakyan, E. I. Bagrii, T. G. Vershinnikova, M. V. Alfimov, *Russ. Chem. Bull., Int. Ed.* 2005, **54**, 2752-2756.
61. V. B. Nazarov, V. G. Avakian, M. V. Alfimov, *High Energy Chem.* 2019, **53**, 108-114.
62. Z.-Y. Zhang, Y. Liu, *Chem. Sci.* 2019, **10**, 7773-7778.
63. S. Hirata, K. Totani, J. Zhang, T. Yamashita, H. Kaji, S. R. Marder, T. Watanabe, C. Adachi, *Adv. Funct. Mater.* 2013, **23**, 3386-3397.
64. R. Kabe, N. Notsuka, K. Yoshida, C. Adachi, *Adv. Mater.* 2016, **28**, 655.
65. I. Bhattacharjee, S. Hirata, *Adv. Mater.* 2020, **31**, 2001348.
66. Y. Wang, J. Yang, Y. Gong, M. Fang, Z. Li, B. Z. Tang. *SmartMat.* 2020, DOI:10.1002/smm2.1006.
67. H. Mieno, R. Kabe, N. Notsuka, M. D. Allendorf, C. Adachi, *Adv. Optical Mater.* 2016, **4**, 1015-1021.
68. R. Gao, D. Yan, *Chem. Sci.* 2017, **8**, 590-599.
69. N. Gan, H. Shi, Z. An, W. Huang, *Adv. Funct. Mater.* 2018, **28**, 1802657.

70. T. Ogoshi, H. Tsuchida, T. Kakuta, T. Yamagishi, A. Taema, T. Ono, M. Sugimoto, M. Mizuno, *Adv. Funct. Mater.* 2018, **28**, 1707369.
71. S. Cai, H. Ma, H. Shi, H. Wang, X. Wang, L. Xiao, W. Ye, K. Huang, X. Cao, N. Gan, C. Ma, M. Gu, L. Song, H. Xu, Y. Tao, C. Zhang, W. Yao, Z. An, W. Huang, *Nat. Commun.* 2019, **10**, 4247.
72. M. Hoshi, R. Nishiyabu, Y. Hayashi, S. Yagi, Y. Kubo, *Chem. Asian J.* 2020, **15**, 787-795.
73. S. Wang, D. Wu, S. Yang, Z. Lin, Q. Ling, *Mater. Chem. Front.* 2020, **4**, 1198-1205.
74. L. Gu, H. Wu, H. Ma, W. Ye, W. Jia, H. Wang, H. Chen, N. Zhang, D. Wang, C. Qian, Z. An, W. Huang, Y. Zhao, *Nat. Commun.* 2020, **11**, 944.
75. H. Wu, W. Chi, Z. Chen, G. Liu, L. Gu, A. K. Bindra, G. Yang, X. Liu, Y. Zhao, *Adv. Funct. Mater.* 2019, **29**, 1807243.
76. Z. Wang, Y. Zhang, C. Wang, X. Zheng, Y. Zheng, L. Gao, C. Yang, Y. Li, L. Qu, Y. Zhao, *Adv. Mater.* 2020, 1907355.
77. S. Kuila, S. J. George, *Angew. Chem. Int. Ed.* 2020, **59**, 9393-9397.
78. S. Kuila, S. Garain, S. Bandi, S. J. George, *Adv. Funct. Mater.* 2020, 2003693.
79. H. Thomas, D. L. Pastoetter, M. Gmelch, T. Achenbach, A. Schlogl, M. Louis, X. Feng, S. Reineke, *Adv. Mater.* 2020, **32**, 2000880.
80. M. E. Díaz-García, A. Fernández-González, R. Badía-Laíño, *Applied Spectroscopy Reviews*, 2007, **42**, 605-624.
81. S. M. A. Fateminia, Z. Mao, S. Xu, Z. Yang, Z. Chi, B. Liu, *Angew. Chem. Int. Ed.* 2017, **56**, 12160-12164.
82. X. Zhen, Y. Tao, Z. An, P. Chen, C. Xu, R. Chen, W. Huang, K. Pu, *Adv. Mater.* 2017, 1606665.
83. J. Zhi, Q. Zhou, H. Shi, Z. An, W. Huang, *Chem. Asian J.* 2020, **15**, 947-957.
84. H. Xiang, J. Cheng, X. Ma, X. Zhou, J. J. Chruma, *Chem. Soc. Rev.* 2013, **42**, 6128-6185.

85. X.-Q. Liu, K. Zhang, J.-F. Gao, Y.-Z. Chen, C.-H. Tung, L.-Z. Wu, *Angew. Chem. Int. Ed.* 2020, **59**, DOI:10.1002/anie.202007039.
86. Goudappagouda, A. Manthanath, V. C. Wakchaure, K. C. Ranjeesh, T. Das, K. Vanka, T. Nakanishi, S. S. Babu, *Angew. Chem. Int. Ed.* 2019, **58**, 2284-2288.
87. L. Huang, C. Qian, Z. Ma, *Chem. Eur. J.* 2020, **52**, 11914-11930.
88. L. Gu, X. Wang, M. Singh, H. Shi, H. Ma, Z. An, W. Huang, *J. Phys. Chem. Lett.* 2020, **11**, 6191-6200.
89. Y. Wang, J. Yang, M. Fang, Y. Yu, B. Zou, L. Wang, Y. Tian, J. Cheng, B. Z. Tang, Z. Li, *Matter*, 2020, **3**, 449-463.
90. C. Chen, Z. Chi, K. C. Chong, A. S. Batsanov, Z. Yang, Z. Mao, Z. Yang, B. Liu, *Nat. Mater.* 2020, DOI:10.1038/s41563-020-0797-2.

Chapter 1: Section 2

Introduction to Thermally Activated Delayed Fluorescence Emitters for Lighting Applications

1.2.1 Introduction

Thermally activated delayed fluorescence (TADF) of organic molecules recently emerged as an effective method for harvesting triplet states and converting them to light. Hence the area has emerged as promising emitting material for OLEDs. Many organic TADF molecules have been screened to boost the efficiency of OLEDs by transforming non-emitting T_1 into emitting S_1 states. Through prompt (PF) and delayed fluorescence (DF), TADF materials can harvest both S_1 and T_1 states. The DF is owing to a thermally induced reverse intersystem crossing process that converts the lowest T_1 to S_1 states. Purely fluorescent-based OLEDs have a 25% internal quantum efficiency limit because of 1:3 singlet-triplet ratio caused by charge recombination by negatively charged electrons and positively charged holes. OLEDs based on TADF molecules have nearly 100% IQEs and are mainly manufactured in the green emission range. Blue TADF emitters also made significant improvements. Nevertheless, the red emissive TADFs still perform with low efficiency. Despite notable progress in recent years, considerable obstacles remain in attaining a complete understanding of the TADF mechanism and improving the material stability. TADF materials have mainly been used in the field of OLEDs so far, although applications in other areas, such as sensing and fluorescence microscopies, are also being considered.¹

Perrin *et. al.*² firstly introduced the concept of DF, also called E-type DF, in 1929 and later by Lewis³ in 1941 in fluorescein solutions. Parker and Hatchard^{4,5} discovered E-type DF in eosin and benzyl in 1961, and in 1968, Wilkinson and Horrocks⁶ identified the delayed luminescence as TADF. This popular and conceptually novel TADF was reawakened by Adachi,⁷ who explained that TADF is a phenomenon in which non-emissive triplet states can harvest in OLEDs.

Based on the spin statistics, upon electrical excitation, the 1:3 ratio of singlet and triplet states are formed. Hence, in OLEDs, the yield of singlet state formation *via* charge recombination is restricted to 25%, while the remaining

75% produces triplet states that are generally non-emissive at ambient temperature. This demonstrates a significant mechanism for OLED efficiency degradation, which has led to the investigation of alternative triplet harvesting techniques in organic materials. Organic molecules containing heavy/halogen atoms are commonly used to overcome this constraint. The presence of heavy/halogen atoms increases SOC and enables efficient mixing between the singlet and triplet states, allowing radiative decay of the triplet state.⁸ Hence, heavy/halogen atoms containing organic molecules became very admired because they made it possible for OLEDs internal quantum efficiency (IQEs) to achieve 100%. Still, metals containing materials, mostly iridium and platinum, assuredly have several benefits. In addition, they exhibit the following significant drawbacks in OLEDs: (1) unstable in the blue spectral range, (2) being expensive because of scarcity, and (3) harmful.

Therefore, transition metals containing iridium or platinum-based materials are not appropriate for applications requiring high output, e.g., display and lighting, to non-economical viability and scarcity worldwide.¹⁰ The introduction of copper-containing compounds aims to replace rare metals. Surprisingly, certain complexes have considerable contributions.¹¹ Yersin research group,¹² have recently reviewed their photophysics and demonstrated how molecular design and host rigidity affect emission properties of Cu(I)-complexes. However, depending on their scarcity, availability, and lack of flexibility of metal complexes, metal-free organic TADF molecules are the favourite.

Another approach for harvesting triplet states in OLEDs is to use triplet fusion, which results from triplet-triplet annihilation (TTA).¹³ In the TTA process, two colliding triplet states interact, forming one singlet excited state that will decay radiatively and result in delayed fluorescence. Woefully, the TTA process mainly depends on the energy alignment of the energy levels and the ordering of S_1 and T_1 excited states.¹⁴ Although the contribution of TTA to the

electroluminescence in OLED has previously been established,¹⁵ still, this process has not yet wholly demonstrated its benefits.

Another way of harvesting triplets excitons in OLED is reverse intersystem crossing in hot excitons, also known as the hot-exciton rISC process.^{16,17} Molecules synthesized for effective hot-exciton rISC have strong CT and higher lying S_n and T_n excited states with nearer energy levels. As a result, the rate of internal conversion within various triplets can compete with rISC rate constant, which occurs between T_n and S_n states. Therefore, higher-level T_n states can be converted into S_n states and subsequently to the lowest S_1 state, from where the emission comes. In short, the rISC hot-exciton process depends on the rate of reverse intersystem crossing between upper T_n and S_n levels having CT character to provide a higher S_1 yield. Thus, the hot-exciton rISC can attain 100% IQE by converting the 75% T_n states into emissive S_n states, although designing molecules having efficient hot-exciton rISC is extremely difficult.¹⁸

Contrary to the hot-exciton mechanism, the design of TADF molecules needs to do in such a way that energy levels between the lowest S_1 and T_1 excited states should be much closer, so rISC will take place easier from the lowest T_1 to S_1 states. This ensures that the issues caused by rISC in the hot-exciton mechanism are prevented. Most of the molecules have a comparatively large energy gap between T_1 and S_0 states, it will effectively compete with rISC process. Many compounds that emit in the green^{22,23} and blue^{19,21} spectral areas may achieve triplet harvesting efficiency near 100%; however, in the red-emitting range, the triplet harvesting yields are often lower because non-radiative decay is more prominent. Generally, designing TADF molecules often involves ensuring a narrow energy gap between the lowest S_1 and T_1 states while simultaneously reducing internal conversion and sustaining high fluorescent yields. Covalently connected donor (D) and acceptor (A) components make it relatively simple to create molecules with a minimal S_1 - T_1 energy gap. This results in S_1 and T_1 excited states exhibiting high CT features, which causes little overlap between

the HOMO and LUMO orbitals and decreases the electronic exchange energy, resulting in a narrow energy gap between S_1 and T_1 states.²⁴ Although this purpose appears to be fairly straightforward, it is not an easy task to simultaneously reduce internal conversion and acquire strong fluorescent yield in molecules with potent CT character. Several factors, including molecular geometry, dielectric mixture, and the existence of reduced energy situated in the donor or acceptor components, may affect photophysics and the effectiveness of the TADF molecules.^{22,25}

1.2.2 Fundamental Principles for the Designing of TADF Emitters -

Organic molecules require a narrow energy gap between the S_1 and T_1 excited states (ΔE_{ST}) and the most negligible non-radiative decay for effective TADF. This will improve the probability that the triplet states will last long in order to be produced by the thermally activated rISC, enhancing the fluorescent yield (Figure 1.2.1). A narrow ΔE_{ST} is important for increasing the rate of rISC (k_{rISC}) mentioned in equation (1).

When estimating the energy of the lowest S_1 and T_1 excited states, the following three distinct aspects are generally taken into consideration: 1) Orbital Energy (E_{orb}) 2) Electron Repulsion Energy (K), and 3) First-order quantum mechanical correction, known as Exchange Energy (J) is caused by the Pauli principle and includes electron-electron repulsion.²⁶

Above mentioned aspects contribute equally to S_1 and T_1 excited states. However, S_1 and T_1 states have different spin arrangements, exchange term enhances energy in singlet states while reducing in triplet states by a similar proportion, based on eq.ⁿ 2 & 3.¹⁸ Therefore, the ΔE_{ST} is given in equation 4.

$$krISC = A \exp\left(-\frac{\Delta E_{ST}}{kT}\right) \quad (1)$$

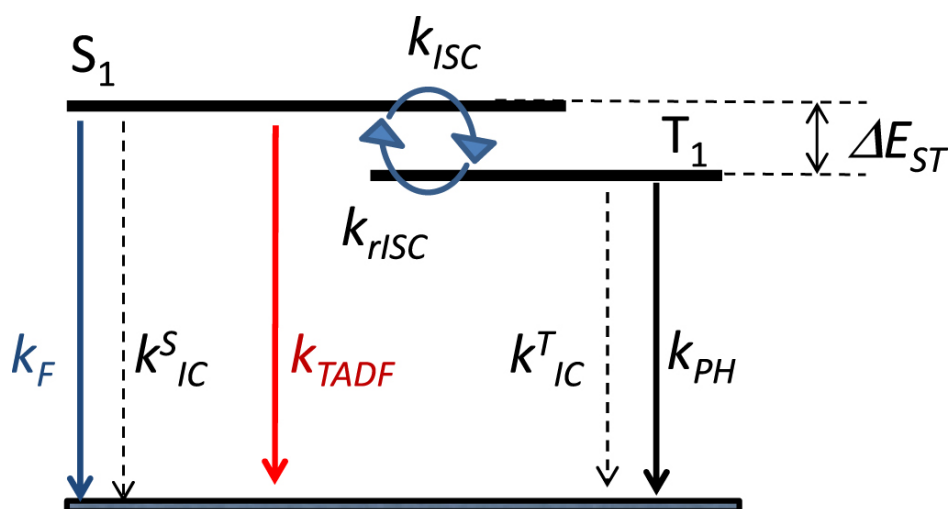


Figure 1.2.1. A simplified illustration of the electronic energy levels, rate constants, and kinetics of the TADF.

$$E_{S_1} = E_{orb} + K + J, \quad (2)$$

$$E_{T_1} = E_{orb} + K - J, \quad (3)$$

$$\Delta E_{ST} = E_{S_1} - E_{T_1} = 2J \quad (4)$$

Equation 4 denotes that the ΔE_{ST} must be reduced by minimising the exchange energy J , which is determined using equation 5. Here, ϕ denotes HOMO and ψ denotes LUMO wavefunctions, and e is the electron charge. From equation 5, it is revealed that J can be reduced by minimising the interaction between HOMO and LUMO orbitals. Therefore, TADF molecules often consist of D and A moiety connected by bridging aromatic compounds to generate characteristic CT characters in excited states. Furthermore, keeping a twist in donor and acceptor around the molecule, achieving donor and acceptor nearly orthogonal or maximising the distance between donor and acceptor using an aromatic bridge can reduce ΔE_{ST} .²⁷

$$J = \iint \phi(r_1)\psi(r_2) \left(\frac{e^2}{r_1-r_2} \right) \phi(r_2)\psi(r_1) dr_1 dr_2 \quad (5)$$

1.2.2.1 Evidence for the Existence of Charge Transfer States-

The presence of solvatochromism in emission provides experimental proof that a particular TADF material produces excited states with charge transfer characteristics. The noticeable spectrum change upon increased solvent polarity is mainly caused by the dipole of excited states, which mainly results from electronic density redistribution attributed to the charge transfer state.^{28,29}

The impact of solvatochromism on a donor-acceptor-donor molecule on the fluorescence spectrum (Figure 1.2.2), with fluorene as the electron donor, and the electron acceptor units are dibenzothiophene-S, and S-dioxide, (**FASAF**) produces excited states of charge transfer nature. The emission of **FASAF** is highly resolved in a non-polar solvent, i.e., in hexane, but when the polarity increases, the emission of **FASAF** redshifted.³⁰

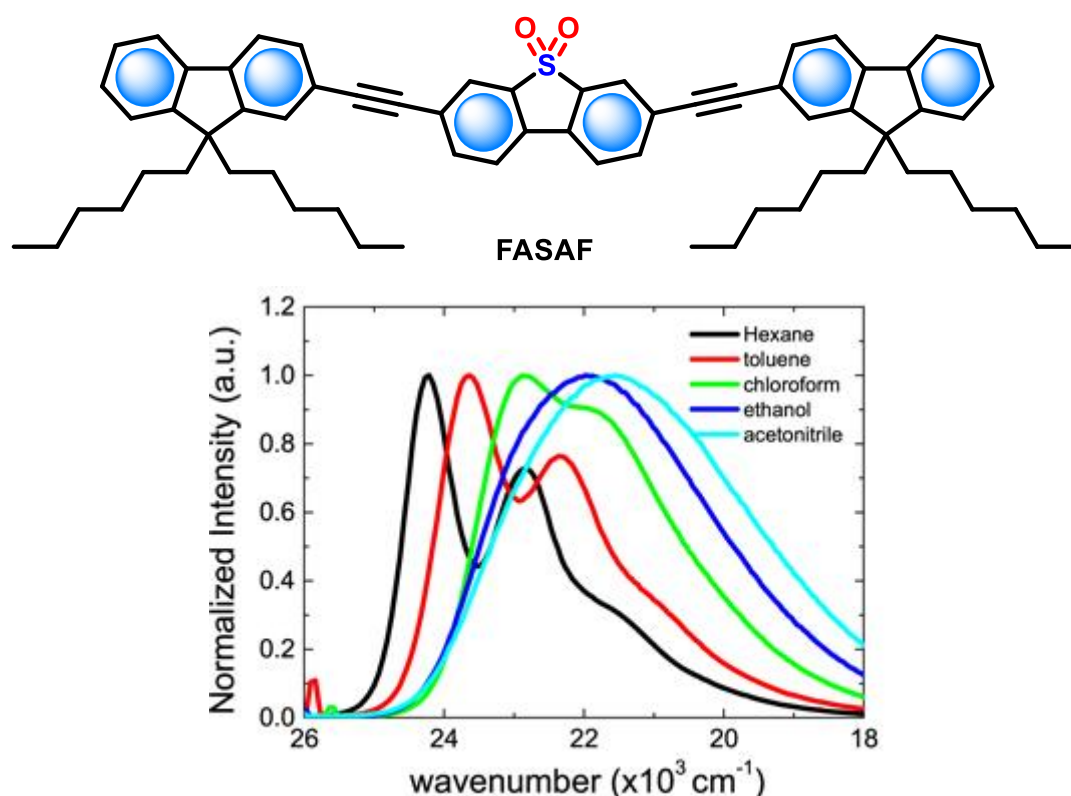


Figure 1.2.2. Solvatochromism of FASAF in different solvents (*Reproduced with permission from ref. 30. Copyright, 2006, American Chemical Society*).

The intensity of the singlet-triplet energy splitting is strongly connected to the charge transfer nature of the excited state. For example, materials having intense charge transfer excited states display broad emissions even in non-polar solvents,

and ΔE_{ST} values are usually below 100 meV.²² But there have been reports on discrepancies in the relationship between the HOMO-LUMO overlap obtained by computations and the EST analyses, which may indicate that other variables may have a substantial impact on the EST, thus the need for further research.³¹

1.2.2.2 Molecular Design -

The most significant influence on the photophysical characteristics of TADF molecules comes from the inclusion of donor and acceptor units used to build TADF emitters. Hence these components should be carefully chosen. The ΔE_{ST} and rate of intersystem crossing are similarly impacted by the coupling between the donor and acceptor units. According to a report by Dias *et al.*,²² the impact of molecular isomerization on TADF material, a noticeable difference in the efficiency of TADF between donor-acceptor-donor isomers that only differ in the position at which carbazole or diphenylamine serve as donor part and dibenzothiophene-S, S-dioxide acceptor moiety. Substitution at the C-2, C-8 of acceptor unit produces TADF, whereas substitution at the C-3, C-7 positions of acceptor unit turns off TADF. (Figure 1.2.3).

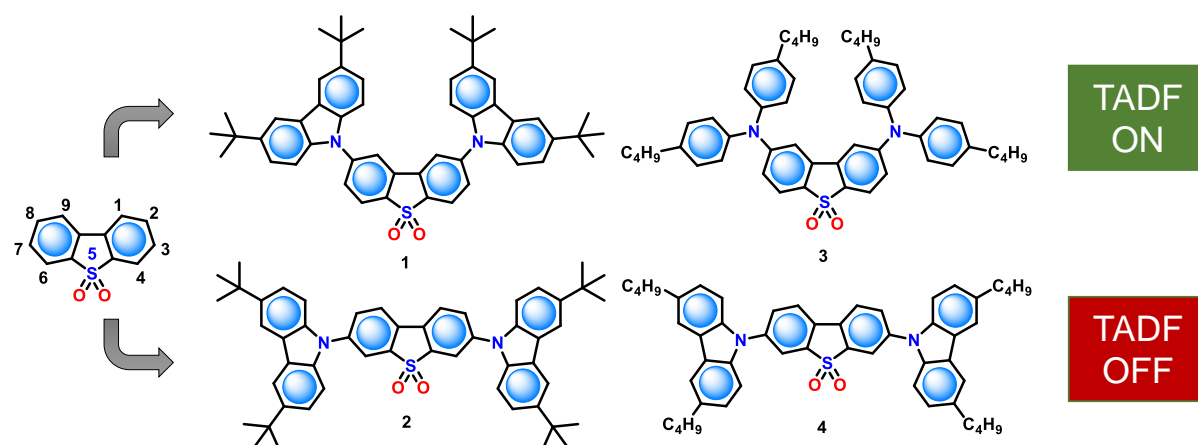
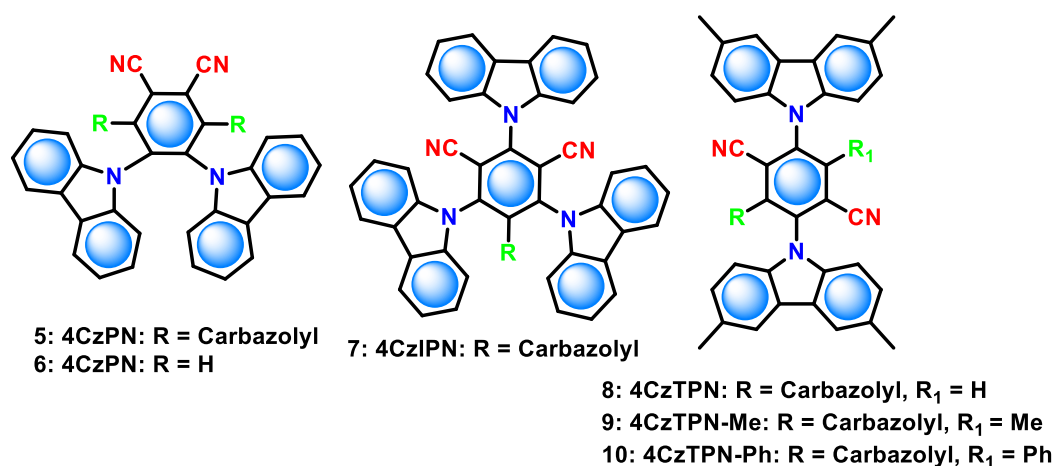


Figure 1.2.3. TADF emitters (**1-4**) have effect of D-A connectivity, molecules **1** and **3** show strong TADF, while molecules **2** and **4** are insufficient to show TADF (Reproduced with permission from ref. 22. Copyright, 2006, American Chemical Society).

The comparison of energy between S_1 and T_1 states in molecules **1-4** was significantly impacted by the host and varied by links between D and A units.

(Figure 1.2.3). The highest TADF contributions are made by compounds **1** and **3**, which have the lowest energy gaps. Mainly, the S-T energy gap minimised by incorporating strong D and A units. Yet, another way is twisted geometries with nearly orthogonal orientation around donor-acceptor linker to achieve an even smaller ΔE_{ST} .^{23,25,32} Similarly, a small ΔE_{ST} can be produced by enhancing the distance between donor and acceptor.^{33,34} Finely confined HOMO and LUMO orbitals are produced by these molecule geometries, which results in reduced ΔE_{ST} values. While negligible HOMO and LUMO orbitals overlap results in small ΔE_{ST} , additionally, it causes low radiative rates, which results in lower fluorescence yields (Φ_f).³² However, weak D and A units cause little localization of HOMO and LUMO, which causes a longer S-T energy gap and reduces the contribution of TADF. In such cases, Lee and co-workers showed the mixing of bicarbazole as a weak donor and diphenyltriazine as a strong acceptor are used to improve the donor nature of TADF molecule with retaining reasonably high Φ_f .³⁵

Adachi⁷ group utilised the above-mentioned strategies and prepared a series of TADF emitters (Scheme 1.2.1) by using carbazolyl dicyanobenzene (**CDCB**) molecule, where dicyanobenzene serves as the electron acceptor and carbazole as the donor. The wavelength of emission maxima and Φ_f of CDCBs are greatly influenced by the number of substitution and their positions in dicyanobenzene. For instance, the emission peak varied from 450 nm to 580 nm for **6** to **10**. Device fabrication using these compounds gave the efficiencies for green, orange, and sky-blue emission OLEDs 19%, 11%, and 8%, respectively.



Scheme 1.2.1. Chemical structure of CDCBs.⁷

Figure 1.2.4 represents the most commonly used derivatives of the molecules having a mixture of donor and acceptor moieties in TADF molecules.

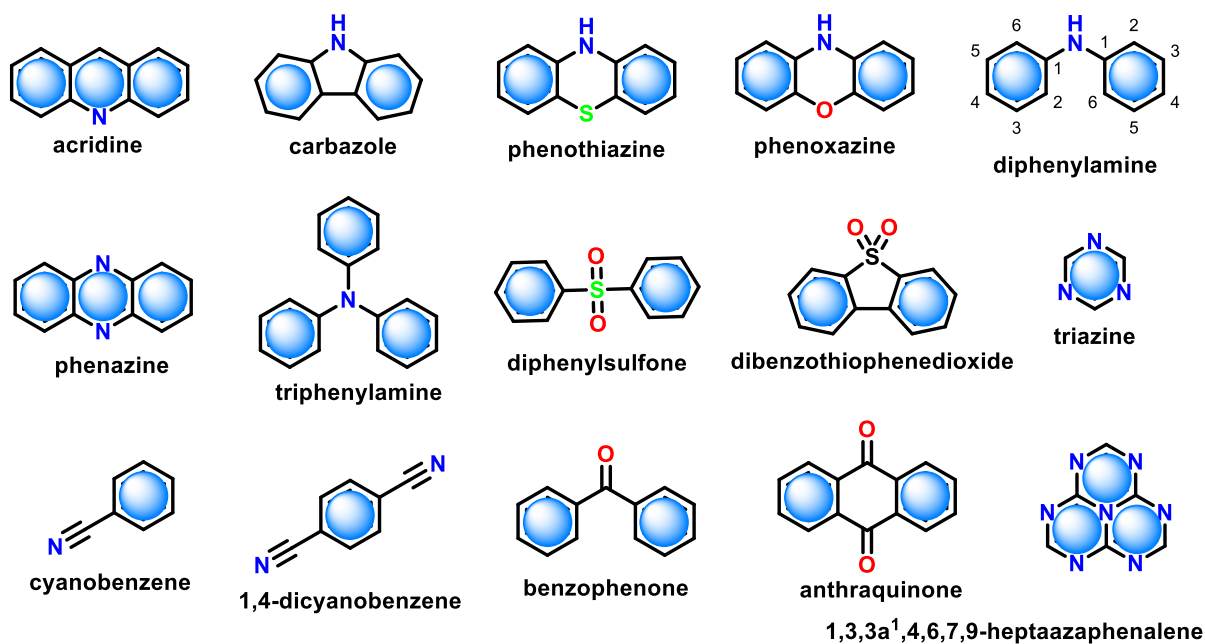


Figure 1.2.4. Electron donor and acceptor units molecular structure used in TADF molecules.¹

1.2.3 Mechanism and Basic Understanding

The luminescence in TADF molecules shows a fast component, identified as prompt fluorescence (PF) after excitation with a fast laser pulse, and the PF is due to the radiative decay of singlet excited states that were directly formed by excitation, according to the scheme in Figure 1.2.1. This fast decay occurs typically within a few nanoseconds and is followed by an emission tail due to the

presence of DF. This happens due to thermally activated reverse intersystem crossing from T_1 to S_1 and is known as TADF.^{18,22,23,36,37} The equilibrium between singlet and triplet excited states due to intersystem crossing (k_{ISC}) and reverse intersystem crossing (k_{rISC}) plays the key role in the observation of TADF. The molecules with a relatively strong yield of triplet formation show strong TADF, whereas the yield of singlet states formed depends on the rate of reverse intersystem crossing.

$$\Phi_{rISC} = \frac{k}{k_{rISC} + k_{IC^T} + k_{PH}} \approx 1$$

These situations occur in compounds where the vibrational decay paths influence the inhibition of triplet excited states., that is, $k_{rISC} \gg k_{PH} + k_{IC^T}$, and the energy difference between S_1 and T_1 states is very small, typically just around 0.1 eV. Then, the maximum emission of TADF emitters (Φ_F) is thoroughly investigated by equation 6, which considers the recycling of S_1 and T_1 states.

$$\begin{aligned} \Phi_F &= \Phi_{PF} + \Phi_{DF} = \sum_{i=0}^n \Phi_{PF} (\Phi_{ISC} \Phi_{rISC})^i \\ &= \Phi_{PF} \frac{1}{1 - \Phi_{ISC} \Phi_{rISC}} \end{aligned} \quad (6)$$

The photophysical measurement of TADF emitters with $\Phi_{DF}/\Phi_{PF} \geq 4$ is thus made simpler, and the triplet yields may be measured based from equation (7) with great accuracy in such circumstances.

$$\begin{aligned} \Phi_{ISC} &= \frac{\Phi_{DF}/\Phi_{PF}}{1 + \Phi_{DF}/\Phi_{PF}} \\ &= \frac{\Phi_{DF}}{\Phi_{PF} + \Phi_{DF}} \end{aligned} \quad (7)$$

The following determination demonstrates all of the other significant photophysical characteristics determined from relatively easy measurements that are given in the following sections.

1.2.3.1 Prompt Fluorescence Yield (Φ_{PF}) and Lifetime (τ_{PF})-

The PF yield (Φ_{PF}) and its lifetime (τ_{PF}) are determined in non-degassed solution, or solid films are crucial methods for the photophysical analysis of TADF emitters. The radiative rate constant (k_F) is determined by knowing Φ_{PF} and τ_{PF} , as per equation 8.

$$k_F = \Phi_{PF} / \tau_{PF} \quad (8)$$

In the presence of oxygen, effective TADF molecules usually have less fluorescence yields. However, upon degassing the sample, $\Phi_F = \Phi_{PF} + \Phi_{DF}$ increases significantly, this is because of DF contribution.

1.2.3.2. Delayed-to-Prompt Fluorescence ratio, (Φ_{DF}/Φ_{PF})-

For efficient TADF emitters, the triplet yield is measured directly from equation (7). Thus, determining the Φ_{DF}/Φ_{PF} fluorescence ratio is of fundamental significance. There are two ways to determine Φ_{DF}/Φ_{PF} : a first method is by collecting the prompt and DF components using degassed samples. The prompt and delayed components are measured in single-time-resolved fluorescence decay. In this case, the fluorescence decay is usually well fitted by the sum of two exponentials, one describing the PF and DF decays, see equation (9).³⁶

$$I_{fl}(t) = A_{PF} \exp(-t/\tau_{PF}) + A_{DF} \exp(-t/\tau_{DF}) \quad (9)$$

The ratio of Φ_{DF}/Φ_{PF} can thus be simply calculated by integrating the PF and DF components, as shown in equation 10.

$$\Phi_{DF} / \Phi_{PF} = A_{DF} \tau_{DF} / A_{PF} \tau_{PF} \quad (10)$$

A second method to determine Φ_{DF}/Φ_{PF} ratio is to use steady-state fluorescence data, and the second method could be much better precise than the first. In view of the fact that the presence of oxygen intensely quenches triplet excited states and generally, the delayed fluorescence is reduced in non-degassed

solution/films, based on the oxygen sensitivity of the host. As a result, intrinsic steady-state fluorescent spectra are proportional to Φ_{PF} obtained in air-equilibrated conditions. Furthermore, both prompt and delayed fluorescence contributes to overall emission in degassed conditions. Thus, in degassed conditions, the integral of the emission spectrum is proportional to the sum $\Phi_{PF} + \Phi_{DF}$.

After determining the Φ_{DF}/Φ_{PF} ratio, the triplet yields is obtained from equation 7. The intersystem crossing rate (k_{ISC}), radiative rate constant (k_F), and internal conversion rate (k_{IC}) are all readily calculated by using fluorescence quantum yield and equations 8, 11 and 12.²³

$$k_{ISC} = \Phi_{ISC}/\tau_{PF} = \frac{1}{\tau_{PF}} \frac{\Phi_{DF}}{\Phi_{PF} + \Phi_{DF}} \quad (11)$$

$$= \frac{1}{\tau_{PF}} - (k_f + k_{isc}) \quad (12)$$

1.2.3.3 Reverse Intersystem Crossing Rate Constant (k_{rISC})-

For photophysical characterisation of TADF molecules, calculating the reverse intersystem crossing rate constant (k_{rISC}) is undoubtedly very important. Keeping fluorescence decay of TADF molecules in equation 9 provides A_{DF} , A_{PF} , τ_{PF} and τ_{DF} . Since $k_{rISC} \tau_{PF} \ll 1$ is usually examined and reverse intersystem crossing rate constant (k_{rISC}) can be measured with the help of equations 13 or 14.³⁶

$$k_{ISC} = \frac{1}{\tau_{DF}} \frac{\Phi_{rISC}}{1 - \Phi_{ISC} \Phi_{rISC}} = \frac{\Phi_{rISC} (\Phi_{PF} + \Phi_{DE})}{\tau_{DF} \Phi_{PF}} \quad (13)$$

If $\Phi_{rISC} \approx 1$, equation 14 improves to equation 15.

$$k_{rISC} = \frac{1}{\tau_{DF}} \frac{1}{1 - \Phi_{ISC}} = \frac{1}{\tau_{DF}} \left(\frac{\Phi_{PF} + \Phi_{DE}}{\Phi_{PF}} \right) \quad (14)$$

1.2.3.4 Temperature Dependence of TADF-

By measuring the temperature-dependent fluorescence decay, rate of reverse intersystem crossing can be determined. The energy gap associated with the reverse intersystem crossing mechanism is estimated by using an Arrhenius type plot of k_{rISC} by utilizing temperature-dependent decay and equation 1. The energy gap related to TADF is usually identical to the S_1 and T_1 energy gap, which is easily measured using S_1 and T_1 energies determined from fluorescence and phosphorescence spectra.

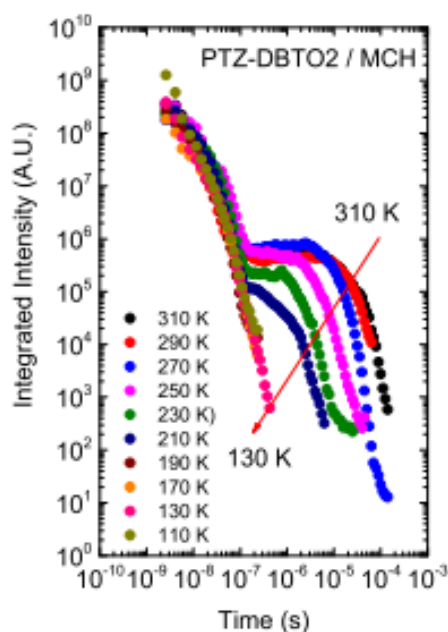


Figure 1.2.5. Fluorescence decay of **PTZ-DBTO2** in MCH, as a function of temperature. (Reproduced with permission from ref. 25 Copyright, 2016, Published by John Wiley and Sons, WILEY-VCH).

For proving the TADF mechanism, the temperature-dependent DF is also important to prove that the DF is because of the TADF mechanism. In the case of the TADF mechanism, when temperature increases, the intensity of DF also will increase, which will appear in time-resolved data as decay or integrated DF. Figure 1.2.5 indicates that in the temperature-dependent fluorescence decay of **PTZ-DBTO2**, the PF decay is unaffected by temperature, whereas the delayed

fluorescence perceives temperature change which is compatible with a thermally activated mechanism responsible for the delayed emission.²⁵

The most difficult part is to calculate Φ_{ISC} once Φ_{DF}/Φ_{PF} ratio is not big and below 3. In such cases, $\Phi_{ISC} \approx 1$ can't be presumed, and a fitting approach has to be applied to estimate Φ_{ISC} . Nonetheless, Berberan-Santos and co-workers^{38,39} described in detail methods to determine Φ_{ISC} . The most suitable way is mentioned in equation 15, where τ_p^0 is a temperature-dependent phosphorescence lifetime where rISC is not active.

$$\tau_{DF} = \tau_p^0 - \left(\frac{1}{\Phi_{ISC}} - 1\right) \tau_p^0 \frac{\Phi_{DF}}{\Phi_{PF}} \quad (15)$$

With the help of equation 16, τ_p^0 and Φ_{ISC} are able to calculate from linear plot of τ_{DF} Vs Φ_{DF}/Φ_{PF} , acquired at various temperatures.³⁸ The reverse intersystem crossing rate constant is then calculated using equation 16, which is stated a little differently than equation 15.

$$k_{ISC} = \frac{1}{\tau_{DF} \Phi_{ISC}} \left(\frac{\Phi_{DF}}{\Phi_{PF}}\right) \quad (16)$$

1.2.3.5 Dependence of TADF with Excitation Dose-

Along with temperature dependency, the variability of the DF integrated intensity with excitation dose is crucial in determining the intramolecular origin of the DF, and it is helpful to distinguish between the TADF and TTA.³⁷ The DF intensity varies with excitation dose in the context of TTA because of a conflict between the rate of collisional quenching of triplets (k_{TTA}) and with the rate of monomolecular decay of triplet states ($k_{PH} + k_{IC}^T$) that is influenced by diffusion, that means, the triplets are deactivated quicker than they are annihilated., the DF due to TTA display a quadratic dependence, and TADF has a linear dependence

with excitation dose. Nevertheless, when TTA dominates, the dependence changes to a linear regime with larger triplet concentrations.^{40,41} In fact, generated DF in the TADF mechanism is exclusively intramolecular, so TADF intensity changes linearly with the excitation dose. Figure 1.2.6 shows such a type of dependence.^{22,23,25,37}

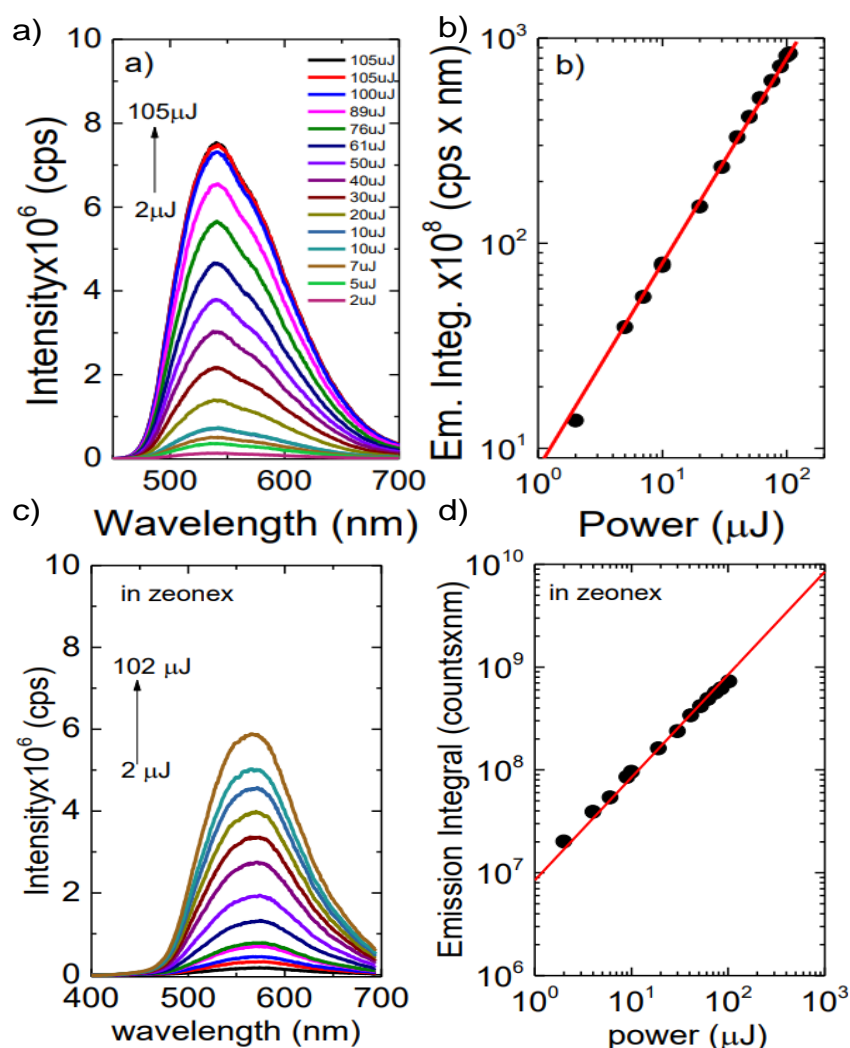


Figure 1.2.6. a) Power-Intensity dependence delayed fluorescence of the **DPTZ-DBTO2** in MCH solution, b) DF intensity linear fit of **DPTZ-DBTO2** as a function of excitation power (*Reproduced with permission from ref. 23. Copyright, 2006, Published by John Wiley and Sons, WILEY-VCH.*

However, a mixture of TADF and TTA has been found in some cases.⁴² Those are demonstrated through the power dependences of the emission intensity

having slopes between 1 and 2. It happens largely in molecules wherein an rISC rate constant will not be quick enough to entirely evacuate the triplet population before annihilating via TTA and is normally caused by the captivity of triplets by host.

1.2.4 Organic TADF Emitters and Applications

1.2.4.1 Diphenyl Sulfone Based TADF Emitters-

Diphenyl sulfone is a prominent acceptor in the development of blue-emissive TADF materials. The electron accepting ability of the diphenyl sulfone is due to the presence of oxygen atoms which is highly electronegative. Furthermore, the diphenyl sulfone group contains a tetrahedral shape, and sulphur has an isolating character, subsequently blocking the conjugation within a molecule.⁴³ Because of this, researchers aim to design TADF emitters of the electron-accepting DPS group. In 2012, Adachi and co-workers published TADF emitters based on blue emissive DPS (**11-13**).⁴⁴ The molecular structures of **11-13** are mentioned in Scheme 1.2.2, while Table 1.2.1 shows related OLED characteristics.

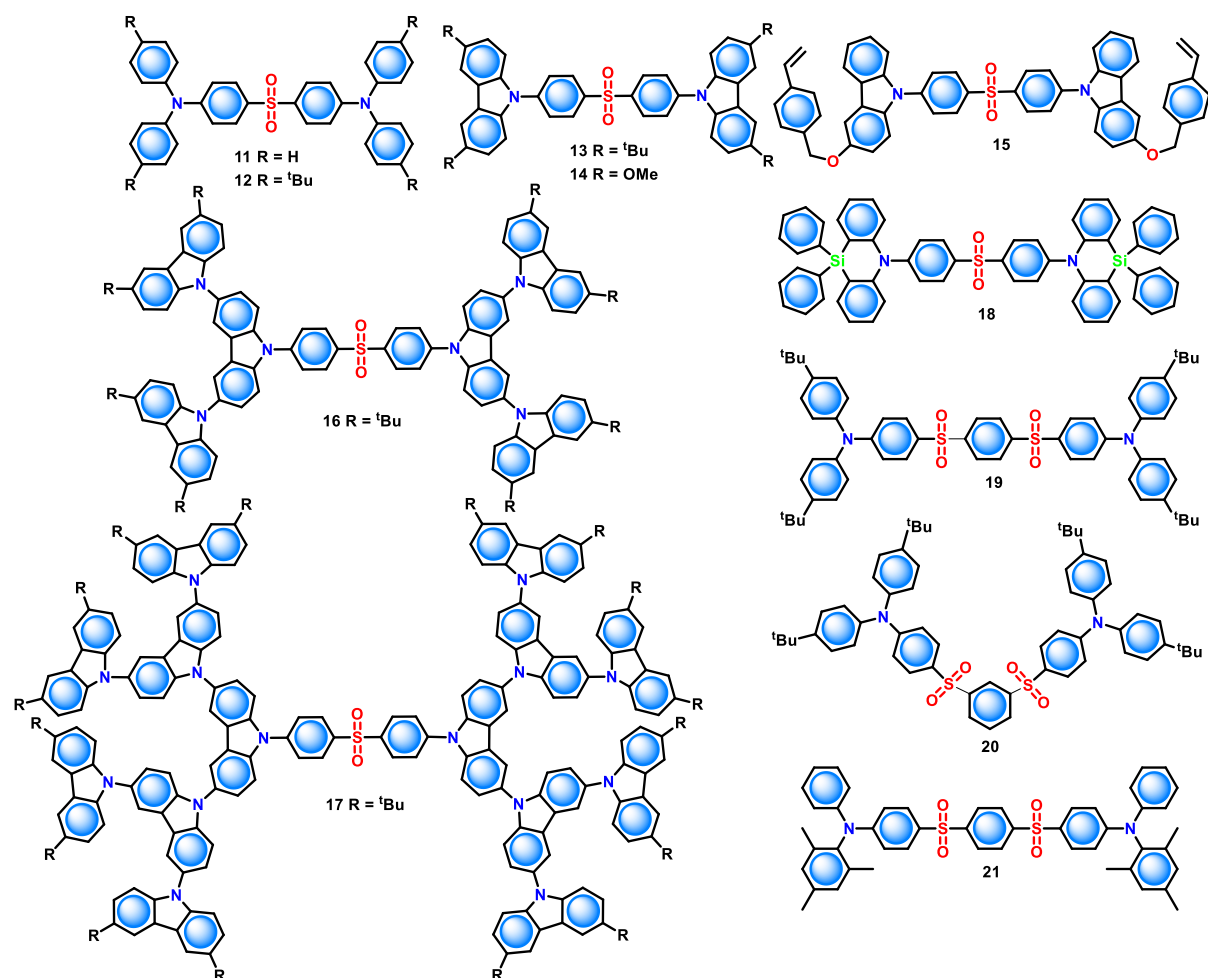
The D-A-D arrangement has been adapted for all of the compounds, where diphenylamine moiety acts as the electron donor in **11** and **12**. In example **13**, the donor is the carbazole group. Based on the fluorescence spectra, their triplet states might be localised on donor groups and attributed to $^3\pi-\pi^*$ transitions. The ΔE_{ST} energy for **11** is 0.54 eV, **12** is 0.45 eV and for **13** is 0.32 eV, respectively. Greater electron-donating characteristics of the **12** relative to **11** were observed after the incorporation of bulky tert-butyl groups on the diphenylamine unit, which shows a red-shift in the CT band shifting to the visible range and reducing CT energy as well as ΔE_{ST} . Destabilization of $^3\pi-\pi^*$ state in **13** was demonstrated when the diphenylamine donor was replaced with the carbazole group, and upon keeping carbazole as a strong donor, a further increase in energy level and decrease in

ΔE_{ST} of molecule **13** was observed. With evidence of TD-DFT computational calculations, larger HOMO-LUMO orbital spacing was observed in **13** with respect to **11** and **12** because of the higher dihedral angle of **13**, which is 49° compared to 32° for **11** and **12**, which results in the decrease of ΔE_{ST} . When multilayer OLEDs were fabricated and employed as dopants, optimum EQEs for **11-13** were 2.9% EQE of **11** < 5.6% EQE of **12** < 9.9% EQE of **13**, respectively. The best EQE procured for OLED is based on **13**, at a high current density, with low-efficiency roll-off for OLED devices. To get a better of efficiency roll-off, emitter **14** was developed by substituting methoxy groups selected for improved electron-donating ability.⁴⁵ Upon inserting methoxy group, ΔE_{ST} reduced by 0.32 eV to 0.21 eV from **13** to **14**, resulting in a decrease in TADF lifetime along with efficiency roll-off. By methoxy addition, the S_1 and T_1 states of **14** could be lower than those of **13**, thus lowering ΔE_{ST} . As a benefit to OLEDs, a delayed lifetime of **14** was estimated to be 93 μ s, which is significantly lesser than **13**, which was 270 μ s. Using an identical device structure and manufacturing condition, the OLED based on **14** achieved a high EQE of 14.5% with a low-efficiency roll-off. The enhancement of OLED performance is because of narrow ΔE_{ST} and lesser TADF lifetime.

Furthermore, Sun and co-workers⁴⁵ proposed **15**, a solution-processable and thermally cross-linkable version of **14**. Although the approach looks viable for addressing stability difficulties, the device efficiencies of 15-based OLEDs were still lower than those of OLEDs made by vacuum-processed, with an EQE of just close to 2.0%. The selection of a host matrix with a higher energy gap is important for TADF emitters having small molecules to prevent quenching of emission of device.⁴⁶ Such OLED doping method may be the cause of insufficient hole and electron injection into an emitting layer.⁴⁷ Moreover, it is necessary to make a less complicated structure, low fabrication costs, and relevant management of doping concentration. Therefore, creating reliable TADF emitters exhibiting

reduced ΔE_{ST} values and solution processability in non-doped devices is essential. To address such issues, Li and co-workers⁴⁸ developed new TADF emitters using sulfone-based dendrimers (**16-17**, Scheme 1.2.2). Dendrimers revealed many advantages compared to monomeric sulfone-based precise molecular structure, specifically tunable molecular diameter and occupied molecular connections.^{49,50} However, dendrimers having TADF showing greenish-blue or green emissions employed in the fabrication for OLEDs with non-doped solution-processed method with satisfactory electroluminescent results.⁵¹⁻⁵⁴ The TADF emitters **16** and **17** were blue-emitting and had similar triplet energy levels of **13**, but better in smaller ΔE_{ST} to facilitate the RISC process. Authors explored such dendrimers in the development of blue-emitting OLED devices by a solution-processed non-doped method having small roll-off efficiency with higher current density. **16**-based OLEDs as non-doped solution-processed blue-emitting OLED devices showed 4.1 cd/A CE. Similarly, the OLED device based on **17** showed minor roll-off efficiency with greater current density.

Sun *et al.* employed azasiline as an electron donor in concert with DPS to synthesize compound **18**, which shows push-pull effect having deep blue emission with CIE coordinates 0.15, 0.11.⁵⁵ Azasiline contains a six-membered core ring, which allows to induce the blockage without resorting to substitution. As a result, azasiline is a suitable donor unit for building TADF materials. Currently, a significantly less number of literature reports based on azasiline-based TADF emitters are available. Sun *et al.*⁵⁵, showed that the extremely distorted structure of **18** helped to lower ΔE_{ST} , enhancing colour purity with improving the performance of electroluminescent devices. A deep blue emitting OLED employing **18** with colour coordinates of (0.15, 0.11) and resulting low EQE of 2.3%.



Scheme 1.2.2. Diphenylsulfone-based (**11-18**) and bis(phenylsulfonyl)benzene-based (**19-21**) TADF emitters.

Later, Liu et al. reported an interesting approach that consists of one and/or more DPS groups in TADF materials.⁵⁶ The electrical parameters are finely controlled while maintaining a broad bandgap and a large triplet energy level by increasing the number of acceptors and adjusting the connectivity among donors and acceptors. Liu et al. effectively synthesized two blue TADF molecules **19-20** containing bis(phenylsulfonyl)benzene group with extremely low ΔE_{ST} through the covalent bonding of interchanged carbazoles (Scheme 1.2.2). Both theoretical and experimental data indicate that adding bis-sulfone units in TADF molecule could significantly minimise ΔE_{ST} relative to structures with a mono-sulfone linker (**13**). However, the authors further demonstrate that molecule **19**, having *p*-substitution induces a bathochromic shift in emission and

electroluminescent properties of **19** shown greater than **20**. In contrast to the prior estimate of 0.32 eV for **13**, the ΔE_{ST} values for **19** was 0.05 eV and 0.24 eV for **20**. The values obtained using DFT are consistent with those found experimentally, and lower values of ΔE_{ST} demonstrate the viability of the design approach for creating TADF emitters with minimal energy splitting. Devices based on **20** generated a blue colored EL having CIE values of 0.15, 0.08, with high CE = 4.4 cd A⁻¹, and EQE = 5.5%. The efficiency of devices based on **19** was more than **20**-based devices with EQE of 11.7% and higher CE of 19.4 cd A⁻¹. The authors attributed the above enhancement to the rISC process being made easier by the comparatively small ΔE_{ST} . Because of the faster ICT and a higher degree of coupling between HOMO and LUMO energy states in **19**, the red-shifted emission was observed, and an EL with sky-blue CIE coordinates of (0.18, 0.19) was found. Later, Jürgensen and co-workers reported a series of extremely soluble triarylamine/bis(phenylsulfonyl)benzene for printable OLEDs application and emitter **21** having the bluest emission shown in Figure 1.2.2.⁵⁷ Compound **21** showed a modest ΔE_{ST} as low as 0.32 eV and considerable steric barrier of the amine donor unit. Compound **21** shows deep-blue emission spanning from 436 to 466 nm with a low CIE value = 0.08. Using such TADF emitters in solution-processed OLEDs resulted in exceptional brightness of around 10,000 cd/m², CE of around 9.5 cd/A, and EQE of around 8.5%. In conclusion, it has been demonstrated that bis(phenylsulfonyl)benzene as an acceptor is an acceptable building block for creating TADF emitters that can be processed in solutions.

1.2.4.2 Triazine-Based TADF Materials-

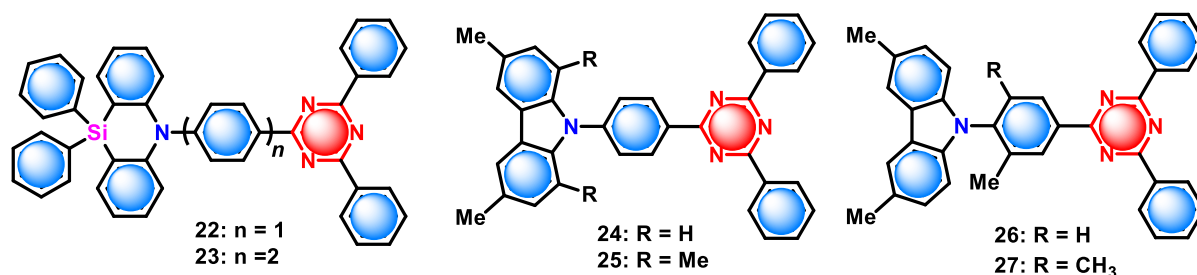
Along with diphenyl sulfone, triazine is a further extensively used acceptor component in the production of TADF materials. OLEDs using the azasiline donor/triazine acceptor (**22**, **23**) groups exhibited exceptional EQE = 22.3%.⁵⁸ As described in the last section, azasiline is a heterocycle compound having a six-

membered ring in which silicon is exchanged with a carbon atom. Thus, azasiline consequently has a lower HOMO energy level and a larger HOMO-LUMO energy gap than the analogous carbon-atom-containing compounds. As the silicon atom is sp^3 hybridised, different groups can be introduced onto the silicon bridge to increase the solubility, rigidify structure, and offer steric hindrance "on-demand".

Sun and co-workers synthesized triazine connected with azasiline moiety **22** and **23** (Scheme 1.2.3)⁵⁵. In terms of structure, **22** differs by π - conjugated bridged length from **23**. Emitter **22** has delayed luminescence of lifetime 25.4 μ s and ΔE_{ST} of 0.14 eV. OLEDs were fabricated by using **22** as the dopant and mCP:TSPO1 as co-host. EL was observed with emission at 463 nm, followed by slight roll-off efficiency. Further, Sun and co-workers modified the structure of **22** with a biphenyl bridge producing **23**. Upon keeping a biphenyl bridge between donor and acceptor, the HOMO and LUMO orbitals of **23** decreased as the distance between the donor and acceptor increased. Consequently, the ΔE_{ST} dramatically dropped to 0.04 eV (Table 1.2.1). OLEDs fabricated using **23** gives blue EL emission with an EQE = 4.7% and CIE = 0.15, 0.09.

A prominent electron donor used in the development of TADF emitters is carbazole. However, because carbazole has a centre 5-membered ring advancing the two peripheral aromatic rings, the steric barrier generated by a functional group can be significantly decreased. Several strategies have been proposed to address this problem, such as keeping a large appropriate dihedral angle to reduce electronic interaction with acceptor. The group of Adachi⁵⁹ synthesized a series of carbazole and triazine-containing molecules **24-27** (Scheme 1.2.3) with methyl groups substituted on carbazole (**24**, **25**) or on central phenyl bridge to assure steric hindrance (**26**, **27**).

DFT calculations showed that the dihedral angle for **24-27** varied as 49.9, 86.8, 71.4, and 82.4°, respectively. Interestingly, ΔE_{ST} shows entirely diverse behaviour (Table 1.2.1). Remarkably, the optical bandgap was significantly reduced when the hydrogen was replaced by methyl groups, which considerably altered the HOMO energy level and redox potential of the system also. On the other hand, the optical bandgap of carbazole remained unchanged when methyl substituents were inserted into the spacer, allowing emitters to keep their wide bandgap. As a result, molecule **24** has the flattest structure and showed the highest ΔE_{ST} in the experiment. The delayed lifetime for **25-27** was found to be 3.5, 13.0, and 10.3 μ s, respectively. Since there was no delayed contribution in its photoluminescence, **24**-based device provided an EQE of only 7.2%. This performance is significantly worse than that of devices fabricated using **25-27**, for which maximum EQEs of 22.0, 19.2, and 18.3%, respectively, were observed.

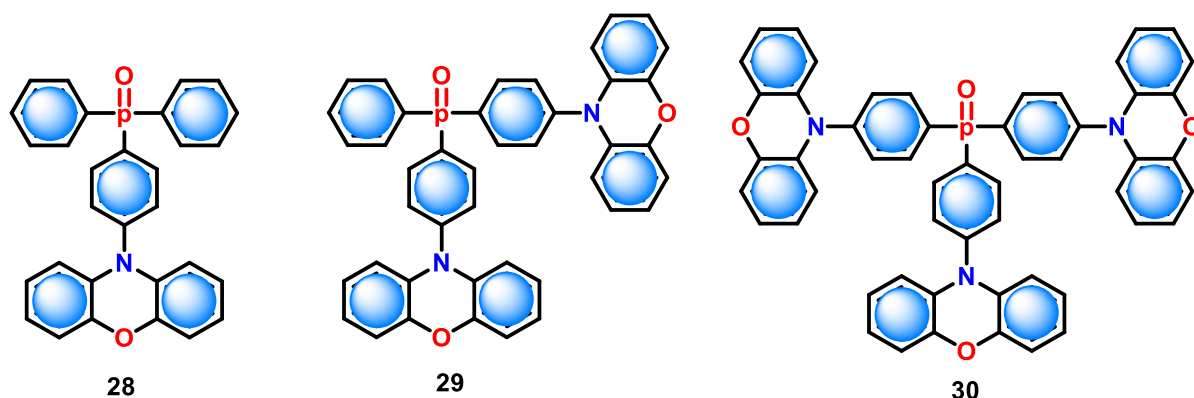


Scheme 1.2.3. Triazine-based (**22-27**) TADF emitters.

1.2.4.3 Phosphine Oxide Derivatives for TADF materials

The reported acceptors for TADF emitters are typically restricted to N-heterocycles, carbonyl, benzonitrile, and sulfone, limiting the versatility of molecular structures. Therefore, the advancement of the acceptors will be essential, and many extremely effective TADF molecules with innovative acceptor units, including phosphine oxides, will be emerged. In this direction, Duan, et al., connected a weak electron-withdrawing group triphenylphosphine oxide (TPPO) to the strong electron-donating group, which is a phenoxazine

(POZ). A series of strong donor-weak acceptor type emitters **28**, **29**, and **30** (Scheme 1.2.4) was synthesized and thus examined their photophysical properties.⁶⁰ It was interesting to note that the ratio of POZ to peak emission intensity was consistent. The three compounds showed PL spectra that were nearly identical, with reasonably high PLQYs of 45, 57, and 65% for **28** to **30**, respectively. The ΔE_{ST} values of **28-30**, 0.26, 0.19, and 0.11 eV were found to be in accordance with the TD-DFT values. According to these findings, fluorescence lifetimes of **28-30** improved from 8 ns to 13 ns to 20 ns. However, delayed contributions were noticed to be 95, 31, and 17 μ s for **28-30**, respectively. Simultaneously, the delayed quantum yields also rose from 36% for **28** to 45% for **29**, and to 51% for **30**, respectively. OLEDs fabricated using **29** gives blue EL at 460 nm, while OLEDs based on **30** emitted blue EL at 464 nm with an EQE =15.3%.



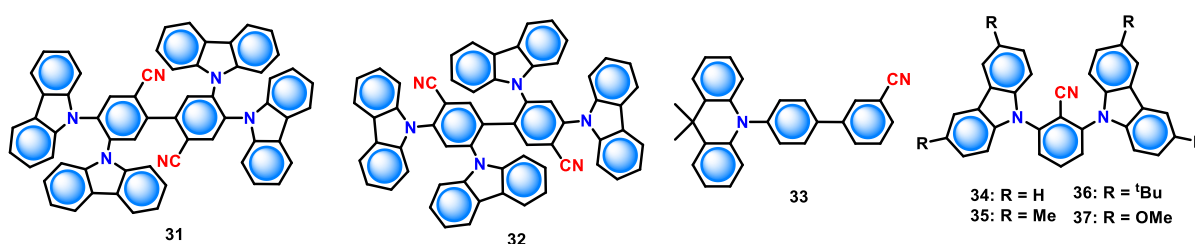
Scheme 1.2.4. Phosphine-oxide-based (**28-30**) TADF emitters.

1.2.4.4 Cyano and Benzonitrile Substituted TADF Emitters-

In search of additional acceptors, benzonitrile was found to be a viable candidate that could help to synthesize blue TADF molecules. The cyano group is one of the strongest electron-accepting groups available to chemists, and it precisely limits the shape of the acceptor group by its capacity. Cyano group as an acceptor and carbazole as a donor group involved in the production of effective TADF molecules. Cho and co-workers developed new TADF molecules using

the carbazole/cyano (donor-acceptor) combination, demonstrating a novel design strategy to enhance the colour purity and broad emission range of TADF molecules.⁶¹ The biphenyl core of compounds **31-33** shown in Scheme 1.2.5 contains a combination of electron-donating and accepting moieties. Comparing the rational structure of **32** against a model compound **31** indicated that an interconnecting donor structure is required for decreasing the FWHM and achieving deep-blue emission, along with high EQE. Although the geometrical structures of the two these compounds differ, both have a nearly similar ΔE_{ST} of 0.27 eV (Table 1.2.1).

The interlocking carbazole units' impact was visible in the PL of **31** and **32**. Molecule **32** exhibited a sharper PL spectrum than **31**. Compared to other TADF emitters, molecule **32** has a substantially reduced FWHM of 55 nm. The TADF emitter **31** has large FWHM (71 nm) than **32**, which means TADF emitter **32** exhibits a narrow emission spectrum. The newly constructed TADF molecule **32** worked as planned to produce OLED shows a deep-blue EL having FWHM of 48 nm with EQE = 14.0%.

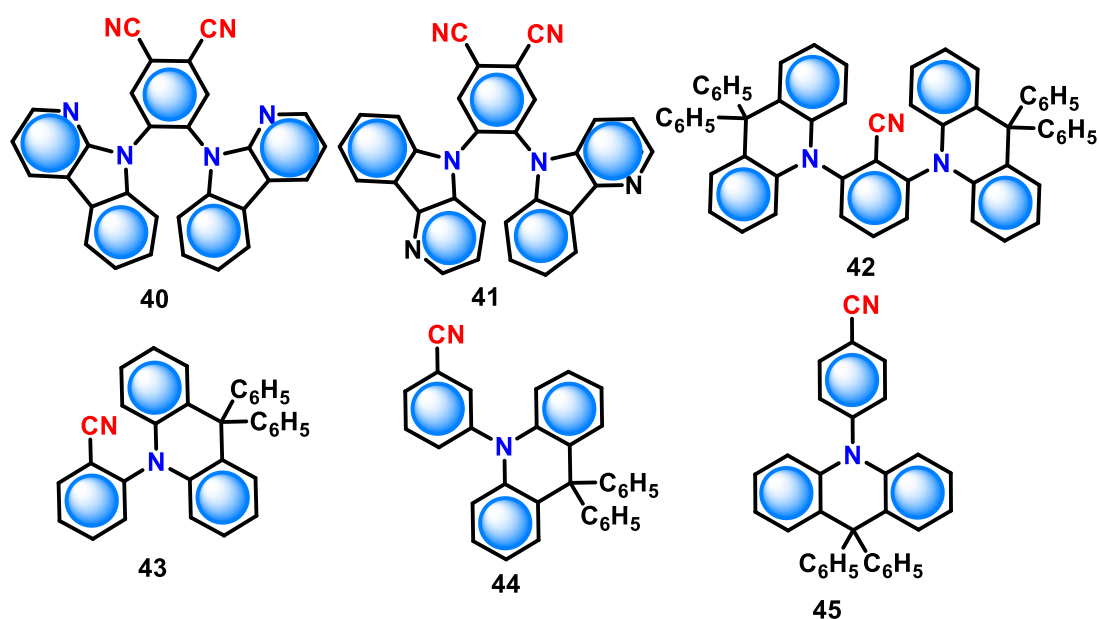


Scheme 1.2.5. Cyano-substituted TADF emitters (**31-37**).

Later, Pan *et.al.* showed cyano moiety as an acceptor while designing TADF emitter **33** (Scheme 1.2.5).⁶² OLED devices of **33** emitted deep blue light with a CIE of (0.16, 0.06). However, the OLED device showed EQE of roughly 1.6% because of its short TADF properties, including a high ΔE_{ST} = 0.40 eV and a low delayed lifetime = 0.01 μ s (Table 1.2.1). A rationalisation of the chemical design to generate a deep blue

colour emission combined carbazole as a donor and benzonitrile as an acceptor in TADF emitters **34-37**.⁶³ The four substituents hydrogen, methyl, *t*-Butyl, and methoxy were examined. The ΔE_{ST} was reduced from 0.31 eV to 0.14 eV by increasing the electron ability of molecules **34** to **37**. The TADF lifetimes of **34** to **37** are collectively decreased from 18 to 5.5 μ s, respectively. After fabricating OLEDs fabrication, deep-blue EL achieved, $\lambda_{EL} = 418$ nm for **34**, $\lambda_{EL} = 436$ nm for **35** and $\lambda_{EL} = 428$ nm for **36**. OLEDs based on **34** show 2.5% EQE, while OLEDs fabricated from **36** showed an improvement of EQE to 10.3%.

Molecules **40**, **41** having highly twisted structures were made by adding nitrogen at α - and δ -positions to the core nitrogen atom in carbazole-derived α - and δ -carboline.⁶⁵ This was accomplished by mixing benzonitrile with the carbazole group and adding a nitrogen atom to the donor (Scheme 1.2.6). Carbolines have been recently discovered as an electron-transport substance with significant triplet energy, which justifies the inclusion of carbolines in these two molecules. Even though adding heteroatoms to aromatic compounds can promote molecular relaxation, doing so will concurrently raise bandgap as well as triplet energy, which lowers the ΔE_{ST} .

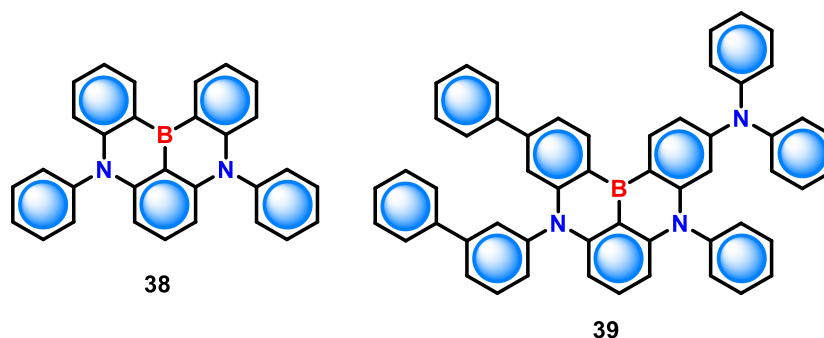


Scheme 1.2.6. Benzonitrile-based TADF emitters (**40-45**).

As an improvement of TADF materials, Adachi and co-workers reported four molecules with extremely twisted structures **42** to **45**, including the combination of a donor unit of 9,9-diphenylacridane linked to a central core of benzonitrile (Scheme 1.2.6).⁶⁶ In this case, the ΔE_{ST} values were almost the same for molecules **42** to **45** ($\Delta E_{ST} = 0.03$ eV), demonstrating that the substituting position seems to have no impact on the up-conversion capabilities. In addition, analysis of the PL spectra of **42** to **45** revealed that the meta-substituted **44** emits at 433 nm, while the para-substituted **45** emits at 428 nm, whereas the PL maxima for **42** and **43** were found to be at 454 and 441 nm, respectively. Thus, it was determined that the ortho-substitution maximised the π -conjugation, and adding two donor units to **42** enhanced the delayed emission intensity, leaving **42** as a good candidate for device testing. OLEDs fabricated using **42** produce blue EL at 463 nm with a high EQE = 15.9%.

1.2.4.5 Triarylborane-based TADF Emitters-

Boron-based TADF molecules have been the research subject over the past ten years, particularly in organic electronics. Many such materials have exceptional electron mobility due to the boron atom's unoccupied p-orbital. Bulkiness and strong electron-withdrawing properties are two other properties of triarylboron derivatives. An innovative method for developing better deep blue emitters, triarylboron-based molecules **38** and **39** (Scheme 1.2.7), was recently reported by Hatakeyama et al.⁶⁴



Scheme 1.2.7. Triarylborane-based (**38-39**) TADF emitters.

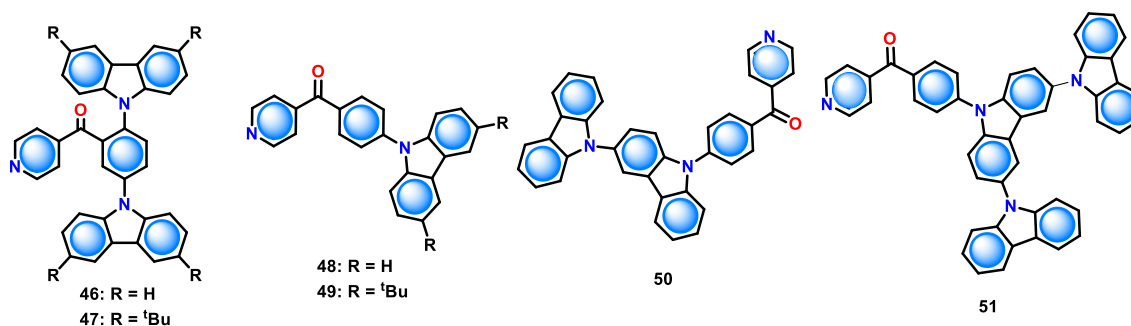
To achieve a pure blue emission, most commercially available OLEDs currently use a colour filter. By using a new design approach to reduce the materials' ΔE_{ST} without extending the PL peaks, Hatakeyama et al. overcame these problems by effectively separating HOMO-LUMO. The authors produced pure blue TADF molecules by using the multiple resonance effect. Molecule **38** depicted in Scheme 1.2.7 is made up of two triphenylamine acceptors fused to a triphenylboron donor. By lengthening the π -conjugated system and adding more electron donors, molecule **39** was created. According to DFT calculations, the HOMOs are localised on the triphenylamine portions, whereas the LUMOs are focused on the triphenylboron moiety. OLEDs fabricated based on **38** showed EL emission at 459 nm including narrow FWHM of 28 nm with EQE = 13.5%, whereas an enhanced OLED device performance was noticed for **39** showing emission at 467 nm with an EQE of 20.2% and FWHM of 28 nm.⁶⁴

1.2.4.6 Benzoylpyridine and Di(pyridinyl)methanone-Carbazole Derivatives-

One of the most potential candidates for OLED is the compounds containing acceptor group as phenyl(pyridin-4-yl)methanone because of efficient rISC and high PLQY. As a first report, the two carbazole donors were initially inserted into the acceptor's phenyl ring at *o*- and *m*-substitution as in **46** and **47** (Scheme 1.2.8).⁶⁷ The codoped films of **46** showed low $\Delta E_{ST} = 0.03\text{eV}$ and 88% PL efficiency whereas codoped films with **47** showed 0.04 eV and high PL efficiency 91.4%, respectively. These numbers are larger than those found for the two molecules in the solution, showing that thin films suppressed the interparticle and intra-molecular quenching. Nonetheless, the carbazole insertion arrangement significantly altered the emission wavelengths and adding tert-butyl substituents to **47** resulted in a bathochromic shift of about 20 nm. Repeated CV scans

revealed that **47** exhibited better electrochemical stability because the *tert*-butyl groups blocked the C₃ and C₆ positions. Notably, sky-blue emitting **46**-based OLEDs showed maximum efficiency of 24% with an EL peak wavelength of 488 nm.

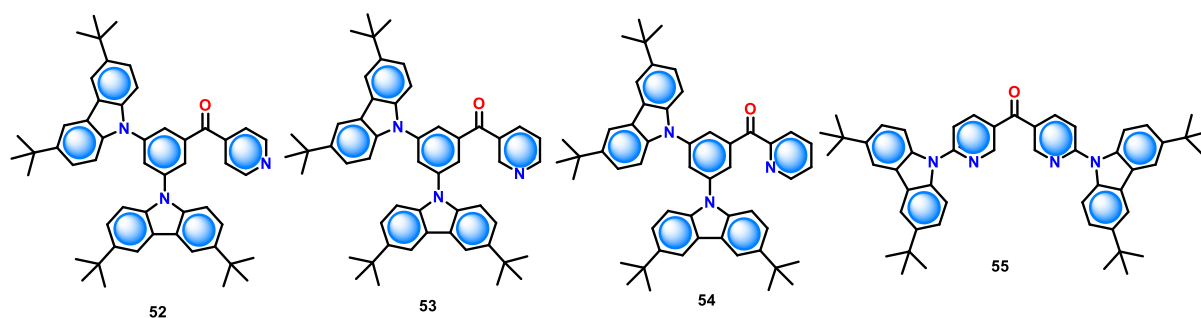
In 2016, the same authors altered their approach and merged all donors, replacing the previous D-A-D triads with D-A diads.⁶⁸ To fine-tune the ability to donate electrons, increasing the unit of carbazoles in the donor helps to minimize the ΔE_{ST} alongside increasing the carbazole group per donor and expanding the size of the donating component. Hence, consequently, ΔE_{ST} decreased from 0.29 to 0.07 to 0.05 eV for **48**, **50**, and **51**, which is compatible with higher HOMO and LUMO orbital separation and a wider molecular distribution of HOMO orbitals.



Scheme 1.2.8. Benzoylpyridine-carbazole derivatives based (**46-51**) TADF emitters.

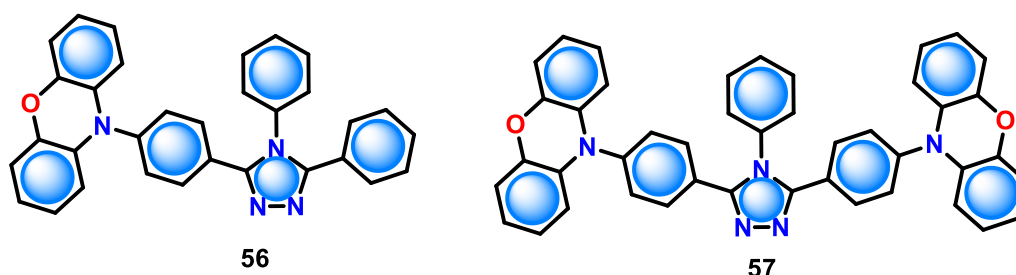
OLED employing **49** as emitter exhibited 9.4% EQE, and further optimisation of the device structure resulted in EQE of 18.4% for **48** based OLED device.⁶⁹ By changing the substitution of the N-atom in the pyridine group of **52-54**, the same authors created a sequence of three fluorescent compounds that were inspired by the structure of **47**.⁷⁰ All compounds had excellent PLQY in thin film ranging between 92 to 97%, as well as very low ΔE_{ST} for **52-54**. Despite these attractive photophysical properties, EL peaks for **52** to **54**-based devices occurred at 490, 476, and 490 nm, respectively. OLED fabricated using **52** to **54** showed

an increase in EQE of 2.1, 24.6, and 28.0%, respectively (Table 1.2.1). In 2017, Cheng et al. reported a highly efficient pure blue TADF emitter containing pyridines groups in bis(6-(3,6-di-tert-butyl-9H-carbazol-9-yl)pyridin-3-yl)methanone (**55**),⁷¹ which are nearly planar with very small ΔE_{ST} and within the co-doped emissive layer, encouraging horizontal molecular orientation. OLEDs manufactured using **55** show EL of 464 nm and achieved a high EQE = 32% despite a comparatively low dopant concentration.



Scheme 1.2.9. Benzoylpyridine and di(pyridinyl)methanone-carbazole derivatives based (**52-55**) TADF emitters.

1.2.4.7 Triazole Derivatives-



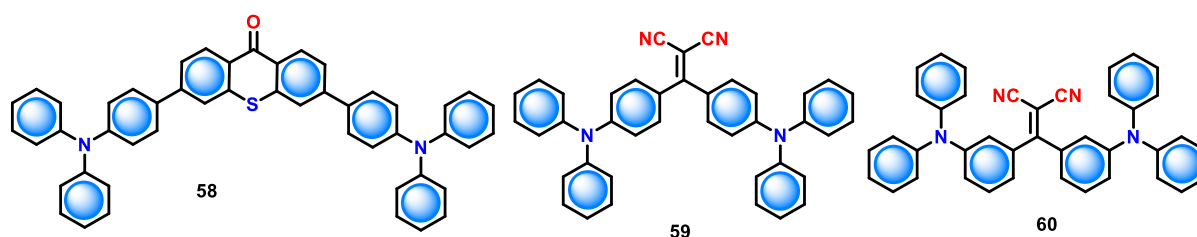
Scheme 1.2.10. Triazole-based (**56** and **57**) TADF emitters.

In addition to being an excellent electron acceptor and outstanding electron-transport material, 3,4,5-triphenyl-4H-1,2,4-triazole is used in several TADF molecules, spanning from charge-transport to OLED materials. Rationally, an electron-donor phenoxazine in combination with 3,4,5-triphenyl-4H-1,2,4-triazole produce TADF emitters when it is appropriately connected, and these

molecules were firstly described in 2013 as shown in Figure 19.⁷² By comparing structures **56** and **57** shown in Scheme 1.2.10, **57** is more luminescent than **56** because of the presence of extra phenoxazine moiety. The PLQYs of **56** is 29.8%, whereas it varied to 43.1% for **57**. The OLED device made with highly luminescent **57** shows sky-blue EL emission ($\lambda_{EL} = 456$ nm) with an EQE of around 6.4%.

1.2.4.8 Triphenylamine Derivatives-

Triphenylamine seems to be a unique electron-donating molecule that has been used in various research areas, including organic photovoltaics and OLEDs. Triphenylamine moieties connected to the thioxanthone core were prepared by Kim and coworkers. Molecule **58** containing triphenylamine units on 9H-thioxanthen-9-one displayed blue PL (Scheme 1.2.11). Theoretical calculations demonstrated a small HOMO/LUMO overlap due to this particular substitution. The PLQY reached 35% in neat or doped films state under ambient conditions, despite the symmetrical substitution on **58**. Utilizing an emissive layer with minimum loading concentration of 1 wt% in a conventional device stacking, OLEDs achieved a high EQE value = 23.7%. In 2017, Kim and co-workers used malononitrile as an electron acceptor in the TADF emitters to produce blue OLEDs.⁷³ The emitting material's molecular orientation is crucial for optimising the electroluminescent properties. If the molecules are horizontally aligned, light-outcoupling effects can be produced that can boost external efficiency by up to 46%.^{74,75} In this study, **59** and **60** share comparable ΔE_{ST} and PL characteristics. However, significant discrepancies were noticed when these two materials were used to fabricate OLEDs. Notably, the current efficiency of **60**-based OLEDs was around nine times higher than that of **59**-based OLEDs. The excellent horizontal alignment of **60** in doped films, in contrast to the poor crystallinity and irregular orientation of **59**, helps to explain these differences and justifies the improved performance of **60**-based devices.



Scheme 1.2.11. Triphenylamine-based TADF emitters (58-60).

Table-1.2.1 TADF emitters with OLED characterization-

TADF Emitter	ΔE_{ST} (eV)	τ_d (μ s)	PE (Lm/w)	EQE (%)	Reference
11	0.54	90.0	n/a	2.9	44
12	0.45	140.0	n/a	5.6	44
13	0.32	270.0	n/a	9.9	44
14	0.21	93.0	n/a	14.5	45
15	0.31	50.0	n/a	2.0	45
16	0.25	464.0	1.6	n/a	48
17	0.17	814.0	0.49	n/a	48
18	0.07	n/a	n/a	2.3	55
19	0.05	1.23	n/a	11.7	56
20	0.24	1.16	n/a	5.5	56
21	0.42	70.0	3.2	8.5	57
22	0.14	25.4	30.4	22.3	58
23	0.04	n/a	n/a	4.7	55
24	0.43	n/a	n/a	7.2	59
25	0.07	3.5	n/a	22.0	59
26	0.17	13.0	n/a	19.2	59
27	0.15	10.3	n/a	18.3	59

28	0.26	95.0	7.6	6.3	60
29	0.19	31.0	16.9	10.6	60
30	0.11	17.0	23.6	15.3	60
31	0.27	24.34	n/a	4.8	61
32	0.27	48.22	n/a	14.0	61
33	0.40	0.01	0.8	1.6	62
34	0.31	18.0	0.6	2.5	63
35	0.22	11.2	2.7	7.7	63
36	0.36	13.5	3.5	10.3	63
37	0.14	5.50	19.0	19.0	63
38	0.013	93.7	8.3	13.5	64
39	0.041	65.3	15.1	20.2	64
40	0.28	57	n/a	4.2	65
41	0.13	180	n/a	22.5	65
42	0.02	n/a	n/a	15.9	66
46	0.03	0.6	n/a	24.0	67
47	0.04	1	n/a	27.2	67
48	0.29	n/a	n/a	4.2	68
49	0.07	n/a	n/a	11.0	68
50	0.05	0.65	n/a	23.9	68
51	0.13	n/a	n/a	9.4	68
52	0.01	18	n/a	28.1	70
53	0.05	7.3	n/a	24.6	70
54	0.02	6.9	n/a	28.0	70
55	0.02	0.27	n/a	31.9	71

56	n/a	0.016	n/a	n/a	72
57	0.03	28.88	n/a	6.4	72
58	0.38	n/a	n/a	23.7	73
59	0.114	10	n/a	1.38 cd/A	73
60	0.098	10	n/a	12.62 cd/A	73

1.2.5 Future Perspective

The above-described section summarizes the recent progress of TADF molecules and the photophysical characterization of these molecules. At the moment, having an extension of electron donor and acceptor combination along with interruption of π -conjugation for producing orthogonality between donor and acceptor in small organic molecules showed efficient TADF with high PLQY. The development of the TADF phenomenon triggered a turning point in the field of OLEDs because TADF molecules are able to achieve 100% internal electroluminescent quantum efficiency by converting non-emissive triplet excitons to emissive in OLEDs. The present research focus on TADF molecules is still on OLED applications. Despite the fact that understanding the photophysics of these systems is still in its early stages, new applications in sensing and biological imaging are currently being investigated. In the upcoming years, a fundamental mechanical understanding, especially by using improved photophysical techniques, will undoubtedly emerge, inspiring creative applications.

Organic TADF materials having emission blue and green colours have been mainly reported, and the red emissive TADF materials are rare for metal-free systems. The availability of red or NIR emissive TADF systems will allow researchers to investigate the use of TADF materials in biological applications.

In recent years, organic TADF materials for flexible display and lighting applications have seen a boom in development. In the case of emissive molecules in solution, the emission for thin films will be altered due to emission quenching by aggregation or photo-bleaching. As a result, novel emitters with higher processability and luminescent properties are required for technologically advanced lighting and display applications. In this regard, solvent-free organic liquids (SOLs) have been extensively researched as a new soft material that can address the aforementioned challenges to some extent.

1.2.6 Conclusion

To summarise, various strategies are now being investigated to generate TADF emitters. The following points obtained from the above-mentioned studies results can serve as a guide to design TADF molecules; (1) Orthogonality between the donor and acceptor to prevent π -conjugation and reduce the connection between the two components, (2) Necessity to keep proximity between the donor and acceptor to avoid proper separation of the donor and acceptor, (3) Extending electron donor and/or electron acceptor π -conjugated system to enhance oscillator strength to increase PLQY, (4) Optimize the rate of reverse intersystem crossing by minimising ΔE_{ST} , (5) Design of OLED materials having a delayed component of TADF lifetime as short as feasible to avoid the issue of excited states annihilation, (6) A precise selection of the linkage built between the electron donor and/or electron acceptor units, as evidenced by the variation in EL performances for materials changing by substitutions (*ortho*-, *meta*- and *para*-position of aromatic rings). TADF materials continue to excite the scientific community with excellent features suitable for efficient OLED devices. The dedicated searches for new efficient candidates improve the performance of the lighting and display devices.

1.2.7 References

1. Dias, F. B., Penfold, T. J. and Monkman, A. P., *Methods Appl. Fluoresc.* 2017, **5**, 012001.
2. Perrin, F., *Ann. Phys. (Paris)*, 1929, **12**, 169-275.
3. Lewis, G. N., Lipkin, D. and Magel, T. T., *J. Am. Chem. Soc.* 1941, **63**, 3005-3018.
4. Parker, C. A. and Hatchard, C. G., *Trans. Faraday Soc.* 1961, **57**, 1894.
5. Parker, C. A. and Joyce, T. A., *Chem. Commun. (London)*, 1968, 1422.
6. Wilkinson, F. and Horrocks, A. R. Phosphorescence and delayed fluorescence of organic substances *Luminescence in Chemistry* ed E. J. Bowen *et al* (Van Nostrand: London) 1968, 116-53.
7. Uoyama, H., Goushi, K., Shizu, K., Nomura, H. and Adachi, C., *Nature*, 2012, **492**, 234-238.
8. Forrest, S. R., Baldo, M. A., O'Brien, D. F., You, Y., Shoustikov, A., Sibley, S. and Thompson, M. E., *Nature*, 1998, **395** 151-154.
9. Schmidbauer, S., Hohenleutner, A. and Konig, B., *Adv. Mater.* 2013, **25**. 2114-2129.
10. Volz, D., Wallesch, M., Flechon, C., Danz, M., Verma, A., Navarro, J. M., Zink, D. M., Bräse, S. and Baumann, T., *Green Chem.* 2015, **17**, 1988-2011.
11. Czerwieniec, R. and Yersin, H., *Inorg. Chem.* 2015, **54**, 4322-4327.
12. Leitl, M. J., Zink, D. M., Schinabeck, A., Baumann, T., Volz, D. and Yersin, H., *Top. Curr. Chem.* 2016, **374**, 1-34.
13. Kondakov, D. Y., Pawlik, T. D., Hatwar, T. K. and Spindler, J. P., *J. Appl. Phys.* 2009, **106**, 124510.
14. Chiang, C. J., Kimyonok, A., Etherington, M. K., Griffiths, G. C., Jankus, V., Turksyoy, F. and Monkman, A. P., *Adv. Funct. Mater.* 2013, **23**, 746.
15. King, S. M., Cass, M., Pintani, M., Coward, C., Dias, F. B., Monkman, A. P. and Roberts, M., *J. Appl. Phys.* 2011, **109**, 74502.
16. Li, W., Liu, D., Shen, F., Ma, D., Wang, Z., Feng, T., Xu, Y., Yang, B. and Ma, Y., *Adv. Funct. Mater.* 2012, **22**, 2797-2803.
17. Li, W., Pan, Y., Xiao, R., Peng, Q., Zhang, S., Ma, D., Li, F., Shen, F., Wang, Y., Yang, B. and Ma, Y., *Adv. Funct. Mater.* 2014, **24**, 1614.
18. Tao, Y., Yuan, K., Chen, T., Xu, P., Li, H., Chen, R., Zheng, C., Zhang, L. and Huang, W., *Adv. Mater.* 2014, **26**, 7931-7958.
19. Zhang, D., Cai, M., Zhang, Y., Zhang, D. and Duan, L., *Mater. Horiz.* 2016, **3**, 145-151.

20. dos Santos, P. L., Ward, J. S., Bryce, M. R. and Monkman, A. P., *J. Phys. Chem. Lett.* 2016, **7**, 3341-3346.
21. Kim, H. M., Choi, J. M. and Lee, J. Y., *RSC Adv.* 2016, **6**, 64133-64339.
22. Dias, F. B., Bourdakos, K. N., Jankus, V., Moss, K. C., Kamtekar, K. T., Bhalla, V., Santos, J., Bryce, M. R. and Monkman, A. P., *Adv. Mater.* 2013, **25**, 3707-3714.
23. Dias, F. B. *et al.*, *Adv. Sci.* 2016, **3**, 1600080.
24. Penfold, T. J., *J. Phys. Chem. C* 2015, **119**, 13535-13544.
25. Nobuyasu, R. S., Ren, Z., Griffiths, G. C., Batsanov, A. S., Data, P., Yan, S., Monkman, A. P., Bryce, M. R. and Dias, F. B., *Adv. Opt. Mater.* 2016, **4**, 597-607.
26. Turro, N. J., Scaiano, J. C. and Ramamurthy, V., *Principles of Molecular Photochemistry: An Introduction*, 2010. (Mill Valley, CA: University Science Books).
27. Milián-Medina, B. and Gierschner, J., *Org. Electron.* 2012, **13**, 985-991.
28. Marini, A., Munoz-Losa, A., Biancardi, A. and Mennucci, B., *J. Phys. Chem. B* 2010, **114**, 17128-135.
29. Grabowski, Z. R., Rotkiewicz, K. and Rettig, W., *Chem. Rev.* 2003, **103**, 3899-4031.
30. Dias, F. B., Pollock, S., Hedley, G., Pålsson, L.-O., Monkman, A., Perepichka, I. I., Perepichka, I. F., Tavasli, M. and Bryce, M. R., *J. Phys. Chem. B* 2006, **110**, 19329-19339.
31. Chen, T., Zheng, L., Yuan, J., An, Z., Chen, R., Tao, Y., Li, H., Xie, X. and Huang, W., *Sci. Rep.* 2015, **5**, 10923.
32. Rajamalli, P. *et al.*, *J. Am. Chem. Soc.* 2016, **138**, 628-634.
33. Zhang, Q., Kuwabara, H., Potscavage, W. J., Huang, S., Hatae, Y., Shibata, T. and Adachi, C., *J. Am. Chem. Soc.* 2014, **136**, 18070-18081.
34. Valchanov, G., Ivanova, A., Tadjer, A., Chercka, D. and Baumgarten, M., *J. Phys. Chem. A* 2016, **120**, 6944-6455.
35. Kim, M., Jeon, S. K., Hwang, S. H., Lee, S. S., Yu, E. and Lee, J. Y., *J. Phys. Chem. C* 2016, **120**, 2485-2493.
36. Baleizao, C. and Berberan-Santos, M. N., *J. Chem. Phys.* 2007, **126**, 204510.
37. Dias, F. B., *Phil. Trans. R. Soc. A* 2015, **373**, 20140447.
38. Baleizao, C. and Berberan-Santos, M. N., *Chem Phys Chem.* 2011, **12**, 1247-1250.

39. Berberan-Santos, M. N. and Garcia, J. M. M., *J. Am. Chem. Soc.* 1996, **118**, 9391-9394.
40. Hertel, D., Bässler, H., Guentner, R. and Schert, U., *J. Chem. Phys.* 2001, **115**, 10007-10013.
41. Jankus, V., Snedden, E. W., Bright, D. W., Whittle, V. L., Williams, J. A. G. and Monkman, A., *Adv. Funct. Mater.* 2013, **23**, 384-393.
42. Jankus, V., Data, P., Graves, D., McGuinness, C., Santos, J., Bryce, M. R., Dias, F. B. and Monkman, A. P., *Adv. Funct. Mater.* 2014, **24**, 6186.
43. Li, Y., Wang, Z., Li, X., Xie, G., Chen, D., Wang, Y.-F., Lo, C.-C., Lien, A., Peng, J. and Cao, Y., *Chem. Mater.* 2015, **27**, 1100-1109.
44. Zhang, Q., Li, J., Shizu, K., Huang, S., Hirata, S., Miyazaki, H. and Adachi, C., *J. Am. Chem. Soc.* 2012, **134**, 14706-14709.
45. Sun, K., Xie, X., Liu, Y., Jiang, W., Ban, X., Huang, B. and Sun, Y., *J. Mater. Chem. C* 2016, **4**, 8973-8979.
46. Wang, H., Xie, L., Peng, Q., Meng, L., Wang, Y., Yi, Y. and Wang, P., *Adv. Mater.* 2014, **26**, 5198-5204.
47. Hu, J.-Y., Pu, Y.-J., Satoh, F., Kawata, S., Katagiri, H., Sasabe, H. and Kido, J., *Adv. Funct. Mater.* 2014, **24**, 2064-2071.
48. Li, J., Liao, X., Xu, H., Li, L., Zhang, J., Wang, H. and Xu, B., *Dyes Pigment.* 2017, **140**, 79-86.
49. Jiang, Y., Wang, L., Zhou, Y., Cui, Y.-X., Wang, J., Cao, Y. and Pei, J., *Chem. Asian J.* 2009, **4**, 548-553.
50. Li, J. and Liu, D., *J. Mater. Chem.* 2009, **19**, 7584.
51. Luo, J., Gong, S., Gu, Y., Chen, T., Li, Y., Zhong, C., Xie, G. and Yang, C., *J. Mater. Chem. C* 2016, **4**, 2442-2446.
52. Albrecht, K., Matsuoka, K., Fujita, K. and Yamamoto, K., *Angew. Chem. Int. Ed.* 2015, **54**, 5677-5682.
53. Ban, X., Jiang, W., Lu, T., Jing, X., Tang, Q., Huang, S., Sun, K., Huang, B., Lin, B. and Sun, Y., *J. Mater. Chem. C* 2016, **4**, 8810-8816.
54. Li, Y., Xie, G., Gong, S., Wu, K. and Yang, C., *Chem. Sci.* 2016, **7**, 5447.
55. Sun, J.W., Baek, J.Y., Kim, K.-H., Huh, J.-S., Kwon, S.-K., Kim, Y.-H. and Kim, J.-J., *J. Mater. Chem. C* 2017, **5**, 1027-1032.
56. Liu, M., Seino, Y., Chen, D., Inomata, S., Su, S.-J., Sasabe, H. and Kido, J., *Chem. Commun.* 2015, **51**, 16353-16356.
57. Jürgensen, N., Kretzschmar, A., Höfle, S., Freudenberg, J., Bunz, U.H.F. and Hernandez-Sosa, G., *Chem. Mater.* 2017, **29**, 9154-9161.

58. Sun, J.W., Baek, J.Y., Kim, K.-H., Moon, C.-K., Lee, J.-H., Kwon, S.-K., Kim, Y.-H. and Kim, J.-J., *Chem. Mater.* 2015, **27**, 6675-6681.
59. Cui, L.-S., Nomura, H., Geng, Y., Kim, J.U., Nakanotani, H. and Adachi, C., *Angew. Chem. Int. Ed.* 2017, **56**, 1571-1575.
60. Duan, C., Li, J., Han, C., Ding, D., Yang, H., Wei, Y. and Xu, H., *Chem. Mater.* 2016, **28**, 5667-5679.
61. Cho, Y.J., Jeon, S.K., Lee, S.-S., Yu, E. and Lee, J.Y., *Chem. Mater.* 2016, **28**, 5400-5405.
62. Pan, K.-C., Li, S.-W., Ho, Y.-Y., Shiu, Y.-J., Tsai, W.-L., Jiao, M., Lee, W.-K., Wu, C.-C., Chung, C.-L. and Chatterjee, T., *Adv. Funct. Mater.* 2016, **26**, 7560-7571.
63. Chan, C.-Y., Cui, L.-S., Kim, J.U., Nakanotani, H. and Adachi, C., *Adv. Funct. Mater.* 2018, **28**, 1706023.
64. Hatakeyama, T., Shiren, K., Nakajima, K., Nomura, S., Nakatsuka, S., Kinoshita, K., Ni, J., Ono, Y. and Ikuta, T., *Adv. Mater.* 2016, **28**, 2781.
65. Kim, G. H., Lampande, R., Im, J. B., Lee, J. M., Lee, J. Y. and Kwon, J. H., *Mater. Horiz.* 2017, **4**, 619-624.
66. Noda, H., Kabe, R. and Adachi, C., *Chem. Lett.* 2016, **45**, 1463-1466.
67. Rajamalli, P., Senthilkumar, N., Gandeepan, P., Huang, P.-Y., Huang, M.-J., Ren-Wu, C.-Z., Yang, C.-Y., Chiu, M.-J., Chu, L.-K., Lin, H.-W. and Cheng, C.-H., *J. Am. Chem. Soc.* 2016, **138**, 628-634.
68. Rajamalli, P., Senthilkumar, N., Gandeepan, P., Ren-Wu, C.-C., Lin, H.-W. and Cheng, C.-H., *ACS Appl. Mater. Interfaces* 2016, **8**, 27026-27034.
69. Rajamalli, P., Senthilkumar, N., Gandeepan, P., Ren-Wu, C.-Z., Lin, H.-W. and Cheng, C.-H., *J. Mater. Chem. C* 2016, **4**, 900-904.
70. Rajamalli, P., Thangaraji, V., Senthilkumar, N., Ren-Wu, C.-C., Lin, H.-W. and Cheng, C.-H., *J. Mater. Chem. C* 2017, **5**, 2919-2926.
71. Rajamalli, P., Senthilkumar, S., Huang, P.-Y., Ren-Wu, C.-C., Lin, H.-W. and Cheng, C.-H., *J. Am. Chem. Soc.* 2017, **139**, 10948-10951.
72. Lee, J., Shizu, K., Tanaka, H., Nomura, H., Yasuda, T. and Adachi, C., *J. Mater. Chem. C* 2013, **1**, 4599-4604.
73. Sohn, S., Koh, B. H., Baek, J. Y., Byun, H. C., Lee, J. H., Shin, D.-S., Ahn, H., Lee, H.-K., Hwang, J., Jung, S. and Kim, Y.-H., *Dyes Pigm.* 2017, **140**, 14-21.
74. Mayr, C., Lee, S. Y., Schmidt, T. D., Yasuda, T., Adachi, C. and Brütting, W., *Adv. Funct. Mater.* 2014, **24**, 5232-5239.
75. Kim, K.-H., Liao, J.-L., Lee, S. W., Sim, B., Moon, C.-K., Lee, G.-H., Kim, H. J., Chi, Y. and Kim, J.-J., *Adv. Mater.* 2016, **28**, 2526-2532.

Chapter 1: Section 3

Introduction to Room-Temperature Solvent-free Luminescent Organic Liquids (SLOLs)

1.3.1 Introduction

Many new organic emitters with excellent quantum efficiencies have been developed using advanced synthetic techniques in organic chemistry. However, with the help of a large π -surface, π -conjugated molecules tend to aggregate and change their optical features. Moreover, it has been demonstrated that aggregation will cause a significant change in electrical and optical properties according to the characteristics of the π -conjugated core and its surroundings.¹ The solvent and its polarity also play a crucial role in the variation of emission. Hence, it is still difficult to find straightforward and facile processing procedures for these emissive organic materials. As a replacement for the current solid organic emitters, room-temperature solvent-free luminous organic liquids (SLOL) have been proposed due to their attractive features described below. In the last decade, much work has been done on SLOLs by isolating the " π -cores" by wrapping them with low-viscosity organic chains.

1.3.2 Features of SLOL-

1. Long and branched side chains support SLOLs by acting as a shield, which results in high stability. Additionally, the side reactions caused by light, molecule oxidation, and heavy atom quenching processes are considerably reduced by these side chains.²
2. Because of the fluidic/honey-type nature, SLOLs have excellent processability as a functional material.³
3. The free-flowing SLOLs can accept a variety of shapes under twisting, bending and stretching conditions.
4. Due to their liquid characteristic, SLOLs may easily accommodate a variety of useful dopants.
5. The donor-acceptor interactions are improved by the nonpolar fluid matrix of SLOLs to deliver effective charge/energy transfer.

6. The free-flowing nature of SLOs supports using a paintable material to coat several substrates, such as glass, wood, paper, etc., to make large-area thin films.

From 1948 onwards, the research on SLOs has been started with 2-*n*-decylnaphthalene with a melting point of 13 °C.⁴ Many alkylated liquid derivatives have been reported in the last decade, comprising the details of their synthesis, characterisation, photophysical characteristics, and applications (Figure 1.3.1).

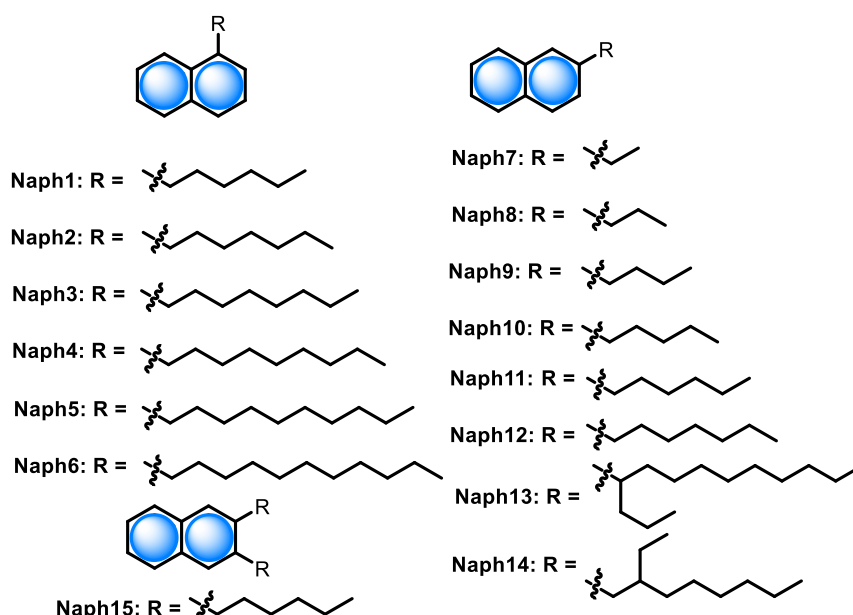


Figure 1.3.1. Chemical structures of naphthalene-based liquid derivatives.

In the solid, crystal or condensed state, it is not easy to maintain the same photophysical property as a monomer due to the strong interchromophoric interactions. The long alkyl side chains introduced in SLOs reduce the aggregation through π - π interactions, although some molecular systems still have weak interactions, that significantly impact the photophysical properties. For example, Shinoda and co-workers studied an alkylated benzothiadiazole liquid (**BZT2**) having red emission in a solution state with 75 % PLQY. The same molecule exhibits 12% PLQY in the neat condensed state, which is very low

compared to the solution state (Figure 1.3.2a and 1.3.2b).⁵ Later, Norioke and co-workers synthesized the oligo(*p*-phenyleneethynylene) liquid (**OPE1**) which demonstrated an efficient energy transfer with the C₆₀ molecule in the liquid mixture (Figure 1.3.2b and 1.3.e).⁶ Additionally, Allain and co-workers developed two tetrazine liquid derivatives (**TTZ1** and **TTZ2**), in which **TTZ1** was substituted with a branched alkyl chain on one side, while **TTZ2** was substituted on both sides (Figure 1.3.2c and 1.3.2f).⁷ Both molecules showed a similar absorption and emission spectra pattern in solution and neat state. Nevertheless, **TTZ1** showed a significant decrease in fluorescence QY from the solution (33%) to the neat liquid state (2.1%). In contrast, **TTZ2** exhibited a similar fluorescence quantum yield in both states (6.6% in solution and 6.9% in neat liquid) (Figure 1.3.2f). The stable fluorescence quantum yield of **TTZ2** in both states is most likely due to the additional side chains, which suppress the interchromophoric interaction.

The restriction of intramolecular interactions typically controls the emission of aggregation-induced emissive compounds (AIE). As a result, AIEgens are weakly emissive in solution but remain strongly emissive when intramolecular interactions are restricted in solvent-free conditions. In 2017, Machida and co-workers successfully synthesized tetraphenylethene (**TPE**)-based AIEgen liquids (**TPE1-4**). Tetraphenylethene liquids were synthesised by covalently linking long branched alkyl chains (Figure 1.3.3a).⁸ In this case, the high viscosity of the liquid medium plays a crucial role in restricting intramolecular motions. In another work, Takeda et al., synthesized another SLOL of TPE-based chromophore (**TPE-5**) by attaching linear tetraethylene glycol (TEG) chains (Figure 1.3.3c).⁹ **TPE5** has an exceptionally low T_g (-60 °C) due to the bent skeleton of **TPE** core and the viscous nature of TEG chains.

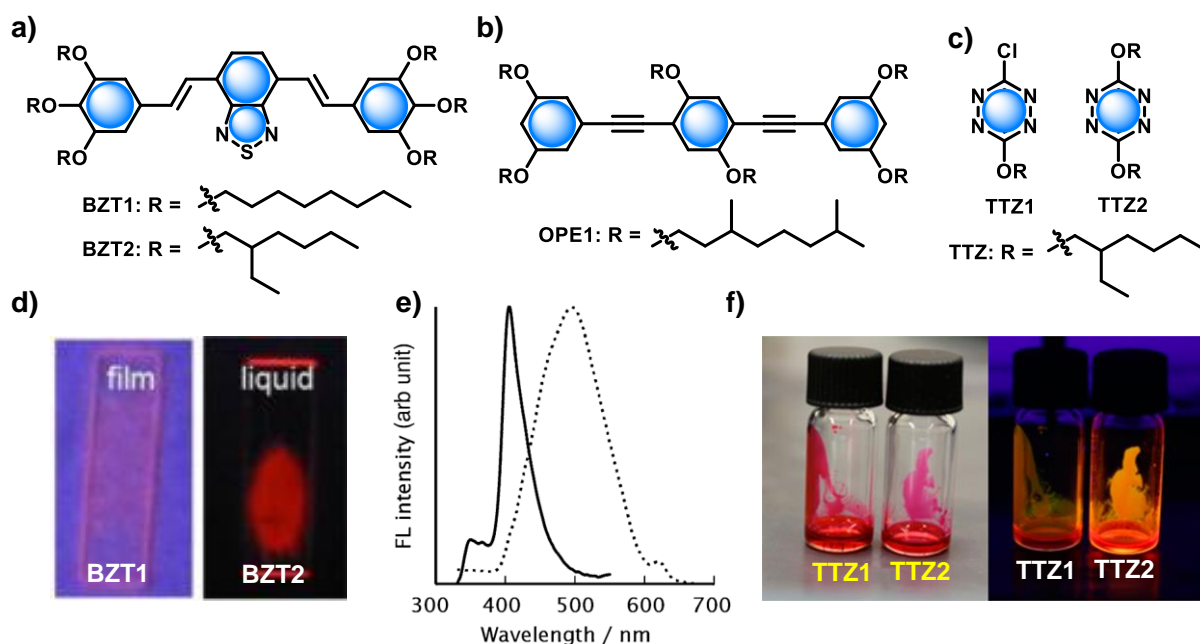


Figure 1.3.2. a) Chemical structures and d) photographs of **BZT1** and **BZT2** under UV light. *Reproduced with permission from ref. 5. Copyright 2013, Elsevier.* b) Chemical structure of **OPE1** (top) and e) fluorescence spectra in CHCl_3 (dotted line: bulk liquid: solid line: CHCl_3 solution) of **OPE1**. *Reproduced with permission from ref. 6. Copyright 2014, the Chemical Society of Japan.* c) Chemical structures and f) photographs of **TTZ1** and **TTZ2** under visible (left) and UV (right) lights. *Reproduced with permission from ref. 7. Copyright 2016, American Chemical Society.*

The mixing of SLOs with a small amount of conventional dopants adds more tunability without changing the inherent liquid nature. Sensible choice of the dopants, masterly tuning ratio of the dopant, and efficient mixing convey exceptional value addition. Babu et al. in 2012 reported the blending nature of blue-emitting liquids **OPV2** or **OPV4** (Figure 1.3.4a) with tris(8-hydroxyquinolinato)aluminum (Alq_3) as a green-emitting and rubrene as a red-emitting dopants.¹⁰ A logical mixing of blue, green, and red-emitting materials produces a white-light-emitting liquid mixture with emissions spanning from 400-700 nm, and the resulting mixture can be painted on a surface with a large

surface (Figure 1.3.4.c). Further, Machida et al., illustrated the white light-emitting liquid composite in a similar way by use of **TPE3** as the host liquid and Nile red used as the dopant.¹⁰

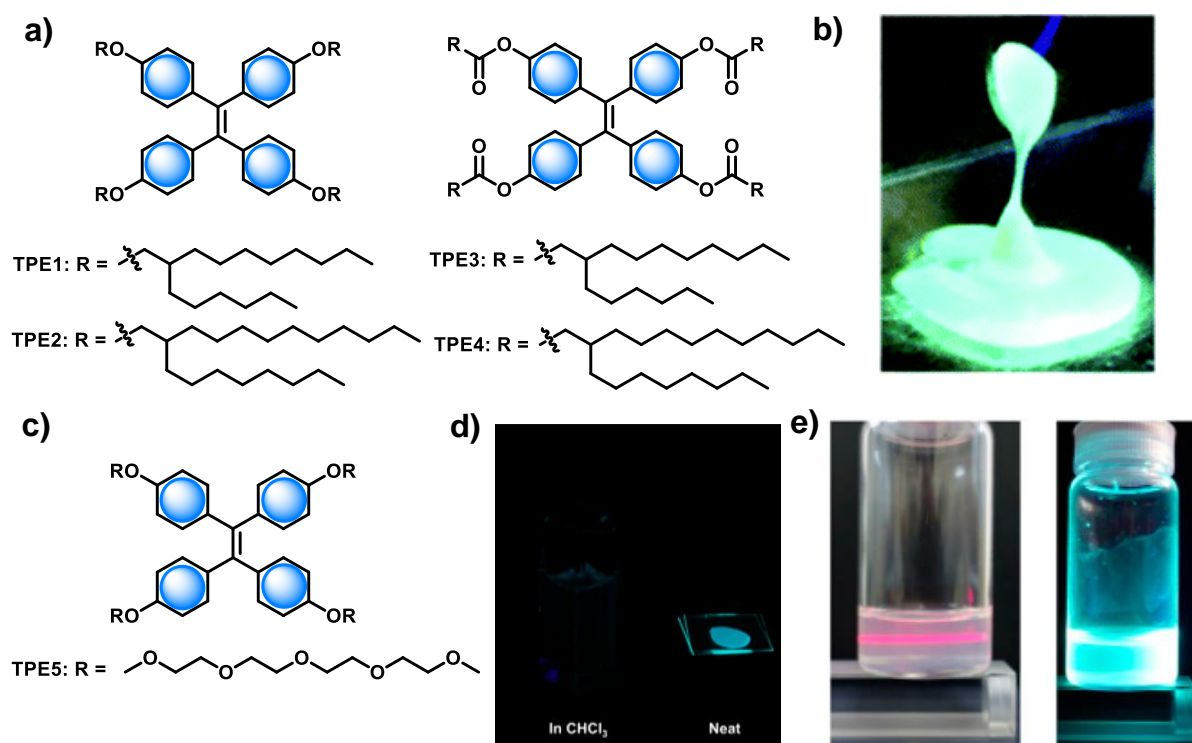


Figure 1.3.3. a) Chemical structures of **TPE1- 4**, and c) **TPE5**. b) Photograph of **TPE3** under UV light. *Reproduced with permission from ref. 8. Copyright 2017, Royal Society of Chemistry.* d) Photograph of **TPE5** under UV light irradiation in CHCl_3 and neat state. e) Tyndall scattering and image under UV light ($\lambda_{\text{ex}} = 365$ nm) of **TPE5** in H_2O . *Reproduced with permission from ref. 9. Copyright 2018, American Chemical Society.*

Later in 2013, Babu and co-workers, reported a series of liquid composites encompassing the entire visible area emission color by using blue-emitting **DPA1** liquid through doping of commercially accessible dyes **D1** and tris(1,3-diphenyl-1,3-propanedionato)(1,10-phenanthroline)europium(III) (**D2**) (Figure 1.3.4b).¹¹ The tunable color emission is achieved by the efficient FRET from **DPA1** to dopants (Figure 1.3.4.f).

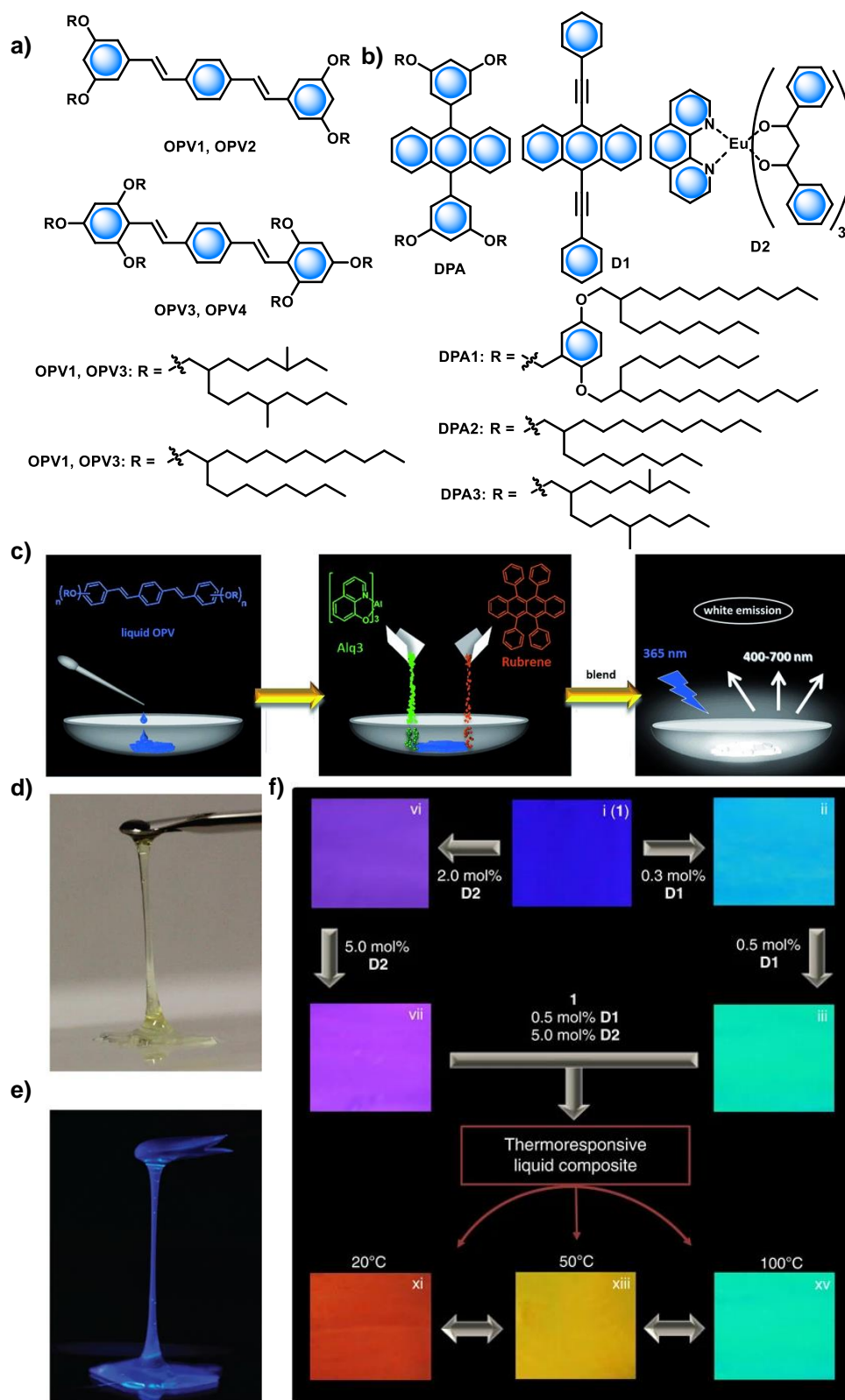


Figure 1.3.4. a) Chemical structures of **OPV1-OPV4**. c) Illustration of the preparation of a solvent-free white-emitting liquid composite. *Reproduced with permission from ref. 10. Copyright, 2012, WILEY-VCH Verlag GmbH & Co.*

KGaA. b) Chemical structures of **DPA1-3**, dopants **D1** and **D2**. Photographs of **DPA2** under d) visible and e) UV light. f) Photographs of the luminescence colour tunability and thermoresponsive feature of the composites of **DPA1**, **D1** (0.5 mol%) and **D2** (5 mol%). Reproduced with permission from ref. 11. Copyright 2013, Springer Nature Publishing AG.

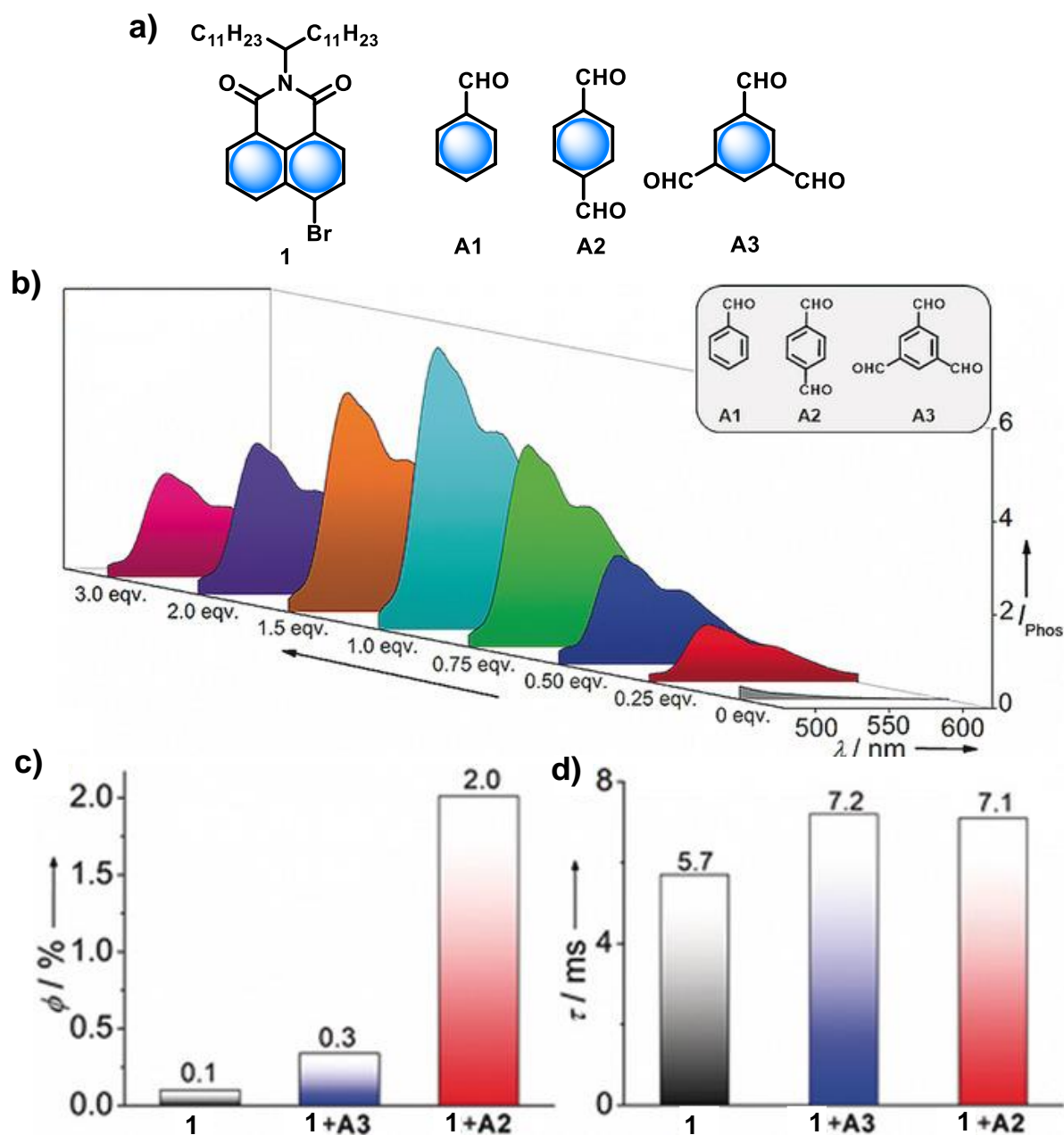


Figure 1.3.5. a) Chemical structures of liquid host **1** and dopants **A1-A3**. b) Phosphorescence spectral changes of **1** with increasing equivalents of **A2** at RT in air. Variation of the c) phosphorescence quantum yield and d) phosphorescence

lifetime of **1** upon composite formation with **A3** and **A2**. (*Adapted with permission from ref. 12, copyright 2019, Wiley-VCH*).

Organic room temperature phosphors (RTP) have been extensively studied in the recent past. It has been emphasised that crystalline molecular ordering is highly required for effective intersystem crossing and to exhibit excellent RTP features. In this context, Goudappagouda et al. investigated the RTP characteristics of an SOL phosphor in air.¹² Upon varying alkyl chain, the physical nature of bromonaphthalimides changed; however, the phosphorescence of solvent-free liquid **1** in the air remained unaltered. RTP organic liquid was made by introducing a long-branched alkyl chain on bromonaphthalimide. As a novel method, by combining the liquid phosphor **1** with carbonyl guests **A2** and **A3**, a paintable RTP composite with greatly increased phosphorescent lifetime and quantum yield was produced. (Figure 1.3.5b). As a result, a large area of paintable phosphorescent liquid composite with a longer lifetime and higher quantum yield was prepared (Figure. 1.3.5c,d). A 10x10 cm large area RTP coating could be realized using liquid composite paint.

Very recently, Wakchaure et al. reported the SLOL by combining donor-acceptor units through exciplex emission and RTP at very low acceptor loading.¹³ The present study showed that D-A interactions in SLOL by using carbazole (**Cbz**) as a donor with naphthalenemonoimide (**NMI**) and naphthalenediimide (**NDI**) derivatives as acceptors in a solvent-free liquid state (Figure. 1.3.6a). As a new strategy, the formation of exciplex was demonstrated with a mixture of **Cbz** and **NMI**, while RTP was shown by a mixture of **Cbz** with **NDI** at a very low loading of the acceptor. This demonstration shows the versatility of doping-assisted tuning of emission features (Figure. 1.3.6c-f).

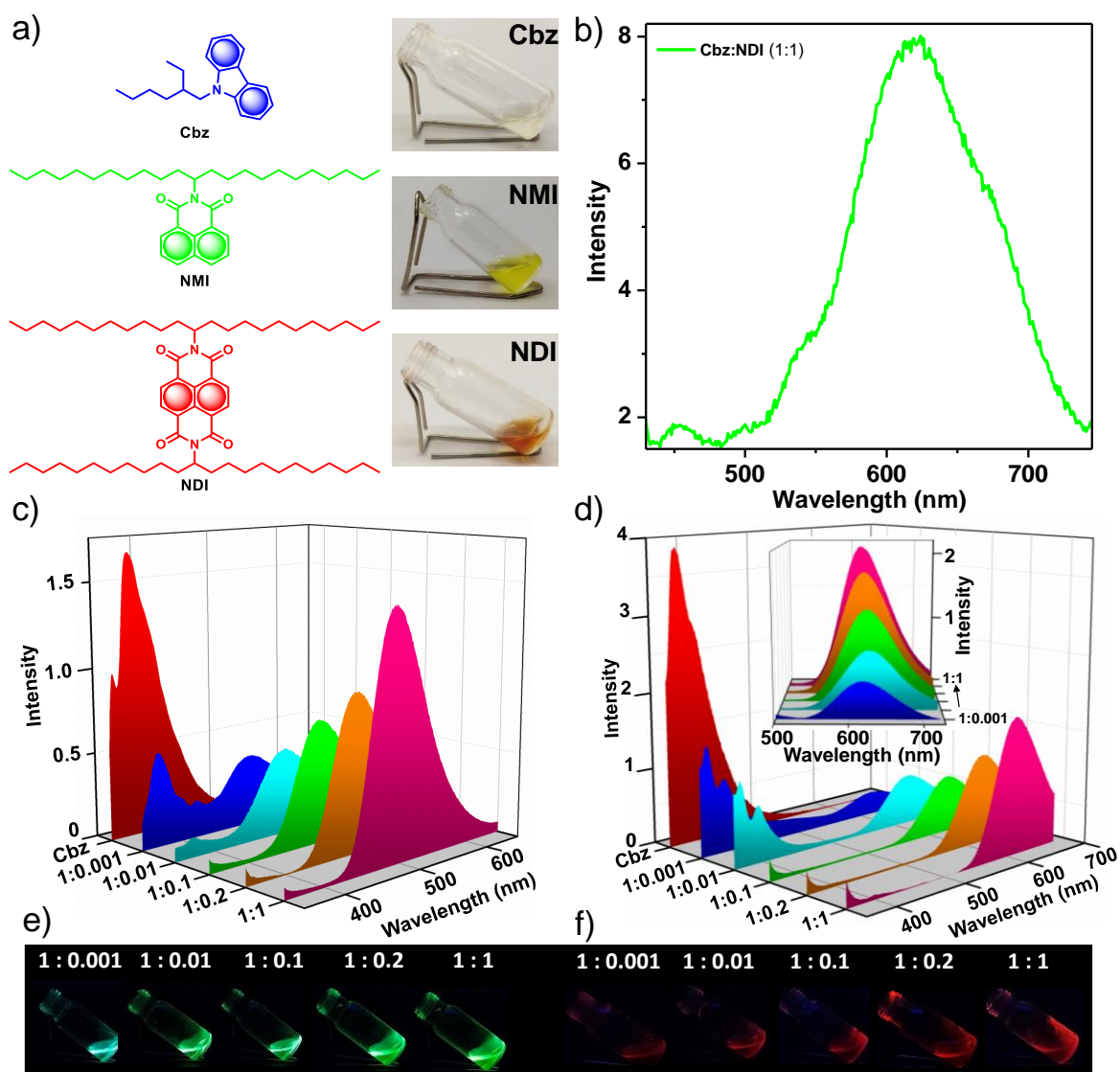


Figure. 1.3.6. a) Chemical structures of **Cbz**, **NMI**, and **NDI** and corresponding photographs under visible light. b) Phosphorescence spectra of **Cbz:NDI** (1:1) at RT in air ($\lambda_{\text{ex}} = 350$ nm). c) Variation of steady-state emission of **Cbz** with an increasing equivalence of **NMI** and corresponding (e) photographs under UV light ($\lambda_{\text{ex}} = 365$ nm). d) Variation of the steady-state emission of **Cbz** with an increasing equivalence of **NDI** ($\lambda_{\text{ex}} = 342$ nm); inset shows the corresponding spectral change by exciting at 370 nm and (f) corresponding photographs under UV light ($\lambda_{\text{ex}} = 365$ nm). (Adapted with permission from ref. 13, copyright 2022, The Royal Society of Chemistry).

1.3.3 Conclusion

In the past few decades, room temperature metal-free organic phosphors and TADF materials have been extensively studied in crystalline and the amorphous state. The liquefaction of such luminophores will provide promising candidates for large-area lighting and display applications. The realization of technologically high potential organic materials as an inventive replacement for the currently used ones requires aesthetic molecular designs. The concept “Solvent-free organic phosphorescent and TADF liquid” is still at the concept level. We aim to accomplish such new diverse methodologies to advance in the research field. Hence, it is anticipated that the SLOs will lead to the realization of new functional materials. Furthermore, to improve the processability of SLOs, a step towards processable polymers will be one of the successful candidates. It is obvious that connecting a long/branched alkyl chain to the chromophore allows one to alter the physical state of small molecules or polymers. Such alterations not only change the physical characteristics of the resulting derivatives but also improves processability as well. Hence, a step toward polymerizable SLOs will be attempted using a large area of paintable solvent-free organic liquid monomers.

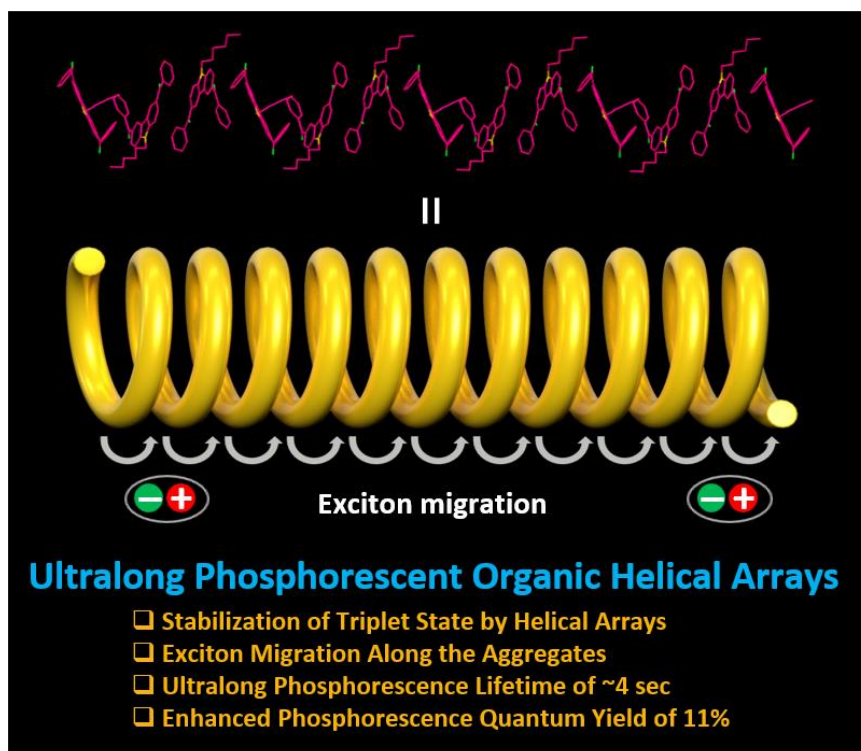
1.3.4 References

1. Pope, M., Kallmann, H. P. and Magnante, P., *J. Chem. Phys.* 1963, **38**, 2042.
2. a) Yoshida, T., Watanabe, H. (Nippon Oil Co., Ltd., Japan), *DE3524186A1*, 1986; b) Yokoyama, N., Imai, F. (Nippon Oil Co., Ltd., Japan), *EP305114A1*, 1989.
3. Hirat, S., Kubota, K., Jung, H. H., Hirata, O., Goushi, K., Yahiro, M. and Adachi, C., *Adv. Mater.* 2011, **23**, 889.
4. a) Hart, R. T., Robinson, S. A., *J. Am. Chem. Soc.* 1948, **70**, 3731; b) Bannister, B., Elsner, B. B., *J. Chem. Soc.* 1951, **0**, 1055; c) Gilman, H., Brannen, C. G., Ingham, R. K., *J. Org. Chem.* 1957, **22**, 685; d) Tutomu, K., Sin-ichi, T., Masayasu, T., *Bull. Chem. Soc. Jpn.* 1949, **22**, 66; e) Kolbel, H., *Erdoel Kohle* 1948, **1**, 308; f) Kato, J., Takeshita, K., *Kyushu*

- Daigaku Kogaku Iho* 1951, **23**, 79; g) Kolbel, H., *Brennst.-Chem.* 1949, **30**, 73.
5. Ishi-I, T., Sakai, M., Shinoda, C., *Tetrahedron* 2013, **69**, 9475.
 6. N. Adachi, R. Itagaki, M. Sugeno, T. Norioka, *Chem. Lett.* 2014, **43**, 1770.
 7. Allain, C., Piard, J., Brosseau, A., Han, M., Paquier, J., Marchandier, T., Lequeux, M., Boissiere, C., Audebert, P., *ACS Appl. Mater. Interfaces* 2016, **8**, 19843.
 8. Machida, T., Taniguchi, R., Oura, T., Sada, K., Kokado, K., *Chem. Commun.* 2017, **53**, 2378.
 9. Takeda, T., Yamamoto, S., Mitsuishi, M., Akutagawa, T., *J. Phys. Chem. C* 2018, **122**, 9593.
 10. Babu, S. S., Aimi, J., Ozawa, H., Shirahata, N., Saeki, A., Seki, S., Ajayaghosh, A., Mohwald, H. and Nakanishi, T., *Angew. Chem. Int. Ed.* 2012, **51**, 3391.
 11. Babu, S. S., Hollamby, M. J., Aimi, J., Ozawa, H., Saeki, A., Seki, S., Kobayashi, K., Hagiwara, K., Yoshizawa, M., Mohwald, H. and Nakanishi, T., *Nat. Commun.* 2013, **4**, 1969.
 12. Goudappagouda, Manthanath, A., Wakchaure, V. C., Ranjeesh, K. C., Das, T., Vanka, K., Nakanishi, T., Babu, S. S., *Angew. Chem. Int. Ed.* 2019, **58**, 2284.
 13. Wakchaure, V. C., Veer, S. D., Nidhankar, A. D., Goudappagouda, Nayak, R. A., Asokan, K., Ravindranathan, S., Babu, S. S., *Chem. Commun.*, 2022, **58**, 1998-2001.

Chapter-2

Self-assembled Helical Arrays for Stabilizing the Triplet State



Room-temperature phosphorescence of metal and heavy atom-free organic molecules has emerged as an area of great potential in recent years. A rational design played a critical role in controlling the molecular ordering to impart efficient intersystem crossing and stabilize the triplet state to achieve room-temperature ultralong phosphorescence. However, in most cases, the strategies to strengthen phosphorescence efficiency have resulted in a reduced lifetime, and the available nearly degenerate singlet-triplet energy levels impart a natural competition between delayed fluorescence and phosphorescence, with the former one having the advantage. Herein, an organic helical assembly supports the exhibition of an ultralong phosphorescence lifetime. Contrary to other molecules,

3,6-phenylmethanone functionalized 9-hexylcarbazole exhibits a remarkable improvement in phosphorescence lifetime (> 4.1 s) and quantum yield (11%) owing to an efficient molecular packing in the crystal state. A right-handed helical molecular array act as a trap and exhibits triplet exciton migration to support the exceptionally longer phosphorescence lifetime.

Publication: *Angew. Chem. Int. Ed.* **2020**, *59*, 13079-13085.

2.1. Introduction

Room-temperature phosphorescence (RTP) of organic molecules has been enthusiastically investigated recently for various applications such as electroluminescence, sensing, bio-imaging, etc.^[1,2] It has been demonstrated that the incorporation of heavy atoms and functional moieties equipped with lone pair of electrons facilitate intersystem crossing (ISC) rate (k_{ST}) through strong spin-orbit coupling (SOC), leading to efficient RTP.^[3-6] In this direction, diverse molecular designs have been explored for ultralong organic phosphorescence (UOP).^[7-10] Hence, successful strategies such as molecular units with n orbitals, which can reduce the singlet–triplet (S-T) splitting energy (ΔE_{ST}) and stabilize the triplet excited state through various interactions, have been widely employed.^[5f] Significant advancement has been noticed in the area of UOP materials, and the maximum lifetime reported for crystalline small molecule-based organic phosphor is circa 2.5 s (Figure 2.1a, Table 1).^[11] Mostly, longer lifetimes under ambient conditions are achieved by stabilization of the triplet state through H-aggregation (Figure 2.1b). However, the already established strategies to improve the phosphorescence efficiency often lead to shortening the lifetime. Moreover, the molecular designs to enhance the nearly degenerate triplet manifolds can, in turn, facilitate reverse intersystem crossing (RISC) to exhibit delayed fluorescence (DF).^[12] Hence it demands a new alternate plan of action to control the competitive decay pathways and efficiently manage the triplet

excitons to enhance phosphorescence lifetime. It can be achieved only through unexplored molecular designs and with the rigorous assistance of molecular packing. Helical arrays of organic small molecules and polymers exhibit exciting optoelectronic properties by controlling the spatial organization of the structural units.^[13] Hence, the design of a helical assembly to modulate the triplet state to achieve a longer phosphorescence lifetime will be highly appreciated. Our continuous attempts in this direction enabled us to successfully utilize the crystalline helical arrays of phenylmethanone functionalized alkylated carbazole to achieve a longer lifetime of above 4 s.

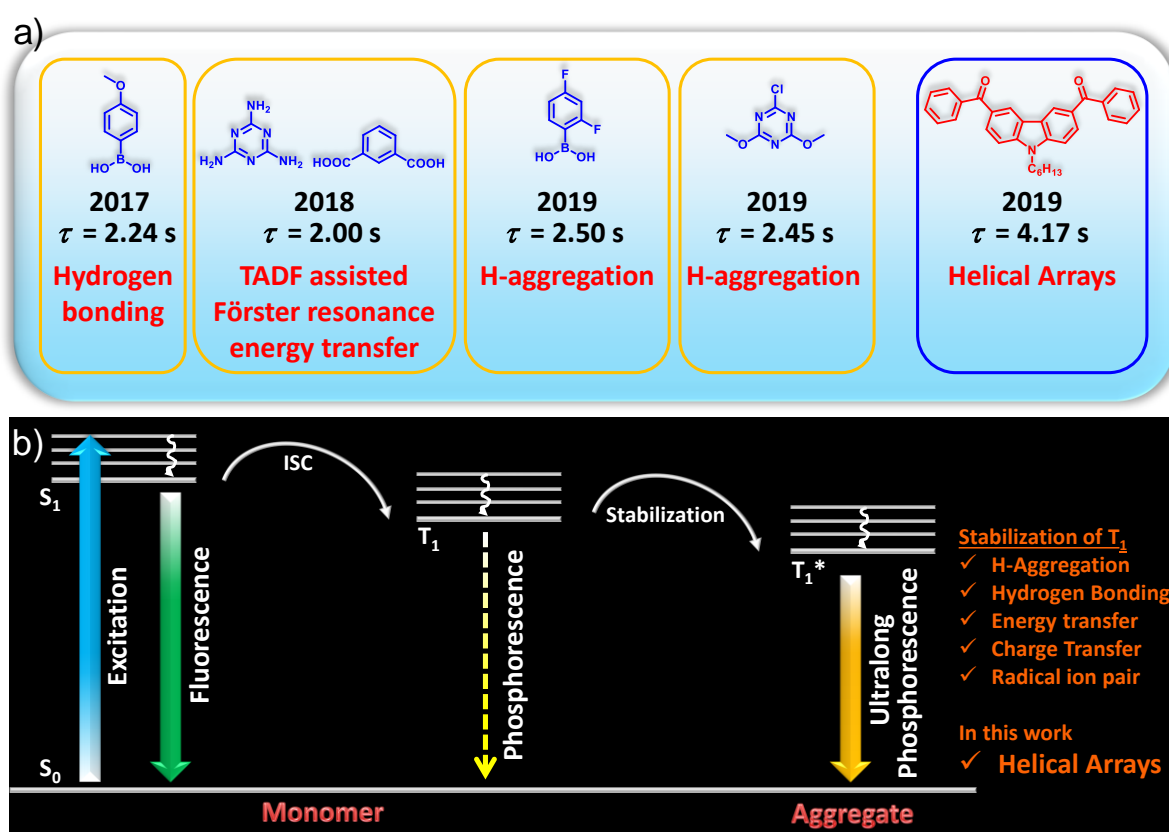


Figure 2.1. a) Recent developments in the area of small molecule-based organic phosphors with lifetime above 2 s and the present work with above 4.17 s. b) Schematic of the stabilization of the triplet state, leading to ultralong phosphorescence.

2.2. Experimental section

2.2.1. Details of DFT Calculations

Ground (S_0) state calculations were performed using restricted density functional theory (DFT). Singlet and triplet excited states were investigated using time-dependent density functional theory (TD-DFT).²³ The ground state singlet (S_0) state was calculated using the B3LYP/6-31+G(d)²⁴ level of theory. Also, the TDDFT calculations were done with same level of theory. All the geometries of the complexes in the S_0 state were optimized. The optimized Cartesian coordinates and total energies are listed below. On the basis of the Frank-Condon principle, the absorption properties were evaluated using the optimized S_0 state structure. The Gaussian09 software²⁵ was used in all the DFT and TD-DFT calculations.

2.2.2. Crystallization

All the single crystal samples were obtained by crystallization using a slow evaporation method from the CH_2Cl_2 solution. To further check the purity of the samples, all the single crystals were dissolved in acetonitrile-water (85:15) mixture (50 μM) and analyzed by HPLC.

2.2.3. Phosphorescence waveguiding

Crystalline rods of **3a** were placed on a glass slide. Home built upright microscope was used for performing the phosphorescence waveguiding experiment. The 532 nm solid-state laser was expanded using a beam expander and was focused onto one of the ends of crystal rods of **3a** using 0.3 NA 10X objective lens. Backscattered light was collected using the same objective lens. The collected light is focussed on the CCD or spectrometer with 150 grooves/mm grating.

2.2.4. X-ray intensity data measurements

X-ray intensity data measurements of all the samples were carried out on a Bruker D8 VENTURE Kappa Duo PHOTON II CPAD diffractometer equipped with Incoatech multilayer mirrors optics. The intensity

measurements were carried out with Mo micro-focus sealed tube diffraction source (MoK α = 0.71073 Å) at 100(2) K temperature. The X-ray generator was operated at 50 kV and 1.4 mA. A preliminary set of cell constants and an orientation matrix were calculated from three sets of 36 frames. Data were collected with ω and φ scan width of 0.5° at different settings of φ , ω and 2θ keeping the sample-to-detector distance fixed at 5.00 cm. The X-ray data collection was monitored by the APEX3 program (Bruker, 2016).²⁶ All the data were corrected for Lorentzian, polarization, and absorption effects using SAINT and SADABS programs (Bruker, 2016). Using the APEX3 (Bruker) program suite, the structure was solved with the ShelXS-97 (Sheldrick, 2008)²⁷ structure solution program, using direct methods. The model was refined with a version of ShelXL-2013 (Sheldrick, 2015)²⁸ using Least Squares minimization. All the hydrogen atoms were placed in a geometrically idealized position and constrained to ride on its parent atoms. An *ORTEP* III²⁹ view of the compound was drawn with 50% probability displacement ellipsoids, and H atoms are shown as small spheres of arbitrary radii. The compound **3a** crystallized in monoclinic chiral space group P21 containing three molecules in the asymmetric unit which are labelled as unprimed, primed, and double primed.

2.2.5. Phosphorescence experiments

All phosphorescence experiments of all crystals have done by keeping the same experimental parameters. The window of maximum delay after flash was kept 0.3-2 ms for RT phosphorescence measurements.

The photophysical parameters were calculated using the following equations.

$$k_r^{Fluo} = \varphi_{Fluo} / \tau_{Fluo}$$

$$k_{nr}^{Fluo} = (1 - \phi_{Phos} - \phi_{Fluo}) / \tau_{Fluo}$$

$$k_{isc} = \phi_{Phos} / \tau_{Fluo}$$

$$k_r^{Phos} = \phi_{Phos} / \tau_{Phos}$$

$$k_{nr}^{Phos} = (1 - \phi_{Phos}) / \tau_{Phos}$$

Where,

k_r^{Fluo} = Radiative rate constant of fluorescence

k_{nr}^{Fluo} = Non-radiative rate constant of fluorescence

k_r^{Phos} = Radiative rate constant of phosphorescence

k_{nr}^{Phos} = Non-radiative rate constant of phosphorescence

ϕ_{Fluo} = Fluorescence quantum yield

ϕ_{Phos} = Phosphorescence quantum yield

τ_{Fluo} = Fluorescence lifetime

τ_{Phos} = Phosphorescence lifetime

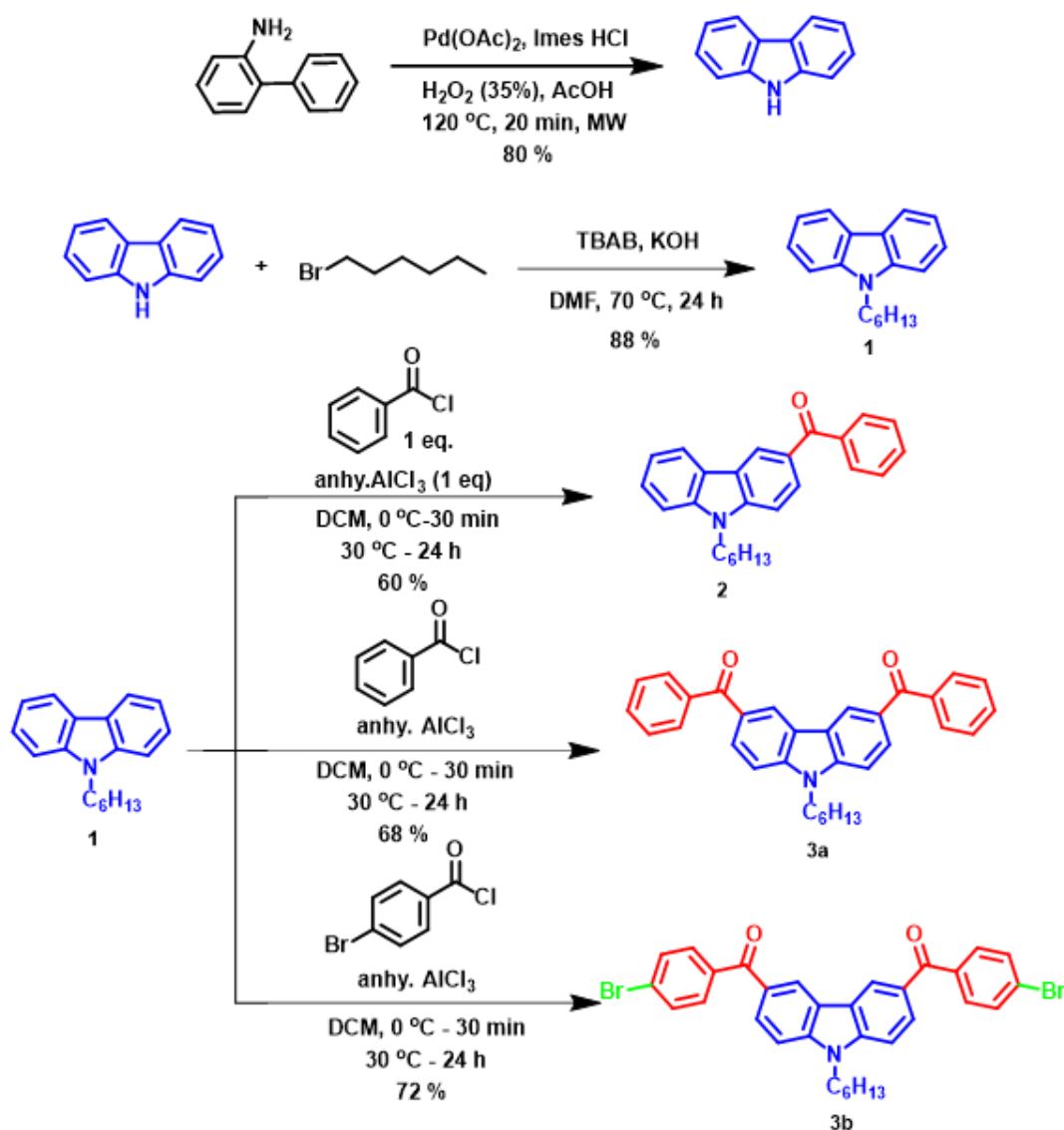
2.3. Synthesis

Synthesis and characterization of molecule carbazole³⁰ and **1**³¹ are conducted according to the reported procedures.

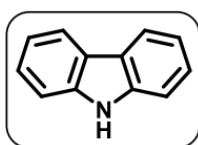
2.3.1. Procedure for synthesis of 9H-carbazole-³⁰

In a microwave tube, 2-aminobiphenyl (100 mg, 456.57 μ mol) was dissolved in glacial acetic acid (5 mL) and then Pd(OAc)₂ (26.53 mg, 118.18 μ mol), IMes·HCl (9 mg, 29.55 μ mol), and H₂O₂ (35 %, 0.158 mL, 2.36 mmol) were added. The vial was sealed, whereupon a magnetic stirrer bar was transferred to the tube. The tube was submerged in the microwave cavity for 20 min at 120 °C. Then, the acetic acid solvent was removed under reduced pressure. The crude product was dissolved in EtOAc (25 mL) and washed with water (20 mL). The aqueous phase

was extracted with EtOAc (2x20 mL). The combined layer was washed with aqueous NaHCO₃ (20 mL). The organic layer was filtered through a pad of Celite and dried with Na₂SO₄. The solvent was evaporated under reduced pressure. The crude product was purified by column chromatography using petroleum ether:EtOAc mixture to obtain the target compound, as white coloured solid, Yield-62.4 mg, 80%.



Scheme 1. Synthetic Scheme for carbazole and target molecules 1-3b.

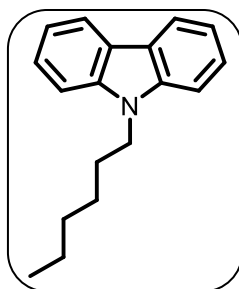


^1H NMR (DMSO- d_6 , 400MHz): δ = 11.24 (br. s., 1 H), 8.10 (d, J = 7.8 Hz, 2 H), 7.48 (d, J = 8.0 Hz, 2 H), 7.34 - 7.41 (m, 2 H), 7.12 - 7.18 (m, 2 H) ppm.

^{13}C NMR (DMSO- d_6 , 100MHz): δ = 139.7, 125.5, 122.4, 120.1, 118.5, 110.9 ppm.

2.3.2. Procedure for synthesis of 9-hexyl-9H-carbazole (1)-³¹

In two-neck round bottom flask were placed carbazole (5.00 g, 0.0299 mol), 1-bromohexane (3.53 mL, 0.0389 mol), KOH (2.18 g, 0.0389 mol), TBAB (tetrabutylammonium bromide, 0.964 g, 0.00299 mol), and DMF (50 mL). Obtained mixture was stirred at 70 °C for 24 hours. After cooling down, water and chloroform were added (each 100 mL) and thoroughly shaken. Organic layer was separated, and inorganic layer was extracted again with chloroform (100 mL). Combined organic extracts were washed with water (100 mL), two times with NaCl saturated solution (2 x 100 mL) and finally dried with anhydrous Na_2SO_4 . Yellowish oil was subjected to column chromatography on silica gel, using petroleum ether as a mobile phase as a white solid, yield-5.56 gm, 89 %.



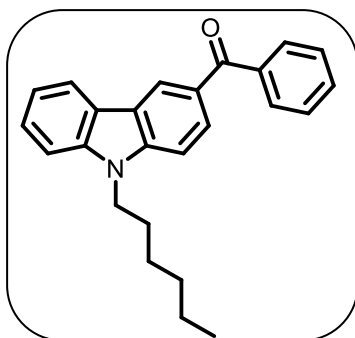
^1H NMR (400MHz, CDCl_3 , 25 °C): δ = 8.15 (d, J = 8.0 Hz, 2 H), 7.48 - 7.53 (m, 2 H), 7.44 (d, J = 8.0 Hz, 2 H), 7.25 - 7.29 (m, 2 H), 4.33 (t, J = 7.4 Hz, 2 H), 1.91 (quin, J = 7.4 Hz, 2 H), 1.40 - 1.47 (m, 2 H), 1.31 - 1.39 (m, 4 H), 0.91 (t, J = 7.1 Hz, 3 H) ppm.

^{13}C NMR (100MHz, CDCl_3 , 25 °C): δ = 140.66, 125.78, 123.05, 120.56, 118.91, 108.87, 43.31, 31.83, 29.16, 27.21, 22.78, 14.24 ppm.

HR-MS-(ESI⁺): calculated for $\text{C}_{18}\text{H}_{22}\text{N}$ [$\text{M}+\text{H}$]⁺ = 252.3730, found 252.1747.

2.3.3. Procedure for synthesis of (9-Hexyl-9H-carbazol-3-yl)(phenyl)methanone (2)-

Benzoyl chloride (462 μ L, 3.98 mmol) and anhydrous aluminium chloride (530 mg, 3.98 mmol) in dry CH_2Cl_2 (15 mL) were placed in two-neck round bottom flask at 0 $^\circ\text{C}$ for 30 min. to this reaction mixture add dropwise 9-hexyl-9H-carbazole (1 gm, 3.98 mmol) CH_2Cl_2 solution for 15 min. Keep reaction mixture for 24 hours at 30 $^\circ\text{C}$. Reaction mixture was quenched by slow addition of saturated ammonium hydroxide (caution: reaction is highly exothermic). The reaction mixture was extracted with CH_2Cl_2 (3x100 mL), and dried with anhydrous Na_2SO_4 . After evaporation of the solvent, the crude product was purified by column chromatography using petroleum ether: CH_2Cl_2 mixture (1:1), as off white coloured solid, Yield-0.85 gm (60%).



$^1\text{H-NMR}$ (400 MHz, CDCl_3 , 25 $^\circ\text{C}$): δ 8.60 (s, 1 H), 8.10 (d, $J = 7.9$ Hz, 1 H), 8.03 (d, $J = 8.5$ Hz, 1 H), 7.84 (d, $J = 7.3$ Hz, 2 H), 7.56 - 7.62 (m, 1 H), 7.50 (t, $J = 7.6$ Hz, 3 H), 7.41 - 7.47 (m, 2 H), 7.24 - 7.29 (m, 1 H), 4.32 (t, $J = 7.3$ Hz, 2 H), 1.89 (quin, $J = 7.3$ Hz, 2 H), 1.37 - 1.42 (m, 2 H), 1.25 - 1.34 (m, 4 H), 0.83 - 0.90 (t, $J = 7.1$ Hz, 3 H) ppm.

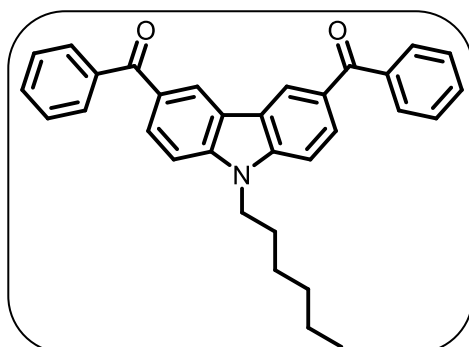
$^{13}\text{C-NMR}$ (100 MHz, CDCl_3 , 25 $^\circ\text{C}$): $\delta = 196.6, 143.0, 141.1, 139.1, 131.6, 129.9, 128.4, 128.4, 128.1, 126.4, 124.0, 123.1, 122.4, 120.7, 119.9, 109.2, 108.2, 43.3, 31.5, 28.9, 26.9, 22.5, 14.0$ ppm.

HR-MS-(ESI $^+$): calculated for $\text{C}_{25}\text{H}_{26}\text{NO}$ $[\text{M}+\text{H}]^+ = 356.4810$ found 356.2009.

General procedure for 3a-b.

Benzoyl chloride and anhydrous aluminium chloride in dry CH_2Cl_2 were placed in two-neck round bottom flask at $0\text{ }^\circ\text{C}$ for 30 min. to this reaction mixture add dropwise 9-hexyl-9H-carbazole CH_2Cl_2 solution for 15 min. Keep reaction mixture for 24 hours at $30\text{ }^\circ\text{C}$. Reaction mixture was quenched by the slow addition of saturated ammonium hydroxide (caution: reaction is highly exothermic). The reaction mixture was extracted with CH_2Cl_2 (3X100 mL), and dried with anhydrous Na_2SO_4 . After evaporation of the solvent, the crude product was purified by column chromatography using petroleum ether: CH_2Cl_2 mixture.

2.3.4. Synthesis of (9-hexyl-9H-carbazole-3,6-diyl)bis(phenylmethanone) 3a- 9-hexyl-9H-carbazole (1 gm 3.98 mmol), Benzoyl chloride (1.3 mL, 11.93 mmol), anhydrous aluminium chloride (2.65 gm, 19.89 mmol), dry CH_2Cl_2 (30 mL), yellow coloured solid, Yield-1.25 gm (68%).



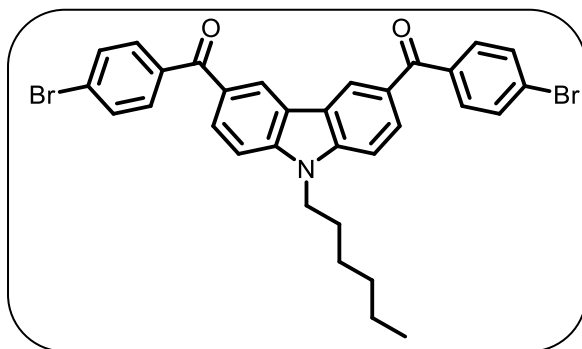
^1H NMR (400 MHz, CDCl_3 , $25\text{ }^\circ\text{C}$): δ = 8.60 (s, 2 H) 8.09 (d, J = 8.54 Hz, 2 H) 7.85 (d, J = 7.32 Hz, 4 H) 7.59 - 7.64 (m, 2 H) 7.53 (t, J = 7.32 Hz, 6 H) 4.40 (t, J = 7.32 Hz, 2 H) 1.90 - 1.99 (m, 2 H) 1.41 - 1.48 (m, 2 H) 1.28 - 1.38 (m, 4 H) 0.86 - 0.92 (t, J = 7.1 Hz, 3H) ppm.

^{13}C NMR (100MHz, CDCl_3 , $25\text{ }^\circ\text{C}$): δ = 196.7, 144.0, 138.9, 132.2, 130.2, 129.9, 129.3, 128.6, 124.4, 123.0, 109.2, 44.0, 31.8, 29.2, 27.2, 22.8, 14.3 ppm.

HR-MS-(ESI $^+$): calculated for $\text{C}_{32}\text{H}_{30}\text{NO}_2$ $[\text{M}+\text{H}]^+ = 460.5890$ found 460.2271.

2.3.5. Synthesis of (9-hexyl-9H-carbazole-3,6-diyl)bis((4-bromophenyl)methanone) (3b)-

9-hexyl-9H-carbazole (1 gm, 3.98 mmol), 4-bromobenzoyl chloride (2.01 gm, 9.15 mmol) anhydrous aluminium chloride (2.65 gm, 19.89 mmol), dry CH₂Cl₂ (30 mL), light yellow coloured solid, Yield-1.72 gm (70%).



¹H NMR (500 MHz, CDCl₃, 25 °C): δ = 8.56 (s, 2 H), 8.05 (dd, J = 8.4, 1.5 Hz, 2 H), 7.72 (d, J = 8.4 Hz, 4 H), 7.67 (d, J = 8.4 Hz, 4 H), 7.53 (d, J = 8.4 Hz, 2 H), 4.41 (t, J = 7.2 Hz, 2 H), 1.89 - 2.00 (m, 2 H), 1.39 - 1.47 (m, 2 H), 1.29 - 1.38 (m, 4 H), 0.88 (t, J = 7.1 Hz, 3 H) ppm.

¹³C NMR (125MHz, CDCl₃, 25 °C): δ = 195.5, 144.1, 137.6, 131.9, 131.7, 129.5, 129.2, 127.2, 124.2, 122.9, 109.3, 44.0, 31.7, 29.2, 27.1, 22.7, 14.2 ppm.

HR-MS-(ESI⁺): calculated for C₃₂H₂₈Br₂NO₂ [M+H]⁺ = 618.3810 found 618.0461.

2.4. Result and discussions

Among the potential RTP candidates, carbazole has undergone diverse functionalization using various combinations of heavy atoms and other functional groups to achieve UOP (Table 2).^[8c,9b,10d,10e] We planned to study the effect of phenylmethanone functionalization on the RTP features of 9-hexylcarbazole, which exhibits a very low RTP lifetime.^[14] Our design strategy comprised of, i. N-alkylation of carbazole to enhance the solubility and impart alkyl- π interaction to promote crystallization, ii. phenylmethanone unit to support a (strain-induced) crystalline assembly formation and stabilize the triplet state by providing hybrid (n,π^*) and (π,π^*) configurations for UOP.^[15] Accordingly, a series of 9-hexylcarbazole molecules with phenylmethanone units at 3 and 3,6-positions were synthesized and unambiguously characterized by ^1H and ^{13}C nuclear magnetic resonance spectroscopies and high-resolution mass spectrometry (Scheme 1). The presence of multi-step synthesis and purification by silica gel column chromatography enabled us to achieve the target molecules in pure form. While our study was progressing, Chen et al., reported the effect of impurity on the afterglow property of carbazoles.^[16] In the purview of this report, we synthesized carbazole in our lab using reported protocols^[17] and confirmed the purity by high-performance liquid chromatography (HPLC) using acetonitrile-water mixture (same condition described in the report) (Scheme 1). After purification by silica gel column chromatography and confirmation of the purity, the lab synthesized carbazole was used for further functionalization. The final molecules were also purified similarly and confirmed the purity by HPLC before starting optical experiments. We compared the results of target molecules synthesized using (purified) commercial and lab synthesized carbazoles, and no appreciable differences were observed. Hence, we would like to mention that the concerns related to the effect of impurity on the present work, if any, are not valid.

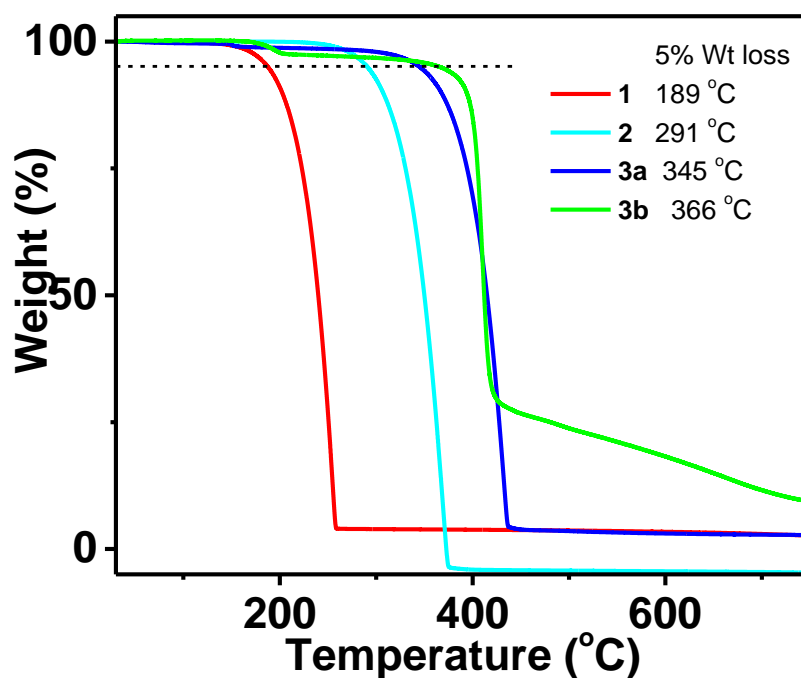


Figure 2.2. Thermogravimetric analysis of 1-3b.

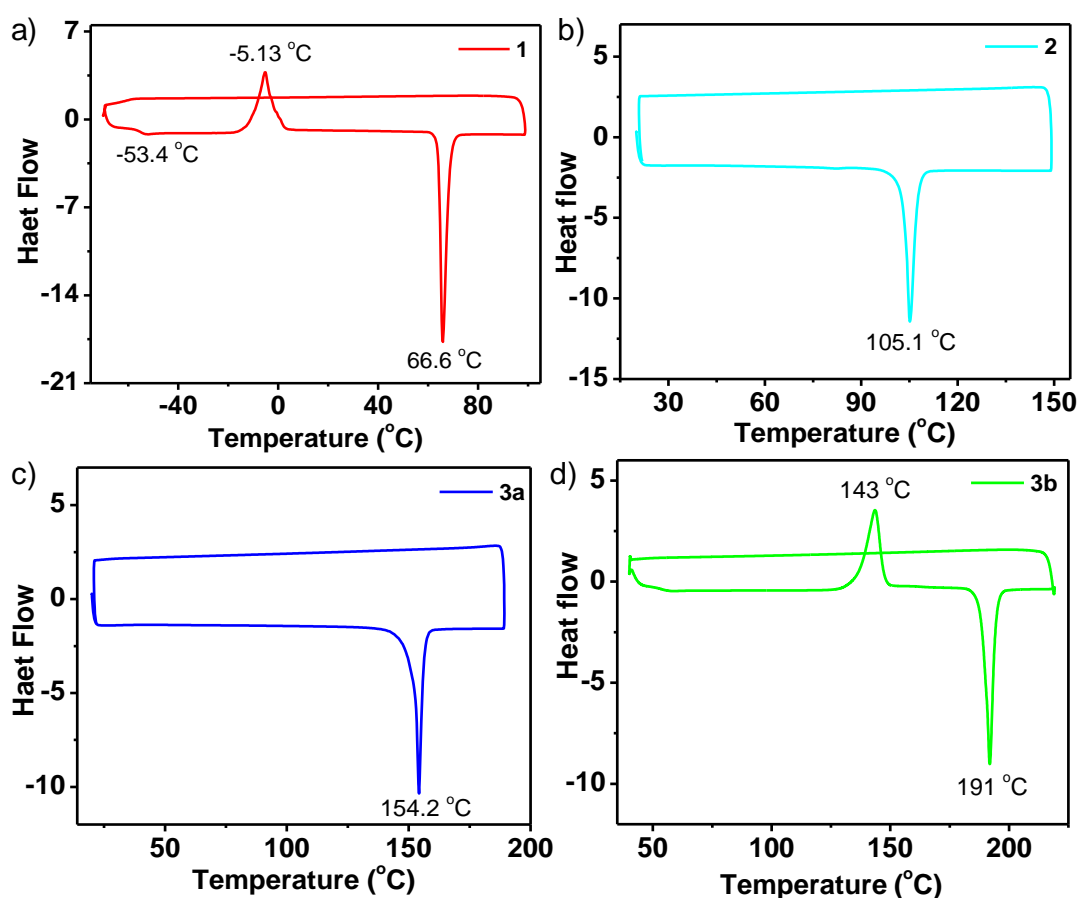


Figure 2.3. DSC thermograms of a) 1, b) 2, c) 3a, d) 3b in the heating trace (second cycle) at a scanning rate of 10 °C/min.

After the complete characterization of the molecules, we checked the thermal stability and followed by optical properties. Thermogravimetric analysis indicated the enhanced stability upon moving from molecule **1** to **3b**, indicating the importance of substitution on 9-hexylcarbazole (Figure 2.2). We observed a similar trend in the melting point of **1-3b** in differential scanning calorimetry experiments as well (Figure 2.3).

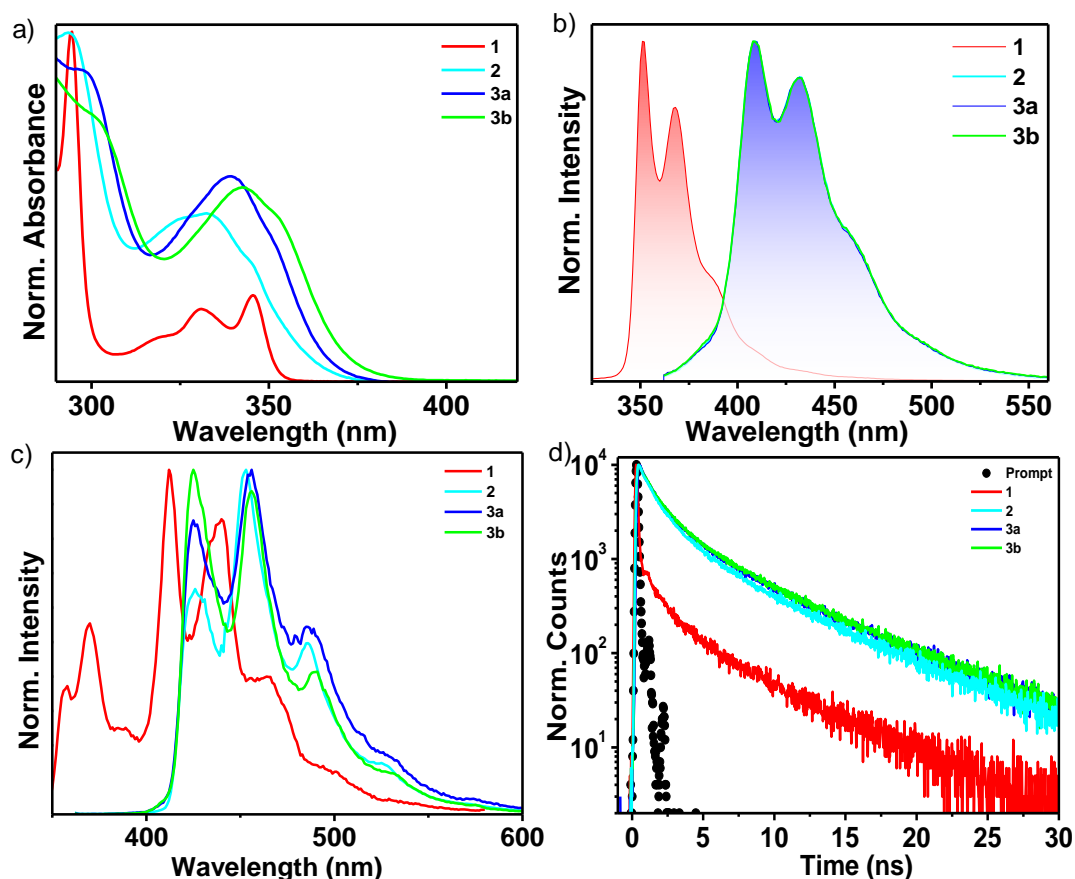


Figure 2.4. Normalized a) absorption, steady-state emission spectra at b) RT c) 77 K of **1-3b** in MTHF solution ($C = 1 \times 10^{-5}$ M, $l = 1$ cm, $\lambda_{\text{ex}} = 294$ nm for **1** and 352 nm for **2-3b**). d) Emission lifetime decay profile of **1-3b** in MTHF solution ($C = 1 \times 10^{-5}$ M, $l = 1$ cm, $\lambda_{\text{ex}} = 374$ nm, $\lambda_{\text{mon}} = 368$ nm for **1** and 408 nm for **2-3b**).

Absorption features of all the luminogens **1-3b** in 2-methyltetrahydrofuran (MTHF) have not varied significantly (Figure 2.4a), compared to **1**, the fluorescence spectra of **2-3b** showed a bathochromic shift of 50 nm due to the increasing electron-withdrawing ability of the carbonyl groups (Figure 2.4b and

Table 3). An increase in the number of benzoyl groups did not alter the fluorescence maximum of **2-3b** in MTHF. Fluorescence lifetime decay profiles in MTHF show that the higher lifetime component varied as 4.11 ns (**1**), 6.39 ns (**2**), 6.04 ns (**3**), and 6.38 ns (**4**) (Figure 2.4d, Table 4 and Table 6). Both red-shifted fluorescence maximum and enhanced fluorescence lifetime for molecules **2-3b** points to the effect of benzylation on carbazole. A comparison of the fluorescence spectra of the MTHF solution at RT (298 K) and 77 K indicates that **1** exhibited additional long-wavelength peaks (400-550 nm) along with a fluorescence peak at 370 nm, whereas a completely red-shifted fluorescence peak appeared for molecules **2-3b** (Figure 2.4c). The fluorescence spectra of **2-3b** both at RT and 77 K match with the red-shifted peak of **1** between 400-550 nm at 77 K (Figure 2.4c).

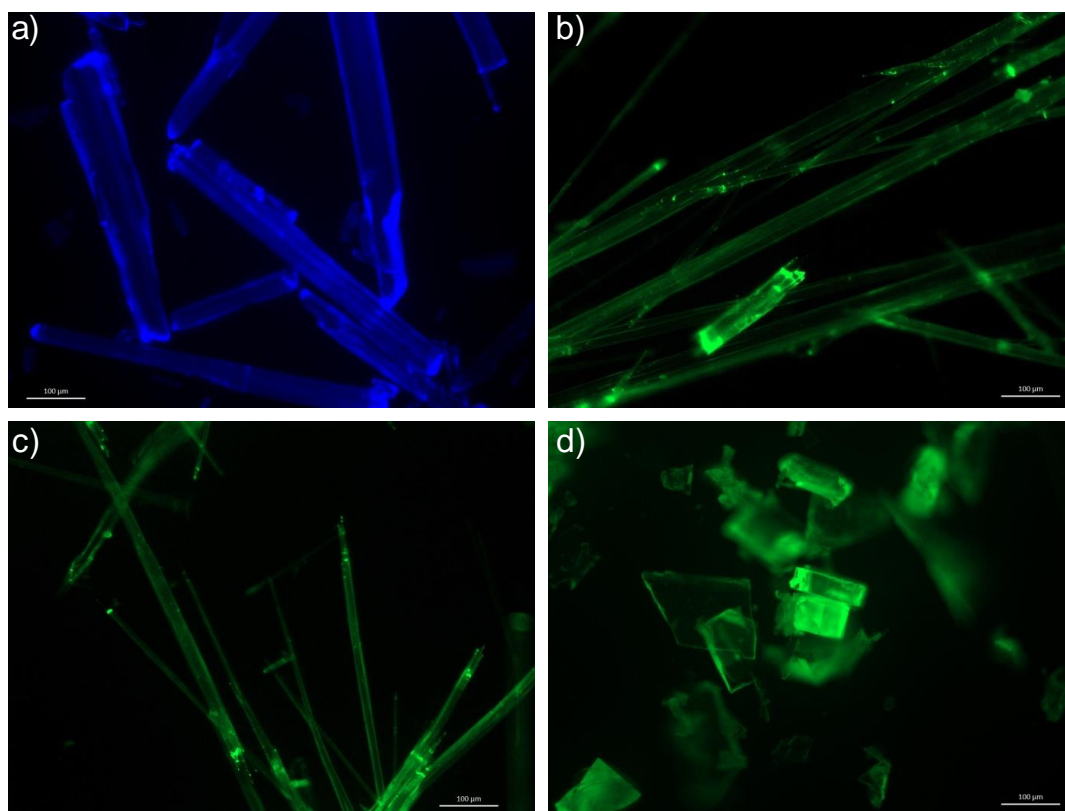


Figure 2.5. Fluorescence microscope images of the crystals of a) **1**, b) **2**, c) **3a**, d) **3b** grown from CH_2Cl_2 , $\lambda_{\text{ex}} = 445$ nm for **1** and 515-565 nm for **2-3b**.

In order to study further, all molecules were crystallized from CH₂Cl₂, and the morphology was visualized by fluorescence microscopy (FM) (Figure 2.5), scanning and transmission electron microscopy (SEM and TEM) images. It was found that molecules **1-3a** formed crystalline rods, whereas flat sheets were formed by **3b**. The bulk purity and ordering of the molecules were confirmed by matching the experimental and theoretical powder X-ray diffraction patterns.

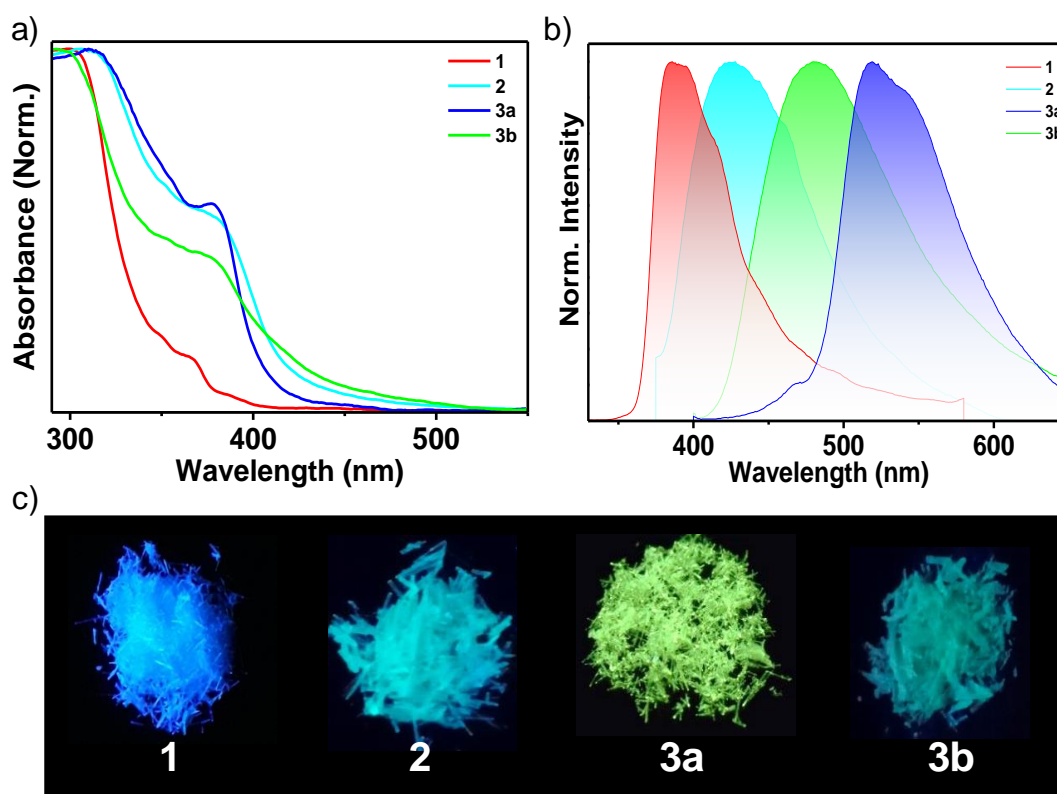


Figure 2.6. Normalized solid-state a) absorption b) emission spectra of **1-3b** crystals at RT. c) Photographs of **1-3b** under UV light (365 nm).

The diffuse reflectance spectra of crystals of **1-3b** exhibited a broad band between 300-450 nm, having an additional absorption band located around 360-380 nm (Figure 2.6a). It is clear from the fluorescence spectra of crystals at RT that molecule **3a** exhibits a far red-shifted peak ($\lambda_{\text{max}} = 517$ nm) than that of **1** ($\lambda_{\text{max}} = 390$ nm), **2** and **3b** ($\lambda_{\text{max}} = 425$ and 490 nm) (Figure 2.6b). Similarly, compared to **1**, molecules **2-3b** exhibited a marked difference in fluorescence features at 77 K in the crystalline state (Figure 2.7). The presence of a long-lived component in the fluorescence lifetime decay of **2-3b** was noticed when the

lifetime was monitored at the fluorescence maxima. Hence, to find out the fluorescence lifetime, the measurement was carried out by monitoring at lower wavelengths and the longer lifetime component varied as 11.1 ns (87%) for **1**, 1.88 ns (17%) for **2**, 3.37 ns (59%) for **3a**, and 3.23 ns (75%) for **3b** (Table 4).

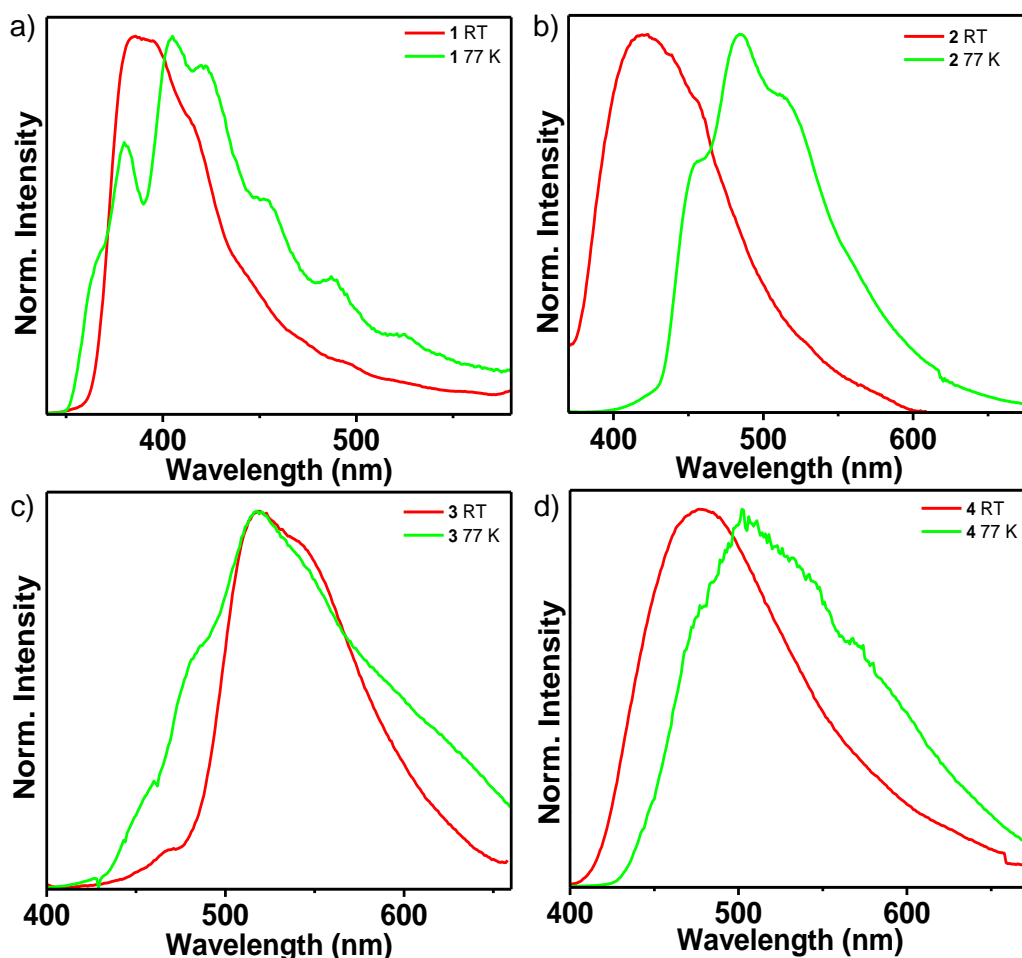


Figure 2.7. Comparison of the normalized crystal state emission spectra of a) **1**, b) **2**, c) **3a** and d) **3b** at RT and 77 K.

The red-shifted fluorescence of the crystals of **2-3b** at RT nearly matches with the corresponding spectra at 77 K, implying RTP for **2-3b** in the crystalline assembly (Figure 2.7). To clarify the presence of RTP for crystals of **2-3b**, phosphorescence spectra were measured and confirmed that the observed red-shifted peak at RT is due to phosphorescence (Figure 2.8a). In the crystalline state, the phosphorescence intensity of **3a** was found to be the highest among all, and it was ~ 27 times higher than that of **1**. The enhanced RTP for **3a** was

visualized by phosphorescence lifetime measurement, and it varied as 5.1, 16.6, 4171, and 114.5 ms for **1-3b**, respectively (Figure 2.8c-f and Table 5,6). Molecule **3a** exhibited a longer phosphorescence lifetime with afterglow for > 12 s upon excitation after just dipping in liquid nitrogen. The phosphorescence quantum yield of the crystals varied as **1** (3.36 %), **2** (0.85 %), **3a** (11.25 %) and **3b** (5.15 %) (Table 6). The observed enhancement in the phosphorescence lifetime of **3a** raised curiosity about the excited triplet state of this particular molecule, and hence we decided to study it in detail.

Time-dependent density functional theory (TD-DFT) computations at the B3LYP/6-31G(d) level of theory for single-molecule in vacuum show that the electron density of the HOMO is located on the carbazole moiety and the LUMO is delocalized over the entire molecule with a considerable extension to the phenylmethanone group (Figure 2.9). The low-lying excited electronic states mainly result from well-described π - π^* transitions along with a significant contribution from the n - π^* character. On examining the relative computed energies for the singlet (S_n) and triplet (T_n) states for **3a**, it has been found that there are many triplet states (T_4 - T_9) nearly degenerate with the first singlet excited state (S_1) (Figure 2.9). As the phenylmethanone functionalization increases, an intense mixing of nearly degenerate excited singlet and triplet states were observed, which could bring out a natural competition between ISC and RISC (Figure 2.9). The energetic proximity of the singlet and the triplet manifold potentials established a small ΔE_{ST} . Thus it appears that molecules **2-3b** have energetically well-matched states that enable efficient singlet-triplet or triplet-singlet crossings. Once T_4 - T_9 levels are populated, relaxation through the triplet manifold to the T_1 state leads to phosphorescence. Besides, we have to consider the strong possibility of RISC in a competitive pathway to exhibit DF. The $\Delta E_{S_1T_1}$ values calculated for the monomer from DFT and phosphorescence spectra varied as 0.72 and 0.32 eV, respectively (Figure 2.8a and 2.9). It shows that the

aggregation of **3a** with the assistance of intermolecular interactions reduces ΔE_{SIT1} to facilitate both ISC and RISC.

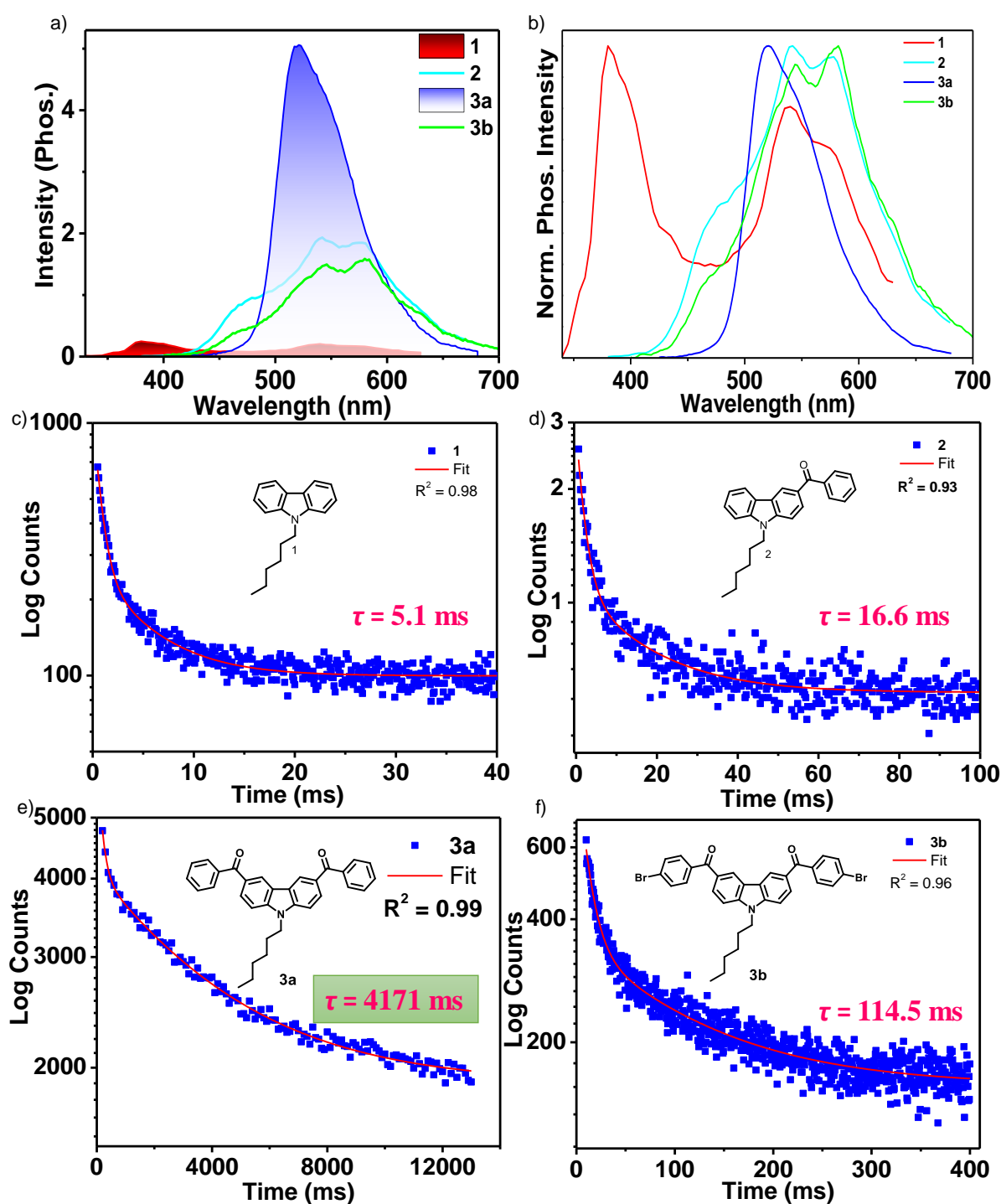


Figure 2.8. a) Phosphorescence spectra and corresponding b) normalized spectra of **1-3b** crystals at RT in air, Phosphorescence lifetime decay of c) **1**, d) **2**, e) **3a**, f) **3b** at RT ($\lambda_{\text{ex}} = 352$ nm, $\lambda_{\text{mon}} = 390$ nm for **1**, 425 nm for **2**, 517 for **3a**, and 480 nm for **3b**).

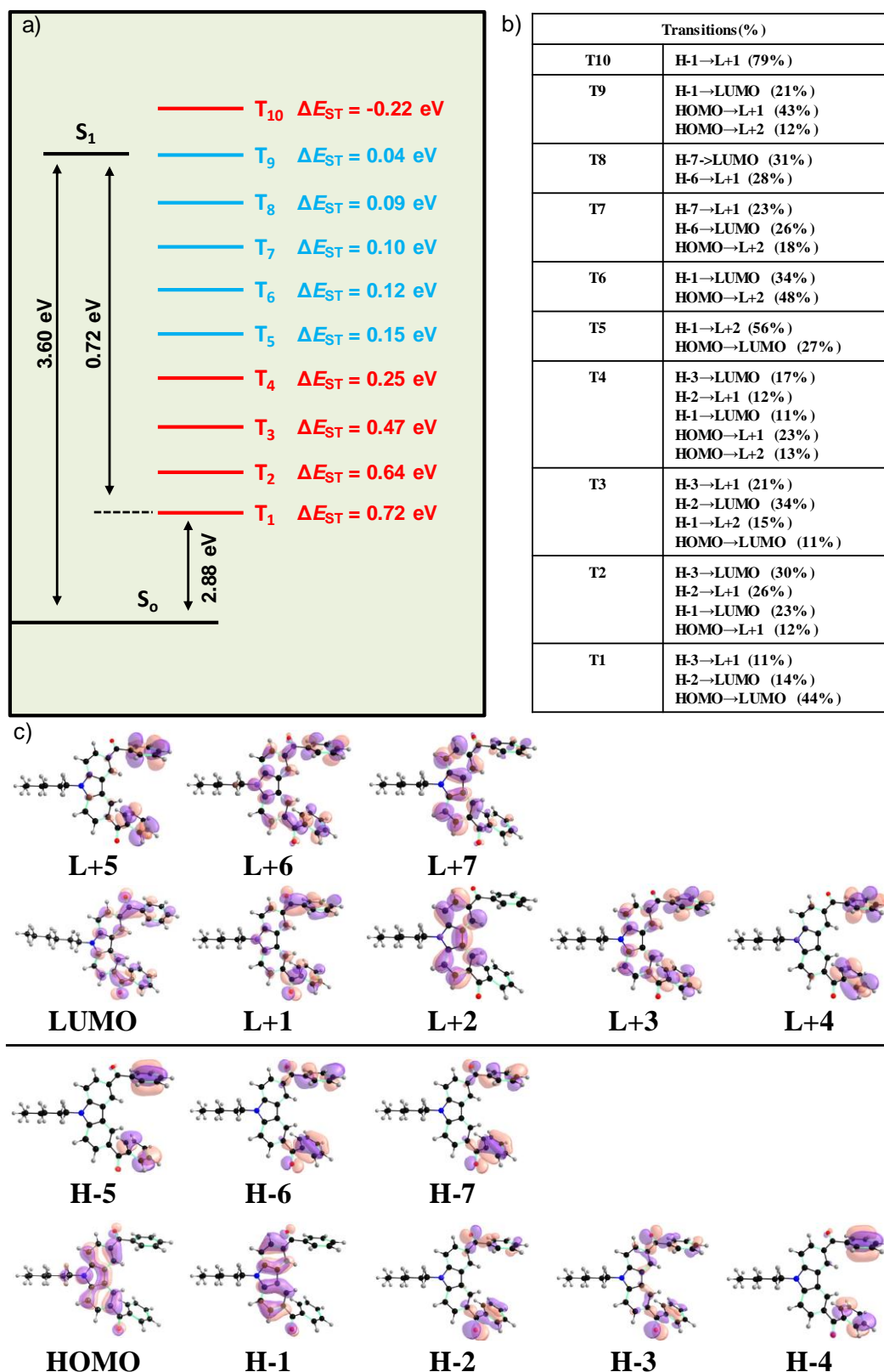


Figure 2.9. Calculated a) energy level diagram showing ΔE_{ST} for **3a** from DFT calculations along with b) probable electronic transitions and c) involved frontier molecular orbitals.

Single-crystal X-ray analysis has been employed to get a deeper structure-property correlation of **1-3b** (Figure 2.10 and 2.11). The unit cell of **3a** contains six molecules arranged in a helical way in two rows along b axis using various intermolecular interactions (Figure 2.10b). An extended molecular array was formed by the arrangement of molecules mainly through π - π interaction (3.34 Å) between carbazole and phenylmethanone units of adjacent molecules (along b-axis) (Figure 2.10a-c). This one-dimensional (1D) helical array is stabilized with the help of CH \cdots π interaction (2.88 Å) between the alkyl chain on carbazole and phenylmethanone unit in the adjacent helical columns to form a three-dimensional network structure. We strongly believe that this kind of space-filled packing (Figure 2.10c) rigidifies the molecular conformations and remarkably blocks the nonradiative decay pathways. The dihedral angle between the aryl groups and carbonyl subunits was found to be around 30° and it enables efficient electronic communication between carbazole and phenylmethanone *via* conjugation (Figure 2.10d). It can be anticipated that better communication between the (n,π^*) from the >C=O and (π,π^*) of carbazole could result in hybrid triplet states. The helical array of **3a** was confirmed by the solid-state circular dichroism (CD) spectrum (Figure 2.10e). A bisignated CD signal observed points to the right-handed helical array of molecules (Figure 2.10a,e). However, no such helical array is present in the case of **1**, **2**, and **3b**, and mainly, a loosely packed crystalline assembly was observed (Figure 2.11). Especially **3b** packs in a kind of slipped molecular arrangement with a carbazole-carbazole distance of 5.7 Å (Figure 2.11c). Hence, the helical array of **3a** is responsible for the enhanced RTP through an efficient space-filled molecular packing by using maximum intermolecular interactions (Figure 2.10a-c).

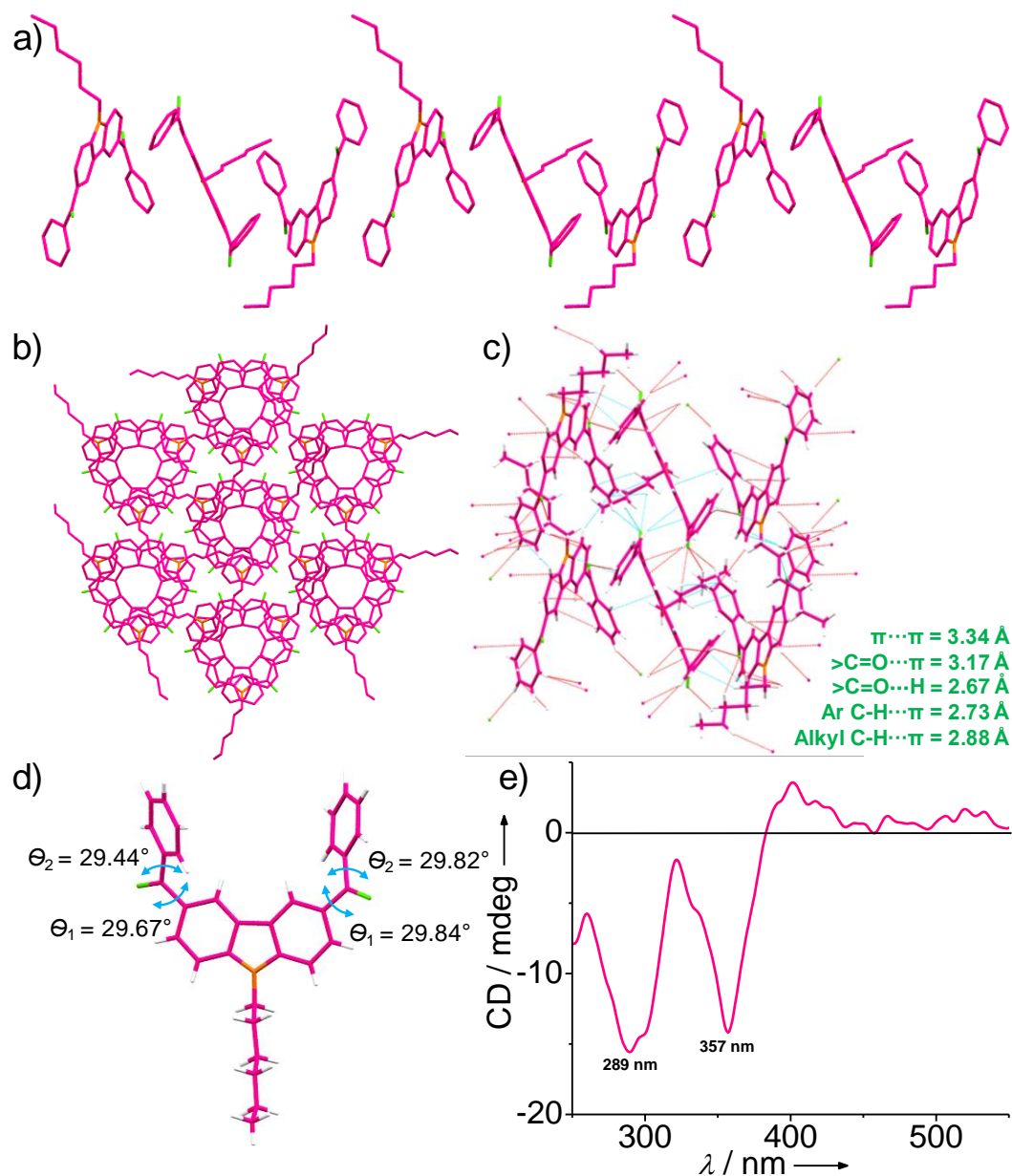


Figure 2.10. (a) The extended molecular packing of **3a** forming the helical 1D-array in the b-axis. (b) Six adjacent helical arrays of **3a** leading to extended columnar packing in the c-axis. (c) All possible intermolecular interactions in a unit cell of **3a** and (d) crystal structure of **3a** showing the dihedral angles. (e) The solid-state CD spectrum of **3a** crystals at RT.

Recently, helical/twisted aromatic systems have been of interest to promote intersystem crossing.^[18] Hariharan and co-workers showed an enhanced intersystem crossing in core-twisted perylene diimide.^{18a} Besides, Juríček, and

coworkers reported the impact of a strain-induced helical twist on the electronic structure that leads to triplet state stabilization of cethrene, a dibenzo-annulated [5]helicene derivative.^[18c,d] Hence, the stabilization of the triplet state of **3a** is strongly supported by the presence of strained helical arrays. In addition, we have tested the emission of **3a** in poly(methyl methacrylate) (PMMA) matrix and found that the spectral feature has been significantly changed, and the lifetime also drastically decreased (8.15 ms) due to the lack of specific molecular ordering.

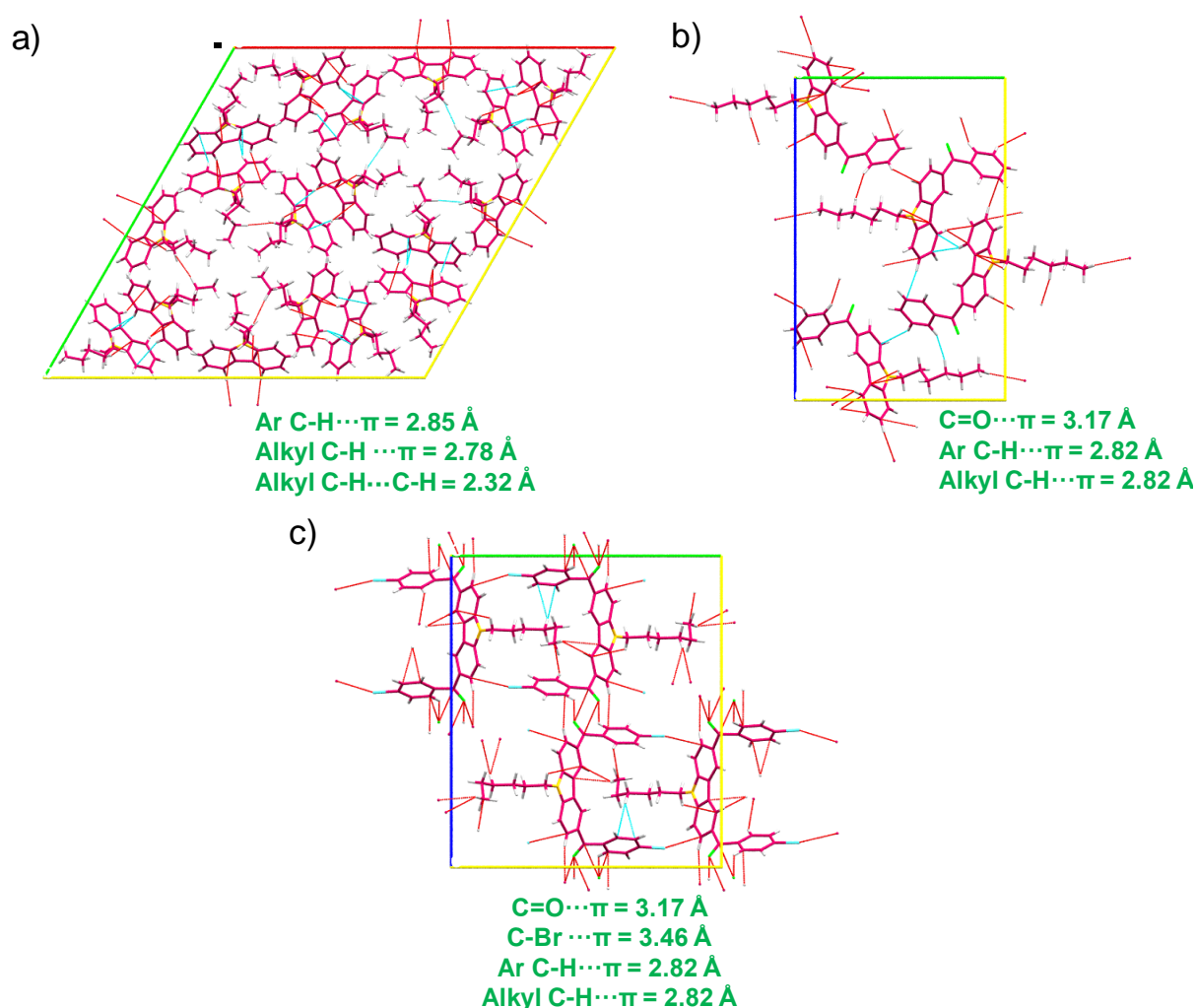


Figure 2.11. The molecular packing of (a) **1** (b) **2** and (c) **3b** in the unit cell.

A perfectly aligned and densely packed fluorescent pi-conjugated molecular array with a large Stokes shift is known for optical waveguiding (WG).^[2a,19] Hence, to check the possibility of WG, one end of the crystals of **3a** was excited

at 532 and 633 nm using a 10X, 0.3 NA objective lens^[20] and found that the micro rods exhibited intense green and red emissions at the distal end, respectively, with characteristic features of the optical WG (Figure 2.12a). The maximum phosphorescence intensity at the distal end was observed when it is excited with polarization along the long axis of the rod, and it has been significantly reduced in the perpendicular polarization. Since molecule **3a** is RTP active, it is obvious that the phosphorescence of **3a** propagates along the long axis of the single crystal rods (Figure 2.12b). The self-waveguided phosphorescence was imaged on a rod with an excitation spot ($\lambda = 532$ nm) positioned at different distances from the end of the rod (Figure 2.12b).

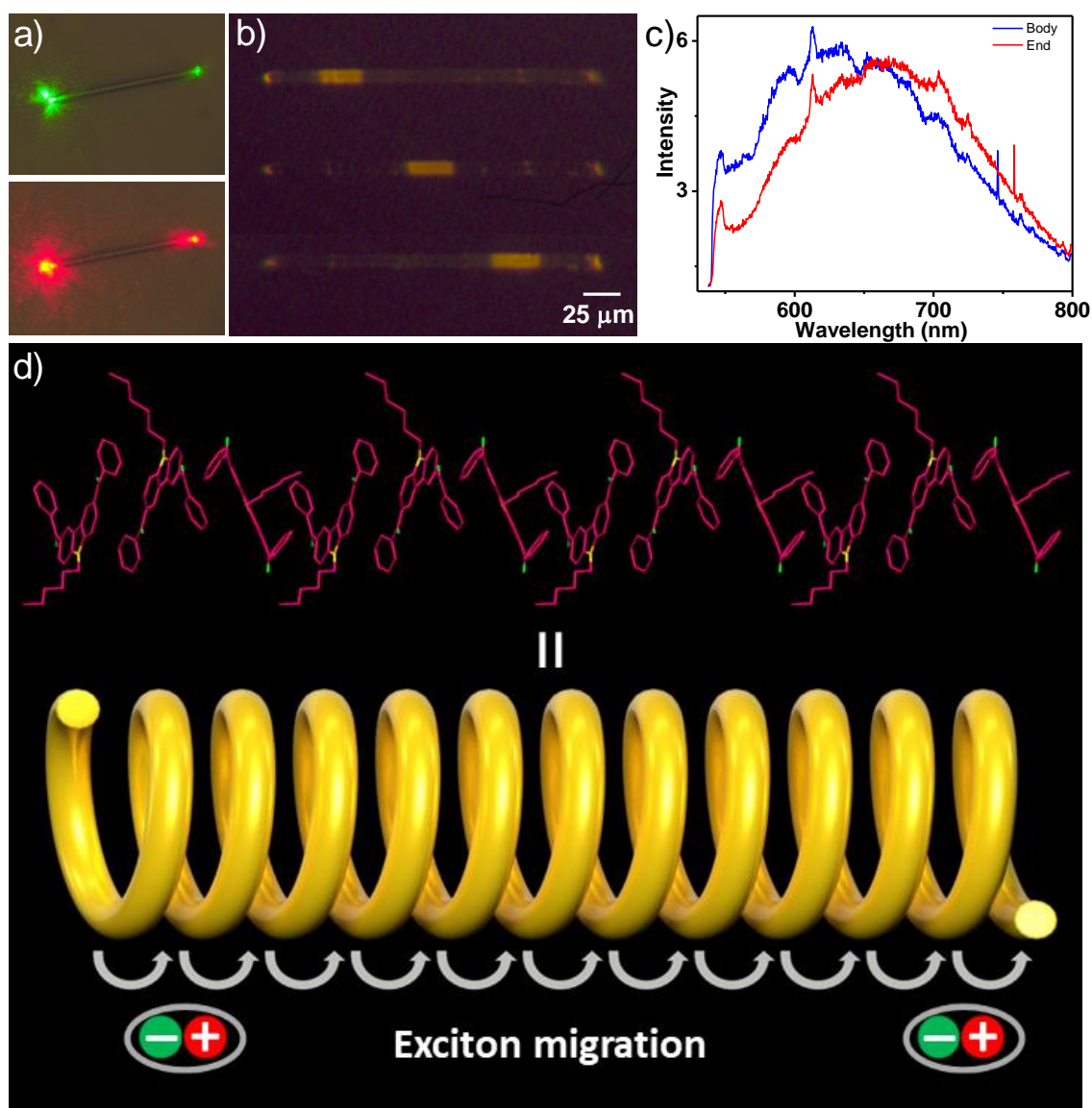


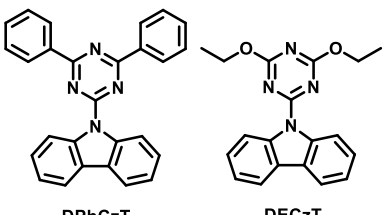
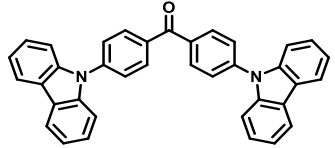
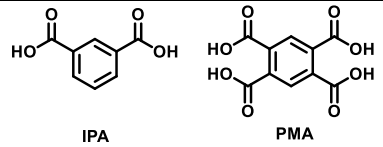
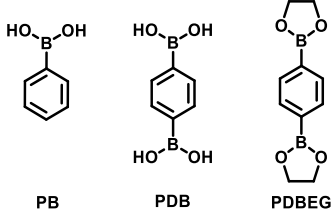
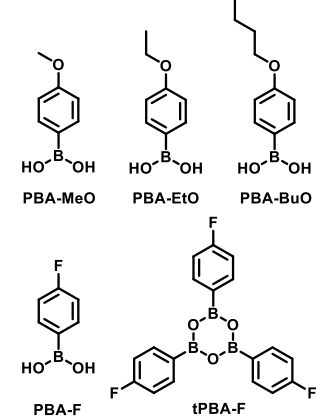
Figure 2.12. (a) Passive waveguiding properties of the crystal of **3a** upon excitation at 532 (above) and 633 nm (below). (b) Phosphorescence waveguiding by the single crystalline rods of **3a**. (c) The red-shifted phosphorescence observed at the distal end of the crystal compared to the body ($\lambda_{\text{ex}} = 532$ nm). (d) Schematic of the helical array of **3a** leading to triplet exciton migration.

The propagation loss coefficient calculated for phosphorescence of **3a** by measuring the intensity at the distal end and the distance from the excitation point is approximately 0.028 dB/ μm . In order to distinguish between the optical WG and exciton migration, we checked the difference in emission from the body and tip of the rods. A red-shifted phosphorescence at the distal end of the crystal compared to the body at RT was observed (Figure 2.12c).^[21] The red-shifted emission is due to the triplet exciton migration^[21,22] from the body to the tip of **3a** single crystal rods and thereby actively supports the long-lived phosphorescence (Figure 2.12d). In the case of other molecules, only waveguiding and no exciton migration was observed, and it points to the critical supportive role of molecular packing assisted exciton migration in achieving a longer phosphorescence lifetime.

TD-DFT studies revealed a qualitative picture of the equal possibility of ISC and RISC for **3a** due to the presence of energetically matching singlet and triplet levels. Even though a shorter component is noticed, the unambiguously confirmed long-lived phosphorescence decay supersedes it with the support of triplet exciton migration through helical molecular arrays. The afterglow observed for more than 12 s after just dipping in liquid nitrogen supports the suppression of RISC and thereby endorses improved radiative decay through the triplet manifolds at low temperatures. The efficient molecular ordering in the helical array of **3a** ensures that the populated triplet decays very slowly. Here T_1 acts as a trap state and plays a vital role in triplet exciton migration, as revealed by the WG results. Hence, it can be concluded that the peculiar helical molecular packing results in a long phosphorescence lifetime of **3a** compared to other

molecules in the series, and it is substantiated by the crystal structure and phosphorescence lifetime. In all other cases, the triplet states mostly undergo nonradiative internal conversions compared to radiative transitions.

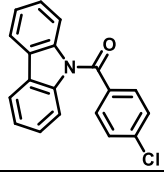
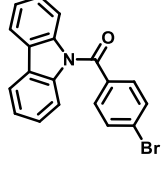
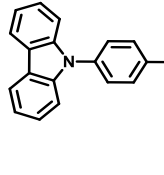
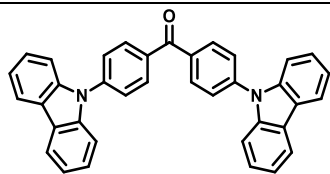
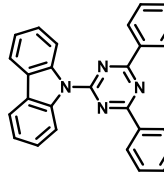
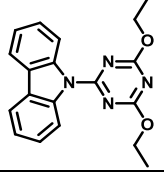
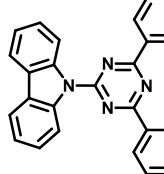
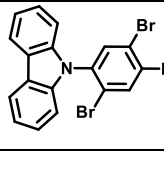
Table 1. Details of the organic phosphors exhibiting phosphorescence lifetime above 1 s.

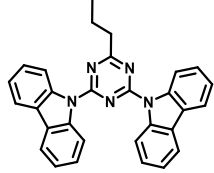
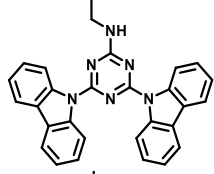
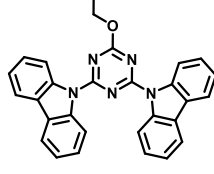
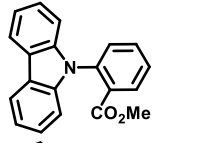
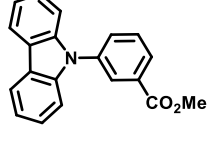
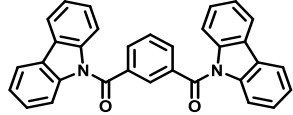
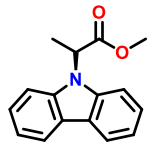
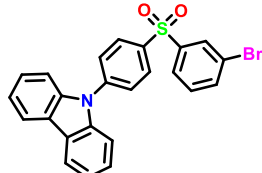
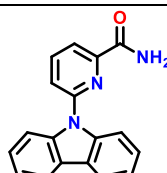
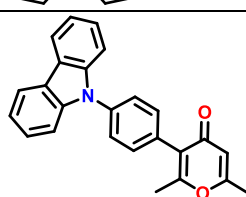
Sl. No.	Molecule	Lifetime	Reason	Reference
1.	 <p>DPhCzT DECzT</p>	1.05 s (DPhCzT) 1.35 s (DECzT)	Effective stabilization of triplet excited states through strong coupling in H-aggregated molecules	<i>Nat. Mat.</i> , 2015 , 14, 685-690.
2.	 <p>1CA Cocrystal of molecule 1CA and trichloromethane</p>	1.7 s (1CA)	Strong interaction between 1CA and trichloromethane through hydrogen bonding.	<i>Adv. Opt. Mater.</i> , 2015 , 3, 1184-1190.
3.	 <p>IPA PMA</p>	0.99 s (IPA) 1.1 s (PMA)	Nuclear spin magnetism-assisted spin exchange of a radical ion pair	<i>Phys. Chem. Chem. Phys.</i> , 2015 , 17, 15989-15995.
4.	 <p>PB PDB PDBEG</p>	1.2 s (PB) 1.6 s (PDBEG)	Charge transfer (CT) assist for the prolonged phosphorescence lifetime	<i>ChemPhotoChem.</i> , 2017 , 1, 102 -106
5.	 <p>PBA-MeO PBA-EtO PBA-BuO</p> <p>PBA-F tPBA-F</p>	2.24 s (PBA-MeO) 1.11 s (PBA-EtO) 1.28 s (PBA-BuO) 1.34 s (PBA-F) 1.96 s (tPBA-F)	Rigid conformation and expanded conjugation induced by molecular alignment contribute to the persistent RTP. And strong intermolecular interactions via hydrogen bonding.	<i>Chem. Sci.</i> , 2017 , 8, 8336-8344.

6.		2.5 s (24FPB)	Stabilisation of triplet excited state by H-aggregation and additional O-H...F interactions in crystal state	<i>Adv. Optical Mater.</i> , 2019 , 1800820.
7.		2.00 s (ME-IPA)	Thermally activated delayed fluorescence (TADF)-assisted Förster resonance energy transfer upto 76% leads to 2 s lifetime.	<i>J. Am. Chem. Soc.</i> , 2018 , 140, 10734-10739. <i>Adv. Funct. Mater.</i> , 2019 , 29, 1807599.
8.		2.45 s (DMOT)	Molecular movement in the same plane and H-aggregation are responsible for the tunable UOP under study.	<i>Nat. Photonics</i> , 2019 , 13, 406-411.
9.		1.74 s (Hydantoin) 1.27 s (MDHA)	Stabilisation of triplet state by abundant intermolecular interactions and fragmental packing in the crystal state	<i>Mater. Horiz.</i> 2020 , 7, 2105-2112.
10.		4171 ms	Triplet exciton migration in helical arrays	This work

Table 2. Details of the carbazole-based phosphors exhibiting phosphorescence lifetime above 500 ms.

Molecules	λ_{em} (nm)	ϕ_p (%)	τ (ms)	Reference
	555	-	910	<i>J. Phys. Chem. Lett.</i> 2018 , 9, 335-339.
	550	-	540	<i>Chem. Commun.</i> 2015 , 51, 10381-10384.
	530	0.7	646	<i>Adv. Mater.</i> 2017 , 29, 1606829.

	570	8.3	847	
	536	3.4	667	<i>Adv. Mater.</i> 2017 , 29, 1701244.
	552	1.4	518	<i>Adv. Mater.</i> 2015 , 27, 6195-6201.
	553	-	1.7 s	<i>Adv. Opt. Mater.</i> 2015 , 3, 1184-1190.
	530	1.25	1066	<i>Nat. Mater.</i> 2015 , 14, 685-690.
	529	0.3	710	
	534	1.59	861	<i>Adv. Mater.</i> 2017 , 29, 1606665.
	546	38.1	560	<i>J. Phys. Chem. Lett.</i> 2019 , 10, 595-600.

	546	1.36	650	
	534	1.70	789	<i>J. Mater. Chem. C</i> 2018 , 6, 226-233.
	553	1.63	632	
	550	2.0	619.2	<i>Angew. Chem. Int. Ed.</i> 2018 , 57, 7997-8001.
	545	2.1	795	
	529	5.7	710.6	<i>Adv. Mater.</i> 2019 , 1807222.
	550	-	603	<i>Angew. Chem. Int. Ed.</i> 2020 , 59, 4756-4762.
	545	3.42	530	<i>Angew. Chem. Int. Ed.</i> 2020 , 59, 17451-17455.
	550	21.3	846.4	<i>Adv. Optical Mater.</i> 2020 , 2001685.
	556	7.5	764	<i>J. Mater. Chem. C</i> , 2020 , 8, 17410-17416.

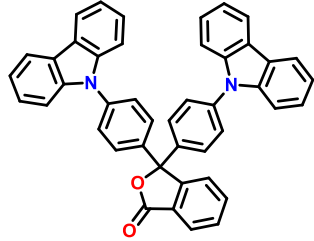
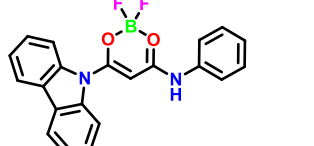
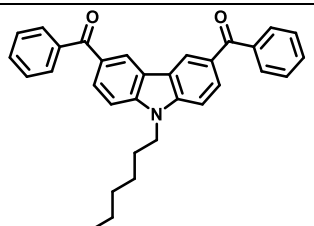
	553	5.1	810	<i>Adv. Optical Mater.</i> 2021 , 2001549.
	543	-	610	<i>Angew. Chem. Int. Ed.</i> 2021 , 60, 24984-24990.
	521	30	4171	<i>This work</i>

Table 3. Photophysical properties of compounds **1-3b** in MTHF (1×10^{-5} M) and solid.

Compound		λ_{ab} (nm)	Log ϵ	λ_{em} (nm)	ϕ (%)
1	Solution	294	4.74	368	-
	Solid	296	-	390	59.00
2	Solution	352	3.99	408	-
	Solid	313	-	425	03.68
3a	Solution	352	4.11	408	-
	Solid	315	-	517	13.58
3b	Solution	352	4.33	408	-
	Solid	310	-	480	27.14

Table 4. Fluorescence lifetime of **1-3b** in MTHF solution and crystal-state.

Compound	λ_{ex}	Lifetime (ns) (solution)	λ_{ex}	Lifetime (ns) (crystal-state)
1	368 nm	0.034 (64.37%) 4.11 (35.63%)	390 nm	11.09
2	408 nm	1.21 (43.17%) 6.39 (56.83%)	425 nm	1.36
3a	408 nm	1.15 (46.42%) 6.04 (53.58%)	517 nm	2.92
3b	408 nm	1.24 (42.85%) 6.38 (57.15)	480 nm	2.53

Table 5. Phosphorescence lifetime of **1-3b** in crystal state.

Compound	λ_{ex}	Lifetime (ms)	R^2
1	390 nm	0.71 (16.87%) 5.11 (83.13%)	0.98
2	425 nm	2.00 (22.98%) 16.63 (77.02%)	0.93
3a	517 nm	106.47 (84.36%) 4171.00 (15.64%)	0.99
3b	480 nm	10.66 (76.5%) 114.46 (23.5%)	0.96

Table 6. Photophysical parameters of compounds **1-3b** based on fluorescence and phosphorescence experiments in the crystal state.

Molecules	QY_{Fl} [%]	τ_{Fl} [ns]	$k_{\text{nr, Fl}} [\times 10^9 \text{ S}^{-1}]$	$k_{\text{r, Fl}} [\times 10^9 \text{ S}^{-1}]$	$k_{\text{isc}} [\times 10^7 \text{ S}^{-1}]$	QY_{Phos} [%]	τ_{Phos} [ms]	$k_{\text{nr, Phos}} [\text{S}^{-1}]$	$k_{\text{r, Phos}} [\text{S}^{-1}]$
1	59.00	11.09	0.033	0.053	0.302	3.36	5.1	189.4	6.50
2	03.68	1.36	0.701	0.027	0.625	0.85	16.6	59.72	0.51
3a	13.58	2.92	0.257	0.046	3.85	11.25	4171	0.212	0.026

3b	27.14	2.53	0.267	0.107	2.03	5.15	114.5	8.28	0.44
-----------	--------------	-------------	--------------	--------------	-------------	-------------	--------------	-------------	-------------

2.5. Conclusion

In summary, we have reported a new series of phenylmethanone functionalized N-alkylated carbazoles exhibiting UOP. A helical array by the peculiar molecular packing of 3,6-bis(phenylmethanone) substituted 9-hexylcarbazole in the crystal state enabled to mix-up of the singlet-triplet states to create hybrid triplets to enhance the intersystem crossings. By optimizing the molecular structure and a strained crystal packing, a metal- and heavy atom-free carbazole derivative resulted in a significant improvement of phosphorescence lifetime and quantum yield. A combined experimental and theoretical study sheds light on the stabilization of the triplet state by the helical arrays, and the presence of triplet exciton migration results in the longer phosphorescence lifetime, so far reported for a single molecule crystal. The findings put forth a new strategy of helical arrays to support long-lived phosphorescence under ambient conditions and definitely will invoke the development of new organic phosphors.

2.6. References

- [1] a) A. Forni, E. Lucenti, C. Botta, E. Cariati, *J. Mater. Chem. C*. **2018** *6*, 4603; b) M. Baroncini, G. Bergamini, P. Ceroni, *Chem. Commun.* **2017**, 53, 2081; c) G. Baryshnikov, B. Minaev, H. Ågren, *Chem. Rev.* **2017**, *117*, 6500; d) X. Yang, G. Zhou, W-Y. Wong, *Chem. Soc. Rev.* **2015**, *44*, 8484.
- [2] a) Z. Yu, Y. Wu, L. Xiao, J. Chen, Q. Liao, J. Yao, H. Fu, *J. Am. Chem. Soc.* **2017**, *139*, 6376; b) S. M. A. Fateminia, Z. Mao, S. Xu, Z. Yang, Z. Chi, B. Liu, *Angew. Chem. Int. Ed.* **2017**, *56*, 12160; *Angew. Chem.* **2017**, *129*, 12328; c) G. Zhang, G. M. Palmer, M. Dewhirst, C. L. Fraser, *Nat. Mater.* **2009**, *8*, 747.

- [3] a) V. C. Wakchaure, K. C. Ranjeesh, Goudappagouda. T. Das, K. Vanka, R. Gonnade, S. S. Babu, *Chem. Commun.* **2018**, *54*, 6028; b) G. He, B. D. Wiltshire, P. Choi, A. Savin, S. Sun, A. Mohammadpour, M. J. Ferguson, R. McDonald, S. Farsinezhad, A. Brown, K. Shankar, E. Rivard, *Chem. Commun.* **2015**, *51*, 5444.
- [4] a) Goudappagouda, A. Manthanath, V. C. Wakchaure, K. C. Ranjeesh, T. Das, K. Vanka, T. Nakanishi, S. S. Babu, *Angew. Chem. Int. Ed.* **2019**, *58*, 2284; *Angew. Chem.* **2019**, *131*, 2306; b) O M. S. Kwon, D. Lee, S. Seo, J. Jung, J. Kim, *Angew. Chem. Int. Ed.* **2014**, *53*, 11177; *Angew. Chem.* **2014**, *126*, 11359; c) Bolten, K. Lee, H. J. Kim, K. Y. Lin, J. Kim, *Nat. Chem.* **2011**, *3*, 205.
- [5] a) Kenry, C. Chen, B. Liu, *Nat. Commun.* **2019**, *10*, 2111; b) S. Hirata, *J. Mater. Chem. C.* **2018**, *6*, 11785; c) S. Xu, R. Chen, C. Zheng, W. Huang, *Adv. Mater.* **2016**, *28*, 9920; d) Y. Li, M. Gecevicius, J. Qiu, *Chem. Soc. Rev.* **2016**, *45*, 2090; e) H. Chen, X. Ma, S. Wu, H. Tian, *Angew. Chem. Int. Ed.* **2014**, *53*, 14149; *Angew. Chem.* **2014**, *126*, 14373; f) S. K. Lower, M. A. El-Sayed, *Chem. Rev.* **1966**, *66*, 199.
- [6] a) S. Kuila, S. J. George, *Angew. Chem. Int. Ed.* **2020**, *59*, DOI:10.1002/anie.202002555; *Angew. Chem. Int. Ed.* **2020**, *132*, DOI:10.1002/ange.202002555; b) S. Kuila, K. V. Rao, S. Garain, P. K. Samanta, S. Das, S. K. Pati, M. Eswaramoorthy, S. J. George, *Angew. Chem. Int. Ed.* **2018**, *57*, 17115; *Angew. Chem.* **2018**, *130*, 17361.
- [7] a) R. Kabe, N. Notsuka, K. Yoshida, C. Adachi, *Adv. Mater.* **2016**, *28*, 655; b) S. Hirata, K. Totani, J. Zhang, T. Yamashita, H. Kaji, S. R. Marder, T. Watanabe, C. Adachi, *Adv. Opt. Mater.* **2013**, *1*, 438; c) C. S. Bilen, N. Harrison, D. J. Morantz, *Nature*, **1978**, *271*, 235.
- [8] a) Y. Xiong, Z. Zhao, W. Zhao, H. Ma, Q. Peng, Z. He, X. Zhang, Y. Chen, X. He, J. W. Y. Lam, B. Z. Tang, *Angew. Chem. Int. Ed.* **2018**, *57*, 7997; *Angew. Chem.* **2018**, *130*, 8129; b) Z. He, W. Zhao, J. W. Y. Lam,

- Q. Peng, H. Ma, G. Liang, I. Shuai, B. Z. Tang, *Nat. Commun.* **2017**, *8*, 416; c) W. Zhao, Z. He, J. W. Y. Lam, Q. Peng, H. Ma, Z. Shuai, G. Bai, J. Hao, B. Z. Tang, *Chem.* **2016**, *1*, 592.
- [9] a) L. Gu, H. Shi, M. Gu, K. Ling, H. Ma, S. Cai, L. Song, C. Ma, H. Li, G. Xing, X. Hang, J. Li, Y. Gao, W. Tao, Z. Shuai, Z. An, X. Liu, W. Huang, *Angew. Chem. Int. Ed.* **2018**, *57*, 8425; *Angew. Chem.* **2018**, *130*, 8561; b) S. Cai, H. Shi, Z. Zhang, X. Wang, H. Ma, N. Gan, Q. Wu, Z. Cheng, K. Ling, M. Gu, C. Ma, L. Gu, Z. An, W. Huang, *Angew. Chem. Int. Ed.* **2018**, *57*, 4005; *Angew. Chem.* **2018**, *130*, 4069; c) Z. An, C. Zheng, Y. Tao, R. Chen, H. Shi, T. Chen, Z. Wang, H. Li, R. Deng, X. Liu, W. Huang, *Nat. Mater.* **2015**, *14*, 685.
- [10] a) Z. He, H. Gao, S. Zhang, S. Zheng, Y. Wang, Z. Zhao, D. Ding, B. Yang, Y. Zhang, W. Z. Yuan, *Adv. Mater.* **2019**, *31*, 1807222; b) T. Ogoshi, H. Tsuchida, T. Kakuta, T. Yamagishi, A. Taema, T. Ono, M. Sugimoto, M. Mizuno, *Adv. Funct. Mater.* **2018**, *28*, 1707369; c) S. Hirata, M. Vacha, *Adv. Optical Mater.* **2017**, *5*, 1600996; d) Y. Xie, Y. Ge, Q. Peng, C. Li, Q. Li, Z. Li, *Adv. Mater.* **2017**, *29*, 1606829; e) Z. Yang, Z. Mao, X. Zhang, D. Ou, Y. Mu, Y. Zhang, C. Zhao, S. Liu, Z. Chi, J. Xu, Y.-C. Wu, P.-Y. Lu, A. Lien, M. R. Bryce, *Angew. Chem. Int. Ed.* **2016**, *55*, 2181; *Angew. Chem.* **2016**, *128*, 2221; f) J. Wei, B. Liang, R. Duan, Z. Cheng, C. Li, T. Zhou, Y. Yi, Y. Wang, *Angew. Chem. Int. Ed.* **2016**, *55*, 15589; *Angew. Chem.* **2016**, *128*, 15818; g) Y. Katsurada, S. Hirata, K. Totani, M. Watanabe, M. Vacha, *Adv. Optical Mater.* **2015**, *3*, 1726.
- [11] a) M. Li, K. Ling, H. Shi, N. Gan, L. Song, S. Cai, Z. Cheng, L. Gu, X. Wang, C. Ma, M. Gu, Q. Wu, L. Bian, M. Liu, Z. An, H. Ma, W. Huang, *Adv. Optical Mater.* **2019**, 1800820; b) B. Zhou, D. Yan, *Adv. Funct. Mater.* **2019**, *29*, 1807599; c) L. Gu, H. Shi, L. Bian, M. Gu, K. Ling, X. Wang, H. Ma, S. Cai, W. Ning, L. Fu, H. Wang, S. Wang, Y. Gao, W.

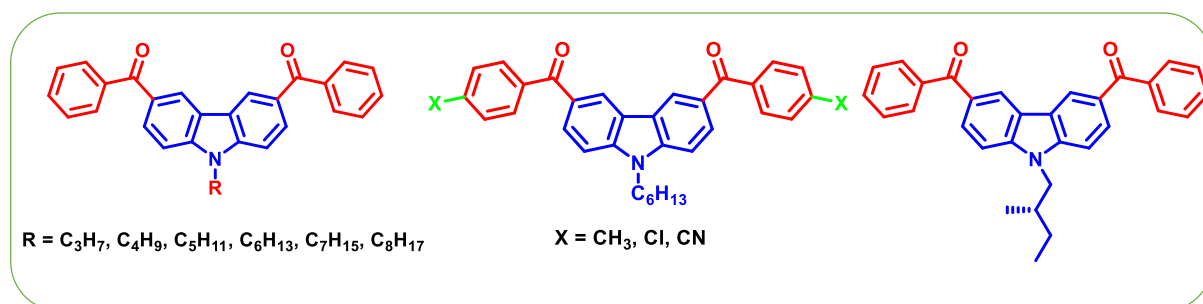
- Yao, F. Huo, Y. Tao, Z. An, X. Liu, W. Huang, *Nat. Photonics* **2019**, *13*, 406; d) L. Bian, H. Shi, X. Wang, K. Ling, H. Ma, M. Li, Z. Cheng, C. Ma, S. Cai, Q. Wu, N. Gan, X. Xu, Z. An, W. Huang, *J. Am. Chem. Soc.* **2018**, *140*, 10734; e) Z. Chai, C. Wang, J. Wang, F. Liu, Y. Xie, Y.-Z. Zhang, J.-R. Li, Q. Lia, Z. Li, *Chem. Sci.* **2017**, *8*, 8336.
- [12] H. Uoyama, K. Goushi, K. Shizu, H. Nomura, C. Adachi, *Nature* **2012**, *492*, 234.
- [13] a) E. Yashima, N. Ousaka, D. Taura, K. Shimomura, T. Ikai, K. Maeda, *Chem. Rev.* **2016**, *116*, 13752; b) C. C. Lee, C. Grenier, E. W. Meijer, A. P. H. J. Schenning, *Chem. Soc. Rev.* **2009**, *38*, 671; c) A Maity, M Gangopadhyay, A Basu, S Aute, SS Babu, A Das, *J. Am. Chem. Soc.* **2016**, *138*, 11113.
- [14] a) W. Li, Q. Huang, Z. Mao, Q. Li, L. Jiang, Z. Xie, R. Xu, Z. Yang, J. Zhao, T. Yu, Y. Zhang, M. P. Aldred, Z. Chi, *Angew. Chem. Int. Ed.* **2018**, *57*, 12727; *Angew. Chem.* **2018**, *130*, 12909; b) Z. Zhang, L. Tang, X. Fan, Y. Wang, K. Zhang, Q. Sun, H. Zhang, S. Xue, W. Yang, *J. Mater. Chem. C.* **2018**, *6*, 8984.
- [15] N. J. Turro, *Modern Molecular Photochemistry*, University Science Books, Sausalito, **1978**.
- [16] C. Chen, Z. Chi, K. C. Chong, A. S. Batsanov, Z. Yang, Z. Mao, Z. Yang, B. Liu, *ChemRxiv.* **2019**, DOI:10.26434/chemrxiv.9895724.
- [17] a) G. Wang, B. Xiong, C. Zhou, Y. Liu, W. Xu, C.-A. Yang, K.-W. Tang, W.-Y. Wong, *Chem. Asian J.* **2019**, *14*, 4365.
- [18] a) K. Nagarajan, A. R. Mallia, K. Muraleedharan, M. Hariharan, *Chem. Sci.* **2017**, *8*, 1776; b) S. Hirata, M. Vacha, *J. Phys. Chem. Lett.* **2016**, *7*, 1539; c) P. Ravat, T. Šolomek, M. Rickhaus, D. Häussinger, M. Neuburger, M. Baumgarten, M. Juriček, *Angew. Chem. Int. Ed.* **2016**, *55*, 1183; *Angew. Chem.* **2016**, *128*, 1198; d) M. Rickhaus, M. Mayor, M. Juriček, *Chem. Soc. Rev.* **2016**, *45*, 1542.

- [19] H. Liu, Z. Bian, Q. Cheng, L. Lan, Y. Wang, H. Zhang, *Chem. Sci.* **2019**, *10*, 227.
- [20] A. B. Vasista, H. Jog, T. Heilpern, M. E. Sykes, S. Tiwari, D. K. Sharma, S. K. Chaubey, G. P. Wiederrecht, S. K. Gray, G. V. P. Kumar, *Nano Lett.* **2018**, *18*, 650.
- [21] D. Chaudhuri, D. Li, Y. Che, E. Shafran, J. M. Gerton, L. Zang, J. M. Lupton, *Nano Lett.* **2011**, *11*, 488-492.
- [22] A. Köhler, H. Bässler, *J. Mater. Chem.* **2011**, *21*, 4003.
- [23] J. P. Stephens, J. J. Pan, F. J. Devlin, J. R. Cheeseman, *J. Natural Prod.* **2008**, *71*, 285.
- [24] J. Tirado-Rives, W. L. Jorgensen, *J. Chem. Theory and Comput.* **2008**, *4*, 297.
- [25] M. J. Frisch, G. W. Trucks, H. B. Schlegel, G. E. Scuseria, M. A. Robb, J. R. Cheeseman, G. Scalmani, V. Barone, B. Mennucci, G. A. Petersson, H. Nakatsuji, M. Caricato, X. Li, H. P. Hratchian, A. F. Izmaylov, J. Bloino, G. Zheng, J. L. Sonnenberg, M. Hada, M. Ehara, K. Toyota, R. Fukuda, J. Hasegawa, M. Ishida, T. Nakajima, Y. Honda, O. Kitao, H. Nakai, T. Vreven, J. A. Montgomery, Jr., J. E. Peralta, F. Ogliaro, M. Bearpark, J. J. Heyd, E. Brothers, K. N. Kudin, V. N. Staroverov, R. Kobayashi, J. Normand, K. Raghavachari, A. Rendell, J. C. Burant, S. S. Iyengar, J. Tomasi, M. Cossi, S. N. Rega, J. M. Millam, M. Klene, J. E. Knox, J. B. Cross, V. Bakken, C. Adamo, J. Jaramillo, R. Gomperts, R. E. Stratmann, O. Yazyev, A. J. Austin, R. Cammi, C. Pomelli, J. W. Ochterski, R. L. Martin, K. Morokuma, V. G. Zakrzewski, G. A. Voth, P. Salvador, J. J. Dannenberg, S. Dapprich, A. D. Daniels, O. Farkas, J. B. Foresman, J. V. Ortiz, J. Cioslowski, D. J. Fox, Gaussian 09 (Revision A.02), Gaussian, Inc., Wallingford CT, 2009.
- [26] Bruker (2016). *APEX2, SAINT and SADABS*. Bruker AXS Inc., Madison, Wisconsin, USA.

- [27] G. M. Sheldrick, *Acta Crystallogr.*, **2008**, A64, 112.
- [28] G. M. Sheldrick, *Acta Crystallogr.*, **2015**, C71, 3-8.
- [29] L. J. Farrugia, *J. Appl. Crystallogr.* **2012**, 45, 849-854.
- [30] H.-R. Bjørsvik, V. Elumalai, *Eur. J. Org. Chem.* **2016**, 5474-5479.
- [31] A. Justyniarski, J. K. Zaręba, P. Hańczyc, P. Fita, M. Chołuj, R. Zaleśny, M. Samoc, *J. Mater. Chem. C*, **2018**, 6, 4384-4388.

Chapter-3

Room-Temperature Phosphorescence from Metal-Free Organic Phosphors



The room-temperature phosphorescence of metal and heavy atom-free organic molecules has attracted increasing attention due to its peculiar photophysical properties. Besides, organic phosphors found potential applications in organic optoelectronics, anti-counterfeiting, organic light-emitting diodes, chemo- and biosensors, bioimaging, data recording, and security protection in recent years. A logical design of organic molecules played an important role in controlling the molecular ordering to provide efficient intersystem crossing and stabilize the triplet state to achieve room-temperature ultralong phosphorescence. As an extension of the previous chapter, herein, we explored the variation of the alkyl chain and chirality-induced room temperature phosphorescence from phenylmethanone containing carbazole-based organic phosphors. The variation of alkyl chains made an impact on photophysical properties assisted by its the molecular packing in the crystal-state. We studied not only the effect of aliphatic chains on 3,6-bis(phenylmethanone) substituted carbazole molecules but also the substitution on phenylmethanone unit to tune RTP features. Compared to other

candidates, molecule **14** decorated with a chiral chain shows green phosphorescence color spanning from 420 nm to 600 nm with a lifetime of 582 ms. Single-Crystal structure helps to find the molecular packing involved in these phosphors. We believe that chiral phosphors can be explored in the circularly polarized phosphorescence which have received attention due to their wide potential applications in various research fields, including 3D-displays, optical data storage, information storage and processing, spintronics devices, sensors, security inks, and biological probes and so forth.

Publication: *Manuscript under Preparation*

3.1. Introduction

The large Stokes shift, high lifetime, and strong afterglow of RTP organic molecules have grabbed scientific interest because they enable applications in organic optoelectronics, bioimaging, sensing, anti-counterfeiting etc.^[1,2] It has been shown that adding heavy atoms and functional groups with a lone pair of electrons increases the intersystem crossing rate (k_{ISC}) through strong spin-orbit coupling (SOC), which results in effective RTP.^[3-6] Hence, diverse molecular designs for ultralong organic phosphorescence (UOP) have been investigated in this direction.^[7-10] As a result, effective ways such as using molecules with n orbitals to lower the singlet-triplet (S-T) splitting energy and stabilise the triplet excited state *via* various interactions have been widely used.^[5d] UOP materials have advanced significantly, and the highest lifetime reported for crystalline small molecule-based organic phosphor is approximately 4.1 s (Figure 3.1).^[11] Interestingly, strategies such as H-aggregation, hydrogen bonding, energy transfer, charge transfer, radical ion pair, exciton migration, helical arrays etc. have been employed for stabilization of triplet state for a longer lifetime.^[12]

Additionally, circularly polarised luminescence (CPL) has gained popularity due to its potential use in optoelectronic devices,²³ probes,²⁴ 3D display,²⁵ and CPL lasers.²⁶ In order to improve device performance, CPL materials should have strong luminescence intensity and a high dissymmetry factor (g_{lum}). The connection between molecular orbitals and transition dipole moments is essential to design CPL molecules because it is directly related to the magnitude of g_{lum} .²⁷ In view of this, we aim to develop a luminescent molecule containing chiral centers and to study how chirality affects the luminescence properties, especially RTP. The chirality of excited states is a powerful tool and attracts growing interest in the development of new optoelectronic devices. While circularly polarized RTP has been observed from many metal complexes, it has not been widely studied for metal-free aromatics molecules. Among the potential RTP candidates,

carbazole has undergone diverse functionalization using various combinations of heavy atoms and other functional groups to achieve UOP. Hence, we aim to develop chiral organic phosphors materials by using carbazole as the basic building block.

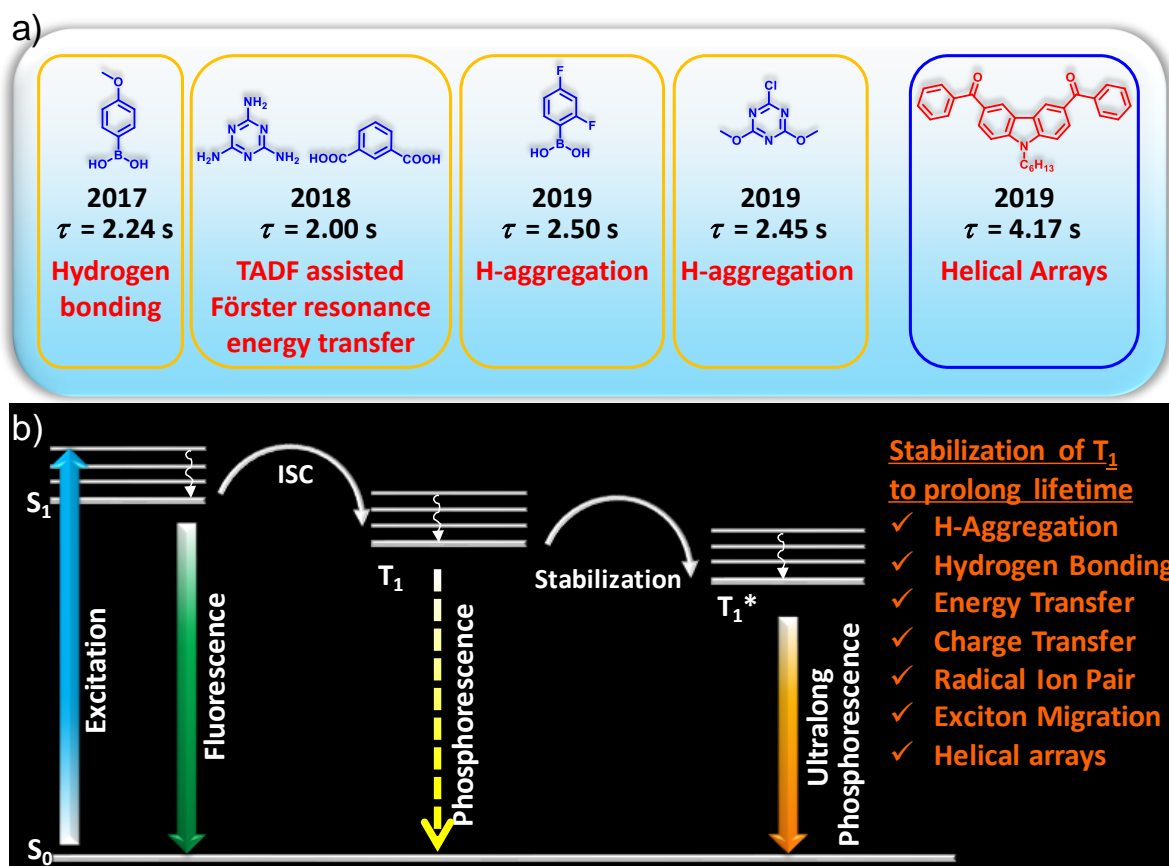


Figure 2.1. a) Recent developments in the area of small molecule-based organic phosphors with lifetime above 4 s b) Schematic of the stabilization of the triplet state, leading to ultralong phosphorescence in organic molecules.

3.2. Experimental section

3.2.1. Crystallization

All the single crystal samples were obtained by crystallization using a slow evaporation method from the CH_2Cl_2 solution.

3.2.2. X-ray intensity data measurements

X-ray intensity data measurements of all the samples were carried out on a Bruker D8 VENTURE Kappa Duo PHOTON II CPAD diffractometer equipped with Incoatech multilayer mirrors optics. The intensity measurements were carried out with Mo micro-focus sealed tube diffraction source ($\text{MoK}_{\alpha} = 0.71073 \text{ \AA}$) at 100(2) K temperature. The X-ray generator was operated at 50 kV and 1.4 mA. A preliminary set of cell constants and an orientation matrix were calculated from three sets of 36 frames. Data were collected with ω and ϕ scan width of 0.5° at different settings of ϕ , ω and 2θ keeping the sample-to-detector distance fixed at 5.00 cm. The X-ray data collection was monitored by the APEX3 program (Bruker, 2016).¹⁵ All the data were corrected for Lorentzian, polarization, and absorption effects using SAINT and SADABS programs (Bruker, 2016). Using the APEX3 (Bruker) program suite, the structure was solved with the ShelXS-97 (Sheldrick, 2008)¹⁶ structure solution program, using direct methods. The model was refined with a version of ShelXL-2013 (Sheldrick, 2015)¹⁷ using Least Squares minimization. All the hydrogen atoms were placed in a geometrically idealized position and constrained to ride on its parent atoms. An *ORTEP* III¹⁸ view of the compound was drawn with 50% probability displacement ellipsoids, and H atoms are shown as small spheres of arbitrary radii.

3.2.3. Phosphorescence experiments

All phosphorescence experiments of all crystals have done by keeping the same experimental parameters. The window of maximum delay after flash was kept 0.3-2 ms for RT phosphorescence measurements.

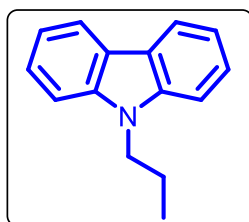
3.3. Synthesis

General procedure for the synthesis of 1-5.¹⁹

In a two-neck round bottom flask were placed carbazole, 1-bromoalkane, KOH, TBAB (tetrabutylammonium bromide), and DMF. The obtained mixture was stirred at 70 °C for 24 hours. After cooling down, water and CH₂Cl₂ were added and thoroughly shaken. Organic layer was separated, and inorganic layer was extracted again with CH₂Cl₂. Combined organic extracts were washed with water, two times with NaCl saturated solution and finally dried with anhydrous Na₂SO₄. Crude product as a yellowish oil was subjected to column chromatography on silica gel, using petroleum ether as a mobile phase as a white solid.

3.3.1. Synthesis of 9-propyl-9H-carbazole (1)-

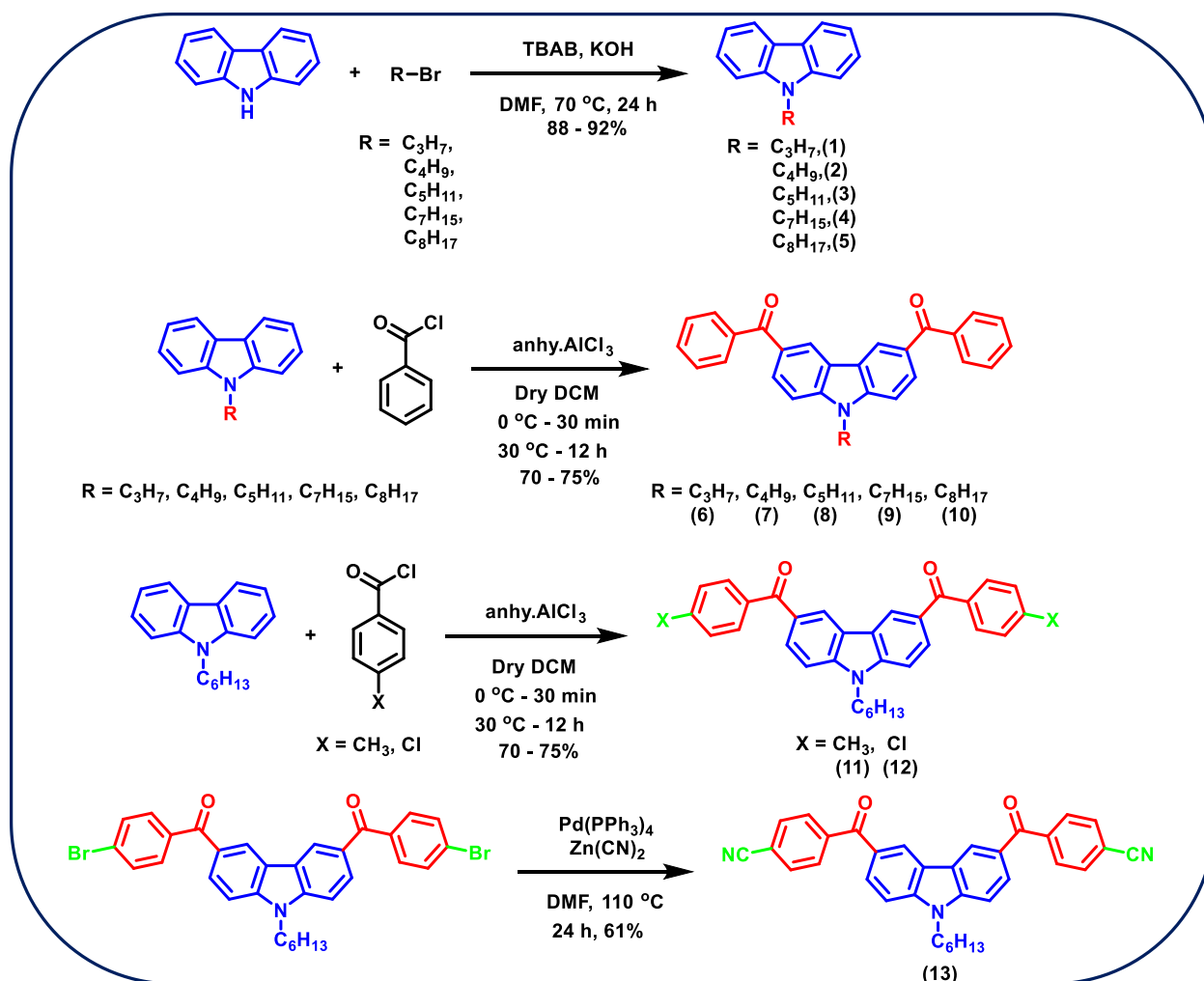
Carbazole (100 mg, 598.05 μmol), 1-bromopropane (70.62 μL, 777.46 μmol), KOH (44 mg, 777.46 μmol), TBAB (20 mg, 59.80 μmol) and DMF (5 ml), white coloured solid, yield-110 mg (88%).



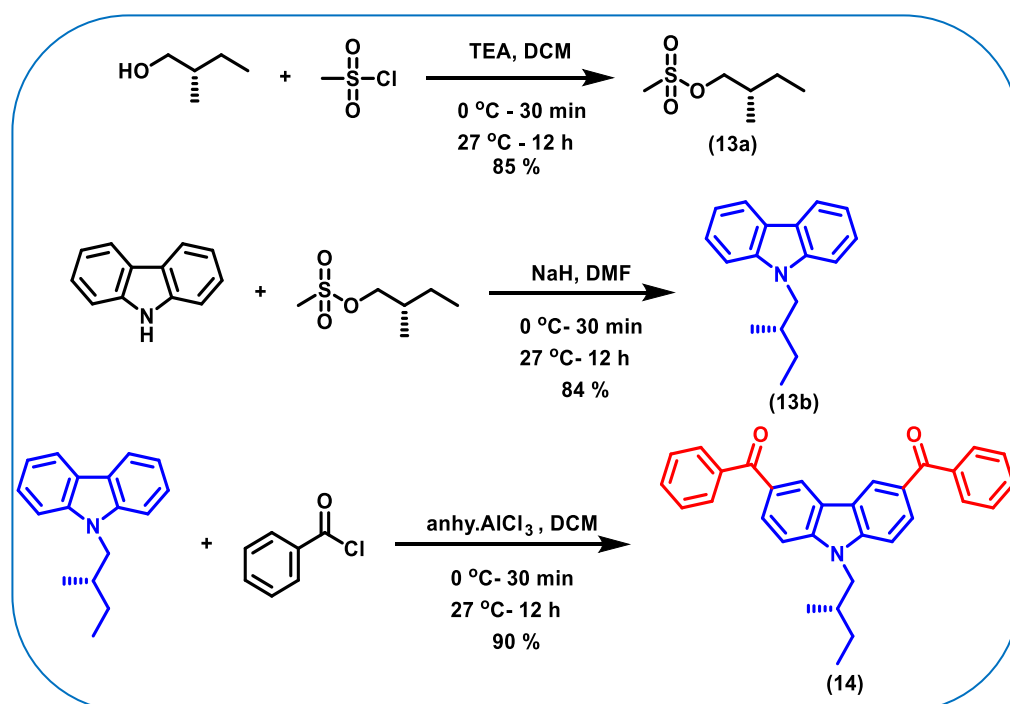
¹H NMR (400MHz, CDCl₃, 25 °C): δ = 8.12 (d, *J*=8.4 Hz, 2 H), 7.42 - 7.50 (m, 4 H), 7.21 - 7.27 (m, 2 H), 4.28 - 4.32 (t, 2 H), 1.91 - 1.98 (m, 2 H), 0.98 - 1.01 (t, 3 H) ppm.

¹³C NMR (100MHz, CDCl₃, 25 °C): δ = 140.5, 125.5, 122.8, 120.3, 118.7, 108.7, 44.6, 22.3, 11.8 ppm.

HR-MS-(ESI⁺): calculated for C₁₅H₁₅N [M]⁺ = 209.2920, found 209.1199.



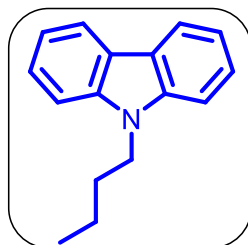
Scheme 3.1. Synthetic Scheme for target molecules 1-13.



Scheme 3.2. Synthetic Scheme for target molecules 14.

3.3.2. Synthesis of 9-butyl-9H-carbazole (2)-

Carbazole (100 mg, 598.0 μmol), 1-bromobutane (83.88 μL , 777.4 μmol), KOH (100 mg, 1.79 mmol), TBAB (20 mg, 59.8 μmol) and DMF (5 ml), white coloured solid, yield- 120 mg (90%).



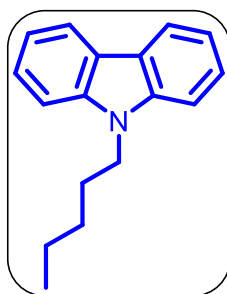
^1H NMR (400MHz, CDCl_3 , 25 $^\circ\text{C}$): δ = 8.15 (d, J = 7.8 Hz, 2 H), 7.44 - 7.53 (m, 4 H), 7.25 - 7.29 (m, 2 H), 4.34 (t, J = 7.1 Hz, 2 H), 1.86 - 1.94 (m, 2 H), 1.41 - 1.49 (m, 2 H), 0.96 - 1.02 (t, 3 H) ppm.

^{13}C NMR (100MHz, CDCl_3 , 25 $^\circ\text{C}$): δ = 140.4, 125.5, 122.8, 120.3, 118.7, 108.6, 42.8, 31.1, 20.6, 13.87 ppm.

HR-MS-(ESI $^+$): calculated for $\text{C}_{16}\text{H}_{17}\text{N}$ $[\text{M}]^+$ = 223.3190, found 223.1356.

3.3.3. Synthesis of 9-pentyl-9H-carbazole (3)-

Carbazole (100 mg, 598.0 μmol), 1-bromopentane (96.41 μL , 777.4 μmol), KOH (100 mg, 1.79 mmol), TBAB (20 mg, 59.8 μmol) and DMF (5 ml), white coloured solid, yield-131 mg (92%).



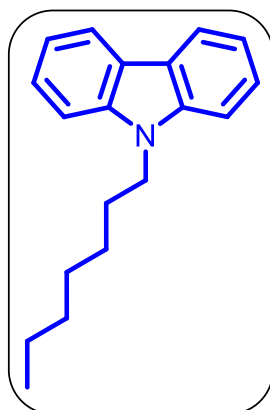
^1H -NMR (400 MHz, CDCl_3 , 25 $^\circ\text{C}$): δ = 8.13 (d, J = 7.8 Hz, 2 H), 7.51-7.47 (m, 2 H), 7.43 (d, J = 8.2 Hz, 2 H), 7.23 - 7.27 (m, 2 H), 4.32 (t, J = 7.3 Hz, 2 H), 1.87 - 1.95 (m, 2 H), 1.35 - 1.43 (m, 4 H), 0.88 - 0.94 (t, 3 H) ppm.

^{13}C -NMR (100 MHz, CDCl_3 , 25 $^\circ\text{C}$): δ = 140.4, 125.5, 122.8, 120.3, 118.7, 108.6, 43.0, 29.4, 28.7, 22.5, 13.9 ppm.

HR-MS-(ESI⁺): calculated for C₁₇H₁₉N [M]⁺ = 237.3460 found 237.1512.

3.3.4. Synthesis of 9-heptyl-9H-carbazole (4)-

Carbazole (100 mg, 598.0 μmol), 1-bromoheptane (122.14 μL, 777.4 μmol), KOH (100 mg, 1.79 mmol), TBAB (20 mg, 59.8 μmol) and DMF (5 ml), white coloured solid, yield- 144 mg (91%).



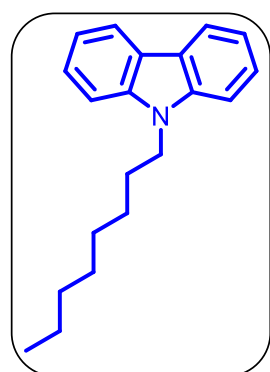
¹H NMR (400MHz, CDCl₃, 25 °C): δ = 8.15 (d, *J* = 7.6 Hz, 2 H), 7.44 - 7.53 (m, 4 H), 7.25 - 7.30 (m, 2 H), 4.34 (t, *J* = 7.2 Hz, 2 H), 1.92 (q, *J* = 7.6 Hz, 2 H), 1.29 - 1.44 (m, 8 H), 0.89 - 0.92 (m, 3 H) ppm.

¹³C NMR (100MHz, CDCl₃, 25 °C): δ = 140.4, 125.5, 122.8, 120.3, 118.6, 108.6, 43.1, 31.7, 29.1, 29.0, 27.3, 22.6, 14.0 ppm.

HR-MS-(ESI⁺): calculated for C₁₉H₂₃N [M]⁺ = 265.4000, found 265.1825.

3.3.5. Synthesis of 9-octyl-9H-carbazole (5)-

Carbazole (100 mg, 598.0 μmol), 1-bromooctane (134.3 μL, 777.4 μmol), KOH (100 mg, 1.79 mmol), TBAB (20 mg, 59.8 μmol) and DMF (5 ml), white coloured solid, yield- 151 mg (90%).



¹H NMR (400MHz, CDCl₃, 25 °C): δ = 8.13 (dd, J = 7.8, 0.9 Hz, 2 H), 7.46 - 7.51 (m, 2 H), 7.41 - 7.44 (m, 2 H), 7.22 - 7.27 (m, 2 H), 4.31 (t, J = 7.3 Hz, 2 H), 1.85 - 1.92 (m, 2 H), 1.26 - 1.43 (m, 10 H), 0.87 - 0.92 ppm (t, 3 H).

¹³C NMR (100MHz, CDCl₃, 25 °C): δ = 140.4, 125.5, 122.8, 120.3, 118.6, 108.6, 43.0, 31.8, 29.4, 29.2, 28.9, 27.3, 22.6, 14.1 ppm.

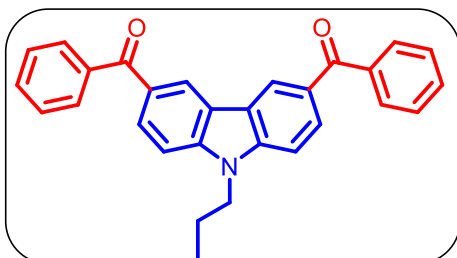
HR-MS-(ESI⁺): calculated for C₂₀H₂₅N [M]⁺ = 279.4270, found 279.1979.

General procedure for 6-12.

Benzoyl chloride and anhydrous aluminium chloride in dry CH₂Cl₂ were placed in two-neck round bottom flask at 0 °C for 30 min. To this reaction mixture, added dropwise 9-hexyl-9H-carbazole CH₂Cl₂ solution for 15 min. Keep reaction mixture for 24 hours at 30 °C. The reaction mixture was quenched by slow addition of saturated ammonium hydroxide (caution: reaction is highly exothermic). The reaction mixture was extracted with CH₂Cl₂ (3x50 mL), and dried with anhydrous Na₂SO₄. After evaporation of the solvent, the crude product was purified by column chromatography using petroleum ether:CH₂Cl₂ mixture.

3.3.6. Synthesis of (9-propyl-9H-carbazole-3,6-diyl)bis(phenylmethanone) (6)-

9-propyl-9H-carbazole (100 mg, 477.80 μ mol), Benzoyl chloride (111.94 μ L, 1.00 mmol), anhydrous aluminium chloride (318 mg, 2.39 mmol), dry CH₂Cl₂ (10 mL), yellow coloured solid, Yield- 150 mg (75%).



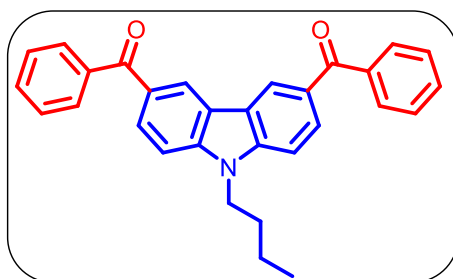
¹H NMR (400 MHz, CDCl₃, 25 °C): δ = 8.60 (d, J =1.4 Hz, 2 H), 8.09 (dd, J = 8.7, 1.8 Hz, 2 H), 7.82 - 7.87 (m, 4 H), 7.59 - 7.65 (m, 2 H), 7.55 (d, J = 2.3 Hz,

2 H), 7.50 - 7.54 (m, 4 H), 4.39 (t, $J = 7.3$ Hz, 2 H), 1.95 - 2.04 (m, 2 H), 1.03 (t, $J = 7.6$ Hz, 3 H) ppm.

^{13}C NMR (100MHz, CDCl_3 , 25 °C): $\delta = 196.4, 143.8, 138.6, 131.9, 129.9, 129.6, 129.0, 128.3, 124.1, 122.7, 109.0, 45.2, 22.3, 11.7$ ppm

HR-MS-(ESI⁺): calculated for $\text{C}_{29}\text{H}_{23}\text{NO}_2$ $[\text{M}+\text{H}]^+ = 418.5080$ found 418.1802.

3.3.7. Synthesis of (9-butyl-9H-carbazole-3,6-diyl)bis(phenylmethanone) (7)-
9-butyl-9H-carbazole (100 mg, 447.7 μmol), Benzoyl chloride (208.0 μL , 1.79 mmol), anhydrous aluminium chloride (298.5 mg, 2.24 mmol), dry CH_2Cl_2 (10 mL), yellow coloured solid, Yield-139 mg (72%).



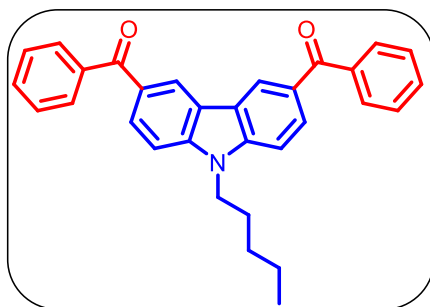
^1H NMR (400 MHz, CDCl_3 , 25 °C): $\delta = 8.60$ (d, $J=1.8$ Hz, 2 H), 8.06 - 8.12 (m, 2 H), 7.82 - 7.87 (m, 4 H), 7.59 - 7.64 (m, 2 H), 7.52 - 7.55 (m, 4 H), 7.50 - 7.52 (m, 2 H), 4.41 (t, $J = 7.1$ Hz, 2 H), 1.89 - 1.97 (m, 2 H), 1.41 - 1.49 (m, 2 H), 0.99 ppm (t, $J = 7.3$ Hz, 3 H).

^{13}C NMR (100MHz, CDCl_3 , 25 °C): $\delta = 196.4, 143.7, 138.6, 131.9, 129.9, 129.5, 129.0, 128.3, 124.1, 122.7, 108.9, 43.4, 31.0, 20.5, 13.8$ ppm.

HR-MS-(ESI⁺): calculated for $\text{C}_{30}\text{H}_{25}\text{NO}_2$ $[\text{M}+\text{H}]^+ = 432.5350$ found 432.1958.

3.3.8. Synthesis of (9-pentyl-9H-carbazole-3,6-diyl)bis(phenylmethanone) (8)-

9-pentyl-9H-carbazole (100 mg, 421.3 μmol), Benzoyl chloride (195.7 μL , 1.69 mmol), anhydrous aluminium chloride (224.7 mg, 1.69 mmol), dry CH_2Cl_2 (10 mL), yellow coloured solid, Yield-137 gm (73%).



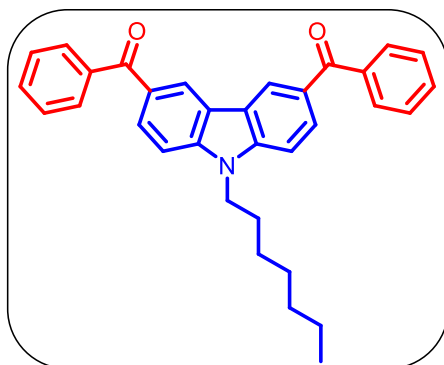
¹H NMR (400 MHz, CDCl₃, 25 °C): δ = 8.60 (d, J = 1.4 Hz, 2 H), 8.09 (dd, J = 8.5, 1.6 Hz, 2 H), 7.82 - 7.88 (m, 4 H), 7.59 - 7.64 (m, 2 H), 7.52 - 7.55 (m, 4 H), 7.50 - 7.52 (m, 2 H), 4.40 (t, J = 7.3 Hz, 2 H), 1.90 - 2.00 (m, 2 H), 1.36 - 1.45 (m, 4 H), 0.87 - 0.93 (m, 3 H) ppm.

¹³C NMR (100MHz, CDCl₃, 25 °C): δ = 196.4, 143.7, 138.6, 131.9, 129.9, 129.5, 129.0, 128.3, 124.1, 122.6, 108.9, 43.6, 29.3, 28.6, 22.4, 13.9 ppm.

HR-MS-(ESI⁺): calculated for C₃₁H₂₇NO₂ [M+H]⁺ = 446.5620 found 446.2111.

3.3.9. Synthesis of (9-heptyl-9H-carbazole-3,6-diyl)bis(phenylmethanone) (9)-

9-heptyl-9H-carbazole (100 mg, 376.7 μ mol), Benzoyl chloride (175.0 μ L, 1.51 mmol), anhydrous aluminium chloride (251.1 mg, 1.88 mmol), dry CH₂Cl₂ (10 mL), yellow coloured solid, Yield-134 mg (75%).



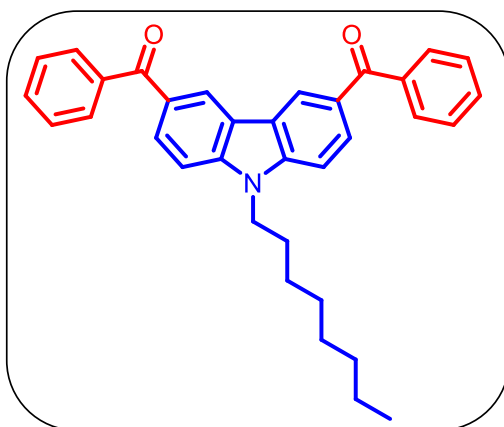
¹H NMR (400 MHz, CDCl₃, 25 °C): δ = 8.60 (d, J = 1.4 Hz, 2 H), 8.09 (dd, J = 8.5, 1.6 Hz, 2 H), 7.81 - 7.89 (m, 4 H), 7.59 - 7.65 (m, 2 H), 7.52 - 7.56 (m, 4 H), 7.51 (s, 2 H), 4.40 (t, J = 7.1 Hz, 2 H), 1.94 (quin, J = 7.3 Hz, 2 H), 1.35 - 1.45 (m, 4 H), 1.24 - 1.32 (m, 4 H), 0.85 - 0.90 (m, 3 H) ppm.

^{13}C NMR (100MHz, CDCl_3 , 25 °C): δ = 196.6, 143.8, 138.7, 132.0, 130.0, 129.7, 129.1, 128.4, 124.2, 122.8, 109.0, 43.8, 31.7, 29.8, 29.1, 27.3, 22.6, 14.1 ppm.

HR-MS-(ESI⁺): calculated for $\text{C}_{33}\text{H}_{31}\text{NO}_2$ $[\text{M}+\text{H}]^+ = 474.6160$ found 474.2428.

3.3.10. Synthesis of (9-octyl-9H-carbazole-3,6-diyl)bis(phenylmethanone) (10)-

9-octyl-9H-carbazole (100 mg, 357.8 μmol), Benzoyl chloride (166.3 μL , 1.43 mmol), anhydrous aluminium chloride (238.5 mg, 1.79 mmol), dry CH_2Cl_2 (10 mL), yellow coloured solid, Yield-129 mg (74%).



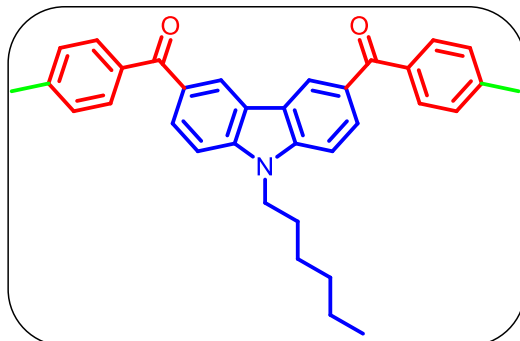
^1H NMR (400 MHz, CDCl_3 , 25 °C): δ = 8.59 (d, J = 1.4 Hz, 2 H), 8.09 (dd, J = 8.5, 1.6 Hz, 2 H), 7.80 - 7.89 (m, 4 H), 7.58 - 7.65 (m, 2 H), 7.52 - 7.56 (m, 4 H), 7.51 (s, 2 H), 4.40 (t, J = 7.1 Hz, 2 H), 1.94 (quin, J = 7.2 Hz, 2 H), 1.34 - 1.44 (m, 4 H), 1.26 - 1.32 (m, 6 H), 0.87 (t, J = 6.9 Hz, 3 H) ppm.

^{13}C NMR (100MHz, CDCl_3 , 25 °C): δ = 196.4, 143.6, 138.6, 131.9, 129.9, 129.5, 129.0, 128.2, 124.1, 122.6, 108.9, 43.6, 31.7, 29.2, 29.1, 28.9, 27.2, 22.5, 14.0 ppm.

HR-MS-(ESI⁺): calculated for $\text{C}_{34}\text{H}_{33}\text{NO}_2$ $[\text{M}+\text{H}]^+ = 488.6430$ found 488.2584.

3.3.11. Synthesis of (9-hexyl-9H-carbazole-3,6-diyl)bis(p-tolylmethanone) (11)-

9-hexyl-9H-carbazole (1 gm 3.98 mmol), p-toluoyl chloride (1.59 mL, 11.93 mmol) anhydrous aluminium chloride (2.65 gm, 19.89 mmol), dry CH₂Cl₂ (30 mL), light yellow coloured solid, Yield-1.41 gm (72%).



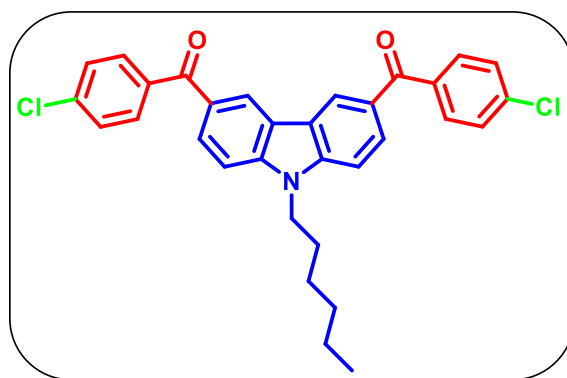
¹H NMR (400 MHz, CDCl₃, 25 °C): δ = 8.57 (d, J = 1.3 Hz, 2 H), 8.07 (dd, J = 8.6, 1.6 Hz, 2 H), 7.77 (d, J = 8.1 Hz, 4 H), 7.51 (d, J = 8.6 Hz, 2 H), 7.33 (d, J = 7.8 Hz, 4 H), 4.40 (t, J = 7.3 Hz, 2 H), 2.48 (s, 6 H), 1.89 - 1.99 (m, 2 H), 1.35 - 1.48 (m, 2 H), 1.26 - 1.34 (m, 4 H), 0.86 - 0.92 ppm (t, 3 H) ppm.

¹³C NMR (100MHz, CDCl₃, 25 °C): δ = 196.3, 143.6, 142.6, 135.9, 130.2, 129.9, 129.0, 128.9, 124.0, 122.6, 108.8, 43.6, 31.5, 28.9, 26.9, 22.5, 21.6, 14.0 ppm.

HR-MS-(ESI⁺): calculated for C₃₄H₃₄NO₂ [M+H]⁺ = 488.6430 found 488.2584.

3.3.12. Synthesis of (9-hexyl-9H-carbazole-3,6-diyl)bis((4-chlorophenyl)methanone) (12)-

9-hexyl-9H-carbazole (1 gm 3.98 mmol), 4-chlorobenzoyl chloride (1.54 mL, 11.93 mmol) anhydrous aluminium chloride (2.65 gm, 19.89 mmol), dry CH₂Cl₂ (30 mL), off white coloured solid, Yield-1.22 gm (77%).



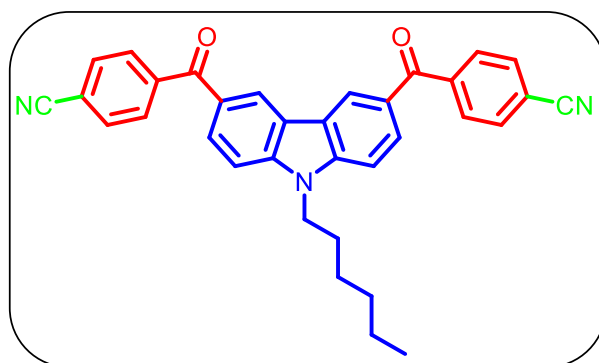
$^1\text{H NMR}$ (400MHz, CDCl_3 , 25 °C): δ = 8.56 (s, 2 H), 8.04 (d, $J=8.5$ Hz, 2 H), 7.79 (d, $J = 7.9$ Hz, 4 H), 7.47 - 7.58 (m, 6 H), 4.40 (t, $J = 7.0$ Hz, 2 H), 1.88 - 2.01 (m, 2 H), 1.29 - 1.49 (m, 6 H), 0.84 - 0.95 ppm (t, 3 H) ppm.

$^{13}\text{C NMR}$ (100MHz, CDCl_3 , 25 °C): δ = 195.1, 143.8, 138.3, 136.8, 131.3, 129.3, 128.9, 128.6, 123.9, 122.7, 109.1, 43.7, 31.5, 28.9, 26.9, 22.5, 13.9 ppm.

HR-MS-(ESI⁺): calculated for $\text{C}_{32}\text{H}_{28}\text{Cl}_2\text{NO}_2$ $[\text{M}+\text{H}]^+ = 528.4730$ found 528.1492.

3.3.13. Synthesis of 4,4'-(9-hexyl-9H-carbazole-3,6-dicarbonyl)dibenzonitrile (**13**).²⁰

A mixture of 9-hexyl-9H-carbazole-3,6-diylbis((4-bromophenyl)methanone (500 mg, 809.87 μmol), tetrakis(triphenylphosphine)palladium(0) ($\text{Pd}(\text{PPh}_3)_4$, 93.59 mg, 80.99 μmol), and zinc cyanide ($\text{Zn}(\text{CN})_2$, 475 mg, 4.05 mmol) in anhydrous DMF (10 mL) was stirred at 110 °C for 22 h. After the completion of the reaction, the reaction mixture was cooled to room temperature, excess chloroform was added and washed with distilled water. The organic layer was washed with brine, dried over anhydrous sodium sulphate and the solvent was evaporated under reduced pressure. The crude product was purified by silica-gel column chromatography using Petroleum ether: CH_2Cl_2 mixture gave **13** (253 mg, 61%) as a yellow solid.



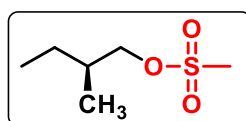
¹H NMR (400MHz, CDCl₃, 25 °C): δ = 8.59 (d, J = 1.5 Hz, 2 H), 8.02 (dd, J = 8.8, 1.5 Hz, 2 H), 7.91 (d, J = 8.4 Hz, 4 H), 7.81 - 7.86 (m, 4 H), 7.55 (d, J = 8.8 Hz, 2 H), 4.42 (t, J = 7.1 Hz, 2 H), 1.91 - 1.99 (m, 2 H), 1.39 - 1.46 (m, 2 H), 1.29 - 1.38 (m, 4 H), 0.88 ppm (t, J = 7.1 Hz, 3 H) ppm.

¹³C NMR (100MHz, CDCl₃, 25 °C): δ = 194.5, 144.1, 142.3, 132.2, 130.1, 129.2, 128.6, 124.0, 122.9, 118.1, 115.3, 109.3, 43.8, 31.4, 28.9, 26.8, 22.5, 13.9 ppm.

HR-MS-(ESI⁺): calculated for C₃₄H₂₈N₃O₂ [M]⁺ = 510.6090 found 510.2176.

3.3.14. Synthesis of (S)-2-methylbutyl methanesulfonate (13a).²¹

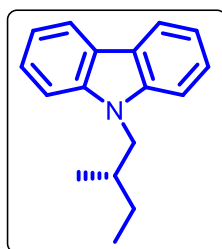
In two-neck round bottom flask were placed (S)-2-methylbutan-1-ol (500 mg, 5.67 mmol), triethylamine (1 mL, 7.65 mmol) in anhydrous CH₂Cl₂ (10 mL) at 0 °C for 30 min. Methanesulfonyl chloride (500 mmL, 6.51 mmol) was syringed into the flask and the reaction mixture was stirred at room temperature for additional 12 h. The reaction was quenched with water and the crude product was extracted with CH₂Cl₂. The organic fractions were washed with distilled water, dried over anhy. Na₂SO₄ and concentrated under reduced pressure. The crude product was used without purification for further step.



¹H NMR (200MHz, CDCl₃, 25 °C): δ = 3.96 - 4.18 (m, 2 H), 3.01 (s, 3 H), 1.82 (dq, J = 13.0, 6.5 Hz, 1 H), 1.39 - 1.57 (m, 1 H), 1.14 - 1.34 (m, 1 H), 0.87 - 1.04 (m, 6 H) ppm.

3.3.15. Synthesis of (S)-9-(2-methylbutyl)-9H-carbazole (13b)²²

In 100 ml two-neck round bottom flask was added carbazole (360 mg, 2.17 mmol) and sodium hydride (87 mg, 3.61 mmol) under argon. Anhydrous DMF (10 mL) was then added to the flask and the suspension was stirred at 0° C for 30 min. (S)-2-methylbutyl methanesulfonate (300 mg, 1.80 mmol) in 5 ml anhy. DMF was dropwise syringed into the flask and the reaction mixture was stirred at room temperature for additional 15 h. The reaction was quenched with water and the crude product was extracted with CH₂Cl₂. The organic fractions were washed with distilled water, dried over anhy. Na₂SO₄ and concentrated under reduced pressure. The crude product was then purified by silica gel chromatography using Petroleum ether:Ethyl acetate mixture gave **15** (360 mg, 84%) as a white solid.



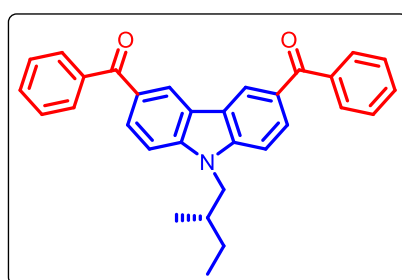
¹H NMR (200 MHz, CDCl₃, 25 °C): δ = 8.11 (d, J = 7.7 Hz, 2 H), 7.35 - 7.55 (m, 4 H), 7.17 - 7.29 (m, 2 H), 4.13 (qd, J = 14.5, 7.4 Hz, 2 H), 2.16 (dd, J = 12.0, 6.7 Hz, 1 H), 1.38 - 1.55 (m, 1 H), 1.21 - 1.36 (m, 1 H), 0.87 - 1.05 (m, 6 H) ppm.

HR-MS-(ESI⁺): calculated for C₁₇H₁₉N [M]⁺ = 237.3460 found 237.1512.

3.3.16. Synthesis of (S)-9-(2-methylbutyl)-9H-carbazole-3,6-diyl)bis(phenylmethanone) (14)

Benzoyl chloride (340 mg, 2.54 mmol) and anhydrous aluminium chloride (295 mmL, 2.54 mmol) in 10 mL dry CH₂Cl₂ were placed in two-neck round bottom

flask at 0 °C for 30 min. to this reaction mixture add dropwise (S)-9-(2-methylbutyl)-9H-carbazole (200 mg, 842.65 μ mol) CH₂Cl₂ solution for 15 min. Keep reaction mixture for 24 hours at 30 °C. The reaction mixture was quenched by slow addition of saturated ammonium hydroxide (caution: reaction is highly exothermic). The reaction mixture was extracted with CH₂Cl₂ (3x50 mL), and dried with anhydrous Na₂SO₄. After evaporation of the solvent, the crude product was purified by column chromatography using petroleum ether:CH₂Cl₂ mixture gives white coloured solid, Yield-338 mg (90%).



¹H NMR (400MHz, CDCl₃, 25 °C): δ = 8.57 - 8.64 (m, 2 H), 8.06 - 8.12 (m, 2 H), 7.81 - 7.90 (m, 4 H), 7.59 - 7.65 (m, 2 H), 7.49 - 7.56 (m, 6 H), 4.31 (dd, J =14.63, 6.88 Hz, 1 H), 4.18 (dd, J =14.63, 8.25 Hz, 1 H), 2.15 - 2.25 (m, 1 H), 1.49 - 1.55 (m, 1 H), 1.34 (dt, J =13.63, 7.75 Hz, 1 H), 0.94 - 1.05 (m, 6 H) ppm.

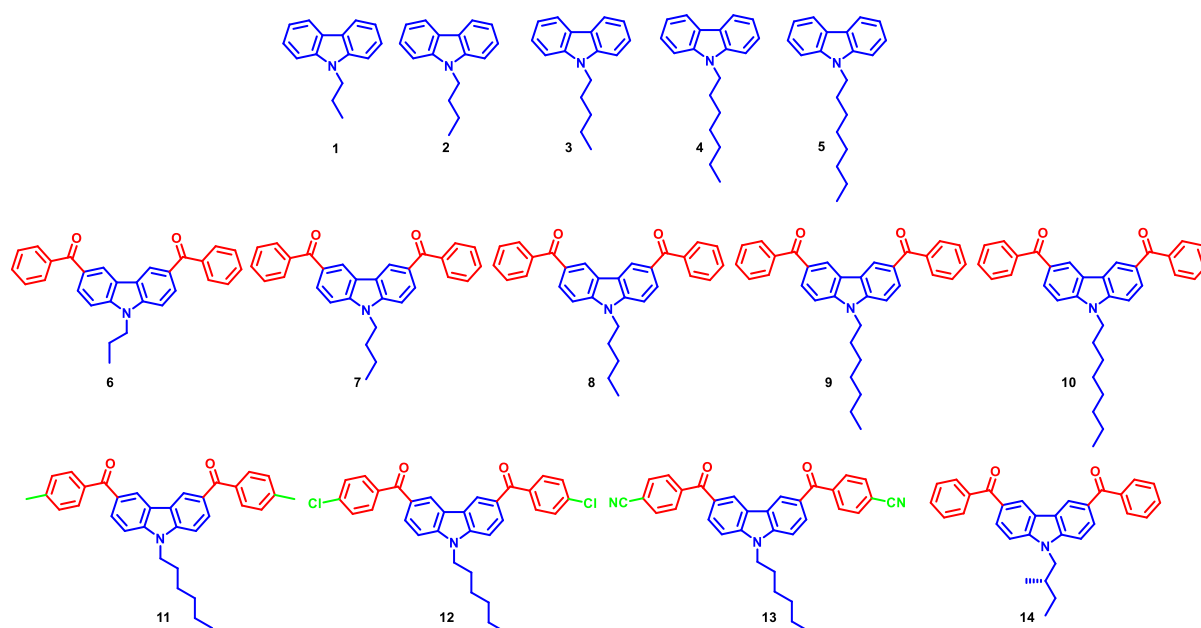
¹³C NMR (100MHz, CDCl₃, 25 °C): δ = 196.6, 144.2, 138.7, 132.0, 130.0, 129.7, 129.1, 128.4, 124.2, 122.7, 109.4, 50.0, 35.4, 27.6, 17.6, 11.6 ppm.

HR-MS-(ESI⁺): calculated for C₃₁H₂₇NO₂ [M]⁺ = 445.5620 found 446.2115.

3.4. Result and discussions

Carbazole is one of the promising RTP candidates which has undergone extensive functionalization through combinations of a variety of heavy atoms and other functional groups to achieve UOP.^[8b,9b,10b,10d] We planned to study the effect of alkyl chain on carbazole and vary the substitution of phenylmethanone functionalization on the RTP features of 9-alkylcarbazole, which exhibits phosphorescence features with low RTP lifetime. In order to facilitate

crystallization and support the formation of strain-induced crystalline assemblies, our design strategy includes: 1) N-alkylation of carbazole with varying alkyl chain to evaluate alkyl- π interaction; and (2) keeping functional group on 4-position of phenylmethanone unit to stabilize the triplet state by contributing hybrid (n,π^*) and (π,π^*) configurations for UOP.^[13] As a result, a group of 9-alkylcarbazole compounds having phenylmethanone units at 3,6-positions was prepared and characterized by using ^1H and ^{13}C nuclear magnetic resonance spectroscopies and high-resolution mass spectrometry (Scheme 3.1, 3.2). We were able to achieve the target molecules in pure after multi-step synthesis and purification by silica gel column chromatography. After the complete characterization of the molecules, we examined the photophysical properties of all molecules in solution and crystal state.



Scheme 3.3. Chemical structure of all the molecules under study in this chapter.

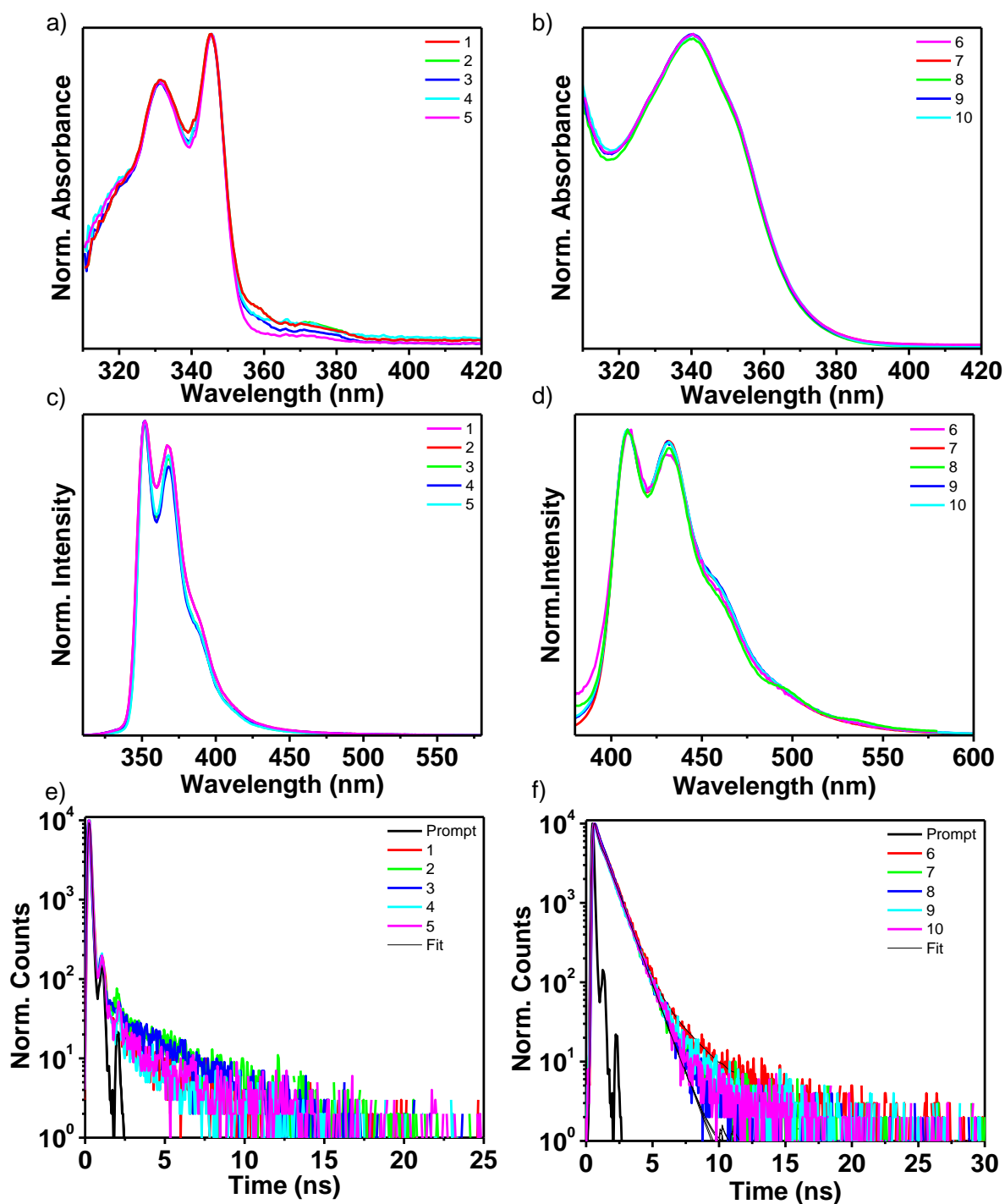


Figure 3.2. Normalized a), b) absorption, c), d) steady-state emission spectra at RT, e), f) emission lifetime decay profile of **1-5** and **6-10** in MTHF solution, respectively ($C = 1 \times 10^{-5}$ M, $l = 1$ cm, $\lambda_{\text{ex}} = 342$ nm for **1-5**, $\lambda_{\text{ex}} = 356$ nm for **6-10**).

Characteristic absorption spectral features of the luminogens **1-5** have not varied significantly in 2-methyltetrahydrofuran (MTHF) (Figure 3.2a). Similarly,

luminogens **6-10** also didn't alter their absorption. By comparing the absorption of luminogens from **1-5** to **6-10**, the later one shows a broad absorption peak ranging from 320-380 nm. Compared to **1-5**, the steady-state emission spectra of **6-10** showed a bathochromic shift of 50 nm due to the increasing electron-withdrawing ability of the carbonyl groups (Figure 3.2c,d and Table 1). Fluorescence lifetime decay of **6-10** in MTHF show that the lifetime varied as 3.01 (94%) for **6**, 0.93 (87%) for **7**, 0.92 (91%) for **8**, 0.96 (86%) for **9** and 0.94 ns (88%) for **10** (Figure 3.2e,f and Table 1).

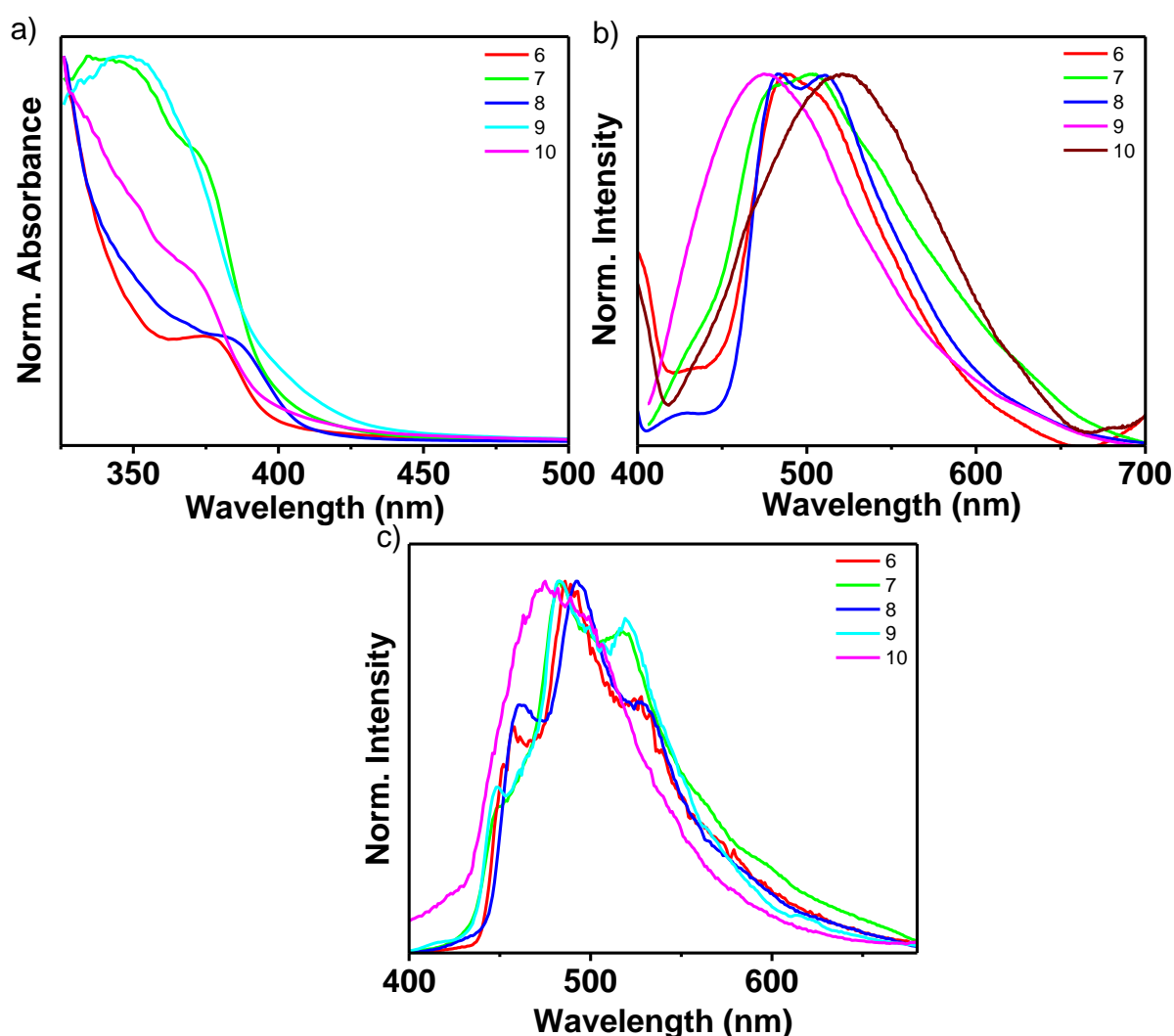


Figure 3.3. Normalized solid-state a) absorption, steady-state emission spectra of **6-10** crystals at b) RT c) 77 K ($\lambda_{\text{ex}} = 375$ nm for **6-10**).

In order to study further, all molecules were crystallized from CH_2Cl_2 . The diffuse reflectance spectra of crystals of **6-10** exhibited a broad band between

300-420 nm, having an additional absorption band located around 360-380 nm (Figure 3.3a). The fluorescence spectra of **6-10** crystals at RT exhibits a red-shifted peak ranging from 400-630 nm (Figure 3.3b). Similarly, molecules **6-10** exhibited a marked difference in fluorescence features at 77 K in the crystalline state (Figure 3.3c). When the lifetime was monitored at the fluorescence maxima, the presence of a long-lived component in the fluorescence lifetime decay of **6-10** was realised. The red-shifted fluorescence of **6-10** crystals at RT is nearly identical to the corresponding spectra at 77 K, implying RTP for **6-10** in the crystalline assembly (Figure 3.4c).

Phosphorescence spectra were measured to confirm the presence of RTP in crystals of **6-10** and confirmed that the observed red-shifted peak at RT is due to phosphorescence (Figure 3.3d). Furthermore, the presence of enhanced RTP for **6-10** was observed by measurements of phosphorescence lifetime, and it varied as 146 ms (**6**), 14 ms (**7**), 11 ms (**8**), 14 ms (**9**) and 14 ms (**10**), respectively (Figure 3.5b and Table 2). Molecule **6** had a longer phosphorescence lifetime with an afterglow lasting for 6 seconds after UV light excitation after dipping in liquid nitrogen. The photoluminescence quantum yield of the crystals varied as **6** (5.57 %), **7** (2.38 %), **8** (2.29 %), **9** (2.58 %) and **10** (3.42 %) (Table 1). The observed phosphorescence lifetime of **6-10** raised curiosity about the excited triplet state of this particular molecule, and further we studied the presence of intermolecular interaction by analysing the crystal packing.

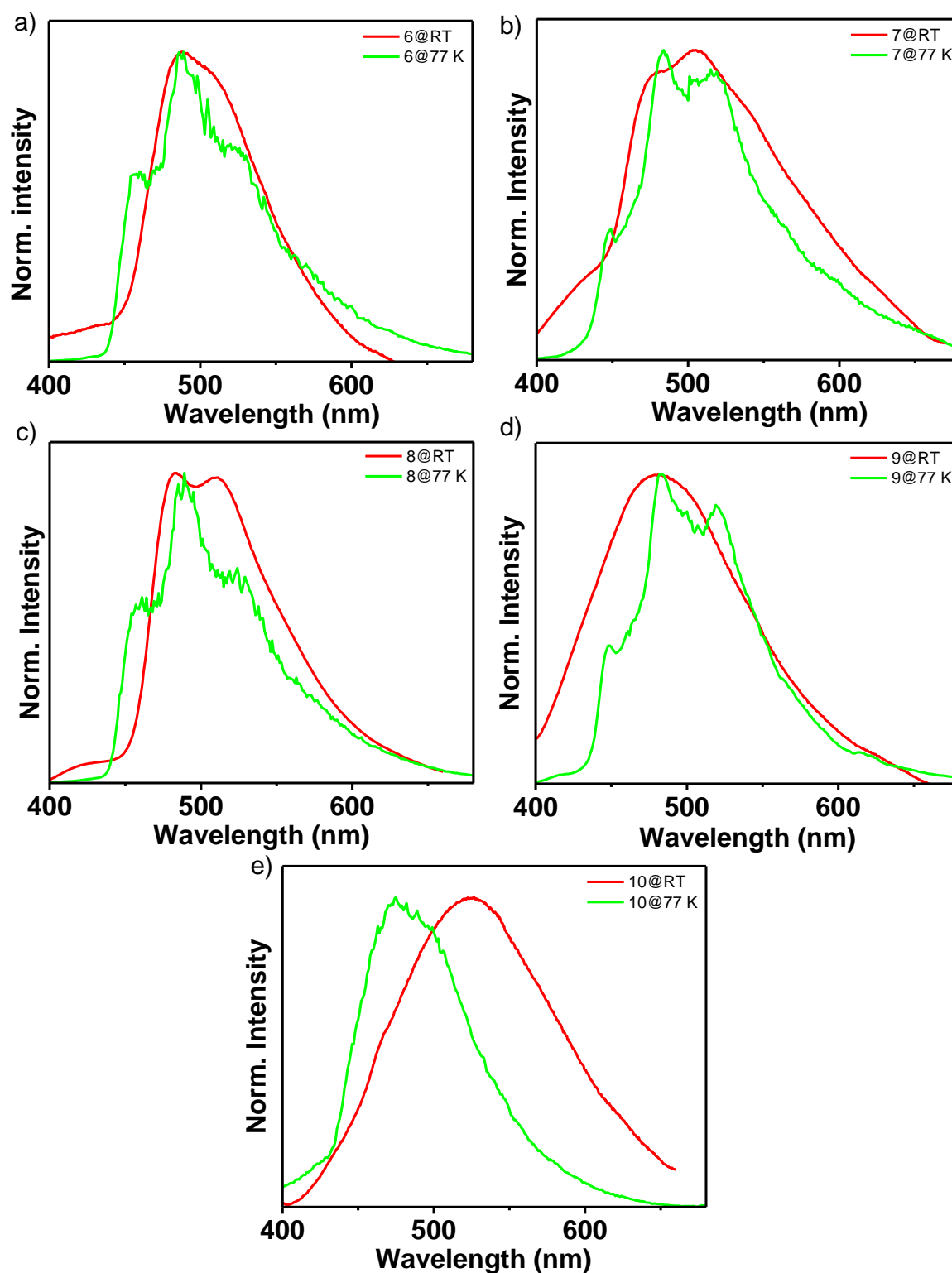


Figure 3.4. Comparison of the normalized crystal state emission spectra of a) **6**, b) **7**, c) **8**, d) **9** and e) **10** at RT and 77 K ($\lambda_{\text{ex}} = 375$ nm for **6-10**).

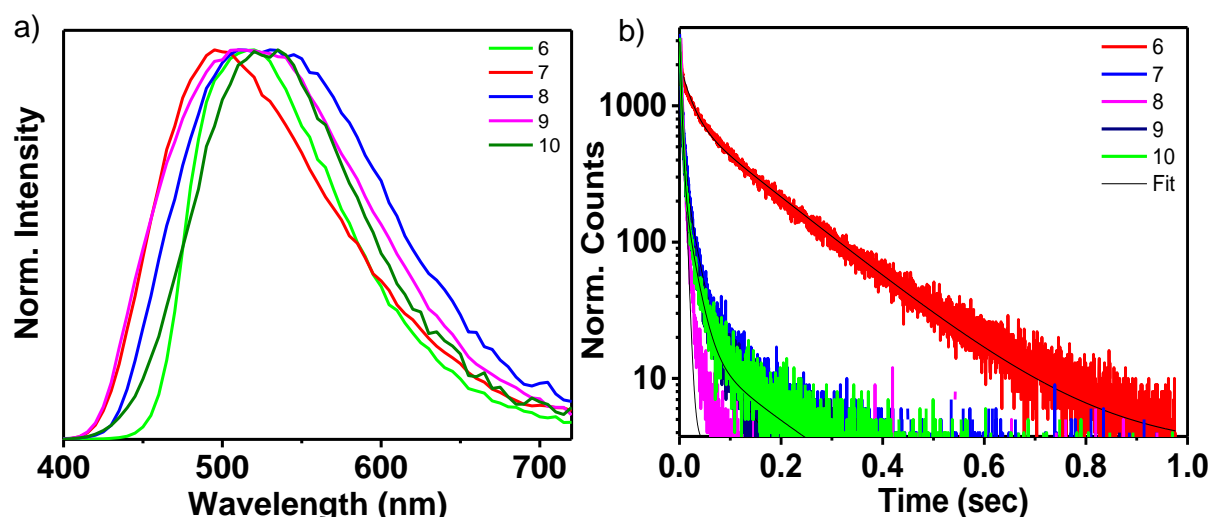


Figure 3.5. a) Normalized Phosphorescence spectra of **6-10** crystals at RT in air ($\lambda_{\text{ex}} = 375$ nm for **6-10**), and b) phosphorescence lifetime decay of **6-10** at RT.

After studying the variation of effect of the alkyl chain on 3,6-phenylmethanone functionalized carbazole molecules, we checked the optical properties of molecules having different functional groups on phenylmethanone unit. In view of this, three different derivatives such as methyl, chloro and cyano group on 4-position of 3,6-phenylmethanone functionalized 9-hexylcarbazole have been prepared. All three different derivatives synthesized in good yield and characterized by ^1H and ^{13}C nuclear magnetic resonance spectroscopies and high-resolution mass spectrometry (Scheme 3.1). After the complete characterization of molecules, the optical properties of three 3,6-phenylmethanone functionalized carbazole derivatives were checked.

Absorption spectra of the luminogens **11-13** show the absorption peak ranging from 290-380 nm in 2-methyltetrahydrofuran (MTHF) (Figure 3.6a), and the steady-state emission spectra of **11** show an emission peak at 360-600 nm, **12** shows at 350-600 nm while the emission peak of **13** is at 400-650 nm in MTHF (Figure 3.6b). The bathochromic shift observed in **13** compared to **11** and **12**, is due to the increasing electron-withdrawing ability of cyanide and carbonyl groups (Figure 3.6b). The emission spectra of **11-13** at 77 K shows structured emission bands covering from 400-600 nm (Figure 3.6c). The fluorescence lifetime decay

profile in MTHF shows that the higher lifetime component varied from 6.42 ns (**11**), 6.99 ns (**12**) and 6.59 ns (**13**) (Figure 3.6b, Table 1).

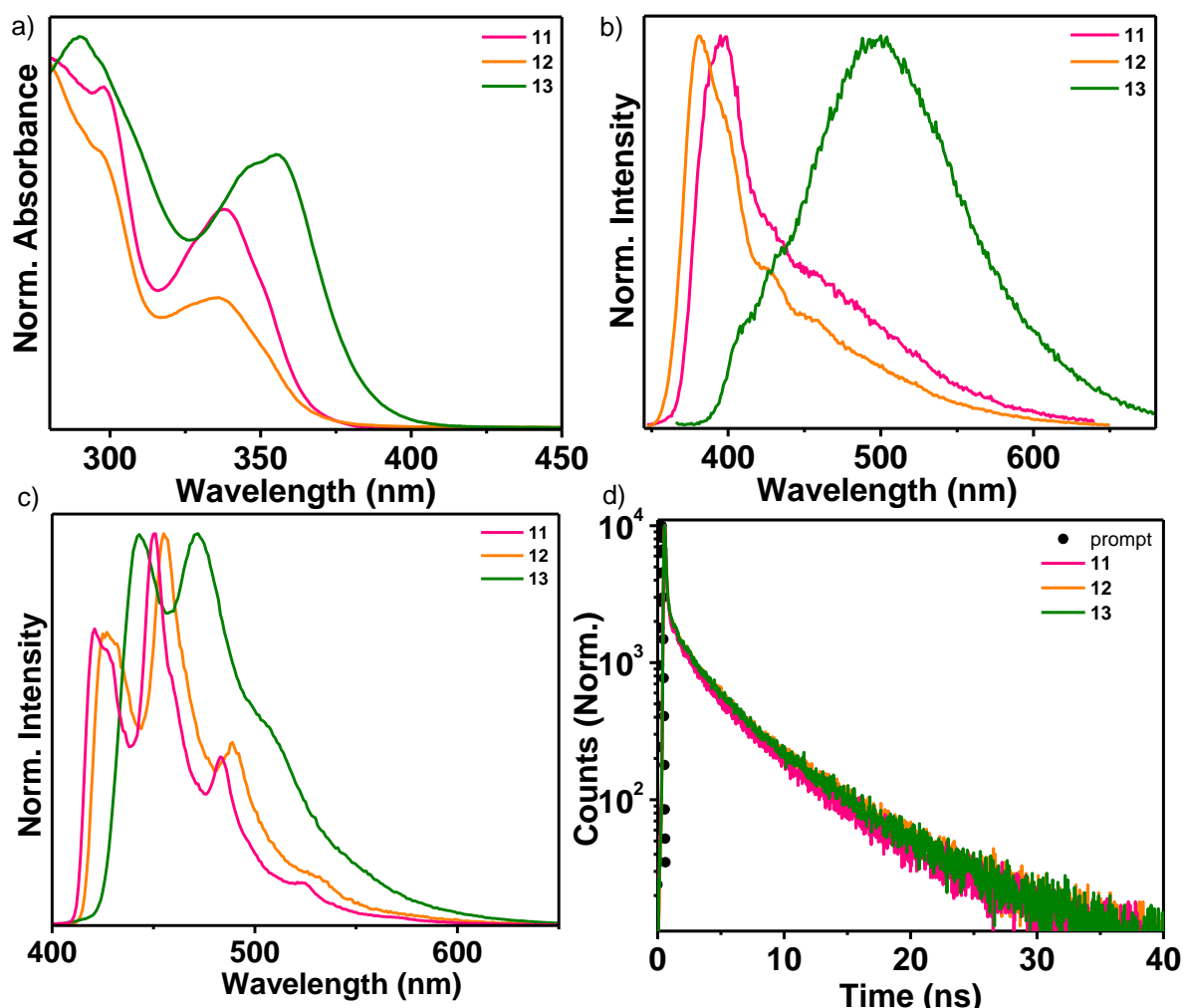


Figure 3.6. Normalized a) absorption, and emission spectra of **11**, **12** and **13** at b) RT and c) 77 K in MTHF solution ($C = 1 \times 10^{-5}$ M, $l = 1$ cm, $\lambda_{\text{ex}} = 338$ nm for **11**, 352 nm for **12**, 356 nm for **13**). d) Emission lifetime decay profile of **11**, **12** and **13** in MTHF solution ($C = 1 \times 10^{-5}$ M, $l = 1$ cm, $\lambda_{\text{ex}} = 374$ nm, $\lambda_{\text{mon}} = 381$ nm for **11**, 397 nm for **12** and 498 nm for **13**) respectively.

Since all the molecules formed crystalline assembly, optical properties were studied in the crystal state. The solid-state diffuse reflectance spectra of **11-13** show a broad band between 330-440 nm (Figure 3.7a). The steady-state emission spectra of **11-13** exhibit emission peaks located around 400-650 nm (Figure 3.7b). Additionally, molecules **11-13** show a little difference in emission

features at 77 K in the crystal state (Figure 3.7c, 3.8). To measure the fluorescence lifetime, the measurement was carried out by monitoring at wavelength maxima and the longer lifetime component varied as 4.40 ns (91%) for **11**, 4.84 ns (76%) for **12** and 3.23 ns (80%) for **13** (Figure 3.7d and Table 1).

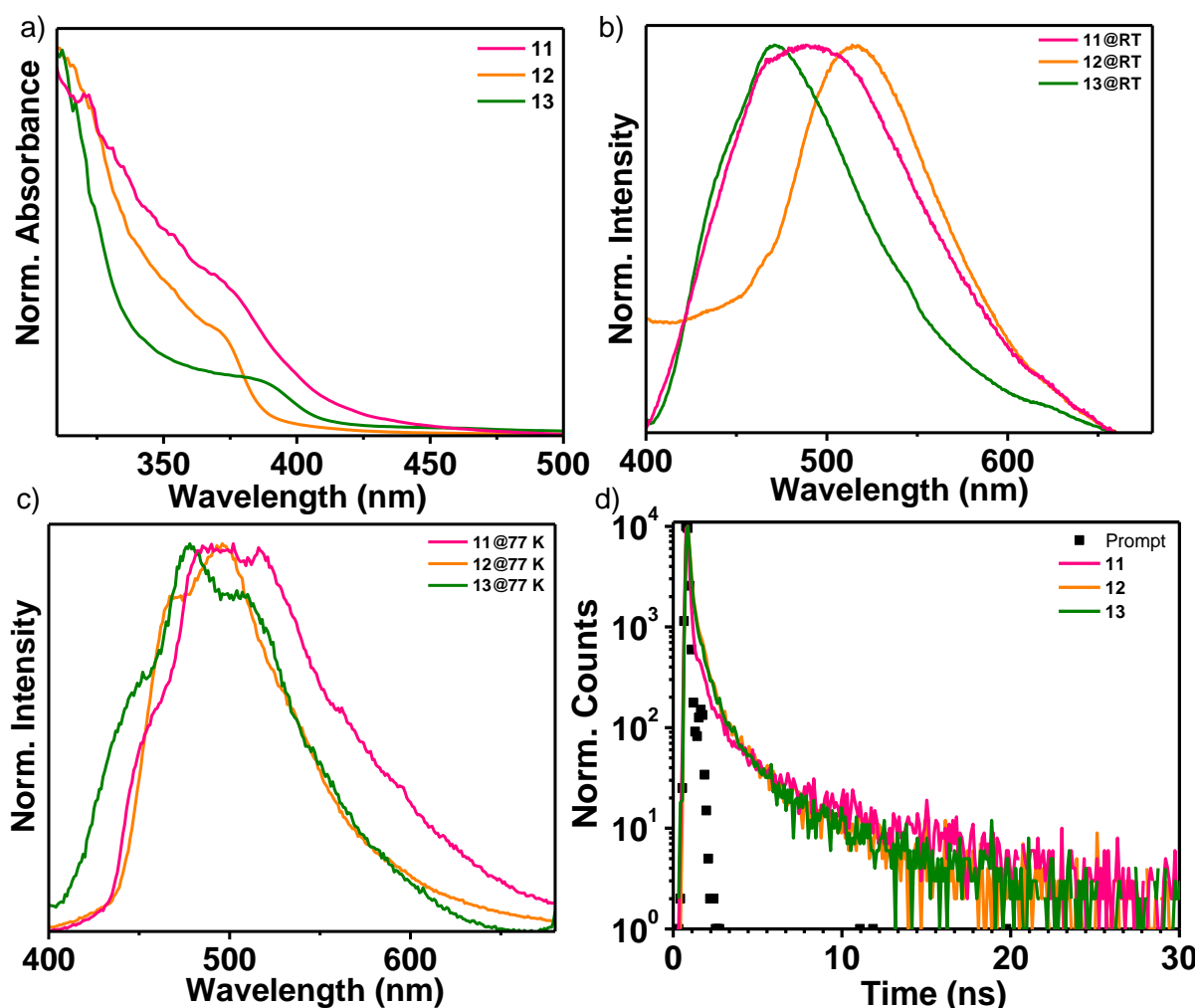


Figure 3.7. Normalized solid-state a) absorption, steady-state emission spectra of **11**, **12**, **13** crystals at b) RT and c) 77 K ($\lambda_{\text{ex}} = 374$ nm for **11**, 378 nm for **12** and 390 nm for **13**). d) Crystal state emission lifetime decay profile of **11**, **12** and **13** ($\lambda_{\text{ex}} = 374$ nm, $\lambda_{\text{mon}} = 491$ nm for **11**, 516 nm for **12** and 472 nm for **13**).

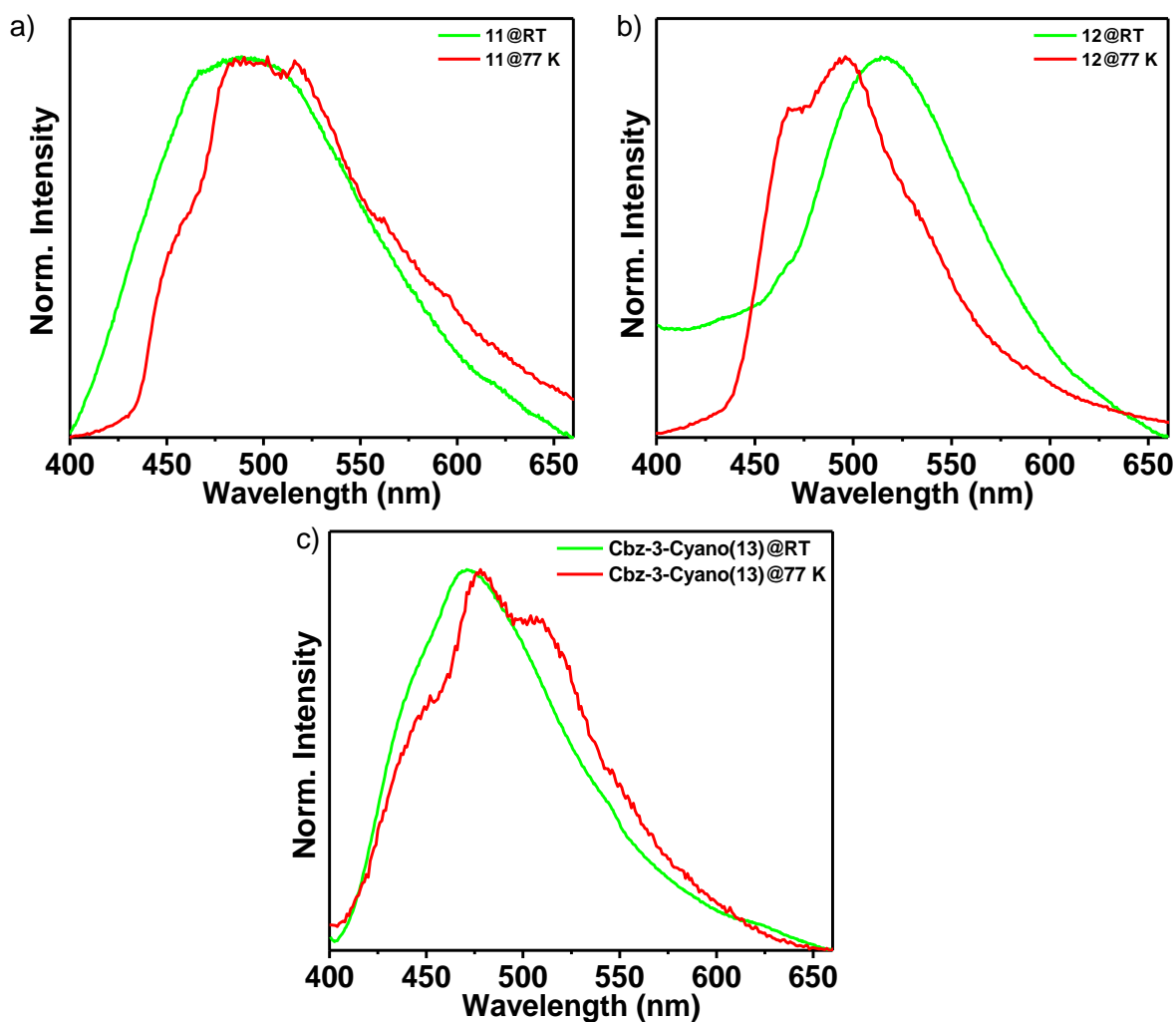


Figure 3.8. Comparison of the normalized crystal state emission spectra of a) **11**, b) **12**, c) **13** at RT and 77 K ($\lambda_{\text{ex}} = 374$ nm for **11**, 378 nm for **12**, and 390 nm for **13**).

The fluorescence of **11** and **13** crystals at RT nearly matches the corresponding spectra at 77 K, indicating RTP for **11** and **13** in the crystalline assembly while molecule **12** shows a slight red-shifted phosphorescence peak (Figure 3.8). Phosphorescence spectra were measured to confirm the presence of RTP in crystals **11-13** and confirmed that the observed red-shifted emission peak at RT is due to phosphorescence (Figure 3.9a). In the crystal state, phosphorescence intensity of **11** was visualized higher than the **12** and **13** and the observed phosphorescence lifetime of **11-13** was found 6.59 ms (**11**), 45.3 ms (**12**) and 11.9 ms (**13**) (Figure 3.9b, Table 2).

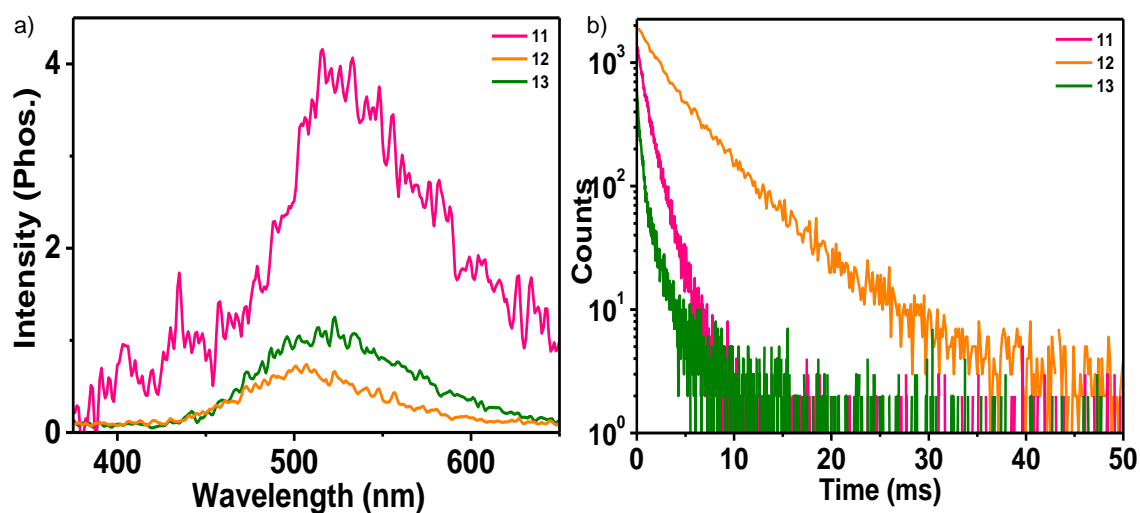


Figure 3.9. Phosphorescence spectra and corresponding phosphorescence lifetime decay profile of **11-13** in the crystal state ($\lambda_{\text{ex}} = 374$ nm, $\lambda_{\text{mon}} = 520$ nm for **11**, 508 nm for **12** and 530 nm for **13**).

Moreover, we aim to develop a luminescent molecule containing chiral center on 3,6-(bis)-phenylmethanone carbazole and to study how molecular chirality affects luminescent properties, especially RTP. Circularly polarized luminescent phosphors are powerful tool to study the chirality of excited states and attracts growing interest in the development of new optoelectronic devices. Moreover, it is advantageous to have chiral phosphors which can be explored in the circularly polarized phosphorescence which have received attention due to their wide potential applications in various research fields, including 3D-displays, optical data storage, information storage and processing, spintronics devices, sensors, security inks, and biological probes and so forth.^[14] While circularly polarized RTP has been observed from many metal complexes, it has not been studied in detail for metal-free organic molecules. Hence, we aim to develop chiral organic phosphors by using 3,6-(bis)-phenylmethanone carbazoles.

Taking into consideration, we aimed to design and synthesis of (S)-(9-(2-methylbutyl)-9H-carbazole-3,6-diyl)bis(phenylmethanone) (**14**) molecule. Target molecule **14** as shown in Scheme 2, was synthesized by using same

synthetic transformations and all the molecules were characterized by ^1H and ^{13}C NMR spectrometry and high-resolution mass spectrometry (HRMS).

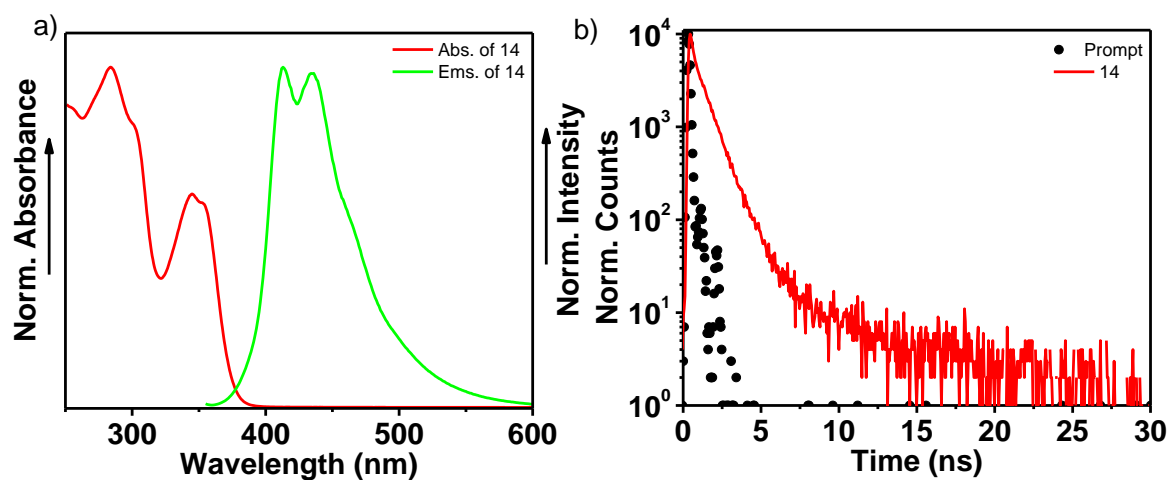


Figure 3.10. a) Normalized absorption and emission spectrum of molecule **14** in MTHF solution b) Fluorescence lifetime decay profile of molecule **14** in MTHF solution monitored at 440 nm wavelength ($C = 10^{-5}$ M, $l = 1$ cm, $\lambda_{\text{ex}} = 360$ nm for **14**).

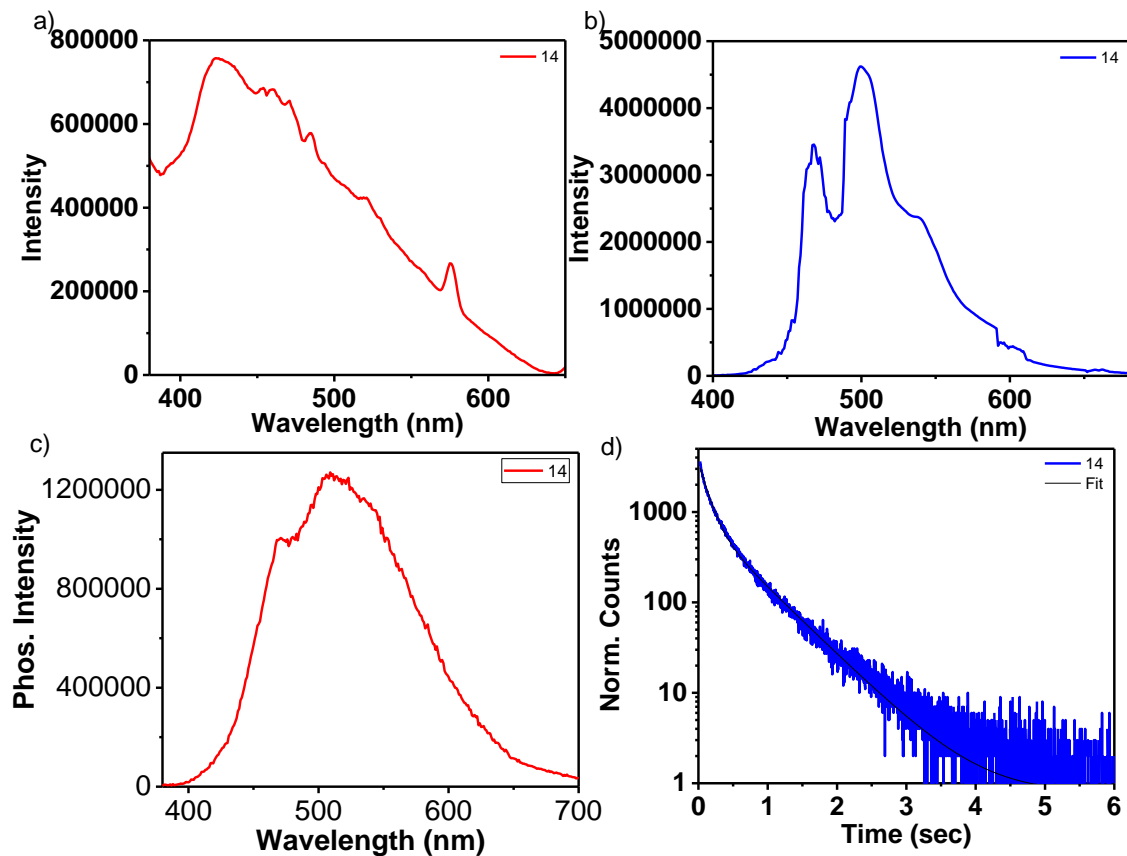


Figure 3.11. Crystal-state fluorescence spectrum of **14** at a) RT and b) 77 K, c) Phosphorescence spectrum ($\lambda_{\text{ex}} = 360$ nm for **14**), d) Phosphorescence lifetime decay profile of **14** monitored at 542 nm at RT.

Molecule **14** is well studied for its absorption, emission, phosphorescence and corresponding lifetime in solution as well as in crystal state. From the absorption spectra, it can be seen that compound **14** absorbs in the UV region ranging from 280-380 nm and the absorption peak at 280 nm is attributed to (π, π^*) transition and peak at 346 nm are due to (n, π^*) transition (Figure 3.10a). The emission spectra of compound **14** measured by exciting at different wavelengths show a broad emission in the range of 390 to 520 nm (Figure 3.10a). Furthermore, the fluorescence spectra of crystals at RT exhibits a red-shifted peak than the solution, which has a broad peak from 400 nm to 620 nm range. A slightly broad phosphorescence spectrum in the same spectral range was noticed (Figure 3.11c). The enhanced RTP for molecule **14** was visualized by phosphorescence lifetime measurement, and it is found as 582 ms for molecule **14**.

Single-crystal X-ray analysis was used to obtain a more detailed structure-property correlation of **6**, **8**, **11-13** and **14** (Figures 3.12 and 3.13). The unit cell of molecule **6** contains four molecules arranged in an alternate way along the a-axis which having intermolecular interactions. The extended packing of molecule **6** involves $>C=O \cdots \pi$ intermolecular interaction with 3.19 Å distance (Figure 3.12a). Similarly, molecule **8** exhibits various kinds of intermolecular interaction in the unit cell packing. The molecule **8** involves $>C=O \cdots \pi = 3.22$ Å, $Ar\ C-H \cdots \pi = 2.89$ Å and $Alkyl\ C-H \cdots C=O = 2.67$ Å interaction (Figure 3.12b). Alike intermolecular interaction seen in the case of molecule **14** in unit cell packing. The unit cell of molecule **14** contains two molecules arranged alternately along the a-axis using various intermolecular interactions. An extended one-dimensional molecular array was formed by the arrangement of molecules mainly through $CH \cdots \pi$ interaction (2.89 Å) between the chiral alkyl chain on carbazole

and phenylmethanone unit in the adjacent columns to form a one-dimensional network structure (Figure. 3.12c).

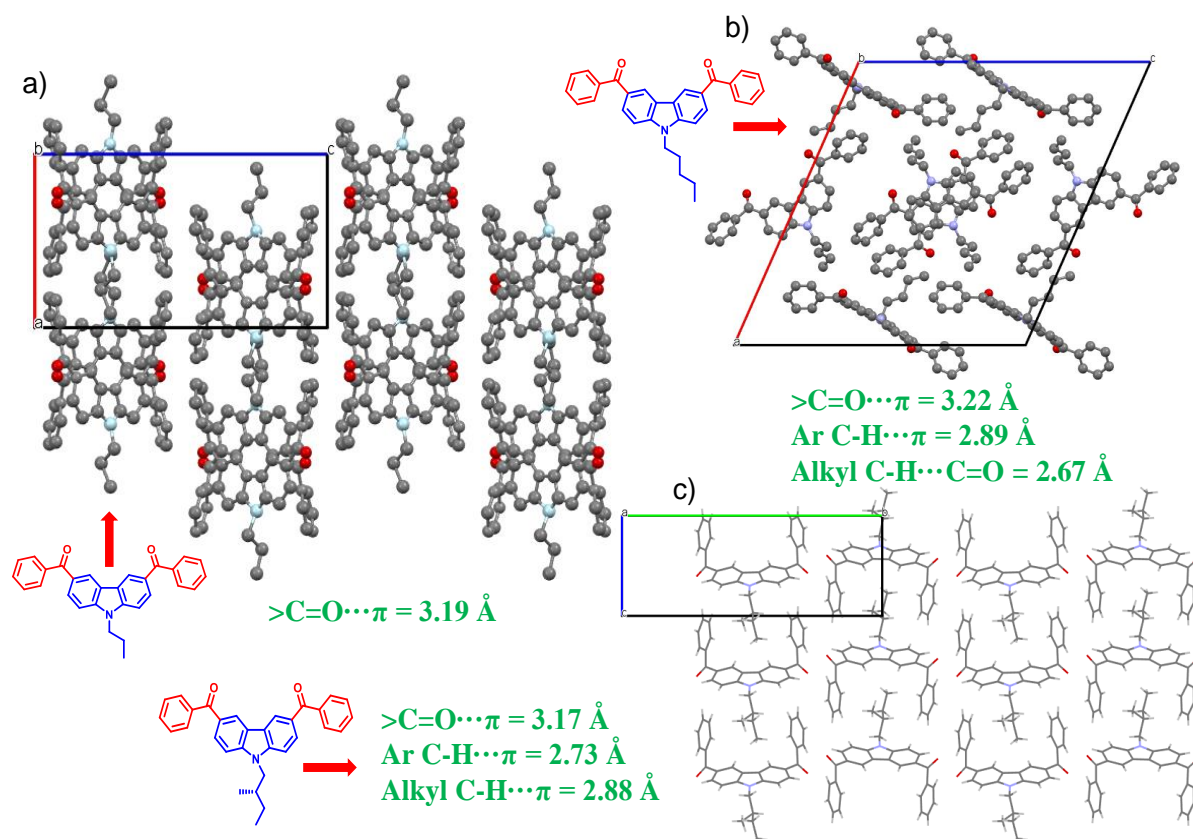


Figure 3.12. Molecular packing of a) **6**, b) **8** and c) **14** in the unit cell.

However, the molecular packing of molecules **11**, **12**, and **13**, on the other hand, shows a loosely packed crystalline assembly with various types of intermolecular interactions (Figure. 3.13). Particularly, molecule **13** is packed in a slipped molecular arrangement with a large distance between two carbazole-carbazole molecules (Figure. 3.13c). As a result of such a loosely packed molecular arrangement between molecules, they have insufficient RTP properties. Most importantly, no helical array packing in crystalline assembly was observed in the whole series of molecules studied. It indicates the lack of enhanced RTP properties even after changing from various alkyl chains as well as substitution of phenylmethanone group. Hence, it can be concluded that the peculiar helical molecular packing results in a long phosphorescence lifetime of

3,6-phenylmethanone functionalized 9-hexylcarbazole compared to other molecules in the series and this is supported by the crystal structure and phosphorescence lifetime.

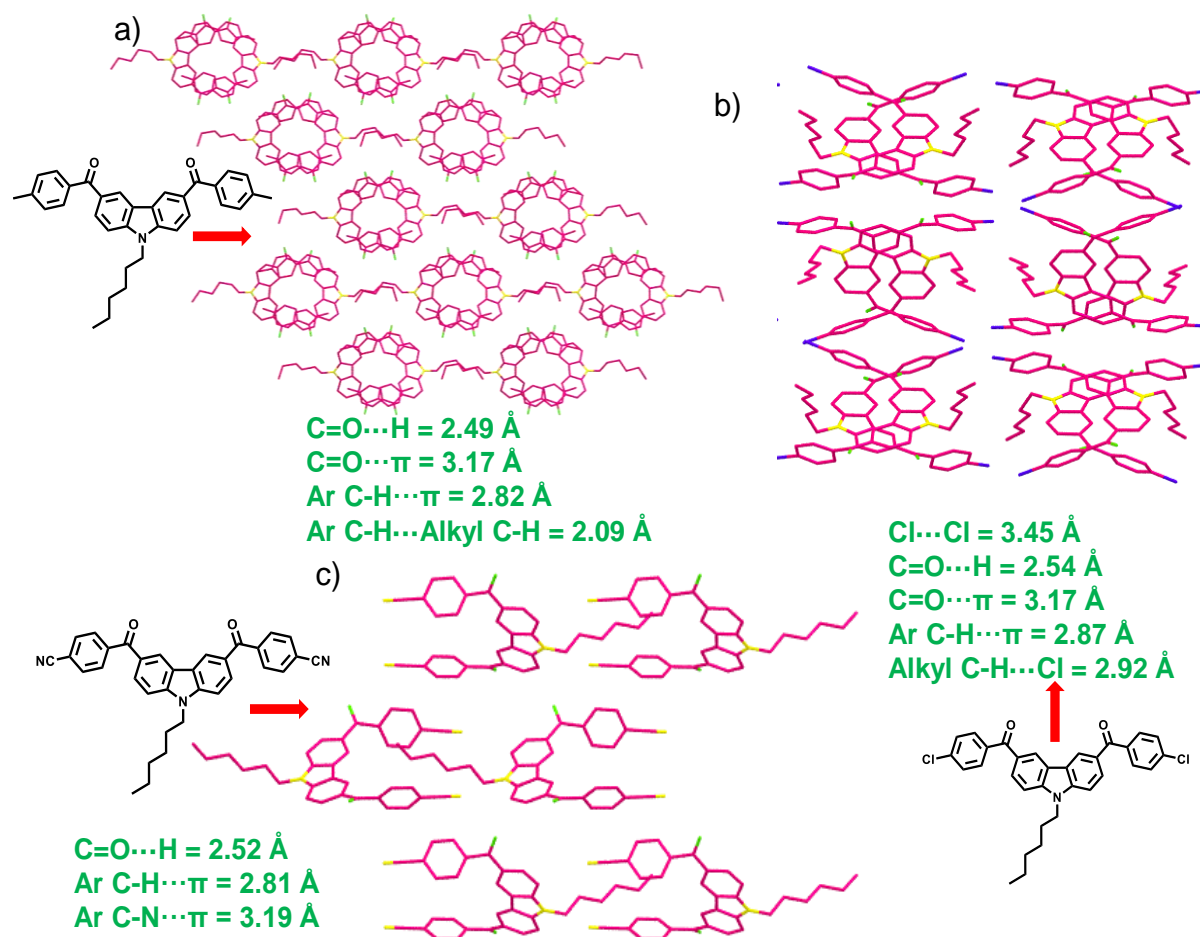


Figure 3.13. Molecular packing of a) **11**, b) **12** and c) **13** in the unit cell.

Time-dependent density functional theory (TD-DFT) computations at the B3LYP/6-31G(d) level of theory for single-molecule in vacuum show that the electron density of the HOMO is located on the carbazole moiety and the LUMO is delocalized over the entire molecule with extension to the phenylmethanone group (Figure 3.14 and 3.15). The low-lying excited electronic states mainly result from well-described π - π^* transitions along with a significant contribution from the n - π^* character. On studying the relative computed energies for the

singlet (S_n) and triplet (T_n) states for **14**, it has been found that T_4 - T_9 triplet states nearly degenerate with the first singlet excited state (S_1) (Figure 3.15d). The energetic proximity of the singlet and the triplet manifold potentials established a small ΔE_{ST} . Thus, it appears that molecules **11-13** have energetically well-matched states that enable efficient singlet-triplet or triplet-singlet crossings. Once T_4 - T_9 levels are populated, relaxation through the triplet manifold to the T_1 state leads to phosphorescence. The $\Delta E_{S_1T_1}$ value were calculated for **14** from DFT as 0.71 eV (Figure 3.15d). It shows that the aggregation of **14** with the assistance of intermolecular interactions reduces $\Delta E_{S_1T_1}$ to facilitate both ISC and RISC.

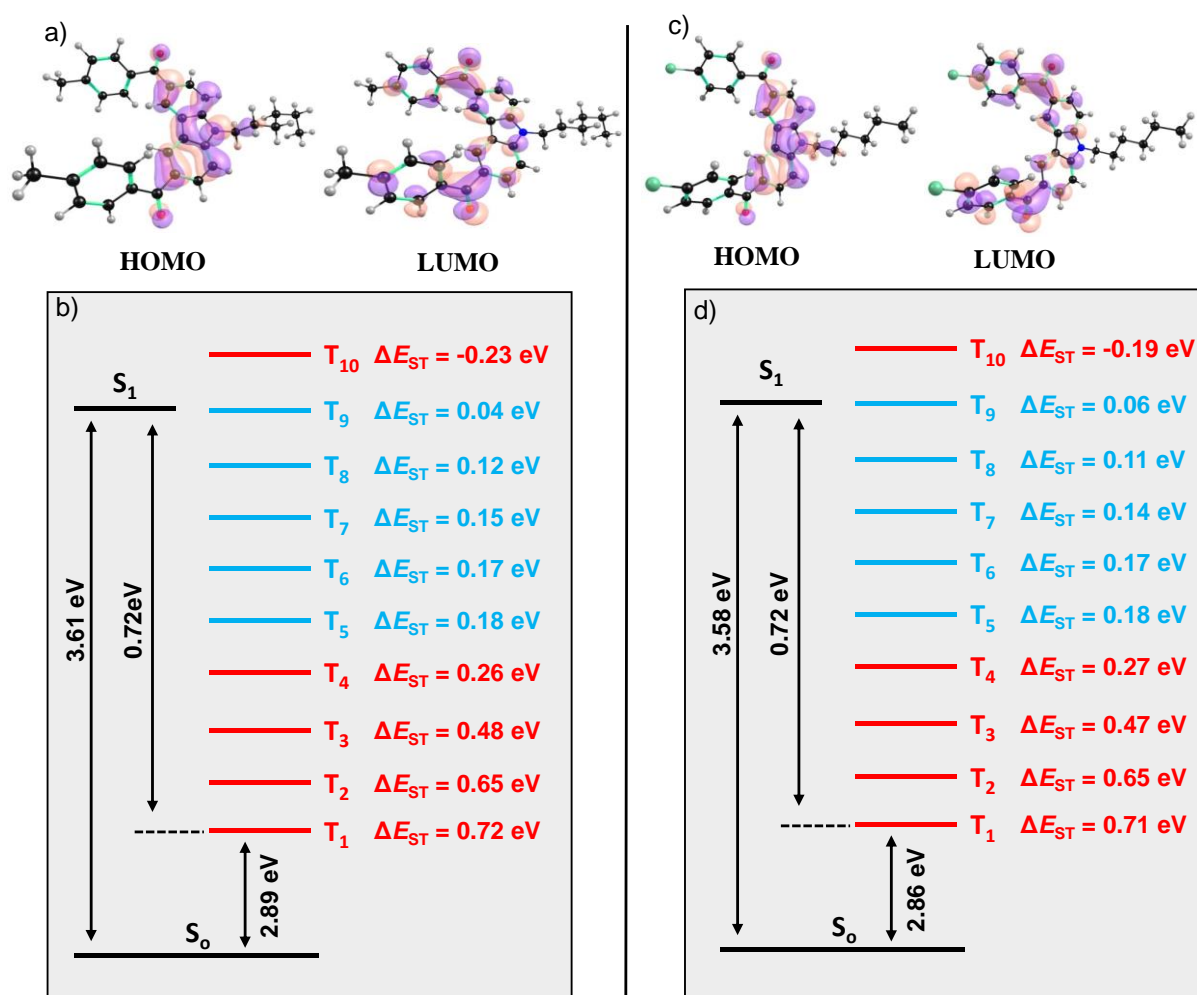


Figure 3.14. HOMO and LUMO frontier molecular orbitals of a) **11** c) **12** and calculated energy level diagram showing ΔE_{ST} for b) **11** d) **12** from DFT calculations.

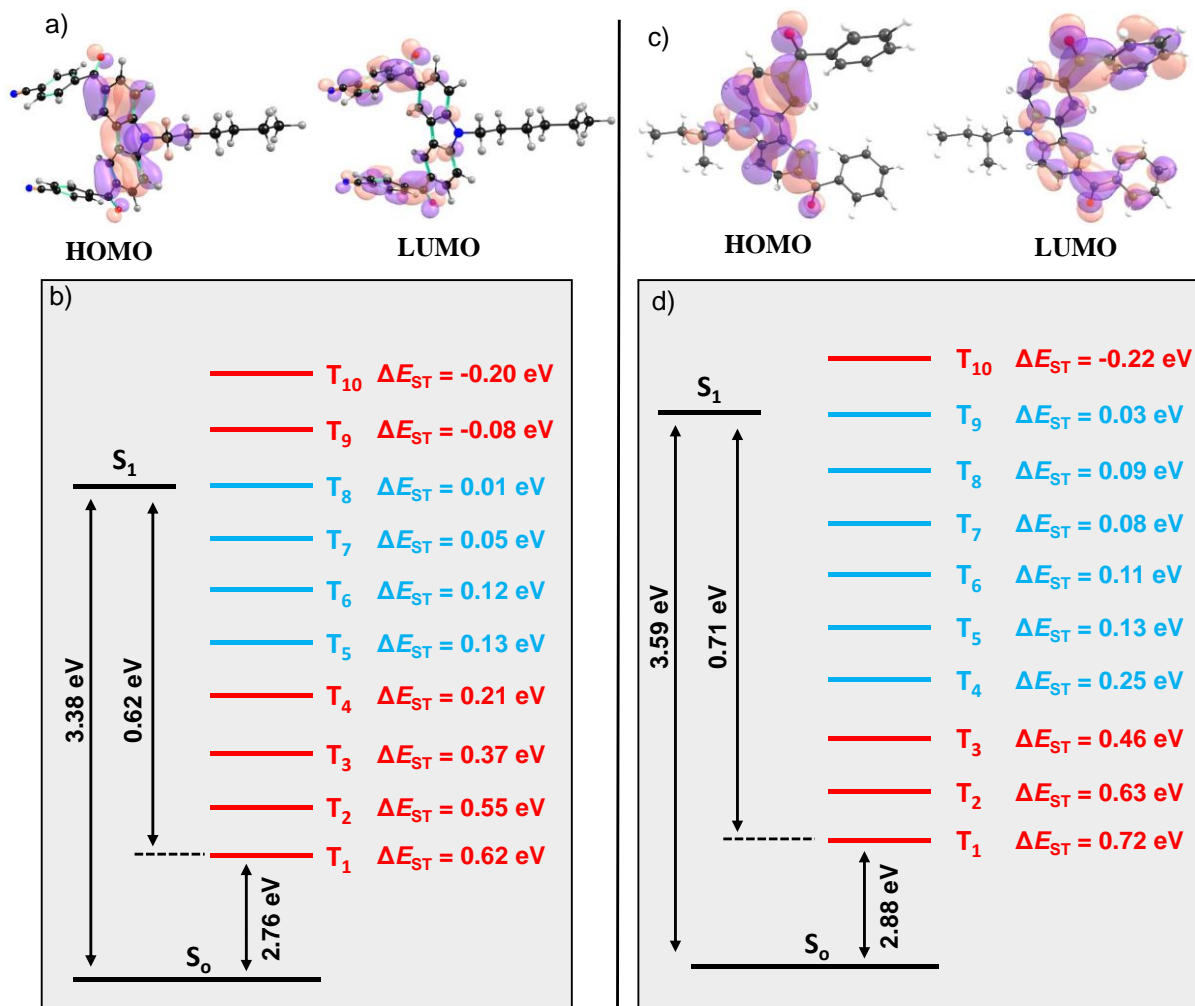


Figure 3.15. HOMO and LUMO frontier molecular orbitals of a) **13** c) **14** and calculated energy level diagram showing ΔE_{ST} for b) **13** d) **14** from DFT calculations.

Table 1. Photophysical properties of compounds **1-14** in MTHF (1×10^{-5} M) and crystal state.

Compound	λ_{ab} (nm)	λ_{em} (nm)	ϕ_{PL} (%)	Lifetime (ns) (solution)

1	Solution	342 nm	370 nm	-	0.69 (08.45 %) 4.12 (91.55 %)
2	Solution	342 nm	370 nm	-	1.08 (12.54 %) 4.33 (87.46 %)
3	Solution	342 nm	370 nm	-	0.66 (08.50 %) 4.12 (91.50 %)
4	Solution	342 nm	370 nm	-	1.50 (38.03 %) 4.26 (45.27 %) 0.05 (16.70 %)
5	Solution	342 nm	370 nm	-	1.80 (38.43 %) 4.45 (49.36 %) 0.07 (12.21 %)
6	Solution	356 nm	434 nm	-	0.84 (05.73 %) 3.01 (94.27 %)
7	Solution	356 nm	434 nm	-	0.10 (11.40 %) 0.93 (88.60 %)
8	Solution	356 nm	434 nm	-	0.12 (09.45 %) 0.92 (90.55 %)
9	Solution	356 nm	434 nm	-	0.09 (14.42 %) 0.96 (85.58 %)
10	Solution	356 nm	434 nm	-	0.08 (11.73 %) 0.94 (88.27 %)
11	Solution	352 nm	397 nm	-	1.49 ns (24.50%) 6.42 ns (49.13%) 0.02 ns (26.37%)
	Solid	360 nm	500 nm	3.52	4.40 ns (91.80%) 3.30 ns (0.64%) 0.06 ns (7.56%)
12	Solution	342 nm	381 nm	-	1.66 ns (25.86%) 6.99 ns (50.29%) 0.02 ns (23.85%)
	Solid	360 nm	520 nm	4.14	1.02 ns (20.56%) 4.84 ns (75.65%) 0.12 ns (3.79%)

13	Solution	360 nm	498 nm	-	1.55 ns (24.48%) 6.59 ns (51.72%) 0.09 ns (23.80%)
	Solid	380 nm	450 nm	4.47	3.23 ns (80.13%) 0.02 ns (02.38%) 0.13 ns (17.49%)
14	Solution	356 nm	434 nm	-	0.10 ns (24.81 %) 0.93 ns (75.19 %)
	Solid	370 nm	480 nm	4.70	1.02 ns (20.56%) 6.84 ns (3.79%) 0.12 ns (75.65%)

Table 2. Phosphorescence lifetime of **6-14** in crystal state.

Compound	λ_{ex}	Lifetime (ms)	CHISQ	ϕ_{Phos} (%)
6	515 nm	146 ms	1.23	2.85
7	495 nm	14 ms	0.91	1.09
8	520 nm	11 ms	1.12	1.78
9	510 nm	14 ms	0.61	1.56
10	525 nm	14 ms	0.88	2.22
11	510 nm	6.59 ms	0.40	2.69
12	505 nm	45.3 ms	0.25	2.61
13	515 nm	11.9 ms	0.21	2.01
14	512 nm	582 ms	1.13	2.32

3.5. Conclusion

In conclusion, we have successfully synthesized and characterized the series of N-alkylated and phenylmethanone functionalized carbazole molecules exhibiting RTP. The prepared molecules show light green to green color phosphorescence spanning from 420 nm to 650 nm with the highest phosphorescence lifetime of **582** ms. The molecular packing in the crystal shows

multiple interactions between phenylmethanone unit and alkyl hydrogen atoms that are helping to enhance the ISC and triplet state of the molecule leading to a moderate lifetime. Crystal structures help in understanding the molecular packing involved in the molecules. It has been concluded that the C-6 alkyl chain plays a crucial role in the helical packing of 3,6-bis(phenylmethanone) substituted 9-hexylcarbazole in the crystal lattice. No such helical molecular packing was observed in other alkyl-substituted carbazole molecules. Hence, helical packing of the metal-free, heavy atom-free 3,6-diphenylmethanone substituted carbazole resulted in a significant improvement of phosphorescence lifetime along with phosphorescence waveguiding. However, molecular chirality also played an essential role in imparting a long phosphorescence lifetime. However, supramolecular chirality is superior to molecular chirality in enhancing the RTP features of phenylmethanone substituted carbazoles in the series.

3.6. References

- [1] a) G. Baryshnikov, B. Minaev, H. Ågren, *Chem. Rev.* **2017**, *117*, 6500; b) M. Baroncini, G. Bergamini, P. Ceroni, *Chem. Commun.* **2017**, *53*, 2081; c) A. Forni, E. Lucenti, C. Botta, E. Cariati, *J. Mater. Chem. C.* **2018** *6*, 4603; d) X. Yang, G. Zhou, W-Y. Wong, *Chem. Soc. Rev.* **2015**, *44*, 8484.
- [2] a) G. Zhang, G. M. Palmer, M. Dewhirst, C. L. Fraser, *Nat. Mater.* **2009**, *8*, 747; b) S. M. A. Fateminia, Z. Mao, S. Xu, Z. Yang, Z. Chi, B. Liu, *Angew. Chem. Int. Ed.* **2017**, *56*, 12160; *Angew. Chem.* **2017**, *129*, 12328; c) Z. Yu, Y. Wu, L. Xiao, J. Chen, Q. Liao, J. Yao, H. Fu, *J. Am. Chem. Soc.* **2017**, *139*, 6376.
- [3] V. C. Wakchaure, K. C. Ranjeesh, Goudappagouda. T. Das, K. Vanka, R. Gonnade, S. S. Babu, *Chem. Commun.* **2018**, *54*, 6028.
- [4] a) Goudappagouda, A. Manthanath, V. C. Wakchaure, K. C. Ranjeesh, T. Das, K. Vanka, T. Nakanishi, S. S. Babu, *Angew. Chem. Int. Ed.* **2019**, *58*,

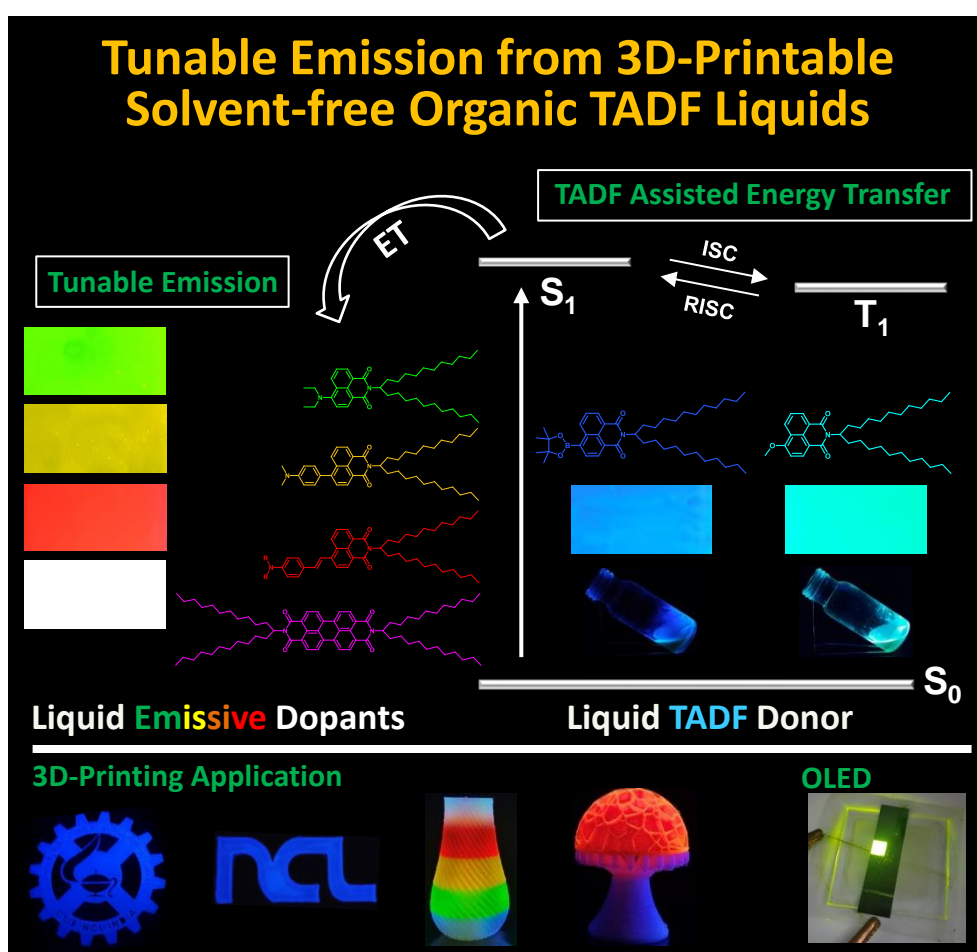
- 2284; *Angew. Chem.* **2019**, *131*, 2306; b) Bolten, K. Lee, H. J. Kim, K. Y. Lin, J. Kim, *Nat. Chem.* **2011**, *3*, 205.
- [5] a) S. Hirata, *J. Mater. Chem. C.* **2018**, *6*, 11785; b) Kenry, C. Chen, B. Liu, *Nat. Commun.* **2019**, *10*, 2111; c) S. Xu, R. Chen, C. Zheng, W. Huang, *Adv. Mater.* **2016**, *28*, 9920; d) S. K. Lower, M. A. El-Sayed, *Chem. Rev.* **1966**, *66*, 199.
- [6] a) S. Kuila, K. V. Rao, S. Garain, P. K. Samanta, S. Das, S. K. Pati, M. Eswaramoorthy, S. J. George, *Angew. Chem. Int. Ed.* **2018**, *57*, 17115; *Angew. Chem.* **2018**, *130*, 17361; b) S. Kuila, S. J. George, *Angew. Chem. Int. Ed.* **2020**, *59*, DOI:10.1002/anie.202002555; *Angew. Chem. Int. Ed.* **2020**, *132*, DOI:10.1002/ange.202002555.
- [7] a) C. S. Bilen, N. Harrison, D. J. Morantz, *Nature*, **1978**, *271*, 235; b) S. Hirata, K. Totani, J. Zhang, T. Yamashita, H. Kaji, S. R. Marder, T. Watanabe, C. Adachi, *Adv. Opt. Mater.* **2013**, *1*, 438; c) R. Kabe, N. Notsuka, K. Yoshida, C. Adachi, *Adv. Mater.* **2016**, *28*, 655.
- [8] a) Z. He, W. Zhao, J. W. Y. Lam, Q. Peng, H. Ma, G. Liang, I. Shuai, B. Z. Tang, *Nat. Commun.* **2017**, *8*, 416; b) W. Zhao, Z. He, J. W. Y. Lam, Q. Peng, H. Ma, Z. Shuai, G. Bai, J. Hao, B. Z. Tang, *Chem.* **2016**, *1*, 592.
- [9] a) Z. An, C. Zheng, Y. Tao, R. Chen, H. Shi, T. Chen, Z. Wang, H. Li, R. Deng, X. Liu, W. Huang, *Nat. Mater.* **2015**, *14*, 685; b) S. Cai, H. Shi, Z. Zhang, X. Wang, H. Ma, N. Gan, Q. Wu, Z. Cheng, K. Ling, M. Gu, C. Ma, L. Gu, Z. An, W. Huang, *Angew. Chem. Int. Ed.* **2018**, *57*, 4005; *Angew. Chem.* **2018**, *130*, 4069.
- [10] a) T. Ogoshi, H. Tsuchida, T. Kakuta, T. Yamagishi, A. Taema, T. Ono, M. Sugimoto, M. Mizuno, *Adv. Funct. Mater.* **2018**, *28*, 1707369; b) S. Hirata, M. Vacha, *Adv. Optical Mater.* **2017**, *5*, 1600996; c) Y. Xie, Y. Ge, Q. Peng, C. Li, Q. Li, Z. Li, *Adv. Mater.* **2017**, *29*, 1606829; d) Z. Yang, Z. Mao, X. Zhang, D. Ou, Y. Mu, Y. Zhang, C. Zhao, S. Liu, Z. Chi, J. Xu, Y.-C. Wu, P.-Y. Lu, A. Lien, M. R. Bryce, *Angew. Chem. Int. Ed.* **2016**,

- 55, 2181; *Angew. Chem.* **2016**, *128*, 2221; e) Y. Katsurada, S. Hirata, K. Totani, M. Watanabe, M. Vacha, *Adv. Optical Mater.* **2015**, *3*, 1726.
- [11] a) M. Li, K. Ling, H. Shi, N. Gan, L. Song, S. Cai, Z. Cheng, L. Gu, X. Wang, C. Ma, M. Gu, Q. Wu, L. Bian, M. Liu, Z. An, H. Ma, W. Huang, *Adv. Optical Mater.* **2019**, 1800820; b) B. Zhou, D. Yan, *Adv. Funct. Mater.* **2019**, *29*, 1807599; c) L. Gu, H. Shi, L. Bian, M. Gu, K. Ling, X. Wang, H. Ma, S. Cai, W. Ning, L. Fu, H. Wang, S. Wang, Y. Gao, W. Yao, F. Huo, Y. Tao, Z. An, X. Liu, W. Huang, *Nat. Photonics* **2019**, *13*, 406; d) L. Bian, H. Shi, X. Wang, K. Ling, H. Ma, M. Li, Z. Cheng, C. Ma, S. Cai, Q. Wu, N. Gan, X. Xu, Z. An, W. Huang, *J. Am. Chem. Soc.* **2018**, *140*, 10734; e) Z. Chai, C. Wang, J. Wang, F. Liu, Y. Xie, Y.-Z. Zhang, J.-R. Li, Q. Lia, Z. Li, *Chem. Sci.* **2017**, *8*, 8336; f) A. D. Nidhankar, Goudappagouda, D. S. M. Kumari, S. K. Chaubey, R. Nayak, R. G. Gonnade, G. V. P. Kumar, R. Krishnan, S. S. Babu, *Angew. Chem. Int. Ed.* **2020**, *59*, 13079-13085.
- [12] A. D. Nidhankar, Goudappagouda, V. C. Wakchaure, S. S. Babu, *Chem. Sci.* **2021**, *12*, 4216-4236.
- [13] N. J. Turro, *Modern Molecular Photochemistry*, University Science Books, Sausalito, **1978**.
- [14] S. Hirata, M. Vacha, *J. Phys. Chem. Lett.* **2016**, *7*, 1539.
- [15] Bruker (2016). *APEX2, SAINT and SADABS*. Bruker AXS Inc., Madison, Wisconsin, USA.
- [16] G. M. Sheldrick, *Acta Crystallogr.*, **2008**, *A64*, 112.
- [17] G. M. Sheldrick, *Acta Crystallogr.*, **2015**, *C71*, 3-8.
- [18] L. J. Farrugia, *J. Appl. Crystallogr.* **2012**, *45*, 849-854.
- [19] A. Justyniarski, J. K. Zaręba, P. Hańczyc, P. Fita, M. Chołuj, R. Zaleśny, M. Samoc, *J. Mater. Chem. C*, **2018**, *6*, 4384.
- [20] F. Lu, K. Hagiwara, M. Yoshizawa, K. Nagura, S. Ishihara, T. Nakanishi, *J. Mater. Chem. C*, **2019**, *7*, 2577-2582.

- [21] H. Gallardo, G. Conte, F. Bryk, M. R. S. Lourenço, M. S. Costa, V. F. Ferreira, *J. Braz. Chem. Soc.*, **2007**, *18*, 1285-1291.
- [22] B. C. Popere, A. M. Della Pelle, A. Poe, G. Balaji, S. Thayumanavan, *Chem. Sci.*, **2012**, *3*, 3093-3102.
- [23] L. Yang, J. Huang, M. Qin, X. Ma, X. Dou, C. Feng, *Nanoscale* **2020**, *12*, 6233-6238.
- [24] R. Tempelaar, A. Stradomska, J. Knoester, F. C. Spano, *J. Phys. Chem. B* **2011**, *115*, 10592-10603.
- [25] F. Zinna, S. Voci, L. Arrico, E. Brun, A. Homberg, L. Bouffier, T. Funaioli, J. Lacour, N. Sojic, L. D. Bari, *Angew. Chem. Int. Ed.*, **2019**, *58*, 6952.
- [26] C. Mowatt, S. M. Morris, M. H. Song, T. D. Wilkinson, R. H. Friend, H. J. Coles, *J. Appl. Phys.*, **2010**, *107*, 043101.
- [27] H. Kubo, D. Shimizu, T. Hirose, K. Matsuda, *Organic Letters* **2020**, *22*, 9276-9281.

Chapter-4

Thermally Activated Delayed Fluorescent Solvent-free Organic Liquid Hybrids for Tunable Emission Applications



The synthetic feasibility and excellent luminescence features of organic molecules attracted much attention and were eventually found useful in lighting applications. In this context, a solvent-free organic liquid having attractive thermally activated delayed fluorescence features in bulk along with high processability has prime importance. Herein, we report a series of naphthalene

monoimide-based solvent-free organic liquids exhibiting blue to red thermally activated delayed fluorescence with luminescence quantum yields up to 80% and lifetimes between 8 to 45 μ s. An effective approach explored energy transfer between liquid donors with various emitters exhibiting tunable emission colours, including white. The high processability of liquid emitters improved the compatibility with polylactic acid and was used for developing multicolour emissive objects using 3D printing. Besides, the first example of a thermally activated delayed fluorescent liquid as an emitter in OLED with moderate performance is promising. Our demonstration will be much appreciated as a processable alternate emissive material suitable for large-area lighting, display, and related applications.

Publication: *Manuscript communicated*

4.1. Introduction

Organic molecules exhibiting thermally activated delayed fluorescence (TADF)¹⁻⁸ and room temperature phosphorescence (RTP)⁹⁻¹⁴ that efficiently harvest triplet excitons and convert to light have emerged as promising light-emitting materials. The advantages of both intersystem crossing (ISC) in RTP and reverse intersystem crossing (rISC) in TADF materials heavily supported achieving an internal quantum efficiency of 100%.^{1,14} Still, conventional fluorescent emitters are preferred due to the comparatively high freedom and simplicity in molecular design. Nonetheless, the inherently reduced internal quantum efficiency (25%) of fluorescent organic light-emitting diodes (OLEDs) and concerns related to the device stability of phosphorescent LEDs urge TADF-sensitized devices.¹⁵ Besides, energy transfer (ET) between the TADF sensitizer and emissive dopants is a promising strategy to achieve tunable emission without compromising the efficiency and operational stability of the devices.¹⁶

Recent years have witnessed a surge in developing organic materials for flexible display and lighting devices.¹⁷⁻²⁰ Mainly, in the case of molecules emissive in the solution, the emission will be altered for thin films upon solvent evaporation due to emission quenching by aggregation or photo-bleaching.²¹⁻²² Hence, the technologically advanced lighting and display applications demand newer emitters with improved processability and luminescence features.²³⁻²⁶ In this direction, solvent-free organic liquids (SOLs) have been keenly investigated as a new soft material to undertake the above-mentioned challenges to a certain extent.^{27,28-48} The recent examples of emissive SOLs project them as a possible alternate soft material to address the balance between efficiency and processability. The present work introduces TADF liquids and efficient ET-assisted tunable emission by doping with emitters (Figure 4.1a). The use of TADF host and fluorescent emitters is proven to improve the device performance by suppressing the efficiency roll-off and reducing the density of triplet excitons of the host.^{1-8,16} Hence, our approach to TADF SOLs and ET-assisted tunable emission offers a new approach to improve the device performance using a processable soft material. Moreover, an inefficient ET due to spin forbidden transition from T_1 of a phosphorescent donor to S_1 of the acceptor also supports ET between TADF and TADF/fluorescent emitters.¹⁶

4.2. Experimental section

4.2.1 RTP and TADF Experiments

The window of maximum delay after flash for phosphorescence measurements was kept as 3 ms for 77 K and 0.1 ms for 298 K ($\lambda_{\text{ex}} = 350$ nm for **1**). Phosphorescence lifetimes were measured at room temperature (298 K) in the air by keeping a 10% delay component and 10% trigger pulse duration, using 355 nm excitation source. All experiments have been done in air by keeping the same experimental parameters.

4.2.2 Temperature-Dependent Emission and Lifetime Decay Measurements

The PTI spectrofluorometer is equipped with thermoelectric cuvette holders, heating stages, and cryostats which allows the measurements to be carried out over a temperature range of 77 K to 353 K. The fluorescence emission and lifetime decays of **1** and **5** from 77 K to 298 K were measured using liquid nitrogen Dewar module.

4.2.3 Preparation of TADF Hybrids for Energy Transfer

The acceptor liquids (**3-6**) were dissolved in dichloromethane (5 mL) to prepare a stock solution ($C = 1 \times 10^{-3}$ M), and the required amounts were added to the donor liquids to prepare the required composition. The sample was mixed well to get a uniform mixture, and the added dichloromethane was evaporated before TADF measurements by heating the hybrid liquid to 80 °C in a vacuum oven for 12 hours. The absence of dichloromethane in the hybrid liquid was confirmed by ¹H NMR experiments in CDCl₃. The homogeneity of the composite is confirmed by the physical appearance and DSC measurements. The experiments were repeated even by mixing the donor and acceptor liquids and obtained comparable results.

4.2.4 Preparation of PLA/ SOL Filaments

All PLA/SOL filaments were prepared by solution mixing followed by melt extrusion. PLA pellets were first dried in a vacuum oven for 4 h at 80 °C to eliminate residual traces of moisture. Dried PLA pellets were dissolved in chloroform, and then the required quantity of SOL was added to it to get a 1wt % SOL/PLA blend. The PLA/SOL solution was mechanically stirred at ambient temperature for 7-8 h to ensure uniform mixing. The PLA/SOL solution was then cast on a glass petri dish and kept for drying at 60 °C under vacuum for 48 h. The completely dried films were then melt compounded in a Haake Mini CTW twin-screw extruder at 210 °C for 5 min. The filaments having a diameter of 2.75 +/- 0.2 mm were extruded from the die of the extruder by tuning the screw speed.

4.2.5 Computational Methods

Ground (S₀) state geometries of all the molecules were optimized using density functional theory (DFT). Singlet and triplet excited states were investigated using time-dependent density functional theory (TDDFT). Ground (S₀) state geometries of all the molecules were optimized using density functional theory (DFT). Singlet and triplet excited states were investigated using time-dependent density functional theory (TDDFT).⁷² B3LYP/6-31+G(d)⁷³ level of theory was employed for the optimization of S₀, S₁ and T₁ states of all the molecules. The Gaussian09 software⁷⁴ was used in all the DFT and TDDFT calculations. To save computational cost, R₂ group was truncated to methyl moiety, for **5**. Single point calculations for the optimized S₀, S₁, and T₁ states were carried out by employing CAM-B3LYP/6-311++G(d,p)⁷⁵ level of theory and PCM⁷⁶ solvation model to take account of long-range interactions as well as the solvation effect of DCM, respectively. The optimized Cartesian coordinates and the related energies are listed below.

4.2.6 Fused Filament Fabrication (FFF) 3D Printing of PLA/SOL Filaments

Prior to 3D printing, the prepared PLA/SOL filaments were dried in a vacuum oven at 80 °C for 4 h. Ultimaker 3 FFF type 3D printer was used to print 3D objects with the following parameters. Nozzle temperature of 210 °C, nozzle diameter of 0.4 mm, bed temperature ~60 °C, Infill density -100%, printing orientation angle of crossed +/-45°, and layer thickness of 0.2 mm. The optimal printing conditions for PLA/SOL blend are given below.

Process parameters

Bed	Glass plate
Nozzle size (mm)	0.4
Nozzle temperature (°C)	210
Bed temperature (°C)	60

Infill degree (%)	100
Orientation angle (°)	Crossed \pm 45
Layer thickness, t (mm)	0.2
Print speed (mm/s)	60

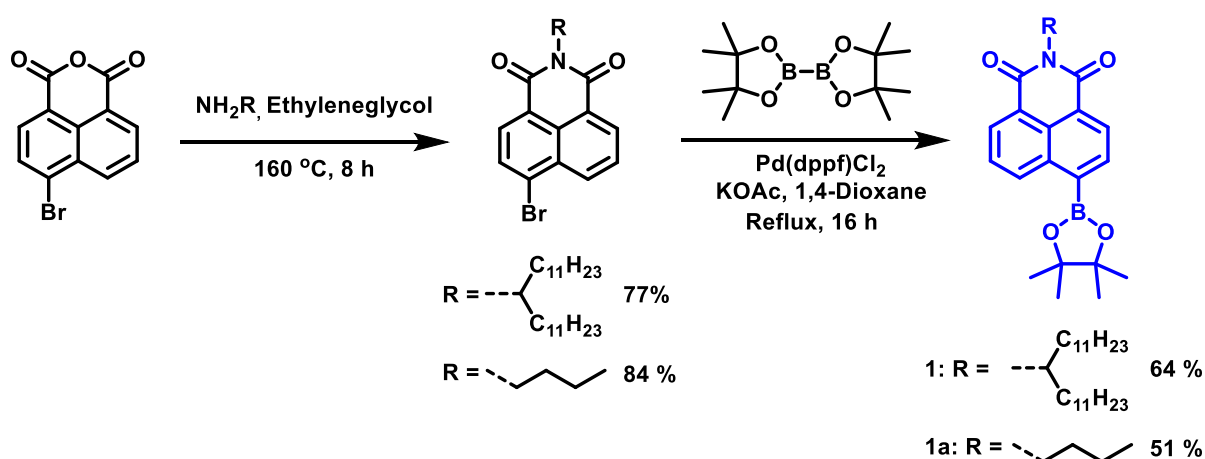
4.2.7 Experimental Details of the OLED device

The OLEDs were fabricated with structures of ITO/PEDOT:PSS(35 nm) /Poly(9-vinylcarbazole) (PVK)(20 nm)/1,3-Bis(N-carbazolyl)benzene(mCP):**4** (60 nm)/2,2',2''-(1,3,5-Benzinetriyl)-tris(1-phenyl-1-H-benzimidazole) TPBi(50 nm)/LiF(1nm)/Al (100 nm). The energy levels and device structure are shown in Figure.4.16.

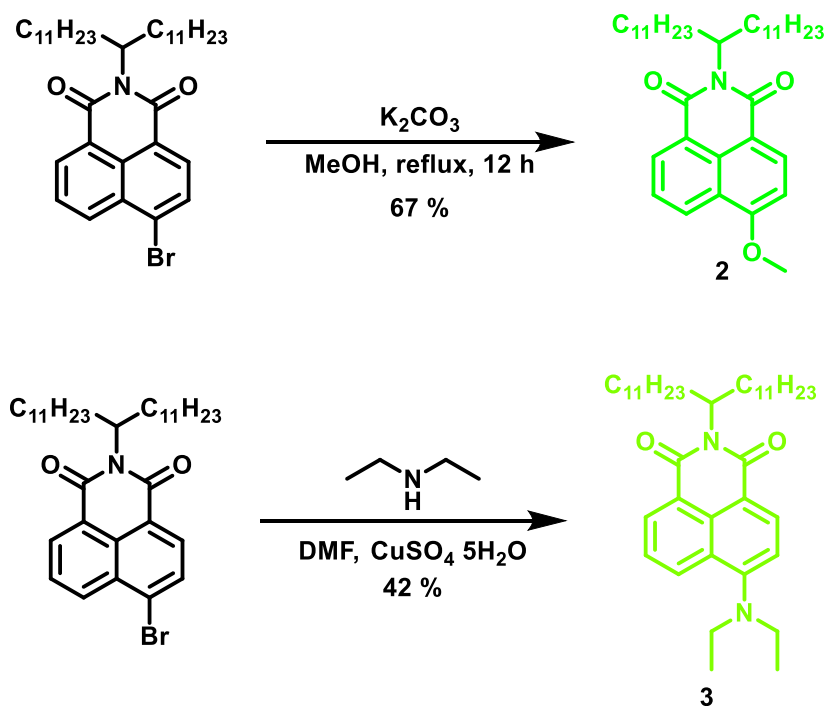
Indium tin oxide (ITO)-coated glass substrates (Kintec Company, Hong Kong) were cleaned in a liquid detergent solution (Alkanox) and subsequently sonicated in deionized water and 2-propanol. After drying, the substrates were UV-ozone-treated (Novascan). The PEDOT:PSS layer was spincoated on the substrates followed by spincoating of PVK in chlorobenzene in a N₂ filled glovebox. Then mCP:NMI (20 w% of **4** in mCP) blend in toluene (42 mg/mL) was spin-coated on top of PVK followed by vacuum annealing for 3 hours. An electron transporting layer of TPBi and Al were deposited by thermal evaporation (Angstrom Inc.) The evaporation process was automatically controlled by Inficon software and thickness of films were optimized using Dektak XT stylus profilometer.

4.3. Synthesis

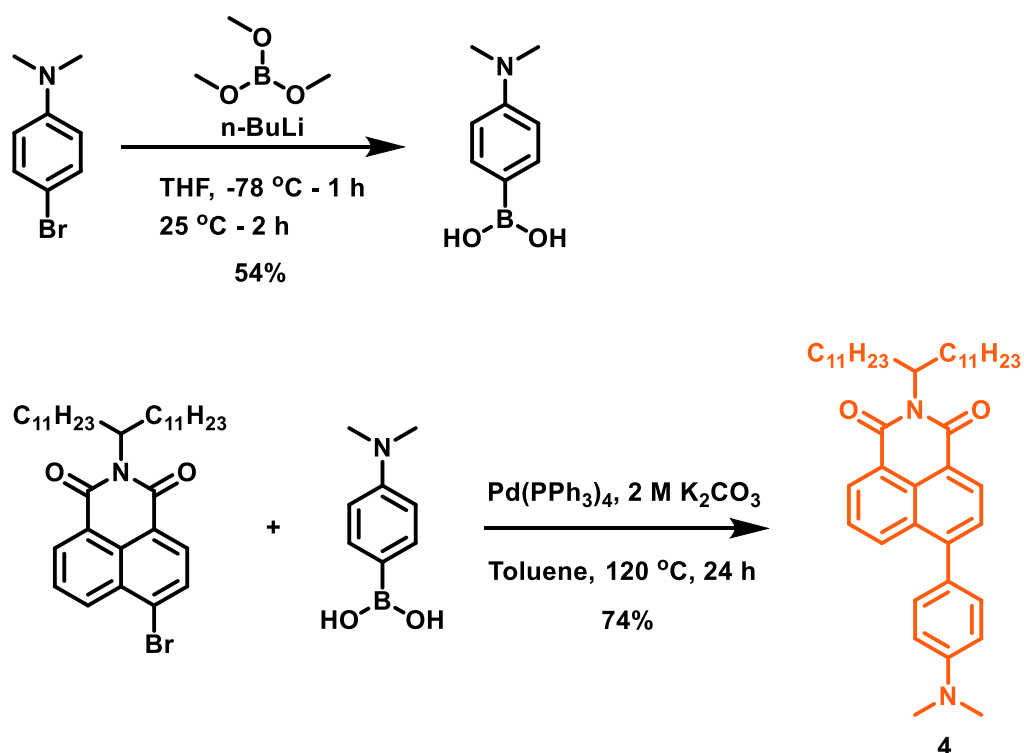
Synthesis of 6-bromo-2-(tricosan-12-yl)-1H-benzo[de]isoquinoline-1,3(2H)-dione and 6-bromo-2-butyl-1H-benzo[de]isoquinoline-1,3(2H)-dione were performed according to the literature procedure.⁷⁷



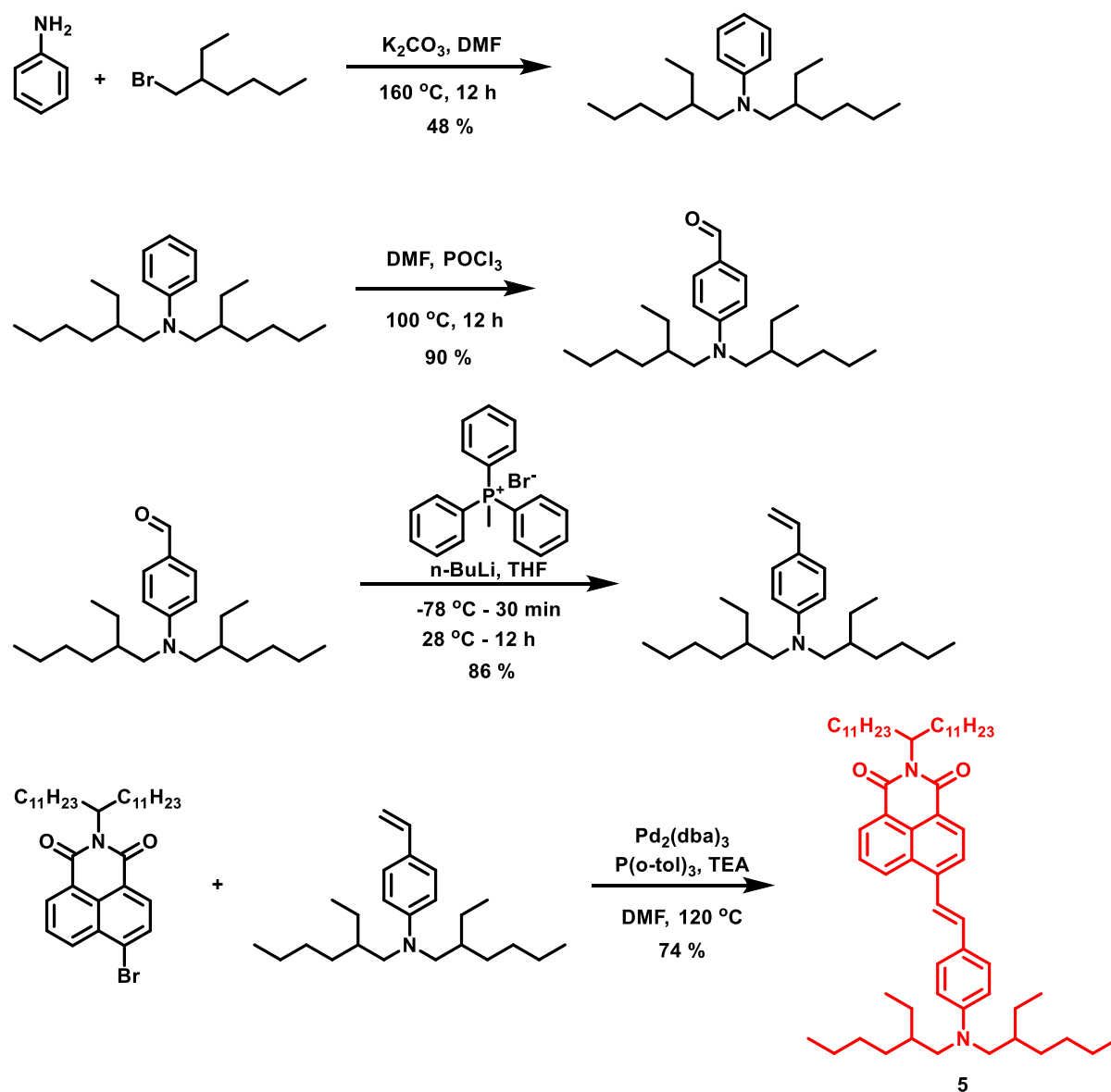
Scheme 4.1. Synthesis of molecules 1 and 1a.



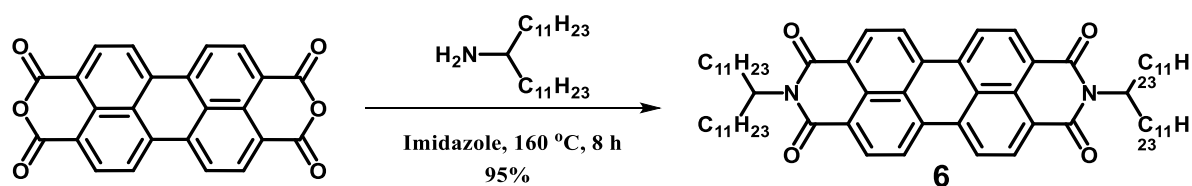
Scheme 4.2. Synthesis of molecules 2 and 3.



Scheme 4.3. Synthesis of molecule 4.



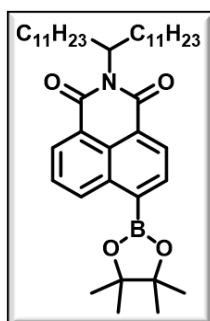
Scheme 4.4. Synthesis of molecule 5.



Scheme 4.5. Synthesis of molecule 6.

4.3.1 Synthesis of 6-(4,4,5,5-tetramethyl-1,3,2-dioxaborolan-2-yl)-2-(tricosan-12-yl)-1H-benzo[de]isoquinoline-1,3(2H)-dione (**1**)⁷⁷

A mixture of 6-bromo-2-(tricosan-12-yl)-1H-benzo[de]isoquinoline-1,3(2H)-dione (2 gm, 3.34 mmol), bis(pinacolato)diboron (B_2pin_2) (1.01 gm, 4.01 mmol), anhydrous potassium acetate (393.42 mg, 4.01 mmol) was weighed and taken in a two neck flask with anhydrous 1,4-dioxane (50 mL). This flask was degassed by repeated *freeze-pump-thaw* cycles. After this, dichloro[1,1'-bis(diphenylphospheno)-ferrocene]palladium(II) (245.10 mg, 0.33 mmol) was added to the reaction mixture and kept for reflux at 110 °C under argon for 12 hours. The progress of the reaction was monitored by TLC (*n*-hexane- CH_2Cl_2). The crude mixture was filtered through celite and washed with CH_2Cl_2 . After the removal of CH_2Cl_2 on a rotary evaporator, the resulting residue was purified by silica column chromatography (100-200 mesh) using *n*-hexane: CH_2Cl_2 (50:50) ($R_f = 0.3$) as eluent to yield **1** (1.38 g, 64%) as a brown colored liquid.



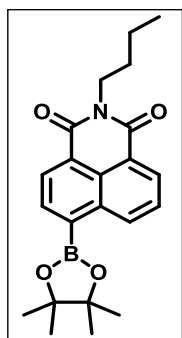
1H NMR (400 MHz, $CDCl_3$), δ (TMS, ppm): 9.13 (d, $J = 7.93$, 1H), 8.58 (d, $J = 7.93$, 2H), 8.35(d, $J = 8.55$, 1H), 7.78 (t, $J = 8.55$, 1H), 5.16 (m, 1H), 2.25 (m, 2H), 1.86 (m, 2H), 1.45 (s, 12H), 1.19 (s, 36H), 0.86 (t, $J = 6.71$, 6H).

^{13}C NMR (100 MHz, $CDCl_3$), δ (TMS, ppm): 165.54, 165.47, 135.77, 135.15, 134.60, 131.23, 130.43, 130.13, 129.34, 128.05, 127.06, 84.50, 54.44, 32.36, 31.87, 29.56, 29.53, 29.51, 29.29, 26.90, 24.94, 22.64, 14.09.

HR-MS (ESI⁺): calcd for $C_{41}H_{64}BNO_4$ [$M+H$]⁺ 645.4928, found: 646.5015.

4.3.2 Synthesis of 2-butyl-6-(4,4,5,5-tetramethyl-1,3,2-dioxaborolan-2-yl)-1H-benzo[de]isoquinoline-1,3(2H)-dione (1a)

A mixture of 6-bromo-2-butyl-1H-benzo[de]isoquinoline-1,3(2H)-dione (2 gm, 6.02 mmol), bis(pinacolato)diboron (B_2pin_2) (1.83 gm, 7.22 mmol), anhydrous potassium acetate (709.04 mg, 7.22 mmol) was weighed and taken in a two neck flask with anhydrous 1,4-dioxane (50 mL). This flask was degassed by repeated *freeze-pump-thaw* cycles. After this, dichloro[1,1'-bis(diphenylphospheno)-ferrocene]palladium(II) (441.74 mg, 0.60 mmol) was added to the reaction mixture and kept for reflux at 110 °C under argon for 12 hours. The progress of the reaction was monitored by TLC (*n*-hexane- CH_2Cl_2). The crude mixture was filtered through celite and washed with CH_2Cl_2 . After the removal of CH_2Cl_2 on a rotary evaporator, the resulting residue was purified by silica column chromatography (100-200 mesh) using *n*-hexane: CH_2Cl_2 (75:25) ($R_f = 0.6$) as eluent to yield **1a** (1.46 g, 51%) as a pale yellow crystals.



1H NMR (400 MHz, $CDCl_3$), δ (TMS, ppm): 9.06 (d, $J = 8.16$, 1H), 8.54 (t, $J = 7.32$, 2H), 8.28 (d, $J = 6.48$, 1H), 7.75 (d, $J = 8.73$, 1H), 4.16 (t, $J = 7.51$, 2H), 1.72 (m, 2H), 1.45 (s, 12H), 1.24 (m, 2H), 0.97 (t, $J = 6.54$, 3H).

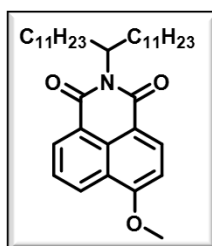
^{13}C NMR (100 MHz, $CDCl_3$), δ (TMS, ppm): 164.32, 135.73, 135.25, 134.88, 133.83, 131.17, 130.82, 129.72, 127.06, 126.91, 124.76, 122.64, 84.31, 40.27, 30.20, 29.68, 29.35, 25.01, 24.96, 24.56, 20.38, 14.11, 13.85.

FTIR (ν_{\max} in cm^{-1}): 3351.60, 3019.30, 2925.30, 2858.21, 1700.36, 1659.39, 1589.86, 1515.28, 1455.00, 1363.76, 1270.98, 1222.11, 1144.65, 1077.50, 962.60, 855.41, 763.26, 666.87.

HR-MS (ESI⁺): calcd for $\text{C}_{22}\text{H}_{26}\text{BNO}_4$ $[\text{M}+\text{H}]^+$ 380.2033, found: 380.2029.

4.3.3 Synthesis of 6-methoxy-2-(tricosan-12-yl)-1H-benzo[de]isoquinoline-1,3(2H)-dione⁷⁸

Compound NMIBr 6-bromo-2-(tricosan-12-yl)-1H-benzo[de]isoquinoline-1,3(2H)-dione (665 mg, 2.0 mmol, 1.0 eq) and K_2CO_3 (1.40 g, 10.0 mmol, 5.0 eq) were dissolved in 30 mL anhydrous MeOH. The mixture was heated to reflux and stirred overnight. After the total consumption of compound 2 (monitored by TLC), the reaction was cooled down. The precipitated solid was filtered and washed with distilled water for several time.



¹H NMR (400 MHz, CDCl_3), δ (TMS, ppm): 8.57 - 8.64 (m, 1H), 8.54 (dd, $J = 8.4, 1.1$ Hz, 2H), 7.70 (dd, $J = 8.2, 7.4$ Hz, 1H), 7.05 (d, $J = 8.3$ Hz, 1H), 5.12 - 5.21 (m, 1H), 4.13 (s, 3H), 2.18 - 2.28 (m, 2H), 1.77 - 1.87 (m, 2H), 1.17 - 1.35 (m, 36H), 0.86 ppm (t, $J = 6.9$ Hz, 6H).

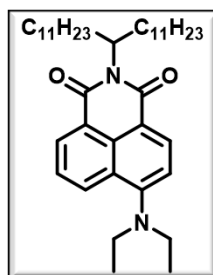
¹³C NMR (101 MHz, CDCl_3), δ (TMS, ppm): 165.7, 164.7, 133.8, 133.0, 131.1, 129.6, 128.3, 125.9, 123.4, 105.2, 56.2, 54.1, 32.4, 31.9, 29.6, 29.6, 29.6, 29.5, 29.3, 26.9, 22.7, 14.1.

HR-MS (ESI⁺): calcd for $\text{C}_{36}\text{H}_{55}\text{NO}_3$ $[\text{M}+\text{H}]^+$ 549.4182, found: 550.4262.

4.3.4 Synthesis of 6-(diethylamino)-2-(tricosan-12-yl)-1H-benzo[de]isoquinoline-1,3(2H)-dione⁷⁹

Compound 6-bromo-2-(tricosan-12-yl)-1H-benzo[de]isoquinoline-1,3(2H)-dione (0.66 g, 2.0 mmol), diethylamine (3 mL, 29.1 mmol) and $\text{CuSO}_4 \cdot 5\text{H}_2\text{O}$ (0.01

g, as catalyst) in DMF (5 mL) were stirred at 90 °C for 12 h. The solvent was evaporated under reduced pressure, and the crude product was purified by column chromatography on silica to afford **3** as a yellow oil (0.24 g, 38.2 %).



¹H NMR (400 MHz, CDCl₃), δ (TMS, ppm): 8.48 - 8.59 (m, 2H), 8.45 (d, *J* = 8.4 Hz, 1H), 7.66 (t, *J* = 7.8 Hz, 1H), 7.22 (d, *J* = 8.4 Hz, 1H), 5.16 (br. s, 1H), 3.41 (q, *J* = 7.0 Hz, 4H), 2.18 - 2.29 (m, 2H), 1.76 - 1.87 (m, 2H), 1.19 - 1.35 (m, 36H), 1.18 - 1.16 (m, 6H), 0.86 ppm (t, *J* = 7.1 Hz, 6H).

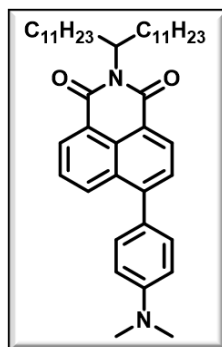
¹³C NMR (126 MHz, CDCl₃), δ (TMS, ppm): 165.3, 164.4, 154.7, 132.4, 131.6, 131.5, 130.5, 130.3, 127.3, 125.2, 116.9, 54.2, 47.4, 32.4, 31.9, 29.6, 29.3, 27.0, 22.7, 14.1, 12.3.

HR-MS (ESI⁺): calcd for C₃₉H₆₂N₂O₂ [M+H]⁺ 590.4811, found: 591.4879.

4.3.5 Synthesis of 6-(4-(dimethylamino)phenyl)-2-(tricosan-12-yl)-1H-benzo[de]isoquinoline-1,3(2H)-dione^{80, 81}

A sealed tube was charged with 6-bromo-2-(tricosan-12-yl)-1H-benzo[de]isoquinoline-1,3(2H)-dione (500 mg, 1 eq.) and 4-(N,N-dimethylamino)phenylboronic acid (207 mg, 1.5 eq.). Both the compounds dissolved in toluene (10 mL) under argon condition. Mixture of 2 M K₂CO₃ (3 mL) added to the sealed tube followed by tetrakis(triphenylphosphine)palladium(0) (97 mg, 0.1 eq.). The mixture was purged with argon for 30 min and then heated to 120 °C for 24 h. The progress of the reaction was monitored by TLC (n-hexane-CH₂Cl₂). The crude mixture was

extracted with CH₂Cl₂ and combined organic layer dried over Na₂SO₄, filtered and concentrated on a rotary evaporator, the resulting residue was purified by silica column chromatography (100-200 mesh) using n-hexane:CH₂Cl₂ (40:60) as eluent to yield **4** (382 mg, 71%) as a as a orange coloured liquid.



¹H NMR (400 MHz, CDCl₃), δ (TMS, ppm): 8.52 (br. d, *J* = 9.1 Hz, 2H), 8.33 (dd, *J* = 8.5, 1.1 Hz, 1H), 7.57 - 7.64 (m, 2H), 7.32 - 7.38 (m, 2H), 6.78 - 6.84 (m, 2H), 5.07 - 5.15 (m, 1H), 3.00 (s, 6H), 2.14 - 2.23 (m, 2H), 1.71 - 1.79 (m, 2H), 1.12 - 1.28 (m, 36H), 0.76 - 0.80 (t, 6H).

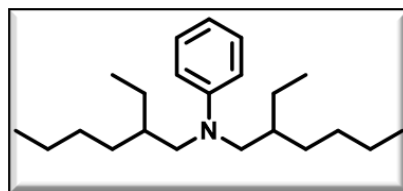
¹³C NMR (101 MHz, CDCl₃), δ (TMS, ppm): 167.3, 166.2, 150.5, 132.8, 130.9, 130.6, 130.0, 129.2, 127.4, 126.5, 126.4, 112.2, 54.4, 40.4, 32.5, 31.9, 30.2, 29.7, 29.6, 29.6, 29.6, 29.3, 27.0, 22.7, 14.1.

HR-MS (ESI⁺): calcd for C₄₃H₆₂N₂O₂ [M+H]⁺ 638.4811, found: 639.4871.

4.3.6 Synthesis of (E)-6-(4-(bis(2-ethylhexyl)amino)styryl)-2-(tricosan-12-yl)-1H-benzo[de]isoquinoline-1,3(2H)-dione (5**)⁸²⁻⁸⁵**

A mixture of aniline (1 equiv., 37.58 mmol, 3.44 mL), 2-ethylhexyl bromide (2.2 equiv., 82.68 mmol, 14.65 mL) and potassium carbonate (3 equiv., 112.75 mmol, 15.58 g) in dry DMF (50 mL) was stirred upon heating at 160 °C for 12 hours. After cooling to room temperature, the excess of potassium carbonate was filtered off and the volatiles were removed under vacuum. To the residue water (100 mL) was added and the mixture was extracted three times with CH₂Cl₂. The organic layer was dried over sodium sulfate and concentrated under vacuum. The

residue was purified by column chromatography on silica gel (eluted with pet ether) to give the product **4a** as a colorless liquid (5.70 g, 48%).

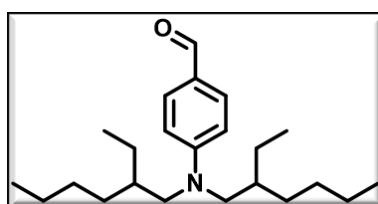


¹H NMR (500 MHz, CDCl₃), δ (TMS, ppm): 7.20 (dd, *J* = 8.8, 7.2 Hz, 2 H), 6.67 (d, *J* = 8.4 Hz, 2 H), 6.62 (t, *J* = 7.2 Hz, 1 H), 3.14 - 3.28 (m, 4 H), 1.75 - 1.85 (m, 2 H), 1.26 - 1.41 (m, 16 H), 0.86 - 0.94 (m, 12 H).

¹³C NMR (126 MHz, CDCl₃), δ (TMS, ppm): 148.4, 128.9, 115.0, 112.8, 56.4, 36.7, 36.7, 30.7, 30.7, 28.7, 28.7, 24.0, 23.2, 14.1, 10.7, 10.7.

HR-MS (ESI⁺): calcd for C₂₂H₃₉N [M+H]⁺ 317.3083, found: 317.5610.

To a cooled solution of N,N-dimethylformamide (5 mL) at 0 °C, was added phosphorous oxytrichloride (POCl₃) (1 mL, 10 mmol) dropwise under argon gas atmosphere. After stirring at that temperature for 1 h, N,N-bis(2-ethylhexyl)aniline (1.25 g, 4 mmol) was introduced into the reaction flask. The reaction mixture was heated at 100 °C for a period of 12 h. After the completion of the reaction, the reaction mixture was neutralized with 2M NaOH solution. The organic mixture was extracted into dichloromethane. The combined organic extracts were dried over anhydrous Na₂SO₄, filtered and evaporated to give the crude product which was further purified by a short-pad filtration using silica-gel. The collected fractions were evaporated to afford the pure product **4b** as yellow-oil. Yield: 91%.

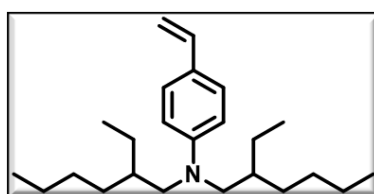


¹H NMR (500 MHz, CDCl₃), δ (TMS, ppm): 9.71 (s, 1 H), 7.64 - 7.76 (d, *J* = 8.8 Hz, 2 H), 6.64 - 6.72 (d, *J* = 8.9 Hz, 2 H), 3.25 - 3.40 (m, 4 H), 1.77 - 1.89 (m, 2 H), 1.26 - 1.41 (m, 17 H), 0.90 (t, *J*=6.7 Hz, 12 H).

¹³C NMR (125 MHz, CDCl₃), δ (TMS, ppm): 190.0, 152.8, 131.9, 124.5, 111.6, 56.3, 36.9, 30.6, 28.6, 23.9, 23.1, 14.0, 10.7.

HR-MS (ESI⁺): calcd for C₂₃H₃₉NO [M+H]⁺ 345.3032, found: 346.3089.

Methyltriphenyl-phosphonium bromide (2.58 g, 7.23 mmol) and THF (20 mL) were added to a 100 mL round-bottom flask. The flask was cooled to -78 °C in a dry ice-acetone bath. A solution of n-BuLi (2.5 M solution in hexane, 3 mL) was added via syringe under nitrogen. The reaction mixture was allowed to stir at -78 °C for 1 h and then was warmed to room temperature for another 1 h. A solution of 4-(bis(2-ethylhexyl)amino)benzaldehyde (**4b**) (1.25 g, 3.62 mmol) in 10 mL of THF was added dropwise. The reaction mixture was stirred at room temperature overnight. After the reaction, most of the THF was evaporated and the solution was diluted with hexane. The compound was purified using a basic alumina column yielding product **4c** (1.07 g, yield 86%) as a colorless oil.

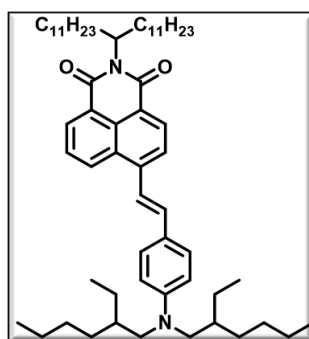


¹H NMR (400 MHz, CDCl₃), δ (TMS, ppm): d = 7.29 (d, *J* = 4.6 Hz, 2 H), 6.57 - 6.69 (m, 3 H), 5.52 (dd, *J* = 17.6, 1.0 Hz, 1 H), 4.99 (dd, *J* = 10.9, 0.9 Hz, 1 H), 3.13 - 3.32 (m, 4 H), 1.76 - 1.85 (m, 2 H), 1.25 - 1.40 (m, 16 H), 0.85 - 0.94 (m, 12 H).

¹³C NMR (101 MHz, CDCl₃), δ (TMS, ppm): 148.0, 136.6, 127.1, 124.7, 112.4, 108.5, 56.4, 36.8, 30.7, 28.7, 23.9, 23.2, 14.1, 10.7.

HR-MS (ESI⁺): calcd for C₂₄H₄₁N [M+H]⁺ 343.3239, found: 344.3312.

Compound 6-bromo-2-(tricosan-12-yl)-1H-benzo[de]isoquinoline-1,3(2H)-dione (500 mg, 1.0 eq), Pd(OAc)₂ (18.75 mg, 0.1 eq.), tris-(ortho-tolyl)phosphine (25.42 mg, 0.1 eq.), triethylamine (0.5 ml) and N,N-bis(2-ethylhexyl)-4-vinylaniline (316 mg, 1.1 eq.) in dry DMF (15 ml) was stirred at 120 °C during 16 h under argon atmosphere. The mixture was cooled to ambient temperature then diluted with water and extracted with CH₂Cl₂. The organic layer was dried with Na₂SO₄ and evaporated in vacuum. the resulting residue was purified by silica column chromatography (100-200 mesh) using pet ether:CH₂Cl₂ (40:60) as eluent to yield **5** (531 mg, 74%) as a red coloured liquid.



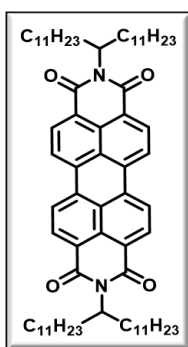
¹H NMR (500 MHz, CDCl₃), δ (TMS, ppm): 8.50 - 8.66 (m, 3 H), 7.97 (d, *J* = 8.0 Hz, 1 H), 7.75 (t, *J* = 7.9 Hz, 1 H), 7.68 (d, *J* = 16.0 Hz, 1 H), 7.49 - 7.56 (d, *J* = 8.9 Hz, 2 H), 7.31 (d, *J* = 15.8 Hz, 1 H), 6.68 - 6.75 (d, *J* = 8.9 Hz, 2 H), 5.15 - 5.21 (m, 1 H), 3.30 (quind, *J* = 14.8, 7.3 Hz, 4 H), 2.17 - 2.31 (m, 2 H), 1.77 - 1.89 (m, 4 H), 1.25 - 1.43 (m, 28 H), 1.20 (br. s., 26 H), 0.89 - 0.95 (m, 12 H), 0.86 (t, *J*=7.0 Hz, 6 H).

¹³C NMR (126 MHz, CDCl₃), δ (TMS, ppm): 165.7, 164.7, 148.9, 142.3, 135.6, 130.7, 129.8, 129.3, 129.1, 128.5, 126.3, 123.6, 122.8, 117.7, 112.5, 56.3, 54.3, 36.9, 32.5, 31.9, 30.7, 29.6, 29.3, 28.7, 27.0, 24.0, 23.2, 22.7, 14.1, 10.7.

HR-MS (ESI⁺): calcd for C₅₉H₉₂N₂O₂ [M+H]⁺ 860.7159, found: 861.7200.

4.3.7 Synthesis of 2,9-di(tricosan-12-yl)anthra[2,1,9-def:6,5,10-d'e'f']diisoquinoline-1,3,8,10(2H,9H)-tetraone (**6**)⁸⁶

In a 100 mL round-bottom flask, perylene-3,4,9,10-tetracarboxylic dianhydride (1g, 2.55 mmol) and tricosan-12-amine (2.16g, 6.37 mmol) was added to imidazole (4.3g, 63.72 mmol). The mixture was stirred at 160 °C for 8 h and then cooled to room temperature. In to that 2N HCl solution (50 mL) was added and stirred for further 2 h, filtered. The precipitate was washed with excess amount of MeOH, and extracted with CH₂Cl₂, and then the compound was purified by silica gel chromatography using CH₂Cl₂ to yield **6** as a red coloured low-melting solid (2.5 g, 95 %).



¹H NMR (400MHz, CDCl₃), δ (TMS, ppm) = 8.68-8.61 (m, 8H), 5.23-5.15 (m, 2H), 2.29-2.21 (m, 4H), 1.90-1.83 (m, 4H), 1.32-1.20 (m, 72H), 0.84 (t, 12H, *J* = 6.67Hz).

¹³C NMR (101 MHz, CDCl₃, 25 °C): δ [ppm] = 164.64, 163.55, 134.49, 131.89, 131.12, 129.59, 126.44, 123.94, 123.20, 123.17, 123, 54.75, 32.34, 31.88, 30.92, 29.58, 29.56, 29.52, 29.30, 26.94, 22.65, 14.08.

MALDI-TOF : m/z calcd for C₇₀H₁₀₂N₂O₄ [M]⁺ 1035.5960, found: 1036.79.

4.4. Result and Discussions

We have chosen an alkylated 1,8-naphthalimide⁴⁴⁻⁴⁶ with boronate ester (BPin) group **1** (Figure 4.1a), a simple molecular design, for exploring TADF in the liquid state. Molecule **1** was synthesized by the Miyaura borylation reaction of the RTP liquid³⁴ and characterized unambiguously (Scheme 4.1). The purity of

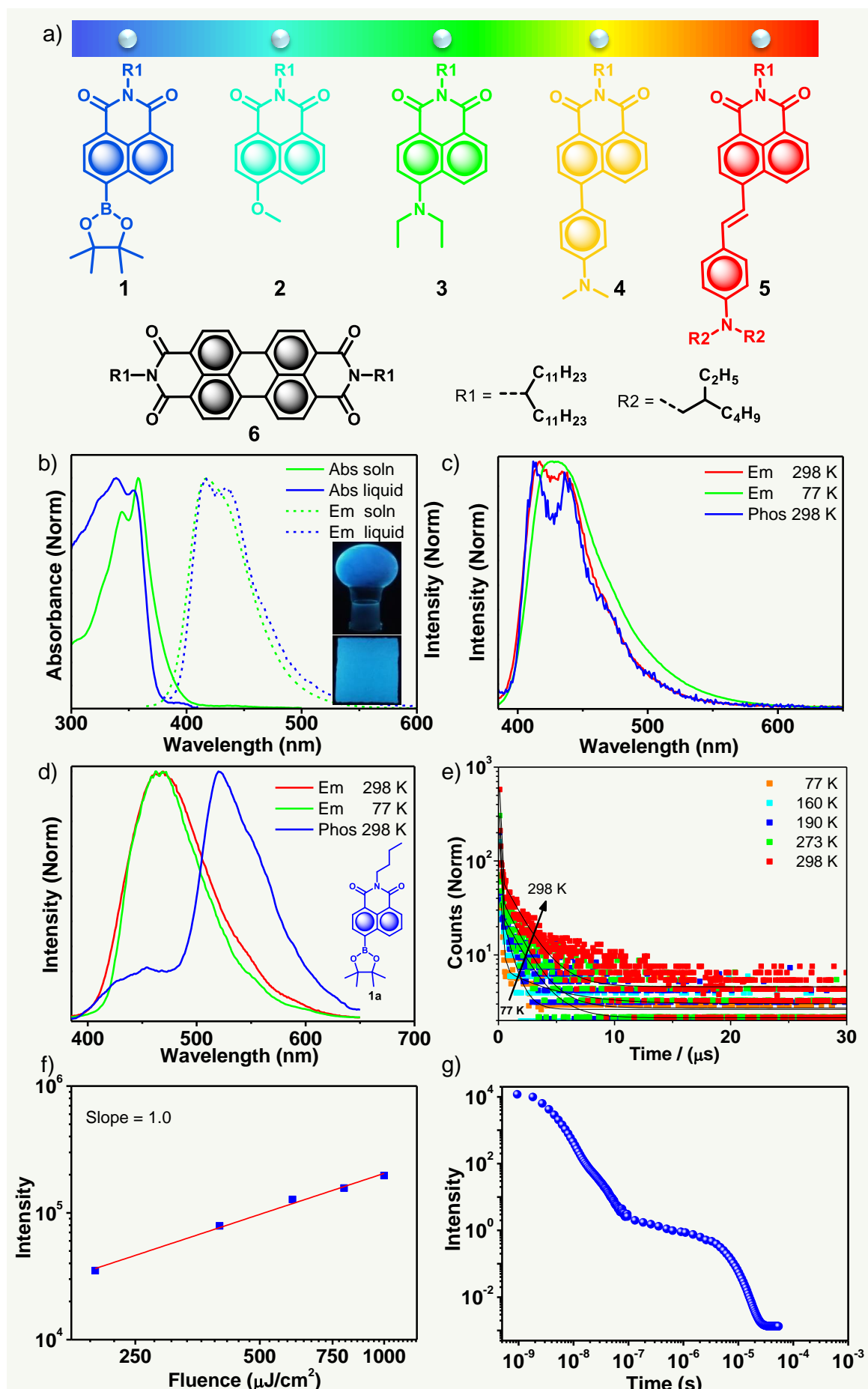


Figure 4.1. a) Chemical structures of TADF emitters **1-5** and fluorescent emitter **6**. b) Comparison of the normalized absorption and emission spectra of **1** in MTHF solution ($C = 1 \times 10^{-5}$ M, $\lambda_{\text{ex}} = 342$ nm) and neat liquid ($\lambda_{\text{ex}} = 360$ nm); insets show the photographs of **1** forming thin film inside a round bottom flask (top) and on glass (10×10 cm²) (bottom) under UV light (365 nm). Comparison of the normalized emission (298 and 77 K) and phosphorescence spectra (298 K) of c) **1** neat liquid and d) **1a** crystals. e) Temperature-dependent TADF lifetime decay curves of **1** ($\lambda_{\text{ex}} = 360$ nm and $\lambda_{\text{mon}} = 450$ nm). f) Excitation intensity-dependent emission profile ($\lambda_{\text{ex}} = 355$ nm) and g) emission decay profile of **1** showing prompt fluorescence at an early time and delayed fluorescence at longer time delays, respectively.

the compounds has been confirmed by CHN analysis. The free-flowing, viscous and amorphous nature of **1** was characterized by differential scanning calorimetry, thermogravimetric analysis, rheology (Figure 4.2), and X-ray diffraction experiments. The amorphous feature seen in **1** is confirmed by two halos at $2\theta = 19.47$ and 4.77° corresponding to branched alkyl chains in the molten state and the random distance among the aromatic moieties.

UV-Vis absorption spectrum of **1** in 2-methyltetrahydrofuran (MTHF) solution shows structured absorption bands located at 344 and 358 nm, and the corresponding steady-state emission has a single band ($\lambda_{\text{max}} = 421$ nm) (Figure 4.1b). Fluorescence lifetime measurements of **1** in solution showed a triexponential decay with major lifetimes of 3.73 ns (84 %) and 1.92 ns (11 %) with no high lifetime component (Table 2). Though an extended lifetime component is missing in the solution, emission intensity and lifetime decreased after purging with oxygen (Table 3). Absorption ($\lambda_{\text{max}} = 350$ nm) and emission ($\lambda_{\text{max}} = 456$ nm) of **1** as a neat liquid offer slightly broad spectra (Figure 4.1b). Molecule **1** shows a redshifted (35 nm) blue emission with a quantum yield (QY) of 66 % (Table-1 & 4) in the neat state (Figure 4.1b). Interestingly, the free-

flowing nature of **1** allowed to form a thin layer inside the round bottom flask and on a large area glass surface (10x10 cm²) (Figure 4.1b; insets). It indicates the enhanced processability and option to handle **1** as paint to apply on large areas.

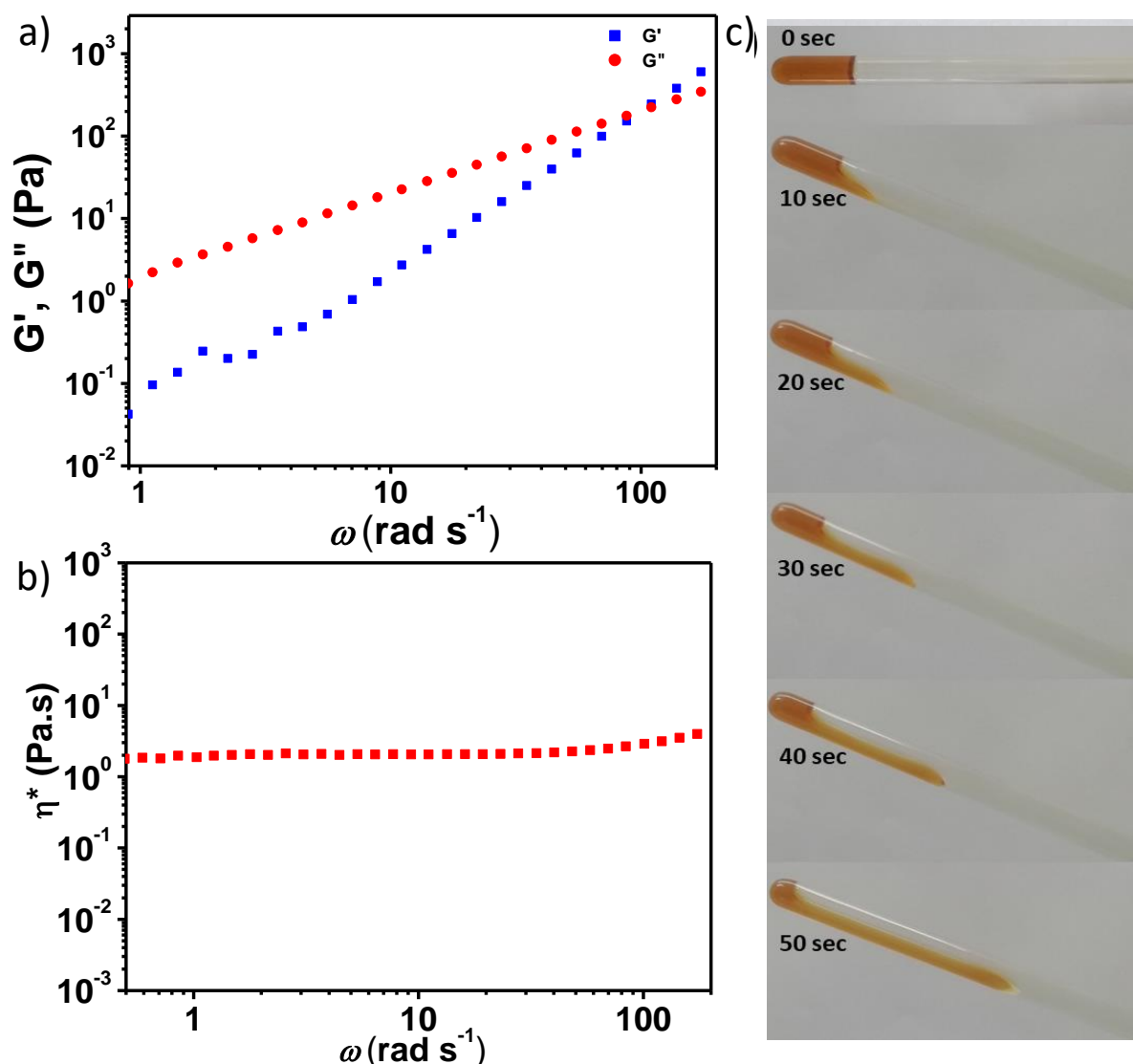


Figure 4.2. Variation of a) loss modulus (G'') (circles), and storage modulus (G') (squares), b) complex viscosity (η^*) versus angular frequency on double logarithmic scale, of **1**. c) Photographs of the free-flowing liquid feature of **1**.

A higher magnitude of G'' in the Rheology plot indicates the presence of an appreciable viscous nature having complex viscosity of 1.87 Pa·s at 1 rads⁻¹ in the liquid state due to the highly dynamic molecular interactions. The rheology

experiments helped to confirm that the identified liquid possesses a certain degree of viscoelasticity (Figure 4.2). We studied the importance of the liquid matrix in imparting TADF for **1** in detail. As shown in Figure 4.1c, a similar spectral feature was noticed for **1** in the steady-state emissions at 298 and 77 K. The exciting fact was the presence of a peak located at 453 nm when 0.1 ms detector delay was applied in the phosphorescence spectral measurement (Figure 4.1c). The similarity and significant overlap between the fluorescence and phosphorescence spectra confirm the minimal singlet-triplet energy gap (ΔE_{ST}).⁴⁷⁻⁴⁸ However, a structural analogue **1a** (Scheme 4.1) exhibits both TADF and RTP emissions in the crystalline assembly *via* radiative decay from both singlet and triplet states to display TADF and RTP, respectively (Figure 4.1d). Though the steady-state emissions at 298 and 77 K look identical, it differs from the phosphorescence spectrum. It validates the support of molecular design and liquid feature in imparting TADF for **1** with a lifetime (τ_{TADF}) of 7.9 μ s (Table-1, 6). Besides, not much change is observed in the prompt (PF), delayed (DF) fluorescence, and RTP spectra, and it shows the narrow energy gap between the singlet and triplet energy levels supporting TADF.

TADF properties of **1** were further confirmed by the changes in the emission spectra and lifetime in the presence of oxygen (Table 7). Here we noticed that the liquid matrix acts as a supportive layer to protect from oxygen, and hence the intensity changes are minimum. Additionally, it has been supported by the temperature-dependent lifetime decay profile of **1**, and it demonstrates the origin of a typical TADF feature (Figure 4.1e and Table 8). Molecule **1** shows an increase in τ_{TADF} upon increasing the temperature from 77 to 298 K (Figure 4.1e). A linear dependence of the DF intensity with excitation power observed for **1** clearly shows that the emission is due to TADF and not by triplet-triplet annihilation (Figure 4.1f). Besides, the long-range lifetime decay profile points to the PF at an early time and DF at longer time delays (Figure 4.1g). Hence, all

these characterizations unambiguously confirm the TADF property, indicating the existence of a thermal activation energy barrier for TADF, and thus more favourable rISC of excitons from triplet to singlet excited state by gradual warming. The k_{ISC} and k_{rISC} for **1** were found to be $3.87 \times 10^8 \text{ s}^{-1}$ and $2.83 \times 10^5 \text{ s}^{-1}$, respectively. However, considering the active support of the liquid matrix in protecting the triplet state, the calculated k_{rISC} may not be accurate to account for the low τ_{TADF} of **1**. The overlap of the emission and RTP spectra, oxygen and temperature-dependent lifetime, together with high QY, support molecule **1** as a potential TADF candidate.⁴⁹⁻⁵⁴

Further, a series of TD-DFT computations were carried out for **1** by using Gaussian 09 program. It has been noticed that HOMO is located on the naphthalene ring (π -type), and LUMO is delocalized between the B-C p-orbital with significant overlap supporting a partially separated frontier energy level for a small ΔE_{ST} (Figure 4.3a). On examining ΔE_{ST} , triplet states T_3 and T_2 are nearly degenerate with the first singlet excited state (S_1) having ΔE_{ST} of 0.06 and 0.25 eV, respectively.⁴⁰⁻⁴¹ Thus, it is clear that molecule **1** has well-matched singlet and triplet energy states and hence helps in efficient rISC from triplet to the singlet state. Natural transition orbitals (NTO) reveal the presence of a reasonable charge transfer (CT) character for S_1 and thereby resulting in CT emission ($f = 0.4663$) (Figure 4.3a). The energetically closer, substantial locally excited (LE) and CT nature of the triplet states and ^1CT support small ΔE_{ST} and subsequently rISC (Figure 4.3a).⁴⁹⁻⁵⁴

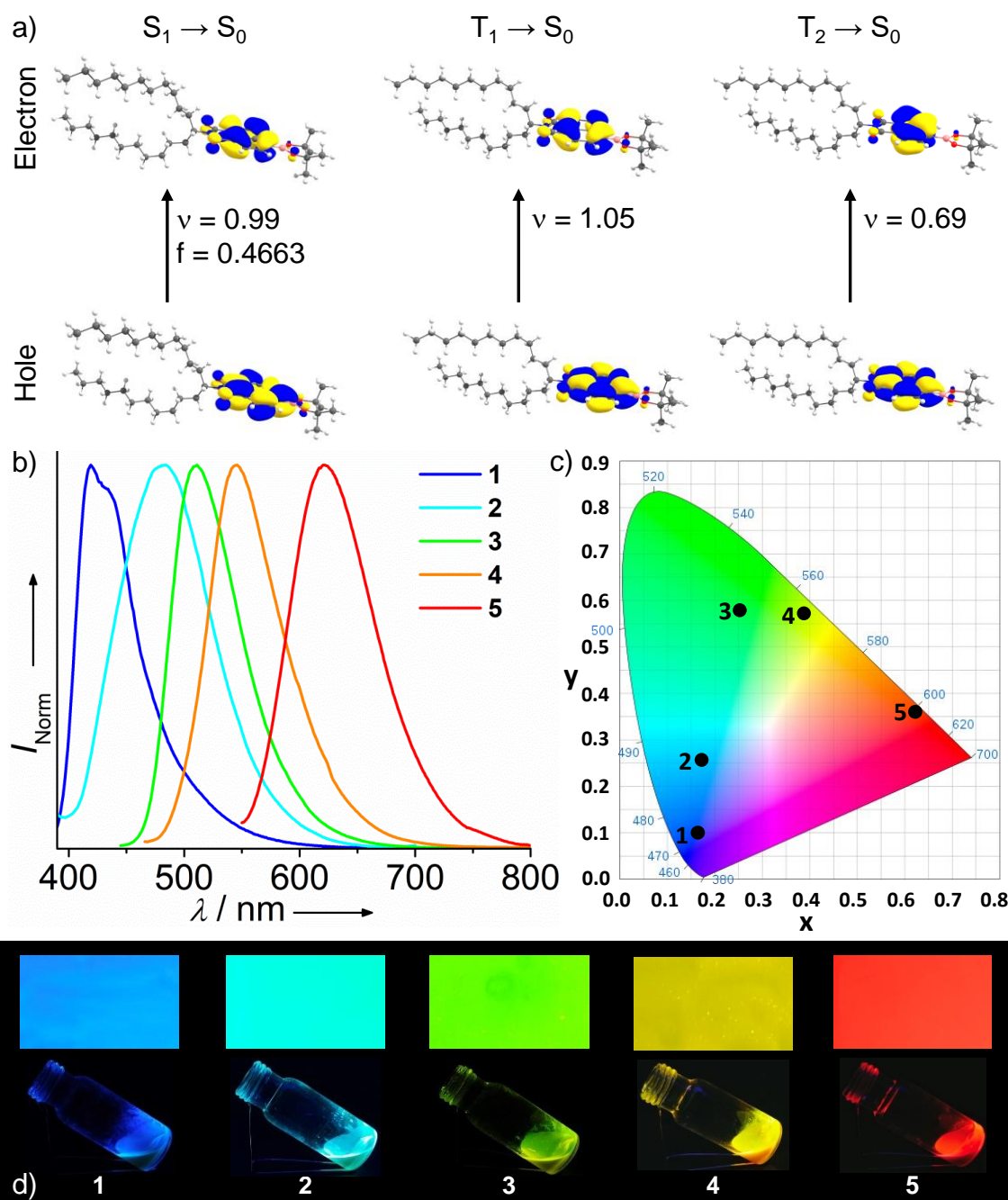


Figure 4.3. a) Natural transition orbitals (NTO) for the emission from the singlet and triplet excited states of 1. b) Normalized emission spectra of 1-5 ($\lambda_{\text{ex}} = 360$ nm (1), 370 nm (2), 430 nm (3), 440 nm (4), 520 nm (5)) along with the corresponding c) CIE coordinate values. d) Photographs of thin films (top) and neat SOLs (bottom) of 1-5 under UV light (365 nm).

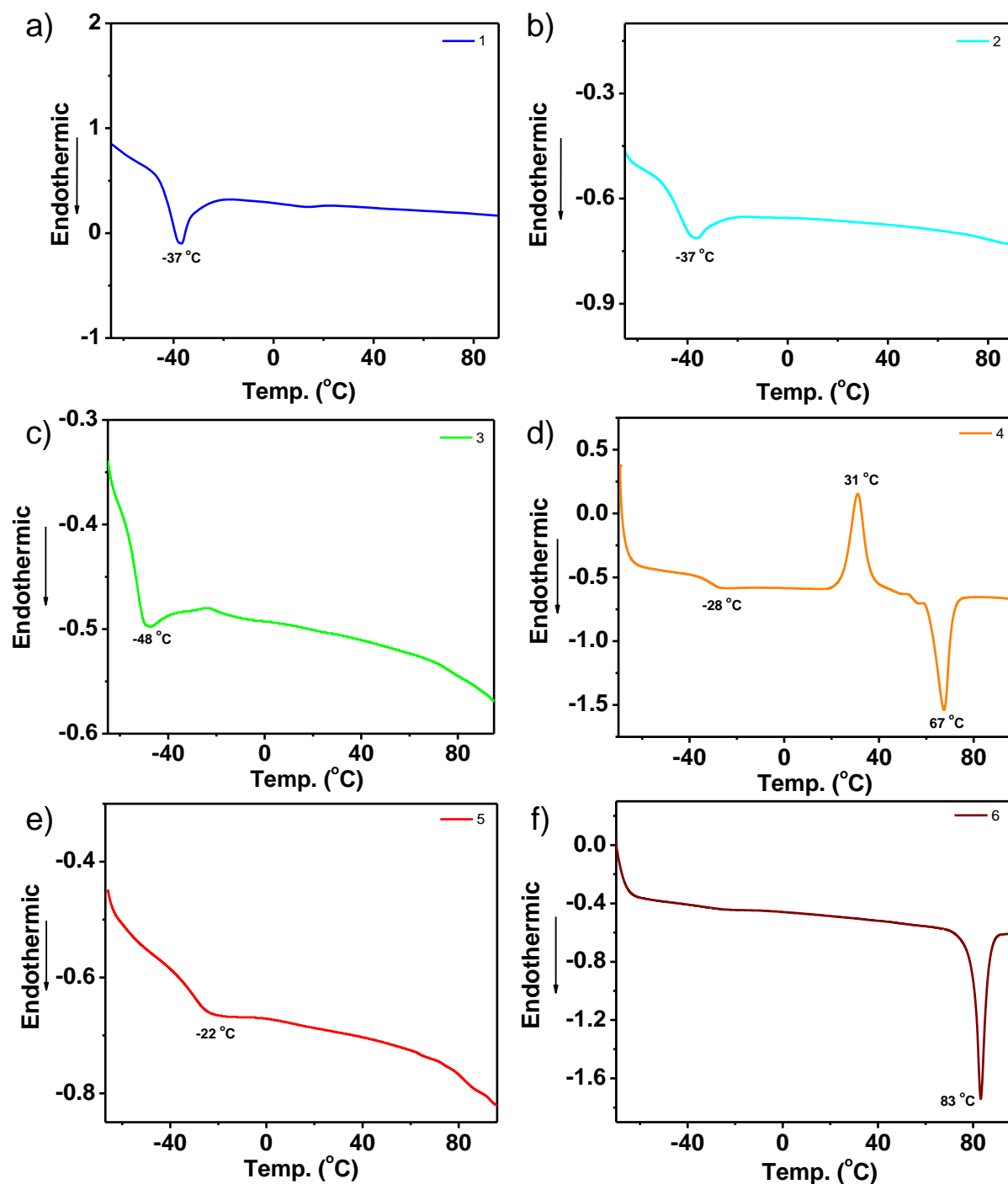


Figure 4.4. DSC thermograms of 1-6 at a scanning rate of 10 °C/min, showing the $T_{g \text{ offset}}$ values.

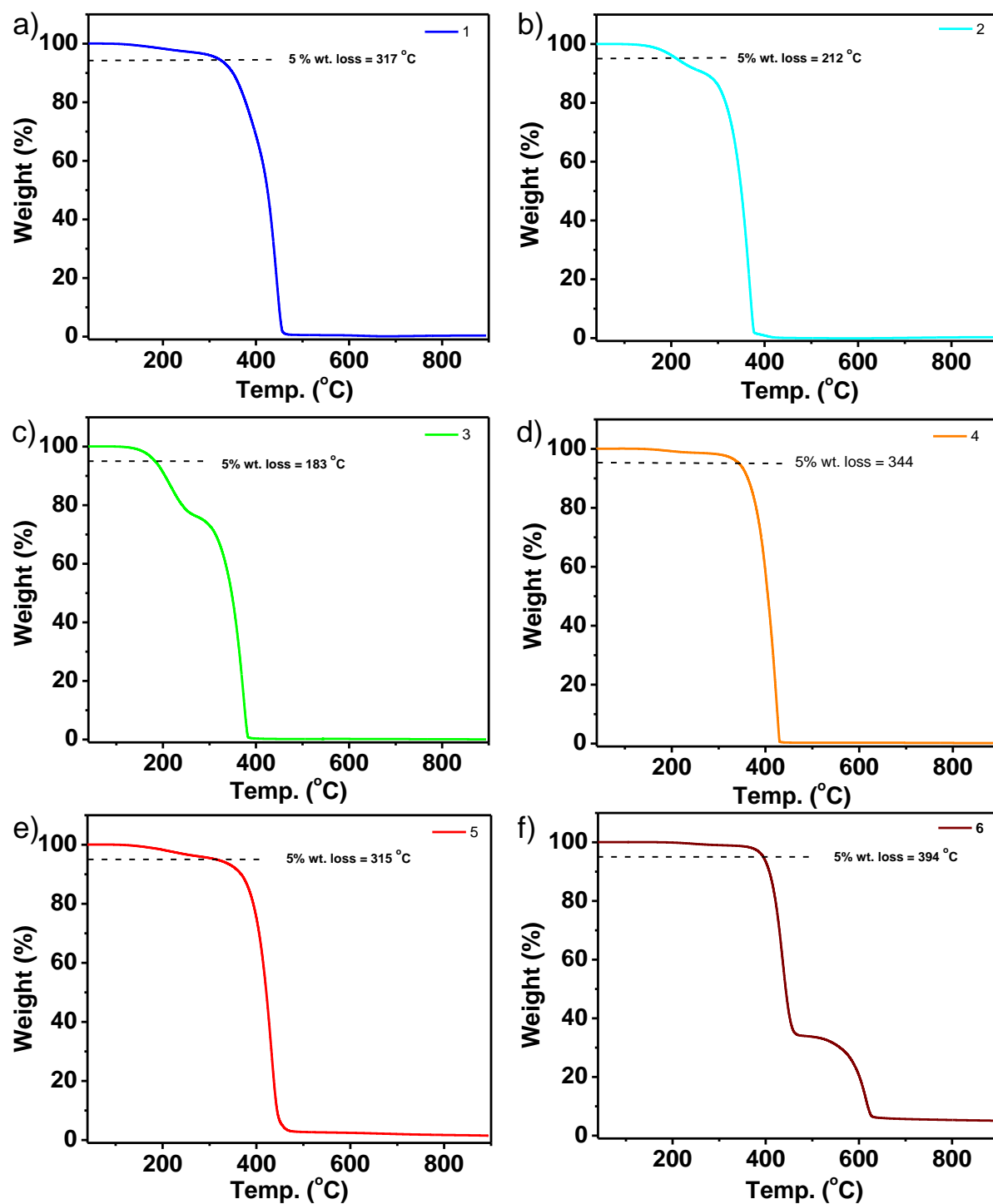


Figure 4.5. TGA analysis of 1-6 at a scanning rate of 10 °C/min, showing the T_{g_offset} values.

After successfully demonstrating the first TADF liquid, a series of naphthalimide derivatives 2-5 (Figure 4.1a and Scheme 4.2-4.4) with emissions spanning from cyan to red have been prepared to diversify the emission features

(Figure 4.3b-d). The emission maxima of **2-5** were varied as 483, 510, 545, and 620 nm, respectively (Figure 4.6 and Table 1). As shown in Figure 4.3d, no significant difference in emission colour was noticed for the thin film and neat SOLs. It points to the monomer-like optical properties in the neat liquid state due to π -core isolation by the long-branched alkyl chains. All SOL molecules showed delayed fluorescence of TADF nature in the neat liquid state, as demonstrated by the lifetime and spectral pattern at 77 and 298 K and high emission QY (Figure 4.8, 4.9 and Table 2-8).

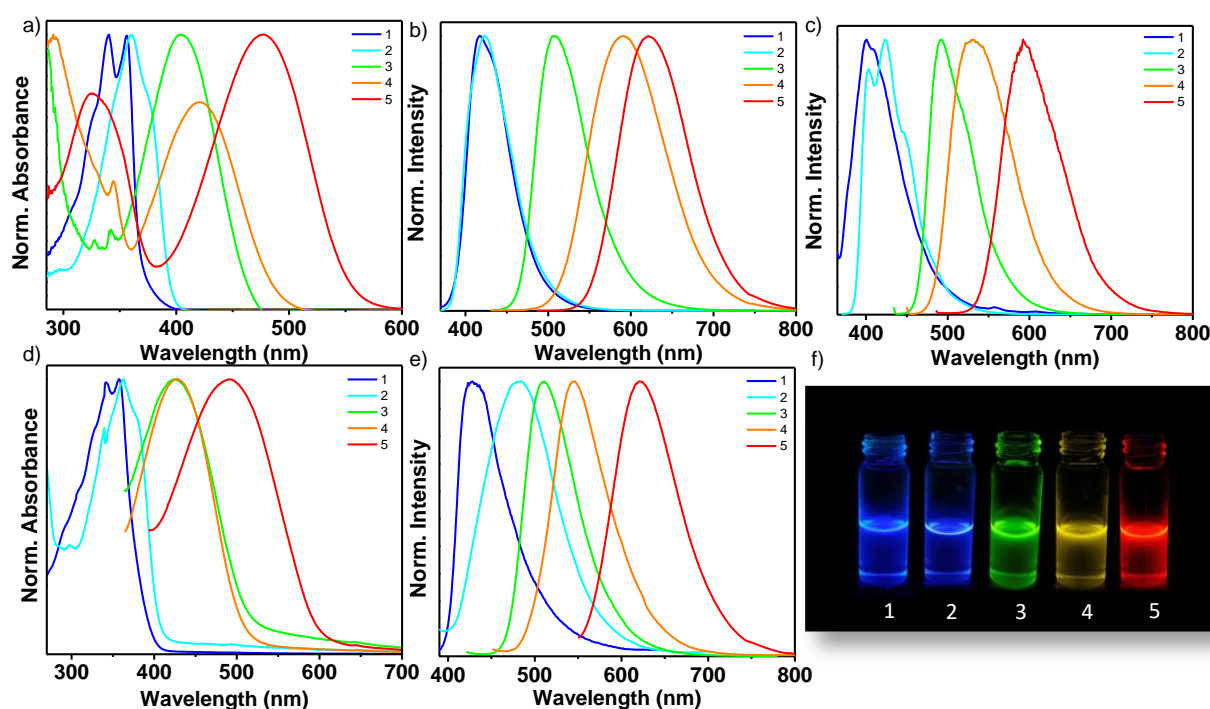


Figure 4.6. Normalized a) absorption and steady-state emission spectra of **1-5** in MTHF solution b) at RT c) at 77 K ($C = 1 \times 10^{-5}$ M, $l = 1$ cm), Normalized d) absorption and e) steady-state emission spectra of **1-5** (neat liquid) ($\lambda_{\text{ex}} = 355$ nm for **1**, $\lambda_{\text{ex}} = 360$ nm for **2**, $\lambda_{\text{ex}} = 424$ nm for **3**, $\lambda_{\text{ex}} = 434$ nm for **4**, $\lambda_{\text{ex}} = 480$ nm for **5**). f) Photograph of MTHF solution of **1-5** under UV (365 nm) light.

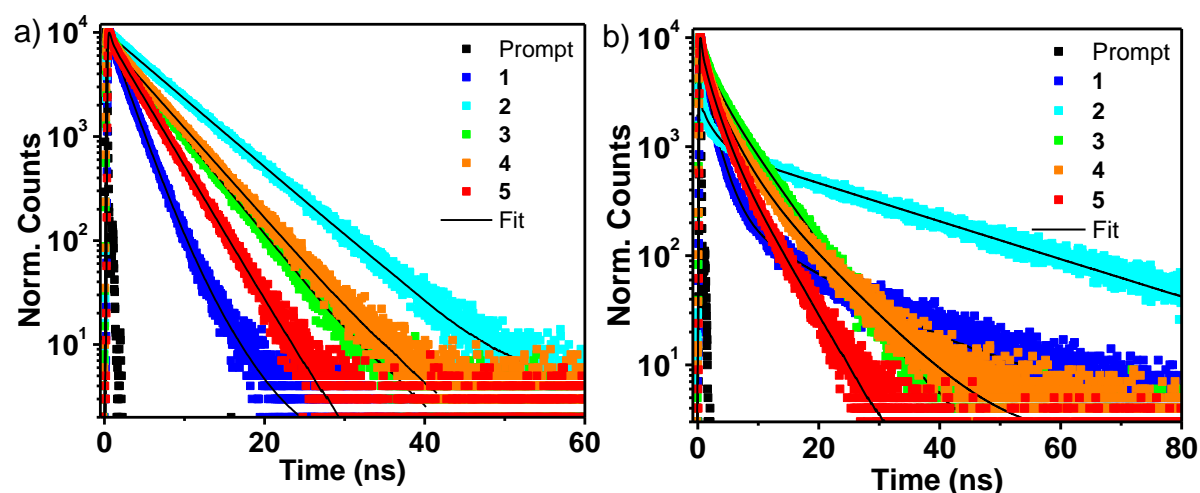


Figure 4.7. Fluorescence lifetime decay profiles of **1-5** in a) in MTHF solution ($C = 1 \times 10^{-5} \text{ M}$) and b) in neat state at 298 K ($\lambda_{\text{ex}} = 374 \text{ nm}$, $\lambda_{\text{mon}} = 420 \text{ nm}$ for **1**, 420 nm for **2**, 524 nm for **3**, 564 nm for **4**, 620 nm for **5**).

A detailed analysis has been performed to establish the TADF feature of molecules **2-5** as well (Figures 4.8-4.11). Temperature-dependent lifetime (Figure 4.10), a linear dependence of the DF intensity with excitation power (Figure 4.11a) and long-range lifetime decay profile (Figure 4.11b) further confirmed TADF of molecules **2-5**. Similar to **1**, the decrease in emission intensity for **2-5** was minimal even after keeping under an oxygen atmosphere for 48 h. The presence of solvatochromism in molecules **1-5** sheds light on the involvement of a CT state in TADF. As the solvent polarity increases, λ_{max} redshifts with a decrease in intensity indicates that the emission originates from S_1 state with a strong CT character.⁴⁹⁻⁵⁴ Similar to **1**, other molecules also exhibit small ΔE_{ST} to facilitate rISC supported by vibrational coupling between ^3LE and ^3CT states.⁴⁹⁻⁵⁴ Hence, donor connected naphthalimides are proven to be efficient TADF candidates due to many supportive structural features.⁵⁵⁻⁵⁸ All the molecules exhibited reasonably high optical stability upon direct irradiation with UV light for five hours.

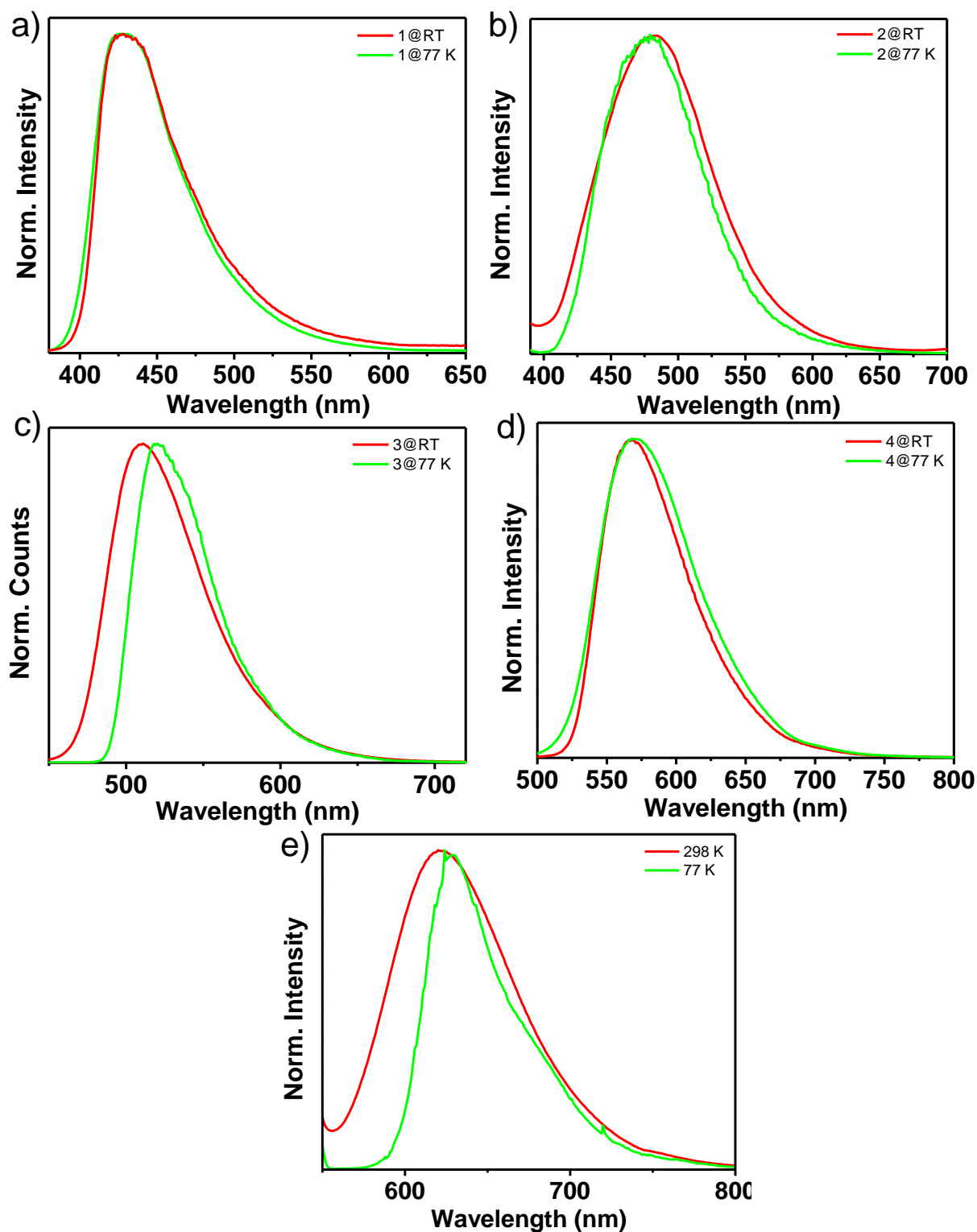


Figure 4.8. Comparison of the emission spectra in of **1-5** in neat state at 298 K and 77 K ($\lambda_{\text{ex}} = 355$ nm for **1**, $\lambda_{\text{ex}} = 360$ nm for **2**, $\lambda_{\text{ex}} = 424$ nm for **3**, $\lambda_{\text{ex}} = 434$ nm for **4**, $\lambda_{\text{ex}} = 480$ nm for **5**).

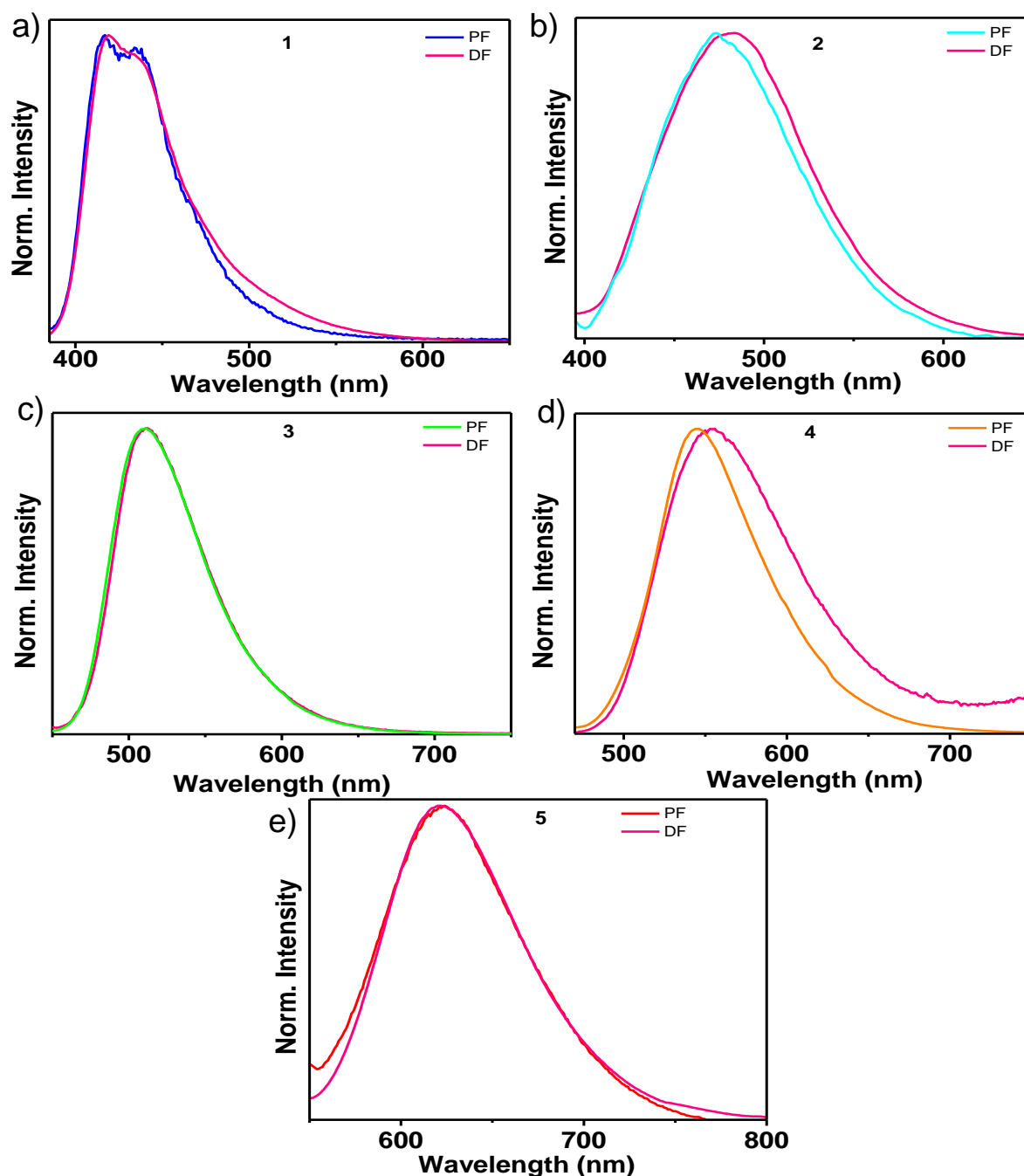


Figure 4.9. Comparison of the PF and DF spectra of **1-5** in neat state at 298 K.

ET between TADF hosts and various TADF, RTP, and fluorescent dopants have been explored as a successful strategy to achieve tunable emission and improved device efficiency. Hence, SOLs **1-5** have been chosen for ET studies due to the significant overlap between the dopants' (**3-5**) absorption spectra with the emission of donors **1** and **2**. An efficient ET was displayed by the combination of **1 + 3**, **1 + 4**, and **1 + 5** with an ET efficiency of 90, 87, 92 %, respectively (Figure

4a-c, 4.12, 4.14 Table 9-19). An extremely low amount of acceptor molecules is only required almost completely to quench the donor emission (~ 4 acceptors for 1000 donors). TADF lifetime of donor gradually reduced with a concomitant increase in acceptor lifetime upon increasing the concentration of dopants due to efficient ET from donor to dopants.

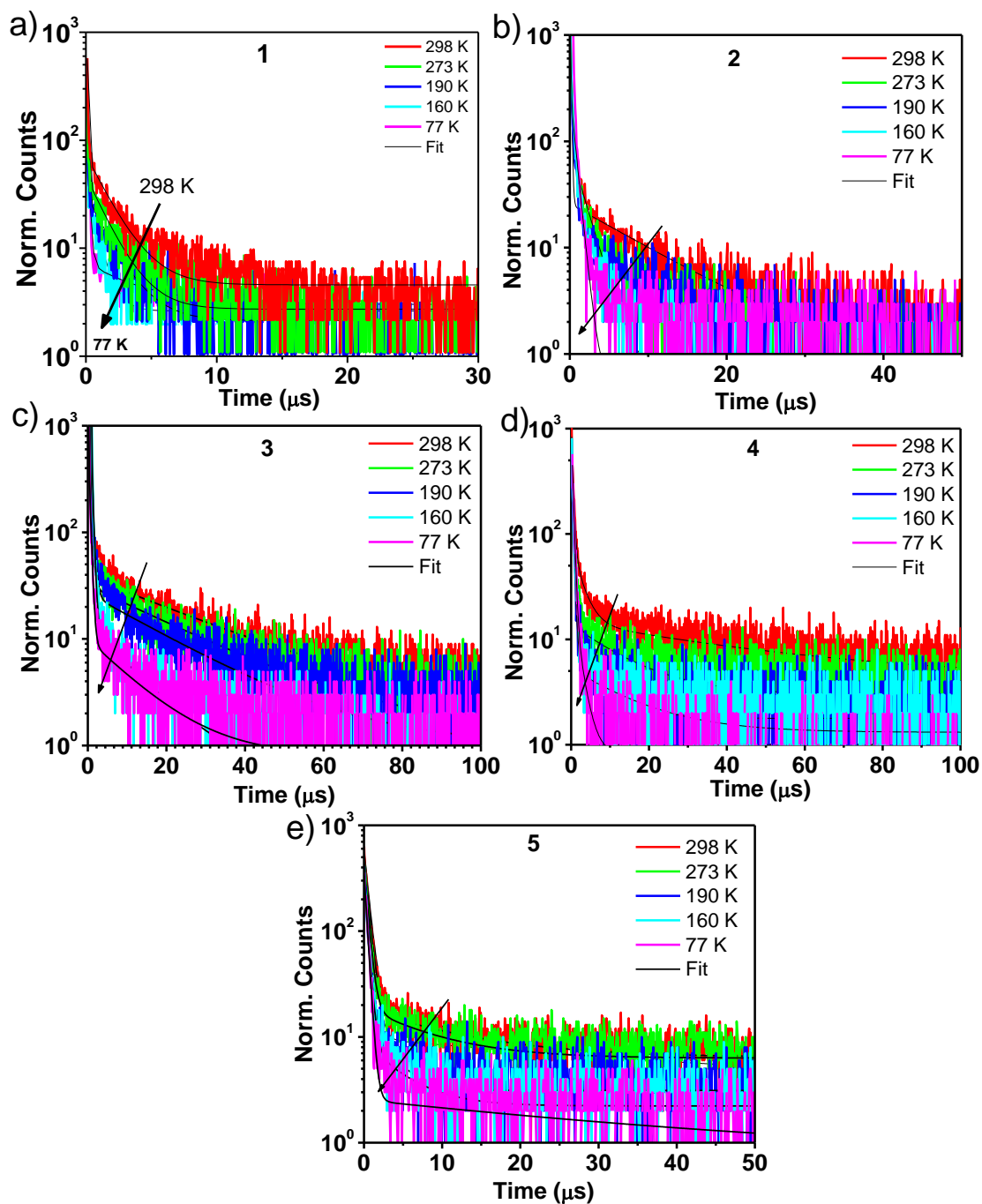


Figure 4.10. Temperature-dependent TADF lifetime for molecule a) **1**, b) **2**, c) **3**, d) **4** and e) **5** in the neat state.

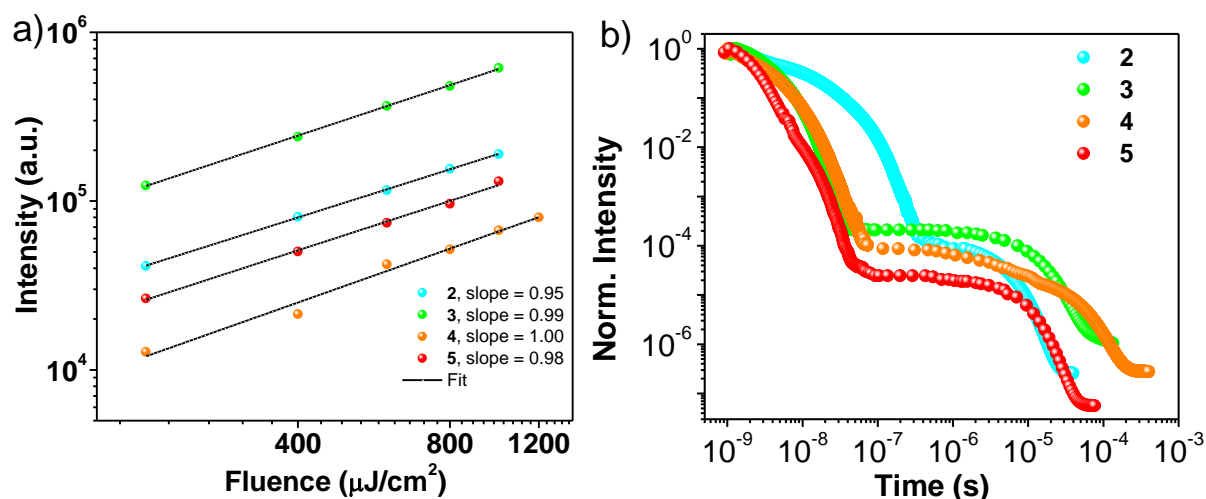


Figure 4.11. a) Excitation intensity-dependent emission profile ($\lambda_{\text{ex}} = 355 \text{ nm}$) and b) emission decay profile of 2-5 showing prompt fluorescence at an early time and delayed fluorescence at longer time delays, respectively.

Molecule **1** acts as an excellent donor to exhibit efficient ET with dopants to deliver tunable emission colours upon exciting at 365 nm (Figure 4.12a-c).⁵⁹⁻⁶² Besides, cascade energy transfer assisted tunable emission hybrid of **1** was developed by mixing varying amounts of **3** and **5** (Figure 4.12d). A logical selection of the components and careful management of the ratio between **1**, **3**, and **5** (1:0.0009:0.0008) resulted in white light emission (Figure 4.12d).⁶³⁻⁶⁵ Further, ET between **2** and **5** has been trialed to reduce the components and thus realized two-component white light emission at the expense of a very low loading of **5** (1:0.002) (Figure 4.12d). All the white light-emitting SOLs prepared through ET between the TADF liquid donors and emitter acceptors exhibit excellent colour stability with time. The samples stored at ambient conditions for five months also retained colour stability.

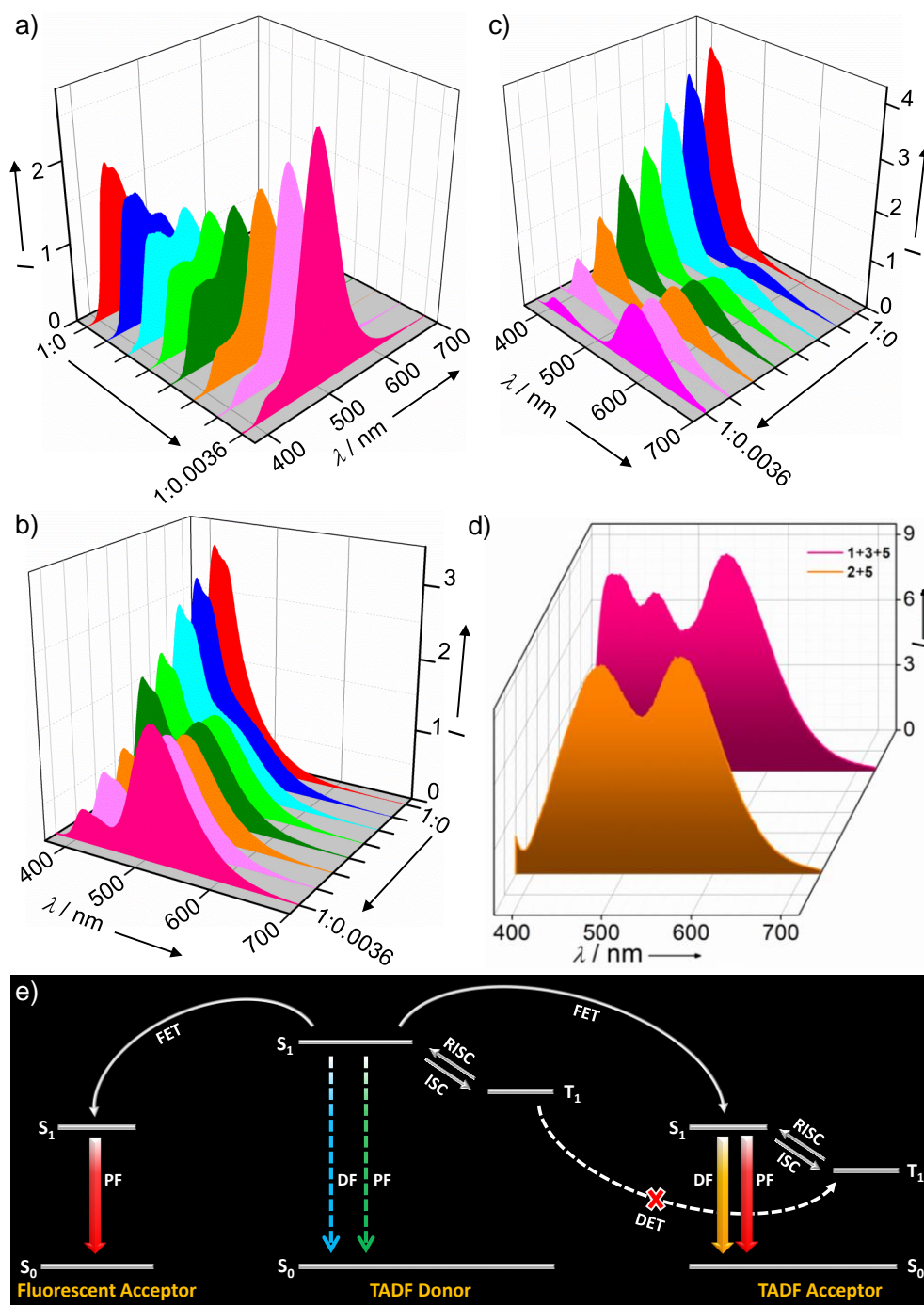


Figure 4.12. ET studies of 1 with increasing equivalents of a) 3, b) 4, c) 5 and d) white light emission achieved by 1+3+5 (1:0.0009:0.0008) and 2+5 (1:0.002). e) The schematic diagram for the ET process. PF-prompt fluorescence, DF-delayed fluorescence, and FET-Förster energy transfer, DET-Dexter energy transfer. The desirable processes are indicated by solid arrows, while the undesirable ones are by dotted arrows. Processes resulting in a loss in efficiency are marked with a cross.

Further, ET between **2** and fluorescent liquid dopant **6** (Figure 4.1a) was also attempted, and ET efficiency of 88% was observed (Figure 4.13 and Table 20). The ET and overall light emission processes are described schematically in Figure 4.12e. Two important facts, such as the significantly low quantity of the acceptors used and the presence of bulky side groups that separate the host and dopants from each other, are expected to manage the Dexter energy transfer loss efficiently. It has to be noticed that the available nonpolar liquid matrix of **1** and **2** shows excellent compatibility with the dopants without any sign of phase separation. Interestingly, an enhanced ET provides an additional relaxation path for TADF donors and thus leads to a reduced exciton concentration and lifetime.¹⁶ In addition, ET of the TADF host is also beneficial for lowering the T_1 -related annihilation process.⁶⁶⁻⁷¹

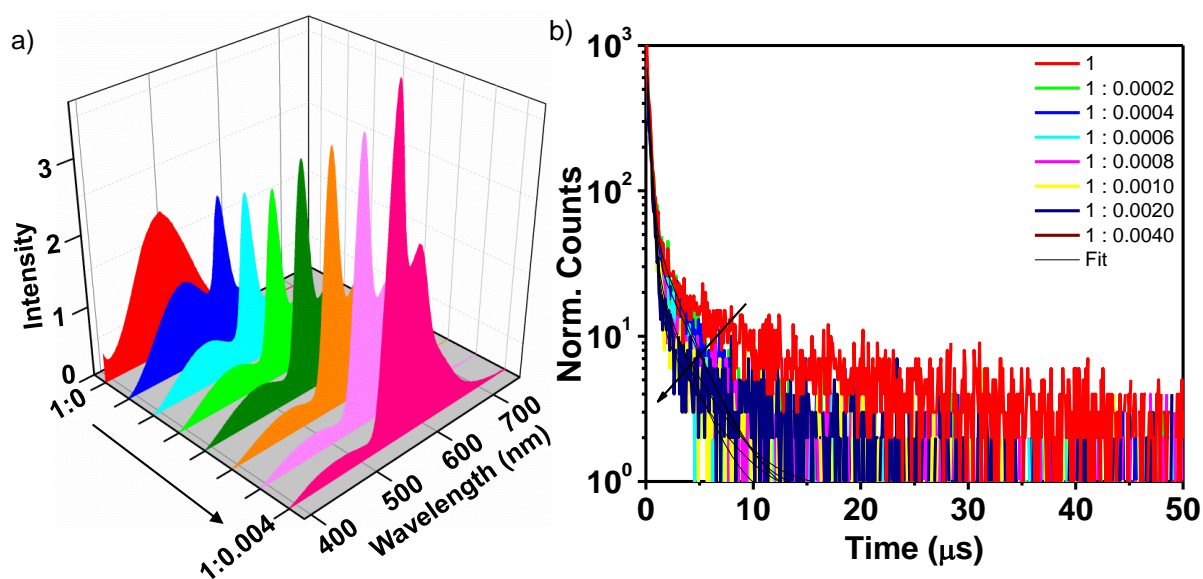


Figure 4.13. a) Energy transfer between **2** and **6**, upon increasing the amount of **6** and b) corresponding lifetime decay profile ($\lambda_{\text{ex}} = 360 \text{ nm}$, $\lambda_{\text{mon}} = 480 \text{ nm}$).

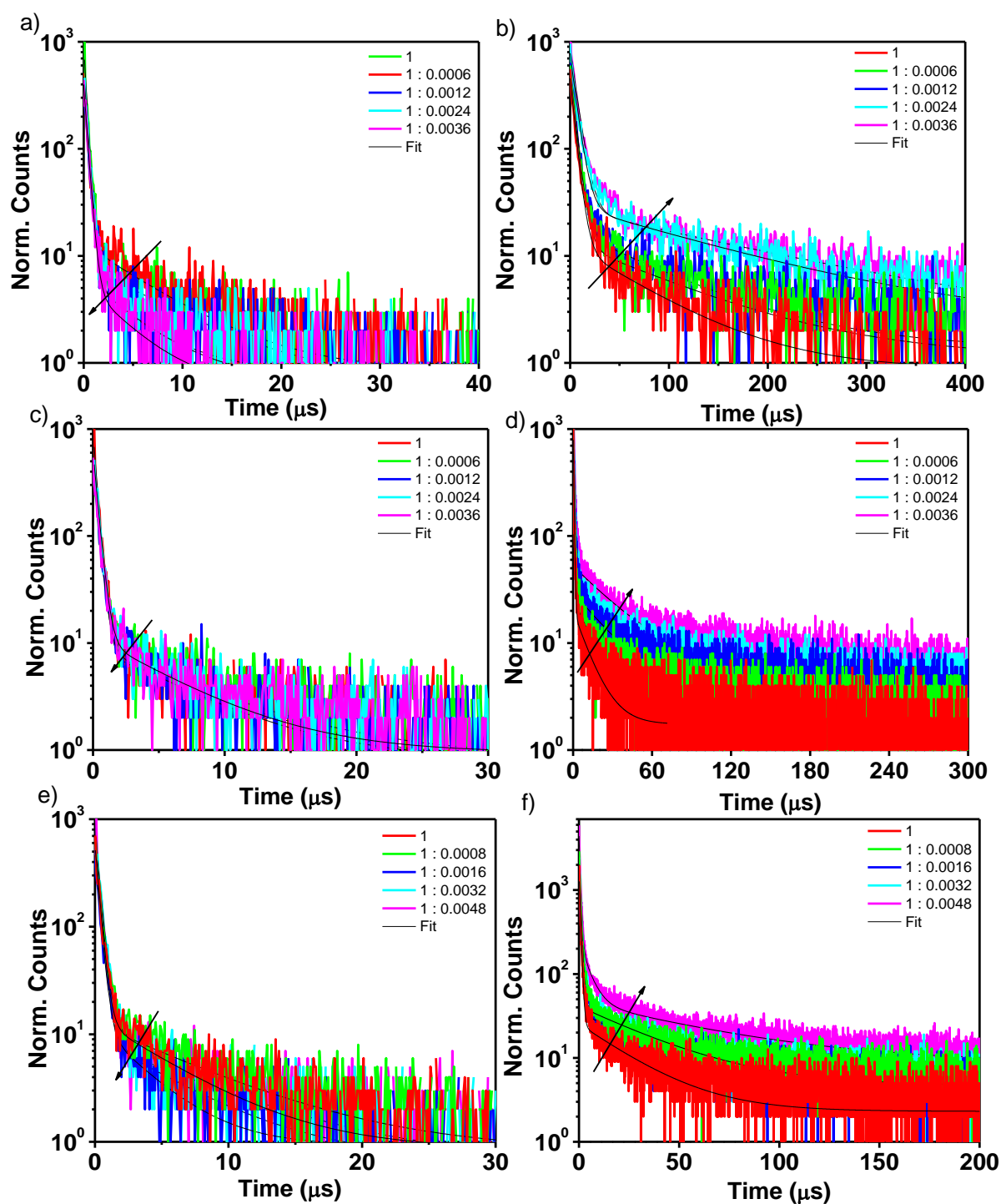


Figure 4.14. TADF lifetime decay of a mixture of **1+3** at 298 K monitored at a) 450 nm (donor) and b) 520 nm (acceptor). TADF lifetime decay of a mixture of **1+4** at 298 K monitored at c) 450 nm (donor) and d) 550 nm (acceptor). TADF lifetime decay of a mixture of **1+5** at 298 K monitored at e) 450 nm (donor) and f) 580 nm (acceptor).

The liquid matrix of SOLs allowed facile mixing with polylactic acid (PLA), a bio-based polymer, to yield solid filament materials ideal for 3D printing applications. We have optimized the minimum amount of SOL as 1 wt% for satisfactory luminescence features with excellent quantum yields for thin films (Figure 4.15a, Table 4). The photographs of the SOL doped (1 wt%) thin films under UV light (365 nm) show similar emission features as the neat SOLs, and it points to the excellent dispersibility of TADF SOLs in the PLA matrix. SOL hybrids individually and in combinations have been used to make a cube having sides with blue (**1**), cyan (**2**), green (**3**), orange (**4**), and red (**5**) along with white (**2+5**) emissions under UV light (365 nm) excitation (Figure 4.15b). PLA-**1** hybrid has been used to 3D print the CSIR and NCL logos, exhibiting deep blue emission (Figure 4.15c). Besides, a flower vase (**2-5** and **2+5**) and a mushroom lamp (**2, 5**) were also prepared (Figure 4.15d). SOLs exhibited excellent thermal stability and processability when melt compounded with thermoplastic polymers such as PLA, rendering their uniform distribution in the PLA matrix. Compared to the solid emitters, the long branched aliphatic chains and liquid matrix of SOLs support the uniform distribution throughout the matrix without any phase separation. The 3D printed objects are stable and retain the emission features for more than one year.

We have attempted the TADF SOLs for light-emitting application, and as a representative example, the LED device was fabricated using **4** as an emitter (Figure 4.16-4.18). The LED device of **4** exhibits reasonably good performance and the details are provided below. To improve the performance, mCP has been selected as the host because of the good overlap of its emission with the absorption of **4** (Figure 4.16). The device showed excellent diode characteristics with a turn-on voltage for light emission around 9V (Figure 4.17). A typical J-V-L characteristic of the LED has been given in Figure 4.17. The device exhibited a maximum luminance of 653 cd/m² at 17 V with a current density of 73 mA/cm².

The electroluminescent spectra showed a peak at 552 nm with CIE coordinates of (0.41,0.56). The emission from mCP is not seen, confirming ET between mCP and **4**. The current efficiency, power efficiency, and external quantum efficiency of 1.26 cd/A, 0.3 lm/W, and 0.33%, respectively, were obtained at 176 cd/m² (at 13V). The variation of the above device parameters with luminescence is shown in Figure 4.18. Further optimization of the transport layers and the doping concentration are expected to improve the device performance.

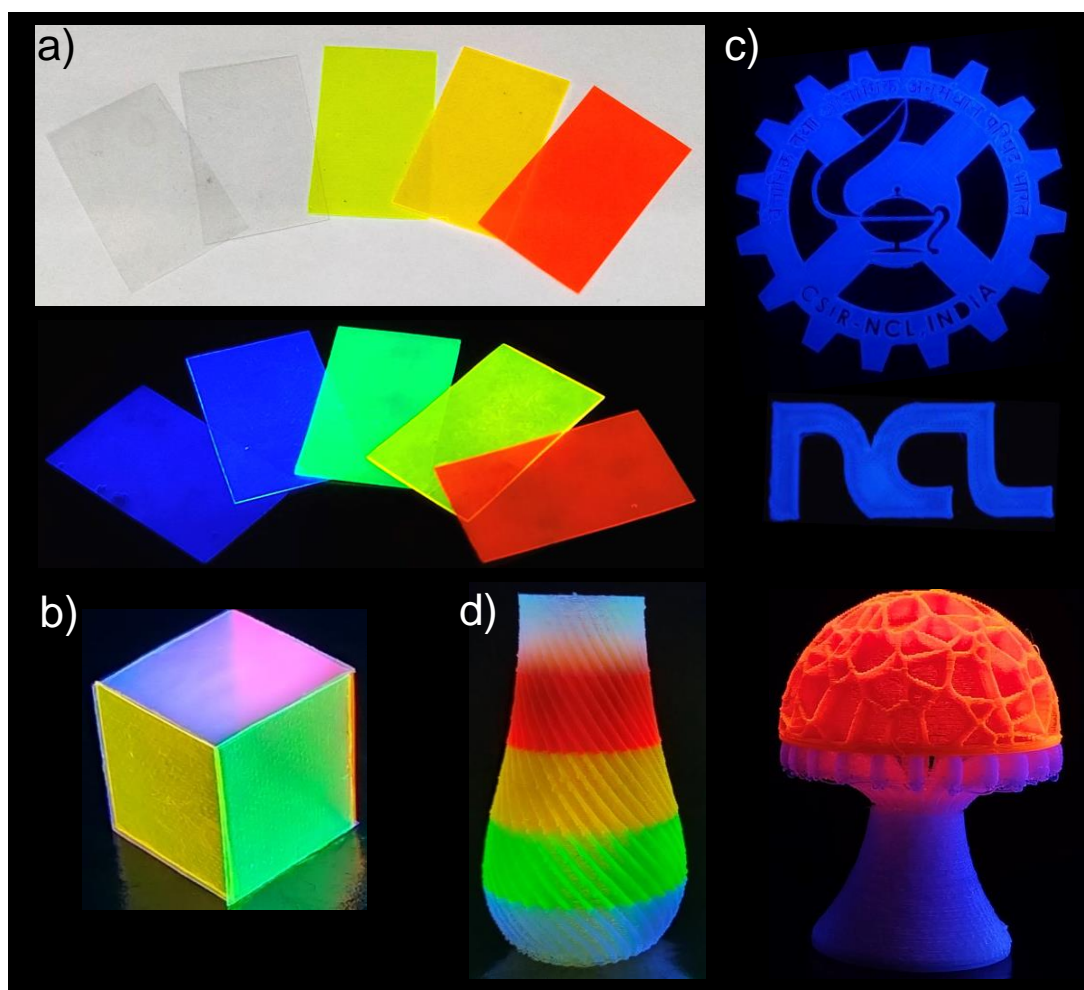


Figure 4.15. a) Photograph of the SOL (**1-5**)-PLA hybrid sheets under visible (top) and UV (365 nm) (bottom) lights, and b) a cube with different emission colours (**2-5**), including white (**2+5**) (1:0.002) made out of hybrid sheets under UV (365 nm) light. Photographs of the 3D printed objects using PLA-TADF SOL (1 wt%) hybrids under UV light (365 nm). c) CSIR and NCL logo using **1**-PLA and d) colourful flower vase (**2-5** and **2+5**) and mushroom lamp (**2, 5**).

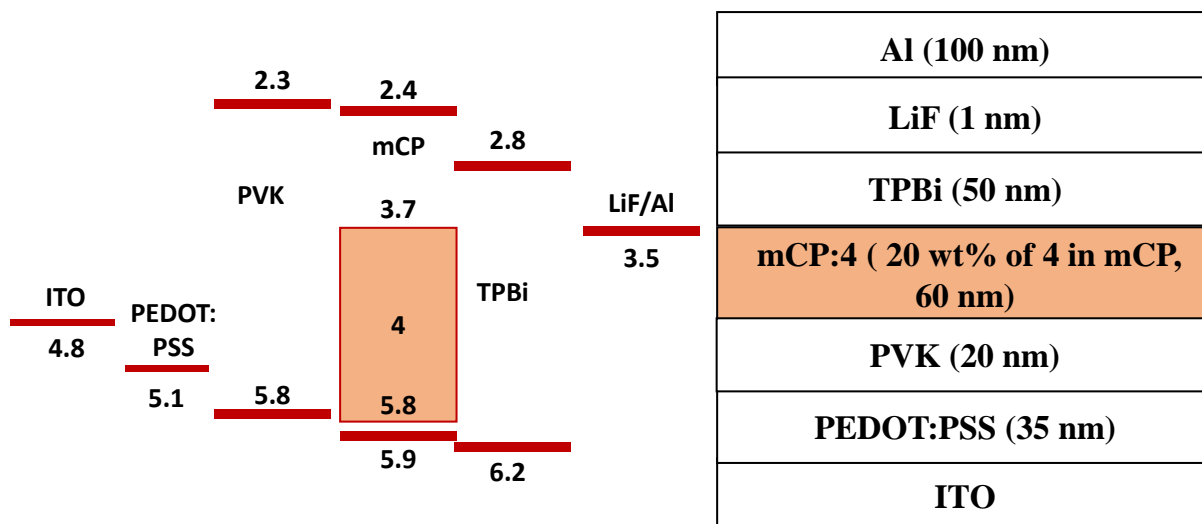


Figure 4.16. Energy levels and device structure of OLED device using **4** as the emitting layer.

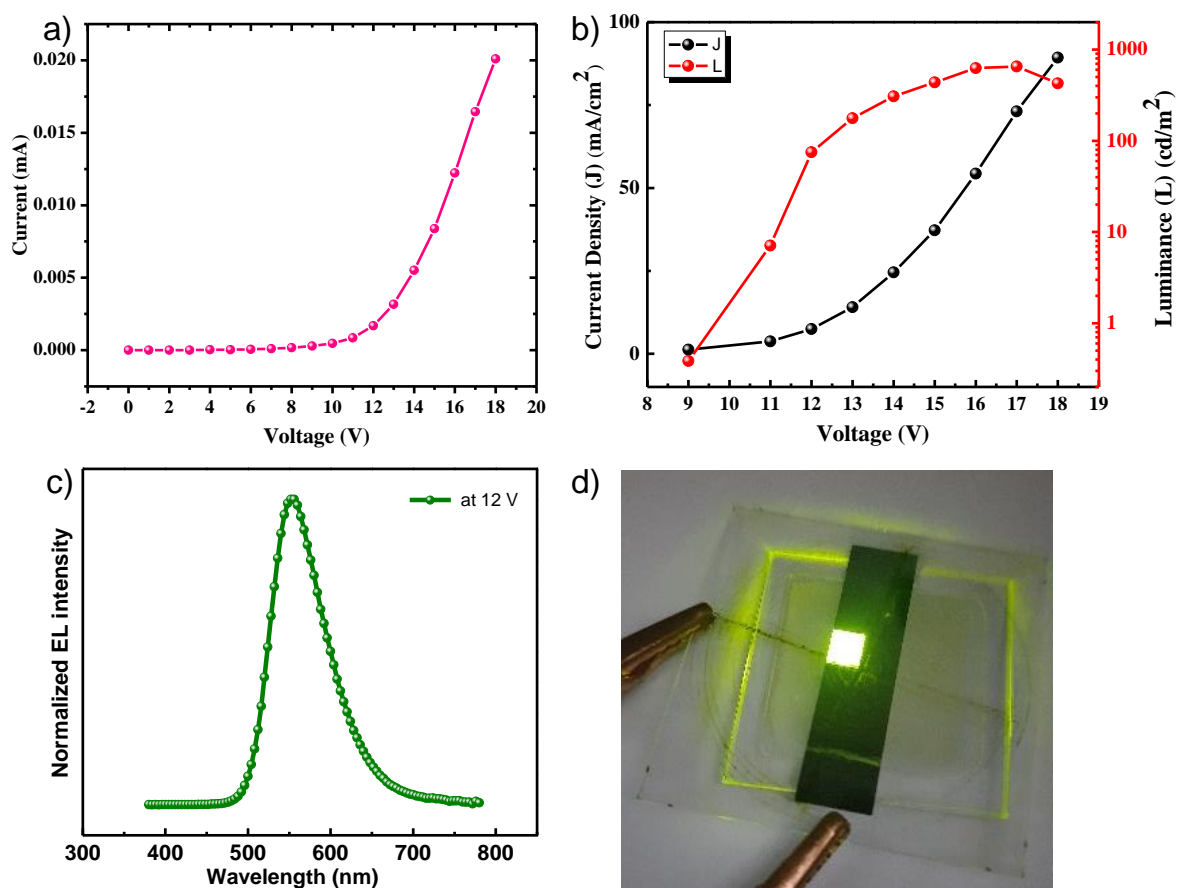


Figure 4.17. a) Current density (J)-Voltage (V)- Luminance (L) characteristics, b) Current(I)-Voltage (V) characteristics, c) Electroluminescence spectra, d) photograph of the device.

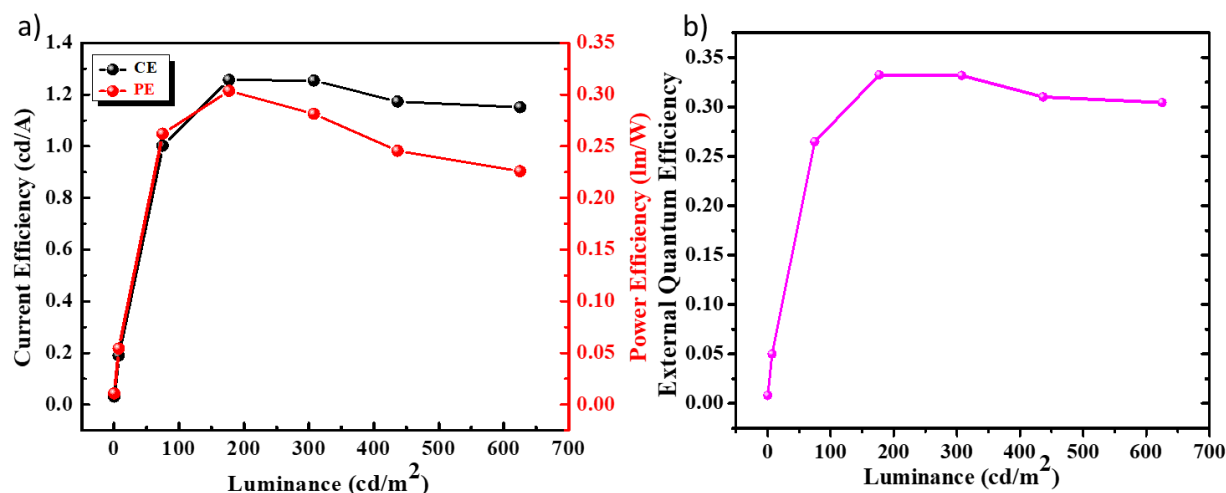


Figure 4.18. a) Current Efficiency and Power Efficiency Vs Luminance plot b) External Quantum Efficiency (EQE) Vs Luminance plot.

Table 1. Photophysical parameters of TADF SOLs

No.	λ_{abs} (nm) (Sol. ⁿ) ^a	λ_{abs} (nm) (Neat) ^a	λ_{em} (nm) (Sol. ⁿ) ^b	λ_{em} (nm) (Neat) ^b	τ (ns) (Neat) ^c	τ (μ s) (Neat) ^d	Φ_{PL} (%) (Sol. ⁿ) ^e	Φ_{PL} (%) (Neat) ^f	S_1 (eV) ^g	T_1 (eV) ^g	ΔE_{ST} (eV) ^g
1	356	358	418	428	12.9	7.90	70	66	3.160	3.126	0.034
2	360	364	424	483	24.7	10.1	59	68	3.091	3.038	0.053
3	404	424	508	510	5.56	28.0	82	79	2.689	2.572	0.117
4	420	430	590	545	7.69	44.8	91	83	2.479	2.388	0.091
5	476	490	620	622	4.50	12.1	95	81	2.254	2.175	0.079

a) Absorption maxima, b) Emission maxima, c) Emission lifetime in Neat State, d) TADF lifetime in Neat State, Photoluminescence Quantum Yield in e) Solution State f) Neat State, g) Experimental S_1 and T_1 energies estimated from the Fluorescence and Phosphorescence spectra in Neat State.

Table 2. Emission lifetime of 1-5 in MTHF solution ($C = 10^{-5}$ M) at 298 K.

Molecules	Lifetime (ns)	CHISQ (χ^2) values
1	$\tau_1 = 3.73$ (84 %) $\tau_2 = 1.92$ (11 %) $\tau_3 = 0.30$ (5 %)	1.10
2	$\tau_1 = 6.62$ (98 %) $\tau_2 = 0.23$ (2 %)	1.24

3	$\tau_1 = 4.61$ (90 %) $\tau_2 = 1.44$ (06 %) $\tau_3 = 0.03$ (03 %)	1.07
4	$\tau_1 = 5.01$ (95 %) $\tau_2 = 0.64$ (3 %) $\tau_3 = 0.04$ (2 %)	1.12
5	$\tau_1 = 0.31$ (5 %) $\tau_2 = 3.36$ (95 %)	0.94

Table 3. Emission lifetime of 1-5 in MTHF solution ($C = 1 \times 10^{-5}$ M before and after purging with oxygen at 298 K.

Molecules	Condition	Lifetime (ns)	CHISQ (χ^2) values
1	Before	$\tau_1 = 0.54$ (20 %) $\tau_2 = 1.85$ (71 %) $\tau_3 = 4.69$ (9 %)	1.21
	After	$\tau_1 = 0.32$ (10 %) $\tau_2 = 1.08$ (43 %) $\tau_3 = 2.27$ (47 %)	1.07
2	Before	$\tau_1 = 0.84$ (23 %) $\tau_2 = 7.27$ (77 %)	1.18
	After	$\tau_1 = 0.67$ (16 %) $\tau_2 = 5.22$ (84 %)	1.16
3	Before	$\tau_1 = 0.41$ (4 %) $\tau_2 = 3.72$ (17 %) $\tau_3 = 8.34$ (79 %)	1.19
	After	$\tau_1 = 0.31$ (5 %) $\tau_2 = 2.66$ (62 %) $\tau_3 = 4.48$ (33 %)	1.12
4	Before	$\tau_1 = 1.32$ (3 %) $\tau_2 = 6.42$ (95 %) $\tau_3 = 0.16$ (2 %)	1.17
	After	$\tau_1 = 0.31$ (7 %) $\tau_2 = 3.38$ (93 %)	1.13

5	Before	$\tau_1 = 0.34$ (5 %) $\tau_2 = 3.59$ (95 %)	1.15
	After	$\tau_1 = 0.34$ (6 %) $\tau_2 = 3.03$ (94 %)	1.09

Table 4. Emission quantum yield of **1-5** in neat state at 298 K.

Compounds	Quantum Yield (%)	
	Neat Liquid	PLA Hybrid Sheets
1	66	60
2	68	64
3	79	76
4	83	79
5	81	76

Table 5. Emission lifetime of **1-5** in the neat state at 298 K.

Molecules	Lifetime (ns)	CHISQ (χ^2) values
1	$\tau_1 = 12.9$ (51 %) $\tau_2 = 1.88$ (22 %) $\tau_3 = 0.55$ (27 %)	1.16
2	$\tau_1 = 24.7$ (82 %) $\tau_2 = 2.13$ (10 %) $\tau_3 = 0.82$ (8 %)	1.24
3	$\tau_1 = 5.56$ (73 %) $\tau_2 = 2.02$ (22 %) $\tau_3 = 0.31$ (5 %)	1.20
4	$\tau_1 = 7.69$ (52 %) $\tau_2 = 2.77$ (36 %) $\tau_3 = 0.52$ (12 %)	1.24
5	$\tau_1 = 1.78$ (47 %) $\tau_2 = 0.28$ (8 %) $\tau_3 = 4.50$ (45 %)	1.00

Table 6. TADF lifetime of **1-5** in the neat state at 298 K.

Samples	TADF lifetime (μs)	CHISQ (χ^2) values
1	$\tau_1 = 7.90$ (25 %) $\tau_2 = 0.27$ (75 %)	1.18
2	$\tau_1 = 10.1$ (45 %) $\tau_2 = 0.09$ (55 %)	0.80
3	$\tau_1 = 28.0$ (49 %) $\tau_2 = 0.73$ (15 %) $\tau_3 = 0.04$ (36 %)	1.16
4	$\tau_1 = 44.8$ (60 %) $\tau_2 = 5.33$ (29 %) $\tau_3 = 0.10$ (11 %)	1.20
5	$\tau_1 = 12.1$ (31 %) $\tau_2 = 0.55$ (69 %)	1.09

Table 7. Variation of TADF lifetime decay of **1-5** in the neat state in the presence of oxygen at 298 K.

Molecules	Condition	Lifetime (μs)	CHISQ (χ^2) values
1	Before	$\tau_1 = 7.90$ (25 %) $\tau_2 = 0.27$ (75 %)	1.18
	After	$\tau_1 = 0.36$ (100 %)	1.16
2	Before	$\tau_1 = 9.47$ (77 %) $\tau_2 = 0.33$ (23 %)	0.94
	After	$\tau_1 = 8.22$ (43 %) $\tau_2 = 0.31$ (57 %)	1.22
3	Before	$\tau_1 = 13.4$ (46 %) $\tau_2 = 0.54$ (54 %)	1.24

	After	$\tau_1 = 11.7$ (40 %) $\tau_2 = 0.48$ (60 %)	1.09
4	Before	$\tau_1 = 10.0$ (34 %) $\tau_2 = 0.44$ (66 %)	1.10
	After	$\tau_1 = 8.09$ (33 %) $\tau_2 = 0.43$ (67 %)	1.19
5	Before	$\tau_1 = 12.4$ (31 %) $\tau_2 = 0.55$ (69 %)	1.26
	After	$\tau_1 = 11.6$ (29 %) $\tau_2 = 0.55$ (71 %)	1.28

Table 8. Temperature-dependent TADF lifetime decay of **1-5** in the neat state.

Molecules	Condition	Lifetime (μ s)	CHISQ (χ^2) values
1	298 K	$\tau_1 = 7.90$ (25 %) $\tau_2 = 0.27$ (75 %)	1.18
	77 K	$\tau_1 = 0.45$ (75 %) $\tau_2 = 0.08$ (25 %)	1.21
2	298 K	$\tau_1 = 10.1$ (45 %) $\tau_2 = 0.09$ (55 %)	0.80
	77 K	$\tau_1 = 0.39$ (48 %) $\tau_2 = 0.05$ (52 %)	0.76
3	298 K	$\tau_1 = 28.0$ (49 %) $\tau_2 = 0.73$ (15 %) $\tau_3 = 0.04$ (36 %)	1.16
	77 K	$\tau_1 = 11.3$ (23 %) $\tau_2 = 0.37$ (12 %) $\tau_3 = 0.04$ (65 %)	0.66
4	298 K	$\tau_1 = 44.8$ (60 %) $\tau_2 = 5.33$ (29 %) $\tau_3 = 0.10$ (11 %)	1.20
	77 K	$\tau_1 = 11.5$ (25 %) $\tau_2 = 0.47$ (75 %)	1.30
5	298 K	$\tau_1 = 12.1$ (31 %) $\tau_2 = 0.55$ (69 %)	1.09

	77 K	$\tau_1 = 2.88$ (39 %) $\tau_2 = 0.19$ (61 %)	0.75
--	------	--	------

Table 9. Variation of the emission lifetime of **1** with increasing equivalents of **3** in the neat state monitored at 450 nm.

Ratio of 1 and 3	Lifetime (ns)	CHISQ (χ^2) values
1	$\tau_1 = 12.9$ (51 %) $\tau_2 = 1.88$ (22 %) $\tau_3 = 0.55$ (27 %)	1.16
1 : 0.0006	$\tau_1 = 1.67$ (66 %) $\tau_2 = 0.44$ (20 %) $\tau_3 = 11.1$ (14 %)	0.33
1 : 0.0012	$\tau_1 = 1.56$ (63 %) $\tau_2 = 0.43$ (25 %) $\tau_3 = 10.6$ (12 %)	0.34
1 : 0.0024	$\tau_1 = 1.04$ (54 %) $\tau_2 = 8.43$ (11 %) $\tau_3 = 0.02$ (35 %)	0.31
1 : 0.0036	$\tau_1 = 0.64$ (37 %) $\tau_2 = 6.97$ (11 %) $\tau_3 = 0.14$ (53 %)	0.33

Table 10. Variation of the emission lifetime of **1** with increasing equivalents of **3** in the neat state monitored at 520 nm.

Ratio of 1 and 3	Lifetime (ns)	CHISQ (χ^2) values
1	$\tau_1 = 12.9$ (51 %) $\tau_2 = 1.88$ (22 %) $\tau_3 = 0.55$ (27 %)	1.16
1 : 0.0006	$\tau_1 = 2.18$ (62 %) $\tau_2 = 0.77$ (21 %) $\tau_3 = 14.1$ (17 %)	1.00
1 : 0.0012	$\tau_1 = 3.97$ (36 %) $\tau_2 = 14.4$ (29 %) $\tau_3 = 1.10$ (35 %)	1.02
1 : 0.0024	$\tau_1 = 5.63$ (44 %)	

	$\tau_2 = 15.0$ (31 %) $\tau_3 = 1.26$ (25 %)	1.05
1 : 0.0036	$\tau_1 = 5.37$ (40 %) $\tau_2 = 15.2$ (31 %) $\tau_3 = 1.30$ (29 %)	1.06

Table 11. Variation of TADF lifetime of **1** with increasing equivalents of **3** in the neat state monitored at 450 nm.

Ratio of 1 and 3	Lifetime (μs)	CHISQ (χ^2) values
1	$\tau_1 = 7.90$ (25 %) $\tau_2 = 0.27$ (75 %)	1.18
1 : 0.0006	$\tau_1 = 6.79$ (36 %) $\tau_2 = 0.31$ (64 %)	0.80
1 : 0.0012	$\tau_1 = 5.02$ (18 %) $\tau_2 = 0.32$ (82 %)	0.98
1 : 0.0024	$\tau_1 = 4.94$ (17 %) $\tau_2 = 0.35$ (83 %)	0.99
1 : 0.0036	$\tau_1 = 4.19$ (14 %) $\tau_2 = 0.33$ (86 %)	0.88

Table 12. Variation of TADF lifetime of **1** with increasing equivalents of **3** in the neat state monitored at 520 nm.

Ratio of 1 and 3	Lifetime (μs)	CHISQ (χ^2) values
1	$\tau_1 = 5.96$ (29 %) $\tau_2 = 0.39$ (71 %)	1.16
1 : 0.0006	$\tau_1 = 7.67$ (36 %) $\tau_2 = 0.40$ (64 %)	1.27
1 : 0.0012	$\tau_1 = 8.59$ (33 %) $\tau_2 = 0.41$ (67 %)	1.09
1 : 0.0024	$\tau_1 = 12.4$ (48 %) $\tau_2 = 0.48$ (52 %)	0.98
1 : 0.0036	$\tau_1 = 0.52$ (52 %) $\tau_2 = 16.2$ (48 %)	0.79

Table 13. Variation of the emission lifetime of **1** with increasing equivalents of **4** in the neat state monitored at 450 nm.

Ratio of 1 and 4	Lifetime (ns)	CHISQ (χ^2) values
1	$\tau_1 = 12.9$ (51 %) $\tau_2 = 1.88$ (22 %) $\tau_3 = 0.55$ (27 %)	1.16
1 : 0.0006	$\tau_1 = 0.34$ (7 %) $\tau_2 = 1.25$ (74 %) $\tau_3 = 5.33$ (19 %)	1.09
1 : 0.0012	$\tau_1 = 0.32$ (6 %) $\tau_2 = 1.13$ (71 %) $\tau_3 = 4.84$ (23 %)	1.15
1 : 0.0024	$\tau_1 = 0.24$ (7 %) $\tau_2 = 0.93$ (69 %) $\tau_3 = 3.97$ (24 %)	1.17
1 : 0.0036	$\tau_1 = 0.53$ (55 %) $\tau_2 = 2.22$ (38 %) $\tau_3 = 0.10$ (7 %)	1.20

Table 14. Variation of the emission lifetime of **1** with increasing equivalents of **4** in the neat state monitored at 550 nm.

Ratio of 1 and 4	Lifetime (ns)	CHISQ (χ^2) values
1	$\tau_1 = 12.9$ (51 %) $\tau_2 = 1.88$ (22 %) $\tau_3 = 0.55$ (27 %)	1.16
1 : 0.0006	$\tau_1 = 1.51$ (17 %) $\tau_2 = 4.56$ (68 %) $\tau_3 = 14.0$ (15 %)	1.20
1 : 0.0012	$\tau_1 = 4.44$ (67 %) $\tau_2 = 1.19$ (18 %) $\tau_3 = 15.0$ (15 %)	1.18
1 : 0.0024	$\tau_1 = 4.57$ (65 %) $\tau_2 = 1.32$ (20 %) $\tau_3 = 15.6$ (15 %)	1.20
1 : 0.0036	$\tau_1 = 4.46$ (57 %) $\tau_2 = 16.1$ (16 %) $\tau_3 = 1.21$ (27 %)	1.19

Table 15. Variation of TADF lifetime of **1** with increasing equivalents of **4** in the neat state monitored at 450 nm.

Ratio of 1 and 4	Lifetime (μs)	CHISQ (χ^2) values
1	$\tau_1 = 7.90$ (25 %) $\tau_2 = 0.27$ (75 %)	1.18
1 : 0.0006	$\tau_1 = 7.54$ (31 %) $\tau_2 = 0.35$ (69 %)	0.91
1 : 0.0012	$\tau_1 = 6.22$ (28 %) $\tau_2 = 0.31$ (72 %)	0.75
1 : 0.0024	$\tau_1 = 5.83$ (29 %) $\tau_2 = 0.32$ (71 %)	0.88
1 : 0.0036	$\tau_1 = 5.02$ (18 %) $\tau_2 = 0.32$ (82 %)	1.30

Table 16. Variation of TADF lifetime of **1** with increasing equivalents of **4** in the neat state monitored at 550 nm.

Ratio of 1 and 4	Lifetime (μs)	CHISQ (χ^2) values
1	$\tau_1 = 11.5$ (36 %) $\tau_2 = 0.49$ (64 %)	1.30
1 : 0.0006	$\tau_1 = 13.7$ (38 %) $\tau_2 = 0.58$ (62 %)	1.21
1 : 0.0012	$\tau_1 = 0.67$ (51 %) $\tau_2 = 27.6$ (49 %)	0.88
1 : 0.0024	$\tau_1 = 0.70$ (49 %) $\tau_2 = 28.8$ (51 %)	1.26
1 : 0.0036	$\tau_1 = 0.72$ (51 %) $\tau_2 = 32.6$ (49 %)	1.23

Table 17. Variation of the emission lifetime of **1** with increasing equivalents of **5** in the neat state monitored at 450 nm.

Ratio of 1 and 5	Lifetime (ns)	CHISQ (χ^2) values
1	$\tau_1 = 12.9$ (51 %) $\tau_2 = 1.88$ (22 %) $\tau_3 = 0.55$ (27 %)	1.16
1 : 0.0008	$\tau_1 = 0.32$ (7 %) $\tau_2 = 1.22$ (75 %) $\tau_3 = 5.18$ (18 %)	1.18
1 : 0.0016	$\tau_1 = 0.28$ (7 %) $\tau_2 = 1.01$ (68 %) $\tau_3 = 4.25$ (25 %)	1.13
1 : 0.0032	$\tau_1 = 0.17$ (7 %) $\tau_2 = 0.72$ (64 %) $\tau_3 = 2.92$ (29 %)	1.07
1 : 0.0048	$\tau_1 = 0.51$ (56 %) $\tau_2 = 2.20$ (39 %) $\tau_3 = 0.14$ (5 %)	1.01

Table 18. Variation of the TADF lifetime of **1** with increasing equivalents of **5** in the neat state monitored at 450 nm.

Ratio of 1 and 5	Lifetime (μ s)	CHISQ (χ^2) values
1	$\tau_1 = 7.90$ (25 %) $\tau_2 = 0.27$ (75 %)	1.18
1 : 0.0008	$\tau_1 = 7.45$ (35 %) $\tau_2 = 0.33$ (65 %)	0.91
1 : 0.0016	$\tau_1 = 5.58$ (26 %) $\tau_2 = 0.33$ (74 %)	0.85
1 : 0.0032	$\tau_1 = 5.29$ (32 %) $\tau_2 = 0.29$ (68 %)	0.96
1 : 0.0048	$\tau_1 = 3.33$ (22 %) $\tau_2 = 0.30$ (78 %)	0.98

Table 19. Variation of TADF lifetime of **1** with increasing equivalents of **5** in the neat state monitored at 580 nm.

Ratio of 1 and 5	Lifetime (μ s)	CHISQ (χ^2) values
------------------	---------------------	---------------------------

1	$\tau_1 = 0.61$ (58 %) $\tau_2 = 24.7$ (42 %)	1.21
1 : 0.0008	$\tau_1 = 0.76$ (52 %) $\tau_2 = 33.6$ (48 %)	1.32
1 : 0.0016	$\tau_1 = 0.74$ (53 %) $\tau_2 = 33.7$ (47 %)	1.31
1 : 0.0032	$\tau_1 = 0.73$ (53 %) $\tau_2 = 35.3$ (47 %)	1.28
1 : 0.0048	$\tau_1 = 0.83$ (51 %) $\tau_2 = 37.9$ (49 %)	1.30

Table 20. Variation of TADF lifetime of **2** with increasing equivalents of **6** in the neat state monitored at 480 nm.

Ratio of 2 and 6	Lifetime (μ s)	CHISQ (χ^2) values
1	$\tau_1 = 10.1$ (45 %) $\tau_2 = 0.09$ (55 %)	0.80
1 : 0.0002	$\tau_1 = 3.04$ (24 %) $\tau_2 = 0.30$ (76 %)	0.76
1 : 0.0004	$\tau_1 = 2.93$ (30 %) $\tau_2 = 0.28$ (70 %)	0.85
1 : 0.0006	$\tau_1 = 2.61$ (46 %) $\tau_2 = 0.28$ (54 %)	0.85
1 : 0.0008	$\tau_1 = 2.24$ (46 %) $\tau_2 = 0.25$ (54 %)	0.84
1 : 0.0010	$\tau_1 = 2.09$ (36 %) $\tau_2 = 0.26$ (64 %)	0.90
1 : 0.0020	$\tau_1 = 1.74$ (20 %) $\tau_2 = 0.21$ (80 %)	1.06
1 : 0.0040	$\tau_1 = 0.42$ (100 %)	1.13

4.5 Conclusion

In conclusion, the successful demonstration of the TADF liquid accomplished a series of molecules having varying TADF emission colours through structural modification. The donor-acceptor combination of TADF liquid emitters exhibited ET-assisted tunable emission. A cascade ET between the TADF SOLs demonstrated hybrid liquids having tunable emission, including white light-emission. The attractive features, such as the capability to form a large-area thin luminescent film and tunable emission by doping, enable TADF liquids to be a potential candidate in lighting and display applications. Interestingly, the high QY and uniform dispersibility of SOLs supported the very low loading of the emitters (1 wt%) to deliver 3D printed objects with multicolour light emission. The detailed photophysical studies indicate that neither the same SOLs in solution nor the crystalline structural analogs exhibit TADF, and it points to the importance of molecular design in developing the hitherto unknown TADF liquids. The high processability of TADF liquids to form large-area thin films without compromising the emission features offer a bright future for TADF SOLs.

4.6 References

1. A. Endo, K. Sato, K. Yoshimura, T. Kai, A. Kawada, H. Miyazaki, C. Adachi, *Appl. Phys. Lett.*, **2011**, 98, 083302.
2. H. Uoyama, K. Goushi, K. Shizu, H. Nomura, C. Adachi, *Nature*, **2012**, 492, 234-238.
3. C. Adachi, *Jpn. J. Appl. Phys.*, **2014**, 53, 060101.
4. Y. Tao, K. Yuan, T. Chen, P. Xu, H. Li, R. Chen, C. Zheng, L. Zhang, W. Huang, *Adv. Mater.*, **2014**, 26, 7931-7958.
5. Z. Yang, Z. Mao, Z. Xie, Y. Zhang, S. Liu, J. Zhao, J. Xu, Z. Chi, M. P. Aldred, *Chem. Soc. Rev.*, **2017**, 46, 915-1016.
6. M. Y. Wong, E. Zsysman-Colman, *Adv. Mater.*, **2017**, 29, 1605444.
7. T. J. Penfold, F. B. Dias, A. P. Monkman, *Chem. Commun.*, **2018**, 54, 3926-3935.

8. Y. Liu, C. Li, Z. Ren, S. Yan, M. R. Bryce, *Nat. Rev. Mater.*, **2018**, *3*, 18020.
9. M. Baroncini, G. Bergamini, P. Ceroni, *Chem. Commun.*, **2017**, *53*, 2081-2093.
10. A. Forni, E. Lucenti, C. Botta, E. Cariati, *J. Mater. Chem. C*, **2018**, *6*, 4603-4626.
11. L. Gu, X. Wang, M. Singh, H. Shi, H. Ma, Z. An, W. Huang, *J. Phys. Chem. Lett.*, **2020**, *11*, 6191-6200.
12. W. Zhao, Z. He, B. Z. Tang, *Nat. Rev. Mater.*, **2020**, *5*, 869-885.
13. A. D. Nidhankar, Goudappagouda, V. C. Wakchaure, S. S. Babu, *Chem. Sci.*, **2021**, *12*, 4216-4236.
14. J. Yang, M. Fang, Z. Li, *Acc. Mater. Res.*, **2021**, *2*, 644-654.
15. D. Wang, C. Cheng, T. Tsuboi, Q. Zhang, *CCS Chem.*, **2020**, *2*, 1278-1296.
16. S. Y. Byeon, D. R. Lee, K. S. Yook, J. Y. Lee, *Adv. Mater.*, **2019**, *31*, 1803714.
17. R.-P. Xu, Y.-Q. Li, J.-X. Tang, *J. Mater. Chem. C*, **2016**, *4*, 9116-9142.
18. T. Huang, W. Jiang, L. Duan, *J. Mater. Chem. C*, **2018**, *6*, 5577-5596.
19. S. Reineke, F. Lindner, G. Schwartz, N. Seidler, K. Walzer, B. Lüssem, K. Leo, *Nature*, **2009**, *459*, 234-238.
20. C. W. Tang, S. A. Vanslyke, *Appl. Phys. Lett.*, **1987**, *51*, 913-915.
21. T. Förster, K. Kasper, *Phys. Chem.*, **1954**, *11*, 275.
22. G. S. Beddard, G. Porter, *Nature*, **1976**, *260*, 366-367.
23. T. Sekitani, H. Nakajima, H. Maeda, T. Fukushima, T. Aida, K. Hata, T. Someya, *Nat. Mater.*, **2009**, *8*, 494-499.
24. J. A. Rogers, T. Someya, Y. Huang, *Science*, **2010**, *327*, 1603-1607.
25. T. Sekitani, T. Someya, *Adv. Mater.*, **2010**, *22*, 2228-2246.
26. M. S. White, M. Kaltenbrunner, E. D. Głowacki, K. Gutnichenko, G. Kettlgruber, I. Graz, S. Aazou, C. Ulbricht, D. A. M. Egbe, M. C. Miron, Z. Major, M. C. Scharber, T. Sekitani, T. Someya, S. Bauer, N. S. Sariciftci, *Nat. Photon.*, **2013**, *7*, 811-816.
27. T. Nakanishi, *Wiley-VCH, Weinheim*, **2019**.

28. S. S. Babu, T. Nakanishi, *Chem. Commun.*, **2013**, 49, 9373-9382.
29. S. S. Babu, *Phys. Chem. Chem. Phys.*, **2015**, 17, 3950-3953.
30. F. Lu, T. Nakanishi, *Adv. Opt. Mater.*, **2019**, 7, 1900176.
31. S. S. Babu, J. Aimi, H. Ozawa, N. Shirahata, A. Saeki, S. Seki, A. Ajayaghosh, H. Möhwald, T. Nakanishi, *Angew. Chem. Int. Ed.*, **2012**, 51, 3391-3395.
32. S. S. Babu, M. J. Hollamby, J. Aimi, H. Ozawa, A. Saeki, S. Seki, K. Kobayashi, K. Hagiwara, M. Yoshizawa, H. Möhwald, T. Nakanishi, *Nat. Commun.*, **2013**, 4, 1969.
33. T. Machida, R. Taniguchi, T. Oura, K. Sada, K. Kokado, *Chem. Commun.*, **2017**, 53, 2378-2381.
34. Goudappagouda, A. Manthanath, V. C. Wakchaure, K. C. Ranjeesh, T. Das, K. Vanka, T. Nakanishi, S. S. Babu, *Angew. Chem. Int. Ed.*, **2019**, 58, 2284-2288.
35. V. C. Wakchaure, Goudappagouda, T. Das, S. Ravindranathan, S. S. Babu, *Nanoscale*, **2021**, 13, 10780-10784.
36. T. Ogoshi, T. Aoki, R. Shiga, R. Iizuka, S. Ueda, K. Demachi, D. Yamafuji, H. Kayama, T. Yamagishi, *J. Am. Chem. Soc.*, **2012**, 134, 50, 20322-20325.
37. N. Giri, M. G. D. Pópolo, G. Melaugh, R. L. Greenaway, K. Rätzke, T. Koschine, L. Pison, M. F. C. Gomes, A. I. Cooper, S. L. James, *Nature*, **2015**, 527, 216-220.
38. S. Hirata, K. Kubota, H. H. Jung, O. Hirata, K. Goushi, M. Yahiro, C. Adachi, *Adv. Mater.*, **2011**, 23, 889-893.
39. N. Kobayashi, T. Kasahara, T. Edura, J. Oshima, R. Ishimatsu, M. Tsuwaki, T. Imato, S. Shoji, J. Mizuno, *Sci. Rep.*, **2015**, 5, 14822.
40. T. Goya, P. Z. Crocomo, T. Hosono, S. Minakata, L. E. de Sousa, P. de Silva, P. Data, Y. Takeda, *Asian J. Org. Chem.*, 2022, **11**, e202100780.
41. T. Hosono, N. O. Decarli, P. Z. Crocomo, T. Goya, L. E. de Sousa, N. Tohnai, S. Minakata, P. de Silva, P. Data, Y. Takeda, *J. Mater. Chem. C*, **2022**, 10, 4905.

42. A. Kamino, T. P. Bender, R. A. Klenkler, *J. Phys. Chem. Lett.*, **2012**, *3*, 1002-1006.
43. T. G. Plint, B. A. Kamino, T. P. Bender, *J. Phys. Chem. C*, **2015**, *119*, 1676-1682.
44. S.-L. Suraru, F. Würthner, *Angew. Chem. Int. Ed.*, **2014**, *53*, 7428-7448.
45. S. V. Bhosale, M. A. Kobaisi, R. W. Jadhav, P. P. Morajkar, L. A. Jones, S. George, *Chem. Soc. Rev.*, **2021**, *50*, 9845-9998.
46. N. Sakai, J. Mareda, E. Vauthey, S. Matile, *Chem. Commun.*, **2010**, *46*, 4225-4237.
47. Q. Zhang, B. Li, S. Huang, H. Nomura, H. Tanaka, C. Adachi, *Nat. Photon.*, **2014**, *8*, 326-332.
48. T. Serevičius, R. Skaisgiris, J. Dodonova, L. Jagintavičius, D. Banevičius, K. Kazlauskas, S. Tumkevičius, S. Juršėnas, *ACS Appl. Mater. Interfaces*, **2020**, *12*, 10727-10736.
49. J. Gibson, A. P. Monkman, T. J. Penfold, *ChemPhysChem*, **2016**, *17*, 2956-2961.
50. M. K. Etherington, J. Gibson, H. F. Higginbotham, T. J. Penfold, A. P. Monkman, *Nat. Commun.*, **2016**, *7*, 13680.
51. T. Hosokai, H. Matsuzaki, H. Nakanotani, K. Tokumaru, T. Tsutsui, A. Furube, K. Nasu, H. Nomura, M. Yahiro, C. Adachi, *Sci. Adv.*, **2017**, *3*, e1603282.
52. P. K. Samanta, D. Kim, V. Coropceanu, J.-L. Brédas, *J. Am. Chem. Soc.*, **2017**, *139*, 4042-4051.
53. I. E. Serdiuk, M. Mońka, K. Kozakiewicz, B. Liberek, P. Bojarski, S. Y. Park, *J. Phys. Chem. B*, **2021**, *125*, *10*, 2696-2706.
54. S. Kuila, S. Garain, G. Banappanavar, B. C. Garain, D. Kabra, S. K. Pati, S. J. George, *J. Phys. Chem. B*, **2021**, *125*, 4520-4526.

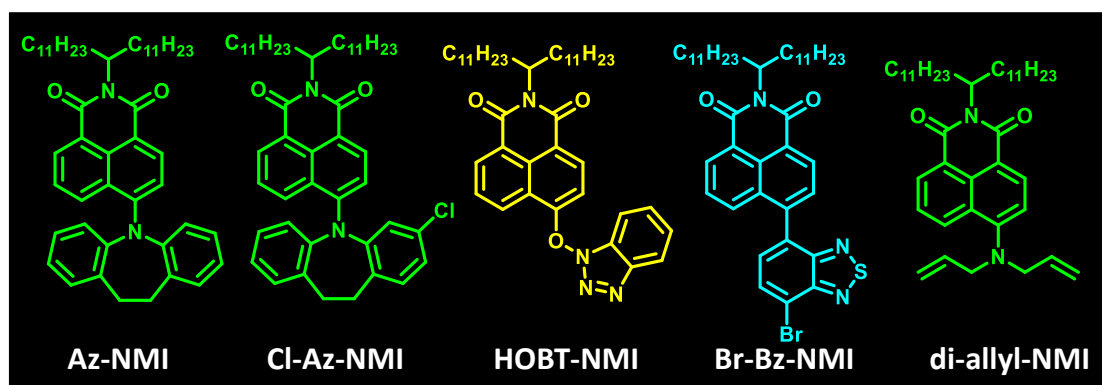
55. W. Zeng, H.-Y. Lai, W.-K. Lee, M. Jiao, Y.-J. Shiu, C. Zhong, S. Gong, T. Zhou, G. Xie, M. Sarma, K.-T. Wong, C.-C. Wu, C. Yang, *Adv. Mater.*, **2018**, *30*, 1704961.
56. Y. Guo, H. Guan, P. Li, C. Wang, Z. Wu, Y. Wang, Z. Yu, Z. Zhang, S. Wang, G. Zhao, *J. Phys. Chem. Lett.*, **2021**, *12*, 9501-9507.
57. G. Tang, A. A. Sukhanov, J. Zhao, W. Yang, Z. Wang, Q. Liu, V. K. Voronkova, M. D. Donato, D. Escudero, D. Jacquemin, *J. Phys. Chem. C*, **2019**, *123*, 30171-30186.
58. Y.-F. Wang, H.-Y. Lu, C. Chen, M. Li, C.-F. Chen, *Org. Electron.*, **2019**, *70*, 71-77.
59. S. P. Dudek, M. Pouderoijen, R. Abbel, A. P. H. J. Schenning, E. W. Meijer, *J. Am. Chem. Soc.*, **2005**, *127*, 11763-11768.
60. A. Ajayaghosh, V. K. Praveen, S. Srinivasan, R. Varghese, *Adv. Mater.*, **2007**, *19*, 411-415.
61. Goudappagouda, V. C. Wakchaure, K. C. Ranjeesh, C. A. R. Abhai, S. S. Babu, *Chem. Commun.*, **2017**, *53*, 7072-7075.
62. A. Sarkar, S. Dhiman, A. Chalishazar, S. J. George, *Angew. Chem. Int. Ed.*, **2017**, *56*, 13767-13771.
63. B. W. D'Andrade, S. R. Forrest, *Adv. Mater.*, **2004**, *16*, 1585-1595.
64. R. Abbel, R. van der Weegen, W. Pisula, M. Surin, P. Leclère, R. Lazzaroni, E. W. Meijer, A. P. H. J. Schenning, *Chem. Eur. J.*, **2009**, *15*, 9737-9746.
65. X. Zhang, S. Rehm, M. M. Safont-Sempere, F. Würthner, *Nat. Chem.*, **2009**, *1*, 623-629.
66. M. A. Baldo, M. E. Thompson, S. R. Forrest, *Nature*, **2000**, *403*, 750-753.
67. B. W. D'Andrade, M. A. Baldo, C. Adachi, J. Brooks, M. E. Thompson, S. R. Forrest, *Appl. Phys. Lett.*, **2001**, *79*, 1045-1047.
68. H. Nakanotani, T. Higuchi, T. Furukawa, K. Masui, K. Morimoto, M. Numata, H. Tanaka, Y. Sagara, T. Yasuda, C. Adachi, *Nat. Commun.*, **2014**, *5*, 4016.

69. D. Zhang, L. Duan, C. Li, Y. Li, H. Li, D. Zhang, Y. Qiu, *Adv. Mater.*, **2014**, *26*, 5050-5055.
70. T. Higuchi, H. Nakanotani, C. Adachi, *Adv. Mater.*, **2015**, *27*, 2019-2023.
71. C.-Y. Chan, M. Tanaka, Y.-T. Lee, Y.-W. Wong, H. Nakanotani, T. Hatakeyama, C. Adachi, *Nat. Photon.*, **2021**, *15*, 203-207.
72. (a) E. Runge, E. K. U. Gross, *Phys. Rev. Lett.*, **1984**, *52*, 997-1000. (b) R. E. Stratmann, G. E. Scuseria, M. J. Frisch, *J. Chem. Phys.*, **1998**, *109*, 8218-8224.
73. (a) S. H. Vosko, L. Wilk, M. Nusair, *Can. J. Phys.*, **1980**, *58*, 1200-1211. (b) C. Lee, W. Yang, R. G. Parr, *Phys. Rev. B Condens. Matter*, **1988**, *37*, 785-789. (c) A. D. Becke, *J. Chem. Phys.*, **1993**, *98*, 5648-5652. (d) P. J. Stephens, F. J. Devlin, C. F. Chabalowski, M. J. Frisch, *J. Phys. Chem. A*, **1994**, *98*, 11623-11627.
74. M. J. Frisch, G. W. Trucks, H. B. Schlegel, G. E. Scuseria, M. A. Robb, J. R. Cheeseman, G. Scalmani, V. Barone, B. Mennucci, G. A. Petersson, H. Nakatsuji, M. Caricato, X. Li, H. P. Hratchian, A. F. Izmaylov, J. Bloino, G. Zheng, J. L. Sonnenberg, M. Hada, M. Ehara, K. Toyota, R. Fukuda, J. Hasegawa, M. Ishida, T. Nakajima, Y. Honda, O. Kitao, H. Nakai, T. Vreven, J. A. Montgomery, Jr., J. E. Peralta, F. Ogliaro, M. Bearpark, J. J. Heyd, E. Brothers, K. N. Kudin, V. N. Staroverov, R. Kobayashi, J. Normand, K. Raghavachari, A. Rendell, J. C. Burant, S. S. Iyengar, J. Tomasi, M. Cossi, N. Rega, J. M. Millam, M. Klene, J. E. Knox, J. B. Cross, V. Bakken, C. Adamo, J. Jaramillo, R. Gomperts, R. E. Stratmann, O. Yazyev, A. J. Austin, R. Cammi, C. Pomelli, J. W. Ochterski, R. L. Martin, K. Morokuma, V. G. Zakrzewski, G. A. Voth, P. Salvador, J. J. Dannenberg, S. Dapprich, A. D. Daniels, O. Farkas, J. B. Foresman, J. V. Ortiz, J. Cioslowski, D. J. Fox, Gaussian 09 (Revision A.02), Gaussian, Inc., Wallingford CT, **2009**.
75. T. Yanai, D. P. Tew, N. C. Handy, *Chem. Phys. Lett.*, **2004**, *393*, 51-57.

76. (a) S. Miertuš, E. Scrocco, J. Tomasi, *Chem. Phys.*, **1981**, *55*, 117-29. (b) S. Miertuš, J. Tomasi, *Chem. Phys.*, **1982**, *65*, 239-245. (c) J. L. Pascual-Ahuir, E. Silla, I. Tuñón, *J. Comp. Chem.*, **1994**, *15*, 1127-38.
77. Goudappagouda, A. Manthanath, V. C. Wakchaure, K. C. Ranjeesh, T. Das, K. Vanka, T. Nakanishi, S. S. Babu, *Angew. Chem. Int. Ed.*, 2019, **58**, 2284-2288.
78. E. R. Triboni, R. G. S. Berlinck, M. J. Politi, P. B. Filho, *J. Chemical Research*, **2004**, *7*, 508-509.
79. Z. Tian, Y. Liu, B. Tian, J. Zhang, *Research on Chemical Intermediates*, **2015**, *41*, 1157-1169.
80. D. Oesch, N. W. Luedtke, *Chem. Commun.* **2015**, *51*, 12641-12644.
81. R. Greiner, T. Schlucker, D. Zgela, H. Langhals, *J. Mater. Chem. C*, **2016**, *4*, 11244-11252.
82. I. A. Karpenko, A. S. Klymchenko, S. Gioria, R. Kreder, I. Shulov, P. Villa, Y. Mely, M. Hibert, D. Bonnet, *Chem. Commun.* **2015**, *51*, 2960-2963.
83. V. Parthasarathy, R. Pandey, P. K. Das, F. Castet, M. Blanchard-Desce, *ChemPhysChem*, **2018**, *19*, 187-197.
84. R. Nazir, E. Balciūnas, D. Buczynska, F. Bourquard, D. Kowalska, D. Gray, S. Mackowski, M. Farsari, D. T. Gryko, *Macromolecules*, **2015**, *48*, 2466-2472.
85. P. A. Panchenko, A. N. Arkhipova, O. A. Fedorova, Y. V. Fedorov, M. A. Zakharko, D. E. Arkhipov, G. Jonusauskas, *Phys. Chem. Chem. Phys.*, **2017**, *19*, 1244-1256.
86. D. Wei, L. Ge, Z. Wang, Y. Wang, R. Guo, *Langmuir*, **2019**, *35*, 11745-11754.

Chapter-5

Luminescent Solvent-free Organic Liquid Naphthalimides for Lighting Applications



Luminescent organic materials have prime importance because of their high colour tunability, stability, processability, and hence have a high demand for processable large-area devices. Recently, an efficient harvest of triplet excitons and convert them into light have emerged for lighting applications. Organic molecules exhibiting thermally activated delayed fluorescence (TADF) have been extensively studied in a short period and gathered much attention. However, organic TADF materials suffer from aggregation caused by quenching in both crystalline and amorphous states. In this context, solvent-free organic liquids with TADF features in bulk with high processability will be promising for practical demonstrations. Herein, we designed and synthesized a series of naphthalimide-based solvent-free TADF liquids exhibiting cyan to yellow colour emission with a delayed lifetime of up to 79 μ s. We sensibly attached a polymerizable group to one of the solvent-free TADF liquids to further utilize for polymerization. The polymerizable liquid can be coated on surfaces to get a stable large area coating after exposure to heat or light. Hence, we aim to develop a polymerizable organic hybrid liquid capable of forming large-area films as a potential candidate for flexible and foldable electronic devices.

Publication: *Manuscript under Preparation*

5.1. Introduction

Self-organization of molecules is an essential tool in organic electronics to control the charge transport features.¹⁻³ Over the last several decades, organic electronics have seen dramatic advancements, resulting in the invention of organic electronic devices such as solar cells, transistors, light-emitting diodes, and so on.⁴ The organised arrangement of molecules to produce a precise transport channel for the generation of holes and electrons has been seen to play a crucial role in determining the efficiency of such devices. However, organic material has restrictions such as stability, crystalline ordering requirements, etc., which slowed down the manufacturing of low-cost, energy-efficient, large-area devices.⁵⁻⁷ It emphasises the significance of an alternate candidate in this research path, and non-volatile solvent-free organic liquid (SOL) is being examined as a potential candidate. As discussed in earlier chapters on SOLs, the main objective is to tune functional properties by synthetic modification or blending with other dopants to fulfill the demand for organic electrical devices.

SOLs have been investigated as a new soft material to undertake the aforementioned challenges to a certain extent.⁸⁻¹¹ SOLs are expected to replace solid crystalline samples, which restrict the manufacturing of large-area thin films with no defects.¹² In this context, luminescent SOLs that can be coated on various surfaces to form continuous thin films are highly promising.⁸⁻¹¹ However, the limitations, including the surface stickiness and the least curability of the films have to be rectified. To overcome the drawbacks of the SOLs without affecting their physical/photophysical properties,¹³⁻¹⁶ polymerizable SOLs can be used to make stable luminescent polymer films. The envisaged polymerizable SOL strategy will allow us to overcome the present hurdles associated with using luminescent organic materials in device applications. In this direction, we aim to develop novel polymerizable luminescent SOLs. In this chapter, we introduce new TADF liquids and a polymerizable version of it.

5.2. Experimental section

5.2.1 RTP and TADF Experiments

The window of maximum delay after flash for phosphorescence measurements was kept as 3 ms for 77 K and 0.1 ms for 298 K. Phosphorescence lifetimes were measured at room temperature (298 K) in the air by keeping a 10% delay component and 10% trigger pulse duration, using 355 nm excitation source. All experiments have been done in the air by keeping the same experimental parameters.

5.2.2 Emission and Lifetime Decay at 77 K and 298 K Temperature Measurements

The PTI spectrofluorometer is equipped with thermoelectric cuvette holders, heating stages, and cryostats which allows the measurements to be carried out over a temperature of 77 K. The fluorescence emission and lifetime decays of all molecules at 77 K and 298 K were measured using a liquid nitrogen Dewar module.

5.2.3 Preparation of Polymerizable Hybrid Liquids

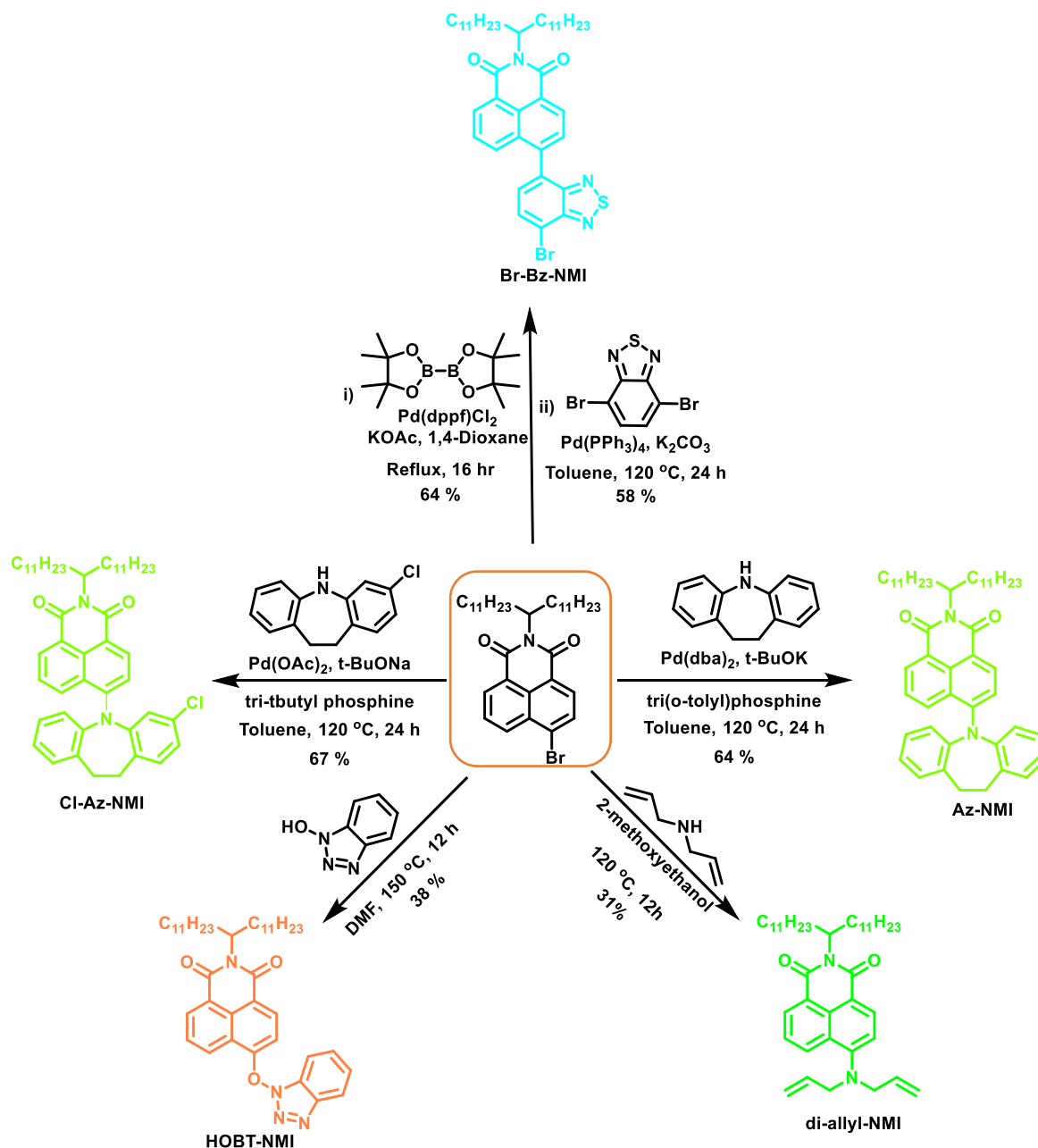
The molecule **Diallyl-NMI** and crosslinker (**CL**) with varying equivalents in glass vials were stirred well with a spatula to get a homogenous hybrid liquid.

5.2.4 Preparation and Purification of Polymer Films¹⁷

The homogenous hybrid liquid was uniformly cast on a glass plate using the doctor blade technique and exposed to UV-visible light (400-800 nm) with 300 Watts power for about **3** hours for photopolymerization to get a stable polymer film. The polymer film was prepared by thermochemical method as well. The homogenous hybrid liquid on a glass plate was kept at 80 °C for **2** hours in the glove box. The polymerization results in stable 2D-sheet films of controllable thickness.

5.3. Synthesis

Synthesis of 6-bromo-2-(tricosan-12-yl)-1H-benzo[de]isoquinoline-1,3(2H)-dione were performed according to the literature procedure.^{9b}

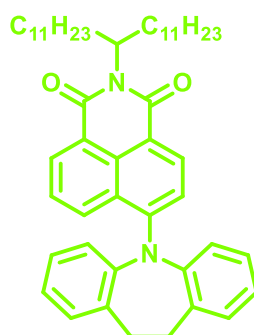


Scheme S1. Synthetic scheme of Naphthalimide-based molecules.

5.3.1 Synthesis of 6-(10,11-dihydro-5H-dibenzo[b,f]azepin-5-yl)-2-(tricosan-12-yl)-1H-benzo[de]isoquinoline-1,3(2H)-dione (Az-NMI)¹⁸

A mixture of 6-bromo-2-(tricosan-12-yl)-1H-benzo[de]isoquinoline-1,3(2H)-dione (200 mg, 334.05 μmol), 10,11-dihydro-5H-dibenzo[b,f]azepine (80 mg,

401 μmol), tri(*o*-tolyl)phosphine (11 mg, 33.41 μmol), anhydrous potassium *t*-butoxide (75 mg, 668.10 μmol) was weighed and taken in a two neck flask with anhydrous toluene (10 mL). This flask was degassed by repeated *freeze-pump-thaw* cycles. After this, and Pd(dba)₂ [Tris(dibenzylideneacetone)dipalladium(0)] (19 mg, 33.41 μmol) was added to the reaction mixture and kept for reflux at 120 °C under argon for 24 hours. The reaction progress was monitored by TLC in a mixture of *n*-hexane-CH₂Cl₂. The reaction mixture was extracted with CH₂Cl₂ and dried with anhydrous Na₂SO₄. The CH₂Cl₂ was removed by a rotary evaporator, and the resulting residue was purified by silica column chromatography using a mixture of *n*-hexane:CH₂Cl₂ to yield **Az-NMI** (153 mg, 64%) as a brown-coloured liquid.



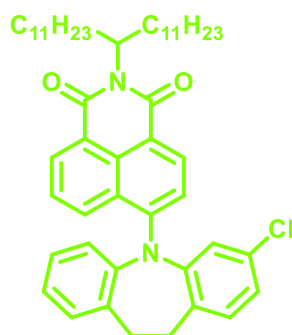
¹H NMR (400 MHz, CDCl₃), δ (TMS, ppm): 8.29 - 8.55 (m, 2 H), 7.89 (d, *J* = 8.6 Hz, 1 H), 7.29 - 7.32 (m, 2 H), 7.25 - 7.28 (m, 4 H), 7.20 - 7.25 (m, 4 H), 5.15 (br. s., 1 H), 3.21 (s, 4 H), 2.15 - 2.29 (m, 2 H), 1.75 - 1.87 (m, 2 H), 1.27 (d, *J* = 6.8 Hz, 12 H), 1.21 (br. s., 24 H), 0.87 (t, *J* = 6.9 Hz, 6 H) ppm.

¹³C NMR (100 MHz, CDCl₃), δ (TMS, ppm): 165.8, 165.0, 149.5, 145.5, 136.5, 133.0, 132.2, 131.4, 131.1, 127.5, 127.2, 127.1, 124.2, 122.6, 114.5, 54.2, 32.5, 32.4, 31.9, 31.3, 29.6, 29.6, 29.3, 26.9, 22.7, 14.1 ppm.

HR-MS (ESI⁺): calcd for C₄₉H₆₄N₂O₂ [M+H]⁺ 714.0630, found: 715.0715.

5.3.2 6-(3-chloro-10,11-dihydro-5H-dibenzo[b,f]azepin-5-yl)-2-(tricosan-12-yl)-1H-benzo[de]isoquinoline-1,3(2H)-dione¹⁸

A mixture of 6-bromo-2-(tricosan-12-yl)-1H-benzo[de]isoquinoline-1,3(2H)-dione (200 mg, 334 μmol), 3-chloro-10,11-dihydro-5H-dibenzo[b,f]azepine (85 mg, 367.46 μmol), tri(*t*-butyl)phosphine (7 mg, 33.41 μmol), anhydrous sodium *t*-butoxide (65 mg, 668.10 μmol) was weighed and taken in a two neck flask with anhydrous toluene (10 mL). This flask was degassed by repeated *freeze-pump-thaw* cycles. After this, Pd(OAc)₂ [Palladium (II) acetate] (8 mg, 33.41 μmol) was added to the reaction mixture and kept for reflux at 120 °C under argon for 24 hours. The reaction progress was monitored by TLC in a mixture of *n*-hexane-CH₂Cl₂. The reaction mixture was extracted with CH₂Cl₂ and dried with anhydrous Na₂SO₄. The CH₂Cl₂ was removed by rotary evaporator, the resulting residue was purified by silica column chromatography using a mixture of *n*-hexane:CH₂Cl₂ to yield **Cl-Az-NMI** (167 mg, 67%) as a brown-coloured liquid.



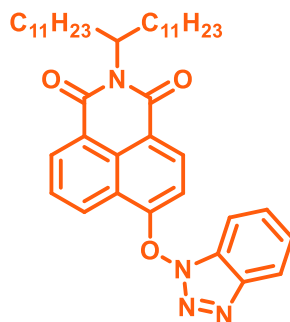
¹H NMR (400 MHz, CDCl₃), δ (TMS, ppm): 8.38 - 8.58 (m, 2 H), 7.93 (d, *J* = 8.9 Hz, 1 H), 7.31 - 7.40 (m, 2 H), 7.29 (br. s., 1 H), 7.18 - 7.24 (m, 4 H), 7.13 - 7.17 (m, 2 H), 5.15 (br. s., 1 H), 3.20 (s, 4 H), 2.19 - 2.27 (m, 2 H), 1.78 - 1.86 (m, 2 H), 1.21 (br. s., 36 H), 0.87 (t, 6 H) ppm.

¹³C NMR (101 MHz, CDCl₃), δ (TMS, ppm): 165.7, 164.7, 145.2, 136.3, 134.3, 133.6, 132.4, 132.2, 131.5, 130.9, 129.7, 127.5, 127.0, 126.5, 125.0, 116.6, 54.1, 32.5, 31.9, 29.6, 29.3, 27.0, 22.7, 14.1 ppm.

HR-MS (ESI⁺): calcd for C₄₉H₆₃ClN₂O₂ [M+H]⁺ 748.5050, found: 749.6150.

5.3.3 Synthesis of 6-((1H-benzo[d][1,2,3]triazol-1-yl)oxy)-2-(tricosan-12-yl)-1H-benzo[de]isoquinoline-1,3(2H)-dione

Compound 6-bromo-2-(tricosan-12-yl)-1H-benzo[de]isoquinoline-1,3(2H)-dione (200 mg, 334.05 μ mol), 1-Hydroxybenzotriazole (68 mg, 501.08 μ mol) in DMF (10 mL) were stirred at 120 °C for 12 h. The solvent was evaporated under reduced pressure, and the crude product was purified by column chromatography on silica to afford **HOBT-NMI** as a dark yellow-coloured liquid (88 mg, 38 %).



¹H NMR (400 MHz, CDCl₃), δ (TMS, ppm): 8.90 - 8.99 (m, 1 H), 8.80 (d, J = 8.4 Hz, 1 H), 8.68 (d, J = 10.9 Hz, 1 H), 8.18 (d, J = 6.8 Hz, 1 H), 8.01 - 8.12 (m, 2 H), 7.85 (t, J = 7.8 Hz, 1 H), 7.72 (t, J = 7.7 Hz, 1 H), 7.56 (t, J = 7.4 Hz, 1 H), 5.19 (br. s., 1 H), 2.17 - 2.33 (m, 2 H), 1.86 (dt, J = 13.5, 4.9 Hz, 2 H), 1.19 - 1.31 (m, 36 H), 0.85 (t, J = 6.9 Hz, 6 H) ppm.

¹³C NMR (126 MHz, CDCl₃), δ (TMS, ppm): 165.3, 164.6, 164.2, 163.5, 151.2, 145.6, 133.0, 132.2, 131.9, 129.9, 129.5, 128.5, 127.1, 125.9, 124.2, 120.8, 119.4, 111.3, 54.6, 32.4, 31.9, 29.7, 29.6, 29.6, 29.6, 29.3, 27.0, 22.7, 14.1 ppm.

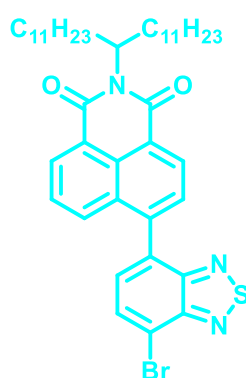
HR-MS (ESI⁺): calcd for C₄₁H₅₆N₄O₃ [M+H]⁺ 653.9240, found: 654.8410.

5.3.4 Synthesis of 6-(4-(dimethylamino)phenyl)-2-(tricosan-12-yl)-1H-benzo[de]isoquinoline-1,3(2H)-dione

Synthesis of 6-(4,4,5,5-tetramethyl-1,3,2-dioxaborolan-2-yl)-2-(tricosan-12-yl)-1H-benzo[de]isoquinoline-1,3(2H)-dione were performed according to the literature procedure.¹⁹

A sealed tube was charged with 6-(4,4,5,5-tetramethyl-1,3,2-dioxaborolan-2-yl)-2-(tricosan-12-yl)-1H-benzo[de]isoquinoline-1,3(2H)-dione (200 mg, 309.70 μ mol), 4,7-dibromobenzo[*c*] [1,2,5]-thiadiazole (365 mg, 1.24 mmol), anhy.

K_2CO_3 (214 mg, 1.55mmol) and tetrakis(triphenylphosphine)palladium (0) (36 mg, 30.97 μ mol) dissolved in toluene (10 mL) under argon condition. The mixture was purged with argon for 30 min and then heated to 120 °C for 24 h. The reaction progress was monitored by TLC (*n*-hexane- CH_2Cl_2). The crude mixture was extracted with CH_2Cl_2 and the combined organic layer dried over Na_2SO_4 , filtered and concentrated on a rotary evaporator, the resulting residue was purified by silica column chromatography using *n*-hexane: CH_2Cl_2 as eluent to yield **Br-Bz-NMI** (132 mg, 58%) as a pale-yellow coloured liquid.



1H NMR (400 MHz, $CDCl_3$), δ (TMS, ppm): 8.72-8.62 (br., 2 H), 8.06 (d, J = 7.38 Hz, 1 H), 7.83 - 7.90 (m, 2 H), 7.59 - 7.69 (m, 2 H), 5.15 - 5.26 (m, 1 H), 2.20 - 2.33 (m, 2 H), 1.77 - 1.91 (m, 2 H), 1.20 - 1.30 (m, 36 H), 0.85 - 0.89 (t, 6 H) ppm.

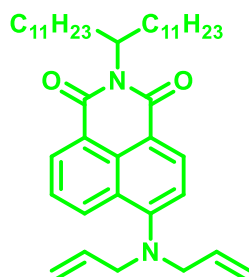
^{13}C NMR (101 MHz, $CDCl_3$), δ (TMS, ppm): 153.7, 153.5, 147.1, 132.0, 131.6, 130.9, 130.1, 128.9, 128.8, 127.1, 124.5, 124.0, 115.2, 54.6, 34.9, 32.4, 31.9, 31.4, 30.2, 29.6, 29.6, 29.6, 29.3, 26.9, 22.7, 14.1 ppm.

HR-MS (ESI⁺): calcd for $C_{41}H_{54}BrN_3O_2S$ $[M+H]^+$ 733.8660, found: 734.8740.

5.3.5 Synthesis of 6-(diallylamino)-2-(tricosan-12-yl)-1H-benzo[de]isoquinoline-1,3(2H)-dione²⁰

Compound 6-bromo-2-(tricosan-12-yl)-1H-benzo[de]isoquinoline-1,3(2H)-dione (200 mg, 334 μ mol), diallylamine (65 mg, 668.10 μ mol) in 2-methoxyethanol (10 ml) was stirred at 120 °C during 24 h under argon atmosphere. The mixture was cooled to ambient temperature, diluted with water,

and extracted with CH₂Cl₂. The organic layer was dried with Na₂SO₄ and evaporated in a vacuum. The resulting residue was purified by silica column chromatography using petroleum ether:CH₂Cl₂ (40:60) as eluent to yield **Diallyl-NMI** (64 mg, 31%) as a yellow-coloured liquid.



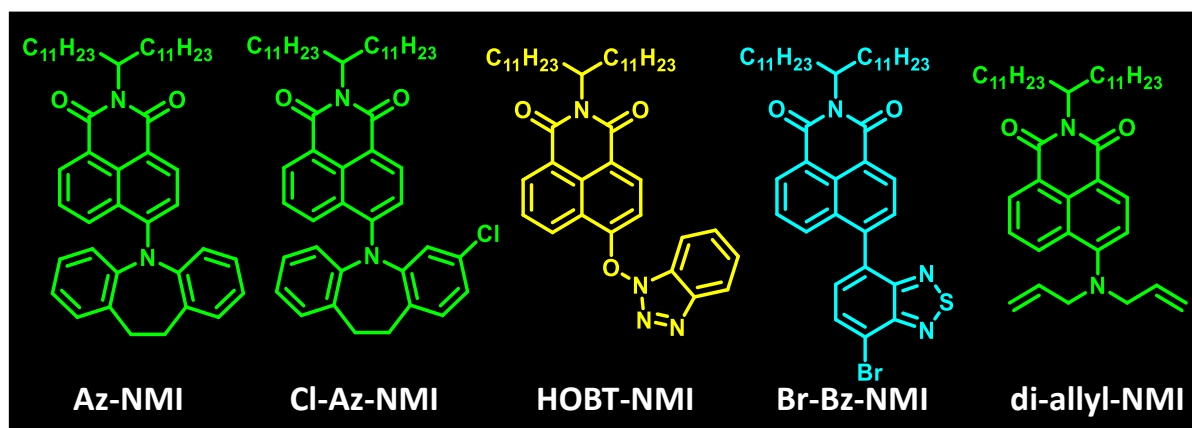
¹H NMR (500 MHz, CDCl₃), δ (TMS, ppm): 8.51 - 8.61 (m, 1 H), 8.39 - 8.50 (m, 2 H), 7.66 (t, *J* = 7.8 Hz, 1 H), 7.19 (d, *J* = 8.2 Hz, 1 H), 5.83 - 5.96 (m, 2 H), 5.34 (d, *J* = 17.4 Hz, 2 H), 5.27 (d, *J* = 10.1 Hz, 2 H), 5.16 (br. s., 1 H), 3.99 (d, *J* = 5.2 Hz, 4 H), 2.17 - 2.29 (m, 2 H), 1.76 - 1.87 (m, 2 H), 1.23 - 1.36 (m, 12 H), 1.20 (br. s., 24 H), 0.86 (t, *J* = 6.9 Hz, 6 H) ppm.

¹³C NMR (126 MHz, CDCl₃), δ (TMS, ppm): 165.8, 165.2, 164.7, 164.3, 154.2, 133.6, 132.4, 131.6, 130.7, 130.3, 130.1, 126.4, 125.4, 123.9, 123.2, 118.2, 116.5, 115.8, 56.0, 54.3, 54.0, 32.5, 32.4, 31.9, 29.6, 29.3, 27.0, 22.7, 14.1 ppm.

HR-MS (ESI⁺): calcd for C₄₁H₆₂N₂O₂ [M+H]⁺ 615.6590, found: 616.9240.

5.4. Result and discussions

Herein, we prepared a series of TADF liquids, including a new polymerizable SOL (Figure 5.1a). The synthesis of TADF liquids and polymerizable SOLs is shown in Scheme 5.1. The TADF liquids and polymerizable derivatives were obtained in moderate to good yields and characterized by ¹H and ¹³C NMR and HR-MS spectroscopy. All the molecules are viscous liquids in nature at 30 °C.



Scheme xx. Chemical structures of naphthalimide-based TADF molecules.

UV-Visible absorption spectra of TADF liquids in 2-methyltetrahydrofuran (MTHF) solution ($C = 1 \times 10^{-5}$ M, $l = 1$ cm) show structured absorption bands ranging from 340 and 480 nm. The absorption maxima were varied as 425, 418, **360**, 355 and 402 nm, respectively, for **Az-NMI**, **Cl-Az-NMI**, **HOBT-NMI**, **4-Br-Bz-NMI**, and **di-allyl-NMI** molecules. Whereas the corresponding steady-state emission in MTHF solution ($C = 1 \times 10^{-5}$ M, $l = 1$ cm) displayed an emission band covering from 390-800 nm (Figure 5.1b, c). Single emission band located at 470 and 494 nm was observed for **4-Br-Bz-NMI** and **di-allyl-NMI**, respectively. At the same time, structured emission bands were noticed in the case of **Az-NMI** (493 nm and 615 nm), **Cl-Az-NMI** (491 nm and 575 nm), and **HOBT-NMI** (432 nm and 492 nm). In accordance with the absorption spectra, **Az-NMI** and **Cl-Az-NMI** exhibited a red-shifted emission peak. Fluorescence lifetime measurements of naphthalimide-based liquids in solution showed a lifetime decay with major lifetimes of 10 ns (98.81 %) for **Az-NMI**, 9.35 ns (64.74 %) for **Cl-Az-NMI**, 9.19 ns (59.51 %) for **HOBT-NMI**, 4.13 ns (51.34 %) for **4-Br-Bz-NMI** and 8.03 ns (95.87 %) for **di-allyl-NMI** (Figure 5.1c and Table 2).

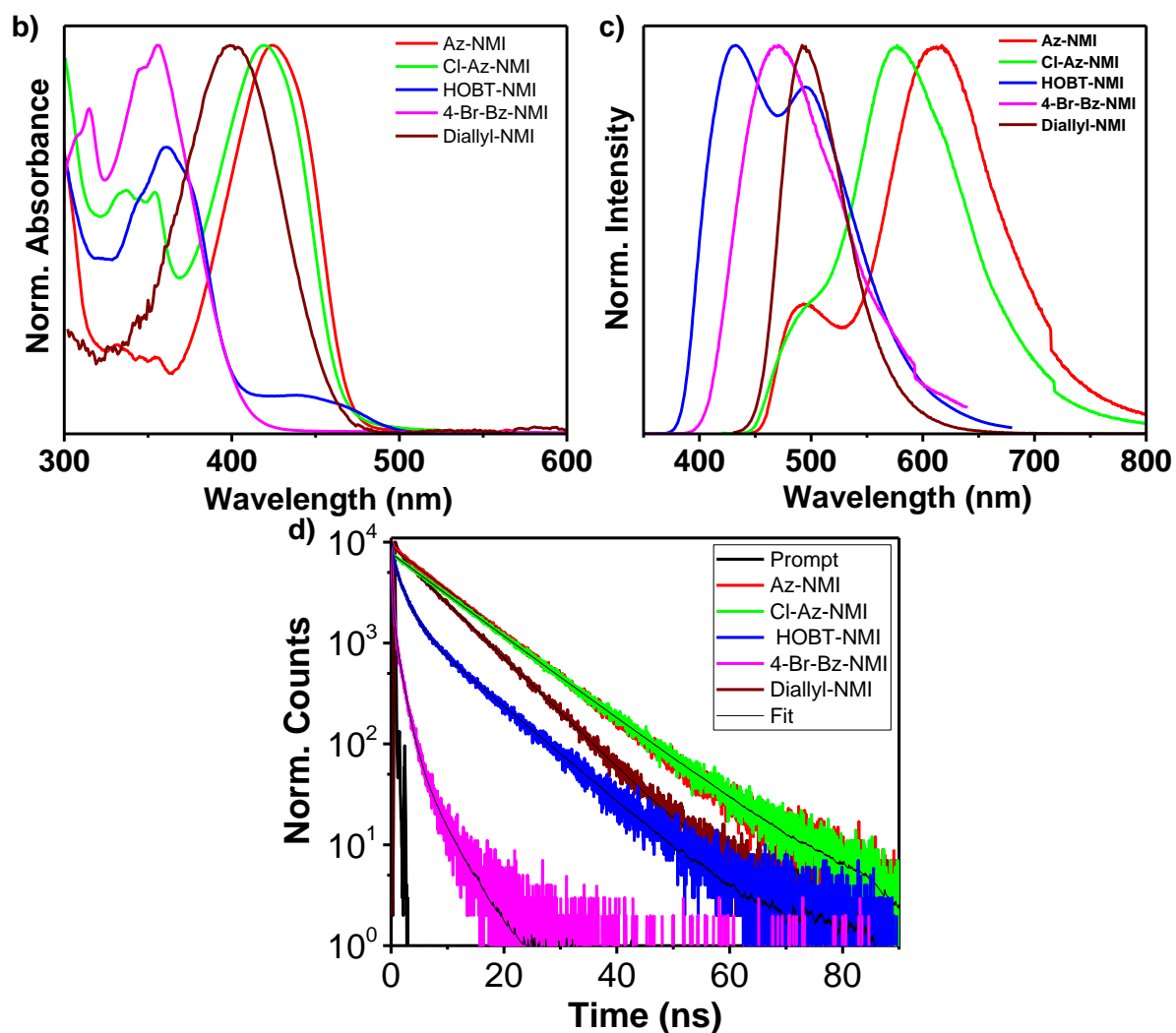


Figure 5.1. Normalized a) absorption and b) emission spectra of naphthalimide-based TADF molecules in MTHF solution ($C = 1 \times 10^{-5}$ M). c) Emission lifetime decay profile of naphthalimide-based molecules at 298 K.

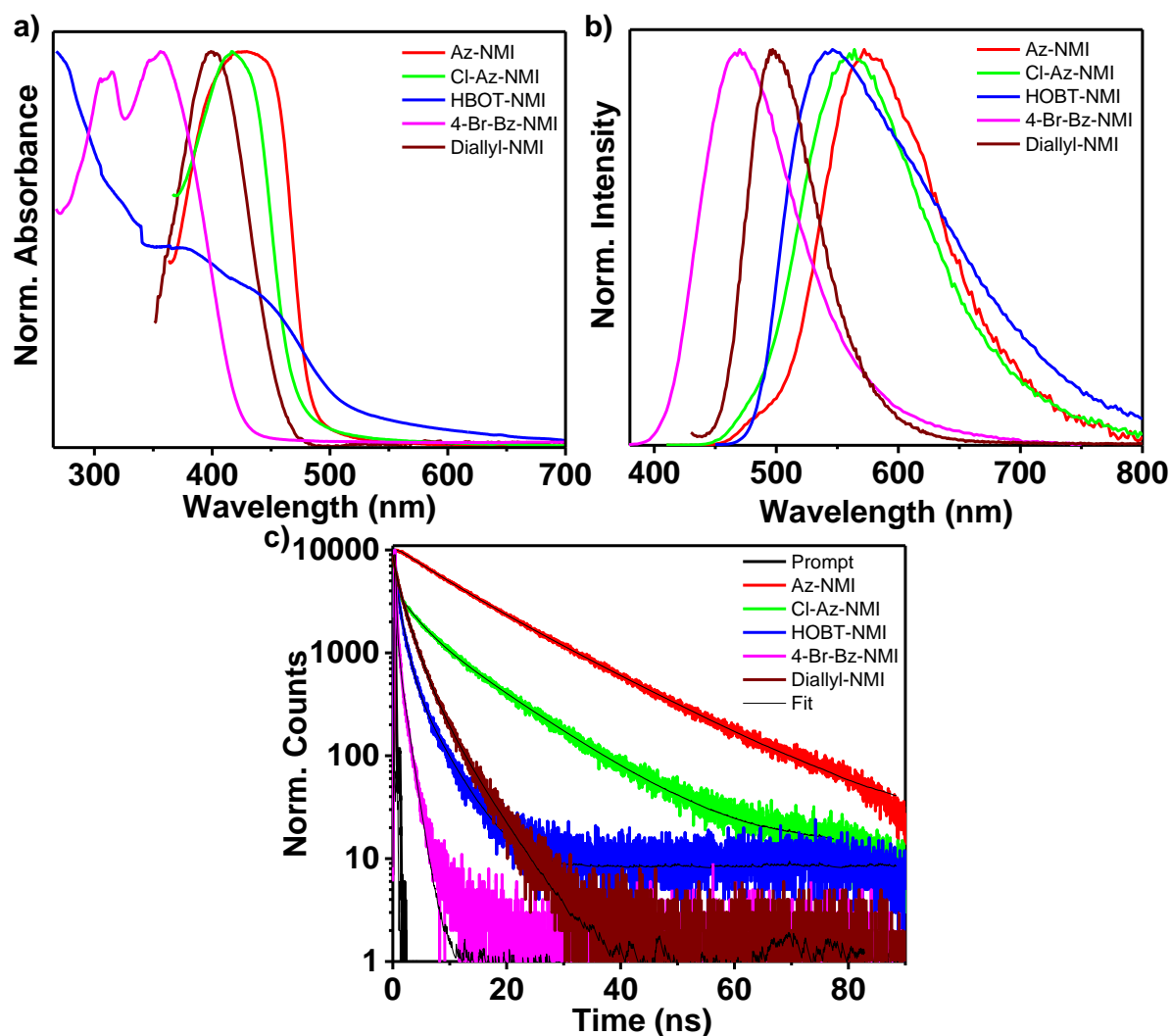


Figure 5.2. Normalized a) absorption and c) emission spectra of naphthalimide-based molecules in a neat liquid state ($\lambda_{\text{ex}} = 425$ nm for **Az-NMI**, $\lambda_{\text{ex}} = 410$ nm for **Cl-Az-NMI**, $\lambda_{\text{ex}} = 450$ nm for **HOBT-NMI**, $\lambda_{\text{ex}} = 360$ nm for **4-Br-Bz-NMI**, $\lambda_{\text{ex}} = 410$ nm for **di-allyl-NMI**). d) Emission lifetime decay profile of naphthalimide-based molecules in a neat liquid state at 298 K ($\lambda_{\text{ex}} = 374$ nm, $\lambda_{\text{mon}} = 580$ nm for **Az-NMI**, 580 nm for **Cl-Az-NMI**, 610 nm for **HOBT-NMI**, 500 nm for **4-Br-Bz-NMI**, 505 nm for **di-allyl-NMI**).

Furthermore, the photophysical properties of TADF liquids in solvent-free conditions were also investigated. The absorption spectra of TADF liquids in a neat liquid state offer slightly broad spectra in the range of 290-500 nm, and the corresponding emission bands cover the range of 400-800 nm (Figure 5.2a, b).

The spectral characteristics of TADF liquids in a neat state slightly vary from that of the solution state due to the possible molecular aggregation *via* weak intermolecular interaction in bulk liquid conditions. Naphthalimide-based solvent-free TADF liquids exhibit cyan to yellow colour emission with the highest quantum yield (QY) of 72 % for **di-allyl-NMI** in the neat liquid state (Table-1, 3). Fluorescence lifetime measurements in the neat state showed lifetime decay with major lifetimes of 14.4 ns (79.72 %) for **Az-NMI**, 11.5 ns (73.16 %) for **Cl-Az-NMI**, 4.24 ns (49.00 %) for **HOBt-NMI**, 1.06 ns (67.45 %) for **4-Br-Bz-NMI** and 5.10 ns (62.41 %) for **di-allyl-NMI**, respectively (Figure 5.2c and Table 1, 4).

As shown in Figure 5.3, a similar spectral feature was noticed for naphthalimide-based liquid in the steady-state emissions at 298 K and 77 K (Figure 5.3a-e). The identical emission spectra at 298 and 77 K points to the existence of a relatively small energy gap between the lowest singlet and triplet energy levels. The emission maxima of naphthalimide-based liquid varied as 570, 550, 530, 475, and 515 nm, respectively (Figure 5.3 and Table 1). No significant difference in emission colour was noticed for the thin film and neat SOLs. All naphthalimide-based liquid molecules showed delayed fluorescence of TADF nature in the neat liquid state, as demonstrated by the lifetime and spectral pattern at 77 K and 298 K (Figures 5.3, 5.4 and Tables 1, 5 and 6).

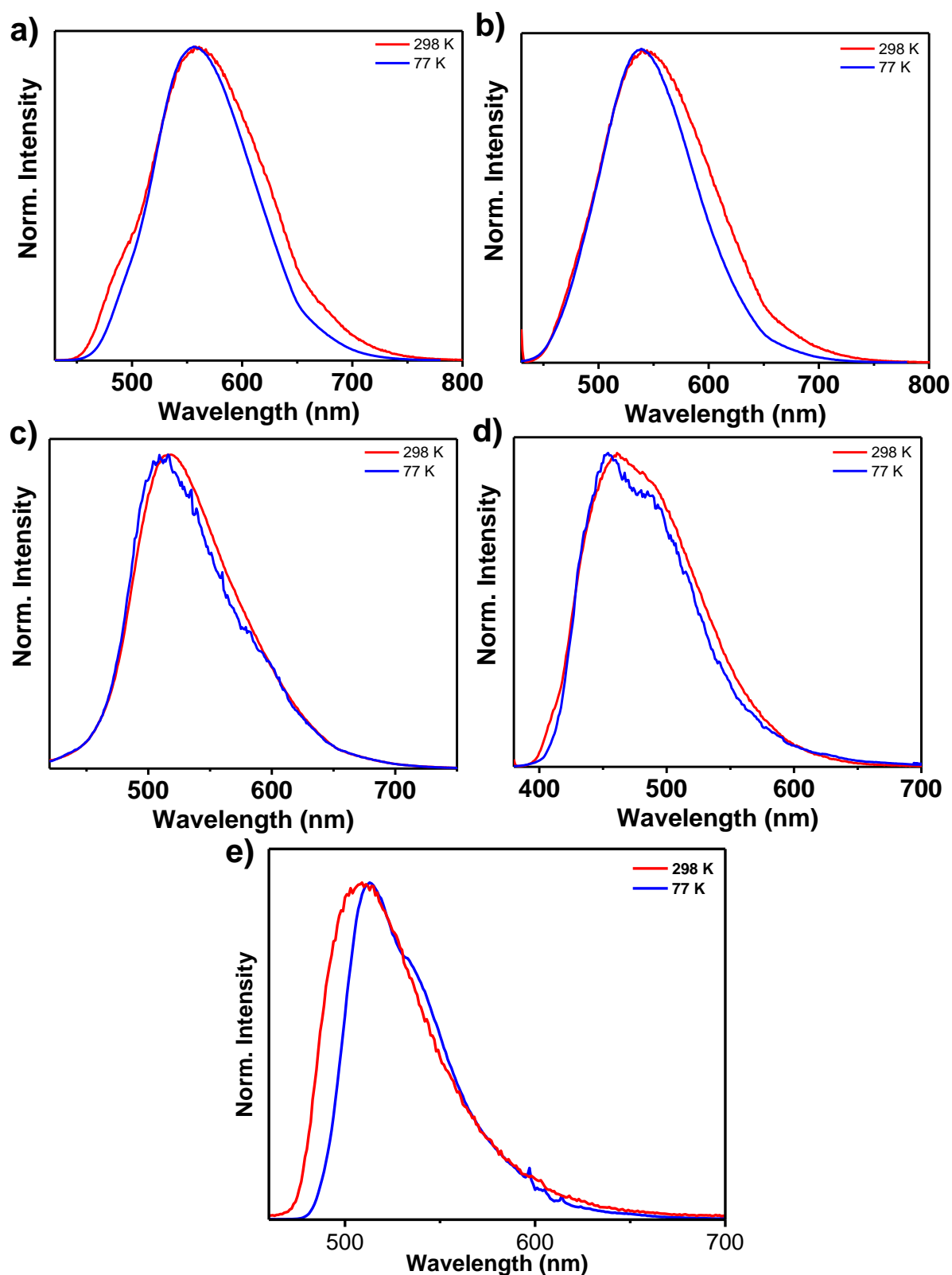


Figure 5.3. Comparison of the emission spectra of naphthalimide-based liquid in neat state at 298 and 77 K ($\lambda_{\text{ex}} = 425$ nm for Az-NMI, $\lambda_{\text{ex}} = 410$ nm for Cl-Az-NMI, $\lambda_{\text{ex}} = 450$ nm for HOBT-NMI, $\lambda_{\text{ex}} = 360$ nm for 4-Br-Bz-NMI, $\lambda_{\text{ex}} = 410$ nm for di-allyl-NMI).

A detailed analysis has been performed to establish the TADF feature of naphthalimide-based liquid molecules. A comparison of the PL and phosphorescence emission spectra (Figure 5.4), temperature-dependent lifetime (Figure 5.5), and excitation intensity-dependent emission profile (Figure 5.6) further confirmed the TADF feature of these molecules. Interestingly, a phosphorescence peak resembling the steady-state emission, located at 585 nm (**Az-NMI**), 575 nm (**Cl-Az-NMI**), 560 nm (**HOBt-NMI**), 480 nm (**4-Br-Bz-NMI**) and 520 nm (**di-allyl-NMI**) was observed when 0.1 ms detector delay was applied in the phosphorescence spectral measurement (Figure 5.4a-e). It has to be noticed that similarity and significant overlap between the fluorescence and phosphorescence spectra exist, and it confirms the minimal singlet-triplet energy gap (ΔE_{ST}) supporting TADF.²¹ Though the steady-state emissions at 298 and 77 K look identical, it slightly differ from the phosphorescence spectra.

Additionally, it has been supported by the temperature-dependent lifetime decay profile of naphthalimide-based liquid, and it demonstrates the origin of a typical TADF feature (Figure 5.5a-e and Tables 1, 5 and 6). Naphthalimide-based liquid molecules show an increase in τ_{TADF} upon increasing the temperature from 77 to 298 K (Figure 5.5a-e). The precisely linear dependence of TADF with excitation intensity confirms the intramolecular origin of the delayed emission. Thus, the source of the delayed emission is conclusively attributed to a thermally activated process, rather than triplet-triplet annihilation (Figure 5.6a-e).

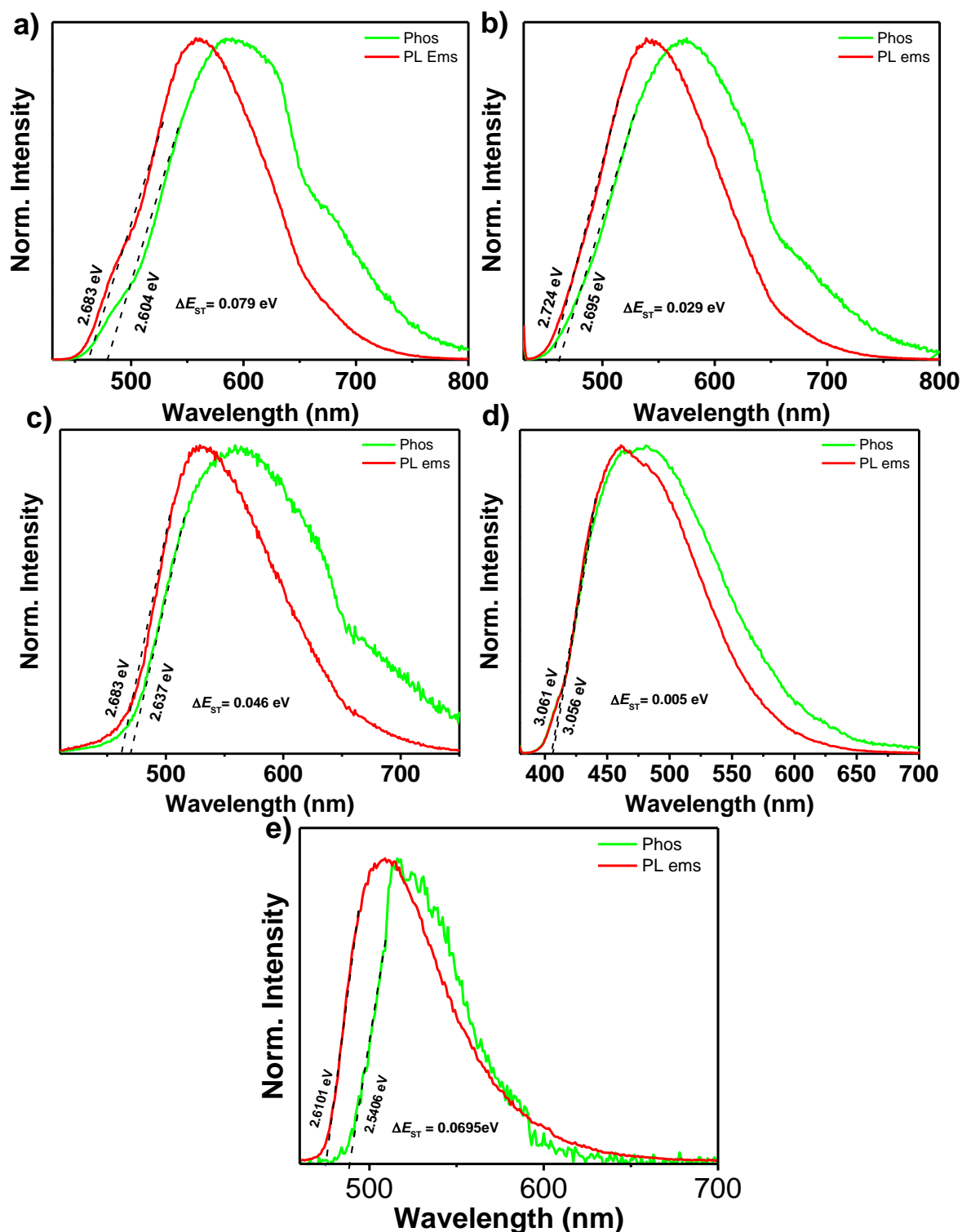


Figure 5.4. Comparison of the PL and phosphorescence emission spectra of naphthalimide-based liquid in neat state at 298 K ($\lambda_{\text{ex}} = 425$ nm for **Az-NMI**, $\lambda_{\text{ex}} = 410$ nm for **Cl-Az-NMI**, $\lambda_{\text{ex}} = 450$ nm for **HOBT-NMI**, $\lambda_{\text{ex}} = 360$ nm for **4-Br-Bz-NMI**, $\lambda_{\text{ex}} = 410$ nm for **di-allyl-NMI**).

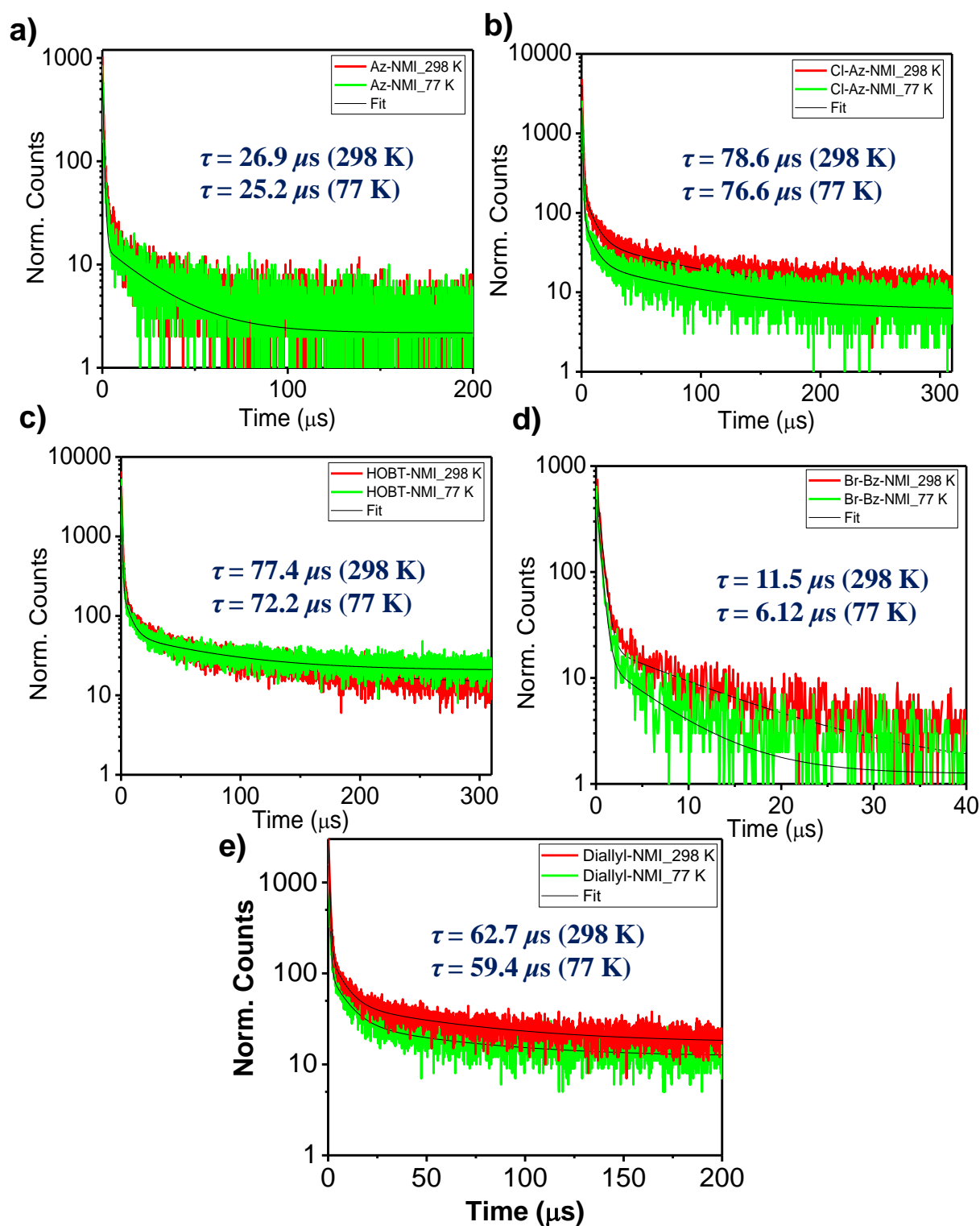


Figure 5.5. Temperature-dependent TADF lifetime for molecule a) Az-NMI, b) Cl-Az-NMI, c) HOBT-NMI, d) 4-Br-Bz-NMI and e) di-allyl-NMI in the neat state.

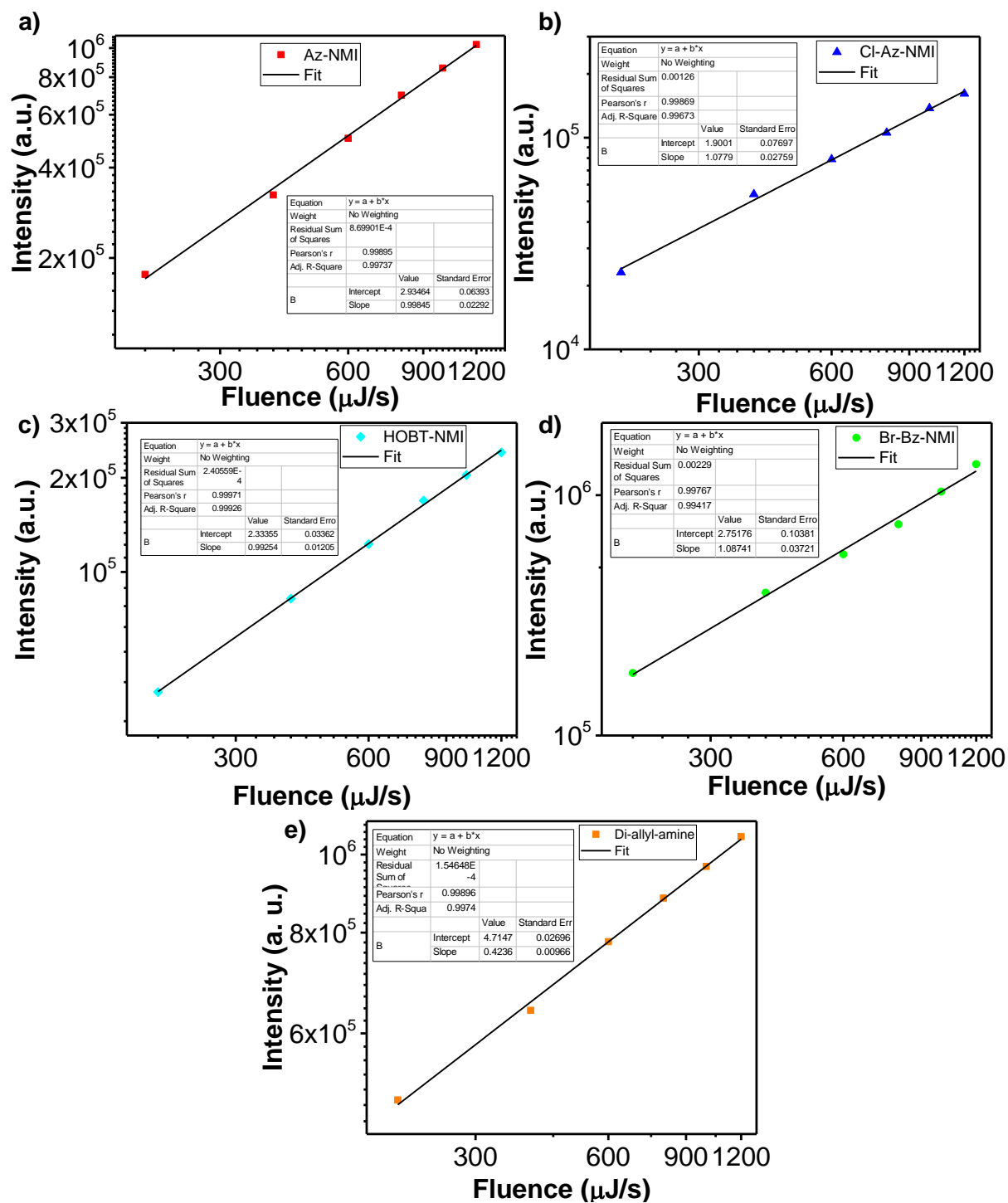


Figure 5.6. Excitation intensity-dependent emission profile of TADF liquids

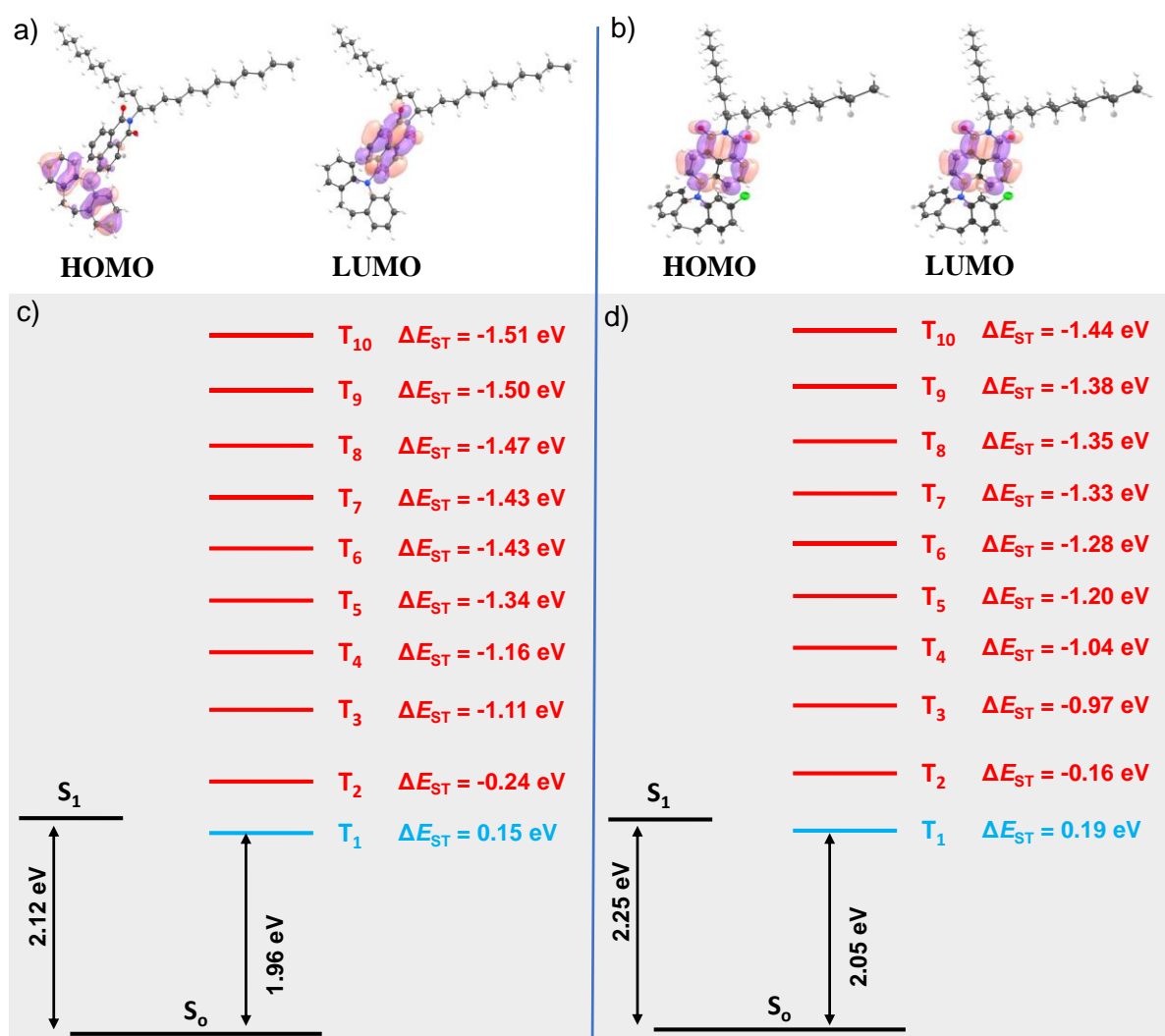


Figure 5.7. HOMO and LUMO frontier molecular orbitals of a) Az-NMI b) Cl-Az-NMI and calculated energy level diagram showing ΔE_{ST} for c) Az-NMI d) Cl-Az-NMI from DFT calculations.

Further, a series of TD-DFT computations were carried out for naphthalimide-based liquid using the Gaussian 09 program. It has been noticed that, in the case of Az-NMI molecule, HOMO is located on the azepine ring (π -type), and LUMO is delocalized on the naphthalene ring with partially separated frontier energy levels for a small ΔE_{ST} (Figure 5.7a). Whereas in the case of Cl-Az-NMI, HOBT-NMI, and 4-Br-Bz-NMI molecules, HOMO is located on the naphthalene ring (π -type), and LUMO is delocalized between the B-C p-orbital with significant overlap (Figure 5.7b, 5.8 a and b). On examining ΔE_{ST} of Az-

NMI molecule, triplet states T_1 is nearly degenerate with the first singlet excited state (S_1) having ΔE_{ST} of 0.15 eV. Similarly, ΔE_{ST} for **Cl-Az-NMI** is 0.19 eV, ΔE_{ST} for **HOBT-NMI** is 1.26 eV, and for **4-Br-Bz-NMI** ΔE_{ST} is 0.95 eV, respectively. The triplet states T_3 and T_4 of **HOBT-NMI** are nearly degenerate, with the first singlet excited state (S_1) having ΔE_{ST} of 0.13 and 0.05 eV, and triplet state T_2 of **4-Br-Bz-NMI** is degenerate with the first singlet excited state (S_1) having ΔE_{ST} of 0.76 eV, respectively. Thus, it is clear that naphthalimide-based liquid molecules have well-matched singlet and triplet energy states and hence help in efficient rISC from triplet to the singlet state.

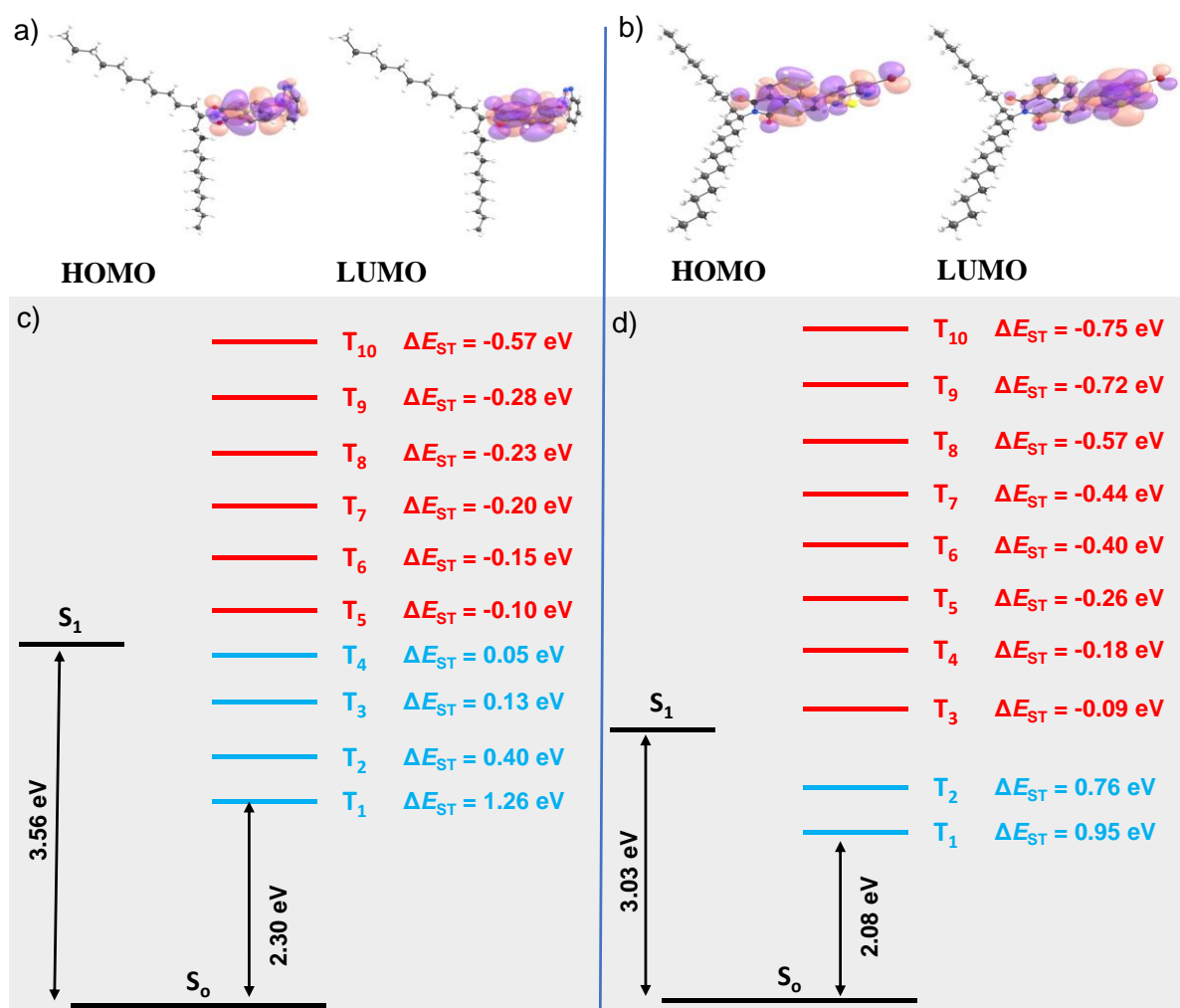


Figure 5.8. HOMO and LUMO frontier molecular orbitals of a) **HOBT-NMI** b) **4-Br-Bz-NMI** and calculated energy level diagram showing ΔE_{ST} for c) **HOBT-NMI** d) **4-Br-Bz-NMI** from DFT calculations.

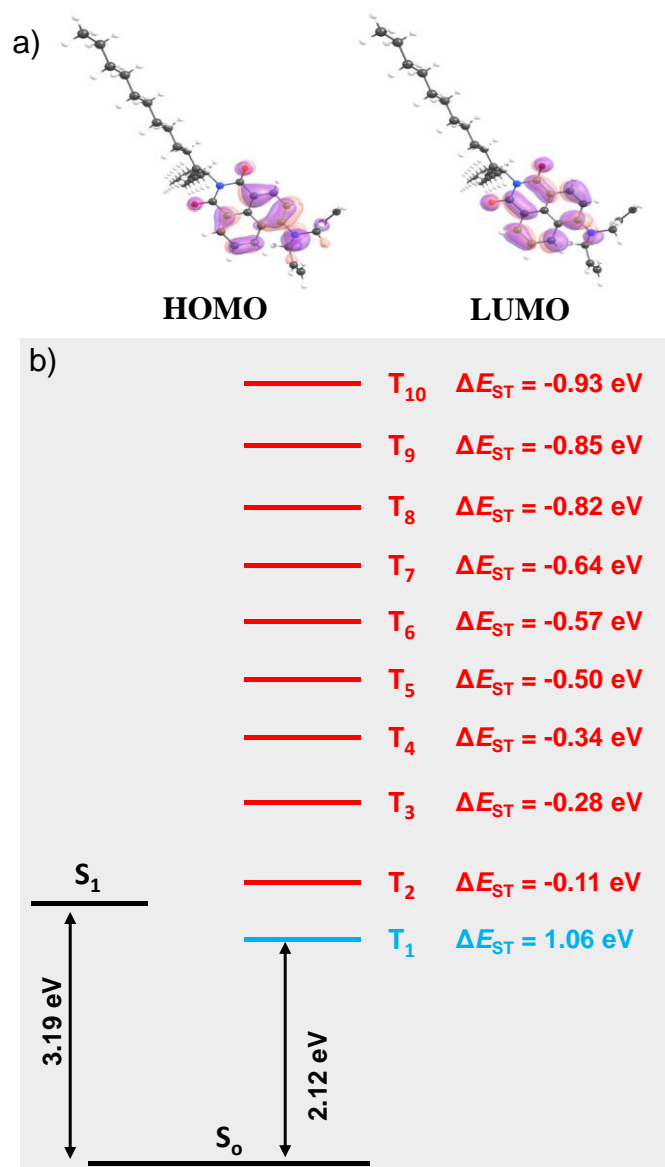


Figure 5.9. a) HOMO and LUMO frontier molecular orbitals of **di-allyl-NMI** b) calculated energy level diagram showing ΔE_{ST} for **di-allyl-NMI** from DFT calculations.

After successful synthesis and photophysical studies of polymerizable luminescent derivative, we synthesized cross-linked 2D-polymer (**NMI2VB**) by visible light-assisted free-radical and thermochemical polymerization methods. A commercially available crosslinker (CL), divinylbenzene was used to widen the scope of polymerizable liquids and prepare stable films. A general procedure is provided as follows, firstly, a polymerisable blend of liquid **di-allyl-NMI** and CL

was prepared, and later photo initiator (**PI**), benzoyl peroxide, was added. SOL hybrid was cast on a quartz plate by the doctor blade method, and the polymerization was carried out by thermal and photo-polymerization. Further, the film was photopolymerized by irradiating with visible light (400-800 nm) irradiation for about 3 hours.

The polymerizable blends were prepared by using 10 mg of liquid **di-allyl-NMI** with varying amounts of **CL** (2, 5, and 10 mol%) in the presence of **PI** (1 wt%) and irradiated for 3 h (**NMI2VB**). No effective polymerization has been observed in the first two cases. An increase in the amount of **CL** from 5 to 10 mol% is the optimum concentration to form a reasonably stable and uniform **NMI2VB** film. The emission spectrum of **NMI2VB** shows emissions ranging from 480 to 680 nm (Figure. 5.10b, d). Further, to improve the polymerization and to reduce the photobleaching of the polymer, the liquid blend was polymerised without using **PI** by both methods (Photo and thermal), and we could able to achieve a stable and uniform film. In the thermal polymerization method, a quartz plate having **SOL** coating was heated on a hot plate at 80 °C for 3 hours under an inert atmosphere. Optimizing the polymer blend by varying the amount of **CL** and **PI** has enabled stable **NMI2VB** polymer films (Table 7). The emission spectrum of **NMI2VB** polymer film without the use of **PI** shows broad emission covering from 500 to 650 nm (Figure 5.10b, d). The corresponding photograph of the **NMI2VB** polymer films under UV light ($\lambda_{\text{ex}} = 365 \text{ nm}$) after photopolymerization and thermal polymerization are shown in Figure 5.10a,b.

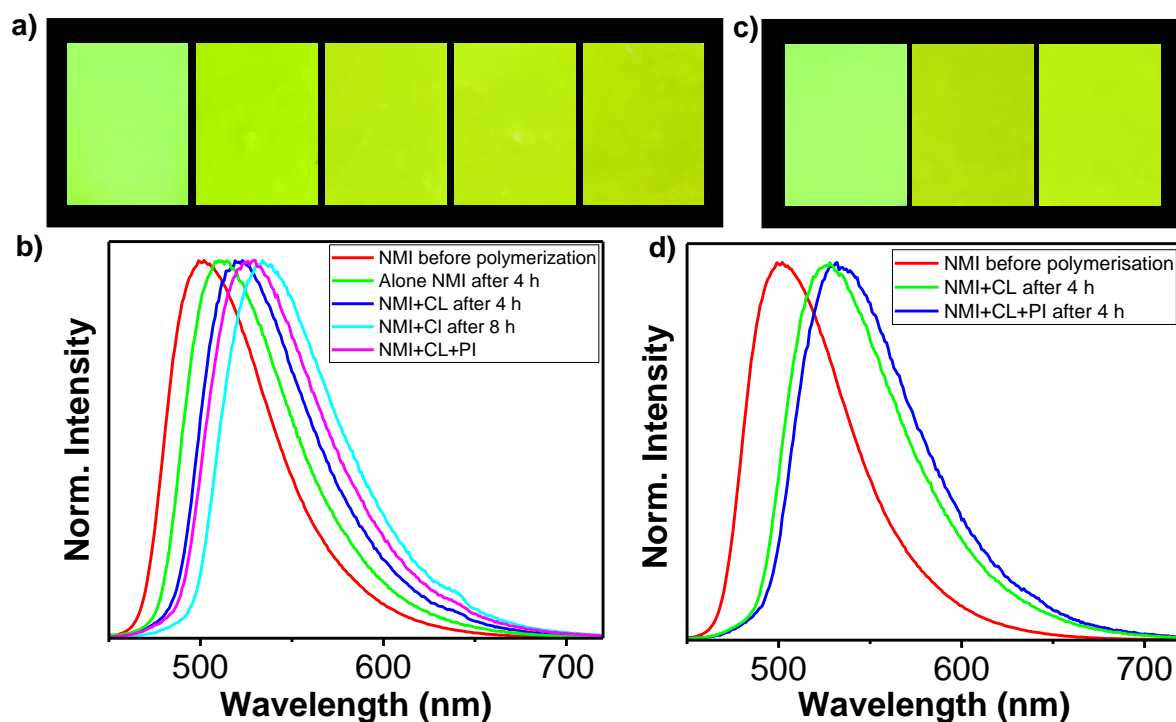


Figure 5.10. Photograph of the **NMI2VB** polymer films under UV light ($\lambda_{\text{ex}} = 365 \text{ nm}$) in the dark a) after photopolymerization, b) thermal polymerization. Comparison of the steady-state emission spectra of **NMI2VB** before and after b) photopolymerization d) thermal polymerization ($\lambda_{\text{ex}} = 425 \text{ nm}$).

Table 1. Photophysical parameters of naphthalimide-based TADF SOLs.

Molecules	λ_{abs} (nm) (Sol. ⁿ) ^a	λ_{abs} (nm) (Neat) ^a	λ_{em} (nm) (Sol. ⁿ) ^b	λ_{em} (nm) (Neat) ^b	τ (ns) (Neat) ^c	τ (μs) (Neat) ^d	Φ_{PL} (%) (Neat) ^f	S_1 (eV) ^g	T_1 (eV) ^g	ΔE_{ST} (eV) ^g
Az-NMI	425	430	612	570	14.4	26.9	42	2.683	2.604	0.079
Cl-Az-NMI	415	420	575	550	11.5	78.6	47	2.724	2.695	0.029
HOBT-NMI	440	450	495	530	4.24	77.4	32	2.683	2.637	0.046
4-Br-Bz-NMI	355	360	470	475	1.06	11.5	67	3.061	3.056	0.005
di-allyl-NMI	400	410	497	515	5.10	62.7	72	2.610	2.540	0.069

a) Absorption maxima, b) Emission maxima, c) Emission lifetime in Neat State, d) TADF lifetime in Neat State, Photoluminescence Quantum Yield in e) Solution State f) Neat State, g) Experimental S_1 and T_1 energies estimated from the Fluorescence and Phosphorescence spectra in Neat State.

Table 2. Emission lifetime of naphthalimide-based liquid in MTHF solution ($C = 10^{-5}$ M) at 298 K.

Molecules	Lifetime (ns)	CHISQ (χ^2) values
Az-NMI	$\tau_1 = 0.17$ (01 %) $\tau_2 = 10.0$ (99 %)	1.23
Cl-Az-NMI	$\tau_1 = 0.93$ (33 %) $\tau_2 = 9.35$ (65 %) $\tau_3 = 0.10$ (02 %)	1.10
HOBT-NMI	$\tau_1 = 1.91$ (35 %) $\tau_2 = 9.19$ (60 %) $\tau_3 = 0.18$ (05 %)	1.19
4-Br-Bz-NMI	$\tau_1 = 1.21$ (39 %) $\tau_2 = 4.13$ (51 %) $\tau_3 = 0.17$ (10 %)	1.13
di-allyl-NMI	$\tau_1 = 0.69$ (04 %) $\tau_2 = 8.03$ (96 %)	1.02

Table 3. Emission quantum yield of naphthalimide-based liquid in neat state at 298 K.

Compounds	Quantum Yield (%)
Az-NMI	42
Cl-Az-NMI	47
HOBT-NMI	32
4-Br-Bz-NMI	67
di-allyl-NMI	72

Table 4. Emission lifetime of naphthalimide-based liquid in the neat state at 298 K.

Molecules	Lifetime (ns)	CHISQ (χ^2) values
-----------	---------------	---------------------------

Az-NMI	$\tau_1 = 5.71$ (19 %) $\tau_2 = 14.4$ (80 %) $\tau_3 = 0.16$ (01 %)	1.25
Cl-Az-NMI	$\tau_1 = 3.29$ (21 %) $\tau_2 = 11.5$ (73 %) $\tau_3 = 0.45$ (06 %)	1.22
HOBt-NMI	$\tau_1 = 1.15$ (34 %) $\tau_2 = 4.24$ (49 %) $\tau_3 = 0.11$ (17 %)	1.19
4-Br-Bz-NMI	$\tau_1 = 0.16$ (33 %) $\tau_2 = 1.06$ (67 %)	1.14
di-allyl-NMI	$\tau_1 = 0.42$ (10 %) $\tau_2 = 2.01$ (28 %) $\tau_3 = 5.10$ (62 %)	1.04

Table 5. TADF lifetime of naphthalimide-based liquid in the neat state at 298 K.

Molecules	TADF lifetime (μs)	CHISQ (χ^2) values
Az-NMI	$\tau_1 = 0.67$ (44 %) $\tau_2 = 26.9$ (56 %)	1.14
Cl-Az-NMI	$\tau_1 = 7.16$ (17 %) $\tau_2 = 78.6$ (44 %) $\tau_3 = 0.60$ (39 %)	1.16
HOBt-NMI	$\tau_1 = 6.42$ (16 %) $\tau_2 = 77.4$ (44 %) $\tau_3 = 0.66$ (40 %)	1.20
4-Br-Bz-NMI	$\tau_1 = 11.5$ (53 %) $\tau_2 = 0.44$ (47 %)	1.08
di-allyl-NMI	$\tau_1 = 6.37$ (19 %) $\tau_2 = 62.7$ (43 %) $\tau_3 = 0.58$ (38 %)	1.10

Table 6. Temperature-dependent TADF lifetime decay of naphthalimide-based liquid in the neat state.

Molecules	Condition	Lifetime (μs)	CHISQ (χ^2) values
------------------	------------------	-------------------------------------	---

Az-NMI	298 K	$\tau_1 = 0.67$ (44 %) $\tau_2 = 26.9$ (56 %)	1.14
	77 K	$\tau_1 = 0.63$ (43 %) $\tau_2 = 25.2$ (57 %)	1.21
Cl-Az-NMI	298 K	$\tau_1 = 7.16$ (17 %) $\tau_2 = 78.6$ (44 %) $\tau_3 = 0.60$ (39 %)	1.16
	77 K	$\tau_1 = 7.38$ (19 %) $\tau_2 = 77.6$ (43 %) $\tau_3 = 0.62$ (38 %)	1.20
HOBt-NMI	298 K	$\tau_1 = 6.42$ (16 %) $\tau_2 = 77.4$ (44 %) $\tau_3 = 0.66$ (40 %)	1.20
	77 K	$\tau_1 = 5.57$ (16 %) $\tau_2 = 72.2$ (44 %) $\tau_3 = 0.59$ (40 %)	1.24
4-Br-Bz-NMI	298 K	$\tau_1 = 11.5$ (53 %) $\tau_2 = 0.44$ (47 %)	1.08
	77 K	$\tau_1 = 6.12$ (68 %) $\tau_2 = 0.39$ (32 %)	1.01
di-allyl-NMI	298 K	$\tau_1 = 6.37$ (19 %) $\tau_2 = 62.7$ (43 %) $\tau_3 = 0.58$ (38 %)	1.10
	77 K	$\tau_1 = 7.87$ (24 %) $\tau_2 = 59.4$ (41 %) $\tau_3 = 0.59$ (35 %)	1.10

Table 7. Optimization of the polymerization condition for the preparation of NMI2VB.

NMI2VB	Di-allyl-NMI	CL	PI	Time (hours)
a	10 mg	2 mol%	1 wt%	3 h

b	10 mg	5 mol%	1 wt%	3 h
c	10 mg	10 mol%	1 wt%	3 h
d	10 mg	10 mol%	-	3 h

CL = Cross-linker, PI = Photoinitiator

5.5 Conclusion

In conclusion, an attempt toward the TADF liquid accomplished a series of solvent-free organic liquid molecules having TADF through minor structural modifications. The solvent-free TADF liquid exhibit cyan to yellow colour emission with a delayed lifetime of up to **79** μ s. Furthermore, a polymerizable group on one of the solvent-free TADF liquid was utilised for both thermal and photo-polymerizations. **Di-allyl-NMI** liquid provides a low viscous fluid matrix for crosslinker (**CL**) by physical mixing to develop polymerizable blends. The hybrid liquid films enabled to develop stable polymer films on glass surface by photo as well as thermal polymerization. Even though we are able to prepare polymer film, our efforts will be continued to make free-standing stable polymer film and its further applications. The high processability of TADF liquids to form large-area thin films without compromising the emission features offer a bright future for TADF SOLs and will emerge as a potential candidate in lighting and display applications.

5.6 References

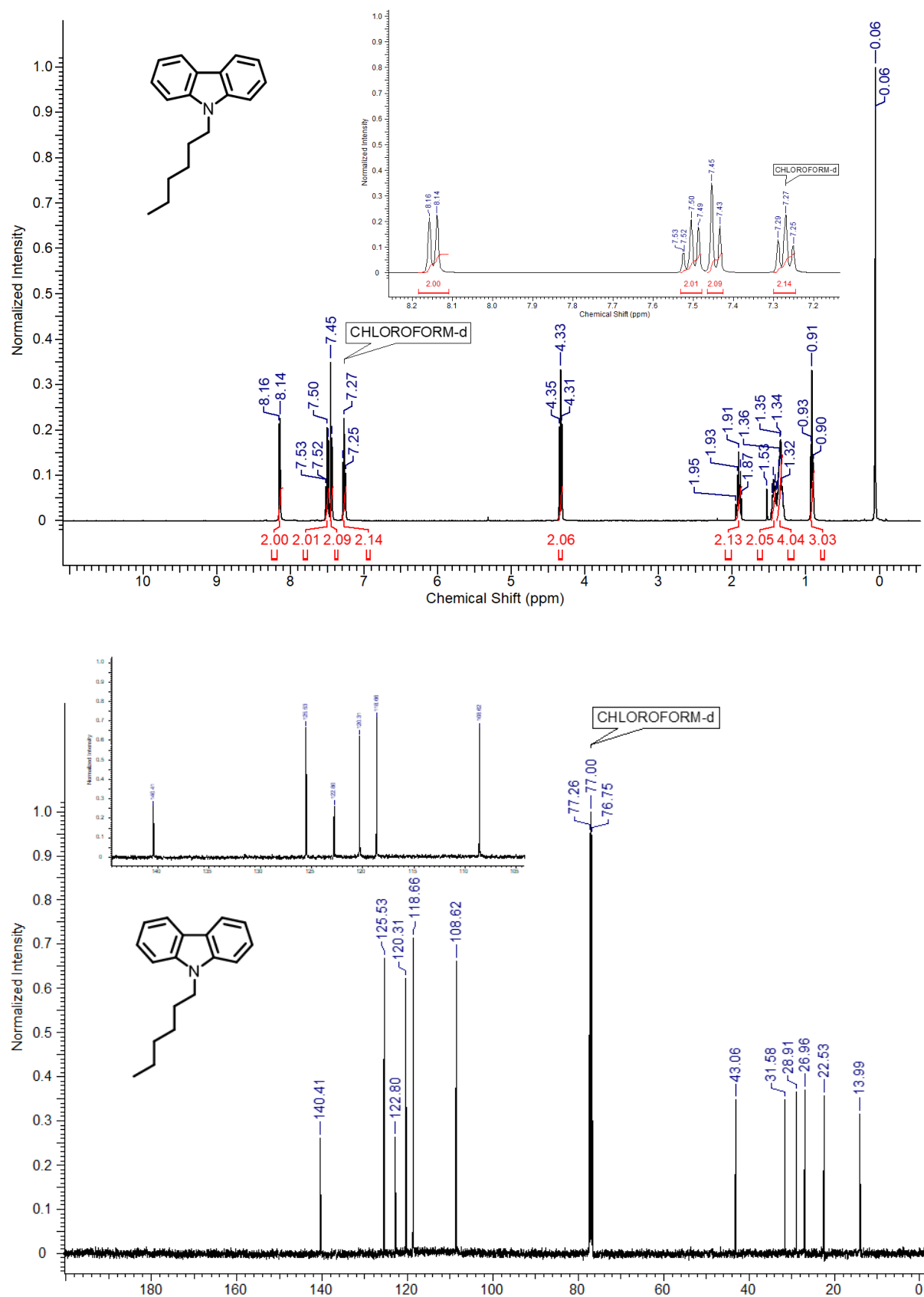
1. a) A. W. Perriman, and S. Mann, *ACS Nano* **2011**, 5, 6085; b) M. Armand, F. Endres, D. R. MacFarlane, H. Ohno, and B. Scrosati, *Nat. Mater.* **2009**, 8, 621.

2. a) W. Perriman, A. P. S. Brogan, H. Cölfen, N. Tsoureas, G. R. Owen, and S. Mann, *Nat. Chem.* **2010**, *2*, 622; b) F. J. M. Hoeben, P. Jonkheijm, E. W. Meijer, A. P. H. J. Schenning, *Chem. Rev.* **2005**, *105*, 1491.
3. L. Maggini, and D. Bonifazi, *Chem. Soc. Rev.* **2012**, *41*, 211; b) M. Wang, and F. Wudl, *J. Mater. Chem.* **2012**, *22*, 24297; c) Y. Yamamoto, *Sci. Technol. Adv. Mater.* **2012**, *13*, 033001; d) G. M. Farinola, and R. Ragni, *Chem. Soc. Rev.* **2011**, *40*, 3467; e) A. P. H. J. Schenning, and E. W. Meijer, *Chem. Commun.* **2005**, 3245.
4. a) H. Li, J. Choi, and T. Nakanishi, *Langmuir* **2013**, *29*, 5394; b) S. S. Babu, and T. Nakanishi, *Chem. Commun.*, **2013**, *49*, 9373.
5. a) T. Weil, E. Reuther, and K. Müllen, *Angew. Chem. Int. Ed.* **2002**, *41*, 1900; b) J. M. Serin, D. W. Brousmiche, and J. M. J. Fréchet, *Chem. Commun.* **2002**, 2605.
6. a) A. Adronov, and J. M. J. Fréchet, *Chem. Commun.* **2000**, 1701; b) S. L. Gilat, A. Adronov, and J. M. J. Fréchet, *Angew. Chem. Int. Ed.* **1999**, *38*, 1422.
7. a) X. Zhang, Y. Zeng, T. Yu, J. Chen, G. Yang, and Y. Li, *J. Phys. Chem. Lett.* **2014**, *5*, 2340; b) A. Ajayaghosh, C. Vijayakumar, V. K. Praveen, S. S. Babu, and R. Varghese, *J. Am. Chem. Soc.* **2006**, *128*, 7174.
8. a) T. Nakanishi, *Functional Organic Liquids*, Wiley-VCH, Weinheim **2019**. b) S. S. Babu, *Phys. Chem. Chem. Phys.* **2015**, *17*, 3950. c) S. S. Babu, J. Aimi, H. Ozawa, N. Shirahata, A. Saeki, S. Seki, A. Ajayaghosh, H. Möhwald, and T. Nakanishi, *Angew. Chem. Int. Ed.* **2012**, *51*, 3391. d) S. S. Babu, and T. Nakanishi, *Chem. Commun.*, **2013**, *49*, 9373. e) S. S. Babu, M. J. Hollamby, J. Aimi, H. Ozawa, A. Saeki, S. Seki, K. Kobayashi, K. Hagiwara, M. Yoshizawa, H. Möhwald, and T. Nakanishi, *Nat. Commun.* **2013**, *4*, 1969.
9. a) F. Lu, and T. Nakanishi, *Adv. Opt. Mater.*, **2019**, *7*, 1900176. b) Goudappagouda, A. Manthanath, V. C. Wakchaure, K. C. Ranjeesh, T. Das,

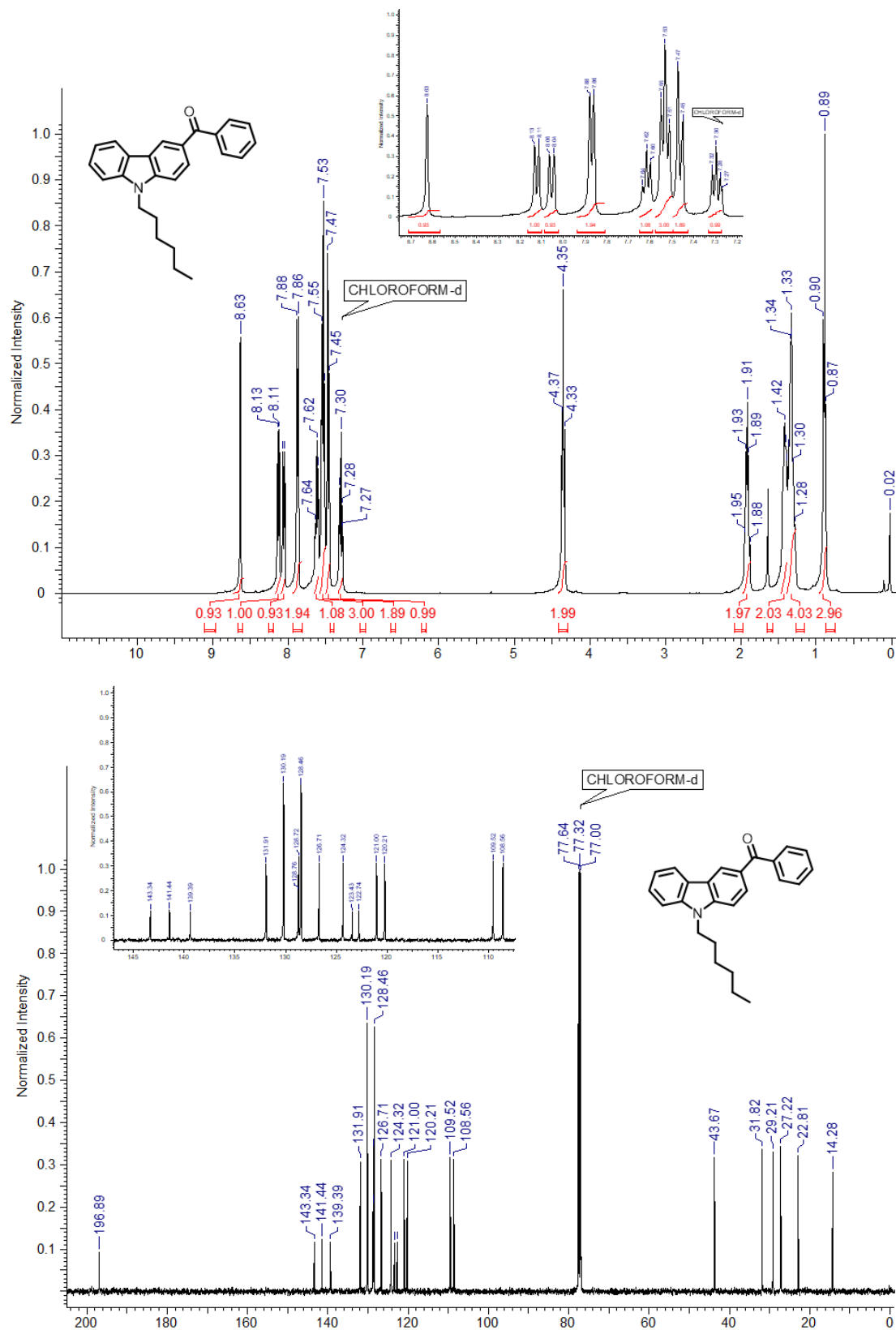
- K. Vanka, T. Nakanishi, and S. S. Babu, *Angew. Chem. Int. Ed.* **2019**, *58*, 2284.
10. a) V. C. Wakchaure, Goudappagouda, T. Das, S. Ravindranathan, and S. S. Babu, *Nanoscale*, **2021**, *13*, 10780. b) N. Kobayashi, T. Kasahara, T. Edura, J. Oshima, R. Ishimatsu, M. Tsuwaki, T. Imato, S. Shoji, and J. Mizuno, *Sci. Rep.*, **2015**, *5*, 14822.
11. a) A. Kamino, T. P. Bender, and R. A. Klenkler, *J. Phys. Chem. Lett.*, **2012**, *3*, 1002. b) Q. Zhang, B. Li, S. Huang, H. Nomura, H. Tanaka, and C. Adachi, *Nat. Photon.*, **2014**, *8*, 326.
12. F. Lu, E. A. Neal, and T. Nakanishi, *Acc. Chem. Res.* **2019**, *52*, 1834.
13. a) P. Duan, N. Yanai, and N. Kimizuka, *J. Am. Chem. Soc.* **2013**, *135*, 19056; b) T. Machida, R. Taniguchi, T. Oura, K. Sada, and K. Kokado, *Chem. Commun.* **2017**, *53*, 2378.
14. J.-C. Ribierre, L. Zhao, M. Inoue, P.-O. Schwartz, J.-H. Kim, K. Yoshida, A. S. D. Sandanayaka, H. Nakanotani, L. Mager, S. Mery, C. Adachi, *Chem. Commun.* **2016**, *52*, 3103.
15. J.-H. Kim, M. Inoue, L. Zhao, T. Komino, S. Seo, J.-C. Ribierre, and C. Adachi, *Appl. Phys. Lett.* **2015**, *106*, 053302.
16. S. Hirata, K. Kubota, H. H. Jung, O. Hirata, K. Goushi, M. Yahiro, and C. Adachi, *Adv. Mater.* **2011**, *23*, 889.
17. a) X. Zhu, Q. Niu, Y. Xu, G. Wu, G. Lia, J. Nie, and G. Ma, *J. Photochem. Photobiol. A*, **2018**, *353*, 101; b) A. Bagheri, and J. Jin, *ACS Appl. Polym. Mater.* **2019**, *1*, 593; c) T. Kooaira, K. Hayashi, and T. Ohnishi, *Polym. J.*, **1973**, *4*, 1; d) V. Vijayakumar, M. Ghosh, M. Kurian, A. Torris, S. Dilwale, M. V. Badiger, M. Winter, J. R. Nair, and S. Kurungot, *Small* **2020**, *16*, 2002528.
18. A. Sanguineti, M. Sassi, R. Turrisi, R. Ruffo, G. Vaccaro, F. Meinardi and L. Beverina, *Chem. Commun.*, **2013**, *49*, 1618.

19. A. D. Nidhankar, Goudappagouda, P. kothavade, S. D. Dongre, S. D. Veer, S. R. Dash, K. Rajeev, K. N. N. Unni, K. Shanmuganathan and S. S. Babu, Thermally Activated Delayed Fluorescent Solvent-free Organic Liquid Hybrids for Tunable Emission Applications, *Manuscript submitted*.
20. Z. Tian, Y. Liu, B. Tian, and J. Zhang, *Res Chem Intermed*, **2015**, *41*, 1157.
21. T. Serevičius, R. Skaisgiris, J. Dodonova, L. Jagintavičius, D. Banevičius, K. Kazlauskas, S. Tumkevičius, and S. Juršėnas, *ACS Appl. Mater. Interfaces*, **2020**, *12*, 10727.

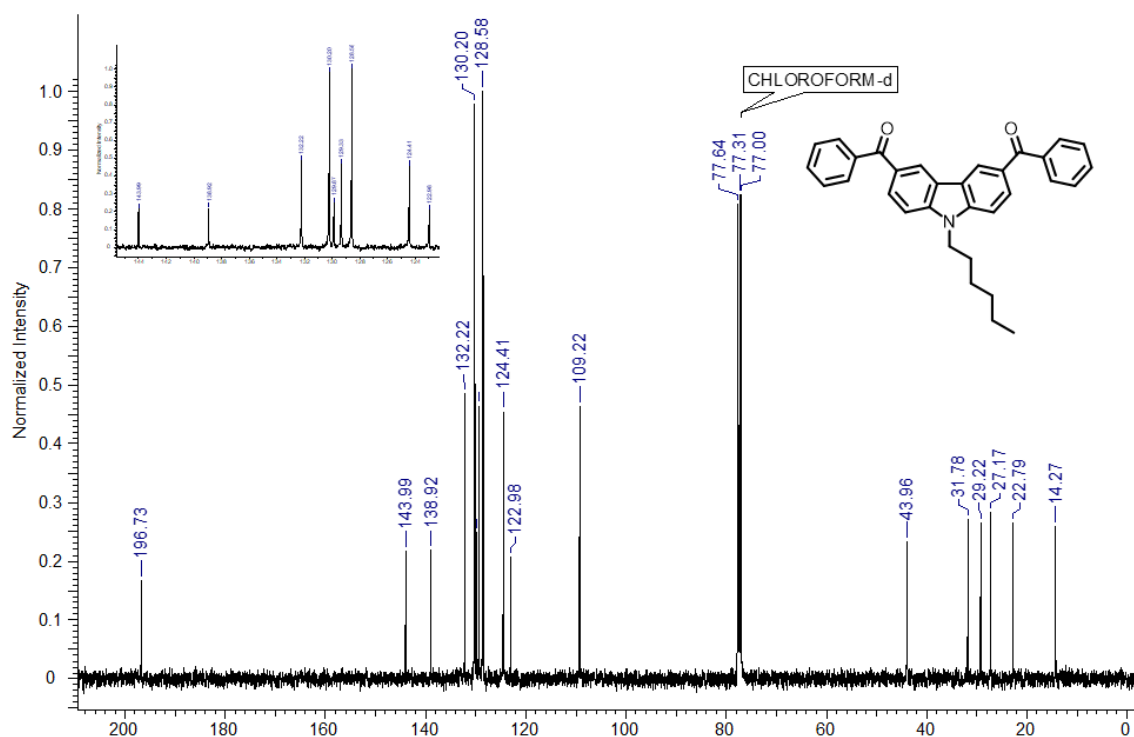
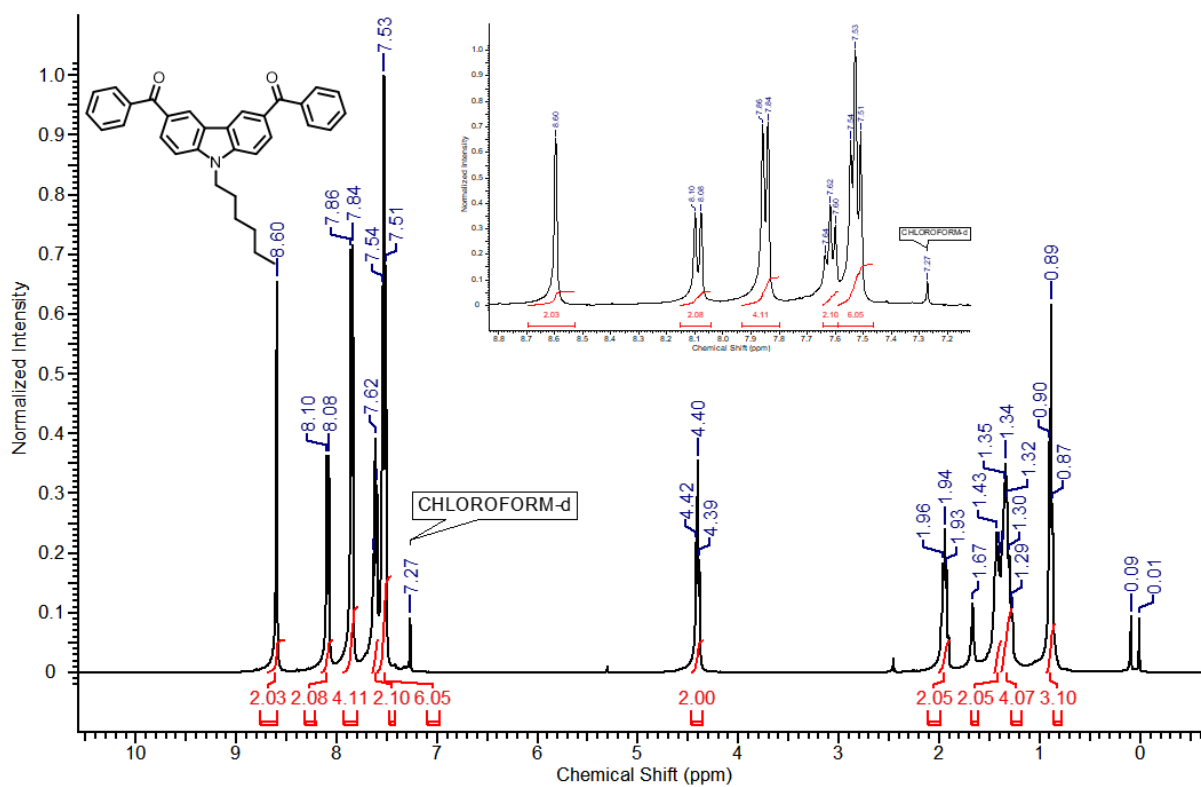
Characterization details of the synthesized compounds



^1H (top) and ^{13}C (bottom) NMR spectra of 9-hexyl-9H-carbazole (1).

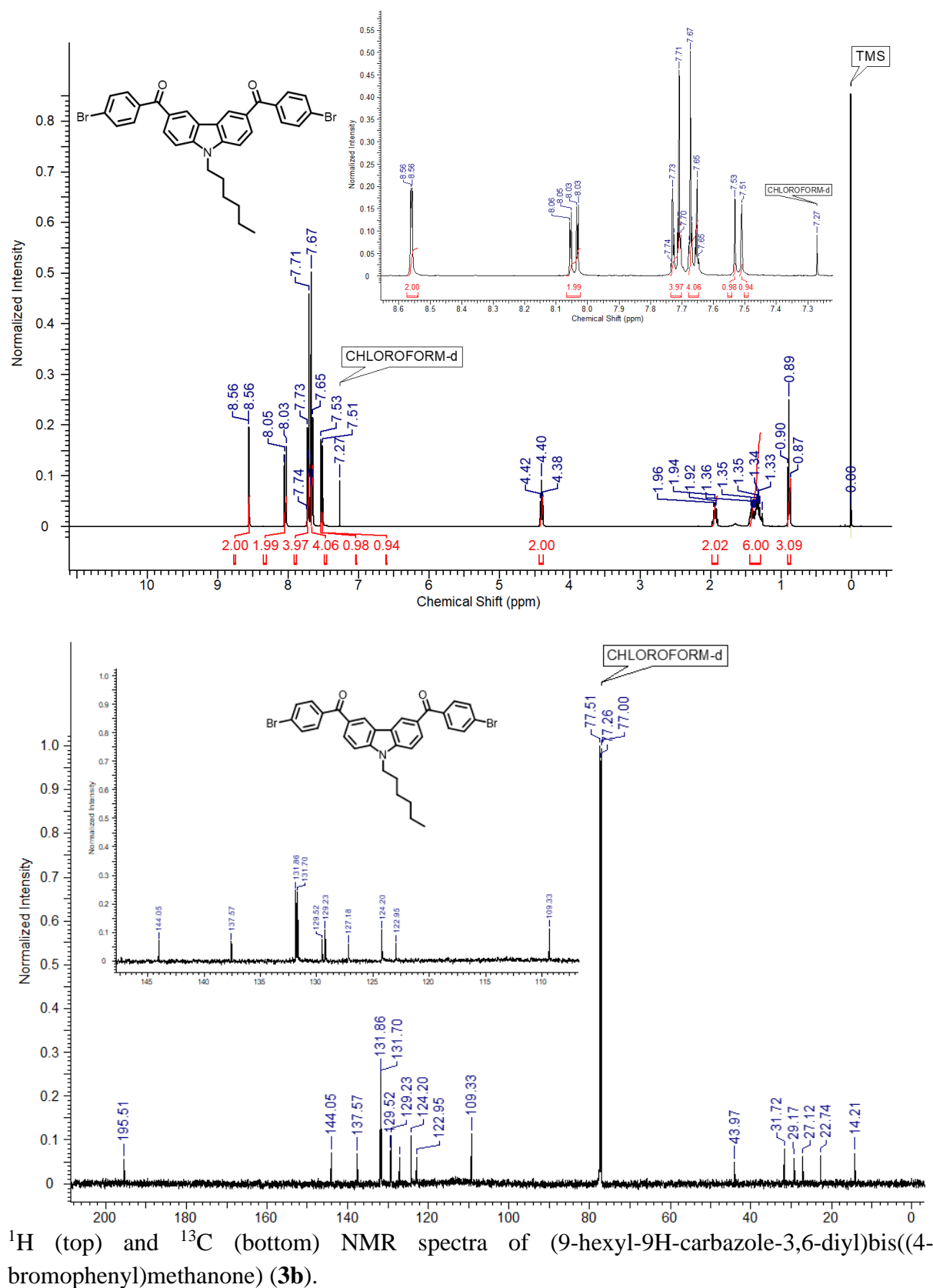


¹H (top) and ¹³C (bottom) NMR spectra of (9-Hexyl-9H-carbazol-3-yl)(phenyl)methanone (2).



¹H (top) and ¹³C (bottom) NMR spectra of (9-hexyl-9H-carbazole-3,6-diyl)bis(phenylmethanone) (**3a**).

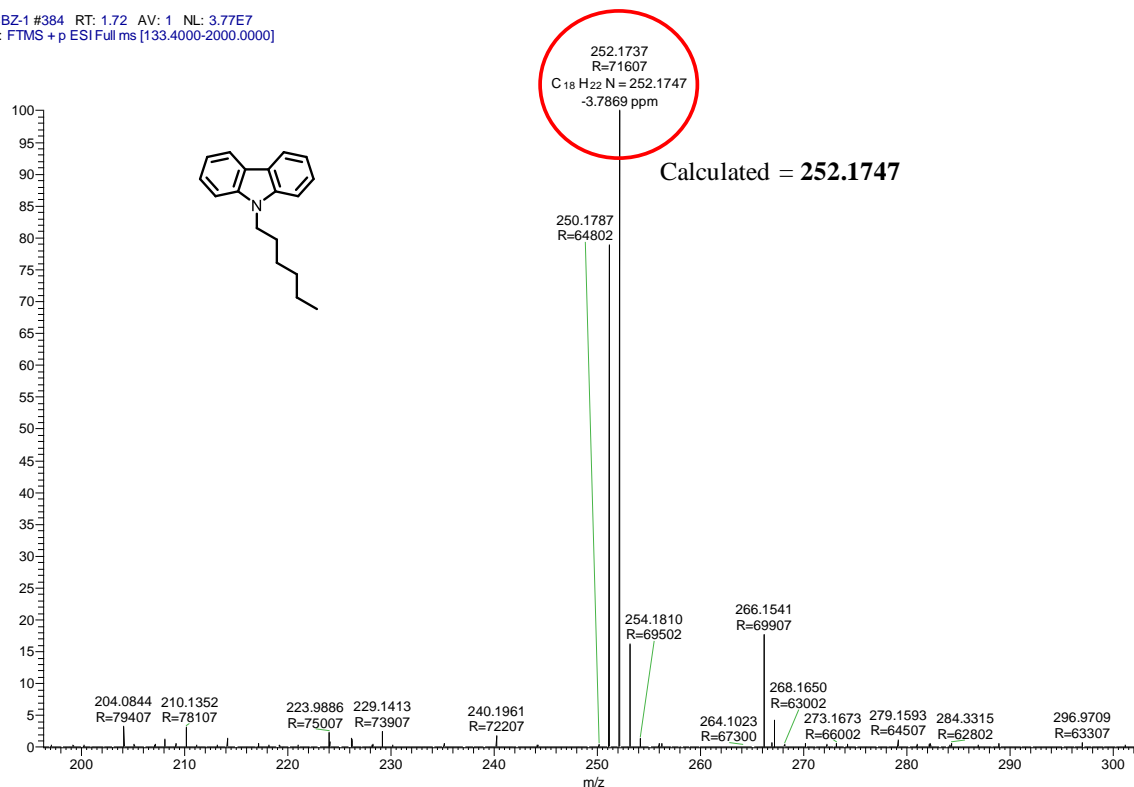
Characterization details of the synthesized molecules



^1H (top) and ^{13}C (bottom) NMR spectra of (9-hexyl-9H-carbazole-3,6-diyl)bis((4-bromophenyl)methanone) (**3b**).

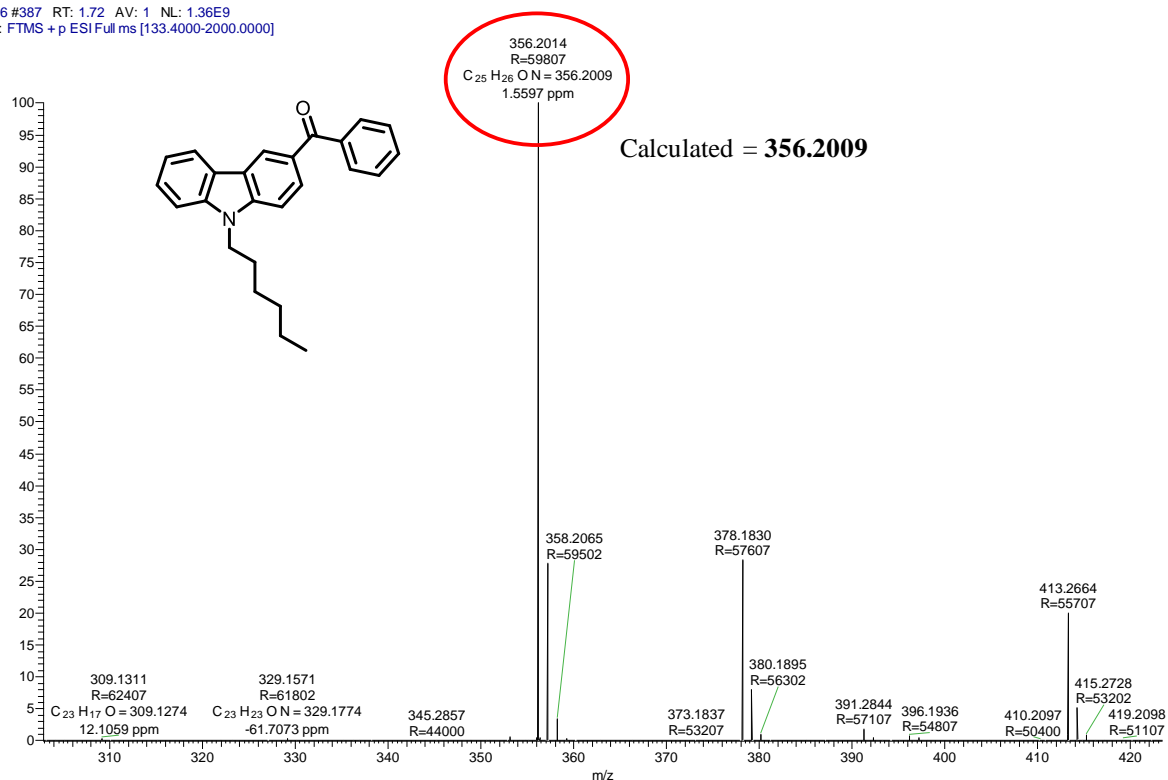
Characterization details of the synthesized molecules

CBZ-1 #384 RT: 1.72 AV: 1 NL: 3.77E7
T: FTMS + p ESI Full ms [133.4000-2000.0000]



HR-MS spectrum of 9-hexyl-9H-carbazole (1).

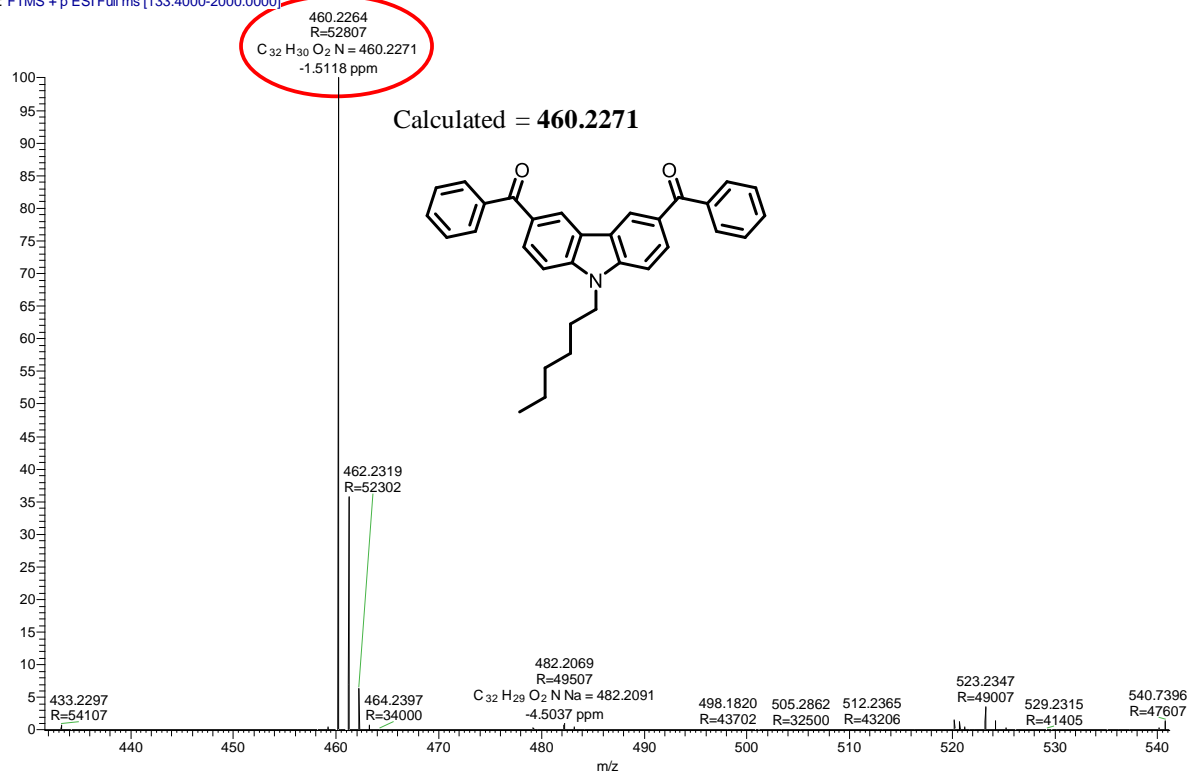
A6 #387 RT: 1.72 AV: 1 NL: 1.36E9
T: FTMS + p ESI Full ms [133.4000-2000.0000]



HR-MS spectrum of (9-hexyl-9H-carbazol-3-yl)(phenyl)methanone (2).

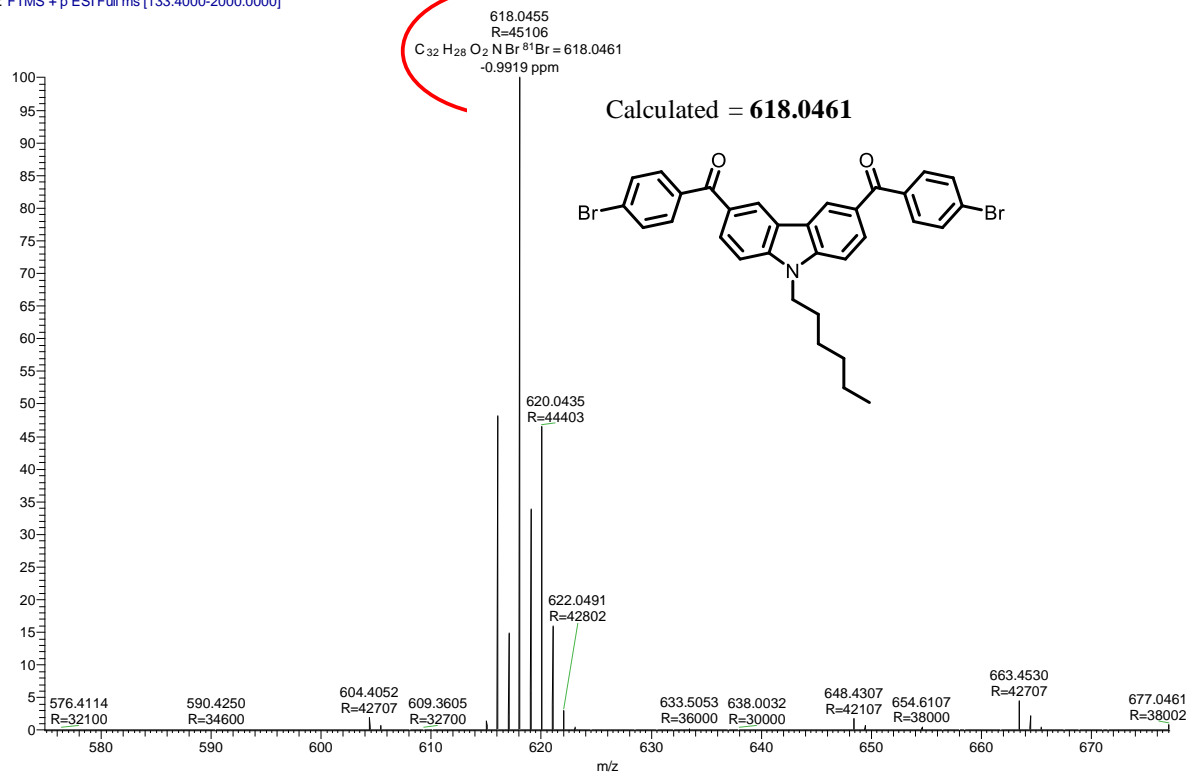
Characterization details of the synthesized molecules

CBZ-2 #373 RT: 1.67 AV: 1 NL: 5.09E8
T: FTMS + p ESI Full ms [133.4000-2000.0000]

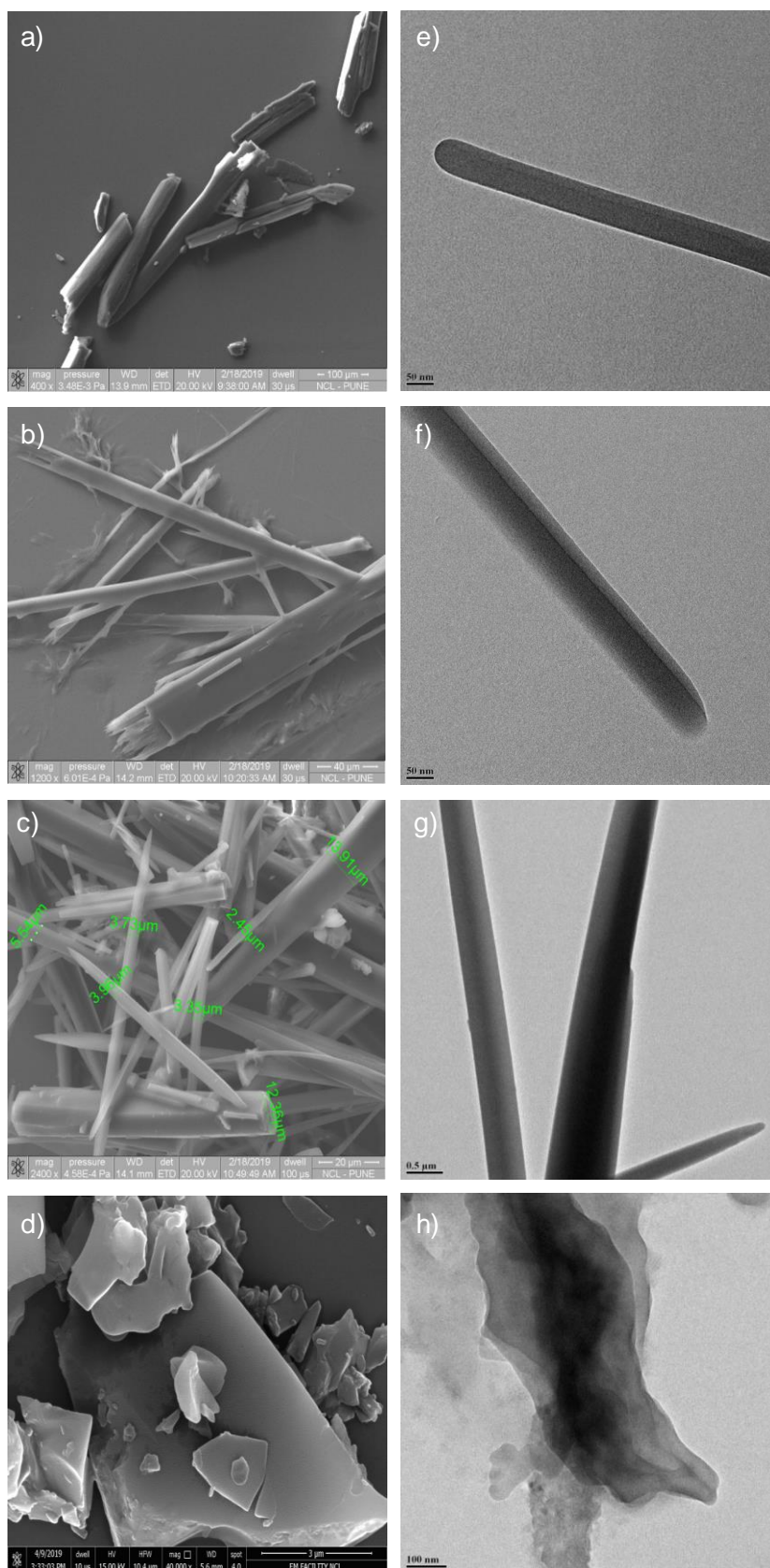


HR-MS spectrum of (9-hexyl-9H-carbazole-3,6-diyl)bis(phenylmethanone) (**3a**).

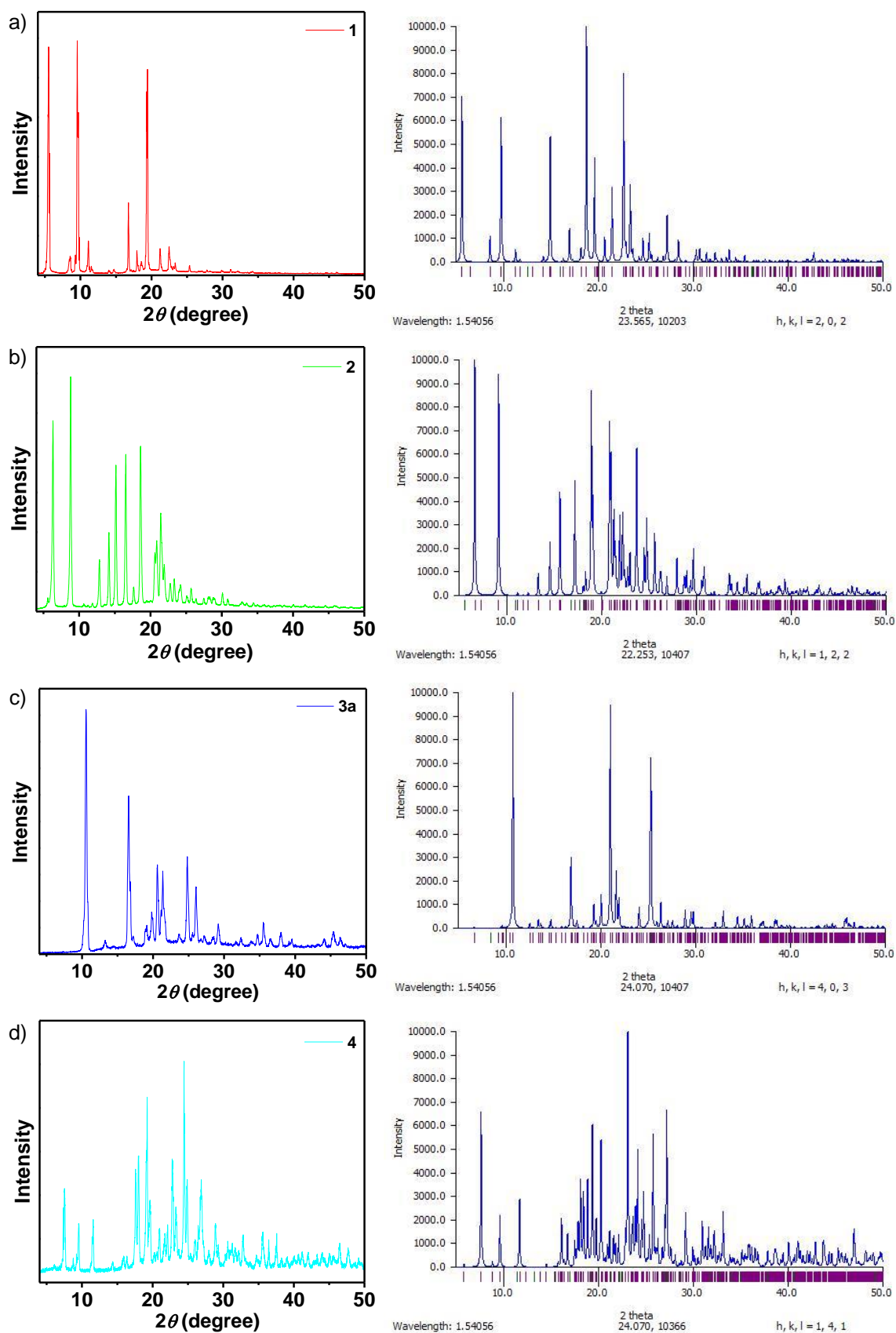
CBZ-4 #527 RT: 2.35 AV: 1 NL: 1.49E7
T: FTMS + p ESI Full ms [133.4000-2000.0000]



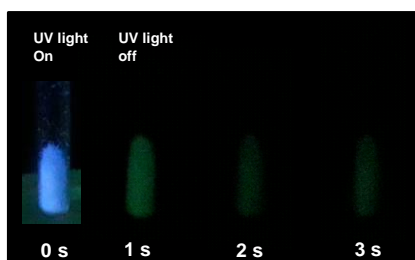
HR-MS spectrum of (9-hexyl-9H-carbazole-3,6-diyl)bis((4-bromophenyl)methanone) (**3b**).



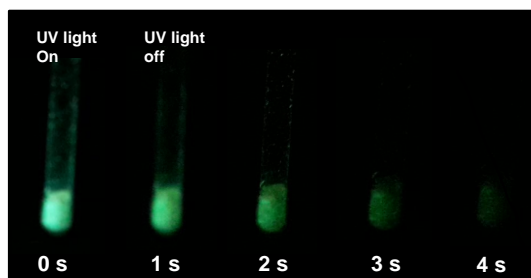
a-d) SEM and e-h) TEM images of the crystals of **1**, **2**, **3a**, **3b**, respectively.



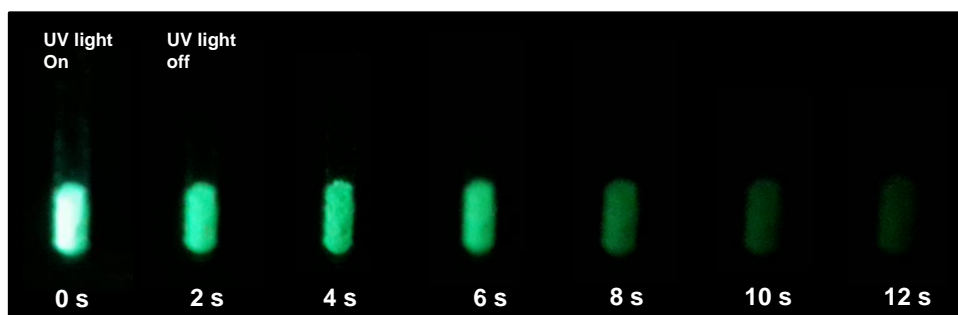
Comparison of the experimental (left) and theoretical (right) PXRD patterns of a) **1**, b) **2**, c) **3a** and d) **3b**. The theoretical PXRD pattern is obtained from the single-crystal XRD.



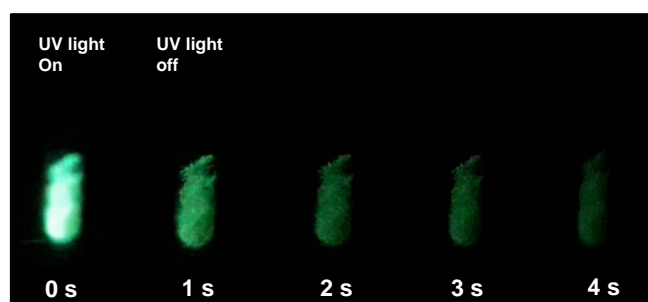
Photographs of the crystals of **1** in a quartz tube (3 mm) (at 77 K for 1 min) recorded at different time intervals upon turning off the excitation source (365 nm) after 3 s exposure.



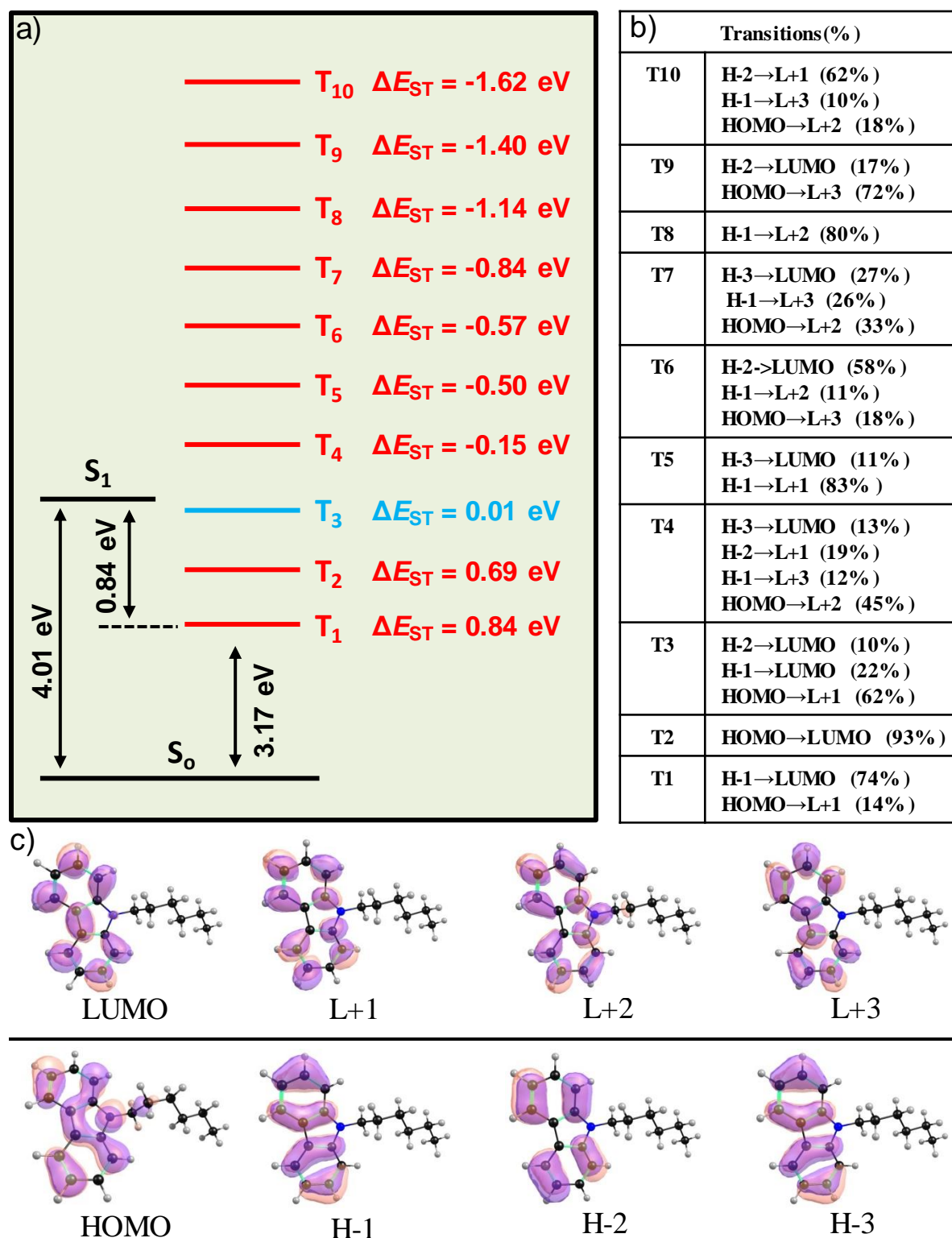
Photographs of the crystals of **2** in a quartz tube (3 mm) (at 77 K for 1 min) recorded at different time intervals upon turning off the excitation source (365 nm) after 3 s exposure.



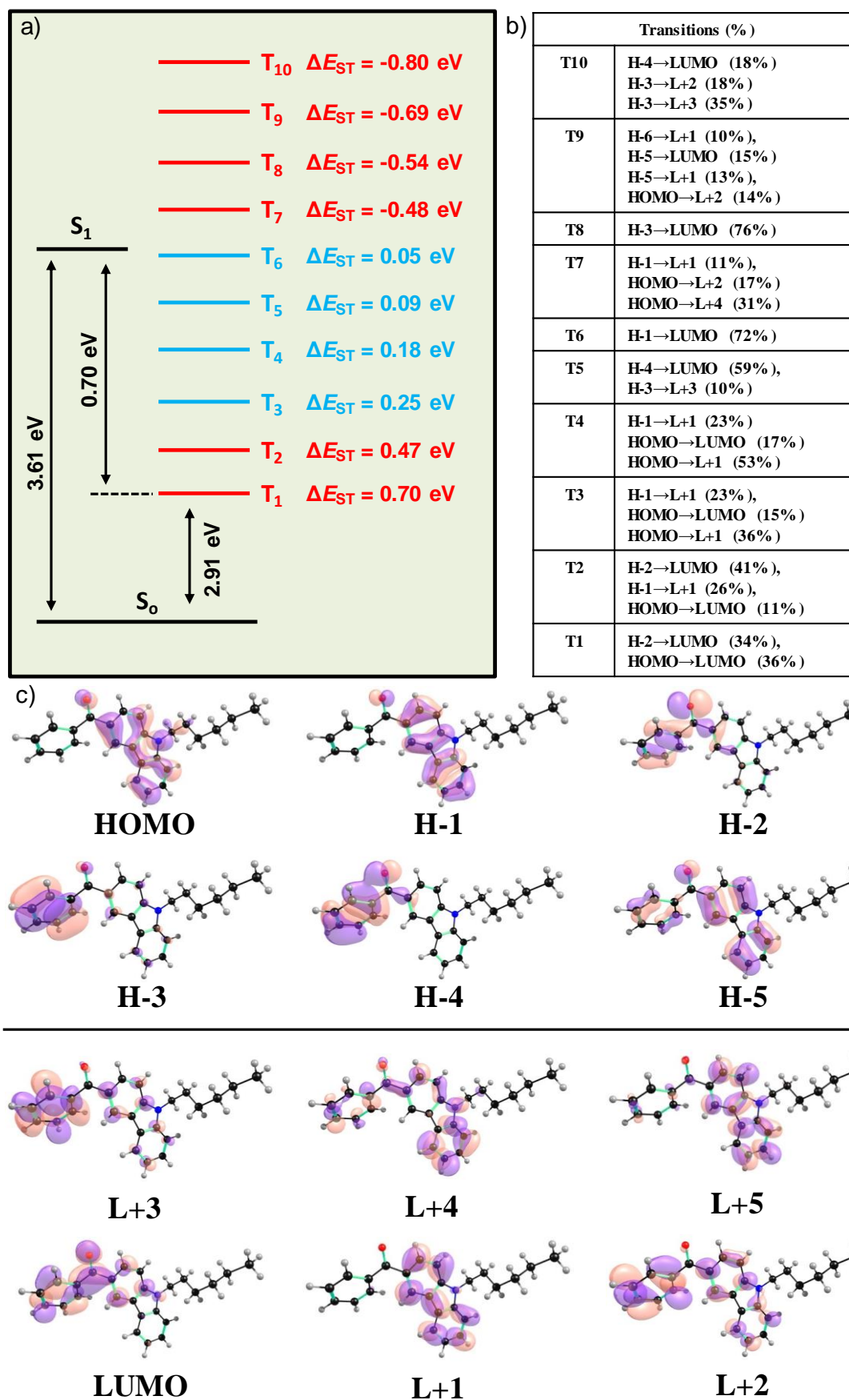
Photographs of the crystals of **3a** in a quartz tube (3 mm) (at 77 K for 1 min) recorded at different time intervals upon turning off the excitation source (365 nm) after 3 s exposure.



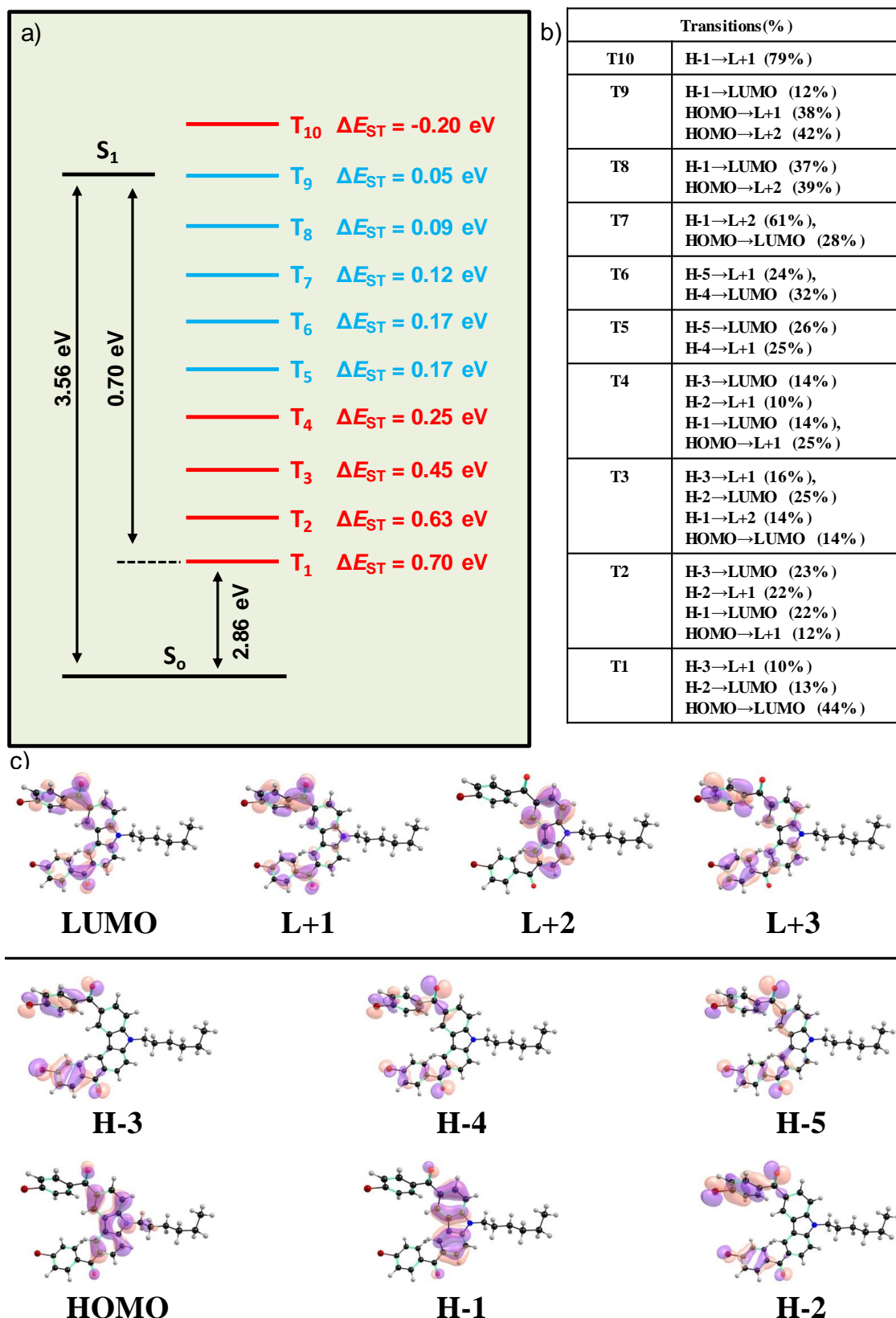
Photographs of the crystals of **3b** in a quartz tube (3 mm) (at 77 K for 1 min) recorded at different time intervals upon turning off the excitation source (365 nm) after 3 s exposure.



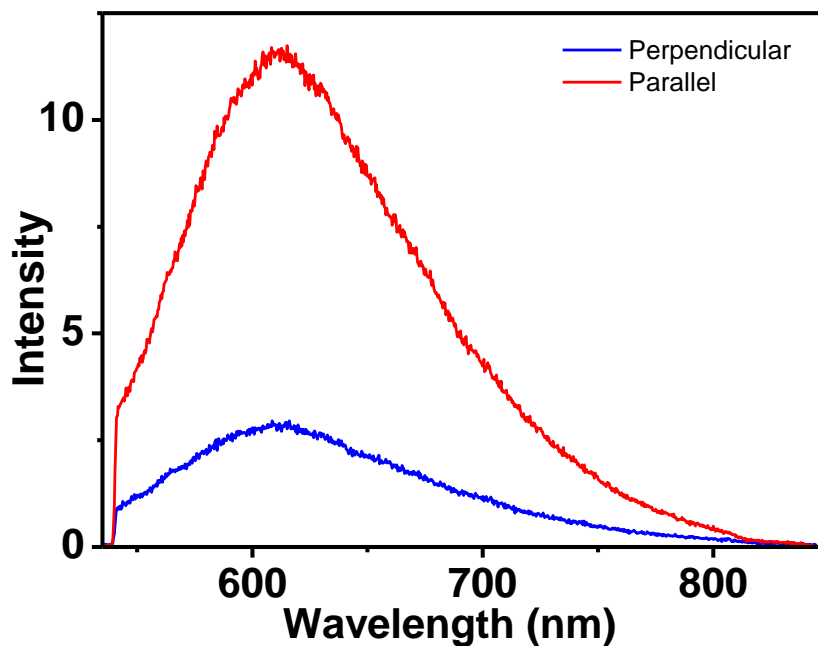
Calculated a) energy level diagram showing ΔE_{ST} for **1** from DFT calculations along with b) probable electronic transitions and c) involved frontier molecular orbitals.



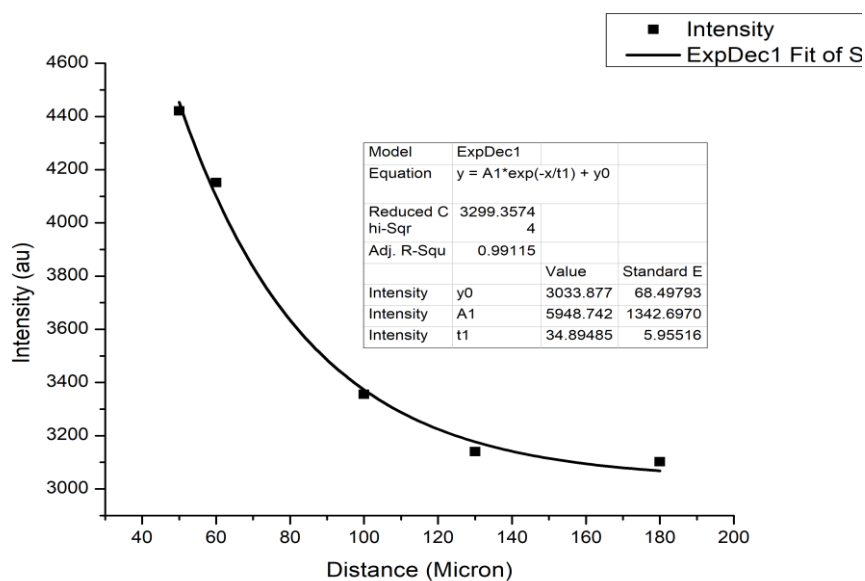
Calculated a) energy level diagram showing ΔE_{ST} for **2** from DFT calculations along with b) probable electronic transitions and c) involved frontier molecular orbitals.



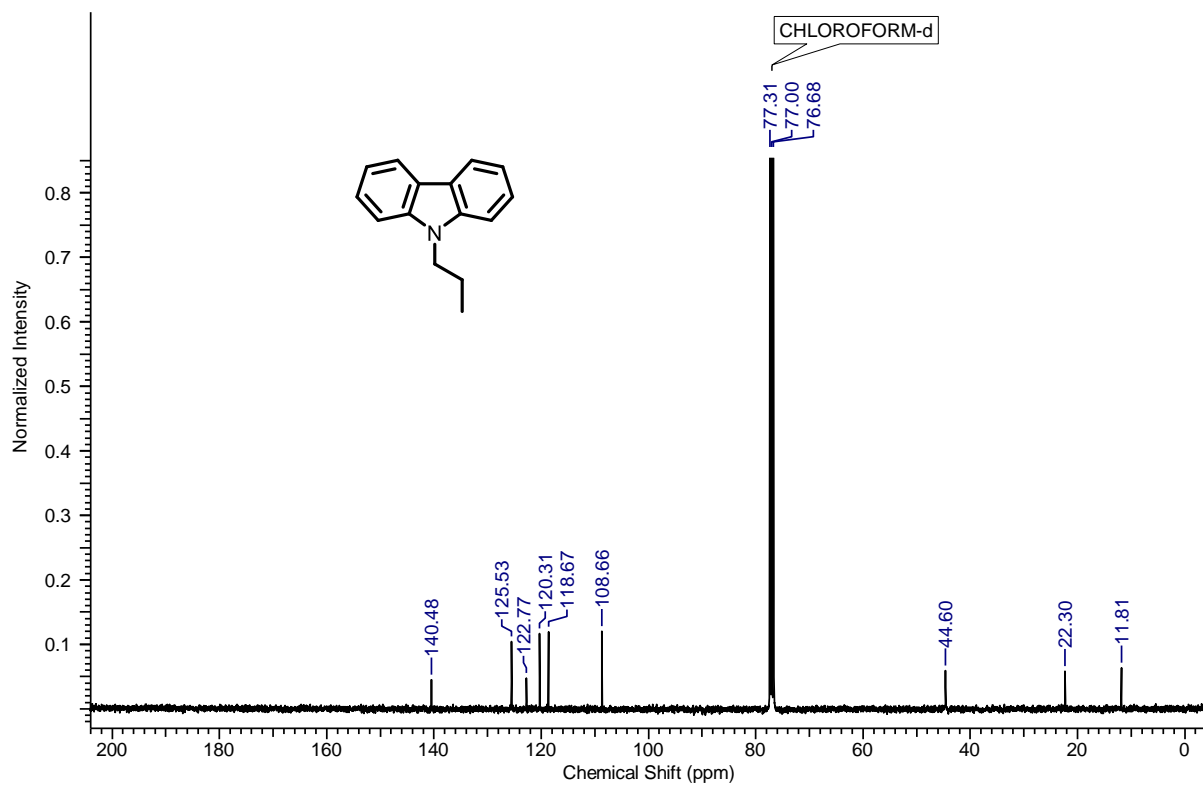
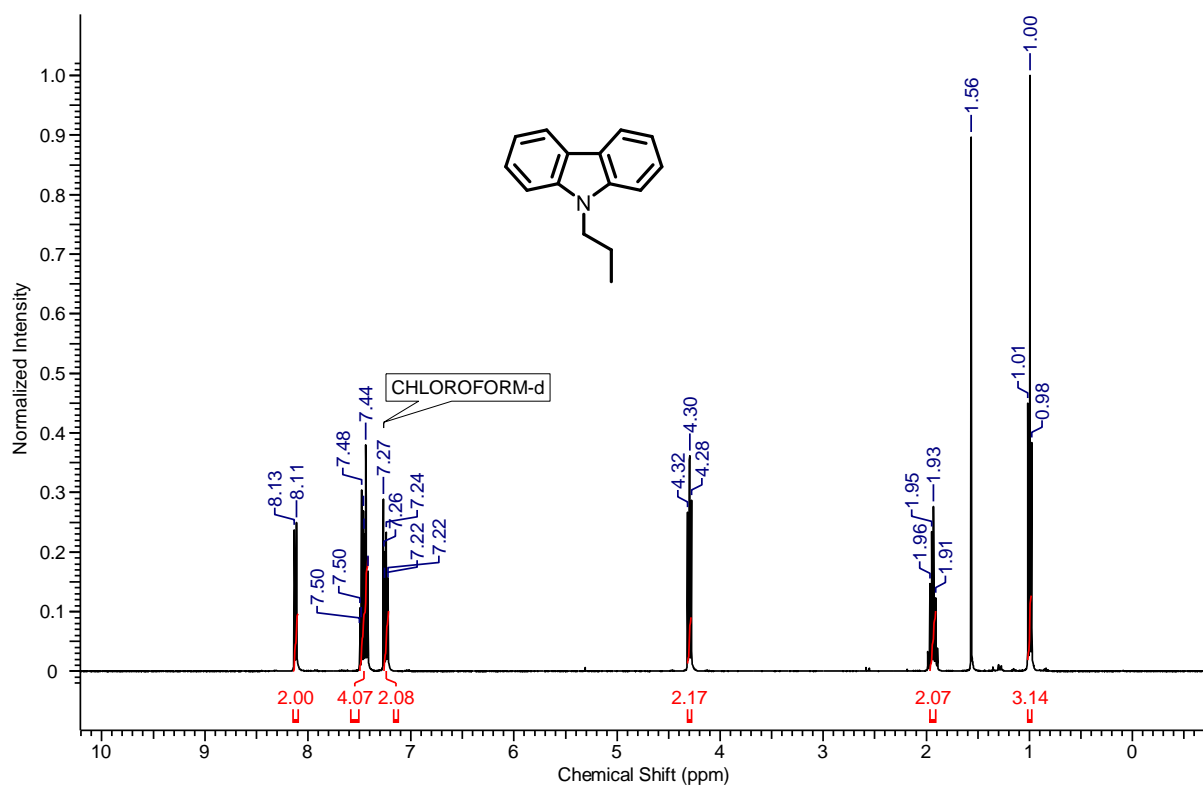
Calculated a) energy level diagram showing ΔE_{ST} for **3b** from DFT calculations along with b) probable electronic transitions and c) involved frontier molecular orbitals.



Comparison of the phosphorescence intensity measured at the distal end of the crystal upon excitation at the parallel and perpendicular polarization to the long axis of the rods ($\lambda_{ex} = 532$ nm).

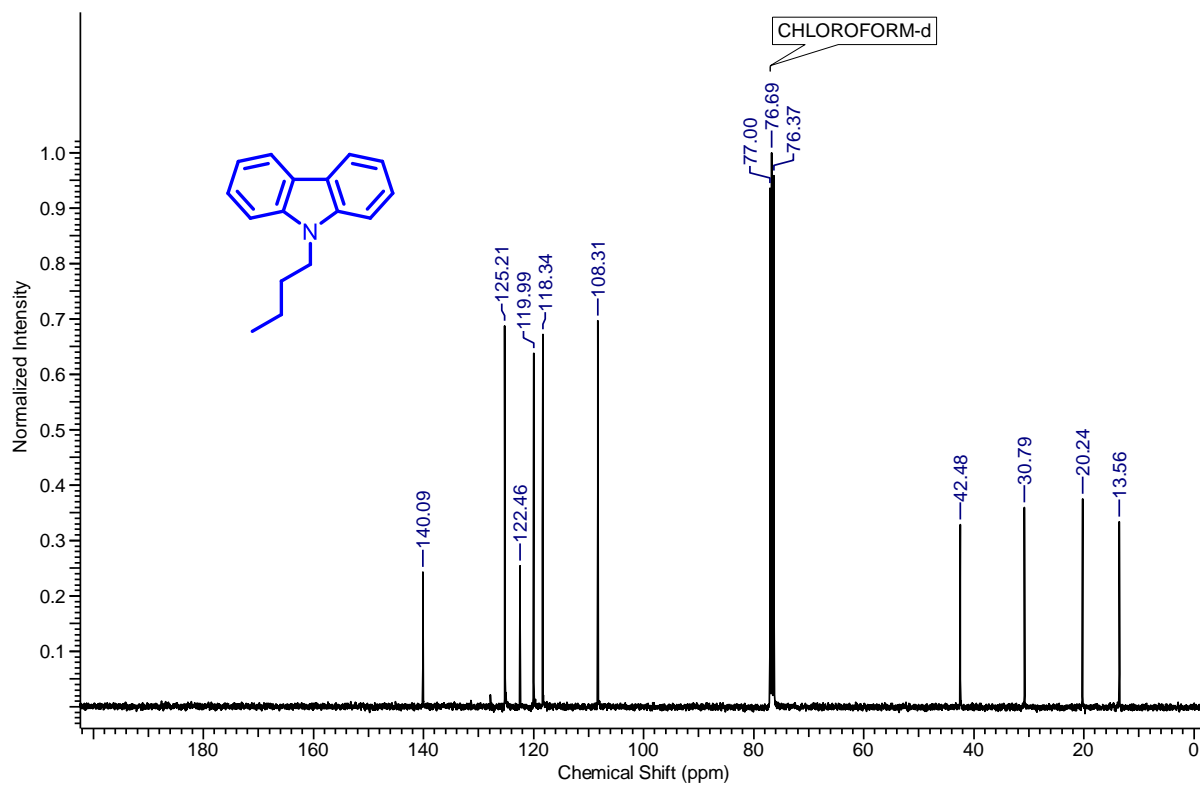
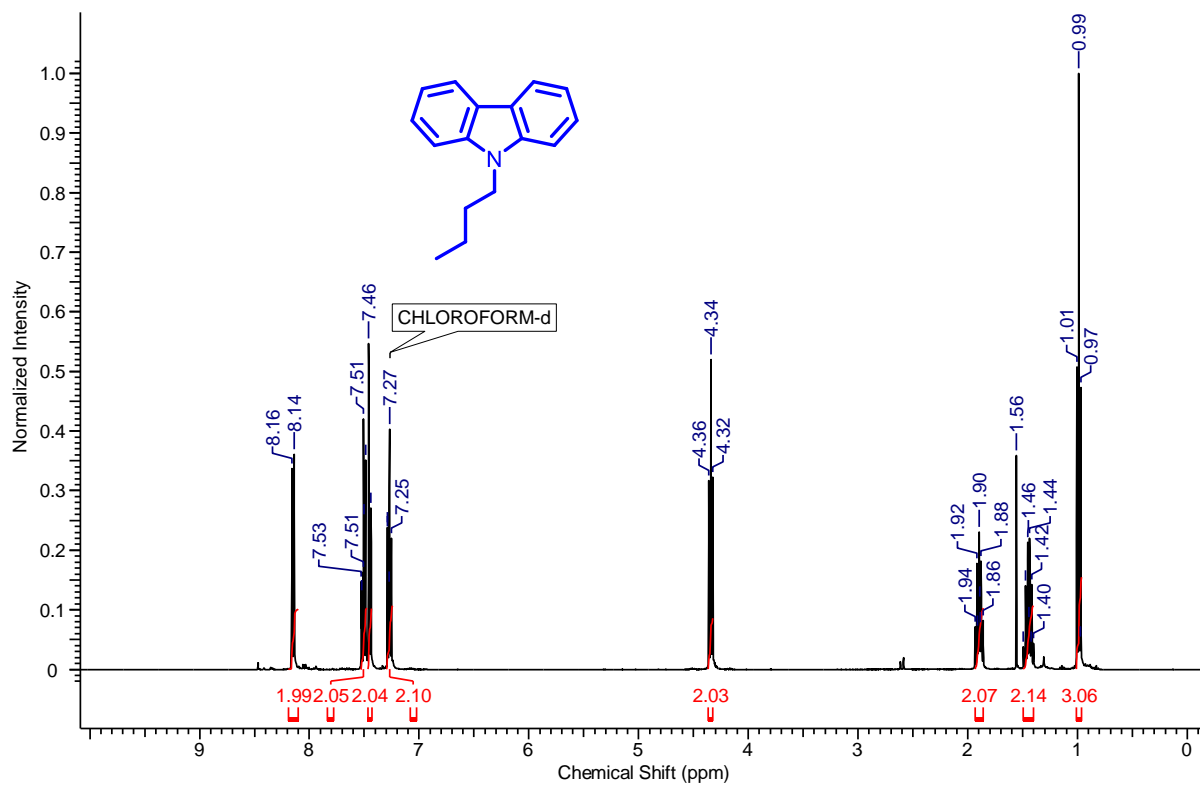


Calculation of propagation loss of crystalline rod of **3a**.

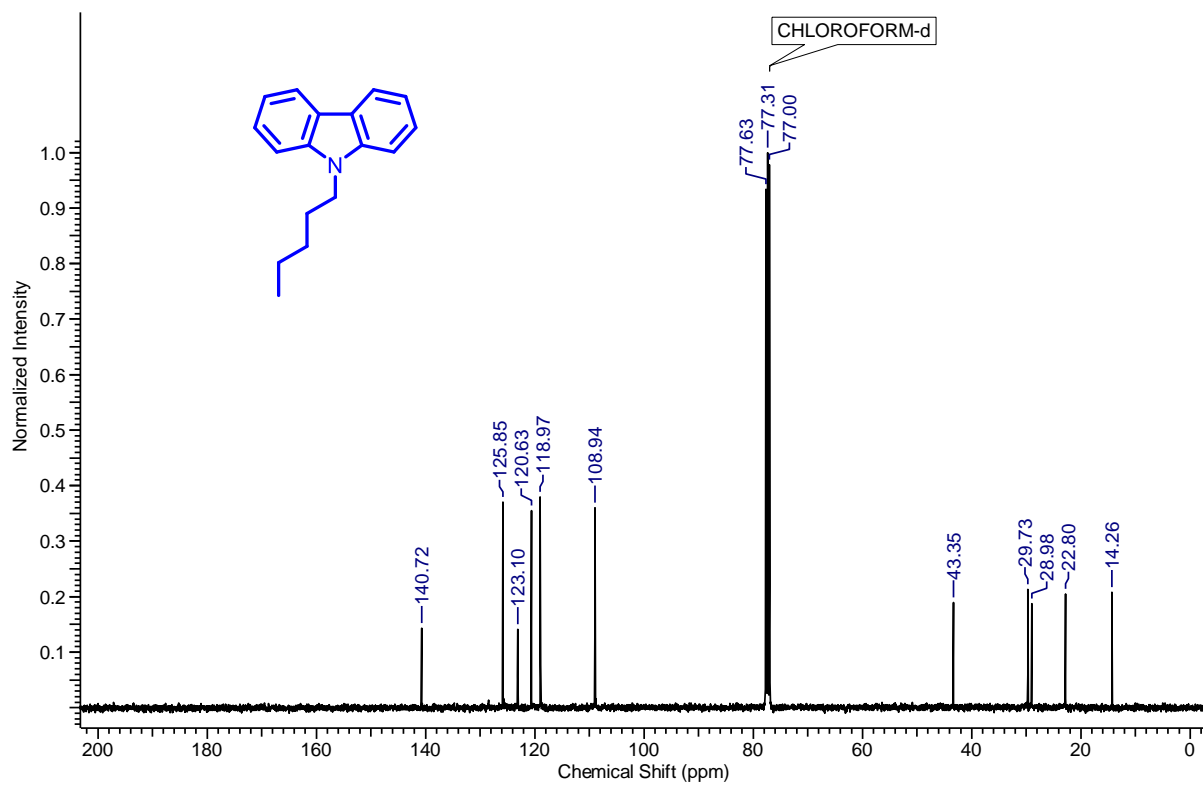
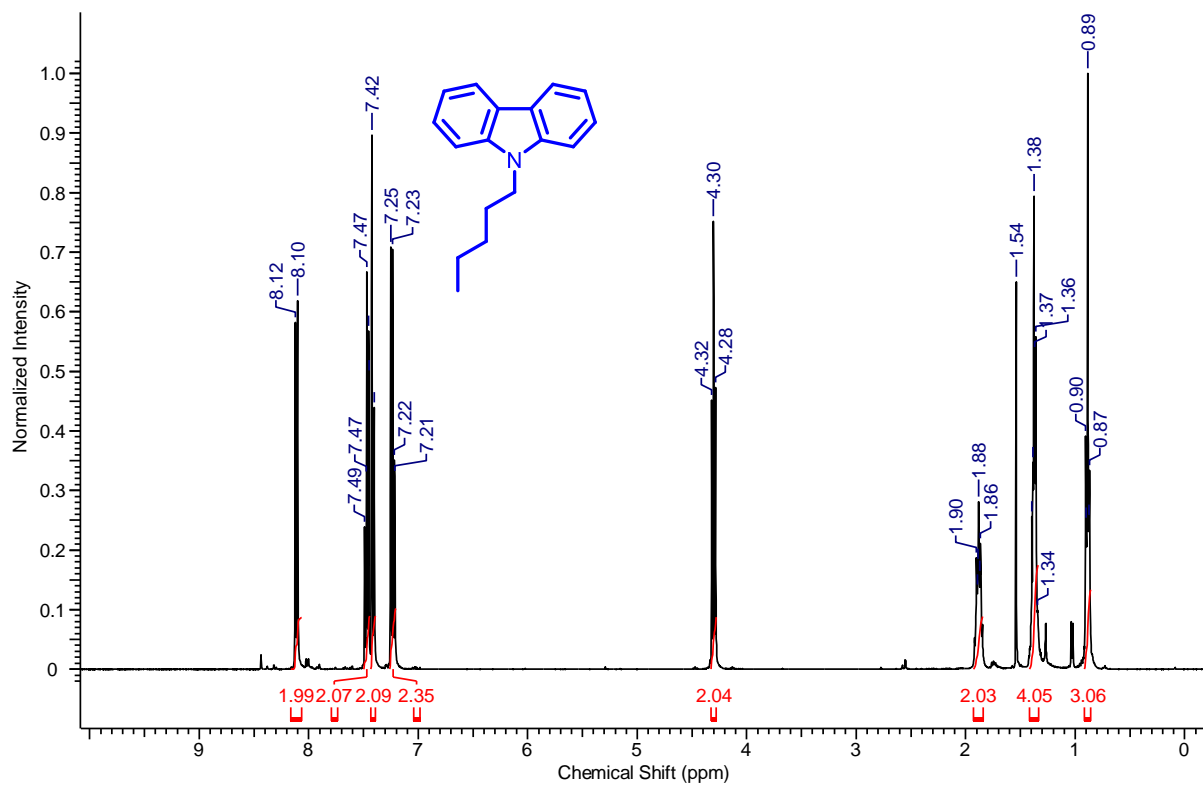


^1H (top) and ^{13}C (bottom) NMR spectra of 9-propyl-9H-carbazole (1).

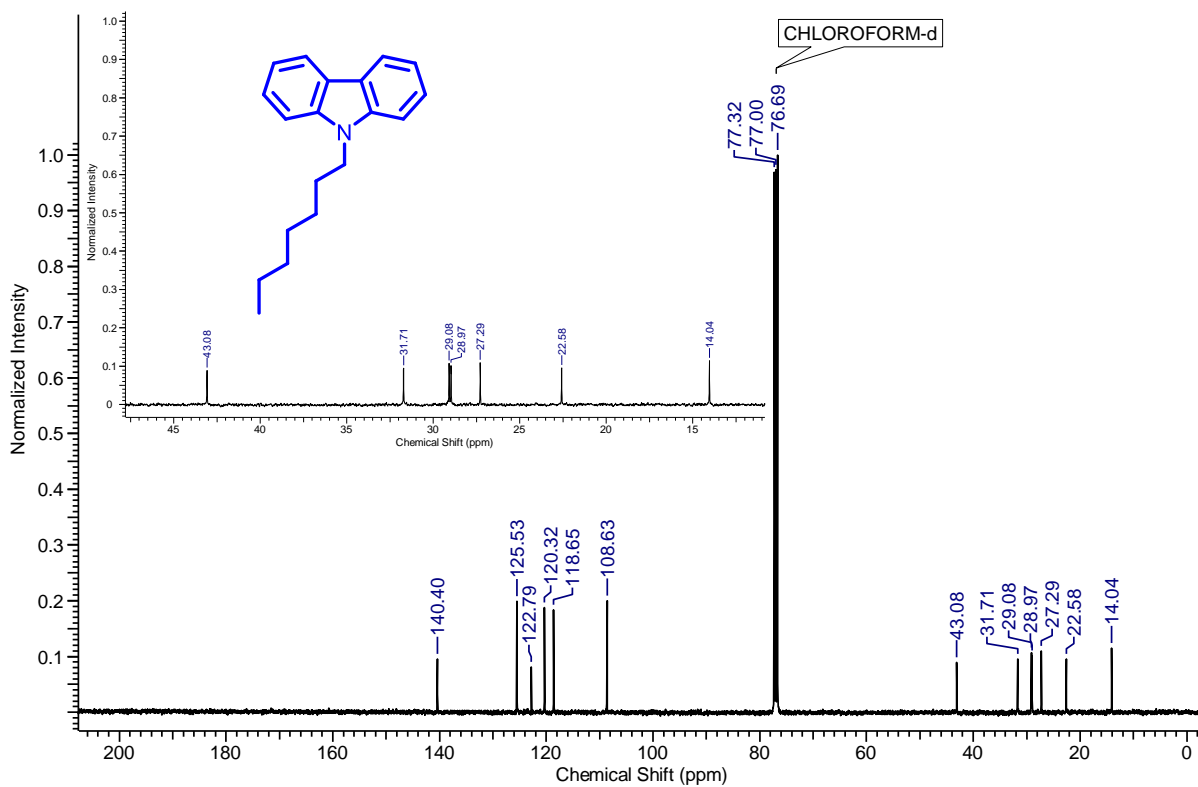
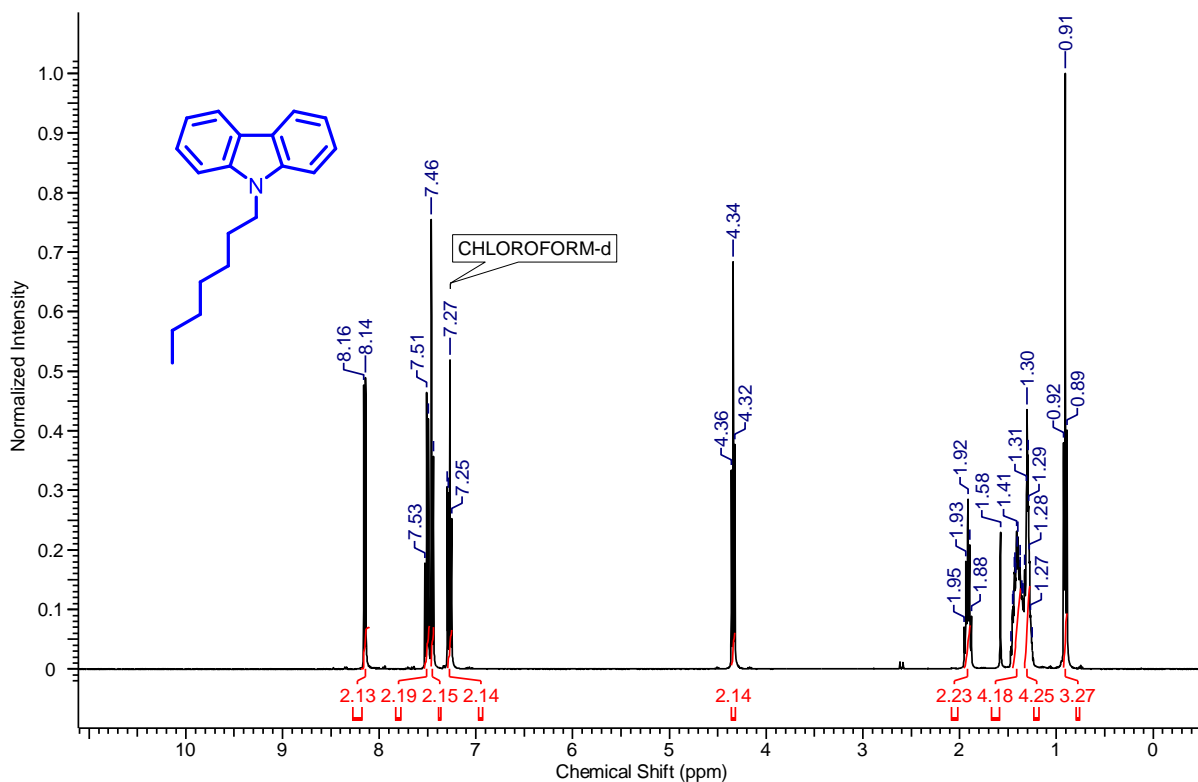
Characterization details of the synthesized molecules



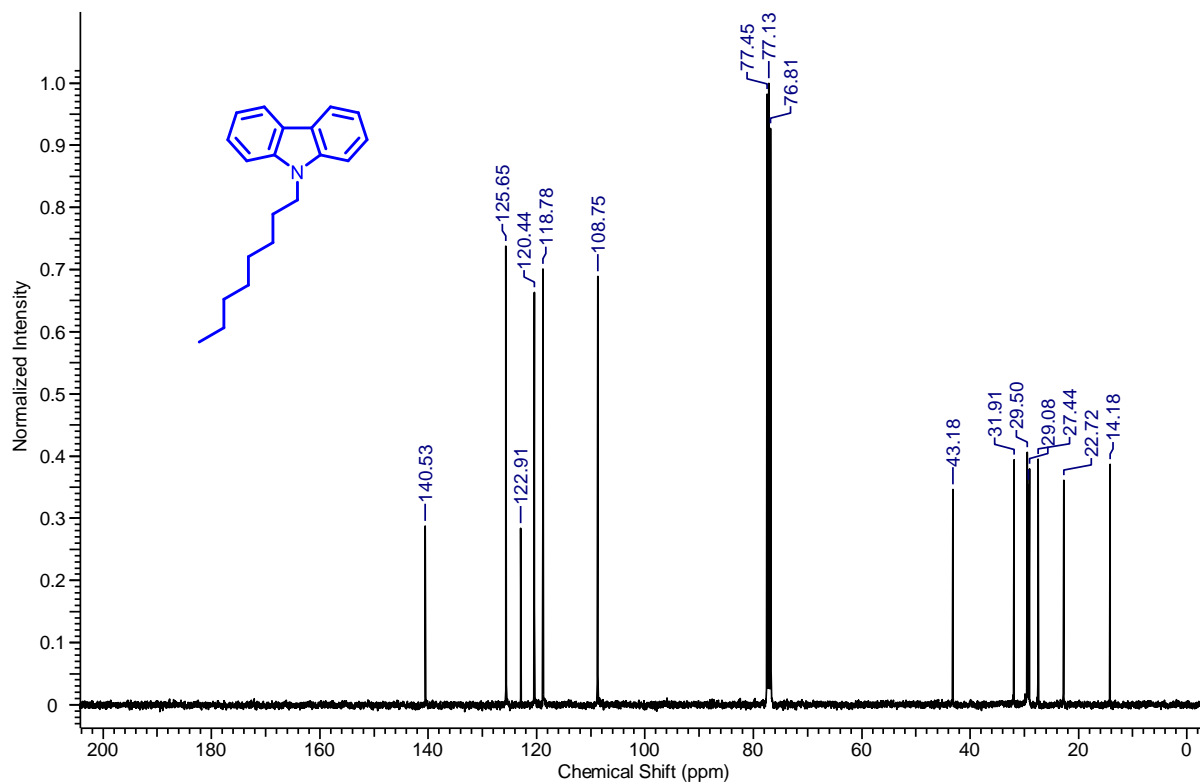
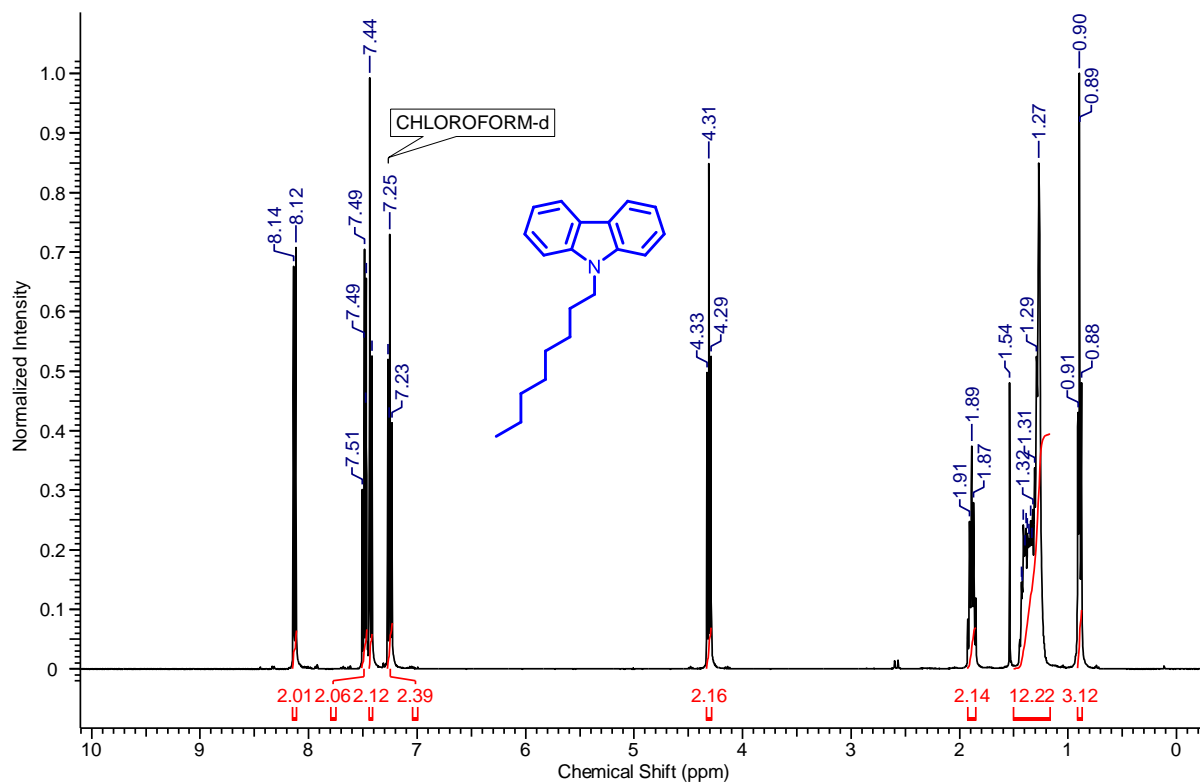
¹H (top) and ¹³C (bottom) NMR spectra of 9-butyl-9H-carbazole (**2**).



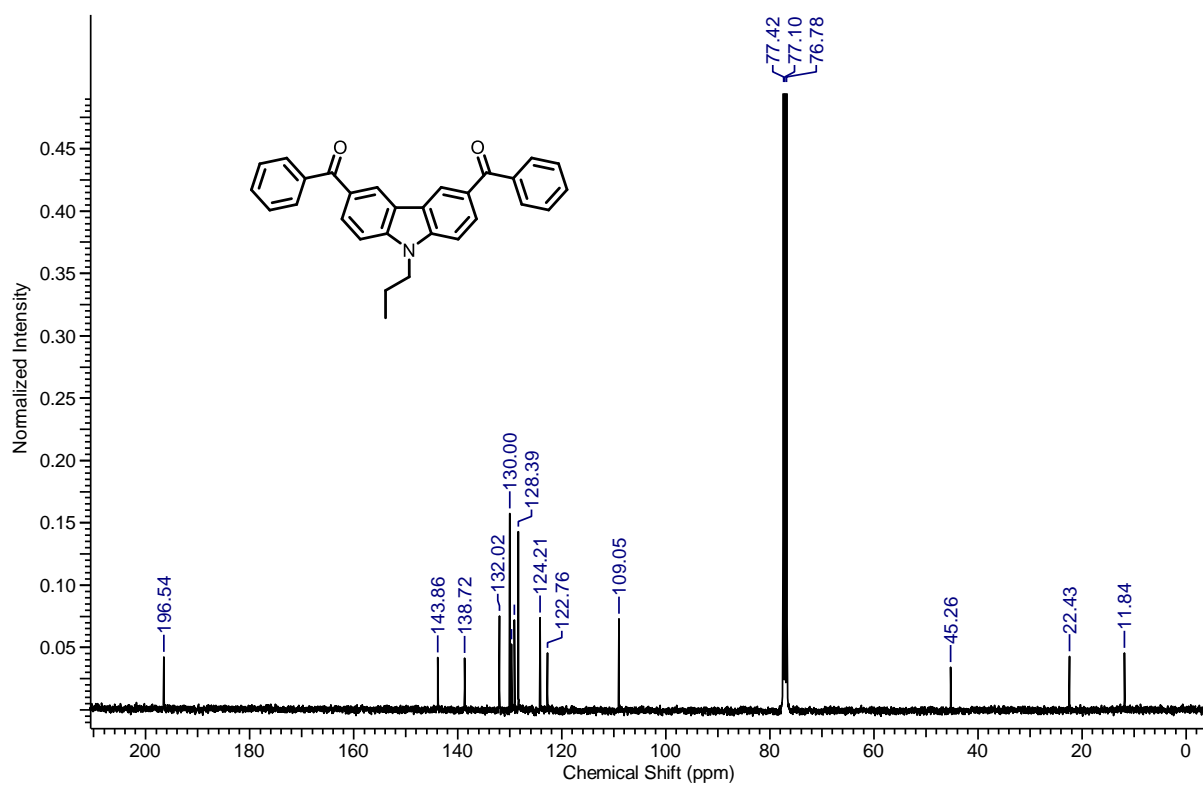
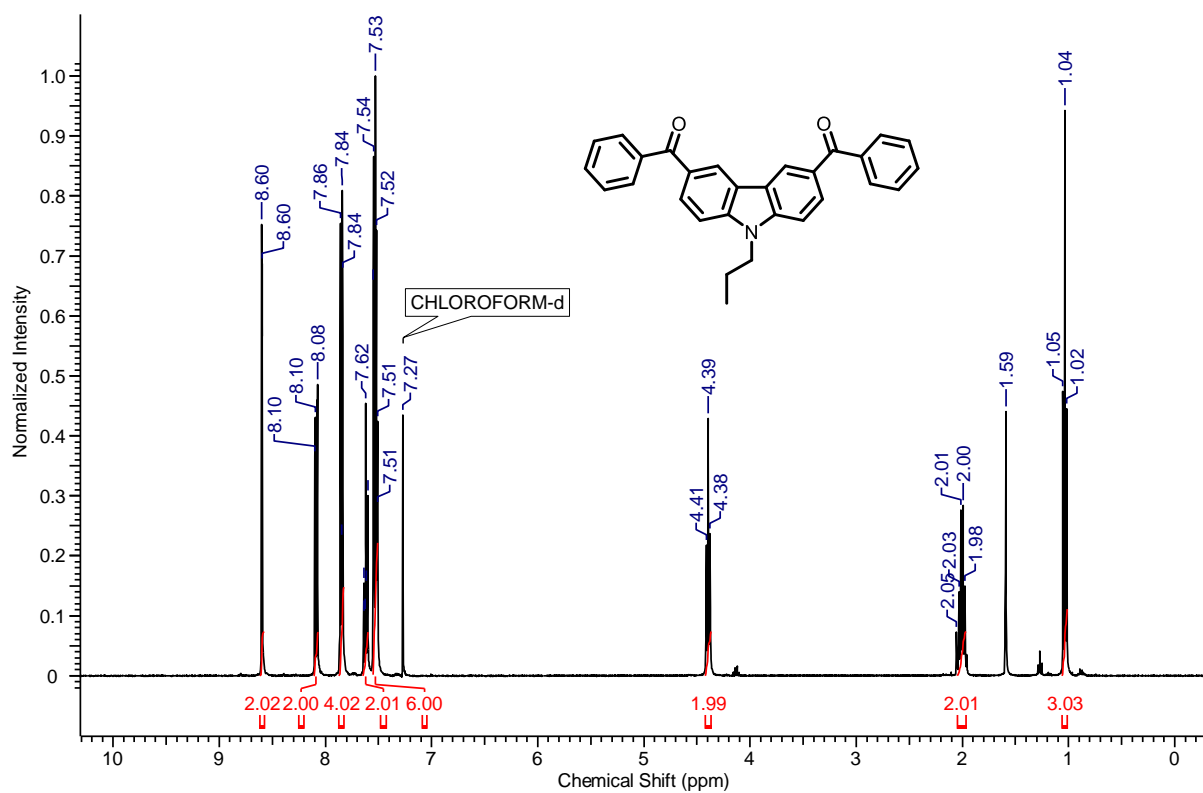
¹H (top) and ¹³C (bottom) NMR spectra of 9-pentyl-9H-carbazole (3).



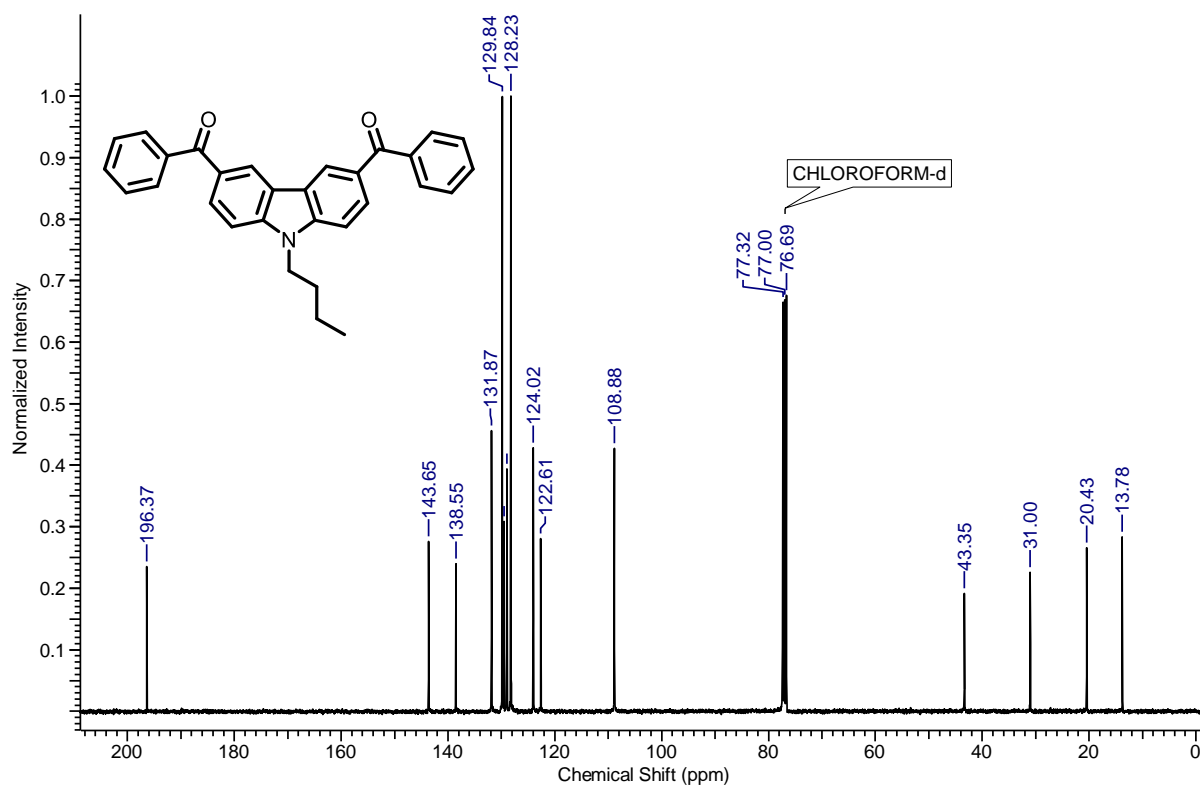
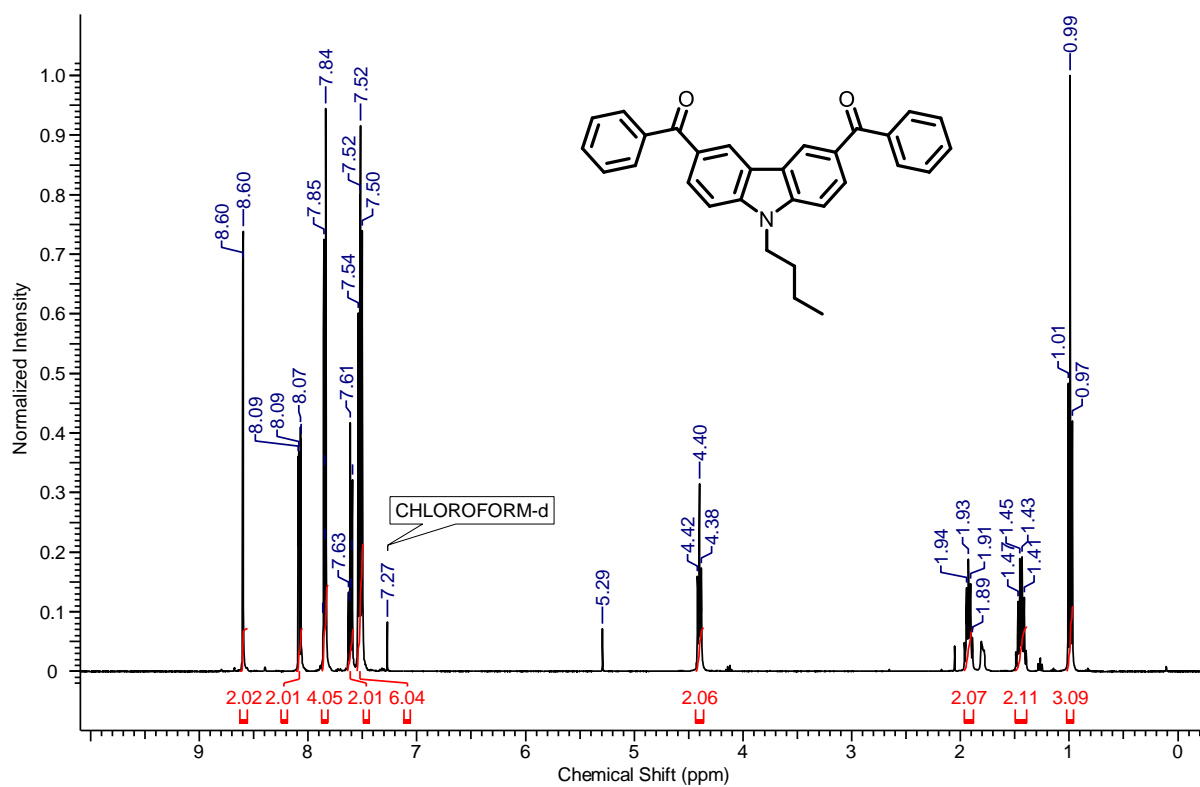
¹H (top) and ¹³C (bottom) NMR spectra of 9-heptyl-9H-carbazole (**4**).



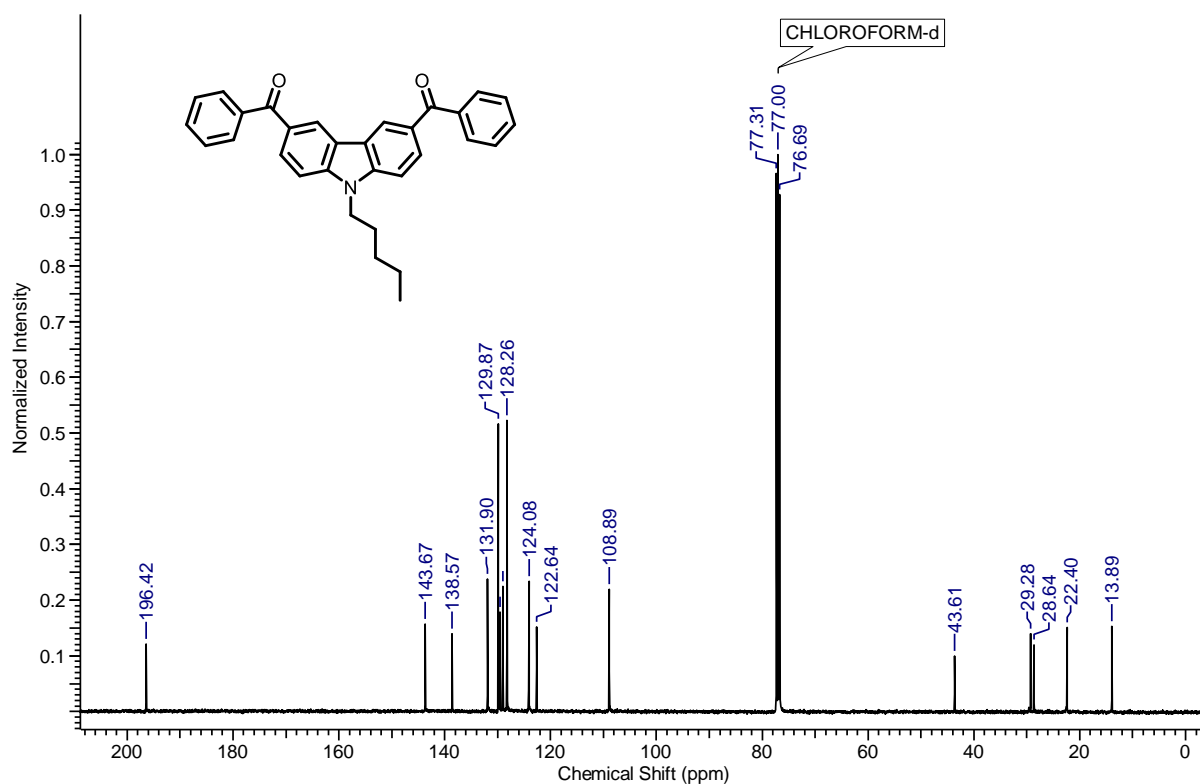
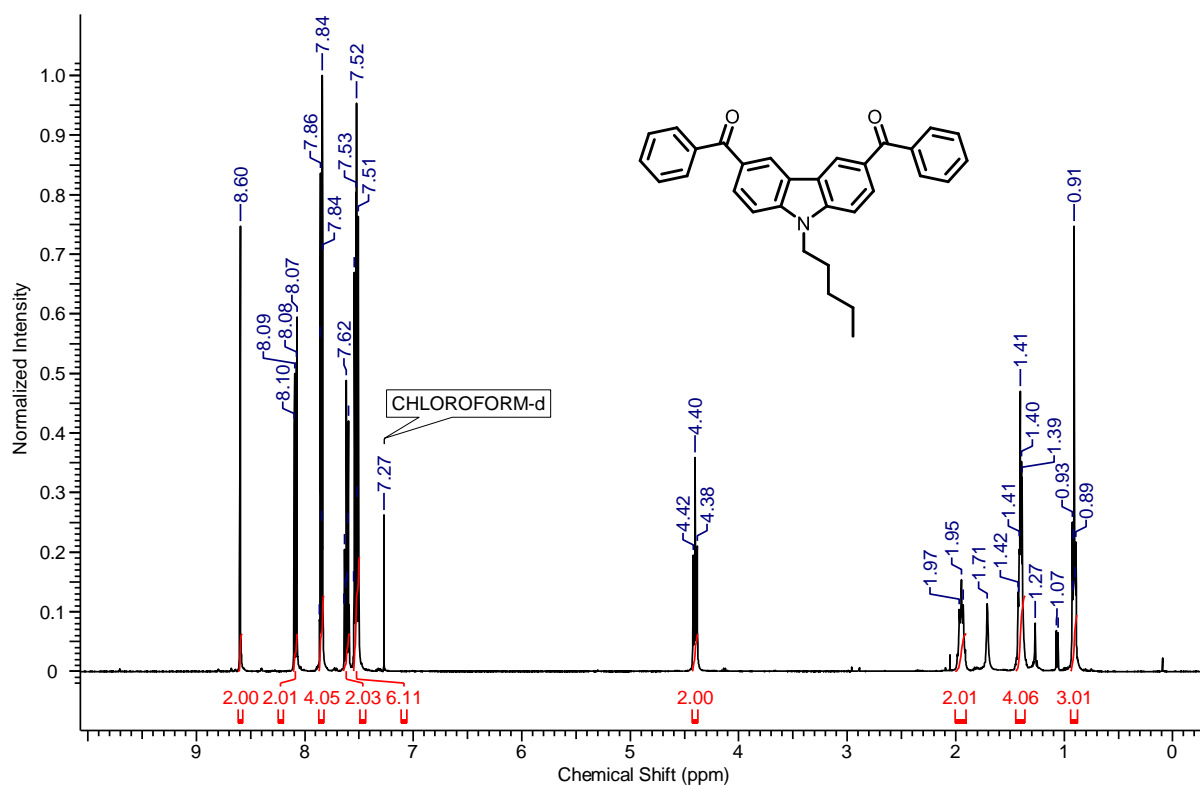
¹H (top) and ¹³C (bottom) NMR spectra of 9-octyl-9H-carbazole (**5**).



¹H (top) and ¹³C (bottom) NMR spectra of (9-propyl-9H-carbazole-3,6-diyl)bis(phenylmethanone) (6).

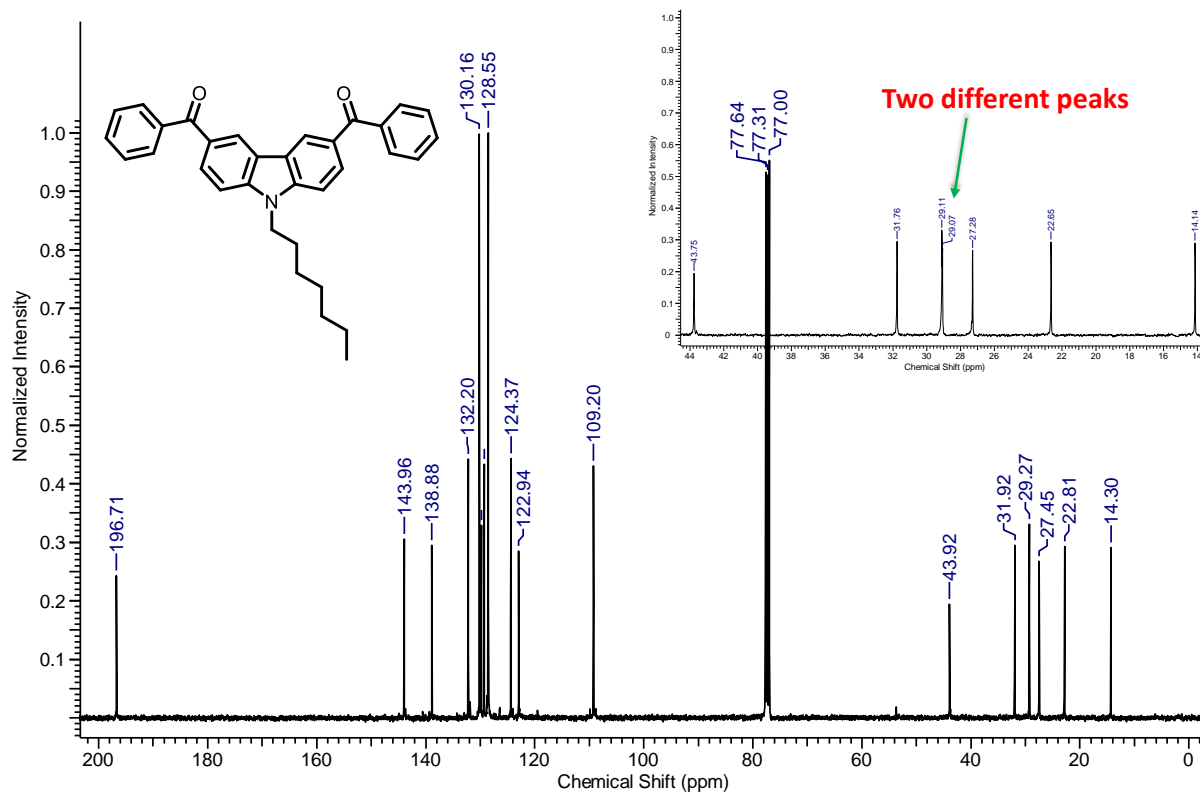
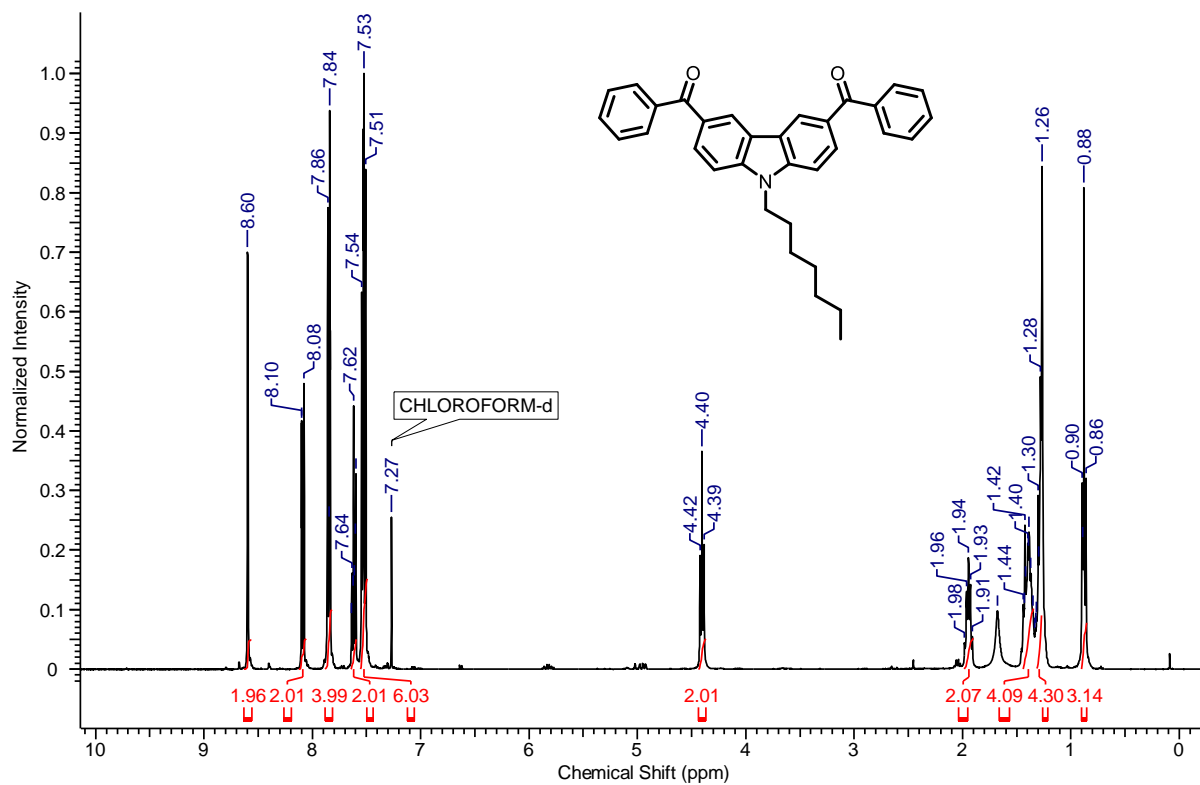


¹H (top) and ¹³C (bottom) NMR spectra of (9-butyl-9H-carbazole-3,6-diyl)bis(phenylmethanone) (7).



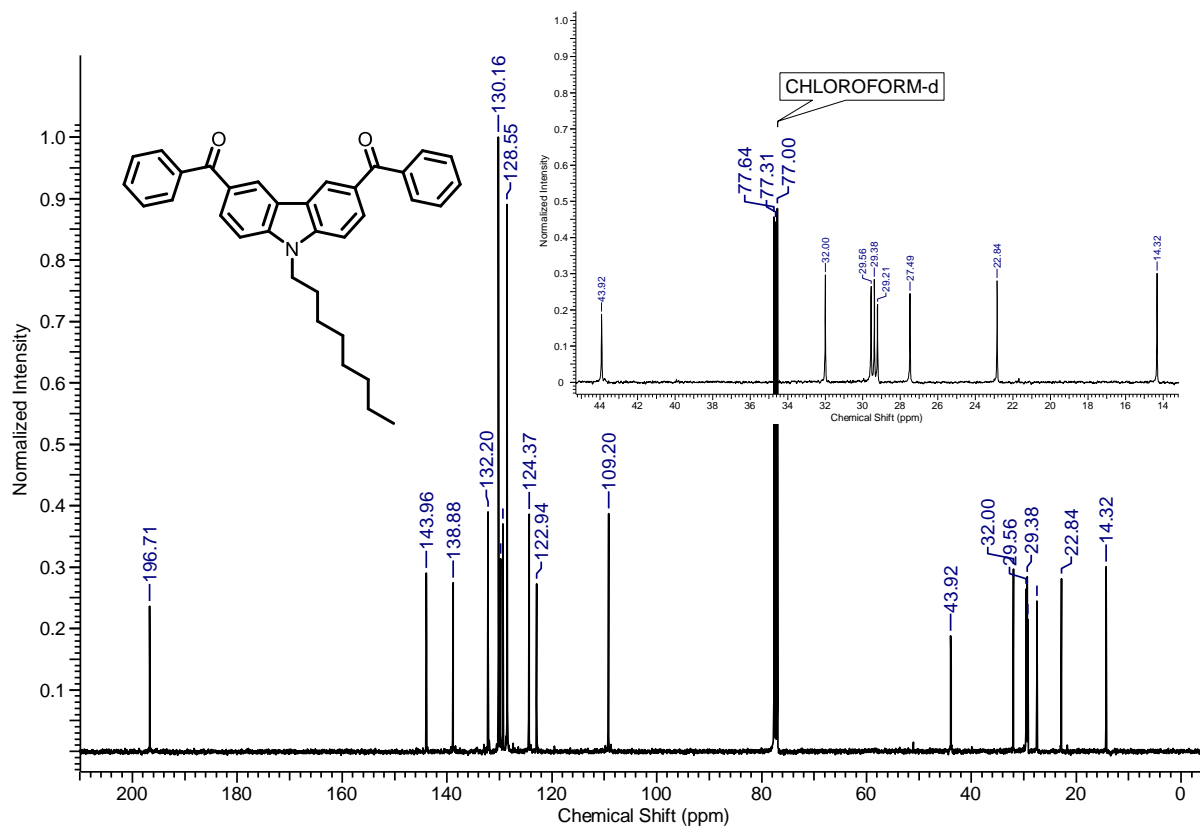
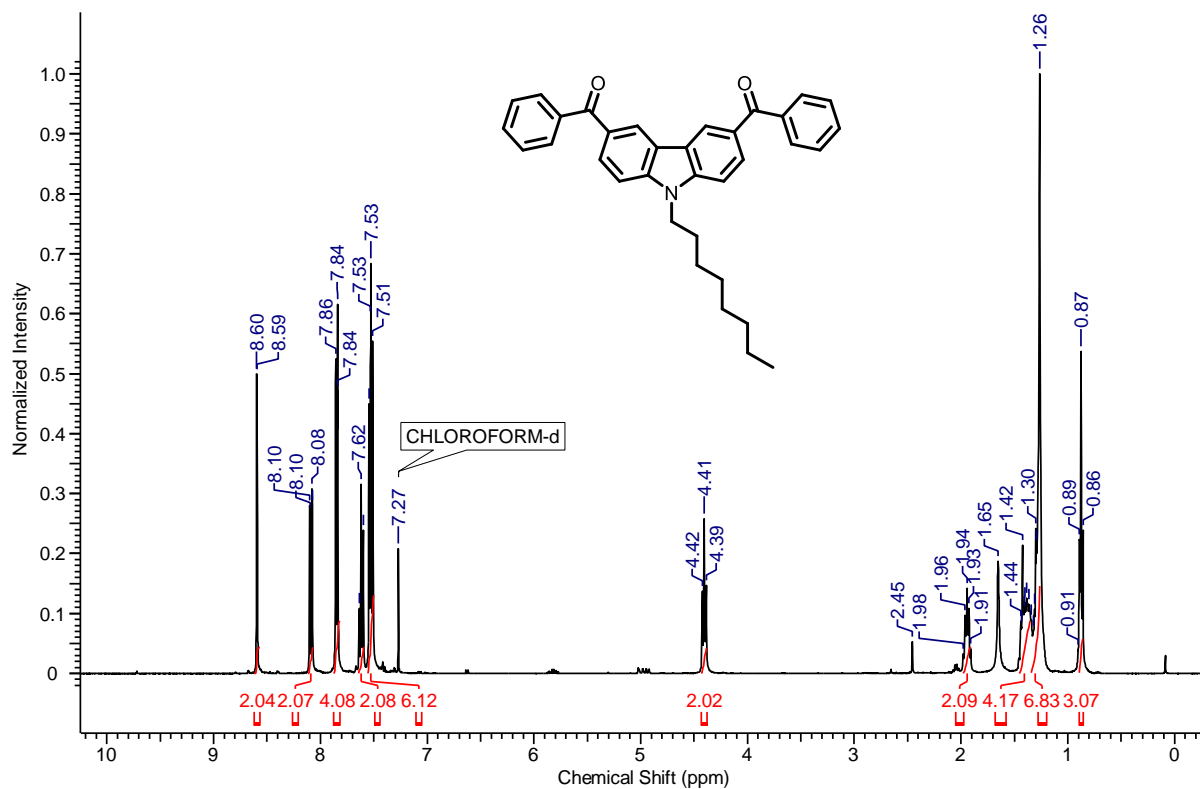
¹H (top) and ¹³C (bottom) NMR spectra of (9-pentyl-9H-carbazole-3,6-diyl)bis(phenylmethanone) (**8**).

Characterization details of the synthesized molecules



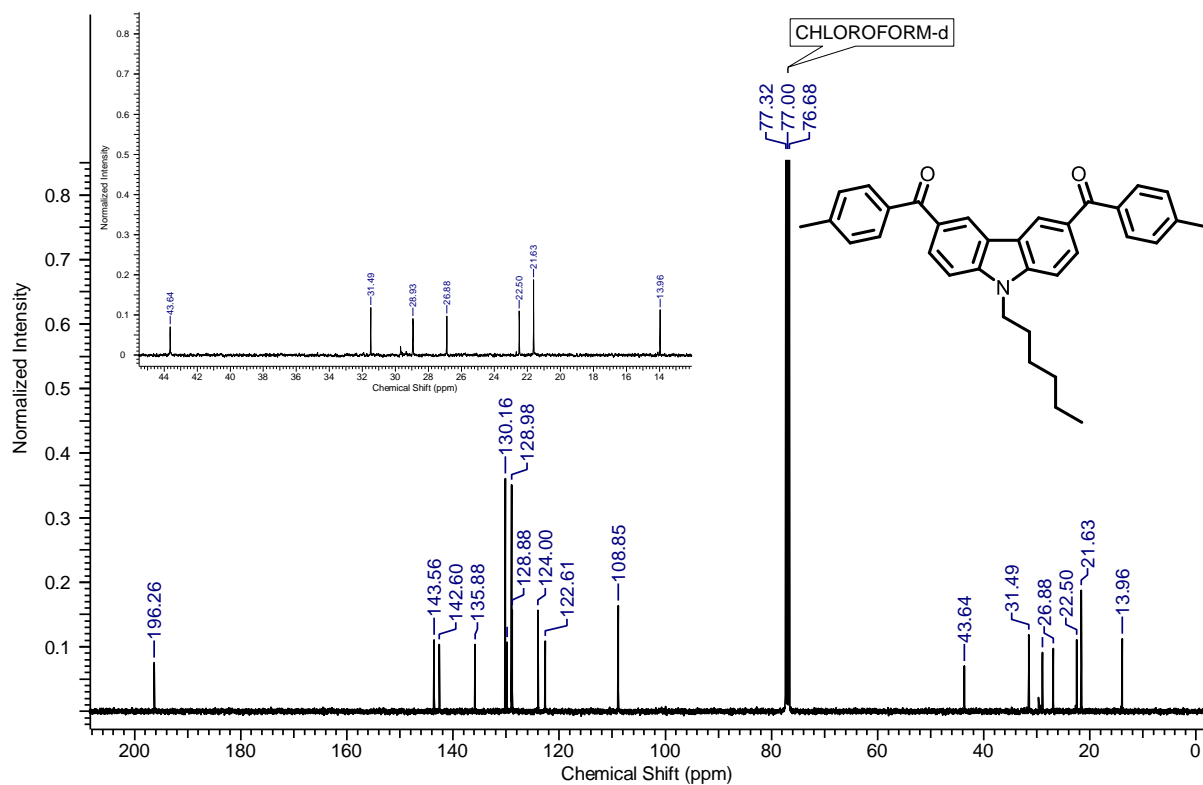
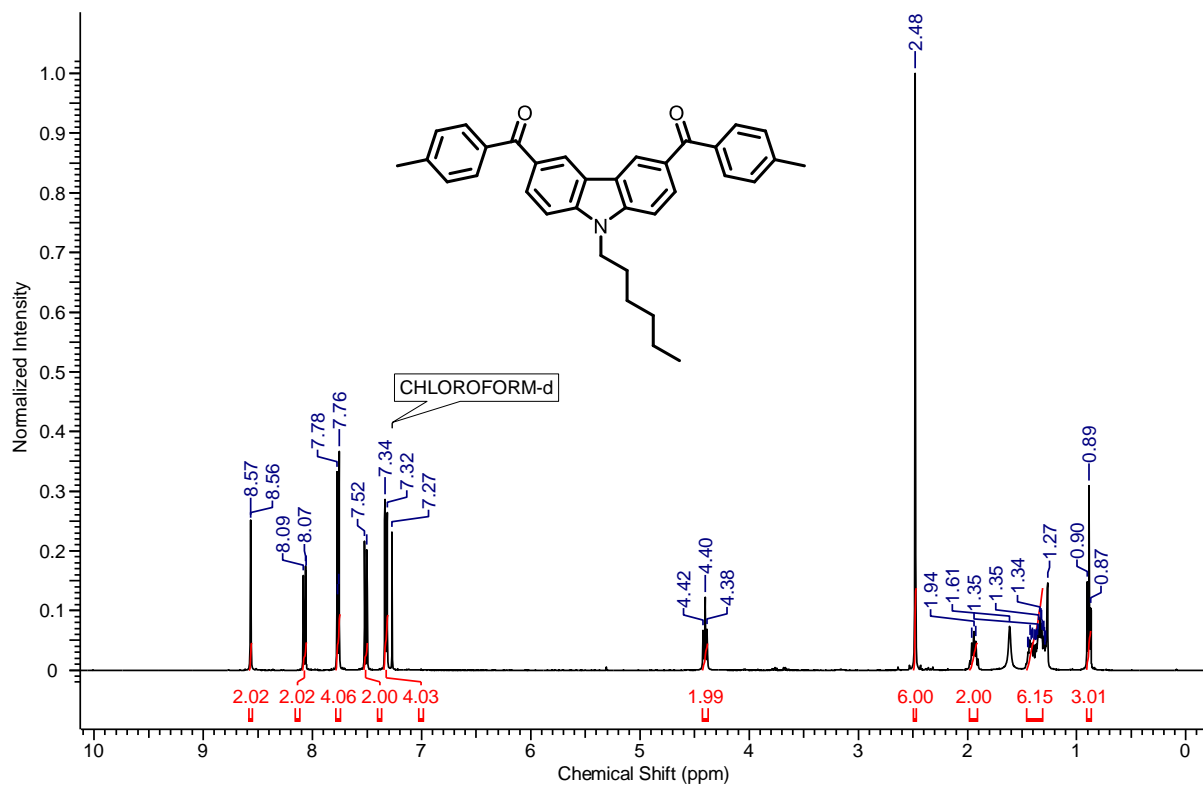
¹H (top) and ¹³C (bottom) NMR spectra of (9-heptyl-9H-carbazole-3,6-diyl)bis(phenylmethanone) (**9**).

Characterization details of the synthesized molecules

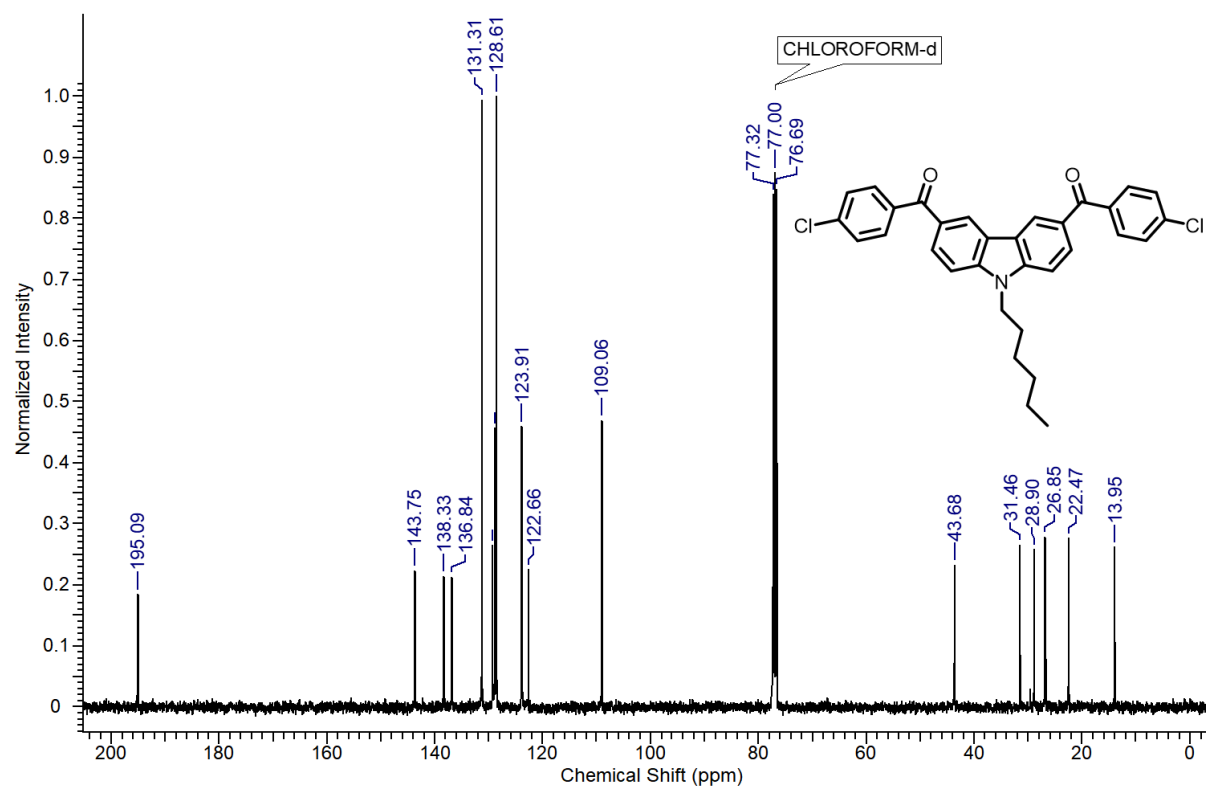
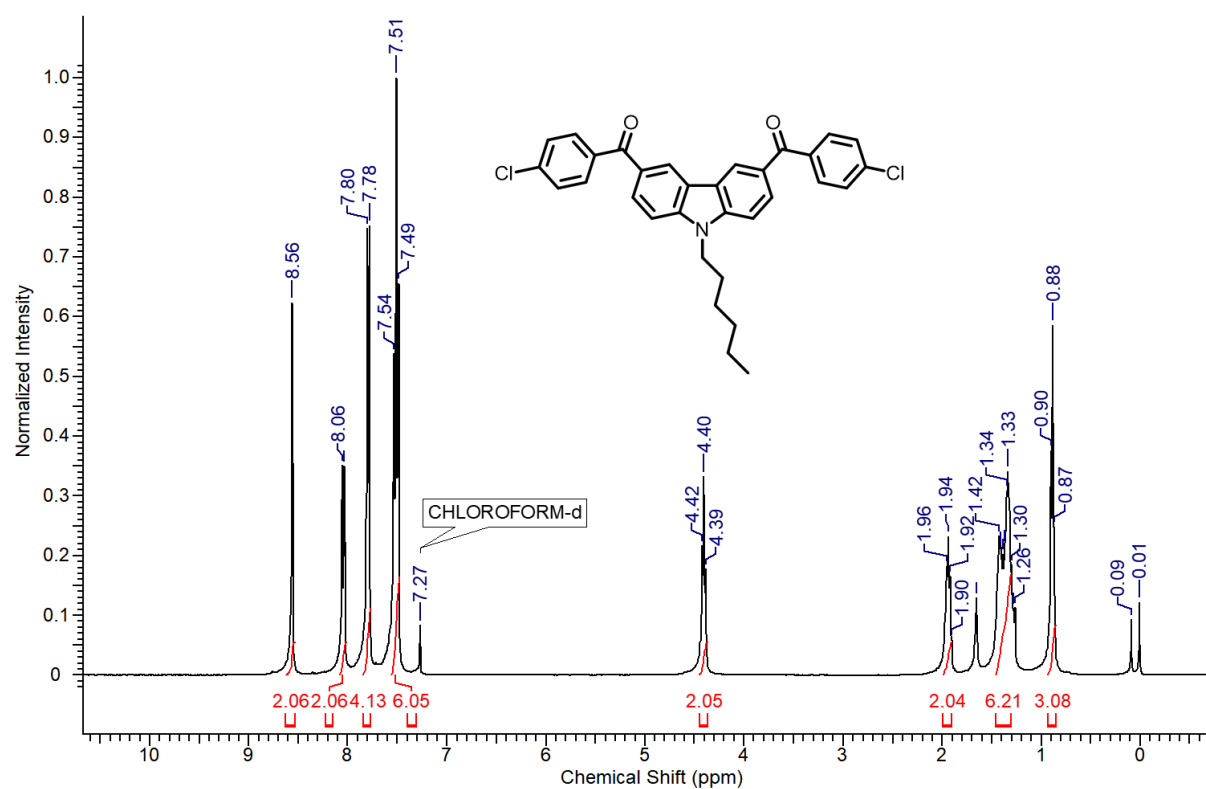


¹H (top) and ¹³C (bottom) NMR spectra of (9-octyl-9H-carbazole-3,6-diyl)bis(phenylmethanone) (10).

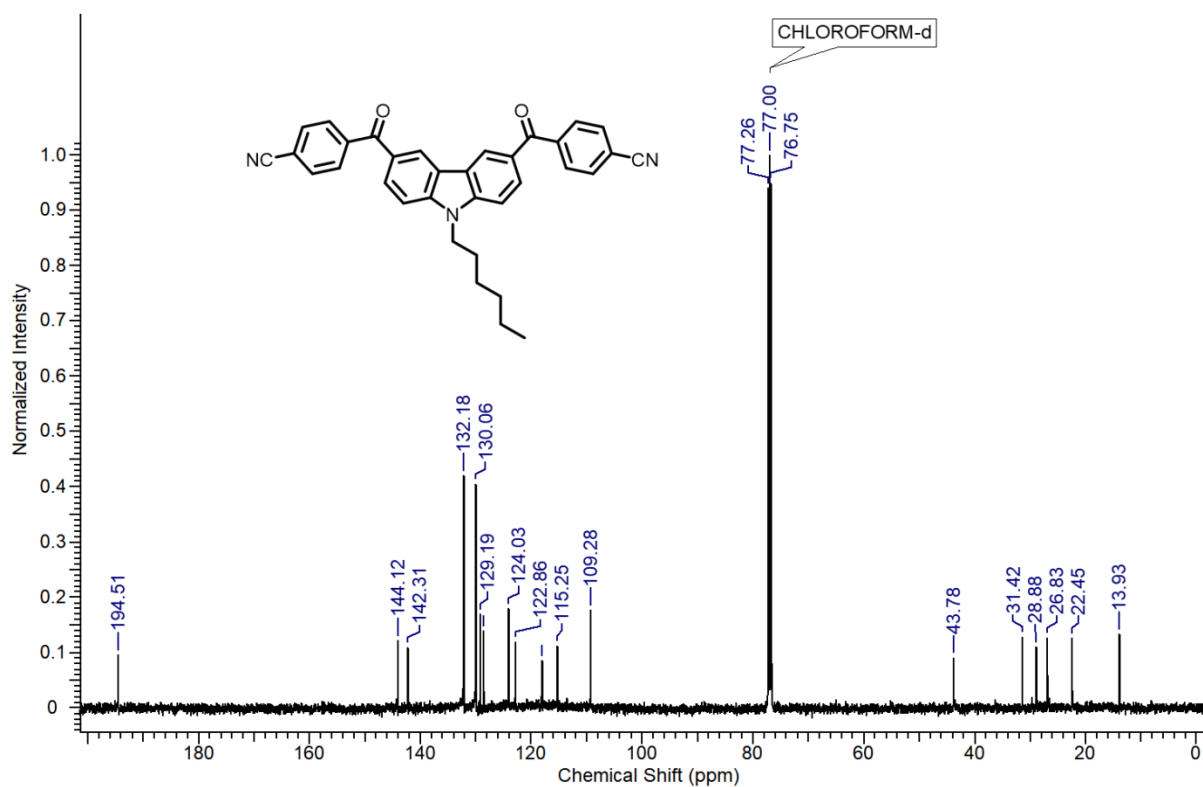
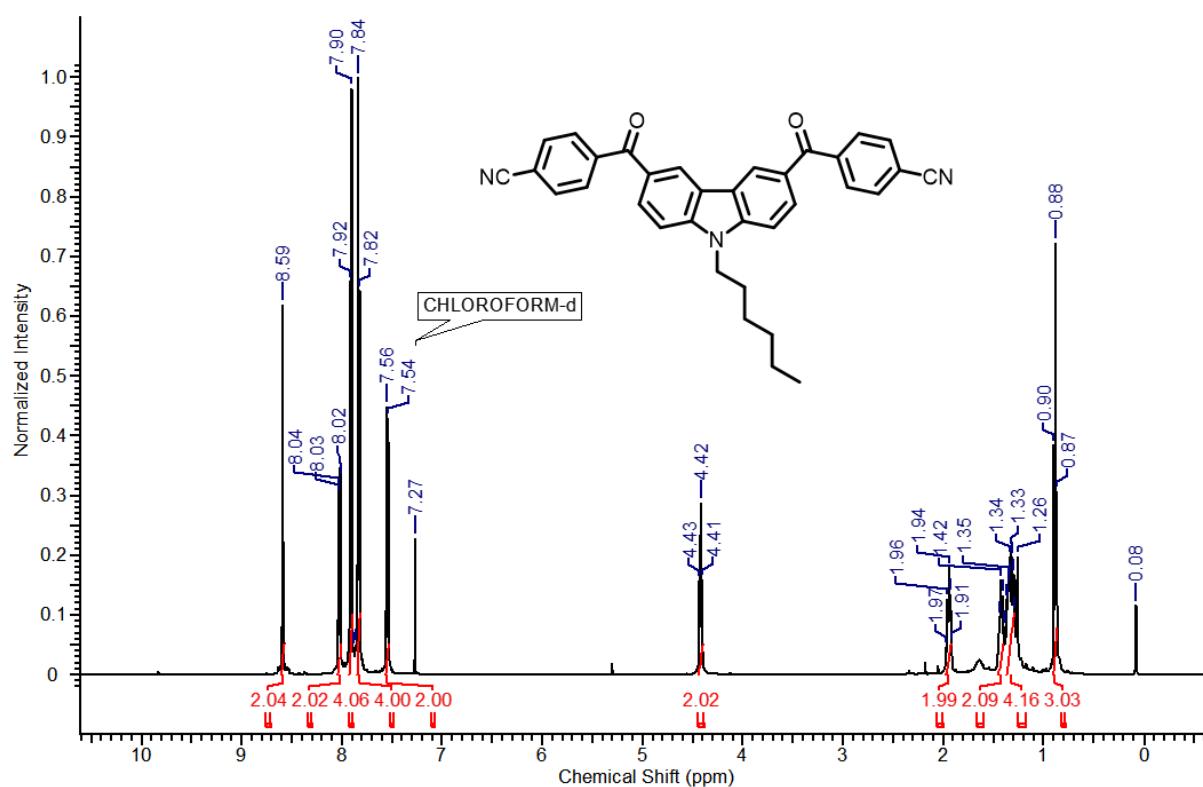
Characterization details of the synthesized molecules



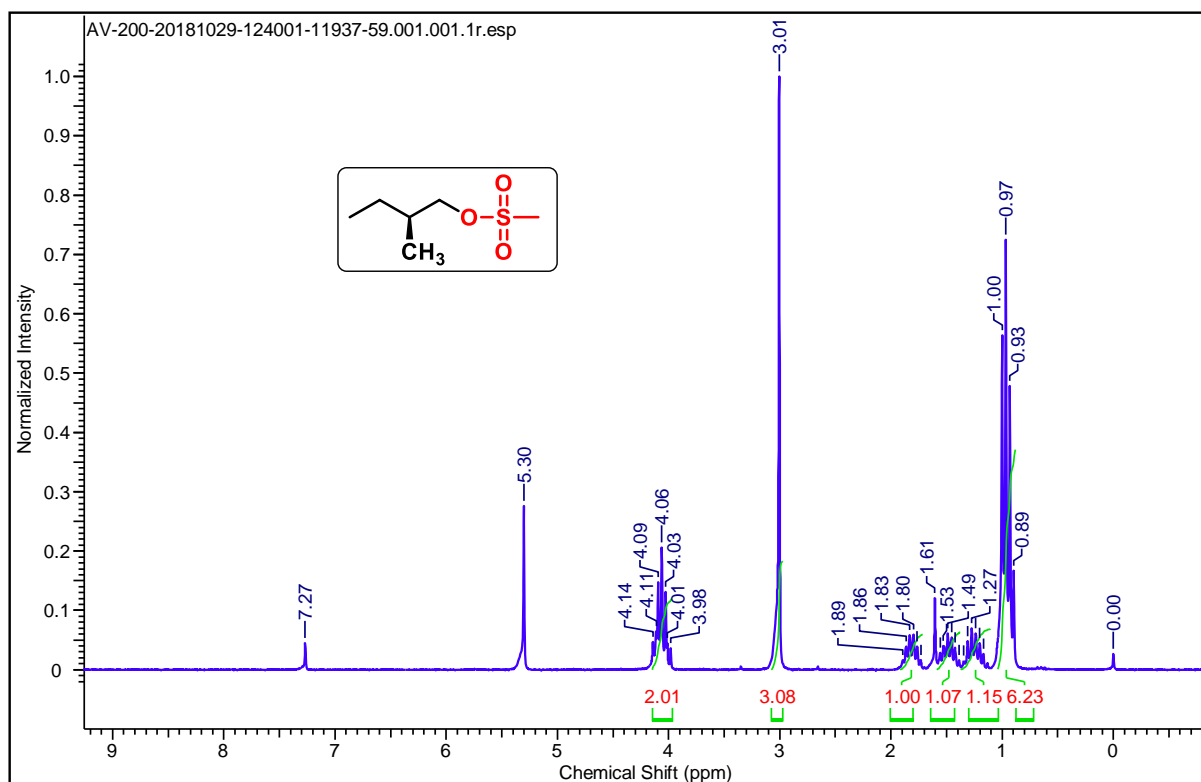
¹H (top) and ¹³C (bottom) NMR spectra of (9-hexyl-9H-carbazole-3,6-diyl)bis(p-tolylmethanone) (**11**).



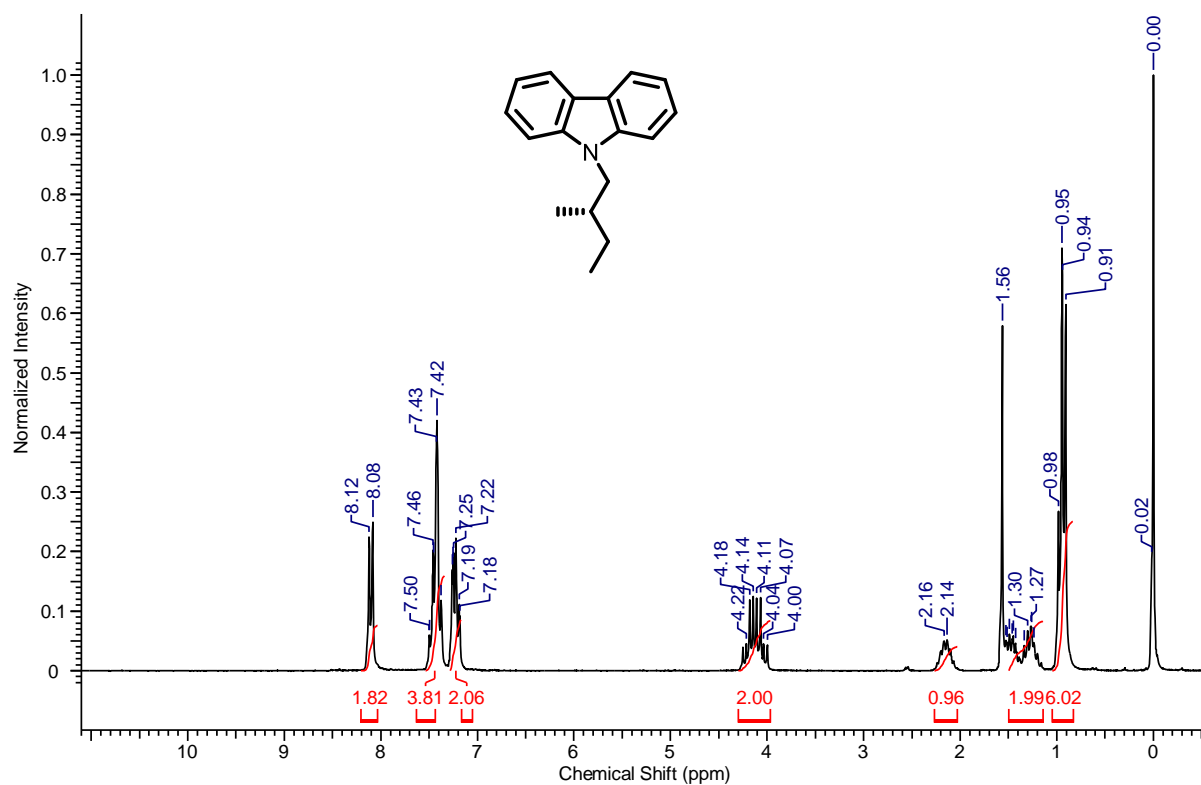
¹H (top) and ¹³C (bottom) NMR spectra of (9-hexyl-9H-carbazole-3,6-diyl)bis((4-chlorophenyl)methanone) (**12**).



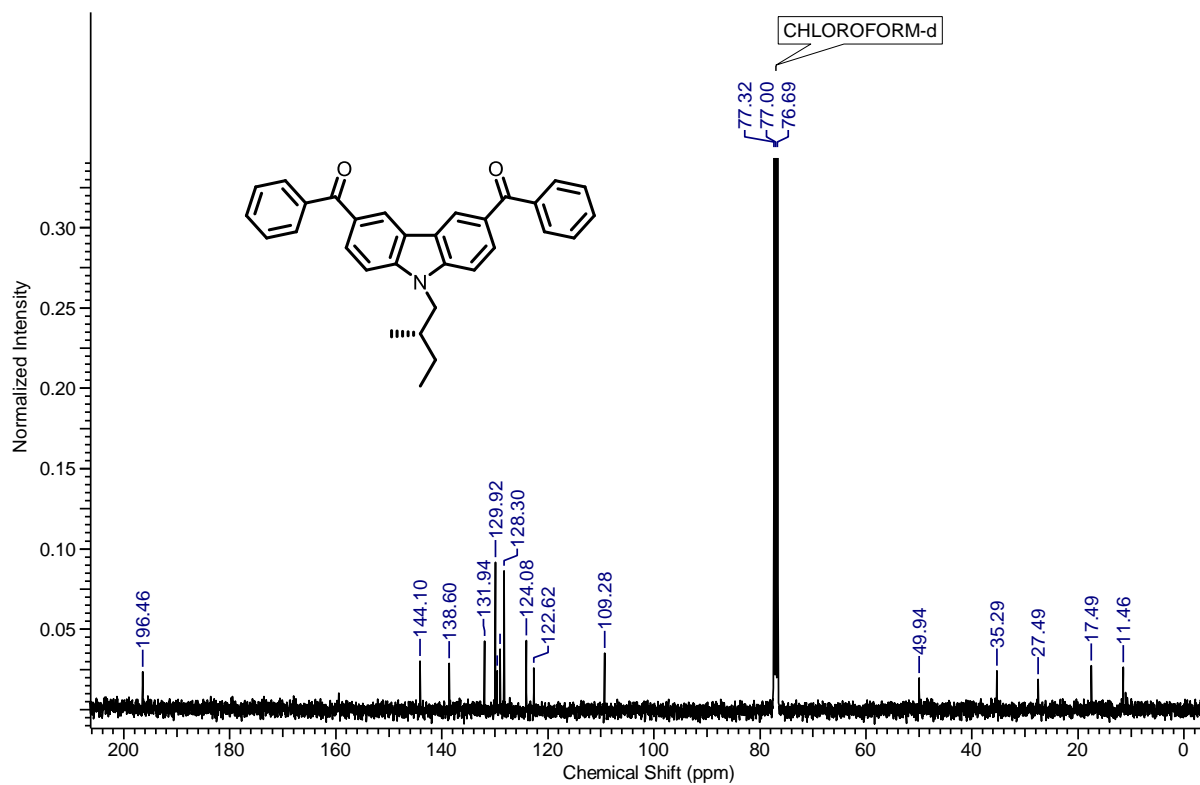
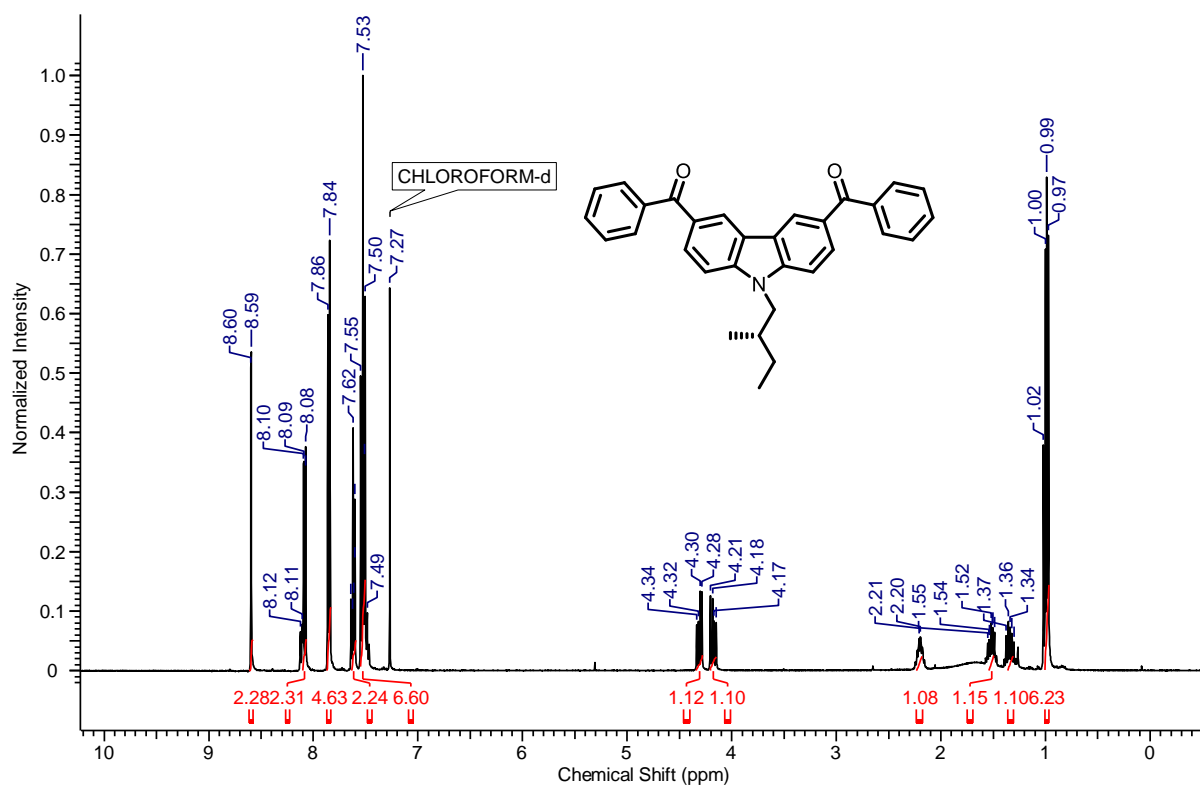
¹H (top) and ¹³C (bottom) NMR spectra of 4,4'-(9-hexyl-9H-carbazole-3,6-dicarbonyl)dibenzonitrile (13).



^1H NMR spectra of (S)-2-methylbutyl methanesulfonate (**14**).



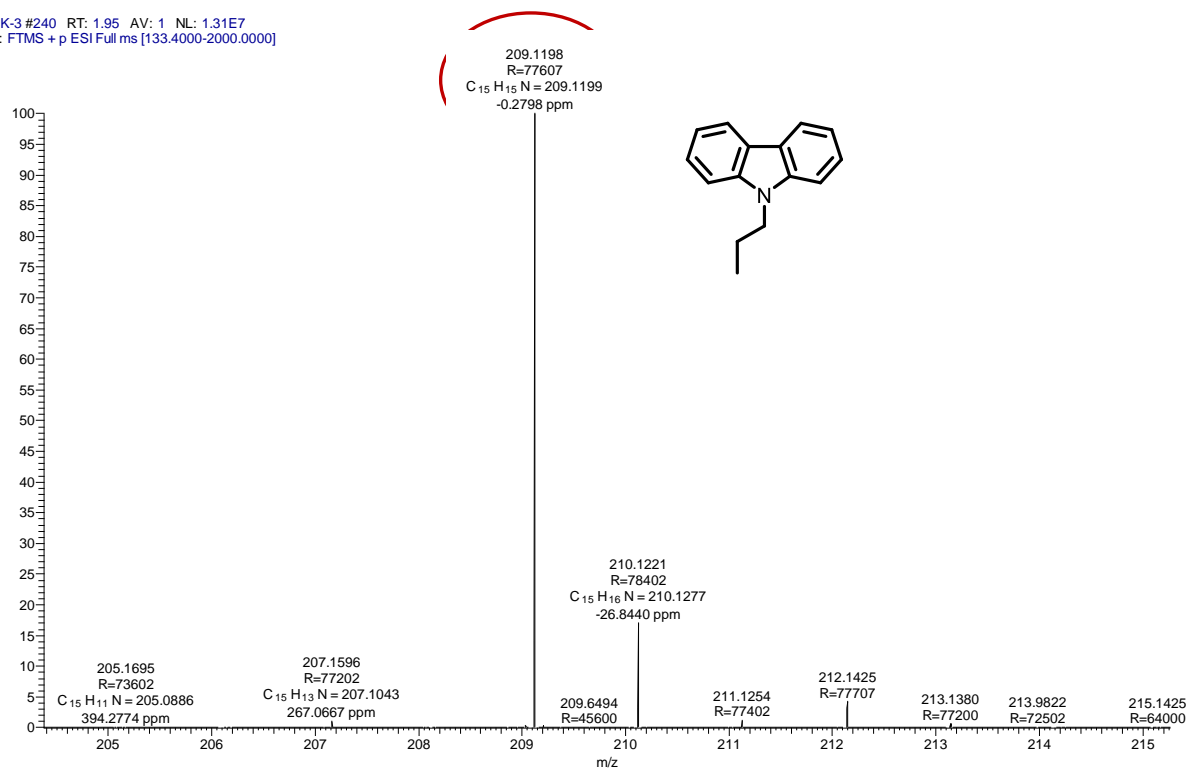
^1H NMR spectra of (S)-9-(2-methylbutyl)-9H-carbazole (**15**).



¹H (top) and ¹³C (bottom) NMR spectra of (S)-9-(2-methylbutyl)-9H-carbazole-3,6-diylbis(phenylmethanone) (**16**).

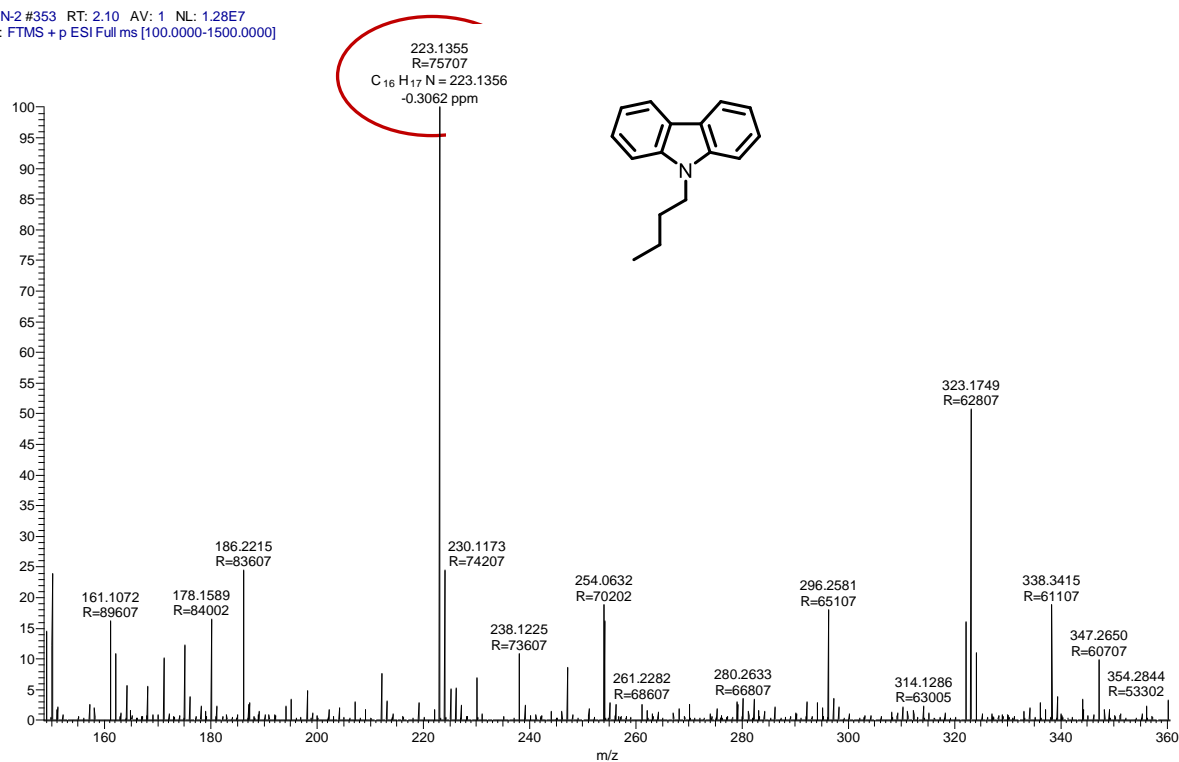
Characterization details of the synthesized molecules

AK-3 #240 RT: 1.95 AV: 1 NL: 1.31E7
T: FTMS + p ESI Full ms [133.4000-2000.0000]



HR-MS spectrum of 9-propyl-9H-carbazole (1).

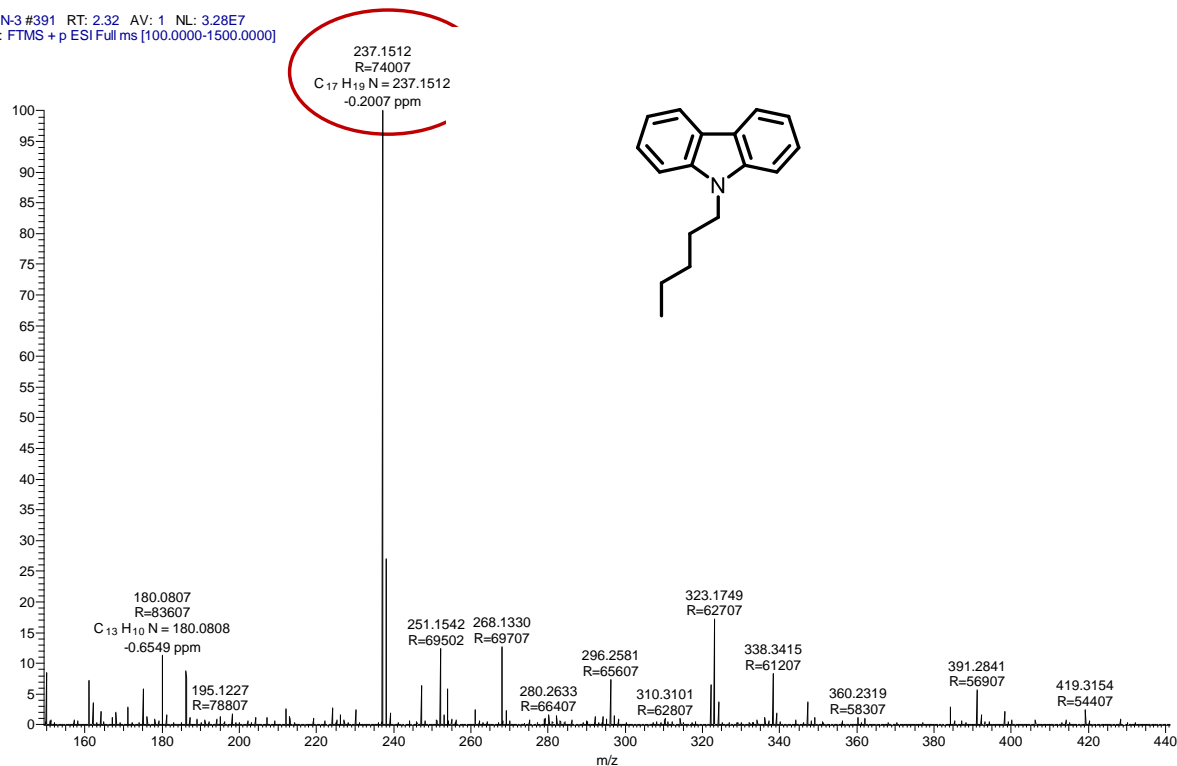
AN-2 #353 RT: 2.10 AV: 1 NL: 1.28E7
T: FTMS + p ESI Full ms [100.0000-1500.0000]



HR-MS spectrum of 9-butyl-9H-carbazole (2).

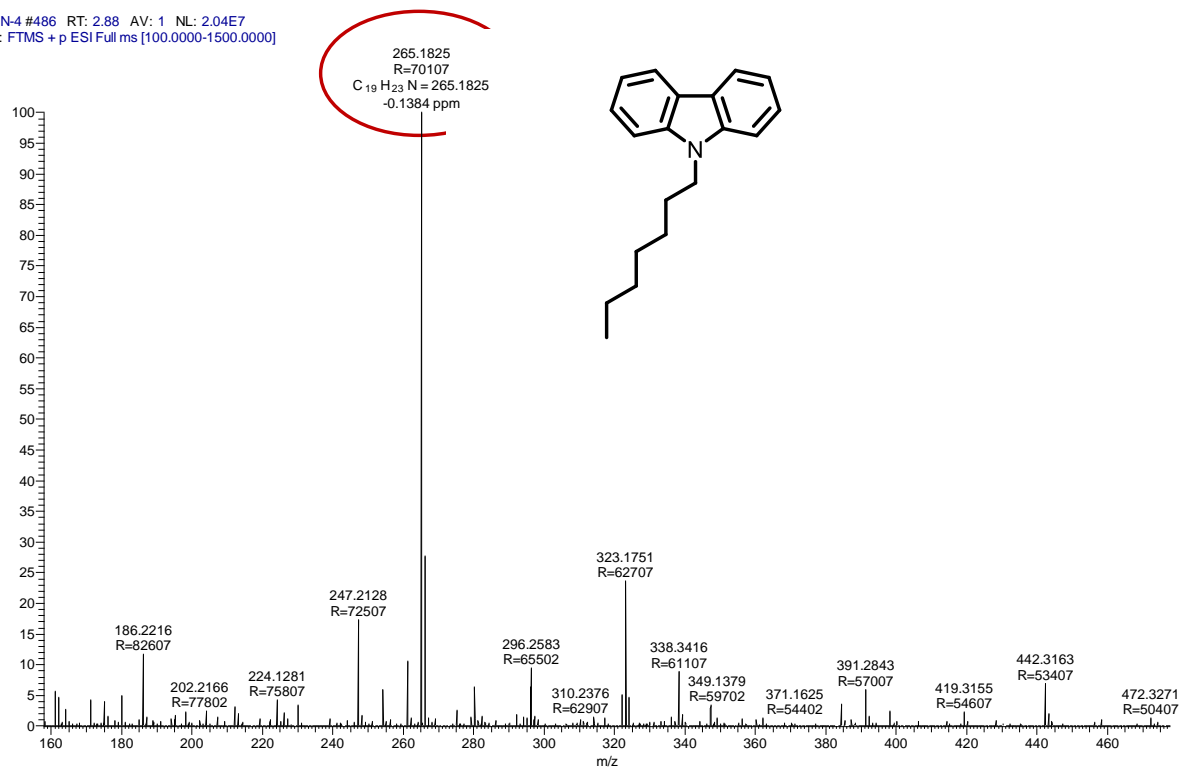
Characterization details of the synthesized molecules

AN-3 #391 RT: 2.32 AV: 1 NL: 3.28E7
T: FTMS + p ESI Full ms [100.0000-1500.0000]



HR-MS spectrum of 9-pentyl-9H-carbazole (3).

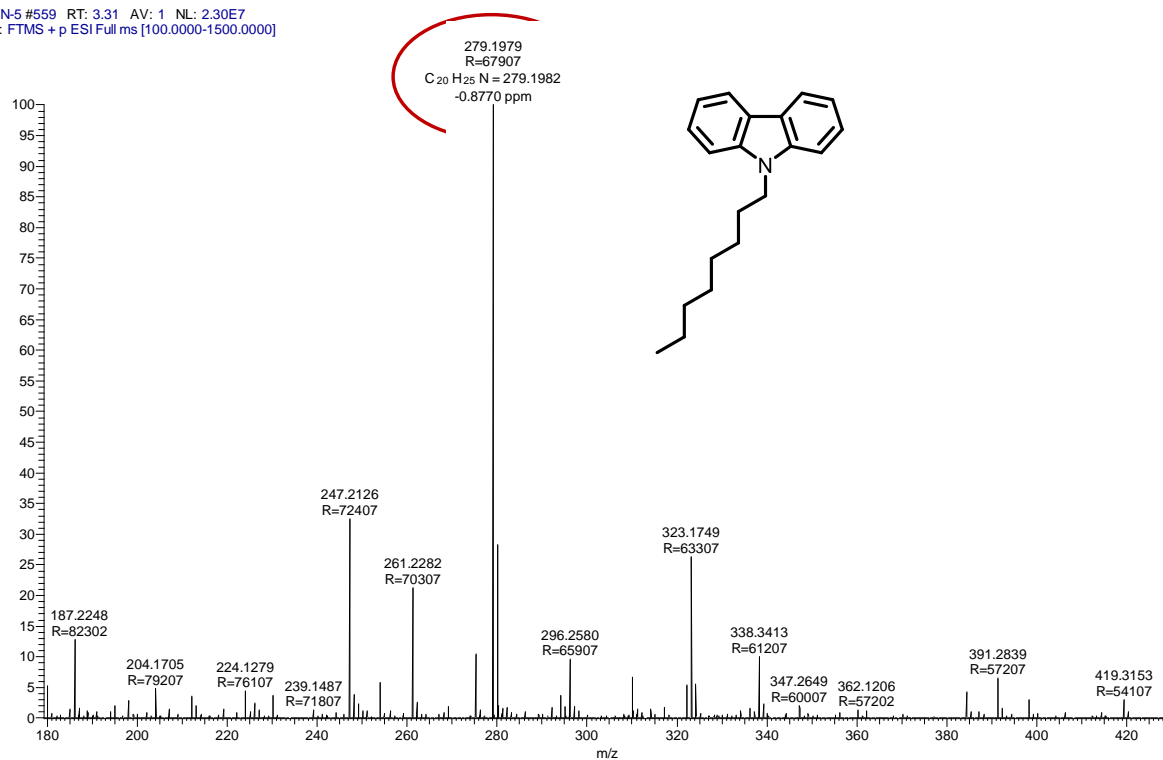
AN-4 #486 RT: 2.88 AV: 1 NL: 2.04E7
T: FTMS + p ESI Full ms [100.0000-1500.0000]



HR-MS spectrum of 9-heptyl-9H-carbazole (4).

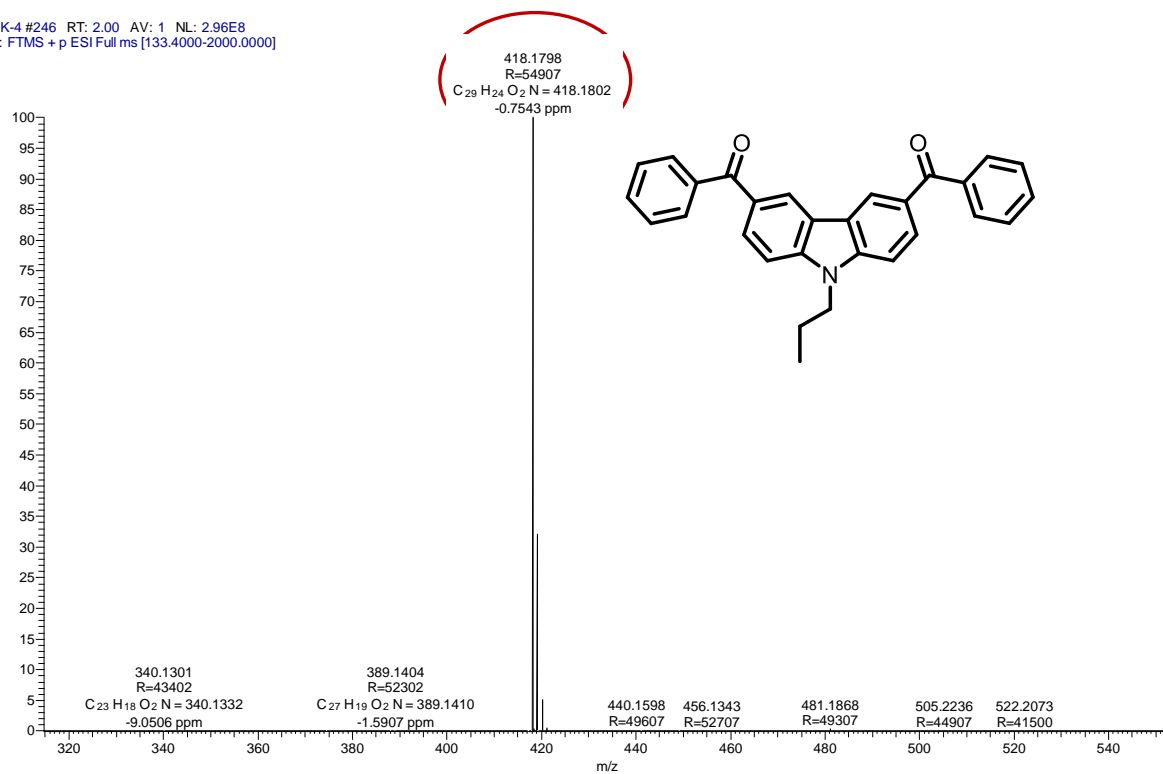
Characterization details of the synthesized molecules

AN-5 #559 RT: 3.31 AV: 1 NL: 2.30E7
T: FTMS + p ESI Full ms [100.0000-1500.0000]



HR-MS spectrum of 9-octyl-9H-carbazole (5).

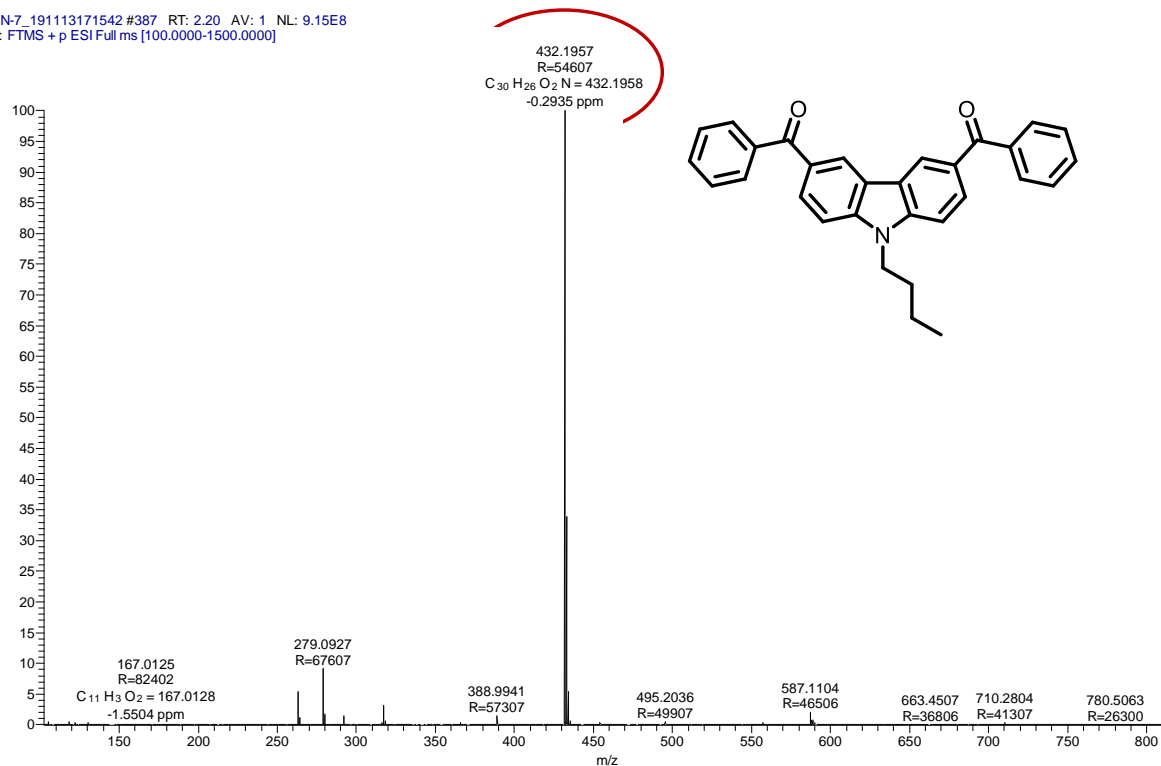
AK-4 #246 RT: 2.00 AV: 1 NL: 2.96E8
T: FTMS + p ESI Full ms [133.4000-2000.0000]



HR-MS spectrum of (9-propyl-9H-carbazole-3,6-diyl)bis(phenylmethanone) (6).

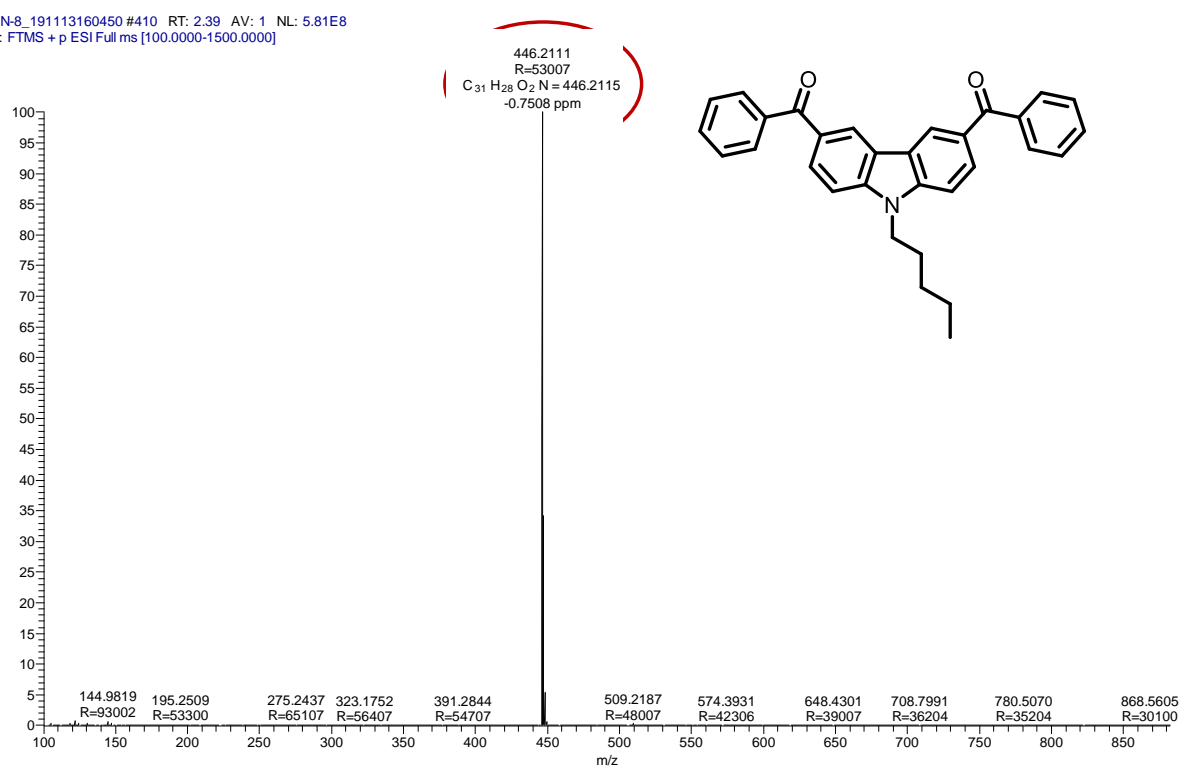
Characterization details of the synthesized molecules

AN-7_191113171542 #387 RT: 2.20 AV: 1 NL: 9.15E8
T: FTMS + p ESI Full ms [100.0000-1500.0000]



HR-MS spectrum of (9-butyl-9H-carbazole-3,6-diyl)bis(phenylmethanone) (**7**).

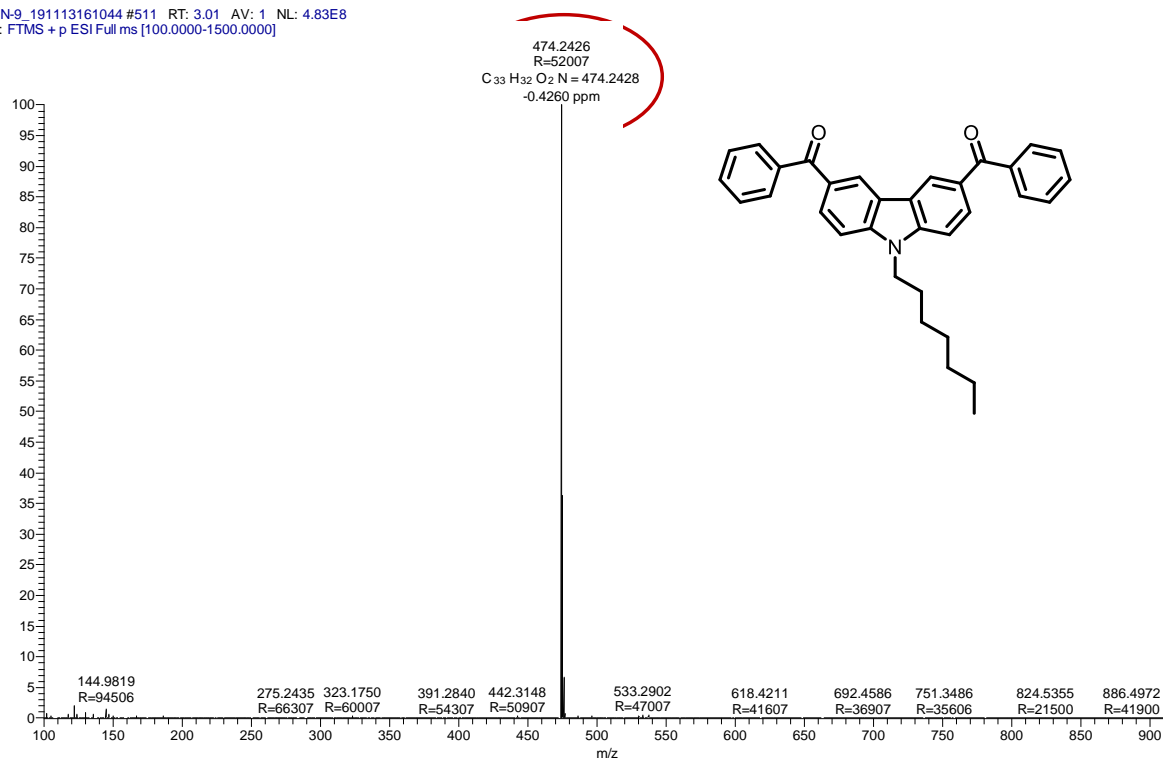
AN-8_191113160450 #410 RT: 2.39 AV: 1 NL: 5.81E8
T: FTMS + p ESI Full ms [100.0000-1500.0000]



HR-MS spectrum of (9-pentyl-9H-carbazole-3,6-diyl)bis(phenylmethanone) (**8**).

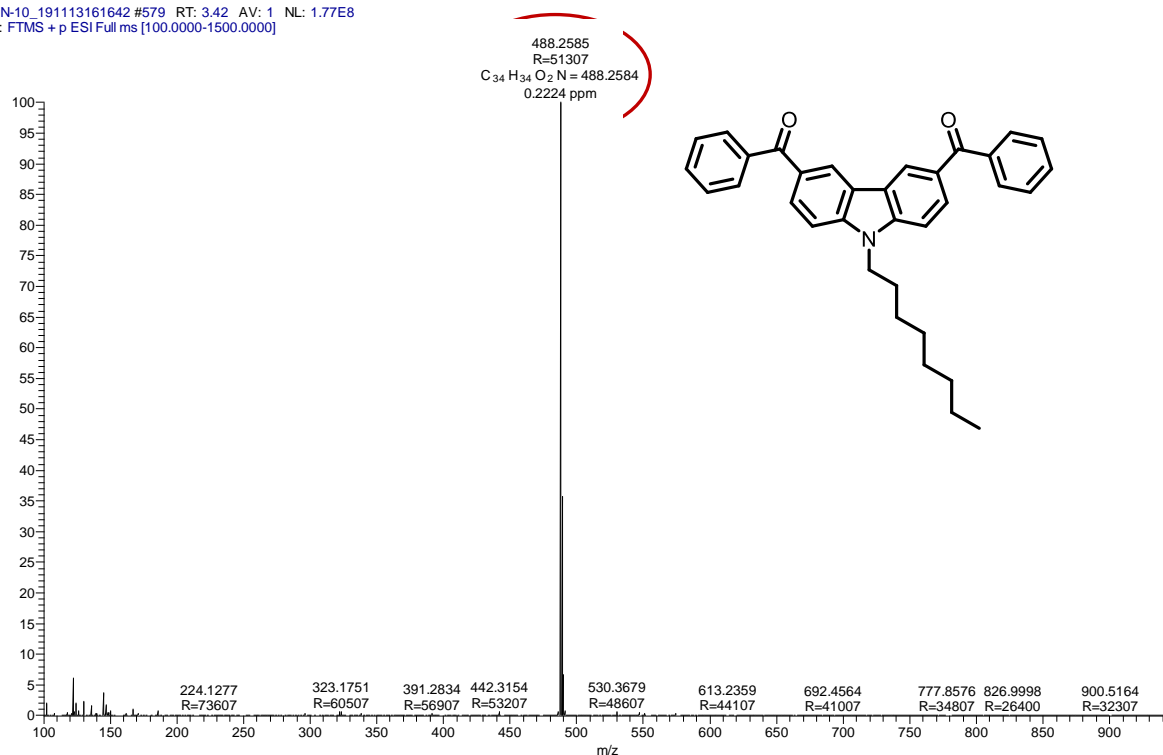
Characterization details of the synthesized molecules

AN-9_191113161044 #511 RT: 3.01 AV: 1 NL: 4.83E8
T: FTMS + p ESI Full ms [100.0000-1500.0000]



HR-MS spectrum of (9-heptyl-9H-carbazole-3,6-diyl)bis(phenylmethanone) (9).

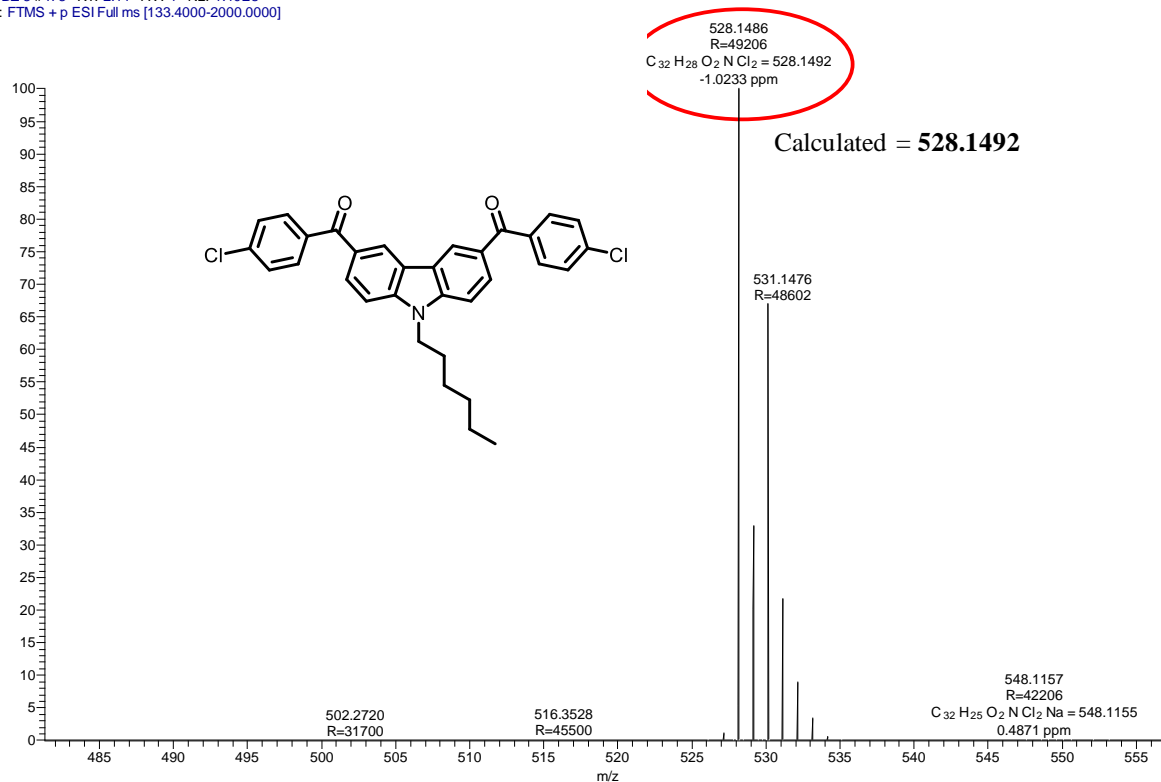
AN-10_191113161642 #579 RT: 3.42 AV: 1 NL: 1.77E8
T: FTMS + p ESI Full ms [100.0000-1500.0000]



HR-MS spectrum of (9-octyl-9H-carbazole-3,6-diyl)bis(phenylmethanone) (10).

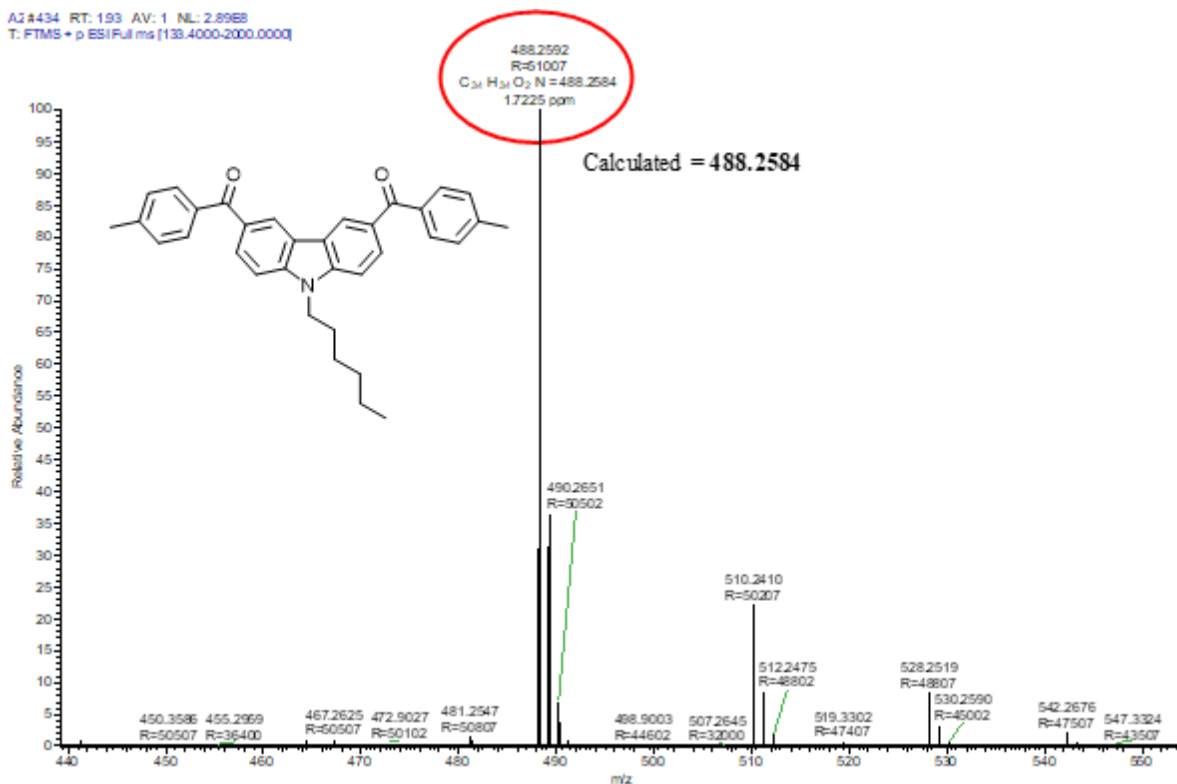
Characterization details of the synthesized molecules

CBZ-3 #473 RT: 2.11 AV: 1 NL: 1.40E8
T: FTMS + p ESI Full ms [133.4000-2000.0000]



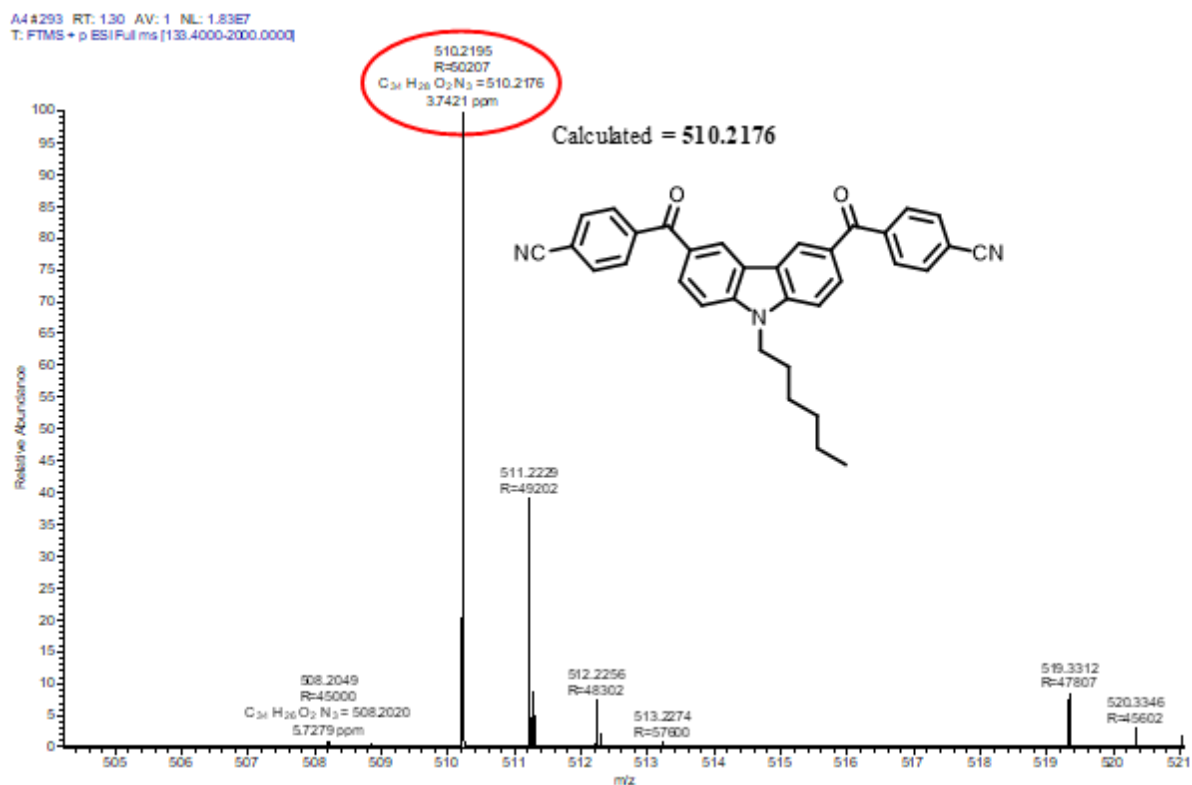
HR-MS spectrum of (9-hexyl-9H-carbazole-3,6-diyl)bis((4-chlorophenyl)methanone) (12).

AJ #434 RT: 1.93 AV: 1 NL: 2.89E8
T: FTMS + p ESI Full ms [133.4000-2000.0000]

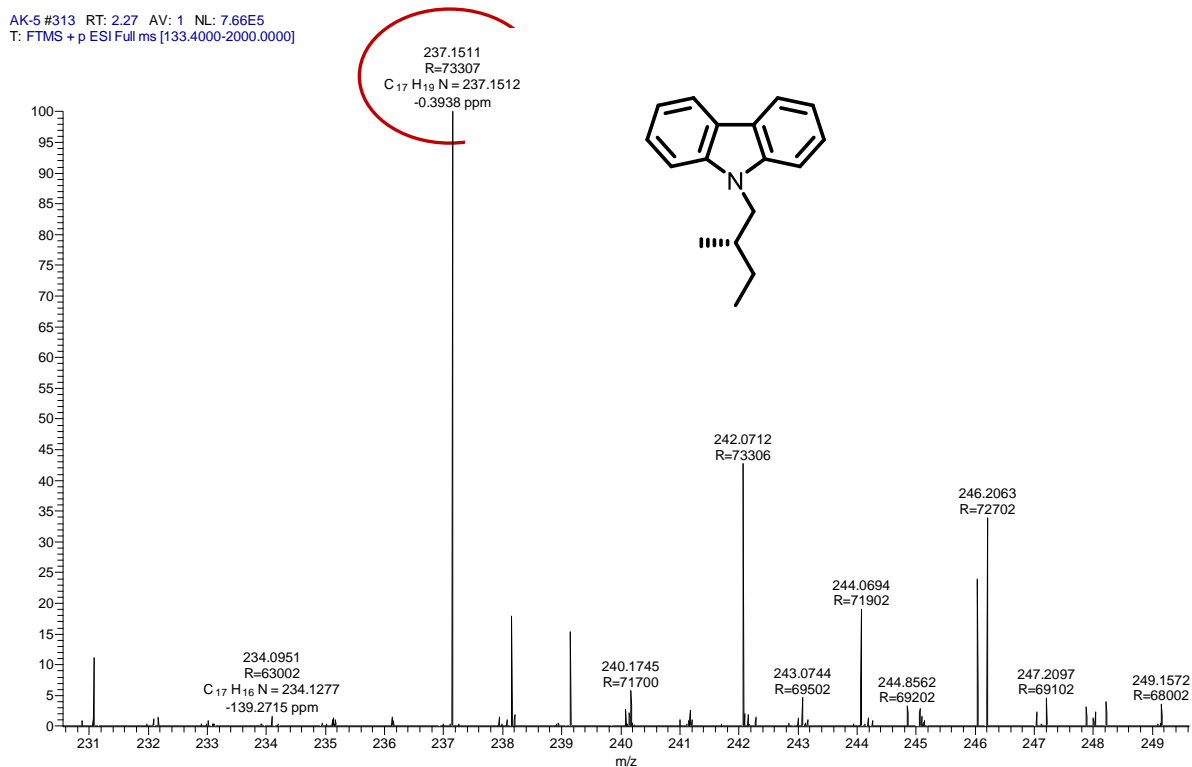


HR-MS spectrum of (9-hexyl-9H-carbazole-3,6-diyl)bis(p-tolylmethanone) (11).

Characterization details of the synthesized molecules



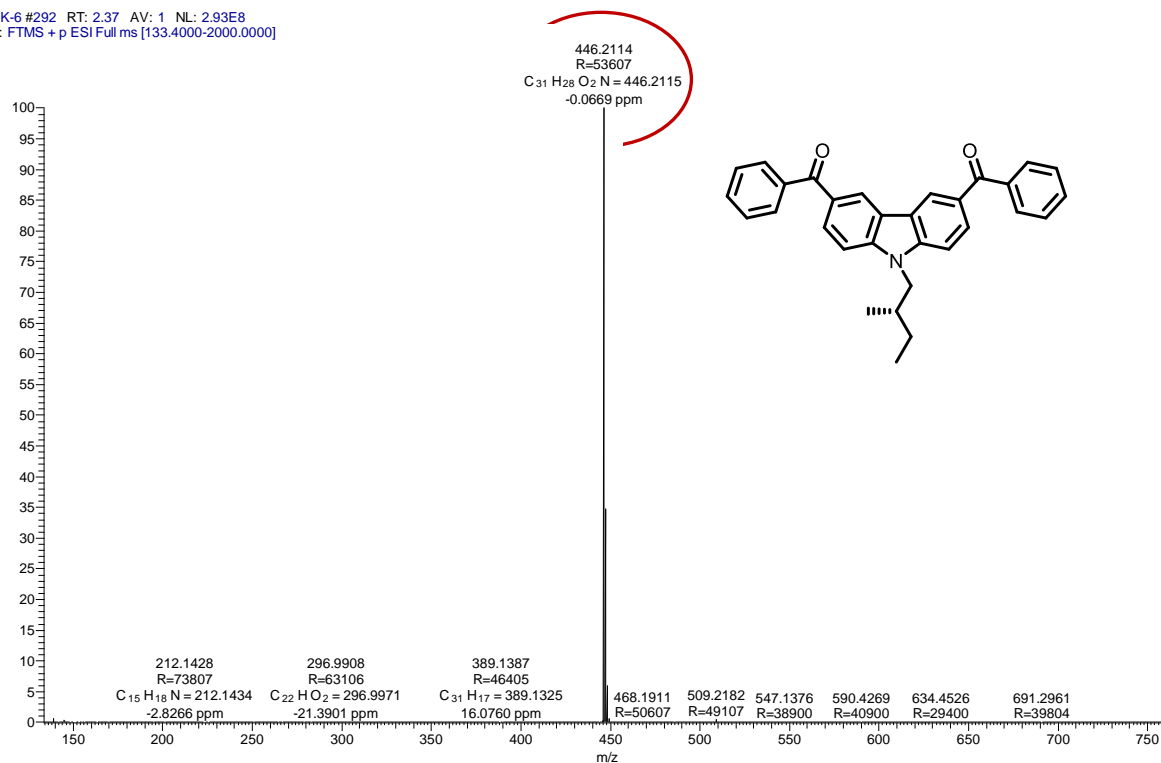
HR-MS spectrum of 4,4'-(9-hexyl-9H-carbazole-3,6-dicarbonyl)dibenzonitrile (**13**).



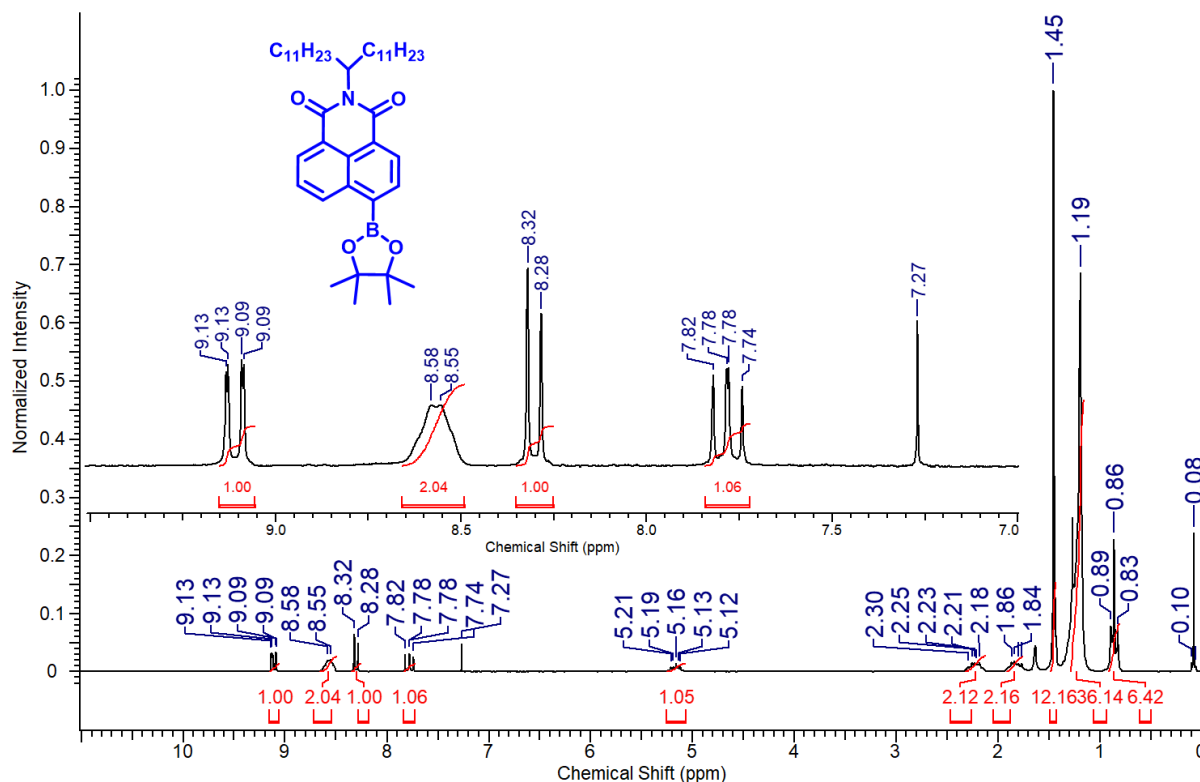
HR-MS spectrum of (S)-9-(2-methylbutyl)-9H-carbazole (**15**).

Characterization details of the synthesized molecules

AK-6 #292 RT: 2.37 AV: 1 NL: 2.93E8
T: FTMS + p ESI Full ms [133.4000-2000.0000]

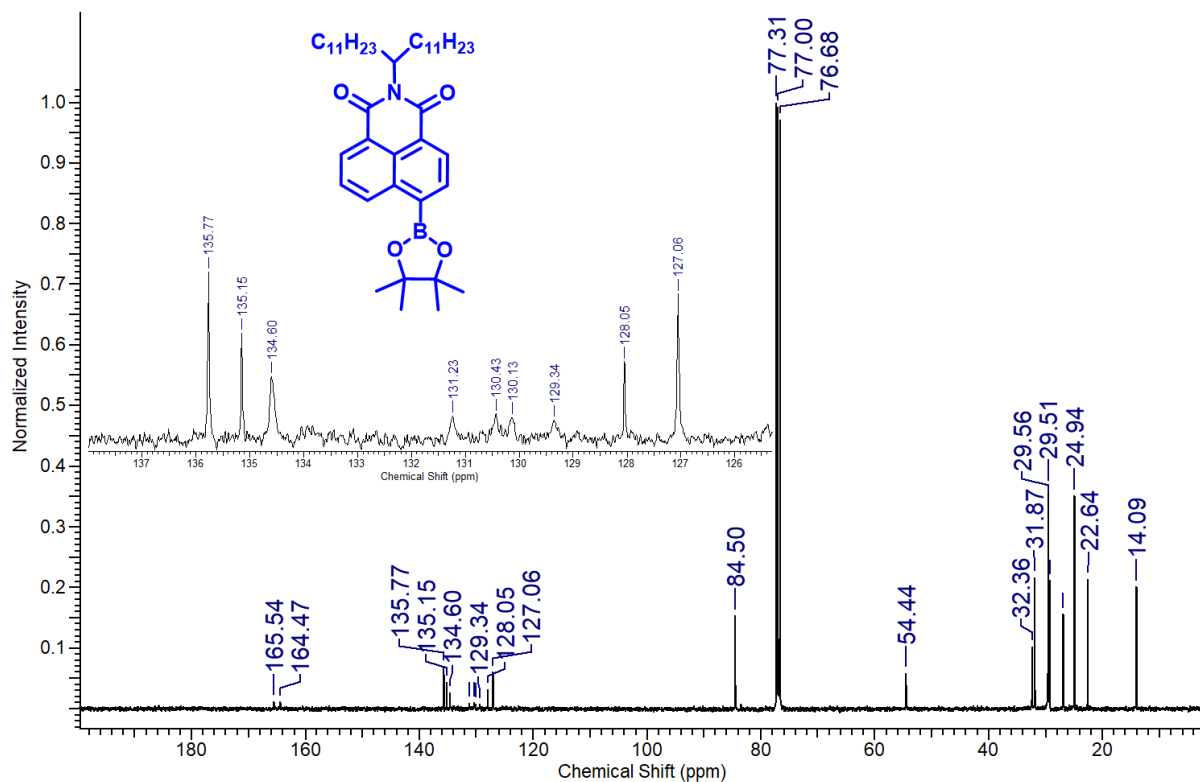


HR-MS spectrum of (S)-(9-(2-methylbutyl)-9H-carbazole-3,6-diyl)bis(phenylmethanone) (16).

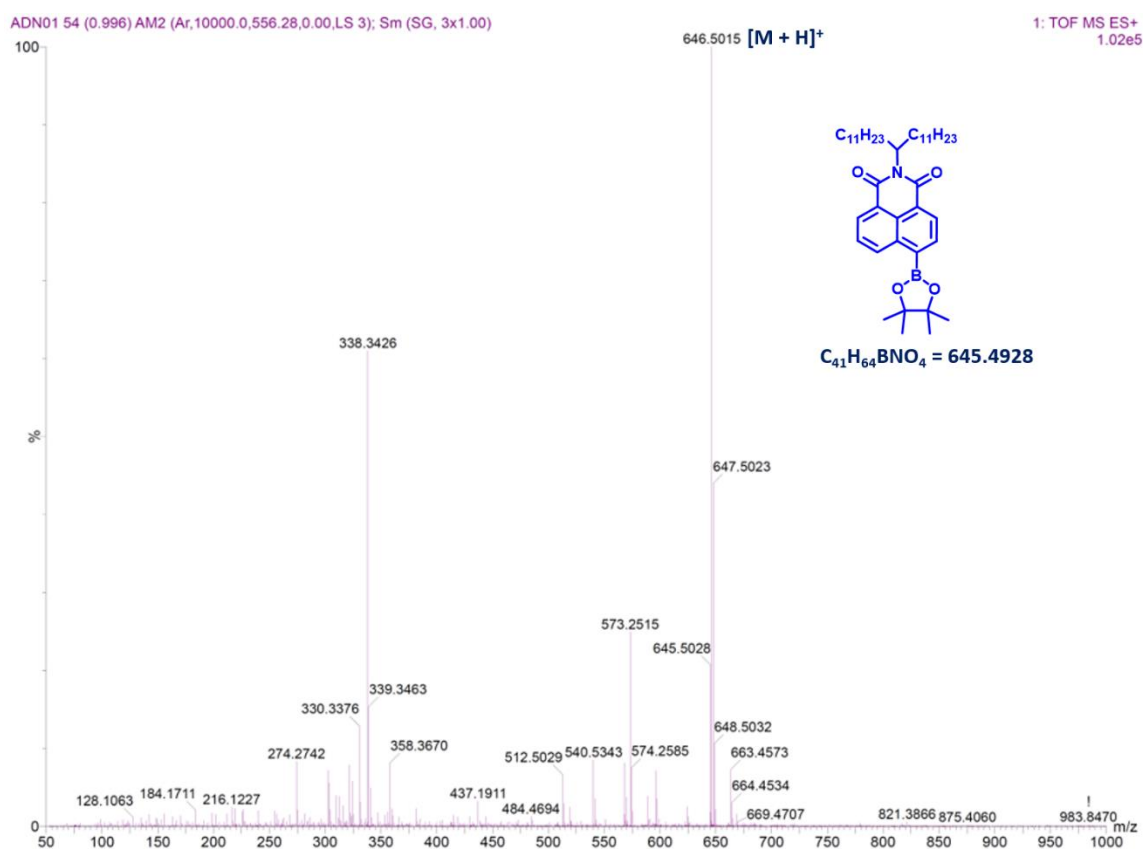


¹H NMR spectra of 6-(4,4,5,5-tetramethyl-1,3,2-dioxaborolan-2-yl)-2-(tricosan-12-yl)-1H-benzo[de]isoquinoline-1,3(2H)-dione (1).

Characterization details of the synthesized molecules

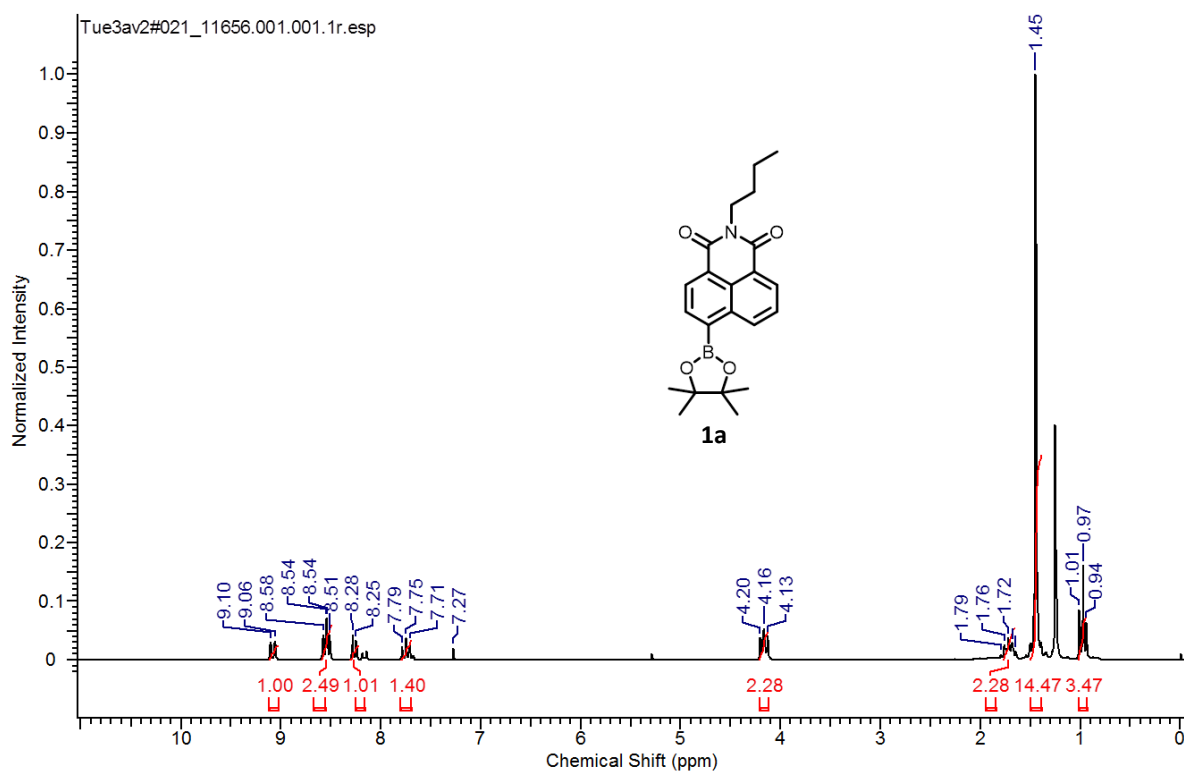


¹³C spectrum spectra of 6-(4,4,5,5-tetramethyl-1,3,2-dioxaborolan-2-yl)-2-(tricosan-12-yl)-1H-benzo[de]isoquinoline-1,3(2H)-dione (**1**).

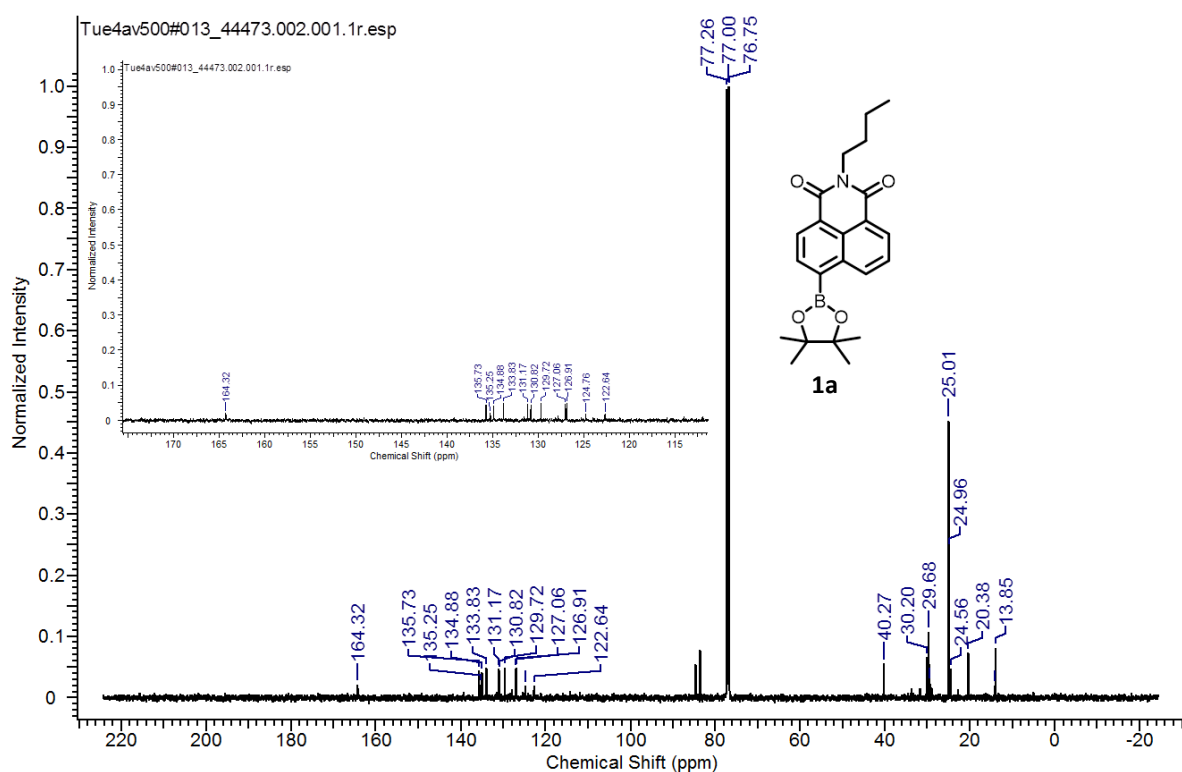


HRMS spectrum of 6-(4,4,5,5-tetramethyl-1,3,2-dioxaborolan-2-yl)-2-(tricosan-12-yl)-1H-benzo[de]isoquinoline-1,3(2H)-dione (**1**).

Characterization details of the synthesized molecules



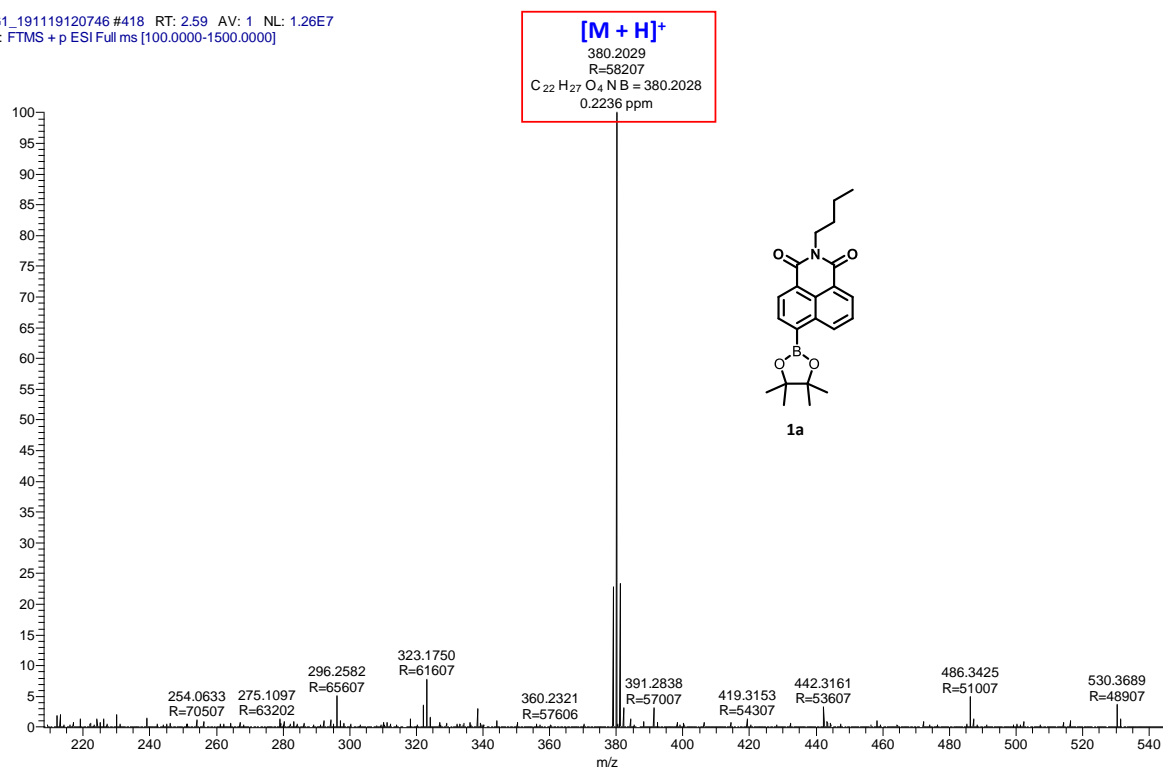
¹H NMR spectra of 2-butyl-6-(4,4,5,5-tetramethyl-1,3,2-dioxaborolan-2-yl)-1H-benzo[de]isoquinoline-1,3(2H)-dione (**1a**).



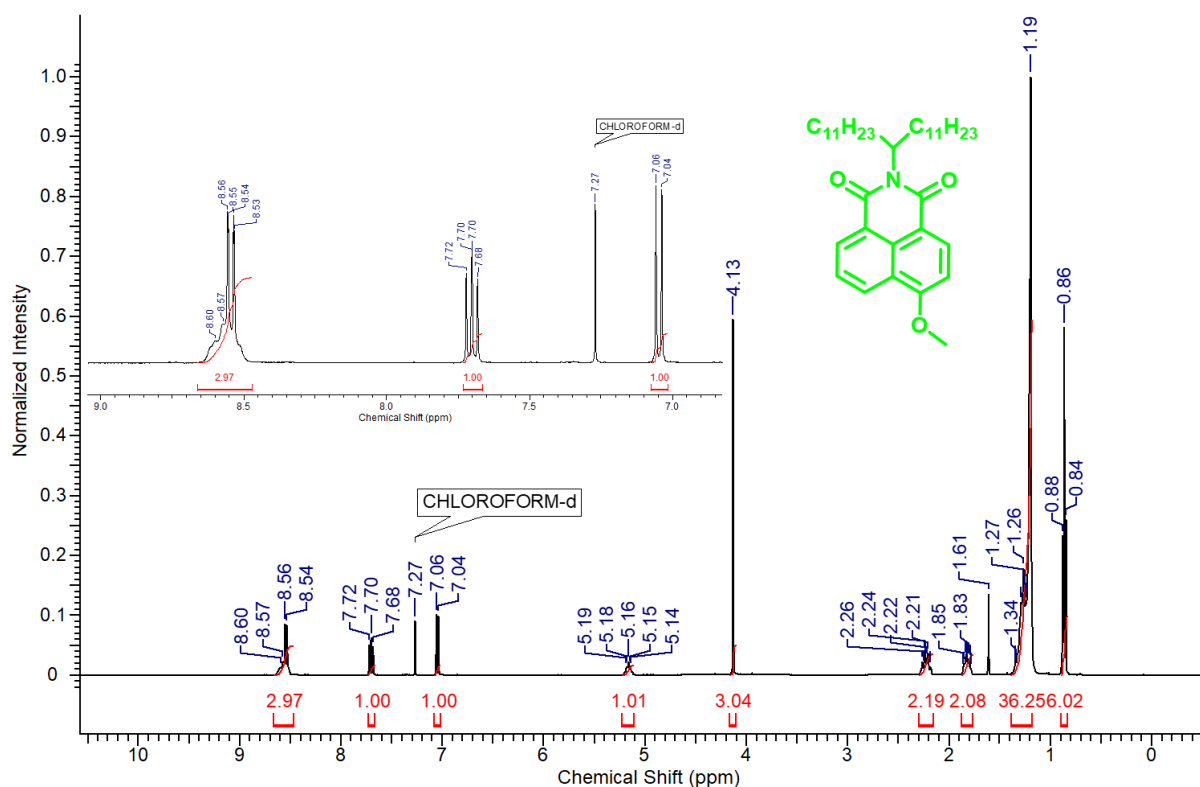
¹³C NMR spectra of 2-butyl-6-(4,4,5,5-tetramethyl-1,3,2-dioxaborolan-2-yl)-1H-benzo[de]isoquinoline-1,3(2H)-dione (**1a**).

Characterization details of the synthesized molecules

G1_191119120746 #418 RT: 2.59 AV: 1 NL: 1.26E7
T: FTMS + p ESI Full ms [100.0000-1500.0000]

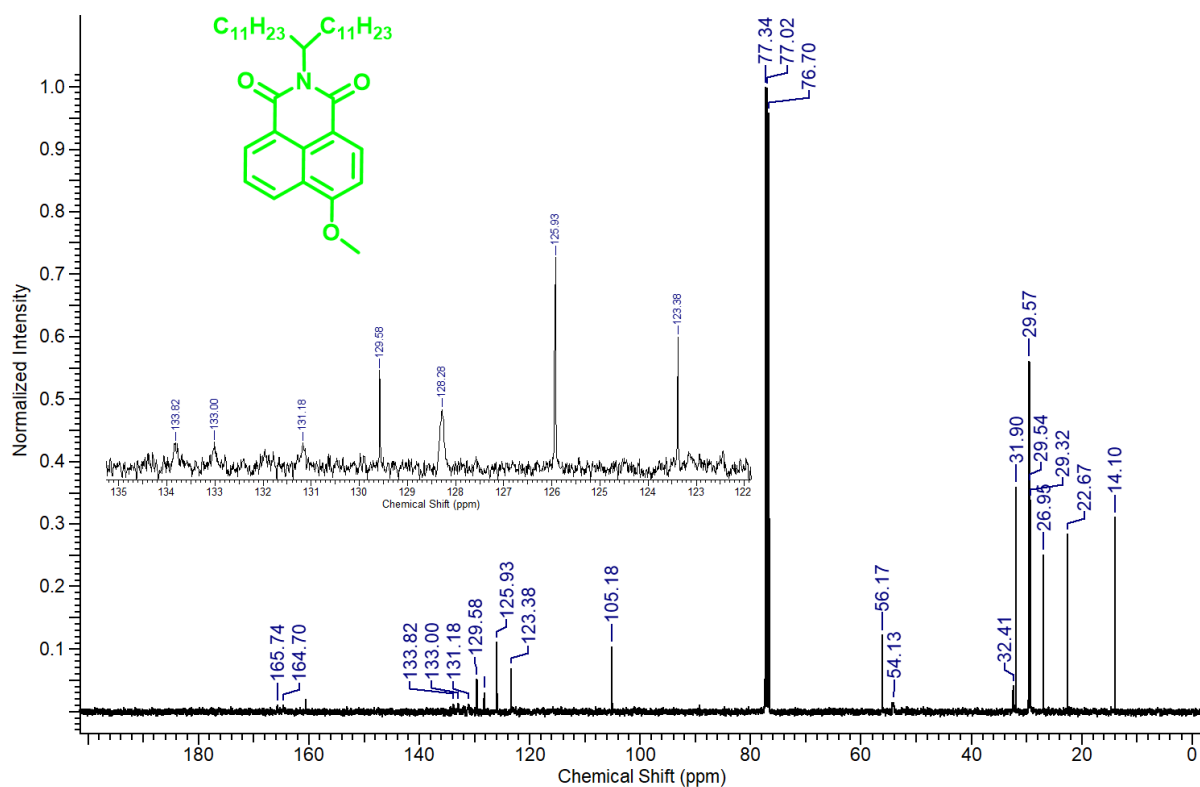


HRMS (ESI) spectra of 2-butyl-6-(4,4,5,5-tetramethyl-1,3,2-dioxaborolan-2-yl)-1H-benzo[de]isoquinoline-1,3(2H)-dione (**1a**).

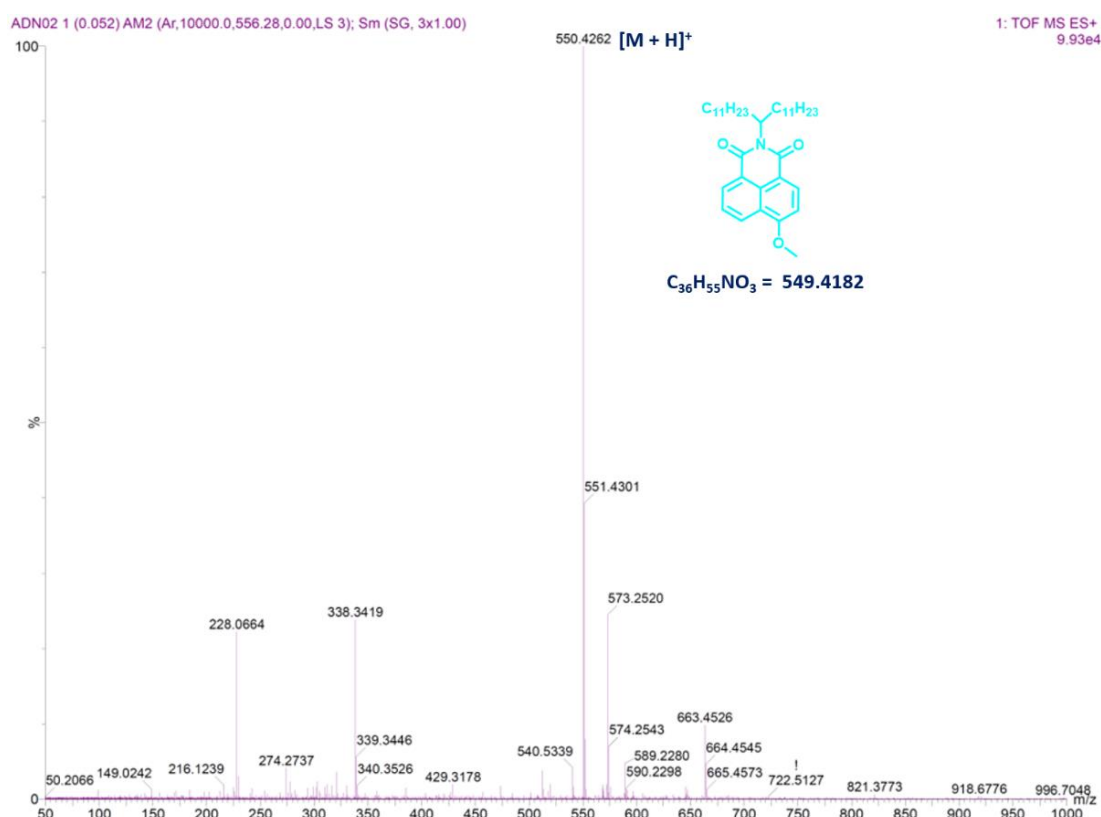


¹H NMR spectra of 6-methoxy-2-(tricosan-12-yl)-1H-benzo[de]isoquinoline-1,3(2H)-dione (**2**).

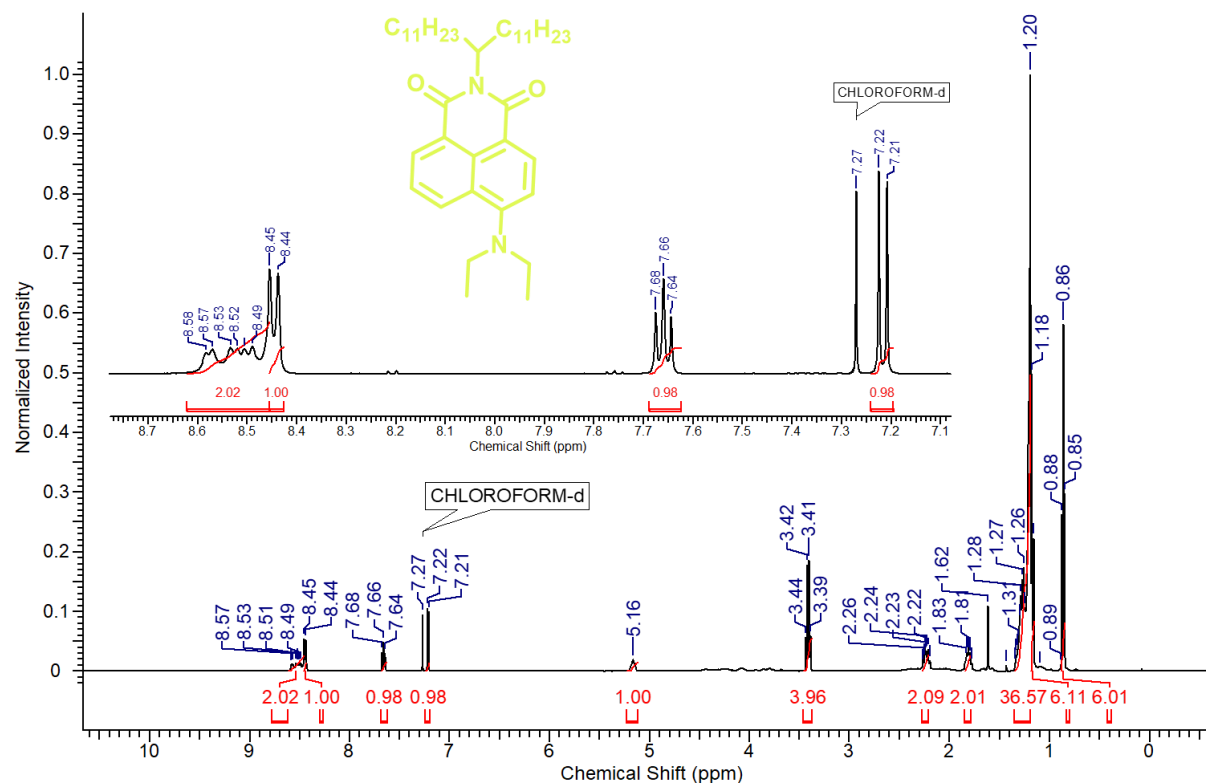
Characterization details of the synthesized molecules



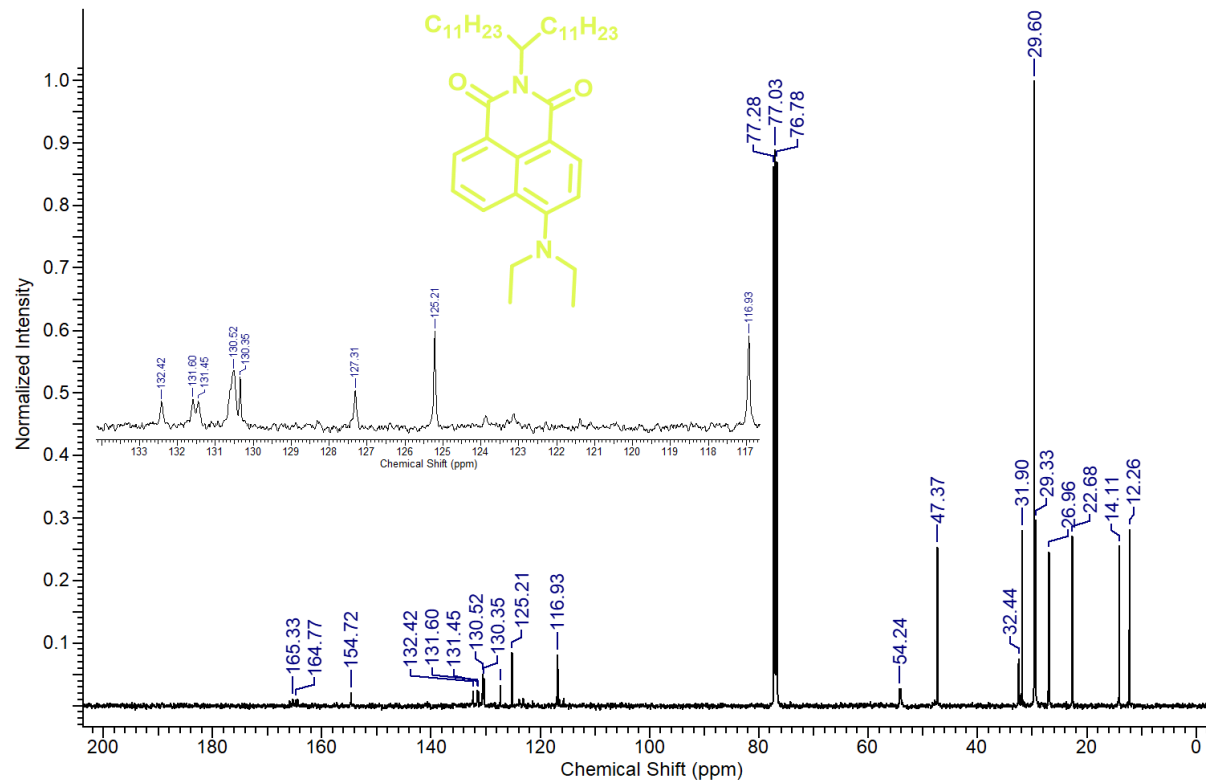
¹³C spectrum spectra of 6-methoxy-2-(tricosan-12-yl)-1H-benzo[de]isoquinoline-1,3(2H)-dione (2).



HRMS spectrum of 6-methoxy-2-(tricosan-12-yl)-1H-benzo[de]isoquinoline-1,3(2H)-dione (2).

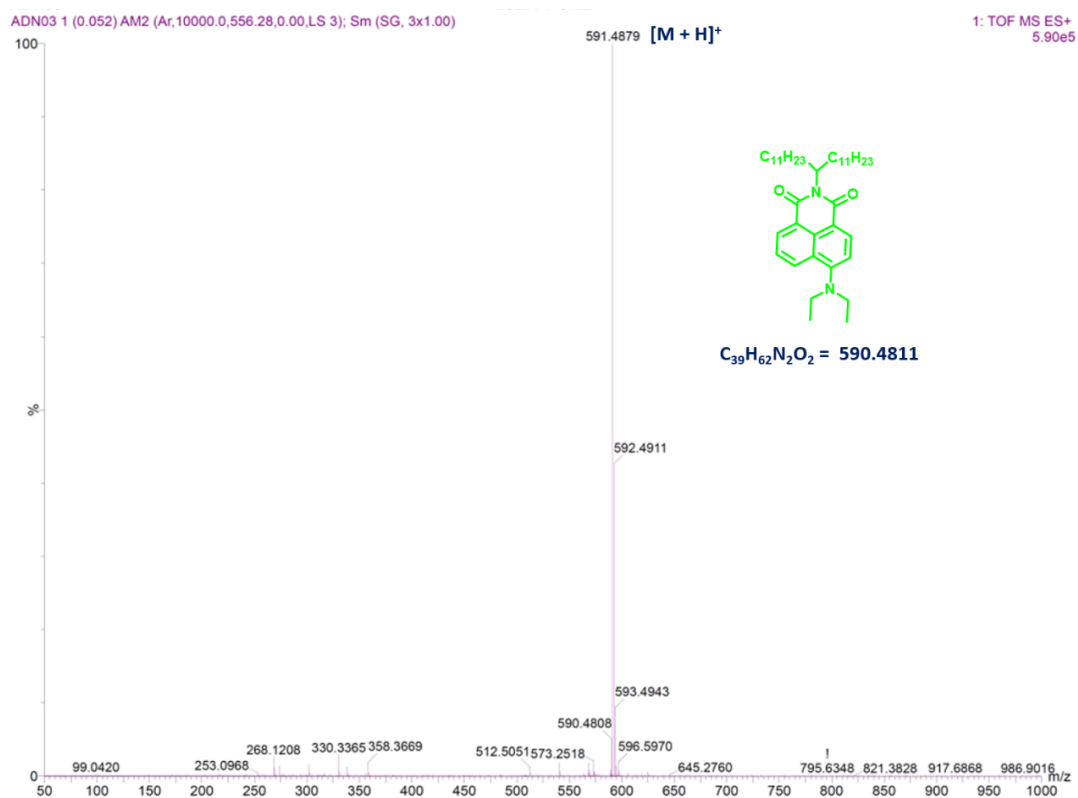


¹H NMR spectra of 6-(diethylamino)-2-(tricosan-12-yl)-1H-benzo[de]isoquinoline-1,3(2H)-dione (3).

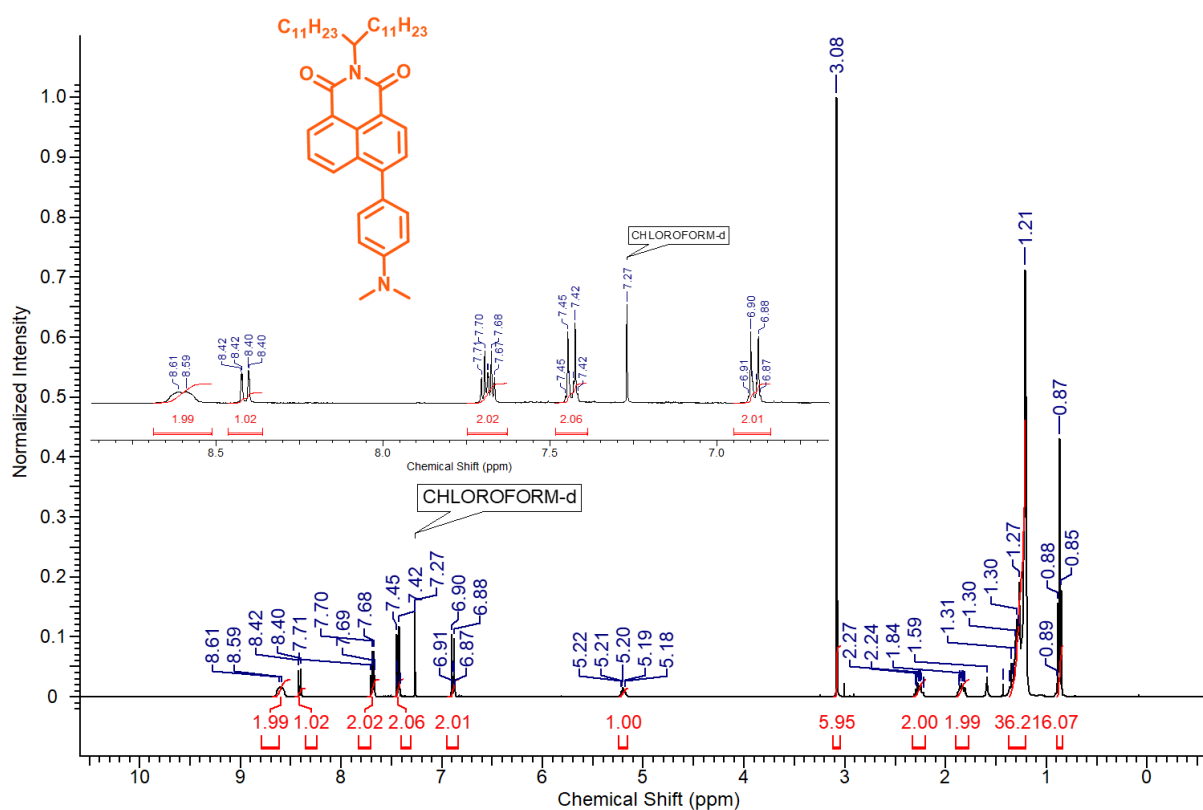


¹³C spectrum spectra of 6-(diethylamino)-2-(tricosan-12-yl)-1H-benzo[de]isoquinoline-1,3(2H)-dione (3).

Characterization details of the synthesized molecules

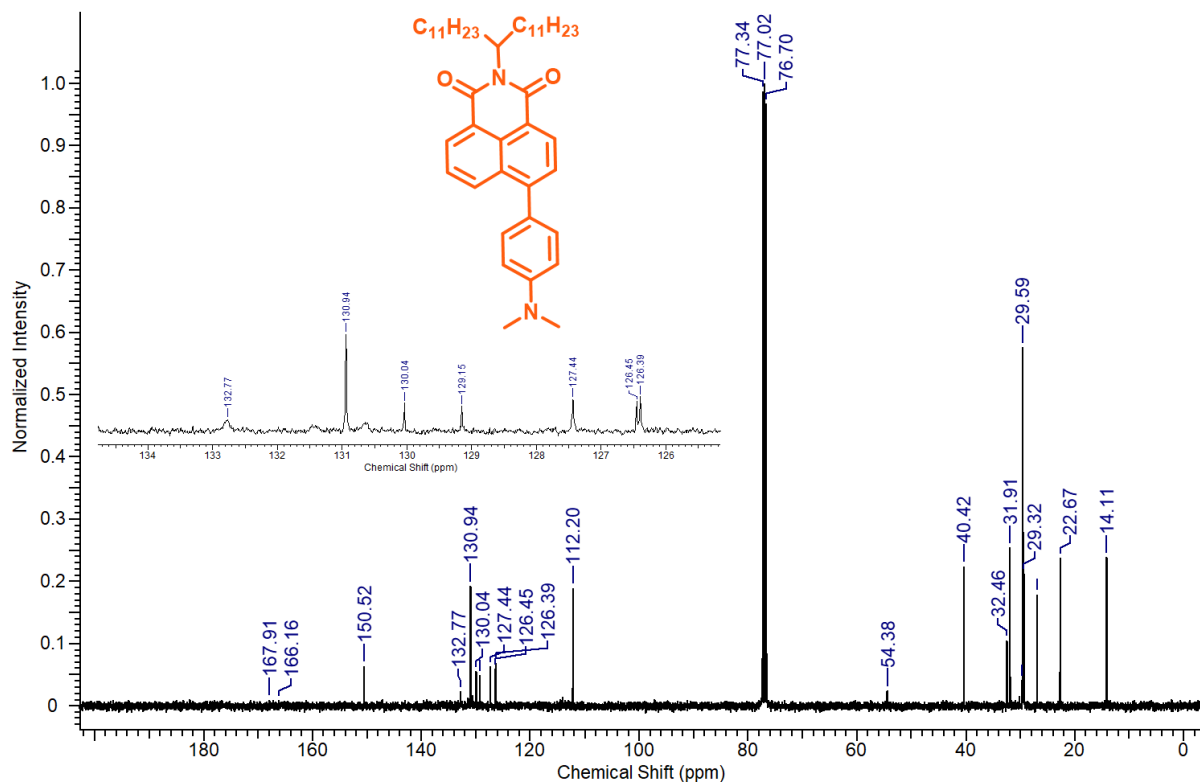


HRMS spectrum of 6-(diethylamino)-2-(tricosan-12-yl)-1H-benzo[de]isoquinoline-1,3(2H)-dione (**3**).

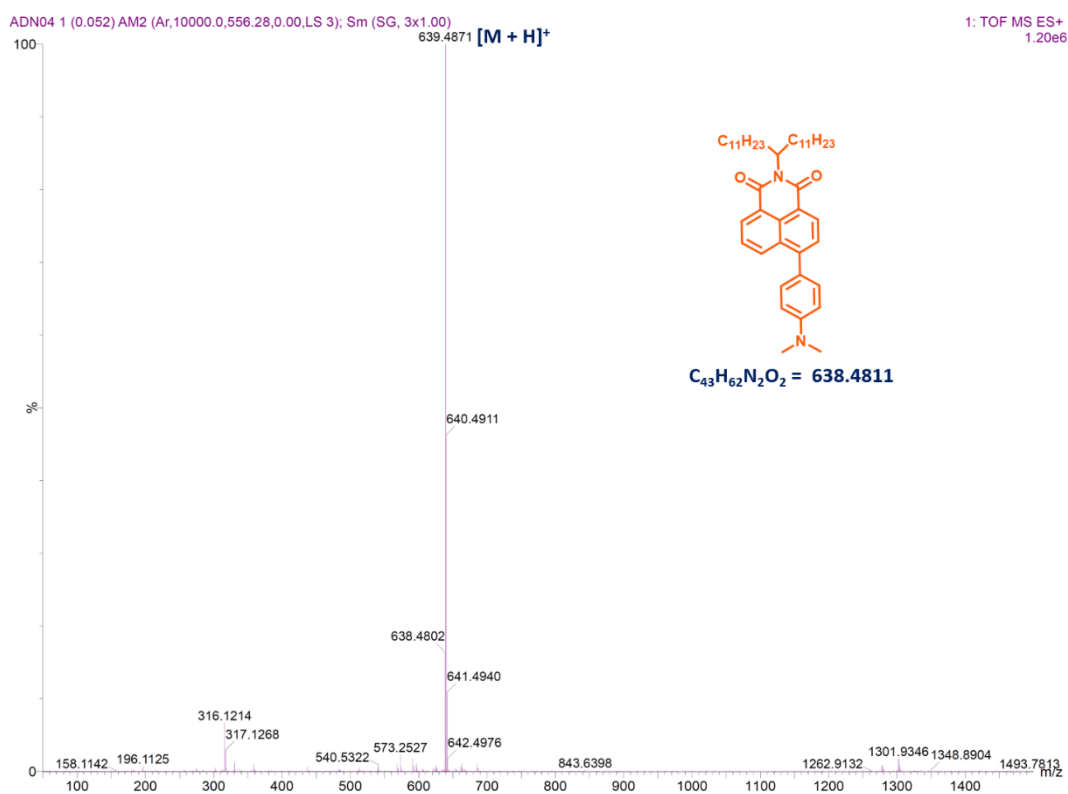


1H NMR spectra of 6-(4-(dimethylamino)phenyl)-2-(tricosan-12-yl)-1H-benzo[de]isoquinoline-1,3(2H)-dione (**4**).

Characterization details of the synthesized molecules

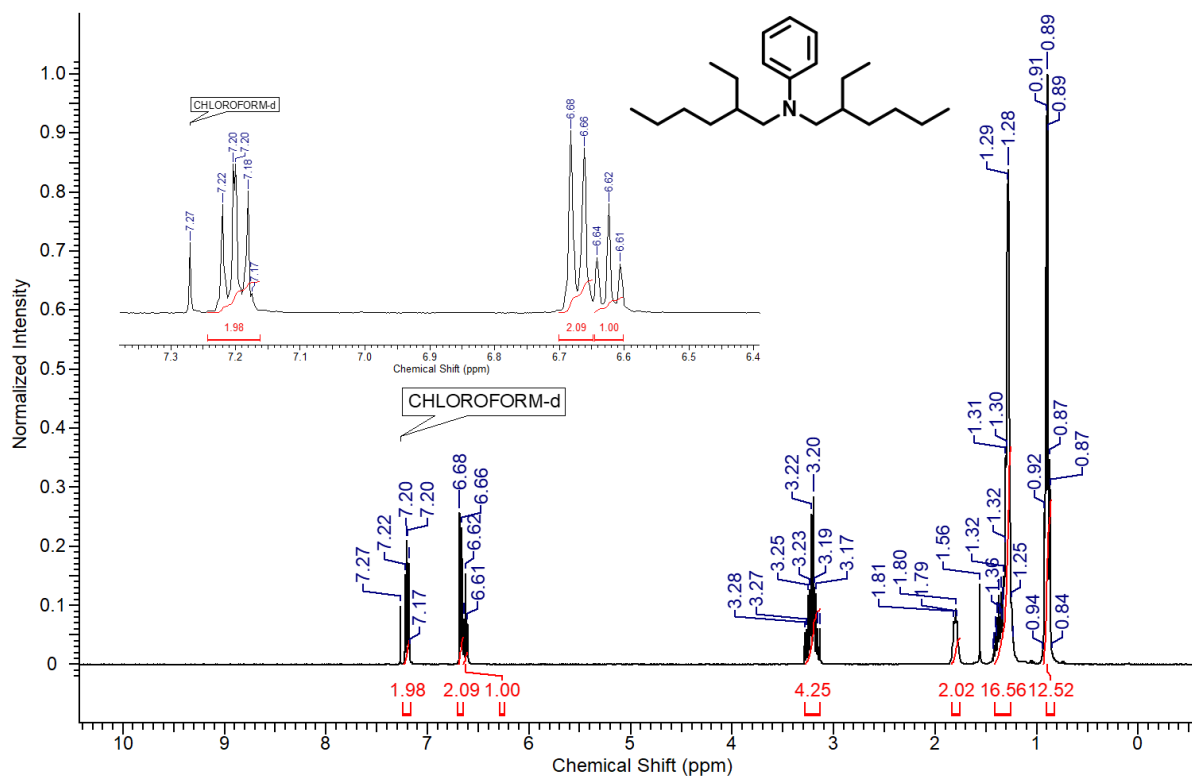


¹³C spectrum spectra of 6-(4-(dimethylamino)phenyl)-2-(tricosan-12-yl)-1H-benzo[de]isoquinoline-1,3(2H)-dione (**4**).

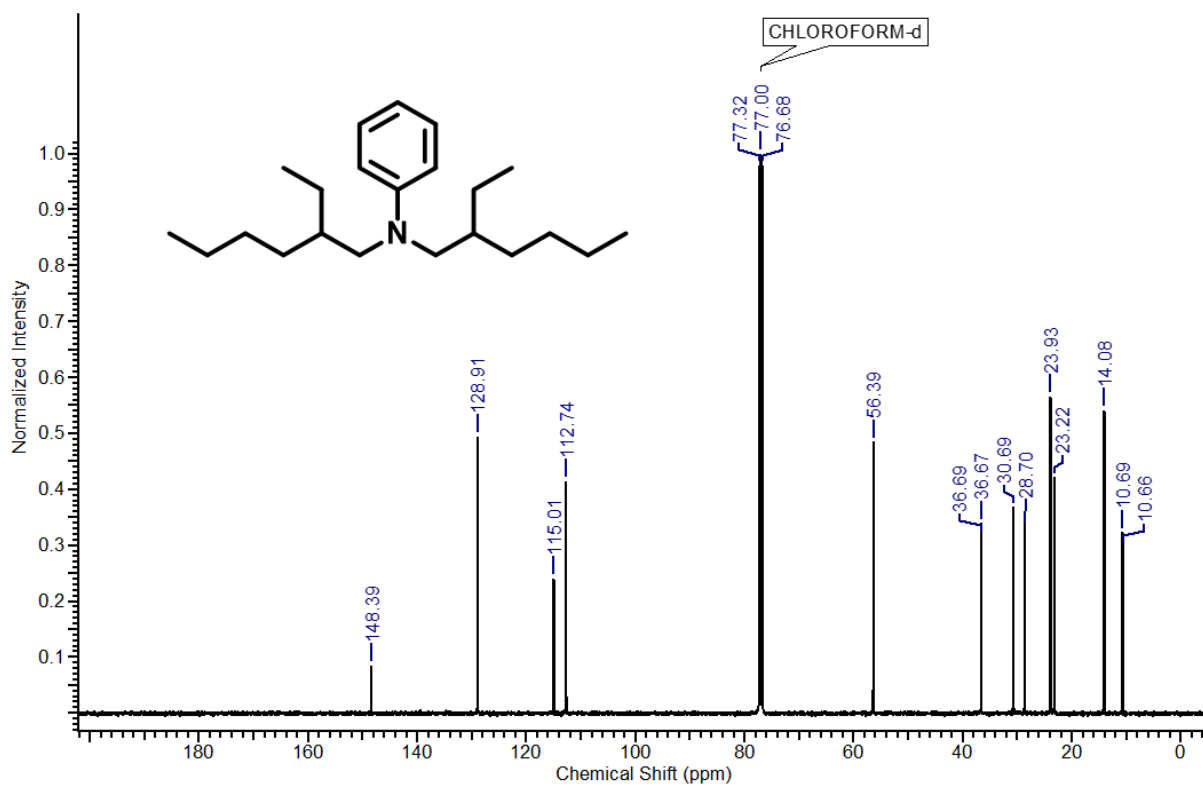


HRMS spectrum of 6-(4-(dimethylamino)phenyl)-2-(tricosan-12-yl)-1H-benzo[de]isoquinoline-1,3(2H)-dione (**4**).

Characterization details of the synthesized molecules



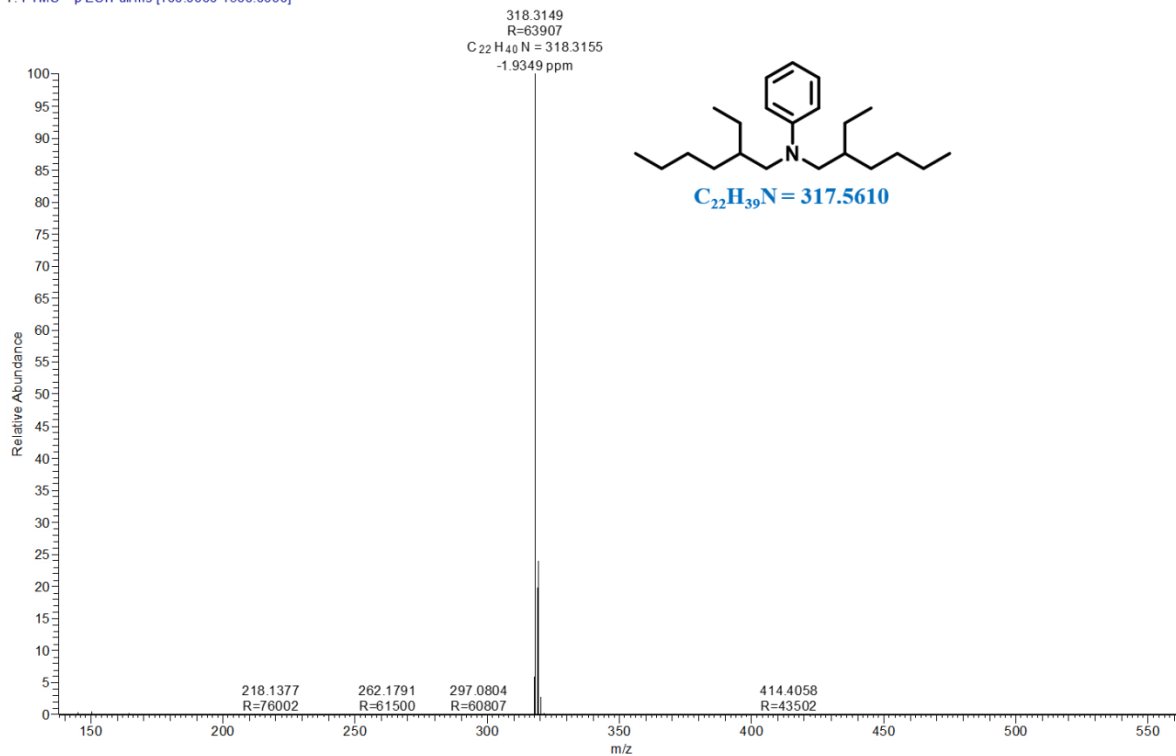
¹H NMR spectra of N,N-bis(2-ethylhexyl)aniline.



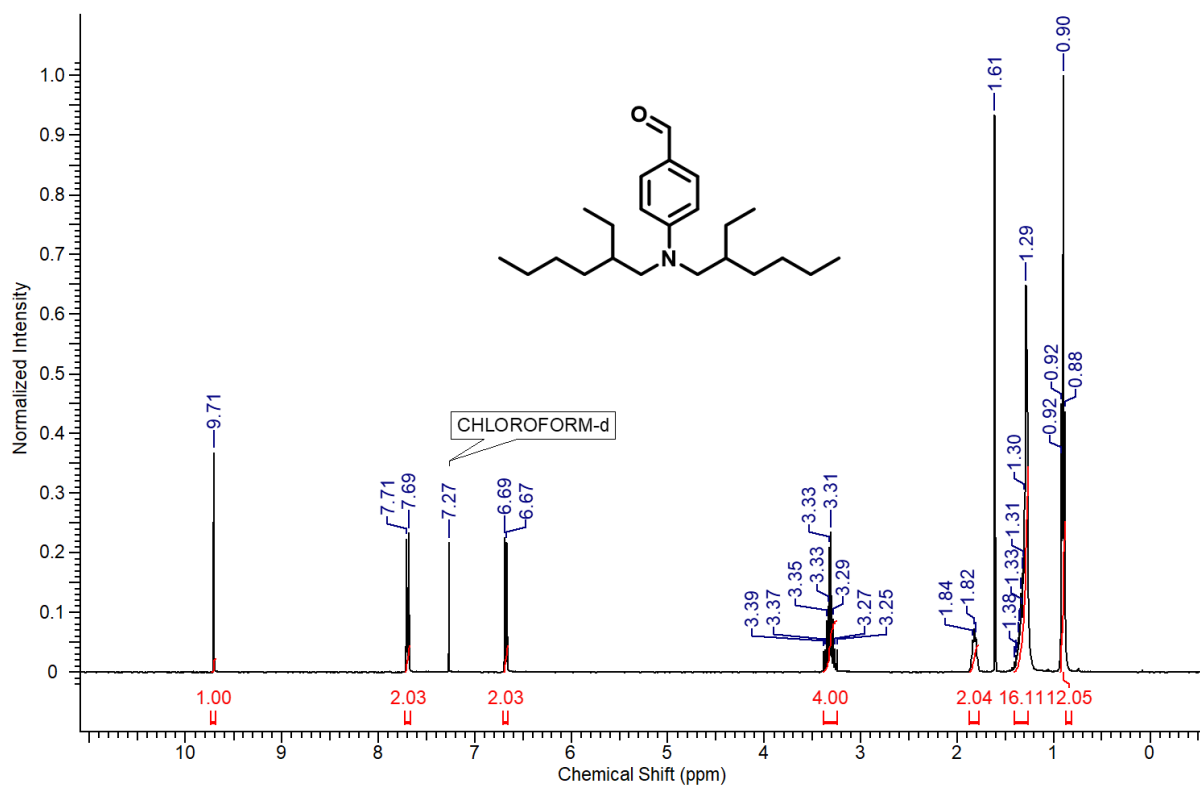
¹³C NMR spectra of N,N-bis(2-ethylhexyl)aniline.

Characterization details of the synthesized molecules

TadF-4A- #521 RT: 2.93 AV: 1 NL: 8.66E8
T: FTMS + p ESI Fullms [100.0000-1500.0000]

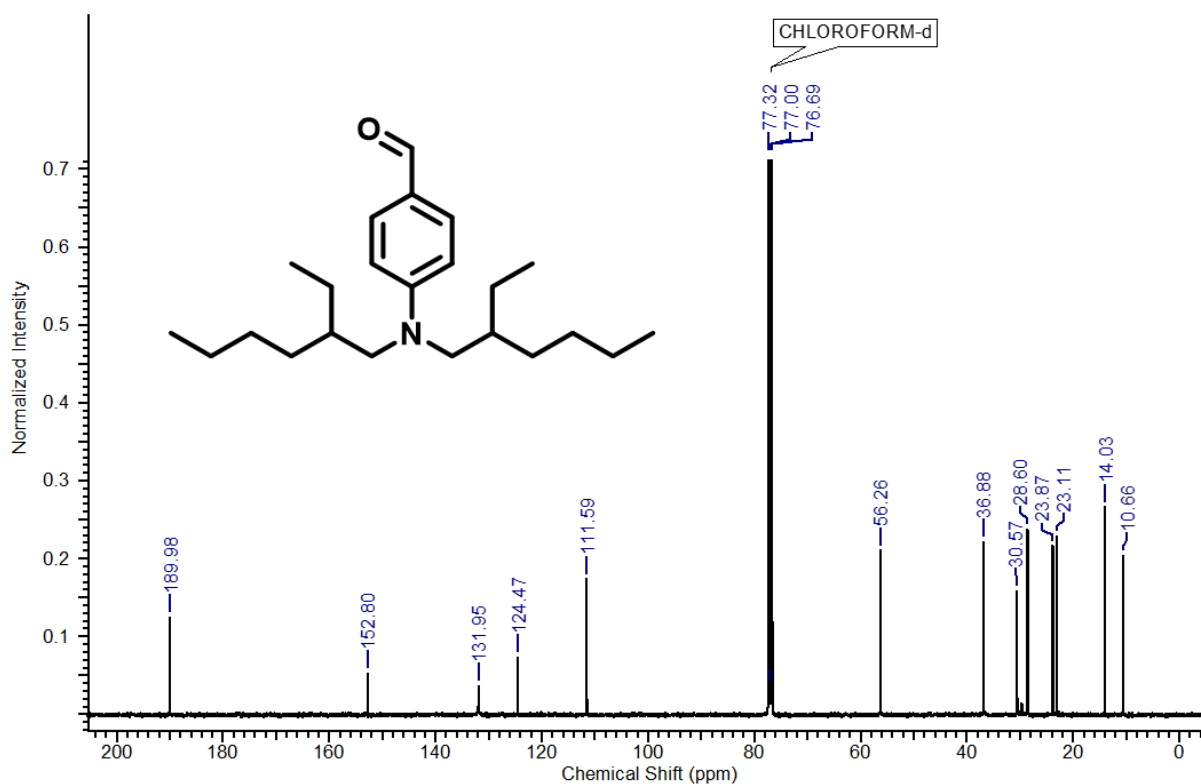


HRMS spectrum of N,N-bis(2-ethylhexyl)aniline.



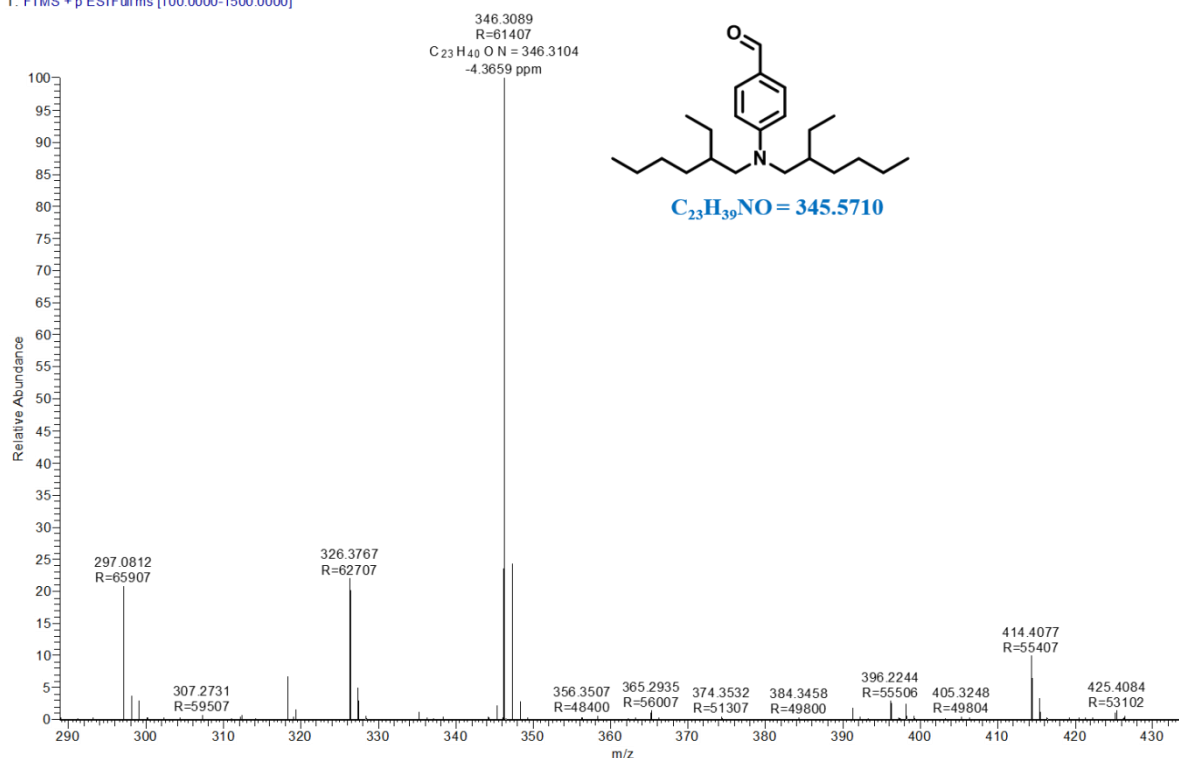
¹H NMR spectrum of 4-(bis(2-ethylhexyl)amino)benzaldehyde.

Characterization details of the synthesized molecules



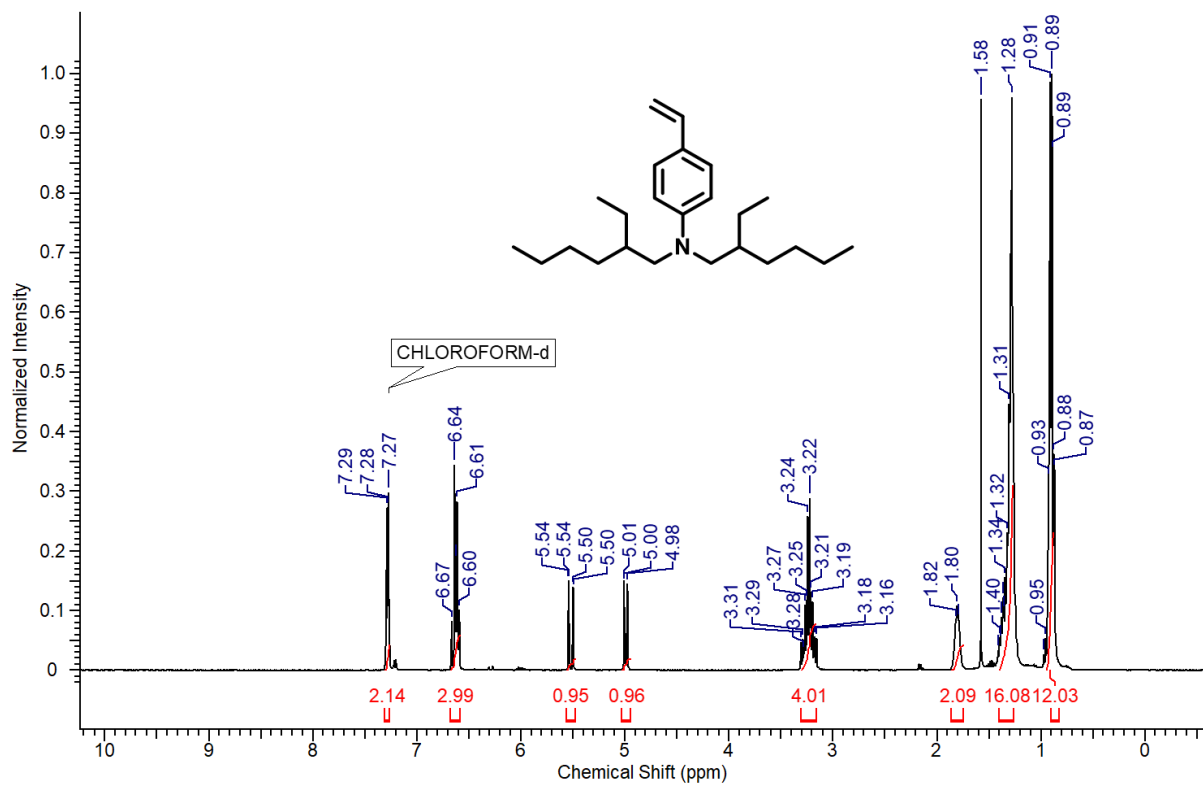
¹³C NMR spectrum of 4-(bis(2-ethylhexyl)amino)benzaldehyde.

TADF-4B- #164 RT: 0.92 AV: 1 NL: 8.46E6
T: FTMS + p ESIFulms [100.0000-1500.0000]

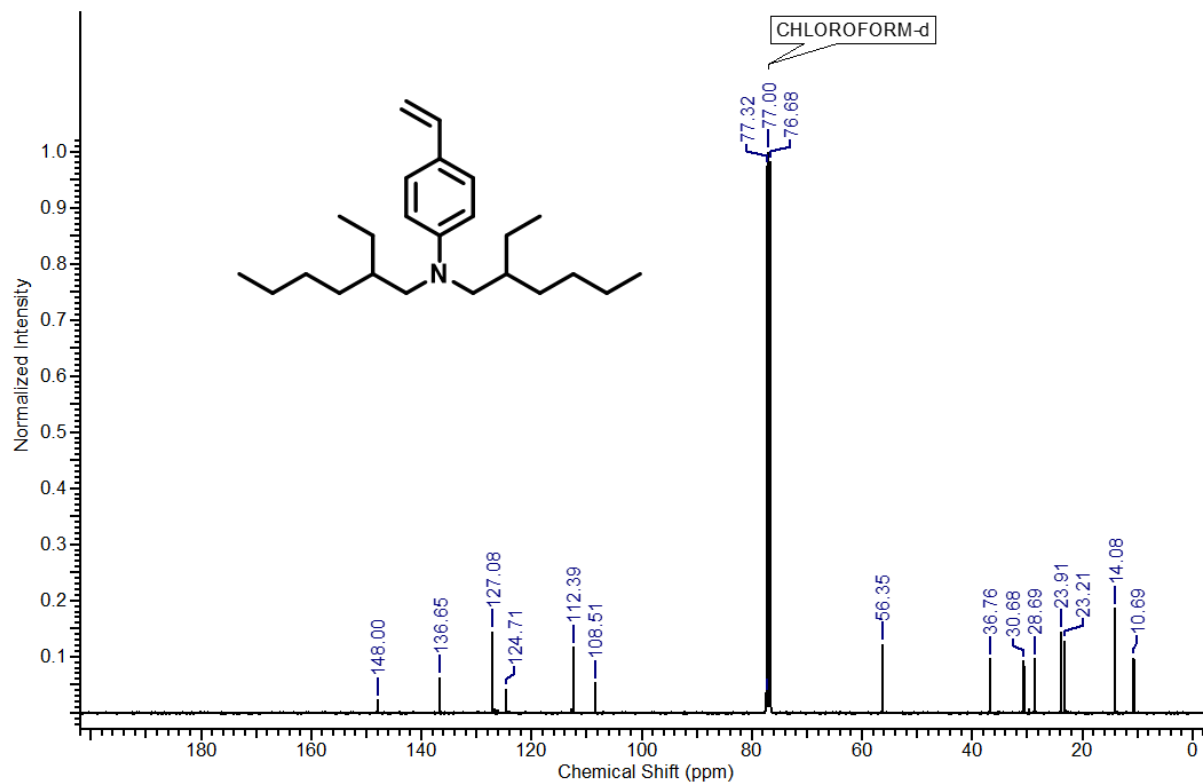


HRMS spectrum of 4-(bis(2-ethylhexyl)amino)benzaldehyde.

Characterization details of the synthesized molecules



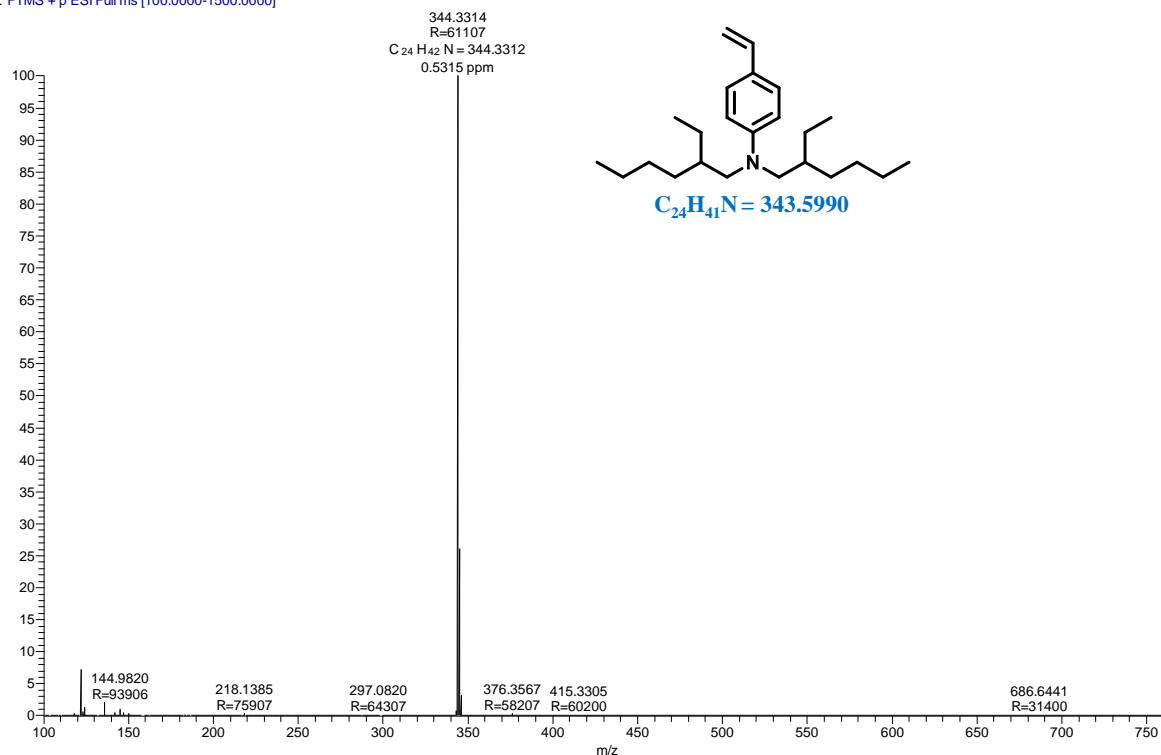
¹H NMR spectrum of N,N-bis(2-ethylhexyl)-4-vinylaniline.



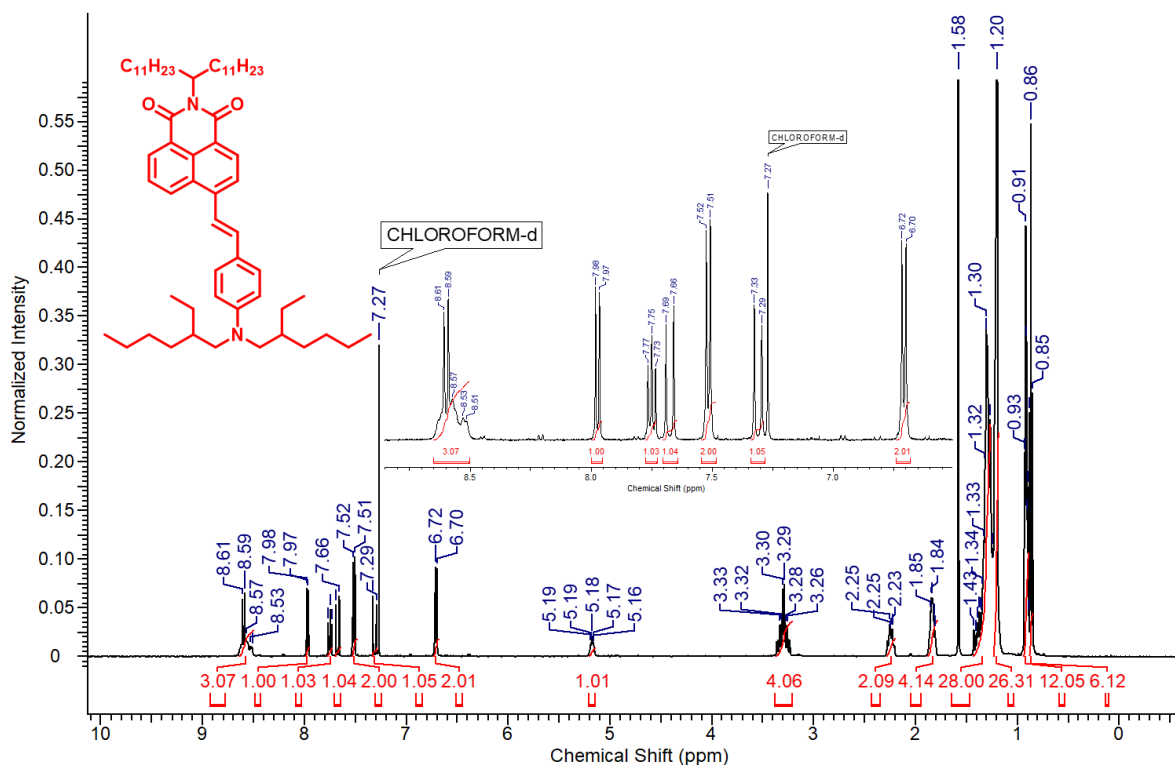
¹³C NMR spectrum of N,N-bis(2-ethylhexyl)-4-vinylaniline.

Characterization details of the synthesized molecules

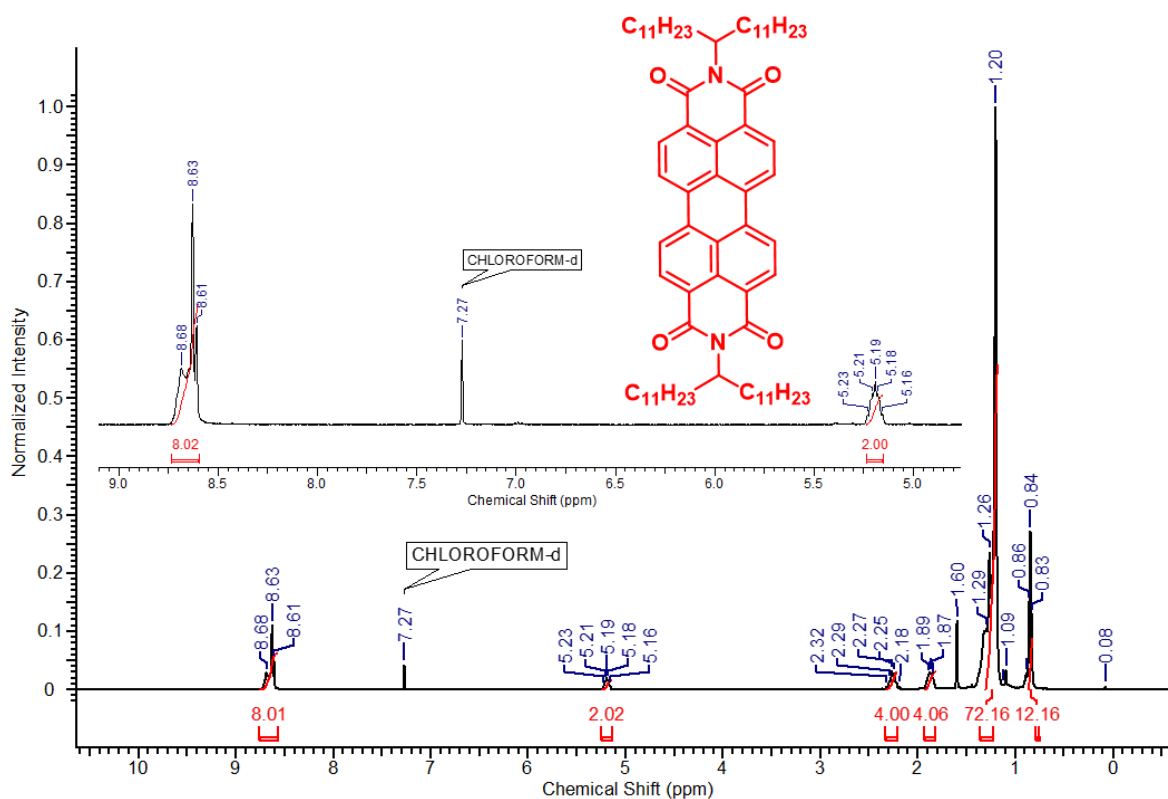
ADN-4- #695 RT: 4.87 AV: 1 NL: 1.68E8
T: FTMS + p ESI Full ms [100.0000-1500.0000]



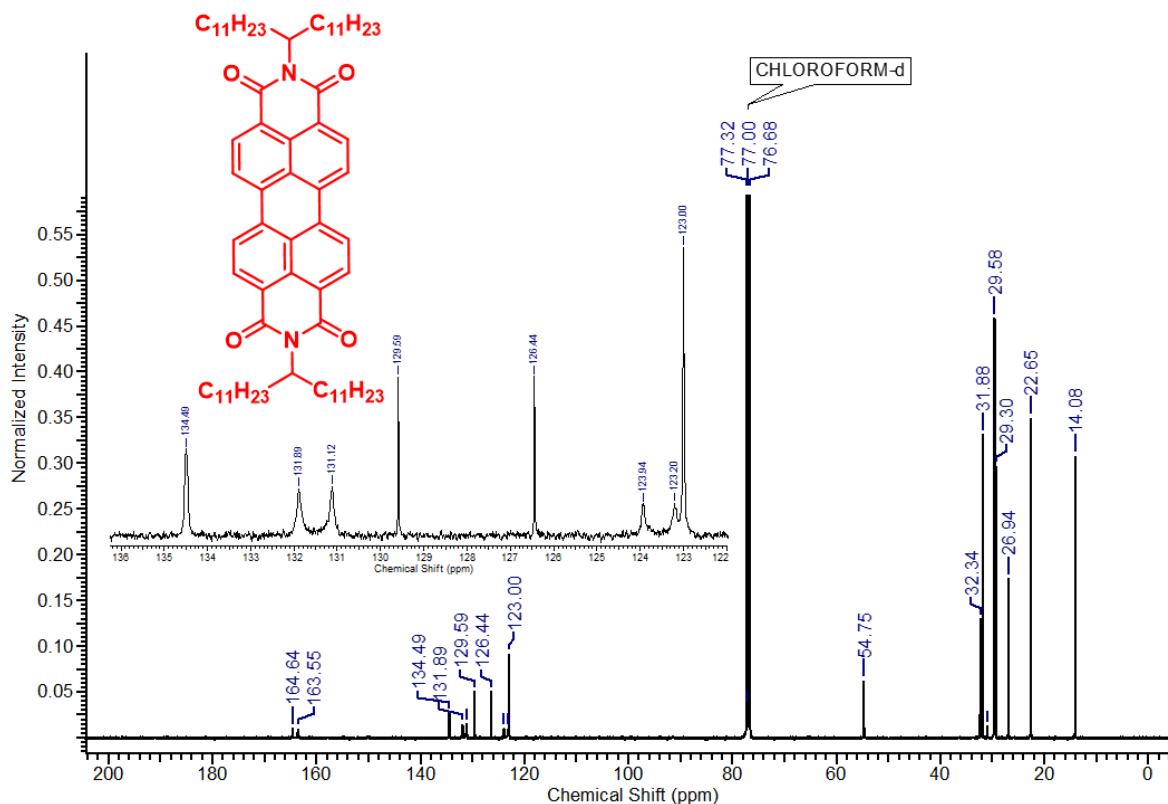
HRMS spectrum of N,N-bis(2-ethylhexyl)-4-vinylaniline.



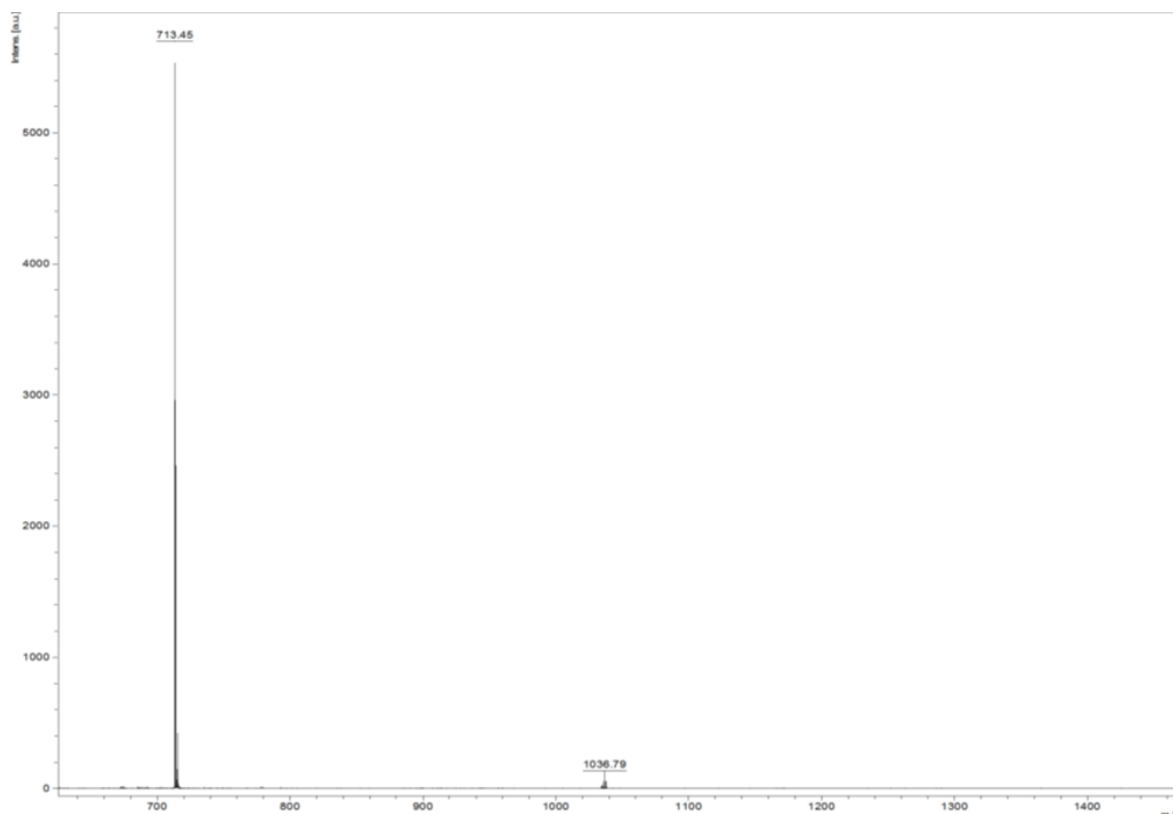
¹H NMR spectra of (E)-6-(4-(bis(2-ethylhexyl)amino)styryl)-2-(tricosan-12-yl)-1H-benzo[de]isoquinoline-1,3(2H)-dione (**5**).



^1H NMR spectra of 2,9-di(tricosan-12-yl)anthra[2,1,9-def:6,5,10-d'e'f]diisoquinoline-1,3,8,10(2H,9H)-tetraone (**6**).



^{13}C NMR spectra of 2,9-di(tricosan-12-yl)anthra[2,1,9-def:6,5,10-d'e'f]diisoquinoline-1,3,8,10(2H,9H)-tetraone (**6**).

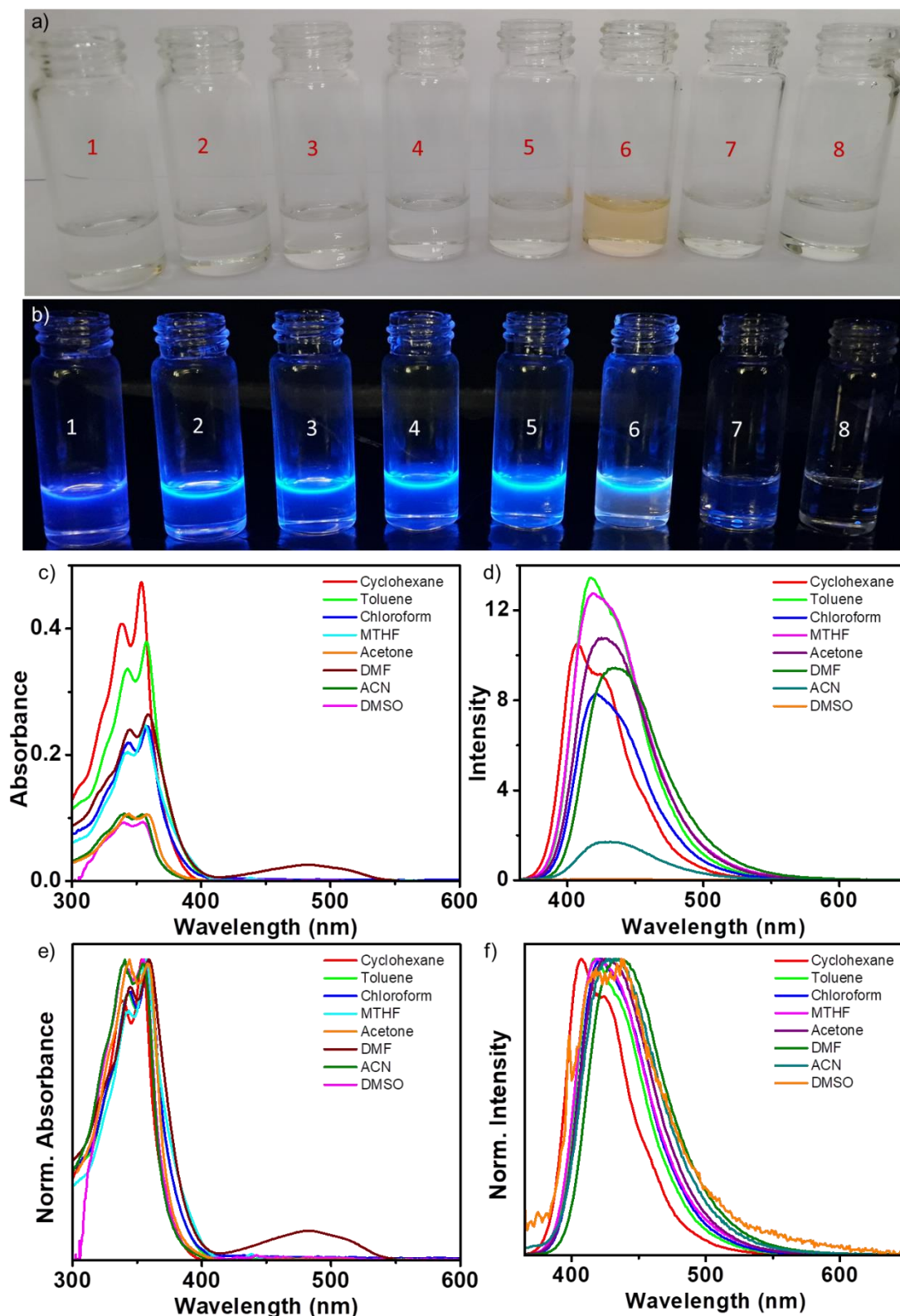


MALDI-TOF MS spectra of 2,9-di(tricosan-12-yl)anthra[2,1,9-def:6,5,10-d'e'f']diisoquinoline-1,3,8,10(2H,9H)-tetraone (**6**).

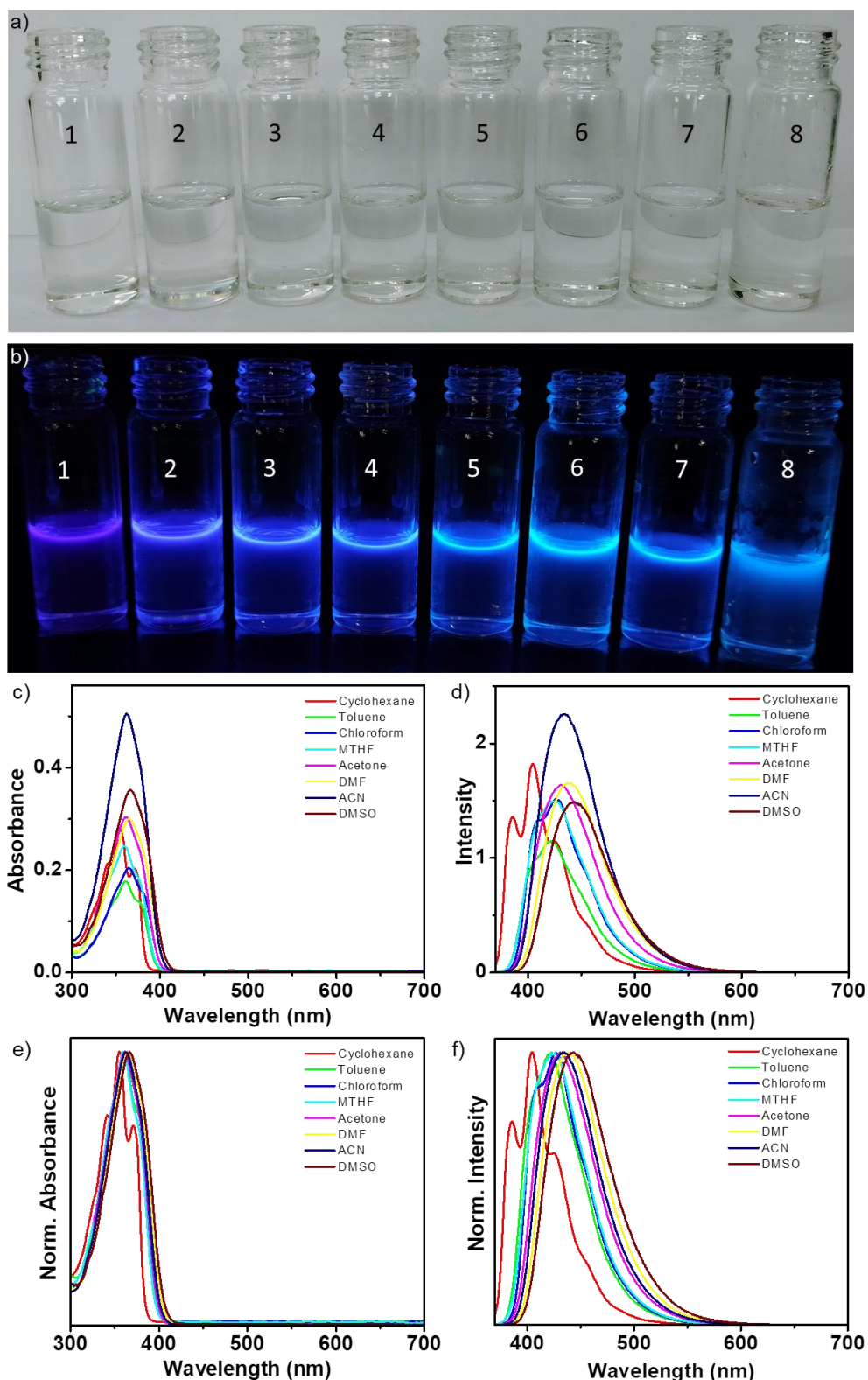
CHN analysis of **1-5**.

Compound	Chemical Formula	Elemental analysis: Theoretical			Elemental analysis: Found		
		C	H	N	C	H	N
1	C ₄₁ H ₆₄ BNO ₄	76.26	9.99	2.17	76.51 (+0.25)	9.68 (-0.31)	2.35 (+0.18)
2	C ₃₆ H ₅₅ NO ₃	78.64	10.08	2.55	78.70 (+0.06)	9.96 (-0.12)	2.65 (+0.10)
3	C ₃₉ H ₆₂ N ₂ O ₂	79.27	10.58	4.74	79.44 (+0.17)	10.46 (-0.12)	4.90 (+0.16)
4	C ₄₃ H ₆₂ N ₂ O ₂	80.83	9.78	4.38	80.95 (+0.12)	9.59 (-0.19)	4.48 (+0.10)
5	C ₅₉ H ₉₂ N ₂ O ₂	82.27	10.77	3.25	82.41 (+0.14)	10.41 (-0.36)	3.49 (+0.24)

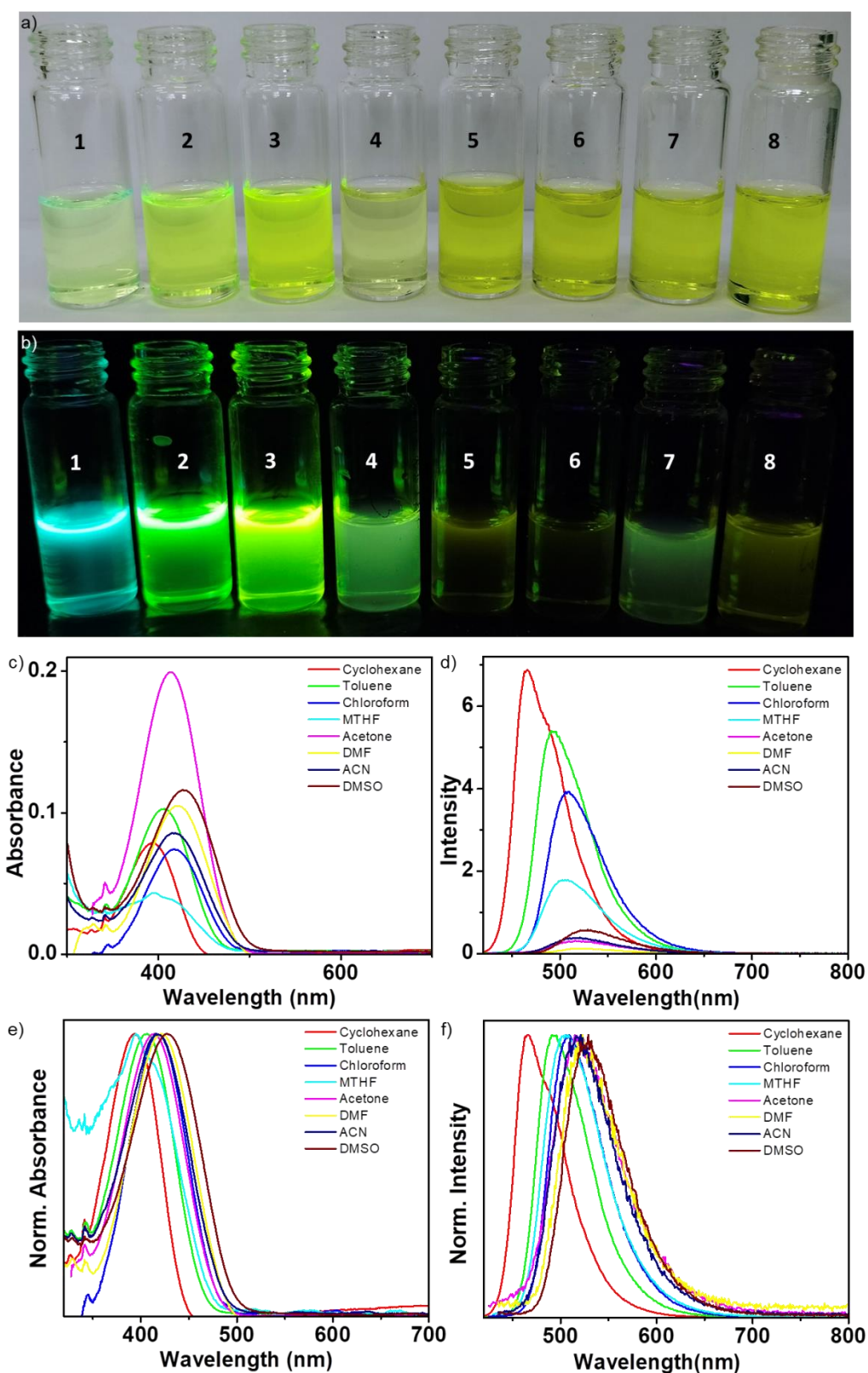
*The deviation of the experimental value from the theoretical value is provided in the bracket.



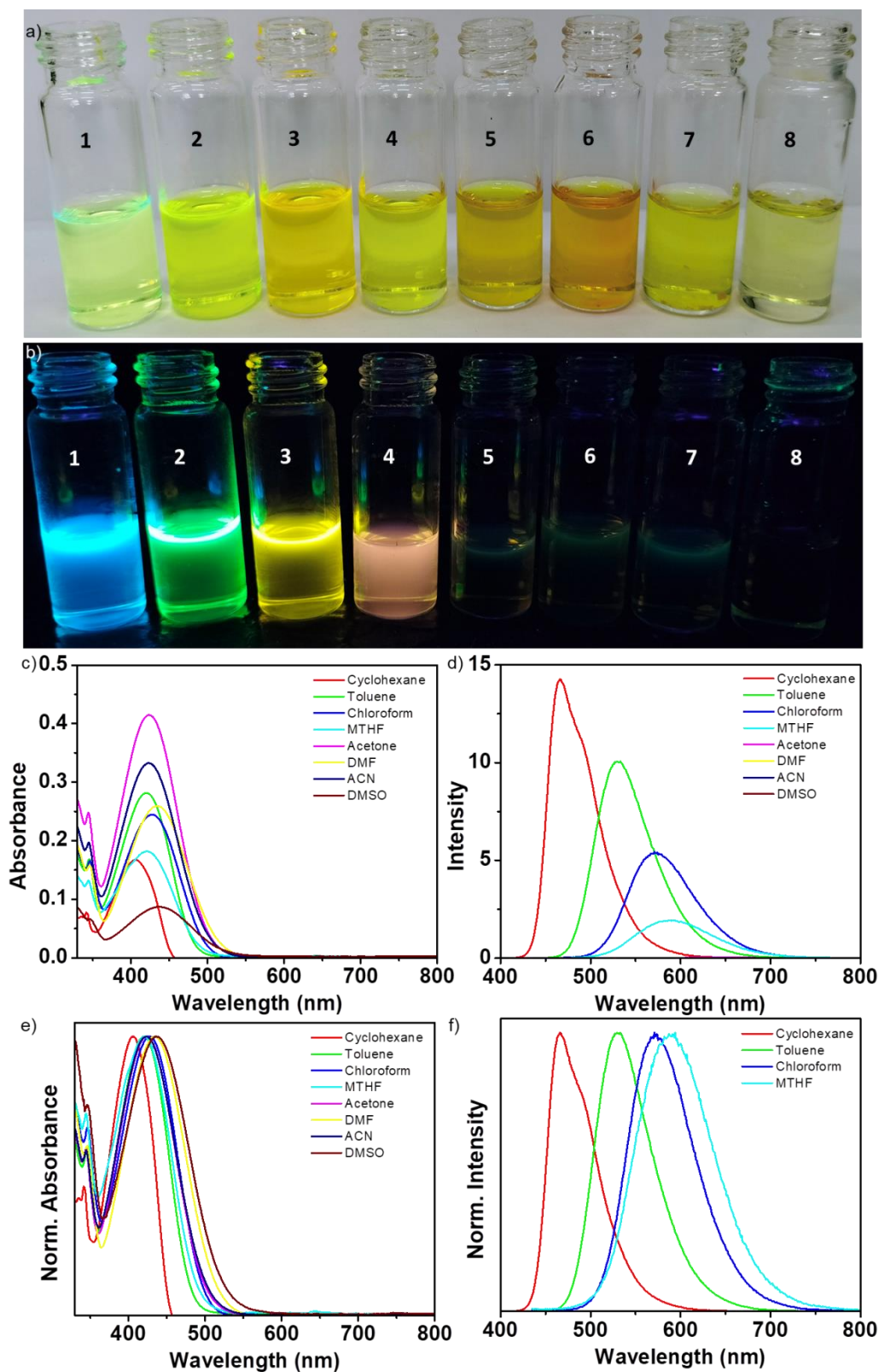
Photographs of **1** in different solvents under a) visible b) UV (365 nm) light. c) absorption, d) steady-state emission spectra of **1** in different solvents and corresponding normalized spectra e) and f), respectively ($C = 1 \times 10^{-5} \text{ M}$, $l = 1 \text{ cm}$, $\lambda_{\text{ex}} = 360 \text{ nm}$). Solvents: 1. Cyclohexane, 2. Toluene, 3. Chloroform, 4. MTHF, 5. Acetone, 6. DMF, 7. Acetonitrile, 8. DMSO



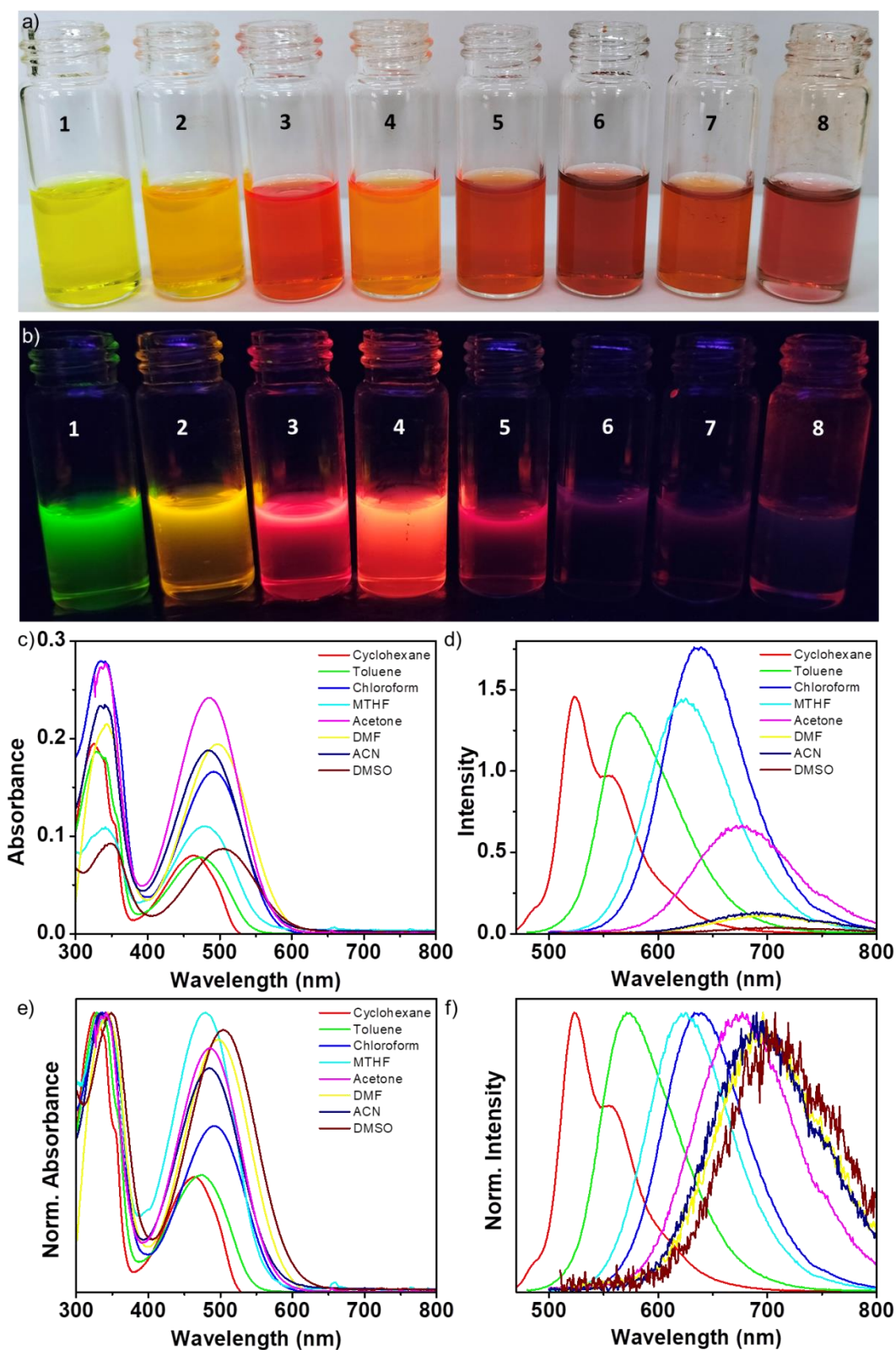
Photographs of **2** in different solvents under a) visible b) UV (365 nm) light. c) absorption, d) steady-state emission spectra of **2** in different solvents and corresponding normalized spectra e) and f), respectively ($C = 1 \times 10^{-5} \text{ M}$, $l = 1 \text{ cm}$, $\lambda_{\text{ex}} = 370 \text{ nm}$). Solvents: 1. Cyclohexane, 2. Toluene, 3. Chloroform, 4. MTHF, 5. Acetone, 6. DMF, 7. Acetonitrile, 8. DMSO



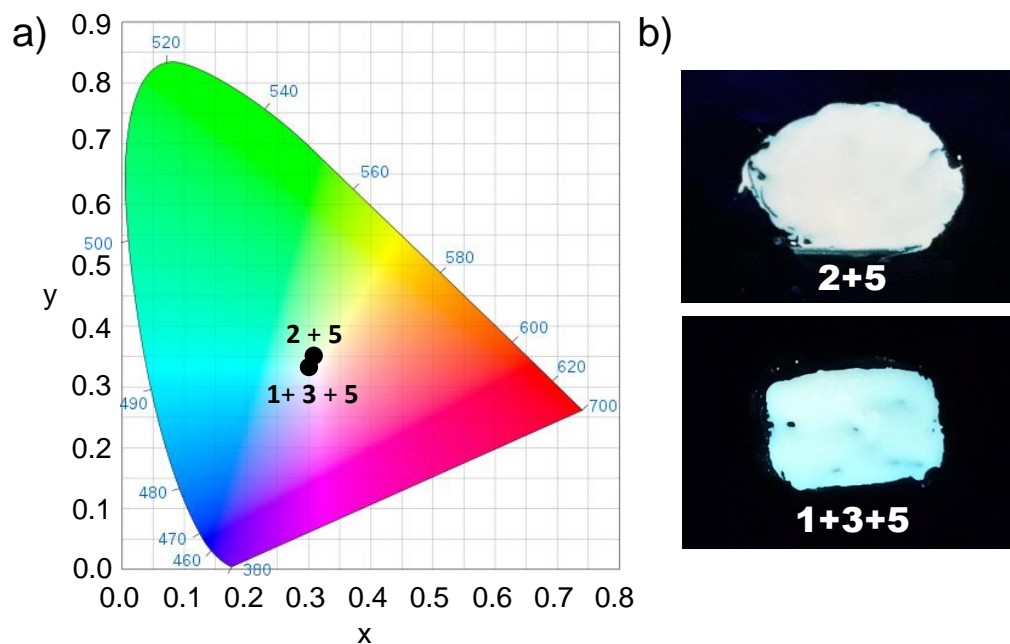
Photographs of **3** in different solvents under a) visible b) UV (365 nm) light. c) absorption, d) steady-state emission spectra of **3** in different solvents and corresponding normalized spectra e) and f), respectively ($C = 1 \times 10^{-5}$ M, $l = 1$ cm, $\lambda_{ex} = 415$ nm). Solvents: 1. Cyclohexane, 2. Toluene, 3. Chloroform, 4. MTHF, 5. Acetone, 6. DMF, 7. Acetonitrile, 8. DMSO



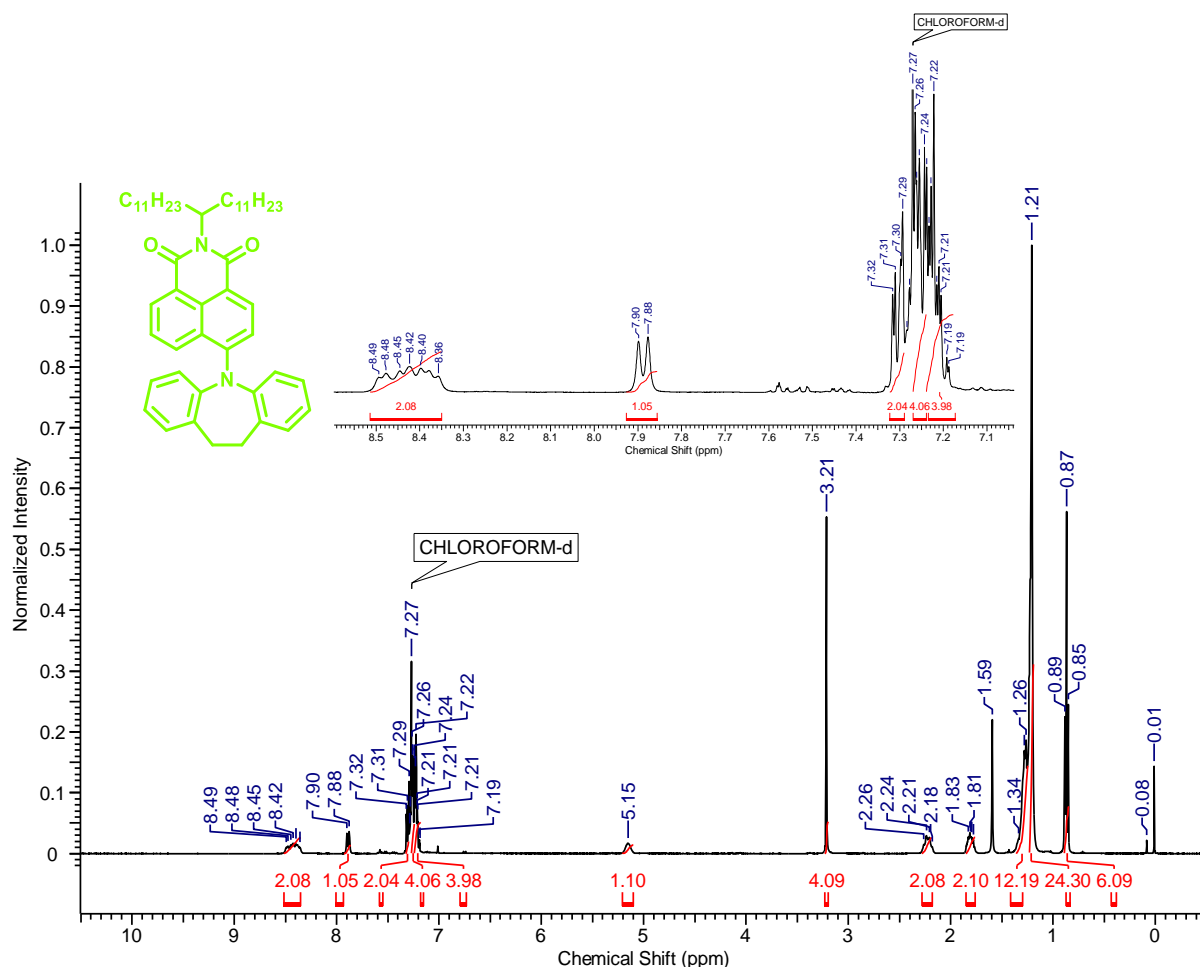
Photographs of **4** in different solvents under a) visible b) UV (365 nm) light. c) absorption, d) steady-state emission spectra of **4** in different solvents and corresponding normalized spectra e) and f), respectively ($C = 1 \times 10^{-5} \text{ M}$, $l = 1 \text{ cm}$, $\lambda_{\text{ex}} = 425 \text{ nm}$). Solvents: 1. Cyclohexane, 2. Toluene, 3. Chloroform, 4. MTHF, 5. Acetone, 6. DMF, 7. Acetonitrile, 8. DMSO



Photographs of **5** in different solvents under a) visible b) UV (365 nm) light. c) absorption, d) steady-state emission spectra of **5** in different solvents and corresponding normalized spectra e) and f), respectively ($C = 1 \times 10^{-5} \text{ M}$, $l = 1 \text{ cm}$, $\lambda_{\text{ex}} = 490 \text{ nm}$). Solvents: 1. Cyclohexane, 2. Toluene, 3. Chloroform, 4. MTHF, 5. Acetone, 6. DMF, 7. Acetonitrile, 8. DMSO

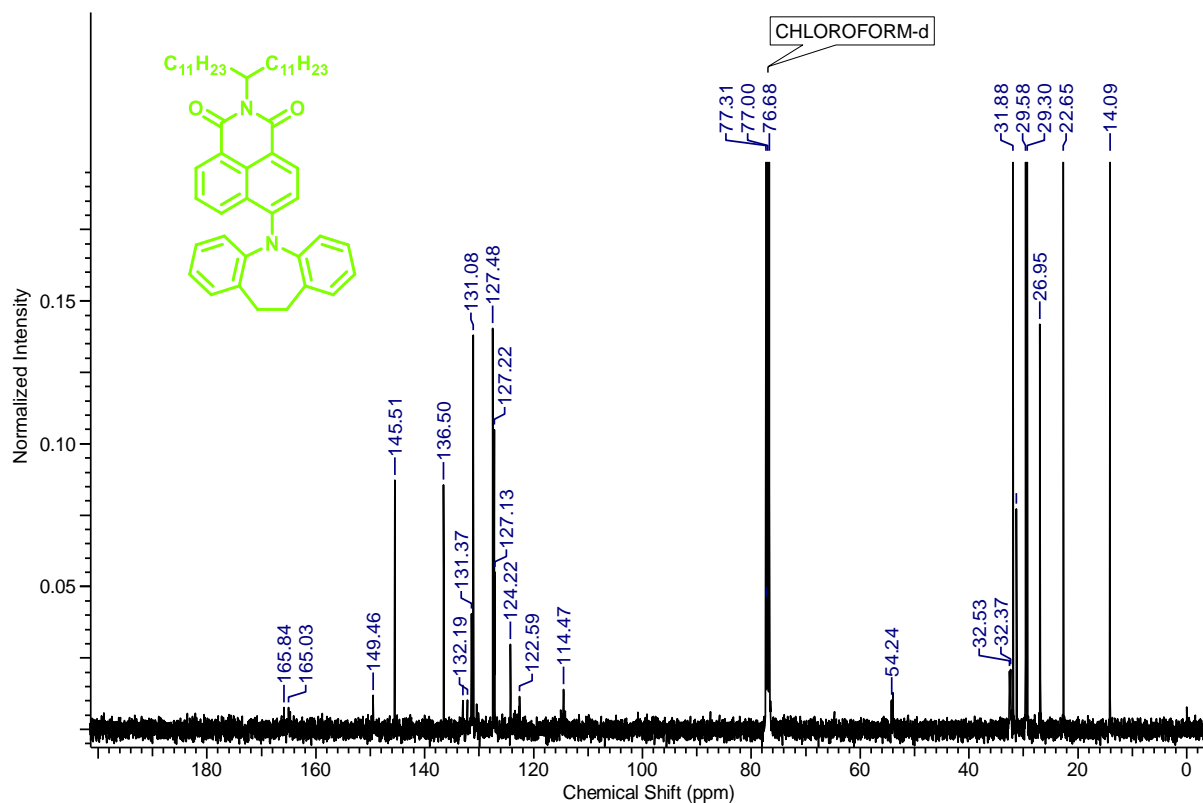


a) CIE coordinate values for white light emission achieved by **1+3+5** (1:0.0009:0.0008) and **2+5** (1:0.002) and b) corresponding photographs under UV light (365 nm).

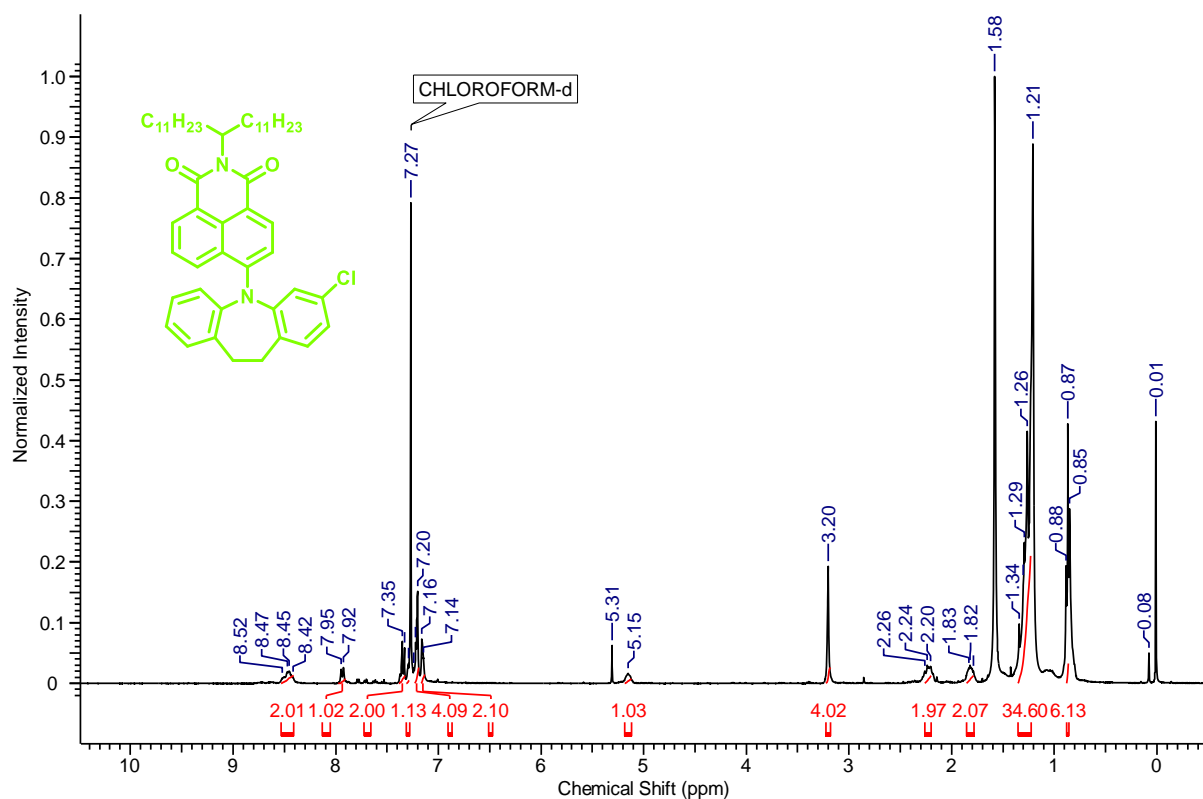


^1H NMR spectra of 6-(10,11-dihydro-5H-dibenzo[b,f]azepin-5-yl)-2-(tricosan-12-yl)-1H-benzo[de]isoquinoline-1,3(2H)-dione (**Az-NMI**).

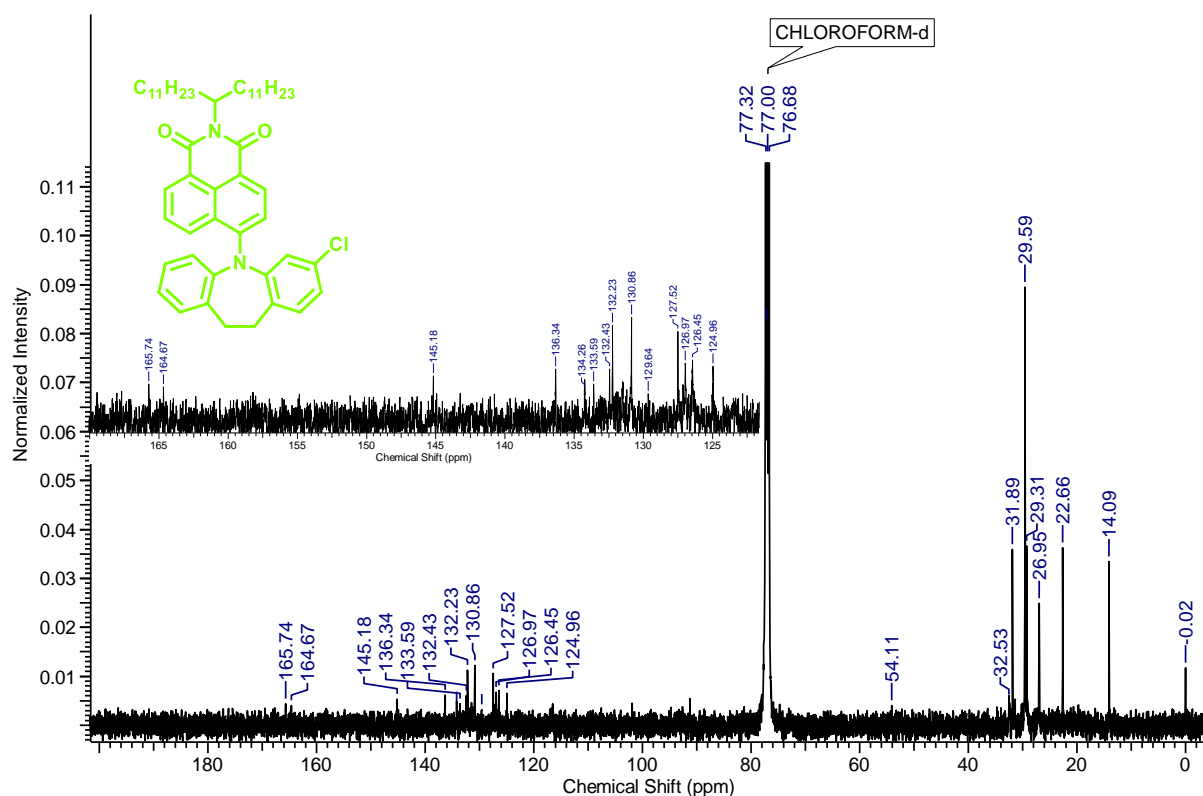
Characterization details of the synthesized molecules



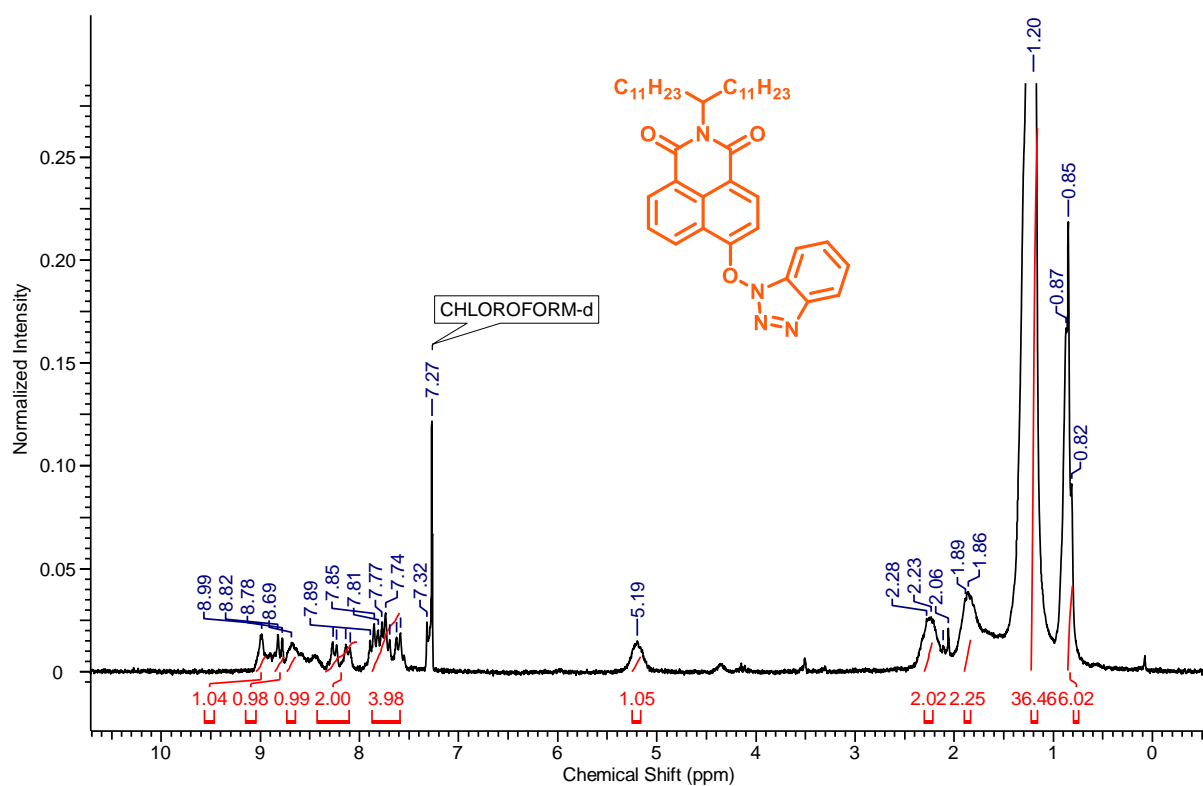
¹³C NMR spectra of 6-(10,11-dihydro-5H-dibenzo[b,f]azepin-5-yl)-2-(tricosan-12-yl)-1H-benzo[de]isoquinoline-1,3(2H)-dione (**Az-NMI**).



¹H NMR spectra of 6-(3-chloro-10,11-dihydro-5H-dibenzo[b,f]azepin-5-yl)-2-(tricosan-12-yl)-1H-benzo[de]isoquinoline-1,3(2H)-dione (**Cl-Az-NMI**).

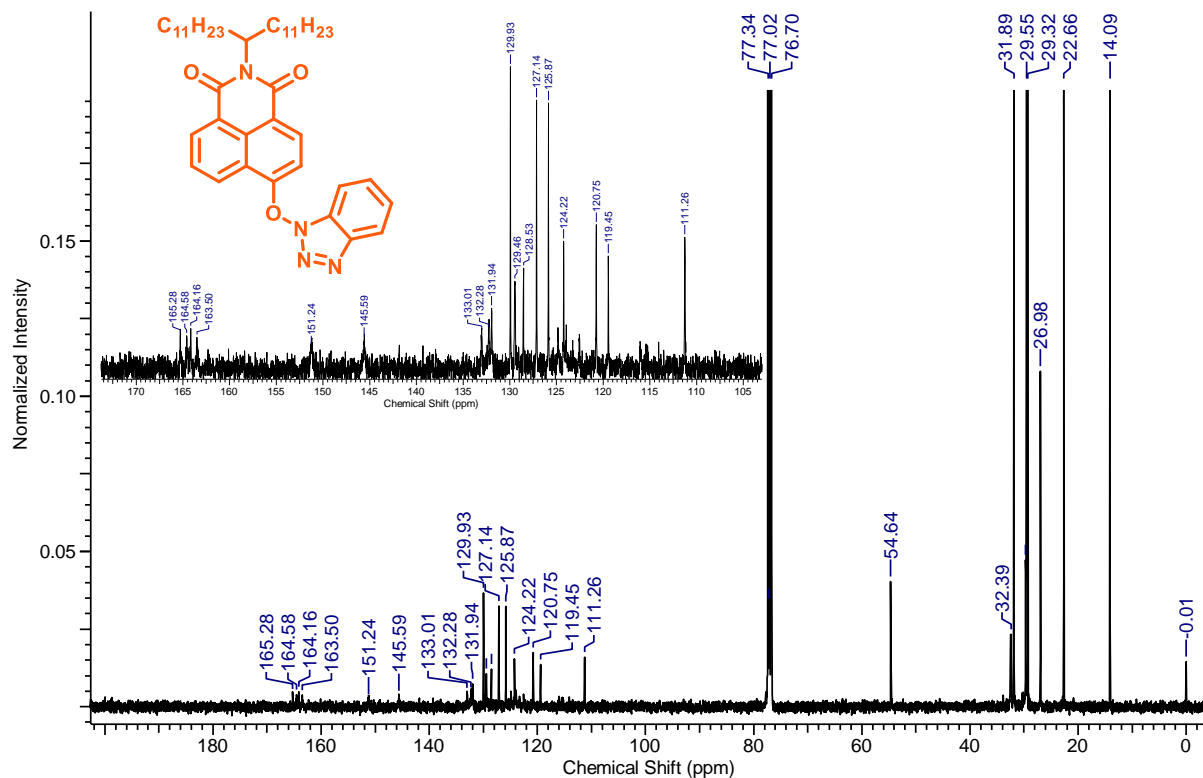


¹³C NMR spectra of 6-(3-chloro-10,11-dihydro-5H-dibenzo[b,f]azepin-5-yl)-2-(tricosan-12-yl)-1H-benzo[de]isoquinoline-1,3(2H)-dione (**Cl-Az-NMI**).

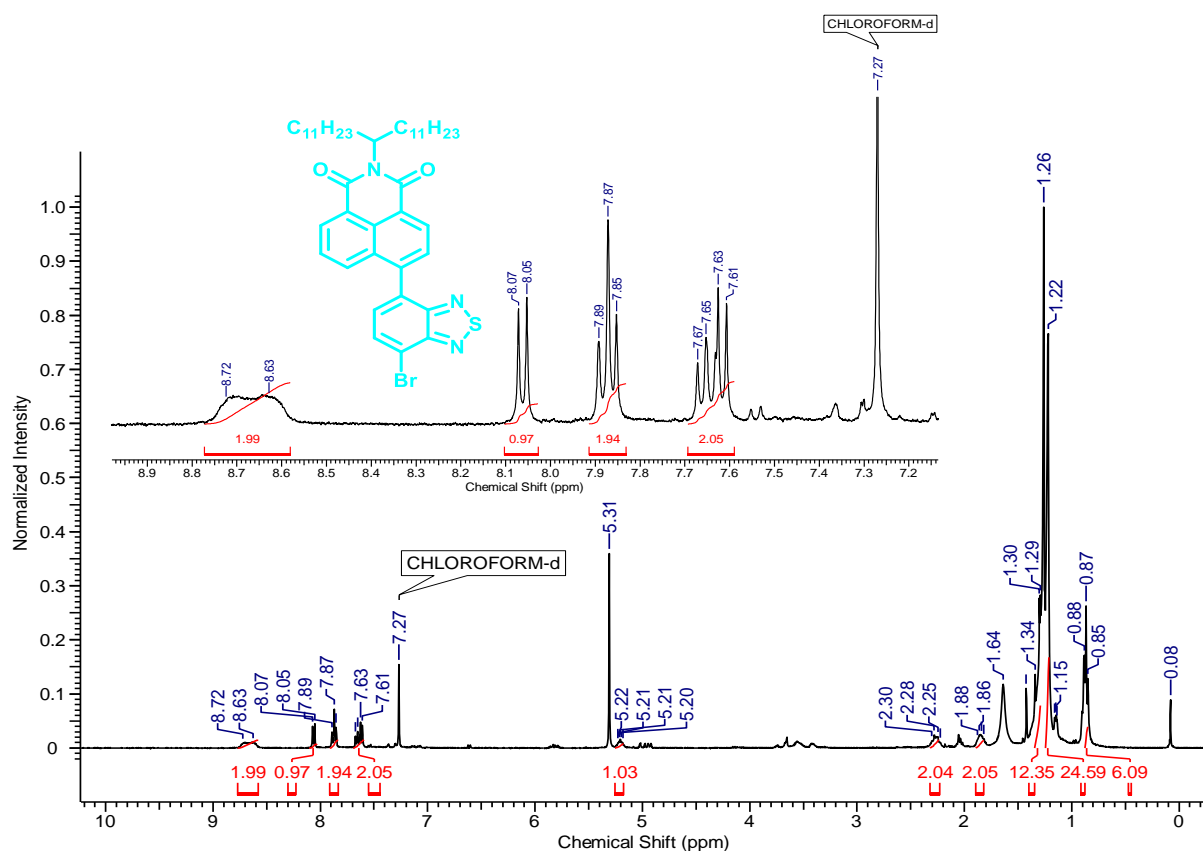


¹H NMR spectra of 6-((1H-benzo[d][1,2,3]triazol-1-yl)oxy)-2-(tricosan-12-yl)-1H-benzo[de]isoquinoline-1,3(2H)-dione (**HOBT-NMI**).

Characterization details of the synthesized molecules

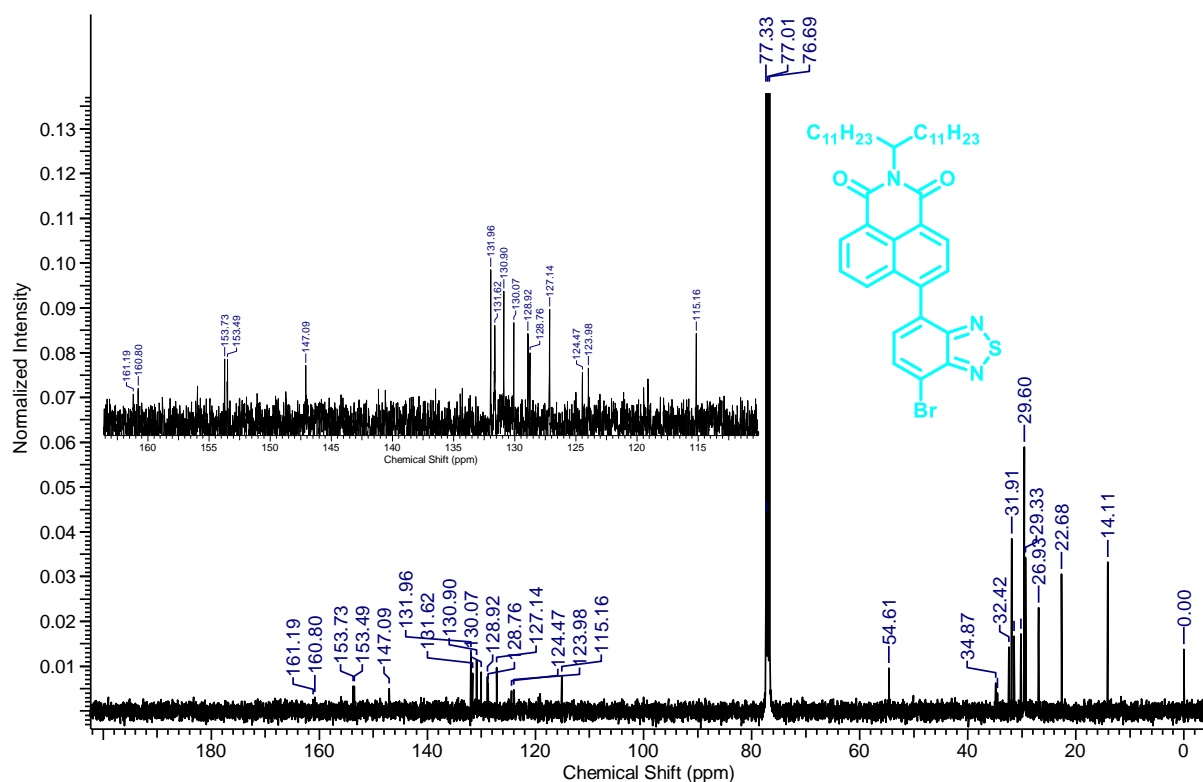


¹³C NMR spectra of 6-((1H-benzo[d][1,2,3]triazol-1-yl)oxy)-2-(tricosan-12-yl)-1H-benzo[de]isoquinoline-1,3(2H)-dione (**HOBT-NMI**).

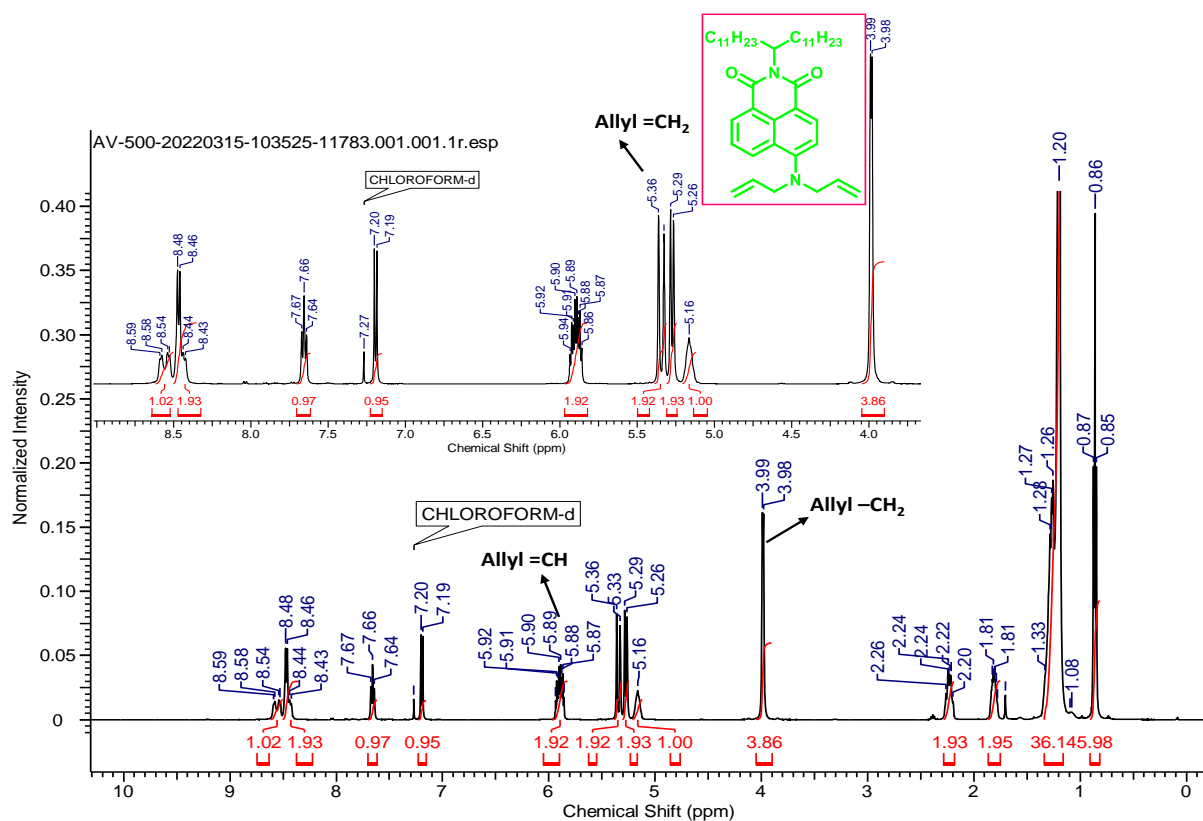


¹H NMR spectra of 6-(4-(dimethylamino)phenyl)-2-(tricosan-12-yl)-1H-benzo[de]isoquinoline-1,3(2H)-dione (**4-Br-Bz-NMI**).

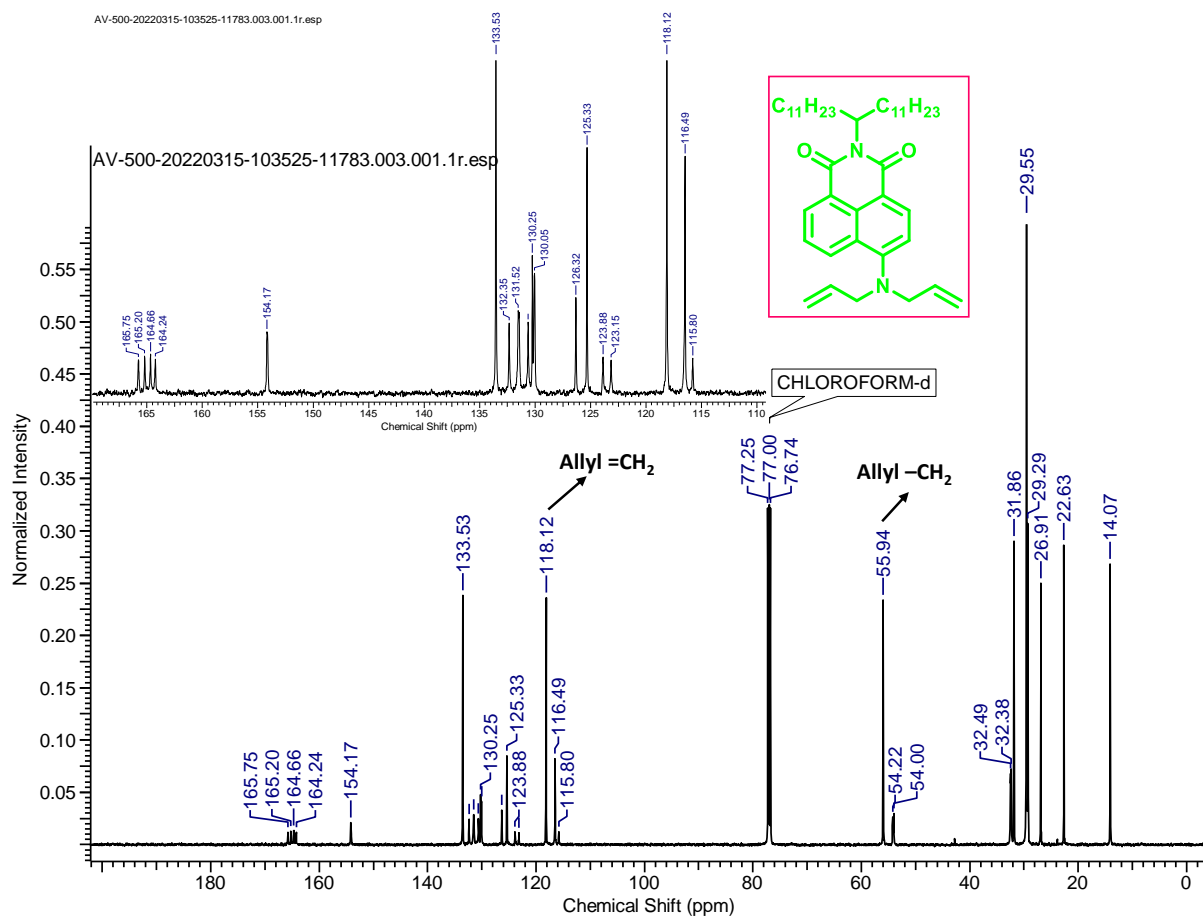
Characterization details of the synthesized molecules



¹³C NMR spectra of 6-(4-(dimethylamino)phenyl)-2-(tricosan-12-yl)-1H-benzo[de]isoquinoline-1,3(2H)-dione (**4-Br-Bz-NMI**).



¹H NMR spectra of 6-(diallylamino)-2-(tricosan-12-yl)-1H-benzo[de]isoquinoline-1,3(2H)-dione (**Diallyl-NMI**).



¹³C NMR spectra of 6-(diallylamino)-2-(tricosan-12-yl)-1H-benzo[de]isoquinoline-1,3(2H)-dione (**Diallyl-NMI**).

ABSTRACT

Name of the Student: Nidhankar Aakash Deepakrao **Registration No.:** 10CC17J26016

Faculty of Study: Organic Chemistry Division **Year of Submission:** 2022

AcSIR academic centre/CSIR Lab: CSIR-NCL

Name of the Supervisor(s): Dr. Santhosh Babu Sukumaran

Name of the Co-Supervisor(s): NA

Title of the thesis: “Organic Room-Temperature Phosphorescent and Thermally Activated Delayed Fluorescent Small Molecules: Efficiency Vs Processability for Lighting Application”

Luminescence is a fascinating word that attracts everyone’s attention. In the past decades, many branches of luminescence flourished with time, and luminescence involving triplet states grabbed much attention. For decades, heavy metal complexes have been explored as triplet harvesters because of the presence of ligand-metal and metal-ligand charge transfer (CT) and strong spin-orbit coupling, which improves the intersystem crossing (ISC) and controls the triplet decay rate. Despite many advantages, organometallic complexes have the drawbacks of high toxicity, limited resources, and high cost. Hence, this situation promoted the search for metal-free organic molecules as alternate candidates. However, for organic materials, the non-radiative (k_{nr}) and quenching (k_q) rates of the triplet states are much larger than the radiative decay rate (k_p) under ambient conditions. Moreover, the triplet states are vulnerable to quenching by molecular oxygen, and hence room-temperature phosphorescence (RTP) and thermally activated delayed fluorescence (TADF) from metal-free organic molecules under ambient conditions continue to be challenging. In this context, we set our approach to develop concisely, practically, and synthetically benign organic molecules which are technologically advanced for lighting and display applications with improved processability and luminescence features.

The current thesis describes the small molecules exhibiting RTP and TADF features and compares their efficiency and processability for lighting applications. This entitled thesis is categorized into five chapters. Initially, we describe the general introduction about RTP and TADF and a summary of related literature reports along with the objectives of the thesis. The important aspects related to two relevant concepts, RTP and TADF, that have emerged as promising techniques in light-emitting materials have been discussed in this chapter. RTP and TADF organic molecules have attracted scientific interest due to their wide applications in bio-imaging, organic optoelectronics, anti-counterfeiting, sensing, flexible display and lighting devices etc. The advantages of both ISC in RTP and reverse intersystem crossing (rISC) in TADF materials that have heavily supported achieving an internal quantum efficiency of 100% are explained in detail. The second chapter deals with self-assembled helical arrays for stabilizing the triplet state, the third chapter deals with room-temperature phosphorescence from metal-free organic phosphors, the fourth chapter deals with thermally activated delayed fluorescent solvent-free organic liquid hybrids for tunable emission applications, and the fifth chapter deals with the processable luminescent solvent-free organic liquid naphthalimides for lighting applications. In short, the present thesis is an attempt toward the development of new triplet harvesting luminescent organic candidates with enhanced efficiency and processability.

List of publication(s) in SCI Journal(s) emanating from the thesis work

1. [A. D. Nidhankar](#), Goudappagouda, V. C. Wakchaure and S. S. Babu, Efficient Metal-free Organic Room Temperature Phosphors, *Chem. Sci.* 2021, 12, 4216-4236.
2. [A. D. Nidhankar](#), Goudappagouda, D. S. M. Kumari, S. K. Chaubey, R. Nayak, R. G. Gonnade, G. V. P. Kumar, R. Krishnan and S. S. Babu, Self-assembled Helical Arrays for Stabilizing the Triplet State, *Angew. Chem. Int. Ed.* 2020, 59, 13079-13085. (Hot Paper)
3. [A. D. Nidhankar](#), Goudappagouda, P. Kothavade, S. D. Dongre, S. D. Veer, S. R. Dash, K. Rajeev, K. N. N. Unni, K. Shanmuganathan and S. S. Babu, Thermally Activated Delayed Fluorescent Solvent-free Organic Liquid Hybrids for Tunable Emission Applications, *Manuscript Communicated*, 2022.
4. [A. D. Nidhankar](#) and S. S. Babu, Room-Temperature Phosphorescence from Metal-Free Organic Phosphors, *Manuscript under preparation*, 2022.
5. [A. D. Nidhankar](#) and S. S. Babu, Processable Luminescent Solvent-free Organic Liquid Naphthalimides for Lighting Applications, *Manuscript under preparation*, 2022.

List of publication(s) in SCI Journal(s) (published & accepted) other than thesis

1. V. C. Wakchaure, S. D. Veer, [A. D. Nidhankar](#), Goudappagouda, R. A. Nayak, K. Asokan, S. Ravindranathan and S. S. Babu, Donor–acceptor based solvent-free organic liquid hybrids with exciplex emission and room temperature phosphorescence, *Chem. Commun.*, 2022, 58, 1998-2001.
2. Goudappagouda, [A. D. Nidhankar](#), R. A. Nayak and S. S. Babu, Aggregation-induced phosphorescence of an anthraquinone based emitter, *Org. Biomol. Chem.* 2021, 19, 1004-1008.
3. V. C. Wakchaure, A. R. Kottaichamy, [A. D. Nidhankar](#), K. C. Ranjeesh, M. Nazrulla, M. Thotiyl and S. S. Babu, Hexaaminobenzene Derived Two-Dimensional Polymer Supercapacitor with High Specific Capacitance and Energy Density, *ACS Appl. Energy Mater.* 2020, 3, 6352-6359.

Patents-

1. Santhosh B. Sukumaran and **Aakash D. Nidhankar**, Ultralong phosphorescent and waveguiding helical arrays of phenylmethanone functionalized carbazole, *India-2019-NF-0134*, (2019).

2. Santhosh B. Sukumaran, **Aakash D. Nidhankar**, and Goudappagouda, Thermally Activated Delayed Fluorescent Solvent-free Organic Liquid, *India-2022-NF-0005*, (2022).

List of National International Conference

1. Participated in the “*15th International Conference on Polymer Science and Technology*” (SPSI MACRO-2018), held during December 19-22, 2018 at Indian Institutes of Science Education and Research, Pune and CSIR- National Chemical Laboratory, Pune, India.
2. Participated in “*NCL-RF Annual Students conference 2018*”, held during November 29-30, 2018, at CSIR- National Chemical Laboratory, Pune, India.
3. Participated in “*NCL-RF Annual Students conference 2019*”, held during November 28-29, 2019, at CSIR- National Chemical Laboratory, Pune, India.
4. Participated in “*FCS-2019, National Workshop on Fluorescence and Raman Spectroscopy*”, held during December 16-19, 2019, at TIFR, Hyderabad.
5. Attended the Winter School on “*Materials and Molecular Simulations Using Open Source Softwares: From Theory to Practice*” during October 16-22, 2019, at Department of Physics, Bishop Moore College, Mavelikara, Kerala, in association with CSIR (New Delhi) & KSHEC (Thiruvananthapuram).
6. Participated in “*Basic Fire Safety & Emergency Preparedness*” on 18th November 2021, at CSIR- National Chemical Laboratory, Pune, India.
7. Participated in “*RSC-IISER Desktop Seminar with PCCP and IISER Thiruvananthapuram*” during May 04-05, 2021, an online conference organized by IISER Thiruvananthapuram.
8. Participated in “*NCL-RF Annual Students conference 2021*”, held during November 29-30, 2021, at CSIR- National Chemical Laboratory, Pune, India.
9. Participated in a Virtual 1st International Conference on “*Emerging Porous Materials (ePorMat-21)*” from July, 29th to 30th 2021.

10. Attended ACS Science Talk on Covalent Organic Frameworks and the Morphology [0-1-2-3] on, 29th January 2021.

LIST OF ORAL AND POSTER PRESENTATION

1. Delivered an oral presentation for ***Krishnan Award for Research Fellow (CSIR-NCL-RF)***, the Best paper award for the paper published with the highest impact factor in material science in 2020), on National Science Day-2021, held on February 26, at CSIR- National Chemical Laboratory, Pune, India.
2. Presented poster in “***National Science Day-2020***”, held on February 26th-28th, 2020, at CSIR- National Chemical Laboratory, Pune, India.
3. Presented poster in “***FCS-2019, National Workshop on Fluorescence and Raman Spectroscopy***”, held during December 16-19, 2019, at TIFR, Hyderabad.
4. Presented poster in “***National Science Day-2021***”, held on February 24th-25th, 2021, at CSIR- National Chemical Laboratory, Pune, India.
5. Presented virtual poster in “***RSC-IISER Desktop Seminar with PCCP and IISER Thiruvananthapuram***” during May 04-05, 2021, an online conference organized by IISER Thiruvananthapuram.

Awards and Honours

1. Awarded for “***Krishnan Award for Research Fellow (CSIR-NCL-RF)***”, the Best paper award for the paper published with the highest impact factor in material science in 2020.
2. Best poster award in “***National Science Day-2020***”, held on February 26th-28th, 2020, at CSIR- National Chemical Laboratory, Pune, India.
3. Best poster award in “***RSC-IISER Desktop Seminar with PCCP and IISER Thiruvananthapuram***” during May 04-05, 2021, an online conference organized by IISER Thiruvananthapuram.

Cite this: *Chem. Sci.*, 2021, 12, 4216

All publication charges for this article have been paid for by the Royal Society of Chemistry

Efficient metal-free organic room temperature phosphors

Aakash D. Nidhankar,^{†ab} Goudappagouda,^{†ab} Vivek C. Wakchaure^{ab} and Sukumaran Santhosh Babu^{ab*}

An innovative transformation of organic luminescent materials in recent years has realised the exciting research area of ultralong room-temperature phosphorescence. Here the credit for the advancements goes to the rational design of new organic phosphors. The continuous effort in the area has yielded wide varieties of metal-free organic systems capable of extending the lifetime to several seconds under ambient conditions with high quantum yield and attractive afterglow properties. The various strategies adopted in the past decade to manipulate the fate of triplet excitons suggest a bright future for this class of materials. To analyze the underlying processes in detail, we have chosen high performing organic triplet emitters that utilized the best possible ways to achieve a lifetime above one second along with impressive quantum yield and afterglow properties. Such a case study describing different classes of metal-free organic phosphors and strategies adopted for the efficient management of triplet excitons will stimulate the development of better candidates for futuristic applications. This Perspective discusses the phosphorescence features of single- and multi-component crystalline assemblies, host-guest assemblies, polymers, and polymer-based systems under various classes of molecules. The various applications of the organic phosphors, along with future perspectives, are also highlighted.

Received 25th January 2021
Accepted 18th February 2021

DOI: 10.1039/d1sc00446h

rsc.li/chemical-science

1. Introduction

One of the areas where organic molecules excelled in the recent past is room temperature phosphorescence (RTP).^{1–30} RTP organic molecules have attracted scientific interest due to the

large Stokes shift, long lifetime, and strong afterglow that enable applications in bio-imaging, organic optoelectronics, anti-counterfeiting, sensing, *etc.*^{24,25,33,34} For the past many decades, heavy metal complexes were explored as phosphors because of the presence of ligand-metal and metal-ligand

^aOrganic Chemistry Division, National Chemical Laboratory (CSIR-NCL), Dr Homi Bhabha Road, Pune-411008, India. E-mail: sb.sukumaran@ncl.res.in

^bAcademy of Scientific and Innovative Research (AcSIR), Ghaziabad-201002, India

[†] These authors contributed equally to this work.



Aakash D. Nidhankar obtained his M.Sc. (Chemistry) from Yes-hwant Mahavidyalaya, SRTM University, Nanded, India in 2015. He is pursuing his Ph.D. in Chemical Science at the National Chemical Laboratory (CSIR-NCL), Pune, India, under the supervision of Dr Santhosh B. Sukumaran. His research interests are mainly focused on functional organic materials with ultralong phosphorescence.



Dr Goudappagouda obtained his M.Sc. (Chemistry) from Sahyadri Science College, Kuvempu University, Karnataka, India in 2012. Later, he received his Ph.D. in Chemical Science under the guidance of Dr Santhosh Babu Sukumaran from CSIR-National Chemical Laboratory (CSIR-NCL), Pune, India, in 2020. His research work mainly focused on the design and synthesis of donor-acceptor

small organic molecules for lighting and light-harvesting applications. Besides, he worked on charge carrier mobility and conductivity of donor-acceptor co-assemblies for electronic applications.



charge transfer (CT) and strong spin-orbit coupling, which improves the intersystem crossing (ISC) and controls the triplet decay rate.²⁷ Despite many advantages, organometallic complexes have the drawbacks of high toxicity, limited resources, and high cost. Hence this situation promoted the search for metal-free organic molecules as alternative phosphors. However, for organic materials, the nonradiative (k_{nr}) and quenching (k_q) rates of the triplet states are much larger than the radiative decay rate (k_p) under ambient conditions. Moreover, the triplet states are vulnerable to quenching by molecular oxygen, and hence RTP from metal-free organic molecules under ambient conditions continues to be challenging.¹ Nonetheless, the recent past has witnessed a massive jump in the exploration of metal-free organic phosphors through innovative molecular designs and control over the radiative and nonradiative decay processes associated with triplet excitons. The critical parameters that are being considered while designing organic RTP (ORTP) molecules include (1) populating the triplet state by efficient singlet-to-triplet ISC, (2) minimizing the nonradiative relaxation pathways, and (3) delaying the radiative decay. In accordance with that, heteroatoms such as N, O, S, Te, and halogens are incorporated as an integral part of the molecular design of organic phosphors.⁴⁻²⁷ Besides, nonradiative relaxation pathways are controlled by molecular packing in the crystalline state and with the help of supportive media such as polymers and cavitands. The compact molecular packing with the assistance of various intermolecular interactions provided extra stabilization of the triplet excitons to extend the lifetimes beyond seconds. In this way, a synergistic effect of all the supportive features resulted in enhanced RTP of metal-free organic phosphors.⁵⁻⁹ Besides, stabilization of the triplet excitons is found to be a conceptually new and exciting strategy to achieve newer heights for RTPs (Fig. 1).²⁰ Many new concepts such as suppression of the nonradiative deactivation pathways of the triplet state through hydrogen bonding, H-aggregation, helical arrays, and excited-state manipulations

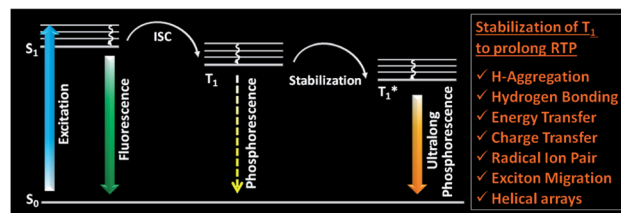


Fig. 1 Schematic of stabilization of the triplet state, leading to ultra-long phosphorescence in organic molecules.

such as CT, energy transfer (ET), radical ion pair formation, energy migration, *etc.* have been introduced to stabilize the triplet state.^{20,21}

Until now, many attempts to understand the relationship between ultralong RTP (URTP) and molecular packing have been reported.⁸⁻¹⁰ Those studies uncovered the vital role of ordered molecular arrays in tailoring lifetime,¹⁴⁻¹⁶ emission efficiency,¹⁸ luminescent colour,¹⁹ and even realizing the unique dynamic URTP features. Even though the structure-property correlation of organic phosphors has been achieved to a certain extent, the involvement of complex factors limits a complete understanding of the underlying mechanism of URTP. Hence a deeper understanding of the supportive role of adequate molecular packing, rigidification by polymers and hosts, and related controlling factors is of great significance. Even though URTP is a fascinating concept, a slow radiative decay leading to a long-lived lifetime is not supportive for any device applications, especially in light-emitting diodes (LEDs).^{31,32} However, compared to short-lived fluorescent materials, the advantages of an ultralong lifetime and large Stokes shifts make URTP materials promising candidates for applications such as bio-imaging, information storage, data encryption, anti-counterfeiting, sensing, and photodynamic therapy.^{24,25,33,34} Besides, the most critical aspect of URTP is that the triplet state excitons are susceptible to deactivation by molecular motions,



Vivek C. Wakchaure completed his M.Sc. (Organic Chemistry) in 2013 from Savitribai Phule Pune University, Pune, India. In 2015, he started his doctoral study under the supervision of Dr Santhosh Babu Sukumaran at the National Chemical Laboratory (CSIR-NCL) Pune, India. His thesis mainly focuses on strategies to develop processable 2D-polymers using organic solvent-free functional liquids.

The thesis describes the synthesis of small organic molecules and two-dimensional polymers for various applications such as sensing, tunable emission, and electrochemical charge storage.



Dr Sukumaran Santhosh Babu obtained his Ph.D. on oligo(*p*-phenylenevinylene) self-assembly from the National Institute for Interdisciplinary Science and Technology (CSIR-NIIST), Trivandrum, India. After several years of post-doctoral studies at the Max Planck Institute of Colloids and Interfaces, Germany, National Institute for Materials Science (NIMS), Japan, and the Univer-

sity of Namur, Belgium, he joined the Organic Chemistry Division of the National Chemical Laboratory (CSIR-NCL) in 2014 as a Senior Scientist. His research interests include self-assembly of luminescent organic materials, phosphorescence, and 2D-polymers for catalytic and energy applications.



oxygen, and humidity.^{1,3,35} Hence it has been extremely challenging to prolong the phosphorescent emission of organic materials at room temperature by overcoming all these hurdles. In this context, URTP of small molecule-based metal-free ORTPs has prime importance as a fundamental challenge. The numerous design strategies and self-assembly methods have been found successful in achieving an ultralong lifetime. Here, we firmly believe that a case study describing the different classes of organic phosphors and how to manage the triplet excitons to prolong the lifetime will inspire us to design better candidates for futuristic applications.

Recently, many reviews have appeared on RTP as an update of the field.^{20–25,29,30} However, the present study will mainly focus on the strategies adopted to achieve high performing metal-free organic triplet emitters, including phosphors having lifetimes of more than one second, high quantum yields, and attractive afterglow properties. More importantly, we have provided a comparison of the influence of radiative and nonradiative decay rates on the lifetime and quantum yield of each category of phosphors. Besides, the applications of ORTPs, along with future perspectives, are highlighted at the end.

2. Ways to improve RTP lifetime and quantum yield

The main challenges in metal-free ORTPs include weak spin-orbit coupling (SOC) ($<0.1 \text{ cm}^{-1}$) resulting in inefficient ISC, enhanced k_{nr} due to many deactivation pathways, and the susceptibility of the T_1 state to oxygen and temperature.^{1,3,35} Hence, to design excellent ORTPs and estimate the performance, the following discussion can be helpful. The important parameters, *i.e.* quantum efficiency of ISC (ϕ_{isc}) (from S_1 to T_1), quantum yield (ϕ_{p}), lifetime (τ_{p}), and radiative decay (k_{p}), of phosphorescence can be defined as

$$\phi_{\text{isc}} = k_{\text{isc}} / (k_{\text{f}} + k_{\text{ic}} + k_{\text{isc}}) \quad (1)$$

$$\phi_{\text{p}} = \phi_{\text{isc}} k_{\text{p}} \tau_{\text{p}} \quad (2)$$

$$\tau_{\text{p}} = 1 / (k_{\text{p}} + k_{\text{nr}}) \quad (3)$$

$$k_{\text{p}} = (64\pi^4 / 3h^4 c^2) \Delta E_{T_1 \rightarrow S_0}^3 |\mu_{T_1 \rightarrow S_0}|^2 \quad (4)$$

where k denotes the rates of the singlet emission process such as k_{f} , k_{ic} and k_{isc} related to the fluorescence (from S_1 to S_0), internal conversion (IC) (from S_n to S_1) and ISC (from S_1 to T_1), respectively. At the same time, the rates related to the triplet state are denoted as k_{p} and k_{nr} for radiative and nonradiative decays (from T_1 to S_0), respectively. It has to be noted that all these rate parameters related to singlet and triplet transitions completely control the characteristic phosphorescence features of pure ORTPs. An in-depth analysis of eqn (1)–(3) reveals that an enhanced k_{isc} , a reduced k_{nr} , and a slow k_{p} are essential for an improved RTP lifetime. Another critical parameter not discussed much is the triplet quenching rate k_{q} which can be minimized by rigidification of the phosphor using a host or polymer support.^{20,29,30} Besides, eqn (1)–(3) indicate that

conditions such as enhanced ϕ_{isc} and $k_{\text{p}} > k_{\text{nr}}$ are required to improve ϕ_{p} . However, to achieve long τ_{p} a reduction of both k_{p} and k_{nr} is needed. Hence the impact of k_{p} is ultimate in achieving high ϕ_{p} and long τ_{p} . Eqn (4) shows that an increment in the singlet–triplet energy gap $\Delta E_{T_1 \rightarrow S_0}$ will accelerate k_{p} and eventually reduce k_{nr} . The above two conditions related to k_{p} are contradictory when looking for a long lifetime and a high quantum efficiency. It indicates that simultaneous enhancement of both ϕ_{p} and τ_{p} is challenging. The below sections describe the various parameters controlling the RTP features.

2.1. Rate of intersystem crossing k_{isc}

There have been several attempts to obtain an enhanced k_{isc} necessary for efficient RTP, such as effective SOC and small ΔE_{ST} .^{36–38} In this direction, the major directive for a high k_{isc} through effective SOC has come from El-Sayed's rule, which states that effective orbital overlapping is possible in a singlet to triplet transition with different molecular-orbital configurations.³⁹ In other words, compared to the transition from $^1(n, \pi^*)$ to $^3(n, \pi^*)$ or from $^1(\pi, \pi^*)$ to $^3(\pi, \pi^*)$, effective ISC can be observed in transitions from $^1(n, \pi^*)$ to $^3(\pi, \pi^*)$ or from $^1(\pi, \pi^*)$ to $^3(n, \pi^*)$ states. Many recent successful designs showed that the presence of n orbitals perpendicular to π orbitals is beneficial to facilitate a strong SOC and thereby promote the ISC from singlet to triplet excited states.^{12,14} Hence the presence of hybrid (n, π^*) and (π, π^*) configurations is supportive for URTP. An enhanced k_{isc} through SOC significantly contributed to achieve high ϕ_{p} . However, a long τ_{p} heavily depends on the stabilization of triplet excitons through multiple pathways.

2.2. Energy gap ΔE_{ST}

One of the reasons for the inefficient RTP in organic molecules is the large ΔE_{ST} due to inappropriate molecular designs. It has been noticed that k_{isc} can be significantly promoted by small ΔE_{ST} , which depends on the spatial overlap of the highest occupied molecular orbital (HOMO) and lowest unoccupied molecular orbital (LUMO) wavefunctions. A strong CT interaction between the donor and acceptor building units of a phosphor can be influential because CT interaction can control the spatial overlap. A CT state can be introduced either by bridging donor–acceptor (D–A) groups or through the assistance of intermolecular interactions between donor and acceptor molecules. Such examples for enhanced RTP through small ΔE_{ST} driven by the CT state³⁸ and through aggregation controlled management of ΔE_{ST} (ref. 40) are available in the literature. The formation of various aggregates can dictate ΔE_{ST} values and thereby influence ISC.

2.3. Rate of nonradiative decay k_{nr}

The current era of organic phosphors and the sudden developments are attributed to crystallization to a greater extent. The crystallization of phosphors using intermolecular interactions such as π – π stacking, van der Waals, halogen, and hydrogen bonding suppresses the nonradiative decay pathways to facilitate RTP.⁴¹ Besides, host–guest assemblies, immobilization of phosphors in frameworks, and polymers also protected the



phosphors from nonradiative decay. In this case, the most celebrated “H-aggregation” was found to be effective in stabilizing the triplet excitons to achieve long-lived RTP.⁴² As per eqn (2) and (3), a variation in k_{nr} also significantly alters the values of both ϕ_p and τ_p . Hence the design strategies should consider the incorporation of corresponding functional moieties to impart various noncovalent interactions to regulate k_{nr} . Another vital strategy adopted to reduce k_{nr} by decreasing reorganization energy is deuteration, which blocks the molecular vibrations.⁴³ The high $\Delta E_{T_1 \rightarrow S_0}$ value was also found to be effective in suppressing the nonradiative decay.^{2,3,39}

2.4. Rate of radiative decay k_p

Eqn (4) shows that k_p is complicated and mainly determined by many factors involving both the singlet and triplet states, such as SOC, transition dipole moment $\mu_{T_1 \rightarrow S_0}$, and energy gap $\Delta E_{T_1 \rightarrow S_0}$. A high $\Delta E_{T_1 \rightarrow S_0}$ accelerates k_p to facilitate RTP with a reduced lifetime and it is the same with the transition dipole moment as well.^{2,3,39} It has been found that in ORTPs showing excellent features, an exceptional stabilization of the triplet excitons through various supports delays the radiative decay. In such systems, k_p is suppressed to achieve a long lifetime over seconds. A slow k_p , in turn, enhances τ_p to realize URTP, while it inversely affects ϕ_p .

2.5. Rate of quenching k_q

Along with other factors controlling the efficiency of RTP, the suppression of k_q is also equally important. Even though recent studies have employed crystalline assemblies and the support of polymers, hosts, and porous structures to avoid the effect of moisture and oxygen, the quenching rate of the triplet excitons is found to be crucial to deliver excellent RTP features under ambient conditions. Hence the deactivation patterns of the triplet excitons require more attention. The current studies on ORTPs lack a deeper understanding of the effect of k_q , assuming that stabilization through self-assembly or other supports will control k_q .²⁰

2.6. Triplet exciton diffusion

Recent studies have shown the importance of triplet exciton diffusion length on persistent RTP.⁴⁴ It has been suggested that short-range triplet exciton diffusion can suppress k_q by stopping the excitons from reaching the trap sites. The importance of exciton diffusion length is more dominant in the case of crystalline arrays with more traps. However, a very recent demonstration indicated that the triplet exciton diffusion with the assistance of helical arrays of phosphor played an essential role in delaying the triplet radiative decay to extend lifetime beyond 4 s.⁴⁵ Hence the quality of the generated crystals or thin films and management of triplet excitons can impart excellent RTP features. More studies in this direction are required for detailed understanding and further development. In addition, hyperfine-coupling (HFC) driven intersystem crossing in CT complexes and radical ion pairs (RIPs),⁴⁶ singlet fission,⁴⁷ *etc.* were also found to be useful in controlling the RTP features.

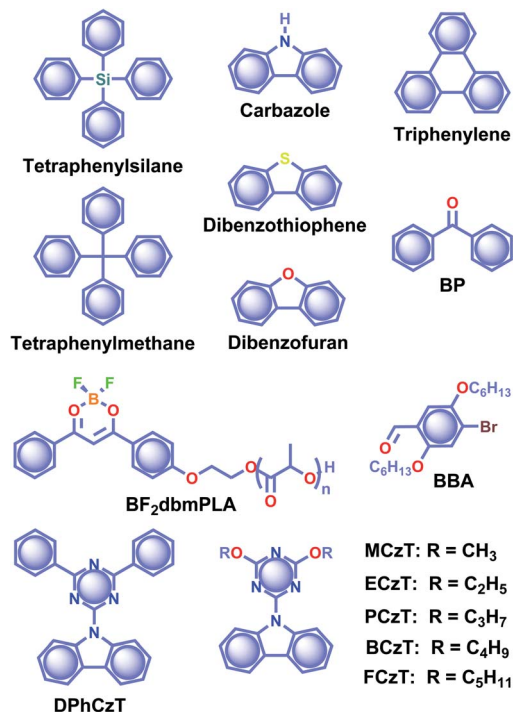
The above sections describe the possible ways for organic phosphors to achieve enhanced RTP features. The implemented molecular designs have been found to be successful to a certain extent and thus delivered some exceptional RTP candidates exhibiting a lifetime longer than one second. In this Perspective, we attempt to reveal the special effects in molecular design and ground state arrangements of metal-free organic phosphors to exhibit prodigious RTP qualities. The recent progress in the lifetime, quantum yield, and afterglow properties of these unusual candidates promoted metal-free ORTPs as a capable material in many functional applications. We want to mention that the dedicated efforts of various research groups worldwide made significant contributions in this area to gain an admirable position for ORTPs in current research.^{1–30}

3. Efficient organic phosphors

RTP of metal-free organic molecules fascinated the scientific community as early as the 1940s, and the exciting demonstrations in the early stages have been summarised in many reviews.^{39,48–50} The initial experiments were limited in solutions, that too under cryogenic and oxygen-free conditions.^{51–54} Later, the developments were focused on RTP of salts of aromatic carboxylic acids, phenols, amines, and sulfonic acids in rigid media including boric acid glass,^{52–54} and filter paper, silica or alumina,^{55–59} micelles,⁶⁰ and hosts such as cyclodextrins,⁶¹ zeolites,⁶² hemicarcerand,⁶³ *etc.* The rigid matrices prepared using glucose, sucrose, citric acid, and tartaric acid have supported the RTP of organic molecules.^{51,64} Similarly, plastics such as poly(methylmethacrylate) and poly(vinyl alcohol) also provided a rigid medium for organic phosphors to excel.^{65–67} The subsequent investigations on ORTP over a few decades emerged the area and found it useful for many potential applications.^{68,69} In between, RTP of crystals was reported in 1939 by Clapp and coworkers.⁷⁰ Crystals of tetraphenylsilane and tetraphenylmethane (Scheme 1) showed RTP afterglow emission up to 23 s visible to the bare eye. Later, in 1978, Bilen and coworkers studied the afterglow of carbazole, dibenzothiophene, dibenzofuran, triphenylene (Scheme 1), *etc.*, having a lifetime up to 4.85 s in the crystal state.⁷¹ After a long gap, the technological improvement in materials chemistry during the last decade resulted in a drastic development in RTP of metal-free organic molecules.^{20–25,29,30} Many new molecular designs and self-assembly models have been experimented with and eventually URTP was realized. The following sections detail the recent advancements of ORTPs.

In 2007, the research group of Fraser came up with boron difluoride dibenzoylmethane (BF₂dbm) conjugated poly(lactic acid) **BF₂dbmPLA** (Scheme 1) having oxygen-sensitive RTP.⁷² Later in 2010, Tang and coworkers reported RTP of a series of benzophenone **BP** derivatives (Scheme 1) and found that the presence of a carbonyl group or halogen atom, and nonplanar conformation are supportive factors in RTP.⁷³ RTP of 2,5-dihexyloxy-4-bromobenzaldehyde **BBA** (Scheme 1) was reported by Kim and coworkers in 2011.⁷⁴ This molecule shows weak fluorescence in solution; however, it exhibits a green phosphorescence emission with a lifetime of 5.4 ms in the crystal





Scheme 1 Chemical structure of phosphors tetraphenylsilane, tetraphenylmethane, carbazole, dibenzothiophene, dibenzofuran, triphenylene, BP, BF₂dbmPLA, BBA, DPhCzT, MCzT, ECzT, PCzT, BCzT, and FCzT.

state. Single-crystal XRD analysis revealed that RTP is due to the presence of close contact between the bromine and the carbonyl oxygen of the neighbouring molecule (C=O...Br-C, 2.86 Å). RTP retains a lifetime longer than 100 ms with an afterglow approaching seconds after cessation of excitation. The above three studies greatly attracted the attention towards organic phosphors and hence resulted in a visible change in the area.

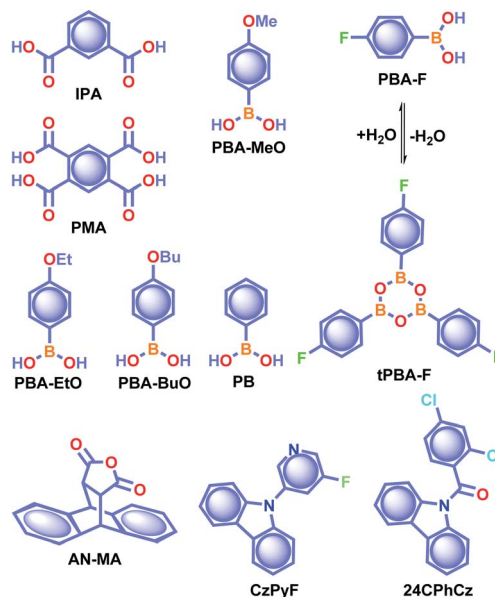
3.1 Single and two-component crystalline organic phosphors

Recently, significant developments have occurred in single-component crystalline assemblies that exhibit long τ_p along with high ϕ_p .⁷⁵ In general, RTP of such single-component assemblies is enhanced by crystallization mainly because of the following reasons: (1) availability of specific intermolecular interaction in the crystal state to improve ISC through SOC; (2) intact molecular packing suppresses the molecular motions and eventually helps to minimize k_{nr} of triplet excitons, (3) crystalline assemblies will provide protection from triplet quenching by oxygen. The recent exciting development of URTPs is strongly supported by molecular organization in the crystal state, which stabilizes the excited triplet state by trapping triplet excitons and controls both radiative and non-radiative decays.

In 2015, Chen, Liu, Huang, and coworkers synthesized a series of pure organic molecules of carbazole and triazine containing O, N, and P atoms (Scheme 1).⁴² Notably, the presence of heteroatoms facilitates the spin-forbidden transfer of

singlet-to-triplet excited states through $n-\pi^*$ transitions to populate triplet excitons. In this series, 9-(4,6-diphenyl-1,3,5-triazin-2-yl)-9H-carbazole **DPhCzT** and 9-(4,6-diethoxy-1,3,5-triazin-2-yl)-9H-carbazole **ECzT** (Scheme 1) exhibited τ_p up to 1.35 s and 1.05 s, respectively. The enhanced ISC in these molecules is due to the increased number of energy transition channels supported by the H-aggregated dimers of **DPhCzT** and **ECzT** in the crystals. The strong coupling *via* $\pi-\pi$ stacking in the H-aggregate dimers with a large transition dipole moment provides stabilization and thus protects the triplet excitons. The stabilized triplet excited state (T_1^*) functions as an energy trap at a lower energy level, offering suppressed radiative and non-radiative deactivation decay rates in favour of long-lived phosphorescence. As a continuation, by varying the alkyl chain length on the triazine unit, the same group achieved photoactivation assisted smart URTP materials.⁷⁶ Among the molecules, the lifetime of **BCzT** (Scheme 1) drastically increased from 1.8 ms to 1.33 s upon photoirradiation for 10 min. The prolonged irradiation of molecules with UV light suppresses k_{nr} by controlling the molecular motion to enhance both RTP emission intensity and lifetime. A significant difference in the distances of intermolecular interactions between adjacent molecules is observed after photoactivation. As the length of the alkoxy chain increased, both the lifetime of photoactivation and deactivation for URTP decreased drastically from **MCzT** to **FCzT**. This study points to the importance of photo-irradiation assisted control of nonradiative transition in ORTPs.

In 2015, Yuasa and his team explained the nuclear spin magnetism-assisted spin-exchange of a radical ion pair (RIP).⁴⁶ In this study, the RTP afterglow of benzoic acid derivatives such as isophthalic acid **IPA** and pyromellitic acid **PMA** (Scheme 2) was observed for several seconds. Phosphorescence



Scheme 2 Chemical structure of benzoic acids IPA and PMA, boron-containing phosphors PBA-MeO, PBA-EtO, PBA-BuO, PBA-F, tPBA-F, and PB, and AN-MA, CzPy, and 24CPhCz.



measurements of **IPA** and **PMA** revealed the presence of bands at 532 and 533 nm with 0.970 and 1.1 s lifetime, respectively. Photoexcitation of these carboxylic acid derivatives leads to the generation of singlet and further triplet RIPs through hyperfine-coupling (HFC) induced spin conversion, mediated through the magnetic field of neighbouring ^1H nuclear spins. Here, deuterium labeling of carboxylic acids suppressed the phosphorescence intensity, confirming the HFC mechanism and a nuclear spin magnetism-assisted spin conversion ($^1\text{RIP} \rightarrow ^3\text{RIP}$) responsible for URTP. In another report, Yan and coworkers reported the phosphorescence lifetime of **IPA** in the crystal state as 1.11 s and explained that the presence of only one type of hydrogen bonding interaction in **IPA** stabilizes the carboxylic acid dimers.⁷⁷

Recently, many aryl boronic acids and esters with stable and extended RTP have been reported. In one of the first reports, Nakai, Fukushima, and coworkers reported long-lived RTP of a series of aryl boronic esters **BE-1-5** (Fig. 2a).⁷⁸ **BE-1** displayed RTP in the solid-state with a green afterglow that lasted for several seconds (Fig. 2b and c). In this series **BE-1-6**, the value of τ_p varied as 1.85, 1.79, 1.65, 1.73, 1.57, and 1.39 s, respectively (Fig. 2c). A combined experimental and theoretical study revealed that an out-of-plane distortion is introduced at the (pinacol) B-C_{ipso} moiety in the T_1^* state, and it enables the mixing of π and σ orbitals to enhance SOC and thereby lead to URTP. Later, Li and coworkers studied the RTP of many

commercially available phenylboronic acids and their thermally prepared triphenylborazine derivatives.⁴¹ The phosphorescence spectrum of 4-methoxyphenyl boronic acid **PBA-MeO** (Scheme 2) revealed two resolved emission peaks at 457 and 488 nm with τ_p of 2.24 and 2.19 s, respectively. The long lifetime is due to rigid conformation and strong intermolecular interactions *via* hydrogen bonds, which decrease k_{nr} . An effective π - π stacking stabilizing the triplet excitons also contributes to bright and prolonged RTP. The importance of π - π stacking interactions was further analyzed by theoretical calculations of dimers, indicating that strong π - π stacking decreases ΔE_{ST} to favour ISC. The authors studied RTP by varying the length of the alkyl chain and found that **PBA-EtO** and **PBA-BuO** also showed RTP with τ_p of 1.11 s and 1.28 s, respectively. In this series of boronic acids, the support of H-bonds through C-H \cdots F interactions enabled **PBA-F** and the thermally prepared triphenylborazine **tPBA-F** derivative (Scheme 2) to show a long lifetime of 1.34 and 1.96 s, respectively.

In the same year, HFC driven ISC in CT complexes was reported by Yuasa and coworkers using phenylboronic acid derivatives (**PBs**) such as phenyl-mono-boronic acid **PB** (Scheme 2) and *p*-phenylenediboronic acid ethyleneglycol ester **BE-3** (Fig. 2a) as examples.⁷⁹ The phosphorescence intensities of **PBs** mainly depend on the magnetic-field and spin-isotope effects controlled by HFC. Interestingly, **PB** showed a RT afterglow for several seconds with τ_p of 1.2 s. Furthermore, the authors investigated the effect of steric bulkiness on phosphorescence by taking **BE-3** as an example, which showed a pale blue afterglow for about 12 s with τ_p of 1.6 s. The luminescence quantum yield of **PB** and **BE-1** was found to be 18 and 77%, respectively. The phosphorescence mechanism was summarized to follow the transitions $S_0 \rightarrow ^1\text{CT} \rightarrow ^3\text{CT} \rightarrow T_1 \rightarrow S_0$, indicating the direct involvement of both singlet and triplet CT states. Furthermore, studies on the effect of halogen on RTP of **PBs** showed that among the series, only 2-(4-fluorophenyl)-1,3,2-

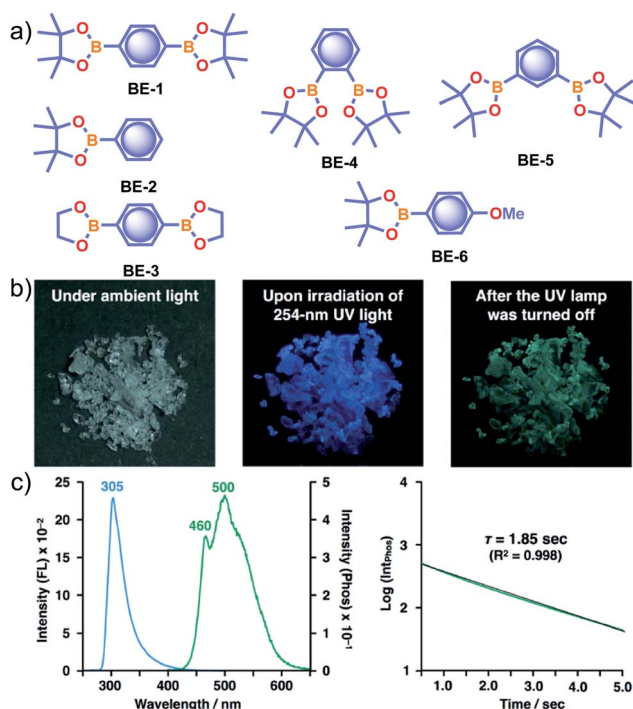


Fig. 2 (a) Chemical structure of aryl boronic esters **BE-1-6**. (b) Photographs of **BE-1** under ambient light (left) and irradiation with 254 nm UV light in the dark (middle), and after the UV light was turned off in the dark (right). (c) Fluorescence and phosphorescence spectra (left) and the corresponding phosphorescence decay profile of **BE-1** (right). Reproduced with permission from ref. 78. Copyright 2017, American Chemical Society.

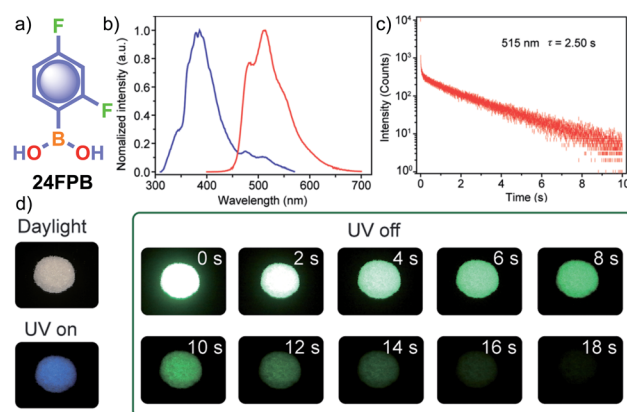


Fig. 3 (a) Chemical structure of **24FPB** and (b) steady-state photo-luminescence (blue line) and phosphorescence (red line) spectra of **24FPB**. (c) Phosphorescence decay profile of the emission band at 515 nm. (d) Photographs of the **24FPB** crystal taken at different time intervals before and after removing the excitation source (a 365 nm UV lamp). Reproduced with permission from ref. 80. Copyright 2019, WILEY-VCH.



dioxaborolane **PBA-F** exhibited long τ_p of 1.7 s. In this line, Huang and his group enhanced τ_p by introducing multiple fluorine atoms on the phenylboronic acid **24FPB** (Fig. 3a and b).⁸⁰ The maximum lifetime of 2.50 s was exhibited by 2,4-difluorophenylboronic acid **24FPB** crystals (Fig. 3c). The prolonged lifetime is because of the stabilization of the triplet excited state by H-aggregation and intramolecular O–H...F hydrogen bonding (2.22 Å) in the crystal. The hydrogen bonding in crystals fixed the dihedral angle (θ) between the benzene ring and the boronic acid group, resulting in rotation confinement leading to a longer lifetime. Interestingly, a persistent green luminescence for **24FPB** was observed for more than 20 s after the UV light was turned off (Fig. 3d).

Since intermolecular interaction assisted packing in the crystalline assembly plays a critical role in ORTP, the examples of polymorphs need a special mention.⁸¹ Polymorphs offer the opportunity to develop crystals with varying sizes, shapes, and optical properties through tuning the cultivation conditions. It has been noticed that even slight variations in the molecular packing impart significant changes in the excited state properties. In this context, the benefit of polymorphism is the informative correlation between molecular packing and the resulting functional properties. In another way, it encourages rational molecular design to improve the optical properties and hence RTP polymorph is an interesting topic of research.

Yuan and coworkers reported a long lifetime for the cycloaddition product **AN-MA** of anthracene and maleic anhydride (Scheme 2).⁸² Out of the two polymorphs form A and form B, afterglow emission of the latter one lasted for several seconds with τ_p of 1.6 s and ϕ_p of 8%, because of its much stronger intramolecular π - π interactions. The presence of the carbonyl group and oxygen atoms with lone pairs, together with the effective intra- and intermolecular interactions, helps **AN-MA** to achieve bright green RTP emission. The relatively low k_{nr} value resulting from the more rigid conformations significantly contributed towards the long lifetime. Cai *et al.* reported that out of the three polymorphs formed by hydrogen-bonded frameworks of benzene-1,3,5-triyltris((9*H*-carbazol-9-yl)methanone), only one with two different types of tetragonal pore in the crystal packing exhibited URTP of 198 ms. The presence of strong intralayer π - π interactions between carbazole units in the framework stabilized the triplet excitons to achieve URTP.⁸³ Similarly, Yang *et al.* demonstrated how the different molecular conformations in the polymorphs of 4-(4*a*,10*a*-dihydro-10*H*-phenothiazin-10-yl)benzoxazole control RTP.⁸⁴ In the series of three polymorphs generated, the one with the more intermolecular interactions has the more extended RTP lifetime of 266 ms. These studies showed that the various modes of packing arising from the different molecular configurations greatly contribute to the incomparable RTP features of the polymorphs. Due to the lower number of reports and nominal performance, RTP polymorphs and the related discussion is restricted in this Perspective.

To understand the effect of a heavy atom to obtain longer RTP, Sasabe, Kido and coworkers studied the RTP features of a series of 3-pyridylcarbazole derivatives with H, F, Cl, Br, and I as substituents on the pyridine ring.⁸⁵ The crystals of the

fluorine-substituted derivative **CzPyF** (Scheme 2) showed an ultralong τ_p of 1.1 s and ϕ_p of 1.2%. Theoretical and experimental data revealed the crucial role of n orbital on the central pyridine ring in enhancing the intersystem crossing between $^1CT^*$ and the locally excited triplet ($^3LE^*$) states. X-ray crystallographic studies indicated that both the pyridine ring and fluorine atom contributed to the enhancement of RTP through restricted motion owing to weak C–H...N and H...F hydrogen-bonding interactions. The presence of a halogen atom with larger electronegativity enabled a longer RTP lifetime in this series. Similarly, in 2019, Shi, An, Huang, and coworkers provided a detailed study related to the critical role of molecular stacking in generating triplet excitons by using a series of carbazole derivatives having chlorine substitution at different positions.⁸⁶ The combined experimental and calculated results revealed that **24CPhCz** (Scheme 2) with robust intermolecular coupling between carbazoles exhibited long τ_p of 1.06 s and ϕ_p of 2.5%. A detailed crystal structure analysis of **24CPhCz** showed that the existence of intermolecular interactions played an essential role in enhancing the lifetime. The molecules were restricted by abundant CCl... π , C=O...Cl, CCl...H–C, Cl...Cl, and C–H... π interactions. The restricted nonradiative transitions through molecular packing in the crystal state prolong the lifetime. However, a weak interchromophoric coupling between carbazoles resulted in weak phosphorescence for the other derivatives in the series.

Tunable emission organic phosphors are rare and are difficult to achieve in a single-component phosphor. A tunable phosphorescence under different excitation wavelengths was reported by Gu *et al.* utilizing the available multiple emitting centers in a phosphor (Fig. 4a).⁸⁷ A triazine derivative, 2-chloro-4,6-dimethoxy-1,3,5-triazine **DMOT** (Fig. 4a and b), contains various heteroatoms that improve the k_{isc} to boost the

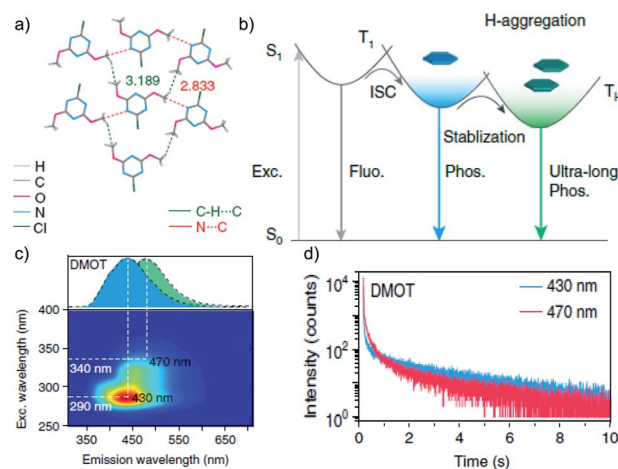


Fig. 4 (a) Top-view crystal structure of DMOT showing detailed information on the intermolecular interactions. (b) Proposed mechanism and molecular design for excitation-dependent colour-tunable URTP. (c) Excitation-phosphorescence mapping of DMOT. (d) Phosphorescence decay profiles of emission bands at 430 and 470 nm for DMOT. Reproduced with permission from ref. 87. Copyright 2019, Springer Nature Limited.



population of triplet excitons. The planar structure of the molecule strongly supports H-aggregation through multiple intermolecular interactions such as N \cdots C, CH \cdots C, and π - π interactions with the surrounding six molecules (Fig. 4a). Besides, H-aggregation assisted restricted molecular motion in the crystal ensures excellent phosphorescence features with τ_p of 2.45 s and ϕ_p of 31.2% (Fig. 4b-d). Interestingly, upon changing the excitation wavelength from 250 to 400 nm, the emission colour of **DMOT** was tuned from violet to sky blue, owing to single-molecule and H-aggregate phosphorescence, respectively (Fig. 4c). Such tunable emission smart RTP material will be useful for displays, sensors, and imaging applications.

Similarly, Yuan and coworkers worked on an unexplored pyrimidine molecule, hydantoin (**HA**) (Scheme 3), with tunable emission colour in response to the excitation wavelength.⁸⁸ The synergistic effect of through-space conjugation between carbonyls (C=O) and nitrogen (N) heteroatoms, and intermolecular interactions through multiple hydrogen-bonds enabled **HA** to be an excellent RTP emitter with τ_p of 1.74 s and ϕ_p up to 21.8%. Crystals of **HA** displayed sky-blue and yellowish-green afterglows lasting for over 10 s upon excitation with 312 and 365 nm UV lights, respectively. A stable self-assembled network with the adjacent molecules using multiple H-bonds, C=O \cdots H and O=C \cdots C=O (π - π) interactions at a relatively shorter distance strengthens the assembly and implies extended through-space delocalization. A dimer of **HA**, 1,1'-methylenehydantoin **MDHA** (Scheme 3), also exhibited tunable URTP, but with comparatively lower efficiency having τ_p of 1.27 and ϕ_p of 3.6%. The tunable RTP feature is supported by a clustering-triggered emission mechanism, where the presence of different clusters with through-space conjugation and conformation rigidification resulted in tunable RTP.

Very recently, Babu and coworkers came up with a new strategy of stabilizing triplet excitons by helical molecular packing (Fig. 5).⁴⁵ An *N*-alkylated carbazole decorated with

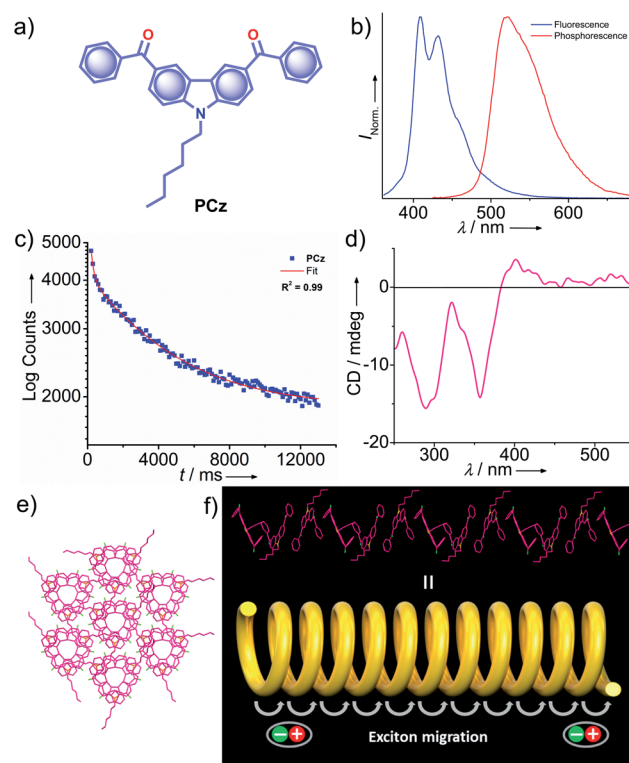
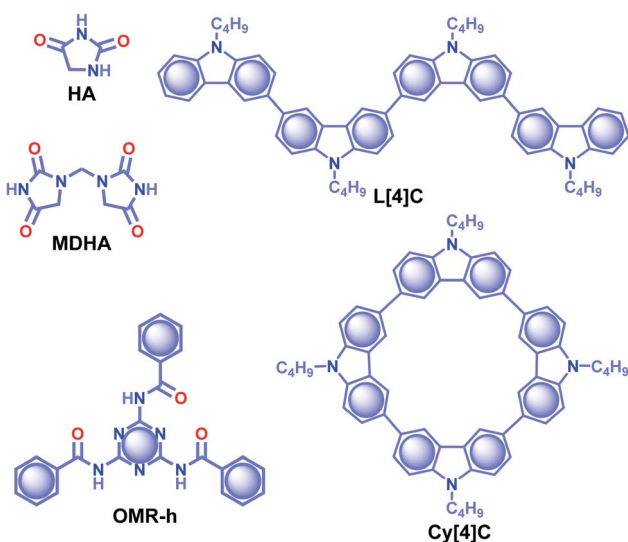


Fig. 5 (a) Chemical structure of PCz. (b) Steady-state photoluminescence (blue line) in solution and phosphorescence (red line) spectra in the crystal state of PCz. (c) Phosphorescence decay profile of PCz crystals. (d) The solid-state CD spectrum of PCz crystals. (e) Six adjacent helical arrays of PCz leading to extended columnar packing in the *c*-axis. (f) Schematic of the helical array of PCz leading to triplet exciton migration. Reproduced with permission from ref. 45. Copyright 2020, WILEY-VCH.

phenylmethanone units **PCz** (Fig. 5a) exhibited URTP with high efficiency ($\tau_p > 4.1$ s and ϕ_p of 11%) (Fig. 5b and c). A helical molecular array of **PCz** in the crystal state enabled the singlet-triplet states to be mixed up to enhance ISC. A right-handed helical molecular array of **PCz** acts as a trap and exhibits triplet exciton migration to deliver the exceptionally long lifetime (Fig. 5d and e). An extended molecular array was formed by the arrangement of molecules mainly through π - π interaction (3.34 Å) between carbazole and phenylmethanone units of adjacent molecules. The thus-formed 1D-helical array is stabilized by CH \cdots π interaction between the alkyl chain on carbazole and phenylmethanone unit in the adjacent helical columns. Space filled packing rigidifies the molecular conformations and remarkably blocks the nonradiative decay pathways. A combined experimental and theoretical study sheds light on the stabilization of the triplet state by the helical arrays. The micro rods of **PCz** exhibit triplet exciton migration that prolongs RTP lifetime (Fig. 5f). In contrast to other carbazole based small molecule phosphors, **PCz** failed to show afterglow emission under ambient conditions.

In 2020, Shan and coworkers reported URTP of organic micro-rods of **OMR-h**, which is synthesized by heating a mixture of melamine and benzoic acid in an aqueous solution (Scheme



Scheme 3 Chemical structure of HA, MDHA, OMR-h, L[4]C and Cy[4]C.



3).⁸⁹ In the presence of water, the micro-rods form a hydrogen-bonded network that rigidifies the molecular motion. A significant enhancement in RTP features with τ_p of 1.64 s and ϕ_p of 11.4% was observed under the wet conditions. The observed lifetime of the hydrogen-bonded structure of **OMR-h** is one of the extended lifetimes of ORTP materials in water. A cyclization-driven enhancement of a less RTP active candidate, *N*-butyl carbazole (τ_p of 1.45 ms), is reported by Zhu *et al.*⁹⁰ An increase in the conjugation resulted in an efficient ISC for both linear **L** [4]**C** and cyclic **Cy**[4]**C** derivatives of *N*-butyl carbazole (Scheme 3) and helped to achieve longer lifetimes of 2.24 and 3.41 s, respectively. The prolonged lifetime is correlated with the significantly lower ΔE_{ST} for **Cy**[4]**C** with a near-planar structure. Moreover, the synergistic effect of rigidification also contributed to suppress the nonradiative decay. The obtained value is highest among the lifetimes for an organic phosphor without any heavy atom or a carbonyl group.

Similar to single component RTPs, many attempts have been reported to stabilize the triplet state through multiple interactions between two different structural units with complementary recognition parts. This section primarily summarizes the

developments in the area of two-component RTP systems. An, Huang and coworkers reported that cocrystals formed by the assembly of melamine **ME** and **IPA** resulted in a stable framework *via* multiple interactions (Fig. 6).⁹¹ The two-component assembly **ME-IPA** exhibited URTP with τ_p of 1.91 s and ϕ_p of 24.3% under ambient conditions (Fig. 6c and d). The rigid framework confined the molecules in a three-dimensional network (Fig. 6e) and thus helped to limit k_{nr} of the triplet excitons and improved k_{isc} . Similarly, the cocrystals of **ME-TPA** also presented excellent RTP features with τ_p of 1.09 s and ϕ_p of 19.4%. The RTP of the cocrystal is confirmed by the faster k_{isc} ($9.3 \times 10^7 \text{ s}^{-1}$) of the **ME-IPA** framework than that of the individual components **ME** ($1.7 \times 10^6 \text{ s}^{-1}$) and **IPA** ($8.7 \times 10^6 \text{ s}^{-1}$). It has to be noted that the SOC $\xi(S_1, T_n)$ of **ME-TPA** and **ME-IPA** increased to 16.1 cm^{-1} and 33.9 cm^{-1} , respectively, compared to the relatively lower values of monomers. If we compare **ME-IPA** and **ME-TPA**, the k_{nr} and k_p varied as 0.13 and 0.18 s^{-1} , and 0.4 and 0.74 s^{-1} , respectively. However, the co-assembly of **ME-PA** exhibited comparatively less RTP efficiency with τ_p of 0.68 s and ϕ_p of 0.82%. The advantages of the two-component phosphor enabled a simultaneous enhancement of τ_p and ϕ_p .

A detailed mechanistic aspect of this significantly high RTP performance of the acid-amine cocrystals was explained by Yan and coworkers through TADF-assisted Förster resonance ET from the energy donor **ME** to the phosphor acceptor acids leading to a longer lifetime (Fig. 6f).⁷⁷ Density functional theory calculations of the D-A assembly showed that the HOMO is located on **ME**, while the LUMO is on **PA/IPA/TPA** for **ME-PA**, **ME-IPA**, and **ME-TPA**, respectively. Furthermore, the possibility of ET was supported by the spectral overlap between the absorption of the acceptors (**PA**, **IPA**, and **TPA**) and the emission of **ME**. The emission peaks at 318, 373, and 342 nm have been shifted to 540, 524, and 554 nm in the delayed spectra with a lifetime of 0.43, 2.00, and 0.77 s, respectively, for **ME-PA**, **ME-IPA**, and **ME-TPA** (Fig. 6g and h). The enhanced RTP lifetime is strictly due to the TADF assisted efficient ET (76%) in the cocrystals. Interestingly, the cocrystals exhibited a strong afterglow lasting for many seconds (Fig. 6i). Two-component assembly promotes triplet state stabilization by additional charge-mediated hydrogen bonding and π - π stacking, resulting in enhanced RTP. A new strategy of multi-component URTP material utilizing both TADF and ET raises hope for further improvement.

The above section pointed out the recent developments in the area of organic crystalline phosphorescent materials. Many single- and multi-component assemblies have been examined to understand the underlying design principles for achieving high quantum yield and extended lifetime up to seconds. However, crystalline RTP materials lack processability and require tedious optimizations for practical applications. This situation demands alternative candidates to troubleshoot the existing barriers in such materials. Hence the organic materials chemists took up this challenge and introduced various new methods to improve RTP features, and the recent developments will be discussed in the following sections.⁹²

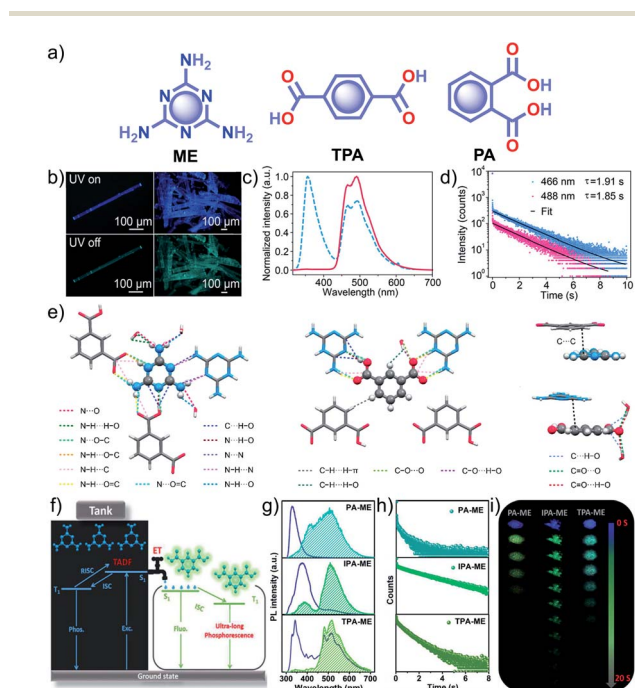


Fig. 6 (a) Chemical structure of **ME**, **TPA** and **PA**. (b) Photographs of emission (top) and phosphorescence (bottom) of the **ME-IPA** cocrystal. (c) Steady-state photoluminescence (blue dotted line) and phosphorescence (red line) spectra along with (d) phosphorescence decay of the emission bands at 466 and 488 nm, respectively, of **ME-IPA**. (e) Molecular packing of **ME-IPA** showing intermolecular interactions from the same plane with **ME** as the center and **IPA** as the center along with **ME** and **IPA** with adjacent planes. (f) Schematic of TADF-assisted transfer from **ME** to **IPA** enhancing the RTP lifetime. (g) Prompt and delayed fluorescence spectra and corresponding (h) time-resolved fluorescence decay profiles, and (i) photographs showing the long-afterglow of **ME-PA**, **ME-IPA**, and **ME-TPA**. Reproduced with permission from (a–e) ref. 91 (copyright 2018, American Chemical Society) and (f–h) ref. 77 (copyright 2019, WILEY-VCH).



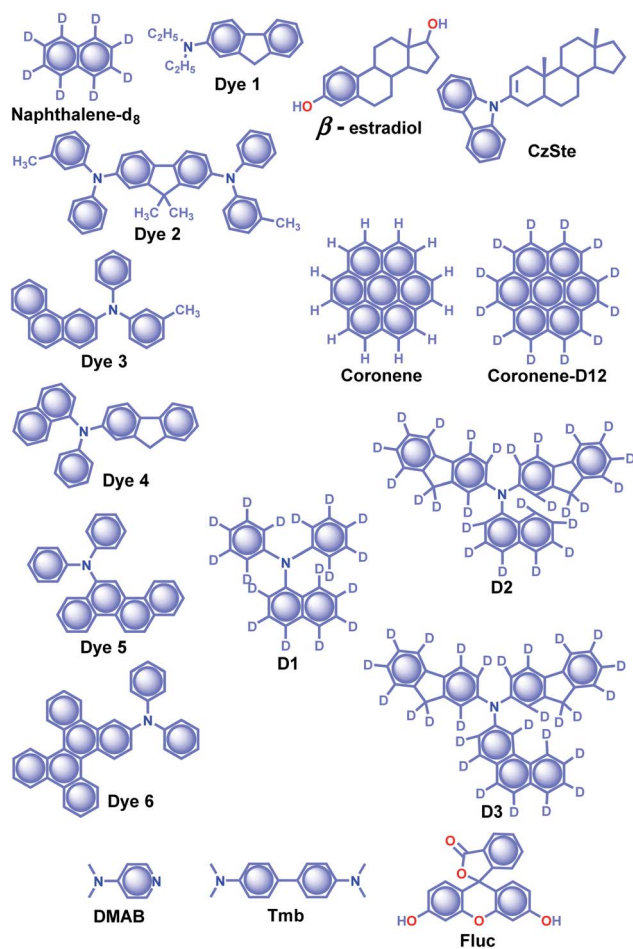
3.2 Host-guest based organic phosphors

The effective control of the host and guest units to create a wide variety of soft materials drew much attention to supramolecular chemistry. Recently, researchers have successfully achieved RTP of pure organic host-guest systems by managing various intermolecular interactions.⁹³ The host-guest interactions are highly selective because multiple factors such as size, shape, charge, polarity, *etc.* limit the host's inclusion. Therefore the selection of appropriate host and guest combinations is very critical. In general, the cavity of the host molecule specifically recognizes the guest molecule and provides a rigid environment to confine the guest molecules. The support is obtained not only from cavitands but other hosts such as small molecules and frameworks, also strongly supported phosphors. Organic host-guest based persistent RTP materials are mainly developed by minimizing k_{nr} of triplet excitons and keeping it smaller than the small k_p .⁹³ Since the fate of the triplet state is heavily dependent on nonradiative deactivation pathways of the guest and quenching by the diffusional motion of the host as well as molecular oxygen, the selection of a suitable host-guest combination remains challenging. Herein, the research

progress of ORTP systems based on host-guest interactions is reviewed.

Alfimov and coworkers achieved long-lived RTP from arene- β -cyclodextrin (β -CD) cage-hydrocarbon complexes in the presence of oxygen.⁹⁴ Among the different combinations, the complex naphthalene- d_8 - β -CD cage (Scheme 4) with various hydrocarbons showed variable RTP lifetime of 11.9 s for diadamantyl, 9.4 s for diamantine, and 10.3 s for adamantine in the presence of oxygen. However, the RTP lifetime of these complexes further increased in the absence of oxygen. The ternary complexes aggregate in water to form micro-particles, which prevent molecular motions and reduce the quenching effect from oxygen to achieve a longer lifetime. In another attempt, the same group demonstrated URTP from the supramolecular complex of naphthalene- d_8 - β -CD-cyclohexane (**I**) with a lifetime of around 16 s while the naphthalene- d_8 - β -CD-cyclohexane-benzophenone (**II**) complex showed 14.7 s.⁹⁵ More interestingly, the long lifetime of complex **II** is attributed to the triplet-triplet (T-T) ET from benzophenone (donor) to naphthalene- d_8 (acceptor).

Another work in the field of host-guest supramolecular systems was reported by Liu and coworkers using cucurbit[6]uril (**CB[6]**) as the host and a heavy-atom-free phenylmethylpyridinium as the guest (Fig. 7a).⁹⁶ The **PBC/CB[6]** complex formed by grinding showed a phosphorescence peak at 510 nm with an ultralong τ_p of 2.62 s and ϕ_p of 9.7% (Fig. 7b-d). The encapsulation in **CB[6]** promotes ISC in phenylmethylpyridinium, which in turn boosts the population of triplet excitons. Moreover, **CB[6]** provides a rigid matrix for the



Scheme 4 Chemical structure of β -estradiol, CzSte and DMAB (host) and naphthalene- d_8 , Dyes1-6, coronene, coronene- d_{12} , D1-3, and Fluc (acceptor) molecules.

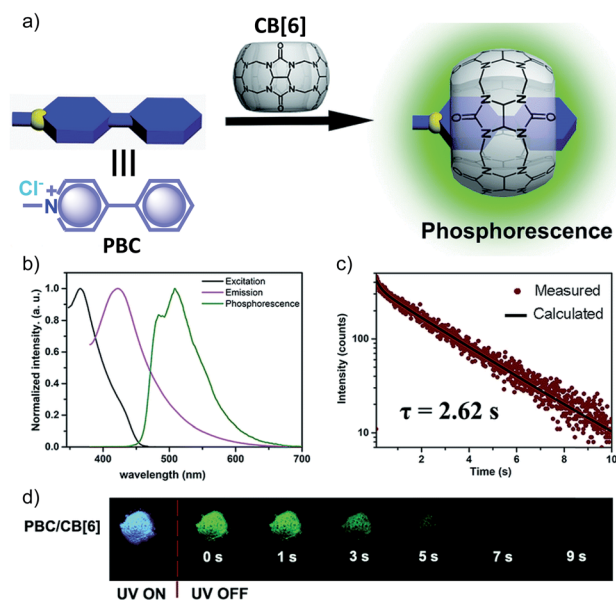


Fig. 7 (a) Schematic illustration of the solid-state supramolecular strategy of PBC and **CB[6]** for URTP. (b) Excitation, emission, and phosphorescence spectra of **PBC/CB[6]** in the solid state. (c) Phosphorescence decay of **PBC/CB[6]** at 510 nm. (d) Photographs of **PBC/CB[6]** powder under 365 nm UV irradiation and at different time intervals after removal of the ultraviolet lamp. Reproduced with permission from ref. 96. Copyright 2019, Royal Society of Chemistry.



guest molecule to suppress molecular motions such as vibrations, rotations, and inter-collisions as well as to provide protection from oxygen. Eventually, the successful **PBC/CB[6]** complex prolonged the phosphorescence lifetime. Notably, the distinct lifetime and robust phosphorescence properties of **PBC/CB[6]** enabled the triple lifetime-encoding for information encryption and anti-counterfeiting applications.

The salient features of a steroidal compound, β -estradiol (Scheme 3), such as rigidity, oxygen barrier, high T_1 energy, *etc.* motivated the research group of Adachi to use it as a host material to suppress the triplet quenching of phosphors.^{97,98} Besides, the use of a deuterated aromatic hydrocarbon as the guest minimized nonradiative deactivation. Red-green-blue persistent RTP with $\tau_p > 1$ s, $\phi_p > 10\%$ and a persistent RTP afterglow for several seconds was realized for dyes **1–6** (Scheme 4).⁹⁷ In 2016, the same group introduced a new host molecule, 3-(*N*-carbazolyl)-androst-2-ene (**CzSte**) (Scheme 4), to enhance the performance of afterglow LEDs.⁹⁸ To maximize the lifetime, the authors used coronene- d_{12} as the emitter and found a significant improvement in RTP features. The planar structure of coronene- d_{12} was found to be suitable for forming a rigid host matrix through intermolecular CH- π interactions with the steroid moiety of **CzSte**. The suppression of molecular vibration and nonradiative decay of the guest emitter resulted in an extended τ_p of 4.7 s and ϕ_p of 5.3%. Furthermore, the prepared host-guest system was found to be useful in LEDs yielding higher external quantum efficiency and longer afterglow.

Hirata and coworkers reported a new heavy atom-free organic molecular design consisting of a secondary amine as an RTP antenna substituted with different RTP centers **D1–3** (Scheme 4) having smaller T_1 energy, exhibiting persistent RTP (Scheme 4).⁹⁹ The notable feature of the molecular design is the steric hindrance introduced between the RTP antenna and the RTP center that decreases k_f and enables efficient ϕ_{isc} . The authors cleverly extended the conjugation of the RTP antenna in anticipation of obtaining $k_p > k_{nr}$. To validate the design strategy, RTP candidates (0.3 wt%) were dispersed in a β -estradiol host and a persistent emission was observed from 470 to 800 nm. The ϕ_p and τ_p of the host-guest systems varied as 11, 50, and 46%, and 1.60, 1.00, and 1.40 s for **D1**, **D2**, and **D3**, respectively.

Recently, a thermoresponsive RTP has been reported by taking advantage of ET and intermolecular CT between *N,N*-dimethylpyridin-4-amine **DMAP** (host) and *N,N,N',N'*-tetramethylbenzidine **Tmb** (guest) (Scheme 4).¹⁰⁰ The cocrystals of **DMAP** and **Tmb** with a mass ratio of 400 : 1 displayed blue RTP emission with τ_p and ϕ_p up to 2.1 s and 13.4%, respectively. In addition, the authors studied the concentration-dependent emission changes by incorporating an additional energy acceptor, fluorescein **Fluc** (Scheme 4), to form a ternary blend. Upon changing the concentration of **Fluc**, a colour-tunable afterglow from blue to yellow was realized. More interestingly, on heating, both **DMAP–Tmb** and **DMAP–Tmb–Fluc** exhibited turn-on RTP with increasing RTP lifetime from 1.4 s to 1.97 s. Here the enhanced intermolecular interactions in **DMAP–Tmb** and **DMAP–Tmb–Fluc** played a significant role in enhancing the phosphorescence lifetime. Furthermore, the thermoresponsive

nature of the host-guest RTP materials has been used for multi-colour thermal printing.

Metal-organic frameworks (MOFs) are capable of encapsulating guest species in their cavities, and the guest confinement can deliver a significant improvement in RTP. Along these lines, Kabe, Adachi, and coworkers demonstrated a long-lived emission from triplet excitons achieved by encapsulating coronene in a zeolitic imidazolate framework (ZIF-8) host.¹⁰¹ It is confirmed that the coronene wholly isolated within the pores of the MOF suppresses the nonradiative decay and molecular vibrations, enabling long-lived RTP. Coronene@ZIF-8 exhibited τ_p of 7.4 s, while an extended lifetime of 22.4 s was achieved for coronene- d_{12} @ZIF-8 under the same experimental conditions. The vibrational energy of the C–D stretching mode is lower than that of the C–H stretching mode, and hence it helps coronene- d_{12} @ZIF-8 to show enhanced lifetime. Moreover, the temperature-dependent lifetime measurement confirmed the suppression of nonradiative deactivation of coronene.

In 2017, Yan and coworkers explored a phosphorescence ET by incorporating donor and acceptor guest molecules in the interlayer nanogallery of an inorganic graphene-like layered double hydroxide (LDH) host material (Fig. 8).¹⁰² The authors used different benzene dicarboxylic acid isomers, namely **IPA** (Scheme 2), **TPA**, and **PA** (Fig. 6a), as potential donors assembled into the interlayer of the Zn–Al-LDH host by the coprecipitation method. Interestingly, among the nanohybrids, the **IPA/LDH** showed a green phosphorescence emission with the longest τ_p up to 1.2 s and ϕ_p of 3.02% (Fig. 8b–d). An H-type aggregation between **IPA** dimers and LDH nanosheets

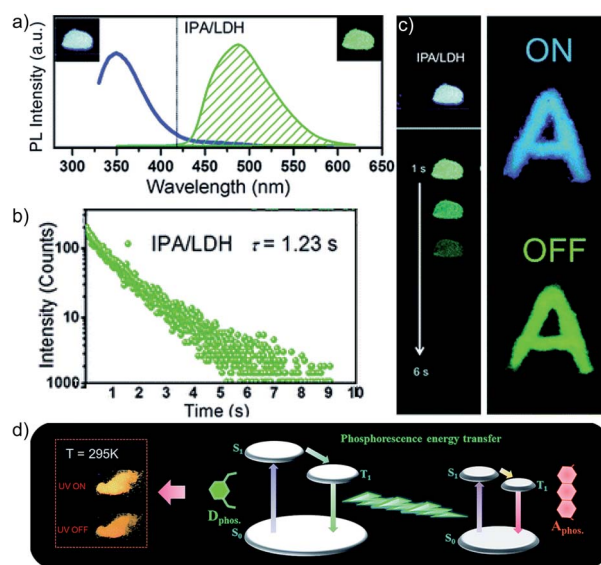
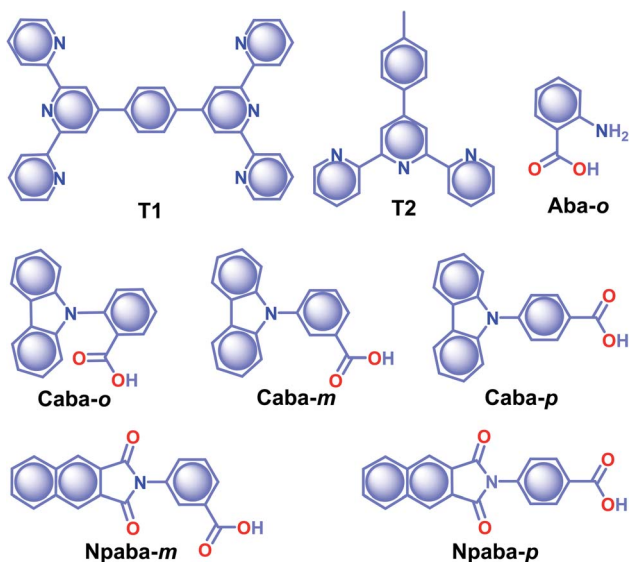


Fig. 8 (a) Steady-state emission (left) and phosphorescence (right) spectra of IPA/LDH nanohybrids (insets show the corresponding photographs). (b) Phosphorescence decay profile of IPA/LDH ($\lambda_{mon} = 489$ nm, $\lambda_{ex} = 320$ nm). (c) The letter 'A' made with IPA/LDH can be unmistakably identified by the naked eye after the excitation is switched off. (d) Schematic representation of the proposed mechanism for PET. Reproduced with permission from ref. 102. Copyright 2017, Royal Society of Chemistry.



stabilized the lowest triplet excited state and minimized the nonradiative decay to prolong the RTP lifetime. Besides, IPA/LDH showed thermoresponsive RTP upon varying the temperature from 295 to 335 K. Subsequently, the co-intercalation of eosin Y as an energy acceptor with the IPA energy donor into the nanogalleries of LDH nanosheets imparted excellent triplet-triplet ET ($E_p = 99.7\%$) (Fig. 8e).

Co-assembly of RTP inactive terpyridine-derivatives **T1** and **T2** (Scheme 5) with LAPONITE® (LP) nanoclay through solvent-free mechanical grinding significantly enhanced the RTP to exhibit green (**T1@LP**) and blue-green (**T2@LP**) emissions.¹⁰³ The long RTP lifetime decay component of both the hybrid materials was around 1.1 s with a strong afterglow lasting for more than 10 seconds. The encapsulation of the emitters in LP helped to achieve ϕ_p of 2.96 and 1.86% for **T1@LP** and **T2@LP**, respectively. A transformation from *trans-trans* to *cis-trans* configuration of **T1** upon protonation has led to a marginal increase in spatial separation of the HOMO and LUMO and eventually narrowed down ΔE_{ST} to facilitate ISC. Moreover, the hydrogen bonding between **T1** and LP reduces the nonradiative decay and protects the triplet excitons. Zhang and coworkers came up with a hybrid material by encapsulating various RTPs (**Aba-o**, **Npaba-m**, **Npaba-p**, **Caba-o**, **Caba-m**, and **Caba-p**) in $[\text{Al}(\text{DMSO})_6]\text{X}_3$, where X is Cl^- or Br^- (Scheme 5).¹⁰⁴ The new approach resulted in a very high RTP lifetime and luminescence quantum yield. The heavy atom effect has a profound impact in this series: as compared to Cl^- hybrids, the analogues with Br^- yield high ϕ_p and a shortened τ_p . The values of τ_p and ϕ_p varied for **Aba-o/Cl** (1.1 s, 2.3%), **Npaba-m/Cl** (1.12 s, 3.9%), **Npaba-p/Cl** (1.26 s, 4.8%), **Caba-o/Cl** (1.81 s, 4.9%), **Caba-m/Cl** (1.84 s, 8.4%) and **Caba-p/Cl** (1.89 s, 2.5%). The presence of many different types of weak interaction between the matrix and RTPs greatly supports RTP by suppressing nonradiative decay.



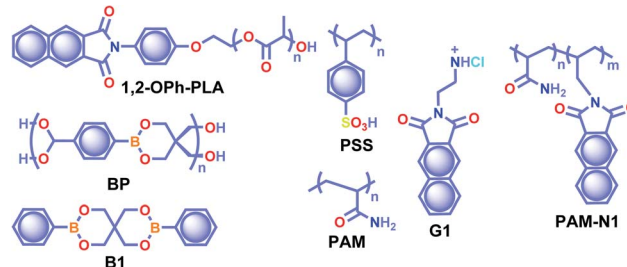
Scheme 5 Chemical structure of **T1**, **T2**, **Aba-o**, **Caba-o**, **Caba-m**, **Caba-p**, **Npaba-m**, and **Npaba-p**.

3.3 Polymer-based organic phosphors

The crystalline URTP materials have drawbacks in terms of reproducibility, processability, and flexibility, which significantly impedes the development of crystalline URTP materials for practical applications.¹⁰⁵ To overcome these fundamental barriers, special attention has been paid to the development of organic polymeric materials capable of URTP. Recently, significant breakthroughs have been achieved by prolonging the lifetime of polymeric materials through homopolymerization, ring-opening polymerization, covalent cross-linking reaction, and radical binary copolymerization, as well as embedding small molecules into a rigid polymer matrix.¹⁰⁵ Polymer-based RTP materials have been receiving increased attention because of the large molecular weight of the polymer and the availability of functional group chains that can help to rigidify the molecular vibrational and rotational motions of the phosphors. Moreover, it can reduce the quenching effects of oxygen and moisture from the ambient environment, allowing the triplet excitons to survive long enough to achieve prolonged lifetimes. More importantly, polymer-based RTPs exhibit easy processability, excellent flexibility, and high thermal stability as well.

In 2016, Chen *et al.* applied the intramolecular CT (ICT) state of *N*-substituted naphthalimide poly(lactic acid)-based polymers to obtain RTP enhancement.⁴⁰ It has been noticed that either the ICT state or a heavy atom (Cl or Br) can ensure enhanced ISC and thus strong RTP. In this series, polymer **1,2-Oph-OLA** (Scheme 6) showed strong ICT and a favourable ΔE_{ST} to support RTP. The existence of an ICT state acted as a bridge between the excited singlet and triplet states and thus accelerated ISC leading to τ_p of 1.12 s. Additionally, *N*-substituted naphthalimides conjugated with natural biomacromolecules such as chitosan and bovine serum albumin also displayed RTP and found useful application in time-resolved bioimaging.

Ogoshi and coworkers reported URTP with a lifetime up to 1.22 s for poly(styrene sulfonic acid) **PSS** in the dry solid-state (Scheme 6).¹⁰⁶ The observed lifetime is one of the most extended RTP lifetimes for non-doped ORTP polymers. The sulfonic acid group in the polymer can form strong inter/intrachain hydrogen bonds in the solid-state that reduce the nonradiative decay and eventually lead to ultralong RTP. The RTP lifetime depends on the introduction ratio of sulfonic acid groups. As the ratio is increased, the phosphorescence lifetime



Scheme 6 Chemical structure of polymers **1,2-Oph-PLA**, **BP**, **PSS**, **PAM**, **G1**, and **PAM-N1**, and model derivative **B1**.



became longer due to strong hydrogen bond formation between sulfonic acid groups. Furthermore, the reversible RTP *via* uptake and removal of water contributed to the lifetime-encoding application. Detailed studies revealed that deuteration of SO₃H and exchanging SO₃Na or SO₃K for SO₃H resulted in an increased RTP lifetime. In contrast, a decrease in RTP lifetime was noticed when PSS was neutralized with NaOH or KOH.

Cai *et al.* demonstrated that the ionic cross-linking between chromophores is critically supportive in suppressing non-radiative transitions for URTP, and by utilizing the concept, a lifetime of 2.1 s for an amorphous polymer is obtained.¹⁰⁷ The replacement of PSS with different ions such as Li⁺, K⁺, Rb⁺, NH⁴⁺, Mg²⁺, Ca²⁺, Al²⁺, and Gd²⁺ imparted a significant effect on the URTP of polymers. The size of the ionic radius is found to control the RTP features, and as the size increases, the URTP lifetime also gradually decreases. The replacement with Li⁺ and Mg²⁺ resulted in a lifetime of 1.3 and 1.1 s, respectively, and thereafter a gradual decrease in the lifetime is observed. It has been concluded that even though the large ionic radius prevents the prolonged URTP, the high ion charge state is found to be supportive. Hence a balance between the ionic radius and charge state can significantly alter the lifetime values. Here the k_{nr} is at least one order of magnitude higher than k_p , indicating that the former one played a dominant role in manipulating the URTP of ionic polymer phosphors. The results of ionic cross-linking assisted URTP have even been extended to nonaromatic ionic polymers and it was found that **PAANa** (Scheme 6) with blue URTP has τ_p of 1.4 ms and 2.1 s, respectively, when monitored at 450 nm and 480 nm bands.

Recently, boronic acid/ester-based organic phosphors also excelled as strong RTP candidates. Along these lines, Kubo and coworkers reported boronate particles **BP** (Scheme 6) as a self-assembled URTP system in both solid state and dispersion in water.¹⁰⁸ Solid **BP** showed phosphorescence peaks located between 450 and 550 nm with a long-lived τ_p of 1.95 s and ϕ_p of 5% under ambient conditions. The RTP properties of **BP** were compared with a model derivative, 3,9-dibenzo-2,4,8,10-tetraoxa-3,9-diborospiro[5.5]undecane **B1** (Scheme 6). Theoretical calculation and the crystal structure of **B1** suggest that boron-containing CT interactions and the presence of intermolecular electron coupling facilitate RTP. Notably, grafting rhodamine B fluorophores on the surface enabled the ET process from the triplet excited state of **BP** to the singlet state of the fluorophore resulting in an afterglow composed of dual luminescence at ~500 and 600 nm.

In 2020, Ling and coworkers reported a colourful afterglow through regulation of clusterization-triggered RTP of non-conjugated amorphous polyacrylamide (**PAM**).¹⁰⁹ The emission features of these non-conjugated polymers containing carbonyl and amine groups depend on the aggregation, which can result in electronic interactions by n- π and π - π interactions. Furthermore, the clusterization of amides can form a rigid conformation of polymer chains, which is helpful to inhibit nonradiative decay of excitons and to stabilize the excited state through hydrogen bonding. When PAM was blended with naphthalimide **G1** (Scheme 6), URTP with τ_p up to 1.7 s and ϕ_p

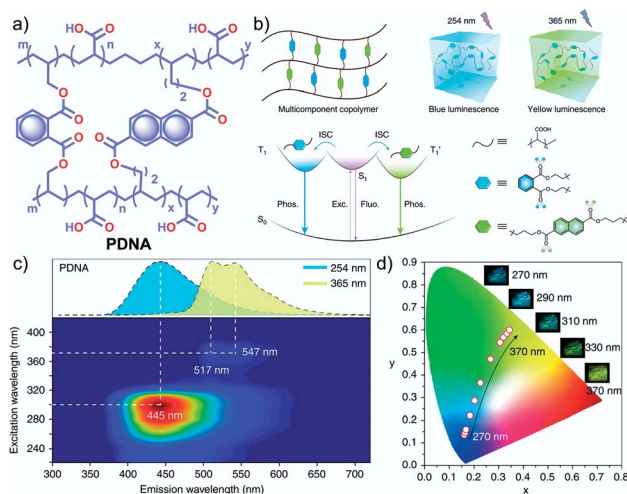


Fig. 9 (a) Chemical structure of PDNA. (b) Schematic illustration of the proposed mechanism of colour-tunable URTP of PDNA. (c) Excitation-phosphorescence mapping of PDNA under ambient conditions; the inset displays the phosphorescence spectra excited at 254 nm (blue) and 365 nm (yellow). (d) CIE chromaticity diagram for PDNA with excitation varied from 270 to 370 nm; the inset shows the UOP photographs of PDNA excited at various wavelengths. Reproduced with permission from ref. 110. Copyright 2020, Springer Nature Limited.

of 13.4% was observed in solid powders. Computational studies revealed the possibility of a clusterization-triggered phosphorescence mechanism. When naphthalimide was covalently linked with the PAMs, **PAM-N1** (Scheme 6) exhibited a visible-light-excited URTP with τ_p of 1.5 s and ϕ_p of 12%.

In 2020, Gu *et al.* discovered a colour-tunable URTP in polymers through multi-component cross-linked polymerization by using acrylic acid and multiple luminophores.¹¹⁰ A copolymer, **PDNA** (Fig. 9a), prepared using vinyl derivatives of naphthalene (MND) and benzene (MDP), and acrylic acid (MND/MDP/AA ratio 1/200/10 000) displayed an excitation dependent multi-colour RTP emission spanning from blue to yellow with a long-lived τ_p of 1.1 s and ϕ_p of 23.2% (Fig. 9b-d). As the ratio of MND/MDP/AA varied, the phosphorescence intensity gradually decreased. Two other polymers with varying ratios of MND/MDP/AA, namely **PDNA-5** (1/5/1000) and **PDNA-10** (1/10/1000), also exhibited excellent RTP features with τ_p of 1.22 and 1.07 s and ϕ_p of 13 and 37.5%, respectively. The excitation spectra of **PDNA** revealed that the blue and yellow emission bands originate from two entirely different excited triplet states of benzene and naphthalene components in the polymer and this is confirmed by the detailed analysis of the individual polymers. The numerous carbonyl and hydroxyl groups of **PDNA** assist in forming inter- or intramolecular hydrogen bonds with polyacrylic acid chains. Thus the eventually created rigid environment suppressed the nonradiative decay of the excited state and prevented the quenching of triplet excitons. The hydrogen bonding assisted RTP in **PDNA** was revealed by a significant decrease in RTP features in the presence of moisture, which breaks the hydrogen bonds between the polymer chains. The overall tunable emission URTP achieved by **PDNA** is demonstrated in Fig. 9d.



3.4 Polymer supported organic phosphors

Apart from incorporating the functional phosphors as a part of the polymer backbones, polymer-supported phosphors also found URTP active. In 2019, Zhao and coworkers achieved URTP from **2-HC** (Fig. 10a) by coassembling with polyvinyl alcohol (**PVA**).¹¹¹ The confinement of **2-HC** in **PVA** restricts the molecular motions to stabilize the triplet state and thereby generate URTP ($\tau_p = 1.21$ s and $\phi_p = 16\%$) with an afterglow lasting for more than four seconds in the dark. The same group demonstrated the excitation-dependent persistent emission by constructing multiple emission centers in polymeric systems with hydrogen bonding.¹¹² A polyphosphazene derivative, **P4**, containing carbazole unit **4-HC** was synthesized and mixed with **PVA** to develop a composite, **PVA-100-P4-1** (Fig. 10a). As shown in Fig. 10b, an excitation wavelength-dependent (340 to 370 nm) redshift of phosphorescence (468 to 522 nm) was observed for **PVA-100-P4-1**. The afterglow of **PVA-100-P4-1** persisted for 12 s, and the corresponding τ_p reached 1.29 s with ϕ_p of 1.0% (Fig. 10c). The presence of strong hydrogen bonding between the polyphosphazene polymer chains and PVA plays a critical role in the afterglow. The k_{nr} for the **PVA-100-P4-1** film has significantly come down to 0.77 s⁻¹ as compared with that of the **PVA-100-4HC-1** precursor film (2.59 s⁻¹). An excitation wavelength-dependent persistent luminescence colour from blue to green indicates the presence of multiple radiation channels in the system (Fig. 10d). Even though the monomer **2-HC-PVA** composite exhibited a longer lifetime, the corresponding polymer **PVA-100-P2-1** failed to extend the lifetime.

Recently, George and coworkers reported a delayed sensitization assisted triplet to singlet ET in polymer-supported D-A

pairs.¹¹³ The authors used a **PVA** matrix to host coronene tetracarboxylate salt **CS** as a triplet energy donor and fluorescent dyes sulpharhodamine101 **SR101** and sulpharhodamine G **SRG** as acceptors to demonstrate PET (Fig. 11a). Since both the donor and acceptors are water-soluble dyes having polar side-groups, it facilitates co-assembly with **PVA** *via* ion-dipole and hydrogen bonding interactions. The **CS-PVA** hybrid showed a phosphorescence band in the range of 500 to 700 nm with an average ultralong τ_p of 2.46 s with ϕ_p of 23.4% (Fig. 11b and c). The emission spectra of **SR101/SRG** doped **CS-PVA** films showed a gradual decrease of **CS** phosphorescence emission

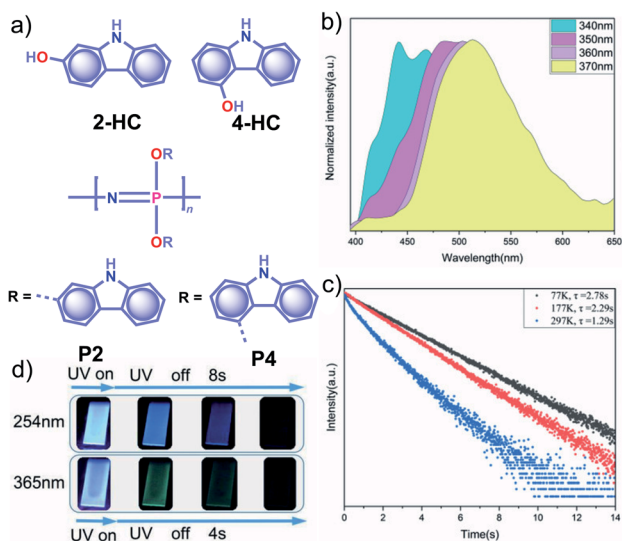


Fig. 10 (a) Chemical structure of monomers **2-HC** and **4-HC**, and polymers **P2** and **P4**. (b) Excitation wavelength-dependent phosphorescence spectra and (c) temperature-dependent phosphorescence decay curves of **PVA-100-P4-1** film. (d) Photographs of persistent luminescence of **PVA-100-P4-1** film under ambient conditions. Reproduced with permission from ref. 112. Copyright 2020, WILEY-VCH.

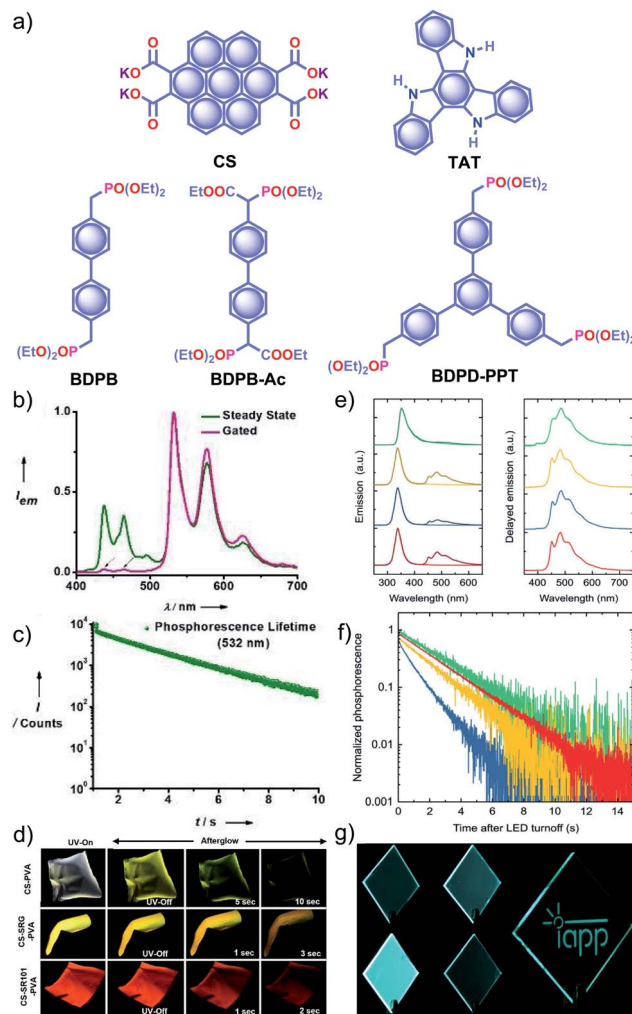


Fig. 11 (a) Chemical structure of **CS**, **TAT**, and aromatic phosphonates **BDPB**, **BDPB-Ac**, and **BDPD-PPT**. (b) Steady-state and gated emission spectra and (c) phosphorescence decay profile of **CS-PVA** film. (d) Photographs of **SRG/SR101** doped **CS-PVA** hybrid films showing ambient afterglow properties. (e) Emission spectra of aromatic phosphonates under an aerated (light colour) and a nitrogen atmosphere (dark colour) (left), and delayed spectra showing RTP in an Exceval, aerated atmosphere (right) along with the corresponding (f) phosphorescence decays. (g) Photographs of **BDPB-Ac**, **BDPB**, and **BDPD-PPT** in Exceval, and delayed phosphorescent image written by masked UV illumination in a **PMMA:BDPB** sample covered with Exceval. Reproduced with permission from (a–d) ref. 113 and (e–g) ref. 115. Copyright 2020, WILEY-VCH.

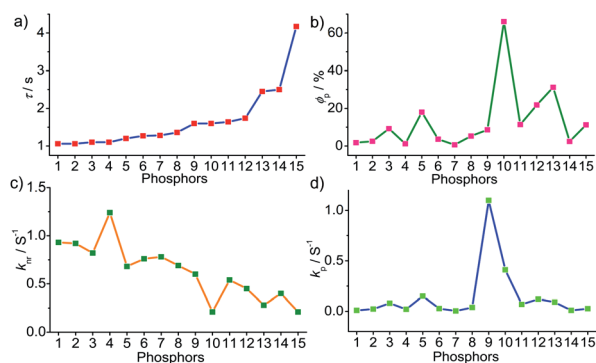


with an enhancement of acceptor emission in the 550–700 nm region due to ET from the triplet state of a donor to the singlet state of the acceptors. The hybrid thin films are self-standing and flexible with stable afterglow features (Fig. 11d). The same group reported deep blue URTP from triazatruxene TAT (Fig. 11a) with an average τ_p of 2.26 s and ϕ_p of 17.5% in a PVA matrix.¹¹⁴ The deep-blue emission of TAT–PVA hybrid films persisted over 10 s, pointing to the RTP from the spatially isolated TAT in the PVA matrix, supported by strong hydrogen-bonding interaction between TAT and PVA. Interestingly, a mixed RTP hybrid of CS–TAT–PVA exhibited excitation-dependent multi-colour afterglow emission, including an ambient white afterglow with the CIE coordinates (0.29, 0.33).

With the understanding of ORTP of amorphous polymer materials, Reineke and coworkers reported a new family of halogen-free organic luminescent derivatives called aromatic phosphonates (Fig. 11a).¹¹⁵ A series of aromatic phosphonates 4,4'-bis(diethylphosphonomethyl)biphenyl BDPB and its derivatives BDPB-Ac and BDPD-PPT were embedded in a polymethyl methacrylate (PMMA) host matrix and covered with Exceval to prepare a hybrid RTP system (Fig. 11e–g). The presence of PMMA and Exceval ensures hydrogen bonding to rigidify the matrix, acts as an oxygen barrier layer, and efficiently suppresses vibrational dissipation to achieve bright long-lived RTP. In the PMMA matrix, when excited at 300 nm, τ_p varied as 1.7 s (BDPB-Ac), 1.8 s (BDPB), and 2.1 s (BDPD-PPT) and further varied as 2.0 s, 2.4 s, and 2.6 s, respectively, when excited at 275 nm (Fig. 11f). Furthermore, RTP of the aromatic phosphonates revealed that the main reason for the long lifetimes is the diethyl-phosphonomethyl units. Interestingly, the lifetime is increased by around 250 ms upon an increase from two to three phosphonate groups.

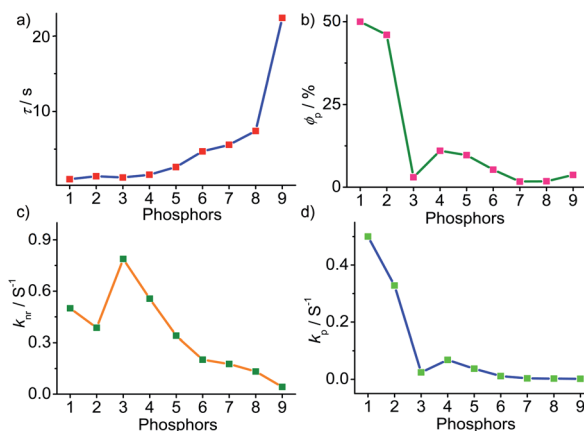
4. Comparative study

To obtain a deeper understanding of the decay pathways, their trends, and their effect on τ_p and ϕ_p , single-component organic phosphors have been selected for detailed analysis (Fig. 12).



Phosphors: 1. DPhCzT, 2. 24CPhCz, 3. PMA, 4. CzPyF, 5. PB, 6. MDHA, 7. ECzT, 8. IPA, 9. AN-MN, 10. PDBEG, 11. OMR-h, 12. HA, 13. DMOT, 14. 24FPB, 15. PCz

Fig. 12 Analysis of (a) τ_p , (b) ϕ_p , (c) k_{nr} and (d) k_p of single-component organic phosphors.



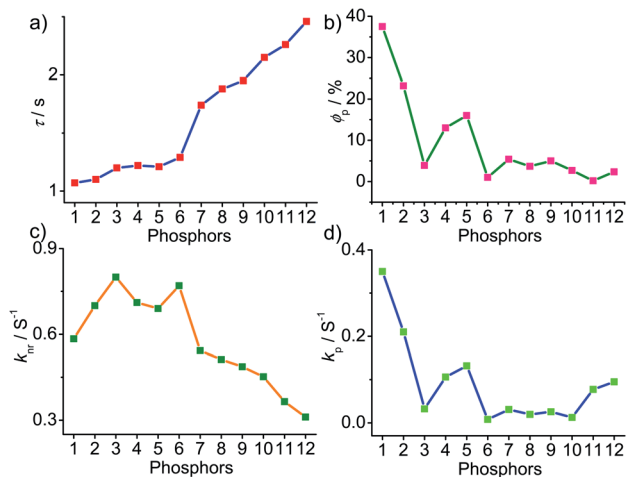
Phosphors: 1. D4, 2. D5, 3. IPA/LDH, 4. D3, 5. PBC/CB[6], 6. Coronene-d₁₂-CzSte, 7. Coronene in PMMA, 8. Coronene@ZIF-8, 9. Coronene-d₁₂@ZIF-8

Fig. 13 Analysis of (a) τ_p , (b) ϕ_p , (c) k_{nr} and (d) k_p of host-guest based phosphors.

However, a few cases with incomplete data are omitted for clarity of the discussion. A comparison made by arranging in the ascending order of lifetimes showed that a variation in τ_p is mostly reflected in k_{nr} than k_p , and this might be due to the significant contribution by k_{nr} in this particular class of molecules (Fig. 12a and c). A detailed analysis indicates that there exists a correlation between τ_p and k_{nr} , as well as ϕ_p and k_p . Compared with the increasing value of τ_p , k_p irregularly varied between 0.01 and 0.15 s⁻¹, while k_{nr} varied inversely as 1.24 to 0.21 s⁻¹, with a few exceptions, in this series. This magnitude difference of k_{nr} and k_p imparts an upper hand for k_{nr} over k_p on lifetime values (Fig. 12c and d). Even though for single component phosphors $k_{nr} > k_p$, the value of ϕ_p varied almost in line with k_p (Fig. 12b and d). We consider this discussion as a qualitative one due to the inconsistencies in sample preparation, quality of crystals, measuring conditions, reproducibility, and so on. Hence, a detailed study is highly required to reveal the underlying details of RTP to go further.

A comparison of the decay pathways connected with τ_p and ϕ_p showed that the variations in decay parameters of the host-guest systems are in line with the expected trend (Fig. 13). The analysis indicates that except for a few cases, the variation of lifetime is reflected on both k_{nr} and k_p (Fig. 13a, c and d). In this series, the value of k_{nr} varies between 0.79 and 0.04 s⁻¹, while k_p gradually decreased from 0.5 to 0.002 s⁻¹ (Fig. 13c and d). However, a longer lifetime is achieved by lowering both k_{nr} and k_p . The presence of the hosts is found supportive to enhance RTP lifetimes. Moreover, the values of both k_{nr} and k_p are observed to be almost in the same range. It has to be noticed that irrespective of the host-guest systems considered, a clear trend is reflected in the value of k_p and ϕ_p (Fig. 13b and d). Compared to single-component organic phosphors, the magnitude difference between k_{nr} and k_p is narrow, and therefore, we can assume that the suppression of k_{nr} is efficient in the host-guest based RTP systems due to the rigidification of the confined phosphors.





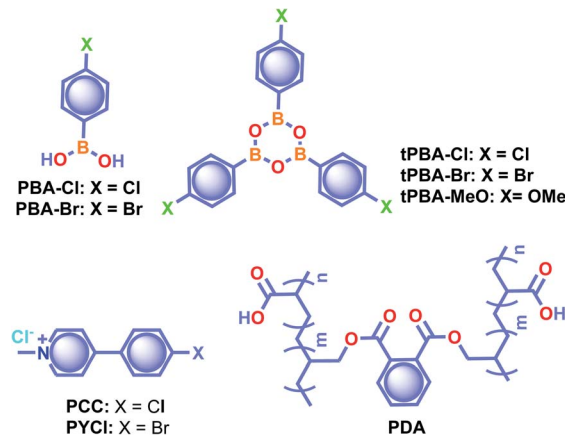
Phosphors: 1. PDNA-10, 2. PDNA, 3. 1,2-Oph-PLA, 4. PDNA-5, 5. 2-HC in PVA, 6. PVA-100-P4-1, 7. BDPB-Ac, 8. BDPB, 9. BP, 10. BDPD-PPT, 11. TAT, 12. CS

Fig. 14 Analysis of (a) τ_p , (b) ϕ_p , (c) k_{nr} and (d) k_p of polymer and polymer-supported phosphors.

In the case of polymer related systems, a reasonable correlation between τ_p and ϕ_p is visible (Fig. 14a and b). As the τ_p is increased from 1 to 2.46 s, an almost steady decrease in ϕ_p from 37.5 to 2.34% is noticed (Fig. 14a and b). Similar to host-guest systems, the comparison of the decay parameters with τ_p and ϕ_p indicates a direct link between τ_p and decay rates k_{nr} and k_p (Fig. 14). The variation of the lifetime is reflected in the values of both k_{nr} and k_p , which decreased from 0.8 to 0.3 s^{-1} and 0.35 to 0.01 s^{-1} , respectively (Fig. 14a, c and d). In polymer and polymer-supported systems, the distinct difference in the magnitude of k_{nr} and k_p is visible. Even though $k_{nr} > k_p$, long lifetimes for polymer-based phosphors have been achieved by lowering the values of both k_{nr} and k_p . Interestingly, a similar trend noticed for ϕ_p and k_p points to the dependence of ϕ_p more on k_p than k_{nr} (Fig. 14b and d). The comparison of three different classes of organic phosphors, crystalline assemblies of single molecules, host-guest, and polymer-based systems revealed that compared to other phosphors, hosts provide a strong support to the guest phosphors and reduce k_{nr} as close to k_p as possible. It indicates the need for newer designs to minimize k_{nr} values to improve the efficiency of organic phosphors. A meaningful conclusion on the various parameters influencing both ϕ_p and τ_p can be generated only by comparing the SOC and k_{isc} values of the phosphors along with k_p and k_{nr} . However, the lack of data in the literature reports prevented us from having such a detailed discussion.

5. Applications

As mentioned in the introduction, the sudden developments of URTPs in recent years have engaged them in various potential applications, including organic electronics, optical recording, anti-counterfeiting, bioimaging, and sensing.^{116–121} Since many reviews have already summarized the applications of various ORTPs,^{21–25,59,80–85} we discuss only the recent developments of



Scheme 7 Chemical structure of the supporting phosphors used for various applications.

very efficient ORTPs. Li and coworkers utilized the strong interactions of aryl boronic acids *via* hydrogen bonds to develop an inkjet printing technology suitable for optoelectronic displays.⁴¹ The comparable intensities of the RTP crystals and samples from solvent evaporation enabled the use of the aryl boronic acid-derived phosphors as a low-cost ink. The fluorescence colour and intensity difference associated with the thermally formed boroxines **tPBA-MeO**, **tPBA-Cl**, and **tPBA-Br** (Scheme 7) from different monomer phosphors **PBA-MeO** (Scheme 2), **PBA-Cl**, and **PBA-Br** (Scheme 7) helped to make distinguishable RTP patterns (Fig. 15a). As a significant advantage, the brightness of the inkjet-printed designs can be improved by cyclic printing (Fig. 15b). The scalable synthesis of phosphors, stability, accuracy, and reproducibility of the images point to an impressive printing process. Besides, **PBA-MeO** exhibited less toxicity when fed to *Bombyxmori* silkworms, making it a potential candidate for biological applications. The excitation-dependent UOP feature of the phosphors has been used for multicolor display applications.⁸⁷ By using **TMOT** and **DCICzT** powders as solid ink for silk-screen printing, different patterns, including a peace dove, panda, Cp rings, and butterfly, were fabricated (Fig. 15c). Since **TMOT** is excitation-dependent UOP active, a change in the excitation wavelength from 254 to 365 nm resulted in a drastic emission color difference (Fig. 15d). The change in the phosphorescence color from sky-blue to green demonstrates as a tool for the detection of UV light.

An encryption algorithm having three different modes of operation has been used to develop information safety applications using URTP materials.⁷⁷ As shown in Fig. 15e, different modes “a”, “b”, and “c” were encrypted by using **ME-IPA**, **MA** and **IPA** (Scheme 2), respectively, and the encryption algorithm enables the real information to be hidden. Besides, the URTP of **MA-IPA** was effectively used to prove personal identity through fingerprints. An inkpad prepared using **MA-IPA** with polyacrylic acid was used to develop the fingerprint on paper (Fig. 15f). Similarly, a 2-dimensional barcode pattern was created by screen-printing the supramolecular framework of **MA-IPA** on



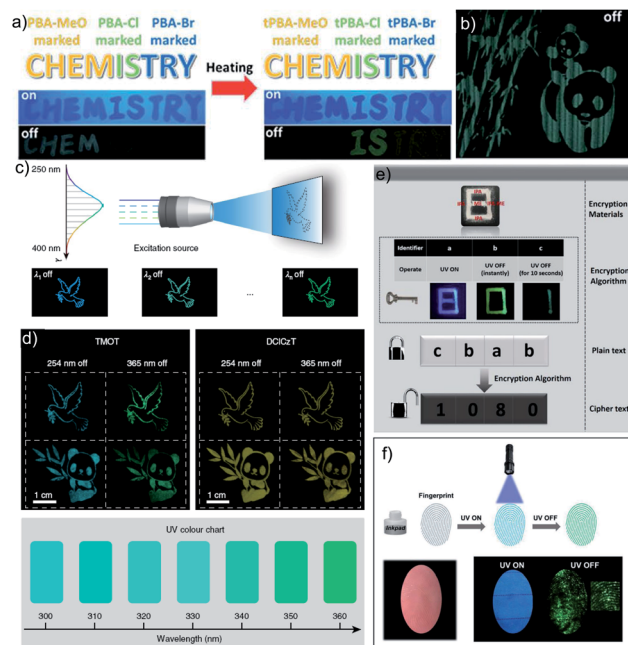


Fig. 15 (a) Demonstration of security documents with tPBA-MeO, tPBA-Cl and tPBA-Br before and after heating. (b) A pattern of panda printed with PBA-MeO for 8 cycles after stopping excitation. (c) The UOP photographs of peace dove and panda patterns, recorded with the TMOT (left) and DCICzT (right) as the ink. (d) UV colour chart showing the ability of TMOT crystalline powder to visually detect specific wavelengths in the UV region. The schematic diagram of (e) encryption to decryption and (f) back-free fingerprint identification with a special inkpad under UV excitation and after stopping UV excitation using IPA, MA and IPA-MA. Reproduced with permission from (a and b) ref. 41 (copyright 2017, Royal Society of Chemistry), (c and d) ref. 87 (copyright 2019, Springer Nature Limited) and (e and f) ref. 77 (copyright 2019, WILEY-VCH).

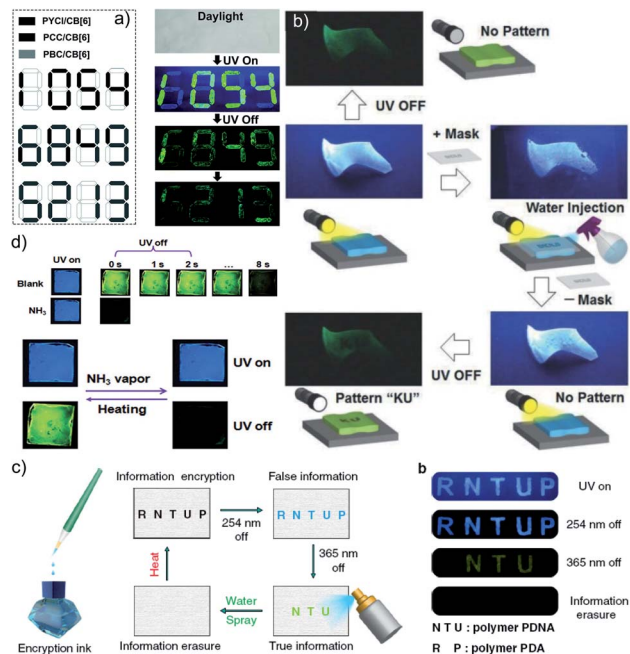


Fig. 16 Lifetime-encoding for security applications using (a) PYCI/CB[6], PCC/CB[6] and PBC/CB[6], and (b) PSS. (c) Process of information encryption by using the multi-component copolymer PDNA (NTU) and PDA (RP) as encryption ink and long-lived luminescence photographs of letters (RNTUP and NTU) before and after switching off the UV light of 254 and 365 nm. (d) Photographs of PAM-N1 films in NH₃ vapors, taken under 365 nm UV light, and after turning off the UV light and afterglow switching based on PAM-N1 films obtained by stimuli of NH₃ vapour and heating. Reproduced with permission from (a) ref. 96 (copyright 2019, Royal Society of Chemistry), (b) ref. 106 (copyright 2018, WILEY-VCH), (c) ref. 110 (Springer Nature Limited) and (d) ref. 109 (copyright 2020, Royal Society of Chemistry).

filter paper.⁹¹ The blue-green URTP of MA-IPA enabled the information to be identified by scanning the barcode in darkness. Similarly, the distinctly different lifetime, quantum yield, and robust RTP features of PBC/CB[6], PCC/CB[6] (Fig. 8a), and PYCI/CB[6] (Scheme 7) complexes were used for triple encoding (Fig. 16a).⁹⁶ The initial colourless pattern turned into a bright green display after excitation at 365 nm due to the high quantum yield of PYCI/CB[6]. Interestingly, the difference in lifetime enabled sequential phosphorescence displays of PYCI/CB[6], PCC/CB[6], and PBC/CB[6].

URTP of amorphous PSS (Scheme 4) and its on/off switching by water vapour has been used for lifetime-encoding application (Fig. 16b).¹⁰⁶ The green RTP emission of PSS film can be masked by making patterns using water. Since the fluorescence remains intact, no change is observed under UV light, even in the presence of water. However, the pattern "KU" created by the water is not anymore RTP active and can be observed by the naked eye. The reversibility of the water-induced patterns increases the applicability of this method. The excitation-dependent URTP has been used for multilevel information encryption using polymers PDA (Scheme 7) and PDNA (Fig. 11a).¹¹⁰ As shown in Fig. 16c, the patterns NTU and RP in the encrypted information

"RNTUP" were fabricated using the polymers PDNA and PDA, respectively, as inks. The initial blue emission under 254 nm irradiation was changed to long-lived blue luminescence to show the false information upon turning off the excitation source. However, after excitation with 365 nm UV light, the correct information of "NTU" was visualized as long-lived yellow emission. Interestingly, the reversibility of encryption has been achieved by erasure using water and regain by thermal treatment. Similarly, the difference in persistent luminescence intensity of PVA-100-2HC-1 and PVA-100-P4-1 (Fig. 12a) inks has also been used for anti-counterfeiting applications.¹¹²

In another attempt, the excellent afterglow properties of PAM-N1 (Scheme 6) films were found to be advantageous for the detection of volatile solvent vapors (Fig. 16d).¹⁰⁹ The strong URTP and green afterglow disappeared in the presence of vapours, and at the same time, NH₃ imparted a drastic emission quenching. The afterglow restoration achieved by thermal removal of NH₃ ensures an afterglow switch using NH₃ vapour and temperature. Moreover, the security ink developed using PAM-N1 was found useful for anti-counterfeiting applications. The flexible and transparent films T1@LP and T2@LP in PVA have been used for relative-humidity sensing and information encryption.¹⁰³ The remarkable RTP characteristics of the hybrid



materials generated from aromatic-acid and Al-DMSO matrices have benefited data encryption and decryption applications through allochroic response recognition and optical logic gates.¹⁰⁴

6. Future perspectives

At the moment, crystallization is a prerequisite for small molecule-based organic phosphors to exhibit RTP with a long lifetime and high quantum yield. One of the limitations associated with crystalline assembly is the processability of such materials for use in optoelectronic devices. The continuous search for noncrystalline RTP materials ended up with amorphous RTP materials such as polymers,^{116–121} polymer-supported phosphors,^{112–115} and organic solvent-free liquids.¹²² However, in most of the systems, the amount of optically inactive molecular components used as a support is high, leading to the content of active luminophores being very low. It necessitates new concepts and designs to develop processable luminogens having excellent RTP efficiency.

ORTPs have exhibited many fascinating features useful for imaging and anti-counterfeiting applications. One of the areas that need to be improved is the stimuli-responsive RTP features, which will enable developing tunable emission smart RTP materials. More concrete demonstrations in the field of multi-stimuli-sensitive and dynamic RTP materials are highly required to widen the scope.^{123–125} Another area that can be explored is the nonlinear optical properties of RTP materials, which will bring out newer concepts in demonstrations. Even though a few attempts have been made with lasing¹²⁶ and waveguiding⁴⁵ applications of ORTPs, more detailed studies are envisioned for RTP materials.

ORTPs with emission spanning from blue to orange colours have been mainly reported; however, red-emitting metal-free RTPs are rare. The availability of red or NIR emissive ORTPs will be appropriate to explore in biological applications. However, such a target seems to be the most awaiting one due to the many hurdles associated with ORTPs. Besides, biological applications demand the biocompatibility of organic phosphors, which is another challenge due to the current scarcity of high performing RTPs under physiological conditions. It provides an opportunity to explore further the exciting molecular design of ORTPs suitable for biological applications. In the same line, RTP molecules with two-photon and multi-photon induced emission will also be highly beneficial due to the possible operation of NIR excitation. The recent initial developments on dynamic ORTPs point to a focus on more such candidates.

Recently, Liu and coworkers reported the effect of impurity on the afterglow features of carbazole derivatives.¹²⁷ An isomer present in the commercially available carbazole significantly contributes to RTP. In another report, Chen *et al.* demonstrated that the presence of a trace amount (0.01%) of structurally similar compound 2-(3,4-dimethoxybenzyl)-5-(dimethylamino)isoindoline-1,3-dione formed by the side reaction of an RTP inactive molecule, 5-bromo-2-(3,4-dimethoxybenzyl)isoindoline-1,3-dione, with solvent (DMF) results in strong RTP with $\phi_p = 25.4\%$ and $\tau_p = 48$ ms.¹²⁸ The RTP of the impurity is activated by the specific

molecular orbital interactions between these two components. It raises serious concerns on the efficiency of organic phosphors. Hence it is advised to check the purity of the samples before analysis.

7. Conclusions

In summary, ORTPs have been widely exploited in the last decade due to the advancement in molecular design, control over intermolecular interactions, and deeper fundamental understanding. In this Perspective, we explained the various successful strategies adopted to improve the RTP efficiency of metal-free organic molecules having an exceptionally long RTP lifetime above one second along with high quantum efficiency and remarkable afterglow properties. The major experiments were centered on important aspects such as boosting the population of the triplet excited state through enhanced ISC (ϕ_{isc}), suppression of nonradiative decay (k_{nr}) pathways, and slowing down the decay rate of the triplet excited state (k_p). The successful examples pointed to the incorporation of heavy atoms, heteroatoms, and carbonyl groups to improve SOC and control the nonradiative decay of the triplet excitons through crystallization, framework formation, host-guest interactions, and polymer support to obtain efficient RTP candidates. A comparison of the lifetime, quantum yield, and decay parameters revealed that host-guest-based RTPs are better than crystalline, small molecules, and polymer-based RTPs. The most interesting observation is the effective utilization of a long lifetime and the strong afterglow of RTPs in applications spanning from data encryption, anti-counterfeiting, and bio-imaging to sensing. Even though many improvised ways to elevate the efficiency of organic phosphors are in place, the real understanding of mechanistic aspects is still missing. Hence this area is expected to make profound revelations shortly through combined experimental and theoretical investigations. The recent increase in both the quality and quantity of publications indicates that RTPs have a bright future. Similarly, the latest developments in this area also point to the vital role of organic functional materials in futuristic applications.

Conflicts of interest

There are no conflicts to declare.

Acknowledgements

ADN, Goudappagouda, and VCW acknowledge the University Grants Commission (UGC), India, for fellowship. This work is supported by the Science and Engineering Research Board (SERB), Govt. of India, CRG/2019/002539.

Notes and references

- N. J. Turro, V. Ramamurthy and J. C. Scaiano, *Principles of Molecular Photochemistry: An Introduction*, University Science Books, 2009.
- T. Itoh, *Chem. Rev.*, 2012, **112**, 4541–4568.



- 3 G. Baryshnikov, B. Minaev and H. Ågren, *Chem. Rev.*, 2017, **117**, 6500–6537.
- 4 M. Baroncini, G. Bergamini and P. Ceroni, *Chem. Commun.*, 2017, **53**, 2081–2093.
- 5 A. Forni, E. Lucenti, C. Botta and E. Cariati, *J. Mater. Chem. C*, 2018, **6**, 4603–4626.
- 6 X. Ma, J. Wang and H. Tian, *Acc. Chem. Res.*, 2019, **52**, 738–748.
- 7 L. Xiao and H. Fu, *Chem.–Eur. J.*, 2018, **25**, 714–723.
- 8 M. Hayduk, S. Riebe and J. Voskuhl, *Chem.–Eur. J.*, 2018, **24**, 12221–12230.
- 9 W. Zhao, Z. He, J. W. Y. Lam, Q. Peng, H. Ma, Z. Shuai, G. Bai, J. Hao and B. Z. Tang, *Chem*, 2016, **1**, 592–602.
- 10 F. B. Dias, K. N. Bourdakos, V. Jankus, K. C. Moss, K. T. Kamtekar, V. Bhalla, J. Santos, M. R. Bryce and A. P. Monkman, *Adv. Mater.*, 2013, **25**, 3707–3714.
- 11 X. Yang, G. Zhou and W.-Y. Wong, *Chem. Soc. Rev.*, 2015, **44**, 8484–8575.
- 12 Z. Yang, Z. Mao, X. Zhang, D. Ou, Y. Mu, Y. Zhang, C. Zhao, S. Liu, Z. Chi, J. Xu, Y. C. Wu, P. Y. Lu, A. Lien and M. R. Bryce, *Angew. Chem., Int. Ed.*, 2016, **55**, 2181–2185.
- 13 G. Zhang, G. M. Palmer, M. W. Dewhurst and C. L. Fraser, *Nat. Mater.*, 2009, **8**, 747–751.
- 14 Y. Xie, Y. Ge, Q. Peng, C. Li, Q. Li and Z. Li, *Adv. Mater.*, 2017, **29**, 1606829.
- 15 J. Yang, X. Zhen, B. Wang, X. Gao, Z. Ren, J. Wang, Y. Xie, J. Li, Q. Peng, K. Pu and Z. Li, *Nat. Commun.*, 2018, **9**, 840.
- 16 S. Tian, H. Ma, X. Wang, A. Lv, H. Shi, Y. Geng, J. Li, F. Liang, Z. Su, Z. An and W. Huang, *Angew. Chem., Int. Ed.*, 2019, **58**, 6645–6649.
- 17 D. Sasikumar, A. T. John, J. Sunny and M. Hariharan, *Chem. Soc. Rev.*, 2020, **49**, 6122–6140.
- 18 H. Wu, W. Chi, G. Baryshnikov, B. Wu, Y. Gong, D. Zheng, X. Li, Y. Zhao, X. Liu, H. Ågren and L. Zhu, *Angew. Chem., Int. Ed.*, 2019, **58**, 4328–4333.
- 19 H. Wu, C. Hang, X. Li, L. Yin, M. Zhu, J. Zhang, Y. Zhou, H. Ågren, Q. Zhang and L. Zhu, *Chem. Commun.*, 2017, **53**, 2661–2664.
- 20 S. Hirata, *Adv. Optical Mater.*, 2017, **5**, 1700116.
- 21 S. Xu, R. Chen, C. Zheng and W. Huang, *Adv. Mater.*, 2016, **28**, 9920–9940.
- 22 Q. Li, Y. Tang, W. Hu and Z. Li, *Small*, 2018, **14**, 1801560.
- 23 S. Mukherjee and P. Thilagar, *Chem. Commun.*, 2015, **51**, 10988–11003.
- 24 Kenry, C. Chen and B. Liu, *Nat. Commun.*, 2019, **10**, 2111.
- 25 W. Zhao, Z. He and B. Z. Tang, *Nat. Rev. Mater.*, 2020, **5**, 869–885.
- 26 V. C. Wakchaure, Goudappagouda, K. C. Ranjeesh, T. Das, K. Vanka, R. Gonnade and S. S. Babu, *Chem. Commun.*, 2018, **54**, 6028–6031.
- 27 W. Wang, Y. Zhang and W. J. Jin, *Coord. Chem. Rev.*, 2020, **404**, 213107.
- 28 Y.-C. Lin, M. Karlsson and M. Bettinelli, Inorganic Phosphor Materials for Lighting, in, *Photoluminescent Materials and Electroluminescent Devices*, ed. N. Armaroli and H. J. Bolink, Springer, Berlin, 2016, pp. 309–355.
- 29 M.-M. Fang, J. Yang and Z. Li, *Chin. J. Polym. Sci.*, 2019, **37**, 383–393.
- 30 S. Tao, S. Zhu, T. Feng, C. Zheng and B. Yang, *Angew. Chem., Int. Ed.*, 2020, **59**, 9826–9840.
- 31 N. C. Giebink, B. W. D'Andrade, M. S. Weaver, P. B. Mackenzie, J. J. Brown, M. E. Thompson and S. R. Forrest, *J. Appl. Phys.*, 2008, **103**, 44509.
- 32 Y. Jin, Y. Zhang, Y. Liu, J. Xue, W. Li, J. Qiao and F. Zhang, *Adv. Mater.*, 2019, **31**, 1900690.
- 33 L. Xu, K. Zhou, H. Ma, A. Lv, D. Pei, G. Li, Y. Zhang, Z. An, A. Li and G. He, *ACS Appl. Mater. Interfaces*, 2020, **12**, 18385–18394.
- 34 H. Shi, L. Zou, K. Huang, H. Wang, C. Sun, S. Wang, H. Ma, Y. He, J. Wang, H. Yu, W. Yao, Z. An, Q. Zhao and W. Huang, *ACS Appl. Mater. Interfaces*, 2019, **11**, 18103–18110.
- 35 H. Ma, Q. Peng, Z. An, W. Huang and Z. Shuai, *J. Am. Chem. Soc.*, 2019, **141**, 1010–1015.
- 36 M. Baba, *J. Phys. Chem. A*, 2011, **115**, 9514–9519.
- 37 C. M. Marian, *WIREs ComputMolSci*, 2012, **2**, 187–203.
- 38 H. Yuasa and S. Kuno, *Bull. Chem. Soc. Jpn.*, 2018, **91**, 223–229.
- 39 M. A. El-Sayed, *Acc. Chem. Res.*, 1968, **1**, 8–16.
- 40 X. Chen, C. Xu, T. Wang, C. Zhou, J. Du, Z. Wang, H. Xu, T. Xie, G. Bi, J. Jiang, X. Zhang, J. N. Demas, C. O. Trindle, Y. Luo and G. Zhang, *Angew. Chem., Int. Ed.*, 2016, **55**, 9872–9876.
- 41 Z. Chai, C. Wang, J. Wang, F. Liu, Y. Xie, Y.-Z. Zhang, J.-R. Li, Q. Li and Z. Li, *Chem. Sci.*, 2017, **8**, 8336–8344.
- 42 Z. An, C. Zheng, Y. Tao, R. Chen, H. Shi, T. Chen, Z. Wang, H. Li, R. Deng, X. Liu and W. Huang, *Nat. Mater.*, 2015, **14**, 685–690.
- 43 S. Hirata, K. Totani, T. Watanabe, H. Kaji and M. Vacha, *Chem. Phys. Lett.*, 2014, **591**, 119–125.
- 44 K. Narushima, Y. Kiyota, T. Mori, S. Hirata and M. Vacha, *Adv. Mater.*, 2019, 1807268.
- 45 A. D. Nidhankar, Goudappagouda, D. S. M. Kumari, S. K. Chaubey, R. Nayak, R. G. Gonnade, G. V. P. Kumar, R. Krishnan and S. S. Babu, *Angew. Chem., Int. Ed.*, 2020, **59**, 13079–13085.
- 46 S. Kuno, H. Akeno, H. Ohtani and H. Yuasa, *Phys. Chem. Chem. Phys.*, 2015, **17**, 15989–15995.
- 47 M. Koch, K. Perumal, O. Blacque, J. A. Garg, R. Saiganesh, S. Kabilan, K. K. Balasubramanian and K. Venkatesan, *Angew. Chem., Int. Ed.*, 2014, **53**, 6378–6382.
- 48 R. T. Parker, R. S. Freedlander and R. B. Dunlap, *Anal. Chim. Acta*, 1980, **119**, 189–205.
- 49 R. T. Parker, R. S. Freedlander and R. B. Dunlap, *Anal. Chim. Acta*, 1980, **120**, 1–17.
- 50 S. K. Lower and M. A. El-Sayed, *Chem. Rev.*, 1966, **66**, 199–241.
- 51 G. N. Lewis, D. Lipkin and T. M. Magel, *J. Am. Chem. Soc.*, 1941, **63**, 3005–3018.
- 52 G. N. Lewis and M. Kasha, *J. Am. Chem. Soc.*, 1944, **66**, 2100–2116.
- 53 G. N. Lewis and M. Kasha, *J. Am. Chem. Soc.*, 1945, **67**, 994–1006.
- 54 M. Kasha, *Chem. Rev.*, 1947, **41**, 401–419.



- 55 M. Roth, *J. Chromatogr.*, 1967, **30**, 276–278.
- 56 E. M. Schulman and C. Walling, *Science*, 1972, **178**, 53–54.
- 57 E. M. Schulman and C. Walling, *J. Phys. Chem.*, 1973, **77**, 902–905.
- 58 T. V. Dinh, E. L. Yen and J. D. Winefordne, *Talanta*, 1977, **24**, 146–148.
- 59 E. M. Schulman and R. T. Parker, *J. Phys. Chem.*, 1977, **81**, 1932–1939.
- 60 N. J. Turro and M. Aikawa, *J. Am. Chem. Soc.*, 1980, **102**, 4866–4870.
- 61 S. Scypinski and L. J. C. Love, *Anal. Chem.*, 1984, **56**, 322–327.
- 62 V. Ramamurthy, D. F. Eaton and J. V. Caspar, *Acc. Chem. Res.*, 1992, **25**, 299–307.
- 63 A. J. Parola, F. Pina, E. Ferreira, M. Maestri and V. Balzani, *J. Am. Chem. Soc.*, 1996, **118**, 11610–11616.
- 64 G. J. Niday and P. G. Seybold, *Anal. Chem.*, 1978, **50**, 1577–1578.
- 65 J. L. Kropp and W. R. Dawson, *J. Phys. Chem.*, 1967, **71**, 4499–4506.
- 66 P. F. Jones and S. Siegel, *J. Chem. Phys.*, 1969, **50**, 1134.
- 67 M. Hilbert and B. Nemet, *Acta Phys. Chem.*, 1978, **24**, 365–370.
- 68 J. H. Fendler, *Photochemistry in Organized Media*, VCH Publishers, 1983, vol. 60.
- 69 T. Vo-Dinh, *Room Temperature Phosphorimetry in Chemical Analysis*, John Wiley & Sons, New York, 1984.
- 70 D. B. Clapp, *J. Am. Chem. Soc.*, 1939, **61**, 523–524.
- 71 C. S. Bilien, N. Harrison and D. J. Morantz, *Nature*, 1978, **271**, 235–237.
- 72 G. Zhang, J. Chen, S. J. Payne, S. E. Kooi, J. N. Demas and C. L. Fraser, *J. Am. Chem. Soc.*, 2007, **129**, 8942–8943.
- 73 W. Z. Yuan, X. Y. Shen, H. Zhao, J. W. Y. Lam, L. Tang, P. Lu, C. Wang, Y. Liu, Z. Wang, Q. Zheng, J. Z. Sun, Y. Ma and B. Z. Tang, *J. Phys. Chem. C*, 2010, **114**, 6090–6099.
- 74 O. Bolton, K. Lee, H.-J. Kim, K. Y. Lin and J. Kim, *Nat. Chem.*, 2011, **3**, 205–210.
- 75 W. Jia, Q. Wang, H. Shi, Z. An and W. Huang, *Chem.–Eur. J.*, 2020, **26**, 4437–4448.
- 76 L. Gu, H. Shi, M. Gu, K. Ling, H. Ma, S. Cai, L. Song, C. Ma, H. Li, G. Xing, X. Hang, J. Li, Y. Gao, W. Yao, Z. Shuai, Z. An, X. Liu and W. Huang, *Angew. Chem., Int. Ed.*, 2018, **57**, 8425–8431.
- 77 B. Zhou and D. Yan, *Adv. Funct. Mater.*, 2019, **29**, 1807599.
- 78 Y. Shoji, Y. Ikabata, Q. Wang, D. Nemoto, A. Sakamoto, N. Tanaka, J. Seino, H. Nakai and T. Fukushima, *J. Am. Chem. Soc.*, 2017, **139**, 2728–2733.
- 79 S. Kuno, T. Kanamori, Z. Yijing, H. Ohtani and H. Yuasa, *Chem. Photo. Chem.*, 2017, **1**, 102–106.
- 80 M. Li, K. Ling, H. Shi, N. Gan, L. Song, S. Cai, Z. Cheng, L. Gu, X. Wang, C. Ma, M. Gu, Q. Wu, L. Bian, M. Liu, Z. An, H. Ma and W. Huang, *Adv. Optical Mater.*, 2019, 1800820.
- 81 J. Bernstein, *Polymorphism in Molecular Crystals*, Oxford University Press, New York, 2002.
- 82 T. Zhang, Z. Zhao, H. Ma, Y. Zhang and W. Z. Yuan, *Chem.–Asian J.*, 2019, **14**, 884–889.
- 83 S. Cai, H. Shi, Z. Zhang, X. Wang, H. Ma, N. Gan, Q. Wu, Z. Cheng, K. Ling, M. Gu, C. Ma, L. Gu, Z. An and W. Huang, *Angew. Chem., Int. Ed.*, 2018, **57**, 4005–4009.
- 84 J. Yang, Z. Ren, B. Chen, M. Fang, Z. Zhao, B. Z. Tang, Q. Peng and Z. Li, *J. Mater. Chem. C*, 2017, **5**, 9242–9246.
- 85 H. Sasabe, Y. Kato, Y. Watanabe, T. Ohsawa, N. Aizawa, W. Fujiwara, Y.-J. Pu, H. Katagiri and J. Kido, *Chem.–Eur. J.*, 2019, **25**, 16294–16300.
- 86 N. Gan, X. Wang, H. Ma, A. Lv, H. Wang, Q. Wang, M. Gu, S. Cai, Y. Zhang, L. Fu, M. Zhang, C. Dong, W. Yao, Hu. Shi, Z. An and W. Huang, *Angew. Chem., Int. Ed.*, 2019, **58**, 14140–14145.
- 87 L. Gu, H. Shi, L. Bian, M. Gu, K. Ling, X. Wang, H. Ma, S. Cai, W. Ning, L. Fu, H. Wang, S. Wang, Y. Gao, W. Yao, F. Huo, Y. Tao, Z. An, X. Liu and W. Huang, *Nat. Photon.*, 2019, **13**, 406–411.
- 88 Y. Wang, S. Tang, Y. Wen, S. Zheng, B. Yang and W. Z. Yuan, *Mater. Horiz.*, 2020, **7**, 2105–2112.
- 89 Y.-C. Liang, Y. Shang, K.-K. Liu, Z. Liu, W.-J. Wu, Q. Liu, Q. Zhao, X.-Y. Wu, L. Dong and C.-X. Shan, *Nano Res.*, 2020, **13**, 875–881.
- 90 H. Zhu, I. Badía-Domínguez, B. Shi, Q. Li, P. Wei, H. Xing, M. C. R. Delgado and F. Huang, *J. Am. Chem. Soc.*, 2021, **143**, 2164–2169.
- 91 L. Bian, H. Shi, X. Wang, K. Ling, H. Ma, M. Li, Z. Cheng, C. Ma, S. Cai, Q. Wu, N. Gan, X. Xu, Z. An and W. Huang, *J. Am. Chem. Soc.*, 2018, **140**, 10734–10739.
- 92 T. Zhang, X. Ma, H. Wu, L. Zhu, Y. Zhao and H. Tian, *Angew. Chem., Int. Ed.*, 2020, **59**, 11206–11216.
- 93 G. Qu, Y. Zhang and X. Ma, *Chin. Chem. Lett.*, 2019, **30**, 1809–1814.
- 94 V. B. Nazarov, V. G. Avakyan, E. I. Bagrii, T. G. Vershinnikova and M. V. Alfimov, *Russ. Chem. Bull.*, 2005, **54**, 2752–2756.
- 95 V. B. Nazarov, V. G. Avakian and M. V. Alfimov, *High Energy Chem.*, 2019, **53**, 108–114.
- 96 Z.-Y. Zhang and Y. Liu, *Chem. Sci.*, 2019, **10**, 7773–7778.
- 97 S. Hirata, K. Totani, J. Zhang, T. Yamashita, H. Kaji, S. R. Marder, T. Watanabe and C. Adachi, *Adv. Funct. Mater.*, 2013, **23**, 3386–3397.
- 98 R. Kabe, N. Notsuka, K. Yoshida and C. Adachi, *Adv. Mater.*, 2016, **28**, 655.
- 99 I. Bhattacharjee and S. Hirata, *Adv. Mater.*, 2020, **31**, 2001348.
- 100 Y. Wang, J. Yang, Y. Gong, M. Fang, Z. Li and B. Z. Tang, *SmartMat*, 2020, **1**, e1006.
- 101 H. Mieno, R. Kabe, N. Notsuka, M. D. Allendorf and C. Adachi, *Adv. Optical Mater.*, 2016, **4**, 1015–1021.
- 102 R. Gao and D. Yan, *Chem. Sci.*, 2017, **8**, 590–599.
- 103 Y. Deng, P. Li, S. Sun, H. Jiang, X. Ji and H. Li, *Chem.–Asian J.*, 2020, **15**, 1088–1093.
- 104 W.-J. Fang, J.-J. Zhang, H. Zhao, J. Ni, S.-Q. Liu, Z. Liu, A.-Y. Ni, P.-P. Zhang and H.-H. Wei, *Adv. Optical Mater.*, 2020, **8**, 2000482.
- 105 N. Gan, H. Shi, Z. An and W. Huang, *Adv. Funct. Mater.*, 2018, **28**, 1802657.



- 106 T. Ogoshi, H. Tsuchida, T. Kakuta, T. Yamagishi, A. Taema, T. Ono, M. Sugimoto and M. Mizuno, *Adv. Funct. Mater.*, 2018, **28**, 1707369.
- 107 S. Cai, H. Ma, H. Shi, H. Wang, X. Wang, L. Xiao, W. Ye, K. Huang, X. Cao, N. Gan, C. Ma, M. Gu, L. Song, H. Xu, Y. Tao, C. Zhang, W. Yao, Z. An and W. Huang, *Nat. Commun.*, 2019, **10**, 4247.
- 108 M. Hoshi, R. Nishiyabu, Y. Hayashi, S. Yagi and Y. Kubo, *Chem.-Asian J.*, 2020, **15**, 787–795.
- 109 S. Wang, D. Wu, S. Yang, Z. Lin and Q. Ling, *Mater. Chem. Front.*, 2020, **4**, 1198–1205.
- 110 L. Gu, H. Wu, H. Ma, W. Ye, W. Jia, H. Wang, H. Chen, N. Zhang, D. Wang, C. Qian, Z. An, W. Huang and Y. Zhao, *Nat. Commun.*, 2020, **11**, 944.
- 111 H. Wu, W. Chi, Z. Chen, G. Liu, L. Gu, A. K. Bindra, G. Yang, X. Liu and Y. Zhao, *Adv. Funct. Mater.*, 2019, **29**, 1807243.
- 112 Z. Wang, Y. Zhang, C. Wang, X. Zheng, Y. Zheng, L. Gao, C. Yang, Y. Li, L. Qu and Y. Zhao, *Adv. Mater.*, 2020, 1907355.
- 113 S. Kuila and S. J. George, *Angew. Chem., Int. Ed.*, 2020, **59**, 9393–9397.
- 114 S. Kuila, S. Garain, S. Bandi and S. J. George, *Adv. Funct. Mater.*, 2020, 2003693.
- 115 H. Thomas, D. L. Pastoetter, M. Gmelch, T. Achenbach, A. Schlogl, M. Louis, X. Feng and S. Reineke, *Adv. Mater.*, 2020, **32**, 2000880.
- 116 M. E. Díaz-García, A. Fernández-González and R. Badía-Laiño, *Appl. Spectrosc. Rev.*, 2007, **42**, 605–624.
- 117 S. M. A. Fateminia, Z. Mao, S. Xu, Z. Yang, Z. Chi and B. Liu, *Angew. Chem., Int. Ed.*, 2017, **56**, 12160–12164.
- 118 X. Zhen, Y. Tao, Z. An, P. Chen, C. Xu, R. Chen, W. Huang and K. Pu, *Adv. Mater.*, 2017, 1606665.
- 119 J. Zhi, Q. Zhou, H. Shi, Z. An and W. Huang, *Chem.-Asian J.*, 2020, **15**, 947–957.
- 120 H. Xiang, J. Cheng, X. Ma, X. Zhou and J. J. Chruma, *Chem. Soc. Rev.*, 2013, **42**, 6128–6185.
- 121 X.-Q. Liu, K. Zhang, J.-F. Gao, Y.-Z. Chen, C.-H. Tung and L.-Z. Wu, *Angew. Chem., Int. Ed.*, 2020, **59**, 23456–23460.
- 122 Goudappagouda, A. Manthanath, V. C. Wakchaure, K. C. Ranjeesh, T. Das, K. Vanka, T. Nakanishi and S. S. Babu, *Angew. Chem., Int. Ed.*, 2019, **58**, 2284–2288.
- 123 L. Huang, C. Qian and Z. Ma, *Chem.-Eur. J.*, 2020, **52**, 11914–11930.
- 124 L. Gu, X. Wang, M. Singh, H. Shi, H. Ma, Z. An and W. Huang, *J. Phys. Chem. Lett.*, 2020, **11**, 6191–6200.
- 125 Y. Wang, J. Yang, M. Fang, Y. Yu, B. Zou, L. Wang, Y. Tian, J. Cheng, B. Z. Tang and Z. Li, *Matter*, 2020, **3**, 449–463.
- 126 Z. Yu, Y. Wu, L. Xiao, J. Chen, Q. Liao, J. Yao and H. Fu, *J. Am. Chem. Soc.*, 2017, **139**, 6376–6381.
- 127 C. Chen, Z. Chi, K. C. Chong, A. S. Batsanov, Z. Yang, Z. Mao, Z. Yang and B. Liu, *Nat. Mater.*, 2020, **20**, 175–180.
- 128 B. Chen, W. Huang, H. Su, H. Miao, X. Zhang and G. Zhang, *Angew. Chem., Int. Ed.*, 2020, **59**, 10109–10112.





Self-Assembled Helical Arrays for the Stabilization of the Triplet State

Aakash D. Nidhankar, Goudappagouda, Divya S. Mohana Kumari, Shailendra Kumar Chaubey, Rashmi Nayak, Rajesh G. Gonnade, G. V. Pavan Kumar, Rethesh Krishnan, and Sukumaran Santhosh Babu*

Abstract: Room-temperature phosphorescence of metal and heavy atom-free organic molecules has emerged as an area of great potential in recent years. A rational design played a critical role in controlling the molecular ordering to impart efficient intersystem crossing and stabilize the triplet state to achieve room-temperature ultralong phosphorescence. However, in most cases, the strategies to strengthen phosphorescence efficiency have resulted in a reduced lifetime, and the available nearly degenerate singlet-triplet energy levels impart a natural competition between delayed fluorescence and phosphorescence, with the former one having the advantage. Herein, an organic helical assembly supports the exhibition of an ultralong phosphorescence lifetime. In contrary to other molecules, 3,6-phenylmethanone functionalized 9-hexylcarbazole exhibits a remarkable improvement in phosphorescence lifetime (>4.1 s) and quantum yield (11 %) owing to an efficient molecular packing in the crystal state. A right-handed helical molecular array act as a trap and exhibits triplet exciton migration to support the exceptionally longer phosphorescence lifetime.

Introduction

Room-temperature phosphorescence (RTP) of organic molecules has been enthusiastically investigated recently for various applications such as electroluminescence, sensing,

bio-imaging, etc.^[1,2] It has been demonstrated that the incorporation of heavy atoms and functional moieties equipped with lone pair of electrons facilitate intersystem crossing (ISC) rate (k_{ST}) through strong spin-orbit coupling (SOC), leading to efficient RTP.^[3–6] In this direction, diverse molecular designs have been explored for ultralong organic phosphorescence (UOP).^[7–10] Hence, successful strategies such as molecular units with n orbitals, which can reduce the singlet–triplet (S–T) splitting energy (ΔE_{ST}) and stabilize the triplet excited state through various interactions, have been widely employed.^[5f] Significant advancement has been noticed in the area of UOP materials and the maximum lifetime reported for crystalline small molecule-based organic phosphor is circa 2.5 s (Figure 1 a, and Table S1 in the Supporting Information).^[11] Mostly, longer lifetimes under ambient condition are achieved by stabilization of the triplet state through H-aggregation (Figure 1 b). However, the already established strategies to improve the phosphorescence efficiency often lead to shortening the lifetime. Moreover, the molecular designs to enhance the nearly degenerate triplet manifolds can, in turn, facilitate reverse intersystem crossing (RISC) to exhibit delayed fluorescence (DF).^[12] Hence it demands a new alternate plan of action to control the competitive decay pathways and efficiently manage the triplet excitons to enhance phosphorescence lifetime. It can be achieved only through unexplored molecular designs and with the rigorous assistance of molecular packing. Helical arrays of organic small molecules and polymers exhibit exciting

[*] A. D. Nidhankar, Goudappagouda, R. Nayak, S. S. Babu
Organic Chemistry Division, National Chemical Laboratory (CSIR-NCL)

Dr. Homi Bhabha Road, Pune-411 008 (India)
E-mail: santhoshsbabu@gmail.com

A. D. Nidhankar, Goudappagouda, R. G. Gonnade, S. S. Babu
Academy of Scientific and Innovative Research (AcSIR)
Ghaziabad-201 002 (India)
E-mail: sb.sukumaran@ncl.res.in

R. G. Gonnade
Center for Materials Characterization (CMC), National Chemical Laboratory (CSIR-NCL)
Dr. Homi Bhabha Road, Pune-411 008 (India)

D. S. Mohana Kumari, R. Krishnan
Department of Chemistry, Government College for Women
Thiruvananthapuram-695 014, Kerala (India)

S. K. Chaubey, G. V. P. Kumar
Department of Physics, Indian Institute of Science Education and Research
Pune-411 008, Maharashtra (India)

Supporting information and the ORCID identification number(s) for the author(s) of this article can be found under:
<https://doi.org/10.1002/anie.202005105>.

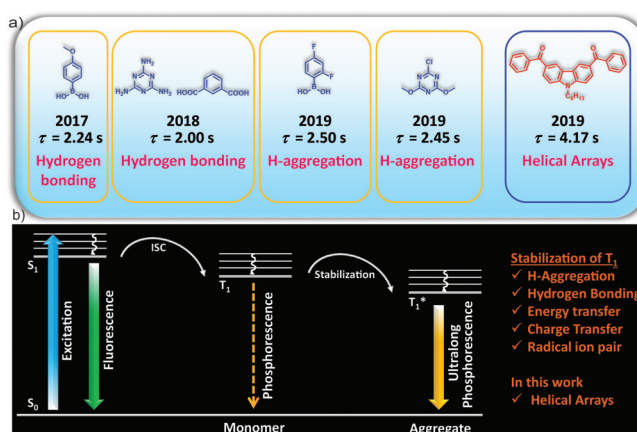


Figure 1. a) Recent developments in the area of small molecule-based organic phosphors with lifetime above 2 s and the present work with above 4.17 s. b) Schematic of the stabilization of the triplet state, leading to ultralong phosphorescence.

optoelectronic properties by controlling the spatial organization of the structural units.^[13] Hence, the design of a helical assembly to modulate the triplet state to achieve a longer phosphorescence lifetime will be highly appreciated. Our continuous attempts in this direction enabled us to successfully utilize the crystalline helical arrays of phenylmethanone functionalized alkylated carbazole to achieve a longer lifetime of above 4 s (Figure 1 b).

Results and Discussion

Among the potential RTP candidates, carbazole has undergone diverse functionalization using various combinations of heavy atoms and other functional groups to achieve UOP (Supporting Information, Table S2).^[8c,9b,10d,e] We planned to study the effect of phenylmethanone functionalization on the RTP features of 9-hexylcarbazole, which exhibits very low RTP lifetime.^[14] Our design strategy comprised of: 1) N-alkylation of carbazole to enhance the solubility and impart alkyl- π interaction to promote crystallization. 2) Introduction of a phenylmethanone unit to support a strain-induced crystalline assembly formation and stabilize the triplet state by providing hybrid (n,π^*) and (π,π^*) configurations for UOP.^[15] Accordingly, a series of 9-hexylcarbazole molecules with phenylmethanone units at 3 and 3,6-positions were synthesized and unambiguously characterized by ^1H and ^{13}C nuclear magnetic resonance spectroscopies and high-resolution mass spectrometry (Figure 2 a, Scheme 1). While our

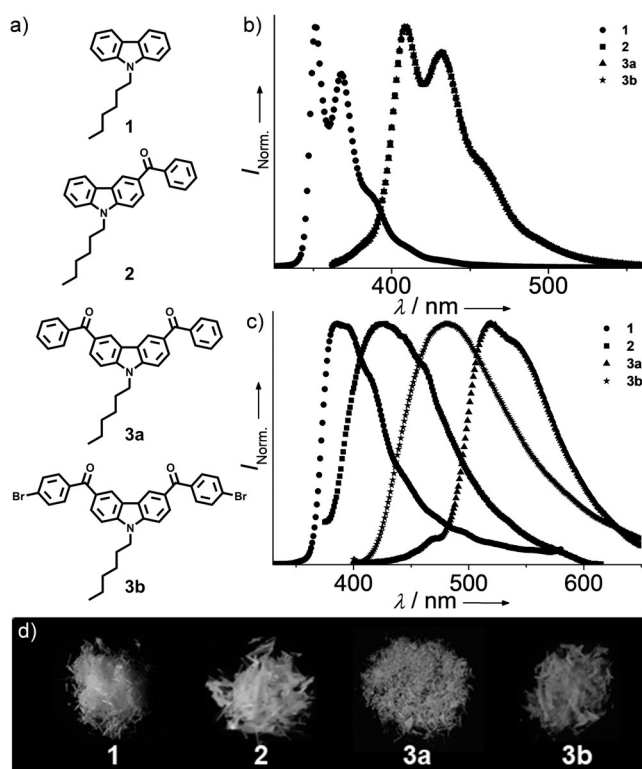
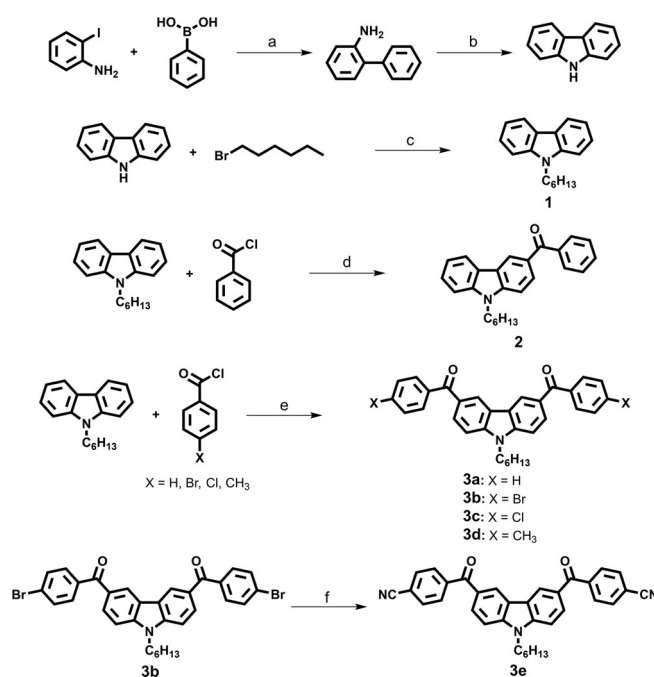


Figure 2. a) Chemical structure of 1–3b. Normalized steady-state fluorescence spectra of 1–3b in b) MTHF solution and c) crystals at RT. d) Photographs of 1–3b crystals under UV light (365 nm).



Scheme 1. Synthetic Scheme for carbazole and target molecules 1–3e, a) $\text{Pd}(\text{PPh}_3)_4$, K_3PO_4 , EtOH, 90 °C, 12 h, 91%. b) $\text{Pd}(\text{OAc})_2$, lmes HCl, H_2O_2 (35%), AcOH, 120 °C, 20 min, MW, 80%. c) TBAB, KOH, DMF, 70 °C, 24 h, 89%. d) Anhy. AlCl_3 (1 equiv.), anhy. CH_2Cl_2 , 0 °C – 30 min, 30 °C – 12 h, 62%. e) Anhy. AlCl_3 (2.5 equiv.), anhy. CH_2Cl_2 , 0 °C – 30 min, 30 °C – 12 h, 70–75%. f) $\text{Pd}(\text{PPh}_3)_4$, $\text{Zn}(\text{CN})_2$, DMF, 110 °C, 24 h, 61%.

study was progressing, Chen et al., reported the effect of impurity on the afterglow property of carbazoles.^[16] In the purview of this report, we synthesized carbazole in our lab using reported protocols^[17] and confirmed the purity by high-performance liquid chromatography (HPLC) using acetonitrile-water mixture (Scheme 1). All the final molecules were also purified similarly and hence, we would like to mention that the concerns related to the effect of impurity on the present work, if any, are not valid.

After the complete characterization of the molecules, we checked the thermal stability and followed by optical properties. Thermogravimetric analysis indicated the enhanced stability upon moving from molecule 1 to 3b, indicating the importance of substitution on 9-hexylcarbazole (Supporting Information, Figure S2). We observed a similar trend in the melting point of 1–3b in differential scanning calorimetry experiments as well (Supporting Information, Figure S3). While absorption features of all the luminogens 1–3b in 2-methyltetrahydrofuran (MTHF) have not varied significantly (Supporting Information, Figure S4), compared to 1, the fluorescence spectra of 2–3b showed a bathochromic shift of 50 nm due to the increasing electron-withdrawing ability of the carbonyl groups (Figure 2 b and Table S3 in the Supporting Information). An increase in the number of benzoyl groups did not alter the fluorescence maximum of 2–3b in MTHF. Fluorescence lifetime decay profiles in MTHF show that the higher lifetime component varied as 4.11 ns (1), 6.39 ns (2), 6.04 ns (3a), and 6.38 ns (3b) (Table 1, and Supporting Information Figure S5 and Table S4). Both red-

Table 1: Photophysical parameters of compounds **1–3e** based on fluorescence and phosphorescence experiments in the crystal state.

No	QY _{Fl} [%]	τ_{Fl} [ns]	$k_{nr, Fl} [\times 10^9 \text{ s}^{-1}]$	$k_{r, Fl} [\times 10^9 \text{ s}^{-1}]$	$k_{isc} [\times 10^7 \text{ s}^{-1}]$	QY _{Phos} [%]	τ_{Phos} [ms]	$k_{nr, Phos} [\text{S}^{-1}]$	$k_{r, Phos} [\text{S}^{-1}]$
1	59.00	11.09	0.033	0.053	0.302	3.36	5.1	189.4	6.58
2	03.68	1.36	0.701	0.027	0.625	0.85	16.6	59.72	0.51
3a	13.58	2.92	0.257	0.046	3.85	11.25	4171	0.212	0.026
3b	27.14	2.53	0.267	0.107	2.03	5.15	114.5	8.28	0.44
3c	4.14	1.06	0.879	0.039	2.46	2.61	45.3	21.49	0.57
3d	4.52	6.23	0.148	0.007	4.431	2.69	6.59	147.6	4.08
3e	4.47	1.11	0.842	0.040	1.81	2.01	11.9	82.34	1.68

shifted fluorescence maximum and enhanced fluorescence lifetime for molecules **2–3b** points to the effect of benzoylation on carbazole. A comparison of the fluorescence spectra of the MTHF solution at room temperature (298 K) and 77 K indicates that **1** exhibits additional long-wavelength peaks (400–550 nm) along with fluorescence peak at 370 nm, whereas a completely red-shifted fluorescence peak appeared for molecules **2–3b** (Table 1 and Figure S6 in the Supporting Information). The fluorescence spectra of **2–3b** both at room temperature and 77 K match with the red-shifted peak of **1** between 400–550 nm at 77 K (Supporting Information, Figure S6).

To study further, all molecules were crystallized from CH_2Cl_2 and the morphology was visualized by fluorescence microscopy (FM) (Supporting Information, Figure S7), and by scanning and transmission electron microscopy (SEM and TEM) images (Supporting Information, Figure S8). It was found that molecule **1–3a** formed crystalline rods, whereas flat sheets were formed by **3b** (Supporting Information, Figure S7,8). The bulk purity and ordering of the molecules were confirmed by matching the experimental and theoretical powder X-ray diffraction patterns (Supporting Information, Figure S9). The diffuse reflectance spectra of crystals of **1–3b** exhibited a broad band between 300–450 nm, having an additional absorption band located around 360–380 nm (Supporting Information, Figure S10). It is clear from the fluorescence spectra of crystals at room temperature that molecule **3a** exhibits a far red-shifted peak ($\lambda_{\text{max}} = 517 \text{ nm}$) than that of **1** ($\lambda_{\text{max}} = 390 \text{ nm}$), **2** and **3b** ($\lambda_{\text{max}} = 425$ and 490 nm) (Figure 2c,d). Similarly, compared to **1**, molecules **2–3b** exhibited a marked difference in fluorescence features at 77 K in the crystalline state (Supporting Information, Figure S11). The presence of a long-lived component in the fluorescence lifetime decay of **2–3b** was noticed when the lifetime was monitored at the fluorescence maxima. Hence, to find out the fluorescence lifetime, the measurement was carried out by monitoring at lower wavelengths and the longer lifetime component varied as 11.1 ns (87%) for **1**, 1.88 ns (17%) for **2**, 3.37 ns (59%) for **3a**, and 3.23 ns (75%) for **3b** (Supporting Information, Figure S12 and Table S4).

The red-shifted fluorescence of the crystals of **2–3b** at room temperature nearly matches with the corresponding spectra at 77 K, implying RTP for **2–3b** in the crystalline assembly (Supporting Information, Figure S11, S13–16). To clarify the presence of RTP for crystals of **2–3b**, phosphorescence spectra were measured and confirmed that the observed red-shifted peak at room temperature is due to phosphorescence (Figure 3a). In the crystalline state, the

phosphorescence intensity of **3a** was found to be highest among all, and it was about 27 times higher than that of **1**. The enhanced RTP for **3a** was visualized by phosphorescence lifetime measurement and it varied as 5.1, 16.6, 4171, and 114.5 ms for **1–3b**, respectively (Figure 3b, and Figure S17 and Table S5 in the Supporting Information). Molecule **3a** exhibited a longer phosphorescence lifetime with afterglow for > 12 s upon excitation after just dipping in liquid nitrogen (Supporting Information, Figure S15). The phosphorescence quantum yield of the crystals varied as **1** (3.36%), **2** (0.85%), **3a** (11.25%), and **3b** (5.15%) (Supporting Information, Table S6,7). The observed enhancement in the phosphorescence lifetime of **3a** raised curiosity about the excited triplet state of this particular molecule, and hence we decided to study it in detail.

Time-dependent density functional theory (TD-DFT) computations at the B3LYP/6-31G(d) level of theory for single-molecule in vacuum show that the electron density of the HOMO is located on the carbazole moiety and the LUMO is delocalized over the entire molecule with a considerable extension to the phenylmethanone group (Figure 3c, Figures S18–21 and Tables S6–9 in the Supporting Informa-

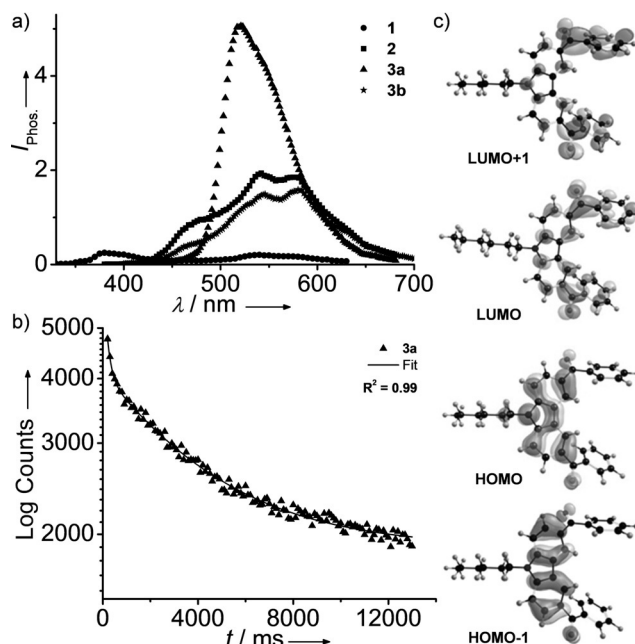


Figure 3. a) Phosphorescence spectra of **1–3b** crystals at RT in air. b) Phosphorescence lifetime decay profile of **3a** crystal recorded at RT in air. c) The frontier molecular orbitals of **3a** from DFT calculations.

tion). The low-lying excited electronic states mainly result from well-described π - π^* transitions along with a significant contribution from the n - π^* character. Upon examining the relative computed energies for the singlet (S_n) and triplet (T_n) states for **3a**, it has been found that there are many triplet states (T_4 - T_9) nearly degenerate with the first singlet excited state (S_1) (Supporting Information, Figure S20 and Table S8). As the phenylmethanone functionalization increases, an intense mixing of nearly degenerate excited singlet and triplet states were observed, which could bring out a natural competition between ISC and RISC (Supporting Information, Figure S20). The energetic proximity of the singlet and the triplet manifold potentials established a small ΔE_{ST} . Thus, it appears that molecules **2-3b** have energetically well-matched states that enable efficient singlet-triplet or triplet-singlet crossings. Once T_4 - T_9 levels are populated, relaxation through the triplet manifold to the T_1 state leads to phosphorescence (Supporting Information, Figure S18-21). Besides, we have to consider the strong possibility of RISC in a competitive pathway to exhibit DF. The ΔE_{SIT_1} value calculated for the monomer from DFT and phosphorescence spectra were varied as 0.72 and 0.32 eV, respectively (Figure 3 a, Figure S20, and Table S8 in the Supporting Information). It shows that the aggregation of **3a** with the assistance of intermolecular interactions reduces ΔE_{SIT_1} to facilitate both ISC and RISC.

Single-crystal X-ray analysis has been employed to get a deeper structure-property correlation of **1-3b**. (Figure 4 and Figures S22-27 in the Supporting Information). The unit cell of **3a** contains six molecules arranged in a helical way in two rows along b axis using various intermolecular interactions. An extended molecular array was formed by the arrangement of molecules (Figure 4a) mainly through π - π interaction (3.34 Å) between carbazole and phenylmethanone units of adjacent molecules (Figure 4b) along b-axis. This one-dimensional (1D) helical array is stabilized with the help of $CH\cdots\pi$ interaction (2.88 Å) between the alkyl chain on carbazole and phenylmethanone unit in the adjacent helical columns to form a three-dimensional network structure (Figure 4c). We strongly believe that this kind of space filled packing (Figure 4c,d) rigidifies the molecular conformations and remarkably blocks the nonradiative decay pathways. The dihedral angle between the aryl groups and carbonyl subunits was found to be around 30° and it enables efficient electronic communication between carbazole and phenylmethanone by conjugation (Figure 4e). It can be anticipated that better communication between the (n,π^*) from the $>C=O$ and (π,π^*) of carbazole could result in hybrid triplet states. The helical array of **3a** was confirmed by the solid-state circular dichroism (CD) spectrum (Figure 4f). A bisignated CD signal observed points to the right-handed helical array of molecules (Figure 4a,f). However, no such helical array is present in the case of **1**, **2**, and **3b**, and mostly, a loosely packed crystalline assembly was observed (Figure 5, and Figures S21-23 in the Supporting Information). Especially, **3b** packs in a kind of slipped molecular arrangement with a carbazole-carbazole distance of 5.7 Å (Supporting Information, Figure S24). Hence, the helical array of **3a** is responsible for the enhanced RTP through an efficient space filled molecular packing by

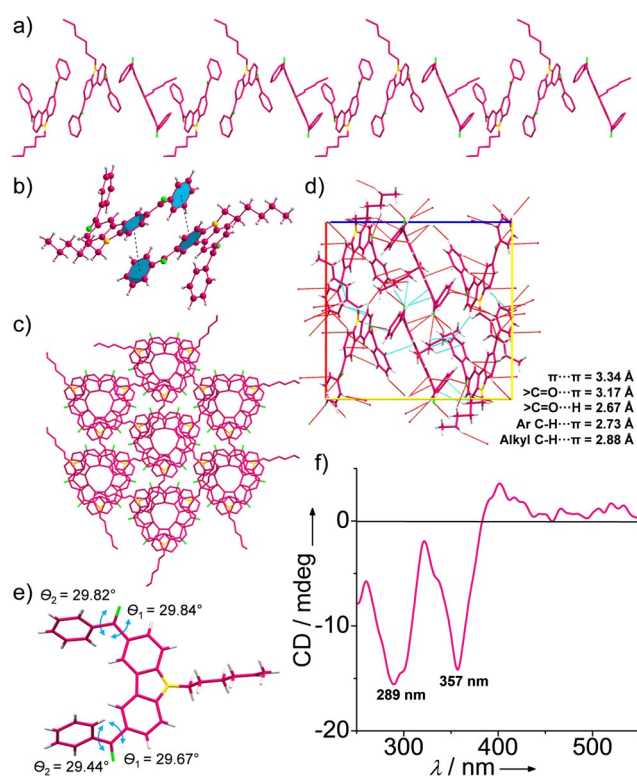


Figure 4. a) The extended molecular packing of **3a** forming the helical 1D-array in the b-axis with the help of b) π - π interaction between carbazole and phenylmethanone unit of the adjacent molecule. c) Six adjacent helical arrays of **3a** leading to extended columnar packing in the c-axis. d) All possible intermolecular interactions in a unit cell of **3a**. e) Crystal structure of **3a** showing the dihedral angles. f) The solid-state CD spectrum of **3a** crystals at RT.

making use of maximum intermolecular interactions (Figure 4a-d).

Recently, helical/twisted aromatic systems have been of interest to promote intersystem crossing.^[18] Hence, the stabilization of the triplet state of **3a** is strongly supported by the presence of strained helical arrays. To ascertain the impact of helical arrays on such a longer phosphorescence lifetime, we prepared a series of carbazole molecules by varying the functional moieties on the phenylmethanone unit (**3c-e**) (Supporting Information, Scheme S1 and Figures S25-37). However, molecules **3c-e** packed differently (Figure 5, Figures S25-27 and Tables S5, S10-12 in the Supporting Information) and hence exhibited lower phosphorescence lifetimes (Supporting Information, Figure S34 and Table S5). It indicates the critical supportive role of helical arrays to impart a longer lifetime for **3a**. Besides, we have tested the emission of **3a** in poly(methyl methacrylate) (PMMA) matrix and found that the spectral feature has been significantly changed and the lifetime also drastically decreased (8.15 ms) due to the lack of specific molecular ordering (Supporting Information, Figure S38).

A perfectly aligned and densely packed fluorescent pi-conjugated molecular array with a large Stokes shift is known for optical waveguiding (WG).^[2a,19] Hence, to check the possibility of WG, one end of the crystals of **3a** was excited at

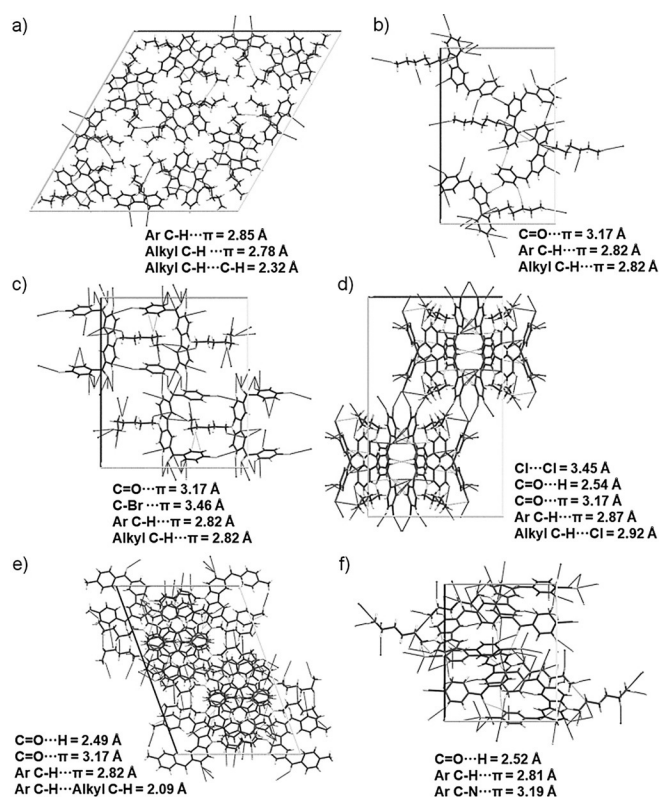


Figure 5. The molecular packing of a) **1**, b) **2**, c) **3b**, d) **3c**, e) **3d**, and f) **3e** in the unit cell.

532 and 633 nm using a 10X, 0.3 NA objective lens^[20] and it was found that the micro rods exhibit intense green and red emissions at the distal end, respectively, with characteristic features of the optical WG (Figure 6a). The maximum phosphorescence intensity at the distal end was observed when it is excited with polarization along the long axis of the rod, and it has been significantly reduced in the perpendicular polarization (Supporting Information, Figure S39). Since molecule **3a** is RTP active, it is obvious that phosphorescence of **3a** propagates along the long axis of the single crystal rods (Figure 6b). The self-waveguided phosphorescence was imaged on a rod with an excitation spot ($\lambda = 532$ nm) positioned at different distances from the end of the rod (Figure 6b). To examine the secondary emission, we filtered out the excitation wavelength using an edge filter. The propagation loss coefficient calculated for phosphorescence of **3a** by measuring the intensity at the distal end and the distance from the excitation point is approximately $0.028 \text{ dB } \mu\text{m}^{-1}$ (Supporting Information, Figure S40). In order to distinguish between the optical WG and exciton migration, we checked the difference in emission from the body and tip of the rods. A red-shifted phosphorescence at the distal end of the crystal compared to the body at RT was observed (Figure 6c).^[21] The red-shifted emission is due to the triplet exciton migration^[21,22] from the body to the tip of **3a** single crystal rods and thereby actively supports the long-lived phosphorescence (Figure 6d). In the case of other molecules, only waveguiding and no exciton migration was observed, and it points to the critical support-

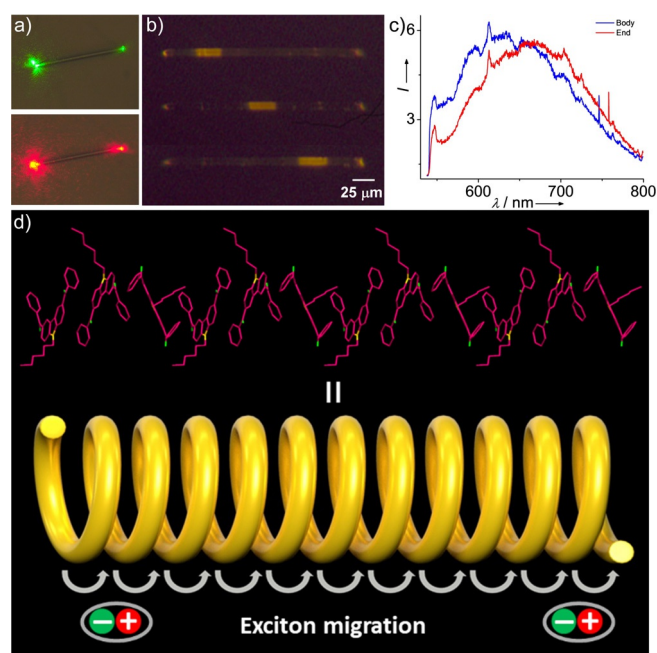


Figure 6. a) Passive waveguiding properties of the crystal of **3a** upon excitation at 532 (above) and 633 nm (below) wavelength, the colors green and red are attributed to the excitation sources, respectively. b) Phosphorescence waveguiding by the single crystalline rods of **3a** after filtering out the excitation wavelength (532 nm). c) The red-shifted phosphorescence observed at the distal end of the crystal compared to the body ($\lambda_{\text{ex}} = 532$ nm). d) Schematic of the helical array of **3a** leading to triplet exciton migration.

ive role of molecular packing assisted exciton migration in achieving longer phosphorescence lifetime.

TD-DFT studies revealed a qualitative picture of the equal possibility of ISC and RISC for **3a** due to the presence of energetically matching singlet and triplet levels. Even though a shorter component is noticed, the unambiguously confirmed long-lived phosphorescence decay supersedes it with the support of triplet exciton migration through helical molecular arrays. The afterglow observed for more than 12 s after just dipping in liquid nitrogen supports the suppression of RISC and thereby endorses improved radiative decay through the triplet manifolds at low temperature. The efficient molecular ordering in the helical array of **3a** ensures that the populated triplet decays very slowly. Here T_1 acts as a trap state and plays a vital role in triplet exciton migration as revealed by the WG results. Hence, it can be concluded that the peculiar helical molecular packing results in a long phosphorescence lifetime of **3a** compared to other molecules in the series and it is substantiated by the crystal structure and phosphorescence lifetime. In all other cases, the triplet states mostly undergo nonradiative internal conversions compared to radiative transitions.

Conclusion

In summary, we have reported a new series of phenylmethanone functionalized N-alkylated carbazoles exhibiting

UOP. A helical array by the peculiar molecular packing of 3,6-bis(phenylmethanone) substituted 9-hexylcarbazole in the crystal state enabled to mix up the singlet-triplet states to create hybrid triplets to enhance the intersystem crossings. By optimizing the molecular structure and a strained crystal packing, a metal- and heavy atom-free carbazole derivative resulted in a significant improvement of phosphorescence lifetime and quantum yield. A combined experimental and theoretical study sheds light on the stabilization of the triplet state by the helical arrays and the presence of triplet exciton migration results in the longer phosphorescence lifetime, so far reported for a single molecule crystal. The findings put forth a new strategy of helical arrays to support long-lived phosphorescence under ambient conditions and will invoke the development of new organic phosphors.

Acknowledgements

ADN and Goudappagouda acknowledge University Grants Commission (UGC), India, for fellowship. R.K. thanks the Department of Higher Education, Government of Kerala for the funding of instrumentation facility in the Government College for Women, Thiruvananthapuram. This work is supported by SERB, Govt. of India, CRG/2019/002539.

Conflict of interest

The authors declare no conflict of interest.

Keywords: carbazole · helicity · phenylmethanone · ultralong phosphorescence · waveguiding

- [1] a) A. Forni, E. Lucenti, C. Botta, E. Cariati, *J. Mater. Chem. C* **2018**, *6*, 4603; b) M. Baroncini, G. Bergamini, P. Ceroni, *Chem. Commun.* **2017**, *53*, 2081; c) G. Baryshnikov, B. Minaev, H. Ågren, *Chem. Rev.* **2017**, *117*, 6500; d) X. Yang, G. Zhou, W.-Y. Wong, *Chem. Soc. Rev.* **2015**, *44*, 8484.
- [2] a) Z. Yu, Y. Wu, L. Xiao, J. Chen, Q. Liao, J. Yao, H. Fu, *J. Am. Chem. Soc.* **2017**, *139*, 6376; b) S. M. A. Fatemina, Z. Mao, S. Xu, Z. Yang, Z. Chi, B. Liu, *Angew. Chem. Int. Ed.* **2017**, *56*, 12160; *Angew. Chem.* **2017**, *129*, 12328; c) G. Zhang, G. M. Palmer, M. Dewhirst, C. L. Fraser, *Nat. Mater.* **2009**, *8*, 747.
- [3] a) V. C. Wakchaure, K. C. Ranjeesh, Goudappagouda, T. Das, K. Vanka, R. Gonnade, S. S. Babu, *Chem. Commun.* **2018**, *54*, 6028; b) G. He, B. D. Wiltshire, P. Choi, A. Savin, S. Sun, A. Mohammadpour, M. J. Ferguson, R. McDonald, S. Farsinezhad, A. Brown, K. Shankar, E. Rivard, *Chem. Commun.* **2015**, *51*, 5444.
- [4] a) Goudappagouda, A. Manthanath, V. C. Wakchaure, K. C. Ranjeesh, T. Das, K. Vanka, T. Nakanishi, S. S. Babu, *Angew. Chem. Int. Ed.* **2019**, *58*, 2284; *Angew. Chem.* **2019**, *131*, 2306; b) O. M. S. Kwon, D. Lee, S. Seo, J. Jung, J. Kim, *Angew. Chem. Int. Ed.* **2014**, *53*, 11177; *Angew. Chem.* **2014**, *126*, 11359; c) O. Bolton, K. Lee, H. J. Kim, K. Y. Lin, J. Kim, *Nat. Chem.* **2011**, *3*, 205.
- [5] a) Kenry, C. Chen, B. Liu, *Nat. Commun.* **2019**, *10*, 2111; b) S. Hirata, *J. Mater. Chem. C* **2018**, *6*, 11785; c) S. Xu, R. Chen, C. Zheng, W. Huang, *Adv. Mater.* **2016**, *28*, 9920; d) Y. Li, M. Gecevicius, J. Qiu, *Chem. Soc. Rev.* **2016**, *45*, 2090; e) H. Chen, X. Ma, S. Wu, H. Tian, *Angew. Chem. Int. Ed.* **2014**, *53*, 14149; *Angew. Chem.* **2014**, *126*, 14373; f) S. K. Lower, M. A. El-Sayed, *Chem. Rev.* **1966**, *66*, 199.
- [6] a) S. Kuila, S. J. George, *Angew. Chem. Int. Ed.* **2020**, <https://doi.org/10.1002/anie.202002555>; *Angew. Chem.* **2020**, <https://doi.org/10.1002/ange.202002555>; b) S. Kuila, K. V. Rao, S. Garain, P. K. Samanta, S. Das, S. K. Pati, M. Eswaremoorthy, S. J. George, *Angew. Chem. Int. Ed.* **2018**, *57*, 17115; *Angew. Chem.* **2018**, *130*, 17361.
- [7] a) R. Kabe, N. Notsuka, K. Yoshida, C. Adachi, *Adv. Mater.* **2016**, *28*, 655; b) S. Hirata, K. Totani, J. Zhang, T. Yamashita, H. Kaji, S. R. Marder, T. Watanabe, C. Adachi, *Adv. Opt. Mater.* **2013**, *1*, 438; c) C. S. Bilen, N. Harrison, D. J. Morantz, *Nature* **1978**, *271*, 235.
- [8] a) Y. Xiong, Z. Zhao, W. Zhao, H. Ma, Q. Peng, Z. He, X. Zhang, Y. Chen, X. He, J. W. Y. Lam, B. Z. Tang, *Angew. Chem. Int. Ed.* **2018**, *57*, 7997; *Angew. Chem.* **2018**, *130*, 8129; b) Z. He, W. Zhao, J. W. Y. Lam, Q. Peng, H. Ma, G. Liang, I. Shuai, B. Z. Tang, *Nat. Commun.* **2017**, *8*, 416; c) W. Zhao, Z. He, J. W. Y. Lam, Q. Peng, H. Ma, Z. Shuai, G. Bai, J. Hao, B. Z. Tang, *Chem* **2016**, *1*, 592.
- [9] a) L. Gu, H. Shi, M. Gu, K. Ling, H. Ma, S. Cai, L. Song, C. Ma, H. Li, G. Xing, X. Hang, J. Li, Y. Gao, W. Tao, Z. Shuai, Z. An, X. Liu, W. Huang, *Angew. Chem. Int. Ed.* **2018**, *57*, 8425; *Angew. Chem.* **2018**, *130*, 8561; b) S. Cai, H. Shi, Z. Zhang, X. Wang, H. Ma, N. Gan, Q. Wu, Z. Cheng, K. Ling, M. Gu, C. Ma, L. Gu, Z. An, W. Huang, *Angew. Chem. Int. Ed.* **2018**, *57*, 4005; *Angew. Chem.* **2018**, *130*, 4069; c) Z. An, C. Zheng, Y. Tao, R. Chen, H. Shi, T. Chen, Z. Wang, H. Li, R. Deng, X. Liu, W. Huang, *Nat. Mater.* **2015**, *14*, 685.
- [10] a) Z. He, H. Gao, S. Zhang, S. Zheng, Y. Wang, Z. Zhao, D. Ding, B. Yang, Y. Zhang, W. Z. Yuan, *Adv. Mater.* **2019**, *31*, 1807222; b) T. Ogoshi, H. Tsuchida, T. Kakuta, T. Yamagishi, A. Taema, T. Ono, M. Sugimoto, M. Mizuno, *Adv. Funct. Mater.* **2018**, *28*, 1707369; c) S. Hirata, M. Vacha, *Adv. Opt. Mater.* **2017**, *5*, 1600996; d) Y. Xie, Y. Ge, Q. Peng, C. Li, Q. Li, Z. Li, *Adv. Mater.* **2017**, *29*, 1606829; e) Z. Yang, Z. Mao, X. Zhang, D. Ou, Y. Mu, Y. Zhang, C. Zhao, S. Liu, Z. Chi, J. Xu, Y.-C. Wu, P.-Y. Lu, A. Lien, M. R. Bryce, *Angew. Chem. Int. Ed.* **2016**, *55*, 2181; *Angew. Chem.* **2016**, *128*, 2221; f) J. Wei, B. Liang, R. Duan, Z. Cheng, C. Li, T. Zhou, Y. Yi, Y. Wang, *Angew. Chem. Int. Ed.* **2016**, *55*, 15589; *Angew. Chem.* **2016**, *128*, 15818; g) Y. Katsurada, S. Hirata, K. Totani, M. Watanabe, M. Vacha, *Adv. Opt. Mater.* **2015**, *3*, 1726.
- [11] a) M. Li, K. Ling, H. Shi, N. Gan, L. Song, S. Cai, Z. Cheng, L. Gu, X. Wang, C. Ma, M. Gu, Q. Wu, L. Bian, M. Liu, Z. An, H. Ma, W. Huang, *Adv. Opt. Mater.* **2019**, *7*, 1800820; b) B. Zhou, D. Yan, *Adv. Funct. Mater.* **2019**, *29*, 1807599; c) L. Gu, H. Shi, L. Bian, M. Gu, K. Ling, X. Wang, H. Ma, S. Cai, W. Ning, L. Fu, H. Wang, S. Wang, Y. Gao, W. Yao, F. Huo, Y. Tao, Z. An, X. Liu, W. Huang, *Nat. Photonics* **2019**, *13*, 406; d) L. Bian, H. Shi, X. Wang, K. Ling, H. Ma, M. Li, Z. Cheng, C. Ma, S. Cai, Q. Wu, N. Gan, X. Xu, Z. An, W. Huang, *J. Am. Chem. Soc.* **2018**, *140*, 10734; e) Z. Chai, C. Wang, J. Wang, F. Liu, Y. Xie, Y.-Z. Zhang, J.-R. Li, Q. Lia, Z. Li, *Chem. Sci.* **2017**, *8*, 8336.
- [12] H. Uoyama, K. Goushi, K. Shizu, H. Nomura, C. Adachi, *Nature* **2012**, *492*, 234.
- [13] a) E. Yashima, N. Ousaka, D. Taura, K. Shimomura, T. Ikai, K. Maeda, *Chem. Rev.* **2016**, *116*, 13752; b) C. C. Lee, C. Grenier, E. W. Meijer, A. P. H. J. Schenning, *Chem. Soc. Rev.* **2009**, *38*, 671; c) A. Maity, M. Gangopadhyay, A. Basu, S. Aute, S. S. Babu, A. Das, *J. Am. Chem. Soc.* **2016**, *138*, 11113.
- [14] a) W. Li, Q. Huang, Z. Mao, Q. Li, L. Jiang, Z. Xie, R. Xu, Z. Yang, J. Zhao, T. Yu, Y. Zhang, M. P. Aldred, Z. Chi, *Angew. Chem. Int. Ed.* **2018**, *57*, 12727; *Angew. Chem.* **2018**, *130*, 12909; b) Z. Zhang, L. Tang, X. Fan, Y. Wang, K. Zhang, Q. Sun, H. Zhang, S. Xue, W. Yang, *J. Mater. Chem. C* **2018**, *6*, 8984.

- [15] N. J. Turro, *Modern Molecular Photochemistry*, University Science Books, Sausalito, **1978**.
- [16] C. Chen, Z. Chi, K. C. Chong, A. S. Batsanov, Z. Yang, Z. Mao, Z. Yang, B. Liu, *ChemRxiv* **2019**, <https://doi.org/10.26434/chemrxiv.9895724>.
- [17] a) G. Wang, B. Xiong, C. Zhou, Y. Liu, W. Xu, C.-A. Yang, K.-W. Tang, W.-Y. Wong, *Chem. Asian J.* **2019**, *14*, 4365; b) H.-R. Bjørsvik, V. Elumalai, *Eur. J. Org. Chem.* **2016**, 5474.
- [18] a) K. Nagarajan, A. R. Mallia, K. Muraleedharan, M. Hariharan, *Chem. Sci.* **2017**, *8*, 1776; b) S. Hirata, M. Vacha, *J. Phys. Chem. Lett.* **2016**, *7*, 1539; c) P. Ravat, T. Šolomek, M. Rickhaus, D. Häussinger, M. Neuburger, M. Baumgarten, M. Juríček, *Angew. Chem. Int. Ed.* **2016**, *55*, 1183; *Angew. Chem.* **2016**, *128*, 1198; d) M. Rickhaus, M. Mayor, M. Juríček, *Chem. Soc. Rev.* **2016**, *45*, 1542.
- [19] H. Liu, Z. Bian, Q. Cheng, L. Lan, Y. Wang, H. Zhang, *Chem. Sci.* **2019**, *10*, 227.
- [20] A. B. Vasista, H. Jog, T. Heilpern, M. E. Sykes, S. Tiwari, D. K. Sharma, S. K. Chaubey, G. P. Wiederrecht, S. K. Gray, G. V. P. Kumar, *Nano Lett.* **2018**, *18*, 650.
- [21] D. Chaudhuri, D. Li, Y. Che, E. Shafran, J. M. Gerton, L. Zang, J. M. Lupton, *Nano Lett.* **2011**, *11*, 488–492.
- [22] A. Köhler, H. Bässler, *J. Mater. Chem.* **2011**, *21*, 4003.

Manuscript received: April 8, 2020

Accepted manuscript online: May 4, 2020

Version of record online: June 5, 2020